Constitutive Modeling of Soils and Rocks

Constitutive Modeling of Soils and Rocks

Edited by
Pierre-Yves Hicher
Jian-Fu Shao

ISTE
WILEY

First published in France in 2002 by Hermes Science/Lavoisier entitled “Modèles de comportement des sols et des roches Vol.1 et 2”
First published in Great Britain and the United States in 2008 by ISTE Ltd and John Wiley & Sons, Inc.

ISTE Ltd
6 Fitzroy Square
London W1T 5DX
UK

www.iste.co.uk

John Wiley & Sons, Inc.
111 River Street
Hoboken, NJ 07030
USA

www.wiley.com

Library of Congress Cataloging-in-Publication Data

[Modeles de comportement des sols et des roches. English] Constitutive modeling of soils and rocks / Edited by Pierre-Yves Hicher Jian-Fu Shao.
p. cm.
Includes bibliographical references and index.
ISBN 978-1-84821-020-2
1. Engineering geology--Mathematical models. 2. Soil mechanics--Mathematical models. I. Hicher, Pierre-Yves. II. Shao, Jian-Fu. III. Title.
TA705.M6113 2008
624.1'51015118--dc22

2007046228

British Library Cataloguing-in-Publication Data
A CIP record for this book is available from the British Library
ISBN: 978-1-84821-020-2

Printed and bound in Great Britain by Antony Rowe Ltd, Chippenham, Wiltshire.

Table of Contents

Preface to the English Edition

The French version of this book appeared in 2002 as part of the "Material Mechanics and Engineering" series. The objective of this book was to create as complete as possible a corpus of knowledge and methods in this field.

In designing this book on the mechanical behavior of soils and rocks, we gathered together a number of internationally known specialists, who each brought a significant contribution to the knowledge of the experimental behavior of these materials, as well as their constitutive modeling. Our goal was to cover as far as possible the theories at the basis of the different approaches of modeling, and also to address the most recent advances in the field.

In translating this book into English, we hope to make available to a wider scientific and engineering public the approaches and school of thought which have dominated the field of geomaterial mechanics in France over the past few decades. We have put together present-day knowledge of mechanical behavior and their theoretical bases in order to construct an original, analytical framework which, we hope, will give readers a useful guide for their own research. Most of the chapters have been updated in order to include the most recent findings on the respective topics.

Finally, we wish to dedicate this book to the memory of Professor Jean Biarez, who not only played a ground-breaking role in the history of soil mechanics in France, but remains a source of inspiration to many of us today.

Pierre-Yves Hicher
Jian-Fu Shao

Preface to the French Edition

Soils and rocks possess a number of similar characteristics: both are highly heterogenous materials formed by natural grains. This alone gives them certain rheological features which distinguish them from other solid materials, such as a strongly non-linear character, a behavior which depends on the mean stress and shearing which induces volume variations, often dilatancy, which leads to unassociated plastic strains.

Soils and rocks can be studied at different scales. At the scale of one or several grains (from μm to cm), we can examine the discrete phenomena which govern the interactions between grains. They can be described using micro-mechanical models or analyzed in order to better understand the material behavior at a larger scale, typically the size of the material specimen: this approach corresponds to passing from a discontinuous to an equivalent continuous medium. Even though the size of the latter can vary, it has to be "sufficiently large" (typically from 1 cm to 1 dm) compared to the size of the material discontinuities in order to be representative of the equivalent continuous medium, whose behavior can be modeled by using certain concepts of continuous medium mechanics which ignore the notion of scaling in its basic equations.

However, some phenomena, such as the development of defects or cracks within the material specimen, are located at an intermediary scale, called the "meso" scale. It is thus necessary, in a constitutive model for continuous medium, to use scaling techniques in order to take into account these intermediary scales. This approach, still recent but potentially strong, can also be adapted to change the scale from the material specimen to the *in situ* soil or rock masses in geotechnical work modeling.

The constitutive models developed to describe the mechanical behaviors at the macroscopic scale can be roughly classified into two categories: those adapted to the behavior of "ductile" materials and those adapted to the behavior of "fragile"

materials. The first category corresponds mainly to sandy or clayey soils, but also to soft rocks subjected to high confining stresses. The second category corresponds mainly to hard rocks, but also to certain soft rocks and highly overconsolidated clays subjected to small confining stresses. In ductile materials, the non-linear behavior is essentially due to irreversible grain displacements, which leads to a more or less significant hardening and to a pore volume change which induces volume changes at the scale of the specimen. In fragile materials, the non-linear behavior is due to the development of cracks, whose size may vary and whose direction depends on the principal stress directions.

In order to model ductile behaviors, plasticity (elastoplasticity or viscoplasticity) has shown to be an operational framework and the large majority of the constitutive models for soils and certain soft rocks belong to this category. However, for non-cohesive soils in particular, the difficulty of characterizing an elastic domain, determining the plastic mechanisms (potential and yield surface) experimentally, has led to the development of specific constitutive models, whose structure can be defined as incrementally non-linear.

In order to model fragile behaviors, the damage mechanics framework has been used to propose constitutive models adapted to describing irreversible phenomena linked to the deterioration of certain physical properties. In particular, they can take into account a large amount of rock properties: irreversible strains, dilatancy, induced anisotropy, hysteresis loop during loading-unloading due to opening and closing of mesocracks and frictional mechanisms along closed mesocracks.

In intermediary materials, the non-linear behavior can be due to microstructural changes, associating damage and hardening phenomena. Models coupling plasticity and damage have been developed to take into account this type of behavior.

After a general presentation of the constitutive models and their internal structures, each chapter will give a brief description of the different approaches mentioned above by focusing on a given class of materials. The first three chapters are devoted to the elastoplasticity theory applied to soils and soft sedimentary rocks. An alternative approach is then presented by means of the so-called incrementally non-linear models. The time-effect in clayey soils is analyzed in the framework of viscoplasticity. The behavior of hard rocks is then studied in Chapters 8 and 9, through the use of the damage theory at different scales. The modeling of the poromechanical behavior is also introduced in order to take into account the hydromechanical coupling in saturated porous rocks.

As the validity of any given model lies in its capacity to reproduce the observed material characteristics, the authors have placed the experimental data, obtained mainly from laboratory testing on intact soil and rock samples, under special consideration. The final chapter is devoted to parameter identification procedures. This is an important topic when dealing with natural materials because, each site being different from another, accurate parameter identification is essential for the quality of geotechnical work calculations, which is the final goal of this modeling approach.

Pierre-Yves Hicher
Jian-Fu Shao

Constitutive Modeling of Soils and Rocks
Edited by Pierre-Yves Hicher & Jian-Fu Shao

Chapter 1

The Main Classes of Constitutive Relations

1.1. Introduction

The study of the mechanical behavior of solid materials and its description by constitutive relations was for many years developed within the framework of isotropic linear elasticity characterized by Hooke's law, plasticity characterized by the Von Mises, Tresca and Mohr-Coulomb criteria, and viscosity characterized in the linear case by Newton's law. However, since the end of the 1960s, the development of more powerful numerical methods such as the finite element method and the use of high-performance computers has revived the study of material behavior, as it became possible to take into account a more realistic visco-elastoplastic modeling, albeit at the expense of much more complex formalisms.

Inside the three sets of equations defining a continuous medium mechanics problem, i.e. general equations (conservation equations), constitutive laws and boundary conditions, constitutive laws correspond to the more difficult part, particularly since the general framework in which the constitutive equations are inscribed remains often numerically imprecise. It is the comprehension of the absence of "physical laws" in this domain which gradually changed the designation of "constitutive laws" to "constitutive models". The latter corresponds better to the objective of giving a mathematical form to the mechanical properties of materials, whose complexity has been demonstrated by the diversity of the experimental results.

Chapter written by Félix DARVE.

During the last 30 years, a large variety of constitutive models have been developed and many workshops organized all over the world have shown that it is important for developers as well as users of models to be able to obtain guiding ideas and a general framework of analysis. The objective of this chapter is to try to formulate both of these.

This general framework will be more useable if it can be unified, and we intend to show that it can be applied to elastoplasticity as well to viscoplasticity or damage theory. We thus invite the reader to a wide presentation of constitutive relations for solid materials.

Two preliminary comments need to be made. First, we should explain why the chapter covers rheology in an incremental form. Two main reasons have made such an incremental presentation indispensable. The first is physical and is linked to the fact that, as soon as some plastic irreversibility is mobilized within the material, the global constitutive functional, which relates the stress state $\sigma(t)$ at a given time t to the strain state $\varepsilon(t)$ history up to this time, is in principle very difficult to formulate explicitly as this functional is singular at all stress-strain states (or more precisely non-differentiable, as will be shown). An incremental formulation enables us to avoid this fundamental difficulty. The second reason is numerical and stems from the fact that material behavior, and usually also the modeling of engineering works, exhibits many non-linearity sources which imply that the associated boundary value problem must be solved by successive steps linked to increments of loading at the boundary. Therefore, such finite element codes need to express the constitutive relations incrementally.

Our second comment concerns the use of incremental stress and strain rather than the stress and strain rates. Here also, it is the physical nature of the phenomena which determines our choice: in elastoplasticity, and more generally for all non-viscous behaviors, physical time does not play any role and, as a consequence, the derivatives with the physical time have no real meaning. Therefore, the incremental form appears to be intrinsically significant and can in fact be attached straightforwardly to the rate: the incremental strain is the product of the strain rate with the time increment, while the incremental stress is the product of Jaumann's derivative of the stress tensor with the time increment. It is, however, incorrect to speak of stress and strain increments, since the incremental strain (for example) corresponds to a small strain variation only in the case of a sufficiently small strain.

This chapter begins with a traditional presentation of the rheological functional. We will show the limits of the functional expression and overcome this limitation by establishing the incremental rheological formalism. First, we will cover the case of non-viscous materials. The notion of "tensorial zones" will allow us to present the

different classes of non-viscous models. Then, we will come back to the general case by considering models which take into account any kind of irreversibility.

1.2. The rheological functional

The basic concepts of continuous medium mechanics are taken for granted. The tangent linear transformation, characterized by the matrix of the gradient of the material particle positions, is assumed to describe correctly the material geometric deformation, even if some theories, called "second gradient theories", consider that this first order approximation by the tangent linear transformation from the positions at a given time to the actual positions is not sufficient, and subsequently introduce second order terms [MUH 91]. We also assume that the constitutive law of a material element does not depend on the neighboring elements (some theories called "non-local theories" consider that the behavior of a basic material particle depends on a finite deformation field around that particle [PIJ 87]). These two hypotheses define a specific class of materials called "simple media" [TRU 74] for which we will develop a theoretical analysis.

The starting point of rheology is thus based upon a principle of determinism, which can be expressed as follows: if a given loading path is applied to a material sample, the material response is determined and unique, i.e., the principle of determinism applies only in conditions where there is uniqueness of the rheological response. Passing through a bifurcation point gives several possible responses. The choice of one of these responses is guided by existing imperfections which are not taken into account in the description of the material mechanical state or in the mode of loading application (control in force or in displacement, for example).

The first expression of the principle of determinism is obtained by stating that stress state $\sigma(t)$ at a given time t is a functional of the history of the tangent linear transformation up to this time t. This implies that it is necessary to know the entire loading path in order to deduce the associated response path.

From a mathematical point of view, this is stated by the existence of a rheological functional F:

$$\sigma(t) = F[\varepsilon(\tau)] \qquad (1.1)$$

$$-\infty < \tau \leq t$$

where E(t) is the strain part of the tangent linear transformation E at time t, also called the deformation gradient. Deformation gradient E is the Jacobian matrix of position f(X,t) of material point X at time t. The existence of such a functional, and

not a function, is related to an essential physical characteristic: for irreversible behaviors, knowing strain ε(t) at time t does not enable us to determine the stress, and vice versa. For example, we can think of viscous or plastic materials where a given level of stress can be related to an infinite number of different strain states.

Since this chapter is devoted to the study of fundamental properties of constitutive relations, the general properties of rheological functional F need to be examined:

– isotropy of F: due to the principle of isotropy of space, F has to be an isotropic function of ε (if σ, ε and the internal variables are subjected to an equal rotation, F remains identical);

– non-linearity of F: the hypothesis of linearity for F is expressed by:

$$\forall \varepsilon_1,\ \varepsilon_2 \text{ and } \forall \lambda_1,\ \lambda_2 \text{ real: } \mathrm{F}\left[\lambda_1\varepsilon_1(\tau)+\lambda_2\varepsilon_2(\tau)\right] \equiv \lambda_1\mathrm{F}\left[\varepsilon_1(\tau)\right]+\lambda_2\mathrm{F}\left[\varepsilon_2(\tau)\right]$$

In such a case, the material response to a sum of histories will simply be equal to the sum of the responses to each history. This constitutes Boltzmann's principle and is the basis of linear viscoelasticity theory, but it is not at all valid in the general case, as in elastoplasticity, for example, where, when we double the strain for example, the stress is obviously not doubled, due to the non-linear behavior.

In the general case, F must be studied in the framework of non-linear functionals:

– F is furthermore non-differentiable as soon as there is some plastic irreversibility. Owen and Williams (1969) showed in fact that the assumptions of non-viscosity and differentiability of stress functional F imply that there is no internal dissipation.

In other words, a non-viscous material whose constitutive functional is differentiable is necessarily elastic. Basically, this is due to the fact that, in plasticity, the tangent loading modulus is not equal to the tangent unloading modulus. Therefore, if we want to describe the behavior of anelastic materials by using a stress-strain relationship, this relation must be formulated using a non-linear and non-differentiable functional:

– degeneration of F: the only case of degeneration of functional F into a function corresponds to elasticity (possibly non-linear and anisotropic), where there is a one-to-one mapping between stress and strain.

Finally, if we want to describe irreversible behavior, we have to consider a non-linear, non-differentiable functional, which, mathematically, is very difficult to use.

We therefore need to study constitutive relations using an incremental formulation rather than a global one.

1.3. Incremental formulation of constitutive relations

We shall now introduce an incremental formulation using a second statement from the principle of determinism. The second principle of determinism, which can be called "in the small" to be distinguished from the first principle "in the large", is obtained by stating that a small load applied during a time increment dt induces a small uniquely determined response.

As stated previously, this principle applies only if the uniqueness of the incremental constitutive relation is maintained. For bifurcation cases, the principle is no longer valid and the choice of the bifurcated branch will depend on the boundary conditions and material imperfections. In addition, the principle assumes implicitly that the loading rate is kept constant during the time increment (even if it can vary from one increment to another), which excludes dynamic loads due to shocks.

We denote by $d\varepsilon = D\,dt$ the incremental strain tensor of order two equal to the product of the second-order strain rate tensor, D (symmetric part of transformation rate $L^{\cdot}$: $L = \dot{E}E^{-1}$ where E is here the deformation gradient) and time increment dt, and by $d\sigma = \sigma\hat{}\,dt$ the incremental stress tensor, equal to the product of an objective time derivative of Cauchy stress tensor σ and dt.

Thus, the second determinism principle implies, from a mathematical point of view, the existence of a tensorial function F_h relating the three quantities:

$$F_h\,(d\varepsilon, d\sigma, dt) = 0 \tag{1.2}$$

What are the properties of this tensorial function F_h?

The first comment concerns the fact that F_h depends on the previous stress-strain history. This history is generally characterized by some scalar and tensorial variables denoted by h which will appear as parameters in the previous relation. These parameters describe, as far as possible, the actual deformed state of the solid. According to various constitutive theories, they are sometimes called "memory variables", "hardening parameters", "internal variables", etc.

Secondly, F_h must satisfy the objectivity principle, which means that F_h must be independent of any observer movement relative to the solid. Thus, F_h is an isotropic function of all its arguments: $d\varepsilon$, $d\sigma$ and also the state tensorial variables, which characterize its presently deformed state. However, if the material is anisotropic

insofar as its mechanical properties are concerned, then F_h is an anisotropic function of $d\varepsilon$ and $d\sigma$.

Finally, F_h is essentially a non-linear function as long as there is some plastic irreversibility. If F_h is linear, we can write:

$$d\varepsilon = Md\sigma + C\,dt$$

which is the general form of viscoelastic laws where M is the fourth-order elastic tensor and C the second-order creep rate tensor of the material.

This property of non-linearity for F_h is directly linked to the non-differentiability of rheological functional F, the property of differentiability of F being equivalent to the linearity of F_h.

In conclusion, relation (1.2) corresponds to the general incremental form of the constitutive relations. We will now distinguish between viscous and non-viscous materials in order to represent this incremental form more precisely.

1.4. Rate-independent materials

For non-viscous materials, the loading rate (characterized by time gradation on a loading path) has no influence on material constitutive behavior: a given loading path, followed at any given rate, gives the same response path. In other words, the behavior class considered is rate-independent. This restriction of the constitutive law implies that constitutive function F_h, which relates $d\varepsilon$ and $d\sigma$, is independent of time increment dt, during which the incremental loading is applied. Therefore, F_h is independent of dt and we can write:

$$d\varepsilon = G(d\sigma) \tag{1.3}$$

or:

$$d\sigma = G^{-1}(d\varepsilon) = H(d\varepsilon) \tag{1.4}$$

The possibility of inversing G or H is linked to the uniqueness of the constitutive relations. This question will not be studied here; for more details see [DAR 94, DAR 95a].

From a mathematical point of view this independence of non-viscous behaviors on loading rates implies the following identity:

$$\forall \lambda \in R^{+} : \lambda d\varepsilon \equiv G(\lambda d\sigma)$$

thus

$$\forall \lambda \in R^{+} : \; G(\lambda d\sigma) \equiv \lambda G(d\sigma) \tag{1.5}$$

which states that if the stress rate is multiplied by any positive scalar, the strain rate response is also multiplied by the same scalar.

This is the first property of G: G is a homogenous function of degree 1 in $d\sigma$ with respect to the positive values of the multiplying parameter. This homogenity property must not be confused with that of "positively homogenous" functions, which is given by;

$$\forall \lambda \in R : \; G(\lambda d\sigma) \equiv |\lambda| G(d\sigma)$$

In addition to this property of homogenity of degree 1, functions G and H, as we have seen in general for function F_h, are non-linear and anisotropic in $d\sigma$ (or in $d\varepsilon$).

1.4.1. *Non-linearity of G and H*

If, in relation (1.3), $d\varepsilon$ is the response to an incremental loading $d\sigma$, the response to an incremental loading $-d\sigma$, following $d\sigma$, is not equal to $-d\varepsilon$, because plastic irreversibility or damage takes place in the material. Therefore, G and H are necessarily non-linear functions of $d\sigma$ and $d\varepsilon$ respectively, which implies that the principle of incremental superposition cannot be rigorously verified, except within the elastic domain, or more generally within a domain of incremental linearity of the constitutive model. Calculus shows, however, that the principle of incremental superposition can be roughly verified along "step-wise" paths, approaching a given loading path [DAR 95b].

1.4.2. *Anisotropy of G and H*

Following the same reasoning as for function F_h, we can deduce that G and H are anisotropic functions of $d\sigma$ and $d\varepsilon$ respectively.

This anisotropy is directly linked to the geometrical meso-structure of the material, which is gradually modified by the strain (particularly irreversible) history. We have seen that this history can be characterized by scalar and tensorial state parameters.

In simple cases, this anisotropy is directly imposed by the choice of these state parameters. If we consider, for example, only scalar memory parameters (such as void ratio), defined independently of any frame, based on the objectivity principle functions G and H will be isotropic functions, which is not supported by experiments.

If we add one single tensor variable (such as the stress tensor) to these scalar memory parameters, G and H are orthotropic functions of $d\sigma$ and $d\varepsilon$ respectively, the orthotropy axes being identified with the principal stress or strain axes. In this case, it means that G and H are invariant by symmetry with respect to any plane containing two principal stress or strain directions.

In the more general case of state variables with at least two second-order non-commutating tensorial variables, anisotropy is not defined. Orthotropy thus becomes a constitutive assumption, which must be considered as an approximation of the real behavior of the material for classes of loading in which stress and strain principal axes rotate.

1.4.3. *Homogenity of degree 1 of G and H*

Having described the three main properties of G, we will now focus on the first (homogenity of degree 1) to see the mathematical consequences of such a property. Let us for this purpose recall Euler's identity for homogenous regular functions of degree 1, by writing it for a function of two variables:

$$\forall x, y : f(x, y) \equiv x \frac{\partial f}{\partial x} + y \frac{\partial f}{\partial y} \tag{1.6}$$

where partial derivatives $\delta f/\delta x$ and $\delta f/\delta y$ are homogenous functions of degree 0.

In formulating constitutive relations, it is often more convenient to replace stress tensor σ and strain tensor ε, which are second order, by two vectors of IR^6 defined in a six-dimensional related space. In this space, vectorial function G is written:

$$G_\alpha(d\sigma_\beta) \equiv \frac{\partial G_\alpha}{\partial(d\sigma_\beta)} d\sigma_\beta \quad (\alpha, \beta = 1, ..., 6)$$

with summation on index β.

The partial derivatives of a homogenous function of degree 1 are homogenous functions of degree 0. Therefore, functions $\partial G_\alpha/\partial(d\sigma_\beta)$ depend only on the direction of $d\sigma$, characterized by the unit vector:

$$u = \frac{\partial \sigma}{\|d\sigma\|}$$

with:

$$\|d\sigma\| = \sqrt{d\sigma_{ij}\ d\sigma_{ij}}$$

Finally, we obtain:

$$d\varepsilon_\alpha = M_{\alpha\beta}(u_\gamma)d\sigma_\beta(u_\gamma = d\sigma_\gamma / \|d\sigma\|) \tag{1.7}$$

or:

$$d\sigma_\alpha = N_{\alpha\beta}(v_\gamma)d\varepsilon_\beta(v_\gamma = d\varepsilon_\gamma / \|d\varepsilon\|) \tag{1.8}$$

Equations (1.7) and (1.8) are the general expressions for all rate-independent constitutive relations. Constitutive tensors M and N also depend on state variables and memory parameters, which characterize the loading history. These two matrices are the gradient matrices of non-linear functions G and H, respectively. In that sense, they can be considered as tangent constitutive tensors and are therefore uniquely defined. However, it is possible to construct from them an infinite number of secant constitutive tensors by adding to the M or N lines the components of any unit vector perpendicular to $d\sigma$ or $d\varepsilon$, respectively.

Relations (1.7) and (1.8) will now allow us to propose a classification of all the existing rate-independent constitutive relations with respect to their intrinsic structure.

1.5. Notion of tensorial zones

First of all, we need to define the notion of a "tensorial zone" [DAR 82]. We will call a tensorial zone any domain in the incremental loading space on which the restriction of G or H is a linear function. In other words, the relationship between $d\varepsilon$ and $d\sigma$ in a given tensorial zone is incrementally linear. If we denote the tensorial zone being considered as Z, the following definition implies:

$$\forall u \in Z : d\varepsilon = M^z \, d\sigma$$

In zone Z, the constitutive relation is characterized by a unique tensor M^z. If u belongs to Z, any vector collinear to u also belongs to Z for all real positive values. Therefore, a zone is defined by a set of half-infinite straight lines, whose apex is the same and is at the origin of the incremental loading space. Tensorial zones thus comprise adjacent hypercones, whose common apex is this origin. What does the constitutive relation become on the common boundary of two (or several) adjacent tensorial zones? If M^{z1} and M^{z2} are constitutive tensors attached, respectively, to tensorial zones Z_1 and Z_2, they must obviously satisfy the condition of continuity of the response to any loading direction u which belongs to the boundary between Z_1 and Z_2:

$$\forall u \in Z_1 \cap Z_2 : \left(M^{z_1} - M^{Z_2}\right) u \equiv 0 \tag{1.9}$$

Relation (1.9) can be called a "continuity condition" for zone change. This condition prohibits, in particular, an arbitrary choice of the constitutive tensors in two adjacent tensorial zones.

Furthermore, we will see that conventional elastoplastic relations satisfy this condition by means of the "consistency condition". This is also the case for damage models when they are built in a rigorous manner. On the other hand, hypoelastic models do not necessarily fulfil this condition, which has to be verified *a posteriori*. It has been proven that this is not the case for some of these models [GUD 79].

The "response-envelopes", as proposed by Gudehus [GUD 79], constitute geometrical diagrams which completely characterize a constitutive relation at a given stress strain state after a given strain history. At this state, all the incremental loadings, having the same norm but oriented in all directions, are considered and all the incremental responses are plotted. The extremities of the response vectors form a hypersurface which is called the "response-envelope". Figure 1.1 gives an example of an elastoplastic model in axisymmetric condition: the continuity of the response at the boundary of two tensorial zones appears well fulfilled. Figure 1.2 gives an example of a model with discontinuities, whereas Figure 1.3 corresponds to a continuous non-elastoplastic model.

In fact, the number of tensorial zones characterizes how a given model describes the irreversibility due to plasticity or damage, and the directional change of behavior, i.e. how constitutive tensor M (or N) evolves with the direction of loading u (or v). More precisely, the number of tensorial zones of a given constitutive model is an intrinsic criterion, which fully represents the model structure. Therefore, we have chosen this criterion to classify, in the next section, the different rate-independent constitutive models.

1.6. The main classes of rate-independent constitutive relations

1.6.1. *Constitutive relations with one tensorial zone*

The first class of relations that we are going to look at is related to the simplest assumption that there is only one tensorial zone. Therefore:

$$\forall u : M(u) = M$$

Therefore:

$$d\varepsilon = M_h \, d\sigma$$

or:

$$d\sigma = N_h \, d\varepsilon.$$

The behavior is therefore entirely reversible (except possibly in the case of the existence of memory parameters h, but this corresponds rather to an artefact in hypoelasticity). As there is a unique linear relationship between dε and dσ (incremental linearity), we have here in this first class all the elastic laws, isotropic or anisotropic, linear or non-linear (in this last case, M and N depend on the actual state of stress).

The best way to reproduce an elastic behavior (without any internal dissipation) in a rigorous manner is to introduce an elastic potential V defined by:

$$dV = \sigma_{ij} \, d\varepsilon_{ij}$$

As V is an exact total differential, we obtain the following expression:

$$\sigma_{ij} = \frac{\partial V}{\partial \varepsilon_{ij}}$$

Therefore:

$$\frac{\partial^2 V}{\partial \varepsilon_{ij} \, \partial \varepsilon_{kl}} \equiv \frac{\partial^2 V}{\partial \varepsilon_{kl} \, \partial \varepsilon_{ij}}$$

using Schwarz's identity. As a consequence, matrices M and N are symmetric and tensors C and D, defined by

$$d\varepsilon_{if} = C_{ijkl} \, d\sigma_{kl} \text{ and } d\sigma_{ij} = D_{ijkl} \, d\varepsilon_{kl}$$

have "major" symmetries

$$C_{ijkl} = C_{klij} \text{ and } D_{ijkl} = D_{klij}.$$

In the general case of non-linear elasticity, the existence of a potential also implies conditions of "integrability" [LOR 85], which have to be satisfied by the components of M and N. All these laws are called "hyperelastic", while, in the absence of a potential, they are called "hypoelastic". The hypoelastic models generate energy dissipation, and should thus not be used in practice, the behavior represented by these models being poorly identified.

1.6.2. *Constitutive relations with two tensorial zones*

In the presence of two tensorial zones, we can call one the "loading zone" and the other the "unloading zone". We thus define two different behaviors (two different constitutive tensors), one representing the loading condition, and the other the unloading condition. Each matrix is attached to a different tensorial zone, these two tensorial zones being separated by a hyperplane in $d\sigma$ or $d\varepsilon$ space. A loading-unloading criterion, a linear and homogenous inequation in $d\sigma$ or $d\varepsilon$, allows us to discriminate between the two behaviors. The hyperplane equation corresponds, by construction, to the zero value of the loading-unloading criterion. The continuity condition at the crossing of the hyperplane gives a link to the two constitutive tensors and the hyperplane equation:

$$\forall u \in \text{hyperplane}: (M^{\text{loading}} - M^{\text{unloading}})u = 0 \tag{1.10}$$

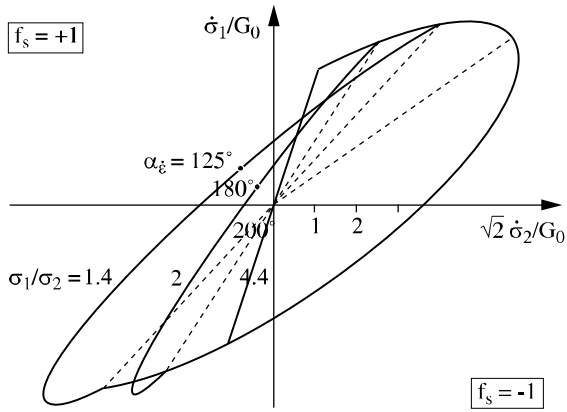

Figure 1.1. *Response envelopes [GUD 79] in axisymmetric conditions for an elastoplastic material with two tensorial zones (characterized by $f_s = \pm 1$) for three different stress levels. The continuity of the response envelopes is verified*

Numerous constitutive models follow these general rules and are therefore based on the definition of two tensorial zones. Their formalisms are basically similar, even if, sometimes, the detailed equations do not clearly show their fundamentally bilinear structure. These models are divided into three different families: elastoplastic models with one plastic potential, hypoelastic models with a unique loading-unloading criterion and damage laws. We will now examine them successively.

1.6.2.1. *Elastoplastic models with one plastic potential*

The first assumption concerns the additive decomposition of the incremental strain into an elastic part (reversible) and a plastic part (irreversible):

$$d\varepsilon = d\varepsilon^e + d\varepsilon^p \tag{1.11}$$

The plastic deformations exist only beyond a given limit surface, "the elastic limit", which depends on the loading history and evolves due to the hardening created by plastic strains, as has been shown experimentally. Its equation is given by:

$$f(\sigma, \varepsilon^p) = 0 \tag{1.12}$$

The loading condition is obtained by writing that the incremental stress is directed outwards from the elastic limit. The unloading condition is obtained if the incremental stress is directed inwards. It follows that:

$$(\delta f/\delta\sigma).d\sigma > 0\text{: loading condition} \tag{1.13}$$

$$(\delta f/\delta\sigma).d\sigma < 0\text{: unloading condition}$$

The equation of the hyperplane, the border between the two zones in the $d\sigma$ space, is thus given by:

$$\partial f/\partial\sigma.d\sigma = 0$$

When the elastic limit is reached, the direction of the incremental plastic strain is given by the flow rule which is often specified in terms of a plastic potential $g(\sigma)$ as:

$$d\varepsilon^p = d\lambda \frac{\partial g}{\partial \sigma} \tag{1.14}$$

where $d\lambda$ is an arbitrary scalar, whose value is determined by the consistency rule which mathematically expresses that, the state of stress reaching the elastic limit and

the loading condition being maintained, the elastic limit follows the state of stress by hardening. Therefore, the consistency condition can be written as:

$$df = 0 \tag{1.15}$$

thus:

$$\frac{\partial f}{\partial \sigma} \cdot d\sigma + \frac{\partial f}{\partial \varepsilon^p} \cdot d\varepsilon^p = 0$$

which gives the value of $d\lambda$:

$$d\lambda = - \left(\frac{\partial f}{\partial \sigma} . \, d\sigma \right) \Big/ \left(\frac{\partial f}{\partial \varepsilon^p} . \, \frac{\partial g}{\partial \sigma} \right) \tag{1.16}$$

Therefore, continuity condition (1.10) is verified:

$$\forall d\sigma \text{ such that } \frac{\partial f}{\partial \sigma} \cdot d\sigma = 0 \text{: } M^{loading} d\sigma - M^{unloading} d\sigma \equiv 0$$

because:

$d\varepsilon - d\varepsilon^e = d\varepsilon^p$ from (1.11)

and:

$$d\varepsilon^p = d\lambda \frac{\partial g}{\partial \sigma} \text{ from (1.14)}$$

with $d\lambda$ proportional to $(\partial f/\partial \sigma . d\sigma)$ from (1.16).

Therefore, the consistency condition in elastoplasticity theory allows us to verify the continuity condition in our general theory. The following equation gives the general mathematical form of the elastoplastic models with one single potential, in which the forms of functions f and g are not developed:

$$d\varepsilon = M^e d\sigma - \alpha \frac{\dfrac{\partial f}{\partial \sigma} . \, \partial \sigma}{\dfrac{\partial f}{d\varepsilon^p} . \, \dfrac{\partial g}{\partial \sigma}} \frac{\partial g}{\partial \sigma} \tag{1.17}$$

where M^e is the elastic tensor and α is a scalar equal to 0 or 1:

$\alpha = 0$ if: $f(\sigma, \varepsilon^p) < 0$

or:

$$f(\sigma, \varepsilon^p) = 0 \text{ and } \frac{\partial f}{\partial \sigma} \cdot \partial \sigma < 0$$

$\alpha = 1$ if:

$$f(\sigma, \varepsilon^p) = 0 \text{ and } \frac{\partial f}{\partial \sigma} \cdot \partial \sigma > 0$$

When $\partial f/\partial \sigma . d\sigma = 0$, α can be equal either to 0 or to 1, indifferently, the value being chosen for internal consistency.

All the elastoplastic models are inherently different from each other depending on the choice of the equations of the elastic limit surface $f = 0$, the plastic potential $g = 0$, and the plasticity criterion obtained when the hardening modulus becomes equal to 0 (the determinant of the elastoplastic tensor N^{ep} is zero with $d\sigma = N^{ep}\, d\varepsilon$). When f and g are identical functions, the elastoplastic model is said to be "associated", otherwise it is "unassociated". In this last case, the elastoplastic tensor is no longer symmetric.

The hardening rule can be "isotropic" when f varies in an homothetic manner in the stress space, "kinematic" when f is translated in the stress space, or "rotational" when f can turn around the origin of the stress space (this last hardening has been introduced more recently, for example in [LAD 97]).

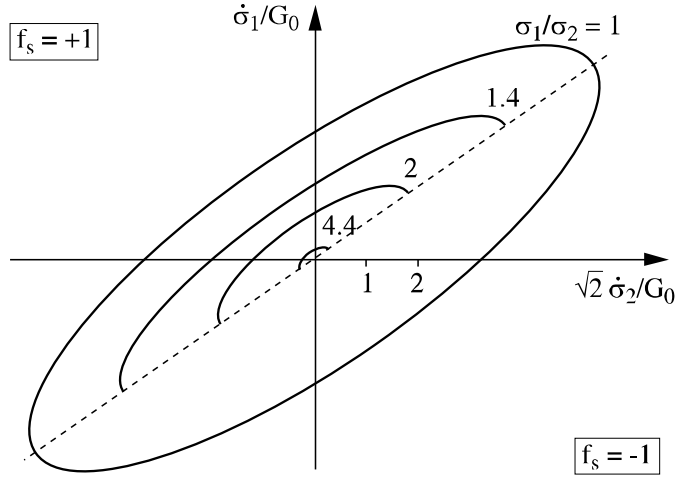

Figure 1.2. *Response envelopes [GUD 79] in axisymmetric conditions for the Duncan-Chang model with two tensorial zones (characterized by $f_s = \pm 1$) for four different stress levels. The continuity of the response envelopes is not verified*

1.6.2.2. *Hypoelastic models with one single loading-unloading criterion*

In this type of model, there is no distinction between elastic and plastic strains and the notion of elastic limit surface is non-existent. The two tensorial zones are separated by a hyperplane, having a linear homogenous equation of the following form:

$$A(\sigma) \,.\, d\sigma = 0$$

The loading zone corresponds to the loading condition:

$$A(\sigma) \,.\, d\sigma > 0 \tag{1.18}$$

with the associated constitutive tensor M^+. The unloading zone is defined by:

$$A(\sigma) \,.\, d\sigma < 0 \tag{1.19}$$

with the associated constitutive tensor M^-.

Here there is a complete similarity with the elastoplasticity theory. Inequations (1.18) and (1.19) correspond to inequations (1.13), whereas tensors M^+ and M^- can be compared to tensors M^{ep} and M^e, respectively.

However, the continuity condition must be fulfilled *a posteriori* here. It can be written:

$$\forall d\sigma \text{ such that } A(\sigma)\cdot d\sigma = 0 \text{: } (M^{+} - M^{-})\, d\sigma \equiv 0 \tag{1.20}$$

Condition (1.20) prevents any arbitrary choice for M^{+} and M^{-}. It corresponds to the consistency condition in elastoplasticity theory. Tensors M+ and M- have to be dependent on memory parameters, which are linked to the stress tensor and to the plastic deformation, as in elastoplastic models.

Figure 1.2 shows the response envelopes obtained for the Duncan-Chang model, which is a non-linear isotropic hypoelastic model with a specific loading-unloading criterion. It is easy to verify that such a model cannot be continuous at the border between the two zones.

1.6.2.3. *Damage models*

The main assumption behind these models is that damaged material loses part of its mechanical elastic properties. This is shown by introducing a damage parameter D, which can be a scalar or a tensor. By introducing the damage parameter into an elastic formulation, we obtain a rheological functional which expresses the elastic behavior of a damaged material [MAZ 86]. This approach has proved to be very easy to use in monotonic loading, but not so much elsewhere, due to the nature of the functional.

In the framework of the incremental expression of the constitutive relations, damage models can be constructed by distinguishing a reversible damaged behavior from an irreversible behavior [MAZ 89]. A limit surface where damage appears is introduced:

$$f(\sigma, D) = 0 \tag{1.21}$$

When the incremental stress is directed towards the outside of this surface, additional damage is created, while the damage remains constant when the incremental stress is directed towards the inside of the surface. The loading-unloading criterion is therefore given by the sign of $\partial f/\partial \sigma . d\sigma$:

$$\begin{cases} \dfrac{\partial f}{\partial \sigma}\cdot d\sigma > 0 \text{: loading condition} \\ \dfrac{\partial f}{\partial \sigma}\cdot d\sigma < 0 \text{: unloading condition} \end{cases} \tag{1.22}$$

When the limit surface is reached and the loading criterion is verified, damage is produced in the direction given by the damage evolution law:

$$dD = d\lambda \frac{\partial g}{\partial \sigma} \tag{1.23}$$

where $g(\sigma) = 0$ is the damage potential. $d\lambda$ is an arbitrary scalar at the present step and can be determined by the consistency equation which expresses that the damage limit surface follows the state of stress as long as the loading condition is verified:

$$df = 0$$

thus

$$\frac{\partial f}{\partial \sigma} . d\sigma + \frac{\partial f}{\partial D} . dD = 0 \tag{1.24}$$

where

$$d\lambda = - \left(\frac{\partial f}{\partial \sigma} . d\sigma \right) \Big/ \left(\frac{\partial f}{\partial D} . \frac{\partial g}{\partial \sigma} \right) \tag{1.25}$$

As in elastoplasticity, we must assure that the consistency equation is always verified.

The incremental strain can then be considered as the sum of two contributions: the first being the "degraded elastic" type, the second, irreversible, is induced by the increase in damage:

$$d\varepsilon = M^e(D)\, d\sigma - \alpha \frac{\dfrac{\partial f}{\partial \sigma} . d\sigma}{\dfrac{\partial f}{\partial D} . \dfrac{\partial g}{\partial \sigma}} \frac{\partial g}{\partial \sigma} \tag{1.26}$$

with $M^e(D)$ the damaged elastic matrix, and α a scalar equal to 0 or 1.

$\alpha = 0$, if $f(\sigma, D) < 0$

or:

$$f(\sigma,\ D) = 0 \text{ and } \frac{\partial f}{\partial \sigma}\cdot\partial\sigma < 0$$

$$\alpha = 1, \text{if} \quad f(\sigma, D) = 0 \text{ and } \frac{\partial f}{\partial \sigma}\cdot\partial\sigma > 0 \tag{1.27}$$

We can see that, by using the notions of tensorial zone and the continuity condition, it is possible to give a unified presentation of elastoplasticity, hypoelasticity with loading-unloading criteria, and damage theory.

1.6.3. *Constitutive relations with four tensorial zones*

In order to describe more precisely the incrementally non-linear behavior of materials, particularly soils, it appears preferable to take into account two plastic mechanisms in the framework of elastoplasticity and two loading-unloading criteria for the hypoelastic constitutive relations. Each criterion can be associated, independently of the other, with a loading or unloading condition according to the direction of the incremental stress, which leads to the definition of four tensorial zones and four constitutive tensors. If the criteria are not independent, another theory, albeit one which is the same in principle, has to be built.

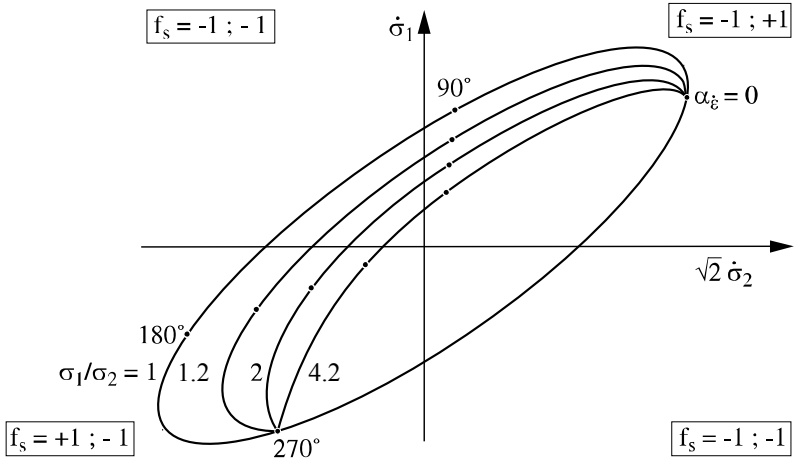

Figure 1.3. *Response envelopes [GUD 79] in axisymmetric conditions for the octo-linear Darve's model [DAR 82] with four tensorial zones (characterized by f_s) for four different stress levels. The continuity of the response envelopes is verified*

1.6.3.1. *Elastoplastic models with double plastic potential*

For each state of stress, following a given loading history, there are two yield surfaces which pass through this state of stress when the first plastic deformations develop:

$$\begin{cases} f_1(\sigma, \varepsilon^p) = 0 \\ f_2(\sigma, \varepsilon^p) = 0 \end{cases} \tag{1.28}$$

For each surface, we define a criterion of loading-unloading defined by the following relation:

$$\begin{cases} \dfrac{\partial f_1}{\partial \sigma} \cdot d\sigma > 0 \text{ or } < 0 \\ \dfrac{\partial f_2}{\partial \sigma} \cdot d\sigma > 0 \text{ or } < 0 \end{cases} \tag{1.29}$$

In the incremental stress six-dimensional space, we can therefore define four tensorial zones separated by two hyperplanes having the following equations:

$$\frac{\partial f_1}{\partial \sigma} \cdot d\sigma = 0 \quad \text{and} \quad \frac{\partial f_2}{\partial \sigma} \cdot d\sigma = 0 \tag{1.30}$$

When the loading condition for criterion *i* is fulfilled, there is a plastic deformation $d\varepsilon^{pi}$, whose direction is given by:

$$d\varepsilon^{pi} = d\lambda_i \frac{\partial g_i}{\partial \sigma} \tag{1.31}$$

where $d\lambda_i$ is an arbitrary scalar and $g_i(s) = 0$ is the plastic potential for mechanism *i*. As in the previous section, the consistency rule for mechanism *i* gives the value of $d\lambda_i$, using equation (1.16). The incremental strain can therefore be written:

$$d\varepsilon = M^e\, d\sigma - \alpha_1 \frac{\dfrac{\partial f_1}{\partial \sigma} \cdot d\sigma}{\dfrac{\partial f_1}{\partial \varepsilon^p} \cdot \dfrac{\partial g_1}{\partial \sigma}} \frac{\partial g_1}{\partial \sigma} - \alpha_2 \frac{\dfrac{\partial f_2}{\partial \sigma} \cdot d\sigma}{\dfrac{\partial f_2}{\partial \varepsilon^p} \cdot \dfrac{\partial g_2}{\partial \sigma}} \frac{\partial g_2}{\partial \sigma} \tag{1.32}$$

where:

$\alpha_i = 0$, if $f_i(\sigma, \varepsilon^p) < 0$
or $f_i(\sigma, \varepsilon^p) = 0$ and $\partial f_i/\partial\sigma.d\sigma < 0$

$\alpha_i = 1$, if $f_i(\sigma, \varepsilon^p) = 0$ and $\partial f_i/\partial\sigma.d\sigma > 0$

The four tensorial zones can be defined by the values of α_1 and α_2 and the correspondent constitutive tensors are:

– tensorial zone I: (0, 0), M^e

– tensorial zone II: (1, 0), $M^{p_1e_2}$

– tensorial zone III: (0, 1), $M^{e_1p_2}$

– tensorial zone IV: (1, 1), $M^{p_1p_2}$

The continuity condition has to be fulfilled between zones I and II for which $\alpha_2 = 0$:

$$\forall d\sigma \text{ such that } \frac{\partial f_1}{\partial \sigma}\cdot d\sigma = 0 : (M^e - M^{p_i e_2})\, d\sigma \equiv 0 \tag{1.33}$$

between zones I and III for which $\alpha_1 = 0$:

$$\forall d\sigma \text{ such that } \frac{\partial f_2}{\partial \sigma}\cdot d\sigma = 0 : (M^e - M^{e_i p_2})\, d\sigma \equiv 0 \tag{1.34}$$

between zones IV and II for which $\alpha_1 = 1$:

$$\forall d\sigma \text{ such that } \frac{\partial f_2}{\partial \sigma}\cdot d\sigma = 0 : (M^{p_i p_2} - M^{p_i e_2})\, d\sigma \equiv 0 \tag{1.35}$$

and between zones IV and III for which $\alpha_2 = 1$:

$$\forall d\sigma \text{ such that } \frac{\partial f_1}{\partial \sigma}\cdot d\sigma = 0 : (M^{p_i p_2} - M^{e_i p_2})\, d\sigma \equiv 0 \tag{1.36}$$

We can easily verify that conditions (1.33) and (1.36) are equivalent, as well as conditions (1.34) and (1.35).

Even if there are four limits, only two continuity conditions have to be satisfied, which correspond to the two consistency conditions. Due to the structure of elastoplastic relations, the two other relations are automatically verified.

1.6.3.2. *Hypoelastic models with two loading-unloading criteria*

For each state of stress, two loading-unloading criteria are defined in order to obtain a more progressive change of the constitutive tensor with the direction of $d\sigma$ (with only one criterion, the tensor can have only two expressions, one corresponding to the loading condition, the other one to the unloading condition):

$$\begin{cases} \text{first criterion: } A_1(\sigma)\cdot d\sigma > 0 \text{ or } < 0 \\ \text{second criterion: } A_2(\sigma)\cdot d\sigma > 0 \text{ or } < 0 \end{cases} \tag{1.37}$$

The two hyperplanes having for equation:

$$A_1(\sigma).d\sigma = 0$$

and:

$$A_2(\sigma).d\sigma = 0$$

define four tensorial zones in the $d\sigma$ space. If we characterize each zone by the signs of expressions (1.37), we get the four different zones with the attached constitutive tensors:

– zone I: (+, +), M^{++}

– zone II: (+, -), M^{+-}

– zone III: (-, +), M^{-+}

– zone IV: (-, -), M^{--}

The four continuity conditions are given by:

$$\begin{aligned} &\forall d\sigma \text{ such that } A_1(\sigma)\cdot d\sigma = 0\text{: } (M^{++} - M^{-+})d\sigma \equiv 0 \\ &\qquad\qquad \text{and } (M^{+-} - M^{--})d\sigma \equiv 0 \\ &\forall d\sigma \text{ such that } A_2(\sigma)\cdot d\sigma = 0\text{: } (M^{++} - M^{+-})d\sigma \equiv 0 \\ &\qquad\qquad \text{and } (M^{-+} - M^{--})d\sigma \equiv 0 \end{aligned} \tag{1.38}$$

We note that, due to the more general structure of the hypoelastic models, the four conditions (1.38) cannot be reduced to two, as in the elastoplastic models with double plastic potential.

1.6.4. *Constitutive relations with n tensorial zones (n > 4)*

All these models have an incrementally piecewise linear structure. In the case of elastoplastic models with *m* plastic potentials, corresponding to *m* loading-unloading criteria, each state of stress can be located at the same time on *m* elastic limits, to which we can associate *m* flow rules. The elastic limit corresponds locally to a vertex, which can be interpreted as the creation of a local singularity by the stress state encountering the elastic limit surface and deforming it locally. Some mechanisms can be associated (yield surface *i* is therefore identical to plastic potential *i*) or unassociated.

With each plastic mechanism is associated a loading-unloading criterion and two tensorial zones. The total number of tensorial zones is therefore equal to:

$$n = 2^m$$

In the case of hypoelasticity, we can find identical structures by the direct introduction of *m* loading-unloading criteria. Obviously, the model has to be constructed so that it will respect the continuity condition at each change of tensorial zone.

An elastoplastic model has been constructed by using three deviatoric mechanisms and one isotropic mechanism, which correspond to 16 tensorial zones [HIC 85, HUJ 85]. A hypoelastic model with eight tensorial zones, the "octo-linear incremental model" [DAR 82], is presented in Chapter 6.

1.6.5. *Constitutive relations with an infinite number of tensorial zones*

A constitutive model can be considered to have an infinite number of tensorial zones, if each direction of $d\sigma$ space is linked to a given tangent constitutive tensor which varies in a continuous manner with this direction. There are three different types of model.

Historically, the first models of this type were developed by Valanis [VAL 71]. They are written in the following form

$$d\varepsilon = M d\sigma + C d\zeta \tag{1.39}$$

where ζ plays the role of an "intrinsic time" for the material (which is at the origin of the designation "endochronic models" for this type of constitutive laws), and corresponds to the length of the path followed in the strain space:

$$d\zeta = \| d\varepsilon \|$$

The incremental non-linearity is thus given by the scalar $||d\varepsilon||$ which always remains positive, regardless of the direction of the incremental loading. Therefore, irreversible strains, independent of the strain rate since the relation is homogenous of degree 1, can be obtained without introducing either loading-unloading criteria or an elastic domain.

In this class of models, we find models with a non-linear incremental term of a tensorial nature, called "interpolation type" models since they are based on a non-linear interpolation between given constitutive responses, the non-linearity being linked to the type of interpolation rule used. Among these models, we can cite the "incremental non-linear of second order" model [DAR 80, DAR 88], which has the following general form:

$$d\varepsilon_{ij} = M_{ijkl}\ d\sigma_{kl} + \frac{1}{\|d\sigma\|} N_{ijklmn} d\sigma_{kl} d\sigma_{mn} \tag{1.40}$$

and some other models with different interpolation forms [CHA 79, DIB 87, ROY 86].

Models with a "bounding surface", proposed by Dafalias [DAF 80], have led to the development of an incrementally non-linear relation called "hypoplasticity" [DAF 86] by creating a dependency of the incremental response on the direction of incremental stress.

The term "hypoplasticity" was also used by Kolymbas [KOL 77] and Chambon [CHA 94] for endochronic type models:

$$\dot{\sigma} = A(\dot{\varepsilon} + b\,\|\dot{\varepsilon}\|) \tag{1.41}$$

which are the object of specific developments unlike the initial model developed by Valanis.

1.6.6. *Conclusion*

Metallic mono-crystals have a finite number of defined directions of sliding planes; therefore, this specific microstructure is the basis of models which have a finite number of plastic potentials. In granular materials, however, plastic sliding can occur in any direction of the space along tangential planes at grain contacts. The mechanical behavior of such materials is thus more likely to be incrementally non-linear.

In order to describe this non-linearity, i.e. the non-linear character of the relationship between the incremental strain and stress, we can use a piecewise linear formalism. Elastoplasticity theory guides us in the construction of such models by the definition of notions such as elastic limit, flow rule and hardening variables. However, calibrating these different elements can be a difficult task and it has been shown that their predictions along non-proportional loading could be of poor quality [WOR 84, WOR 88], mainly due to limitations induced by the difficulty of identifying elastic domains, flow rules and hardening variables.

Hypoelastic models with multiple loading-unloading criteria require fewer initial hypotheses and increase the choice of elaboration of the constitutive tensors, which must however verify *a posteriori* the continuity conditions. We can say that the modeler pays for his increased choice by a lack of constraint, which is certainly a life lesson of broad concern!

The incrementally non-linear formalism increases to an even greater extent the range of choices which is only limited by the homogenity condition. The advantage of the incrementally non-linear constitutive "interpolation type" relations is the reintroduction of some guides strongly linked to the material mechanical properties by proposing a non-linear interpolation between known behaviors in conventional loading conditions. We shall come back to this aspect in Chapter 6.

1.7. The main constitutive relations for rate-dependent materials

Viscosity plays a less central role in solid materials than in fluids. It completes an elastoplastic behavior, either by adding an additional incremental strain, or by influencing the plastic strain. These two hypotheses are the basis of the proposed classification [DAR 90].

1.7.1. *First class of incremental strain decomposition*

The hypothesis for the models belonging to this first class consists of assuming that the incremental strain can be divided into an instantaneous and a delayed part:

$$\mathrm{d}\varepsilon = (\mathrm{d}\varepsilon)_{\text{instantaneous}} + (\mathrm{d}\varepsilon)_{\text{delayed}} \tag{1.41}$$

The instantaneous strain can be interpreted as being of an elastoplastic type and the delayed strain of a viscous type. Therefore:

$$\mathrm{d}\varepsilon = \mathrm{d}\varepsilon^{ep} + \mathrm{d}\varepsilon^{v} \tag{1.42}$$

In the previous section we have seen that $d\varepsilon^{ep}$ can be written:

$$d\varepsilon^{ep} = M(u)d\sigma \quad \text{with} \quad u = d\sigma / \|d\sigma\|$$

Thus:

$$d\varepsilon = M(u)\, d\sigma + d\varepsilon^{v} \tag{1.44}$$

Under the small transformation hypothesis, creep tests correspond to the condition dt = 0. Therefore, $d\varepsilon^{v}/dt$ corresponds to the creep rate, and we obtain:

$$d\varepsilon = M_h(u)\, d\sigma + C_h\, dt \tag{1.45}$$

where M is the elastoplastic constitutive tensor and C the creep rate, both tensors being dependent on the loading history.

We should note that, for saturated materials, the stresses to be considered are effective stresses and that the considered creep tests are drained.

1.7.2. *Second class of incremental strain decomposition*

We assume in this case that incremental strain can be decomposed into a reversible and an irreversible part:

$$d\varepsilon = (d\varepsilon)_{\text{reversible}} + (d\varepsilon)_{\text{irreversible}} \tag{1.46}$$

The reversible part can be considered as purely elastic and the irreversible part as viscoplastic:

$$d\varepsilon = d\varepsilon^{e} + d\varepsilon^{vp} \tag{1.47}$$

If M^e is the elastic tensor, the elastic law being incrementally linear, we have:

$$d\varepsilon^{e} = M^{e}\, d\sigma \tag{1.48}$$

The viscoplastic strain is generally determined by using the viscoplastic potential theory developed by Perzyna [PER 63]:

$$d\varepsilon^{vp} = d\lambda \frac{\partial g}{\partial \sigma}, \tag{1.49}$$

with $g(\sigma) = 0$ being the viscoplastic potential.

Due to the fact that the actual stress state can be outside the actual elastic limit, scalar $d\lambda$ is no longer determined by the consistency condition, but directly by the intensity of the viscoplastic strains.

1.8. General conclusions

Having reviewed all the main classes of constitutive relations, we must emphasize two main choices when constructing a constitutive model.

The first choice concerns the structure of the constitutive model, which should be better adapted to the problem to which it is addressed. This first choice has been widely discussed: is viscosity necessary or not? If yes, which type of viscous behavior is more pertinent: adding viscous behavior to elastoplastic strain or taking into account viscoplastic strains? How many tensorial zones are needed to describe the elastoplastic strains properly? Should we stay in the framework of elastoplasticity or damage theory, well defined and yet restrictive, or should we give ourselves more degrees of freedom by working in the framework of hypoelasticity or incrementally non-linear constitutive equations? Without a precise and solid knowledge of the material microstructure [DAR 05a, DAR 05b], the objective criteria for choosing one direction cannot be well defined, which can partially explain that the use of a given model in finite element analyses is rarely rationally justified. For a better understanding of the limitations of main constitutive models, the reader can refer to the results of two international workshops which took place in Grenoble in 1984 and in Cleveland in 1988, which were devoted to comparing model performances along various loading paths [WOR 84, WOR 88].

The second necessary choice is linked to the description of the loading history and leads to the following questions: which state variables? Which hardening variables? Which memory parameters? These questions have not been fundamentally addressed in this chapter, even if they play a central role in the quality of the model prediction. In the general case of an unproportional loading, our ignorance on this topic remains significant. The only insurance that we have is the major role played by induced anisotropy on the stress-strain response and therefore, the necessity of taking it into account in the modeling. Elastoplasticity also seems to require discrete memory parameters, which can characterize the last changes in the loading direction.

Finally, we should note that the topic concerning constitutive models cannot be developed further without taking into account the significant developments made in the field of discrete numerical simulations concerning granular materials. We also

have to take into consideration the demand coming from practitioners concerning the need for parameter identification methods based on inverse analyses of *in situ* test results, and not only from laboratory testing, which are often more difficult and more expensive to perform.

1.9. References

[CHA 79] R. CHAMBON and B. RENOUD-LIAS, "Incremental non-linear stress-strain relationships for soils and integration by F.E.M.", *Int. Conf. Num. Meth. in Geomech.*, W. Wittke (ed.), publ. Balkema, vol. 1, 405-413, 1979.

[CHA 94] R. CHAMBON, J. DESRUES, W. HAMMAD and R. CHARLIER, "Cloe a new rate-type constitutive model for geomaterials. Theoretical basis and implementation", *Int. J. Num. Anal. Meth. in Geomech.*, 18(4), 253-278, 1994.

[DAF 86] Y.F. DAFALIAS, "Bounding surface plasticity I. Mathematical foundation and hypoplasticity", *J. Eng. Mech.*, 112(9), 966-987, 1986.

[DAF 80] Y. DAFALIAS and L. HERRMANN, "A bounding surface soil plasticity model", *Int. Symp. of Soils under Cyclic and Transient Loading*, Pande and Zienkiewicz (eds.), publ. Balkema, vol. 1, 335-345, 1980.

[DAR 80] F. DARVE, "Une loi rhéologique incrémentale non-linéaire pour les solides", *Mech Res. Comm.*, 7(4), 205-212, 1980.

[DAR 82] F. DARVE and S. LABANIEH, "Incremental constitutive law for sands and clays. Simulations of monotonic and cyclic tests", *Int. J. Num. Anal. Meth. in Geomech.*, 6, 243-275, 1982.

[DAR 87] F. DARVE, "L'écriture incrémentale des lois rhéologiques et les grandes classes de lois de comportement", *Manuel de Rhéologie des Géomatériaux*, F. Darve (ed.), publ. Presses des Ponts et Chaussées, 129-152, 1987.

[DAR 88] F. DARVE and H. DENDANI, "An incrementally non-linear constitutive relation and its predictions", *Constitutive Equations for Granular Soils*, Saada and Bianchini (eds.), publ. Balkema, 237-254, 1988.

[DAR 90] F. DARVE, "The expression of rheological laws in incremental form and the main classes of constitutive equations", *Geomaterials Constitutive Equations and Modeling*, F. Darve (ed.), publ. Elsevier, 123-148, 1990.

[DAR 94] F. DARVE, "Stability and uniqueness in geomaterials constitutive modelling", *3rd Int. Workshop on Localisation and Bifur. Theory for Soils and Rocks*, Chambon Desrues Vardoulakis (eds.), publ. Balkema, 73-88, 1994.

[DAR 95a] F. DARVE, E. FLAVIGNY and M. MEGHACHOU, "Constitutive modelling and instabilities of soils behaviour", *Computers and Geotechnics*, 17(2), 203-224, 1995.

[DAR 95b] F. DARVE, E. FLAVIGNY and M. MEGHACHOU, "Yield surfaces and principle of superposition revisited by incrementally non-linear constitutive relations", *Int. J. of Plasticity*, 11(8), 927-948, 1995.

[DAR 05a] F. DARVE and F. NICOT, "On incremental non-linearity in granular media. Phenomenological and multi-scale views", *Int. J. Num. Analyt. Meth. in Geomech.*, 29(14), 1387-1410, 2005.

[DAR 05b] F. DARVE and F. NICOT, "On flow rule in granular media. Phenomenological and multi-scale views", *Int. J. Num. Analyt. Meth. in Geomech.*, 29(14), 1411-1432, 2005.

[DIB 78] H. DI BENEDETTO, "Modélisation du comportement des géomatériaux", Doctoral thesis, INPG/ENTPE, 1978.

[GUD 79] G GUDEHUS, "A comparison of some constitutive laws for soils under radially symmetric loading and unloading", *Int. Conf. Num. Meth*. in Geomech, W. Wittke (ed.), publ. Balkema, vol. 4, 1309-1324, 1979.

[HIC 85] P.Y. HICHER, "Comportement mécanique des argiles saturées sur divers chemins de sollicitation monotones et cycliques. Application à une modélisation élasto-plastique et visco-plastique", Doctoral thesis, E.C.P., 1985.

[HUJ 85] J.C. HUJEUX, "Une loi de comportement pour les chargements cycliques des sols", *Génie Parasismique*, publ. Presses des Ponts et Chaussées, 1985.

[KOL 77] D. KOLYMBAS, "A rate-dependent constitutive equation for soils", *Mech Res. Comm*., 4(6), 367-372, 1977.

[LAD 97] P. LADE and S. INEL, "Rotational kinematic hardening model for sand. Part I Conception of rotating yield and plastic potential surfaces", *Comp. and Geotechn*., 21(4), 183-216, 1997.

[LOR 85] B. LORET, "On the choice of elastic parameters for sand", *Int. J. Num. Anal. Meth. in Geomech.*, vol. 9, 285-292, 1985.

[MAZ 86] J. MAZARS, "A description of micro and macro-scale damage of concrete", *Eng. Fract. Mech*., 25(5/6), 729-737, 1986.

[MAZ 89] J. MAZARS and G. PIJAUDIER-CABOT, "Continuum damage theory. Application to concrete", *J. Eng. Mech*., 115(2), 345-365, 1989.

[MUH 91] B. MUHLHAUS and E.C. AIFANTIS, "A variational principle for gradient plasticity", *Int. J. Solids Struct*., 28, 845-857, 1991.

[OWE 69] D.R. OWEN and W.O. WILLIAMS, "On the time derivatives of equilibrated response functions", *ARMA*, 33(4), 288-306, 1969.

[PER 63] P. PERZYNA, "The constitutive equations for work-hardening and rate-sensitive plastic materials", *Proc. Vibrational Problems*, 4(3), 281-290, 1963.

[PIJ 87] G. PIJAUDIER-CABOT and Z.P. BAZANT, "Non-local damage theory", *ASCE J. Engng. Mech*., 113, 1512-1533, 1987.

[ROY 86] P. ROYIS, "Formulation mathématique de lois de comportement. Modélisation numérique de problèmes aux limites en mécanique des solides déformables", Doctoral thesis, INPG/ENTPE, 1986.

[TRU 74] C. TRUESDELL, *Introduction à la Mécanique Rationnelle des Milieux Continus*, Masson, 1974.

[VAL 71] K.C. VALANIS, "A theory of viscoplasticity without a yield surface", *Arch. of Mech*., vol. 23, 517-551, 1971.

[WOR 84] GRENOBLE WORKSHOP, "Constitutive Relations for Soils", Gudehus, Darve and Vardoulakis (eds.), publ. Balkema, 1984.

[WOR 88] CLEVELAND WORKSHOP, "Constitutive Equations for Granular Soils", Saada and Bianchini (eds.), publ. Balkema, 1988.

Constitutive Modeling of Soils and Rocks
Edited by Pierre-Yves Hicher & Jian-Fu Shao

Chapter 2

Mechanisms of Soil Deformation

2.1. Introduction

Mechanical soil behavior is generally studied within the framework of continuous medium mechanics, which provides a way of formulating constitutive models adapted to the specific nature of these materials. Given the extremely diverse nature of soils, it is necessary to investigate first of all the possibility of proposing models flexible enough to be adapted to a vast range of natural materials. Secondly, it is necessary to assess the procedure by which the parameters for a given soil are obtained. The field of soil mechanics has always favored the perfect elastic-plastic Mohr-Coulomb model. Numerous elastoplastic models have thus been developed, improving the representation of observable non-linear behavior. However, these models come up against a problem of parameter determination on account of the generally small number of experimental field data. From the outset of our study, we will present a number of experimental results which clearly show the soil's mechanical behavior by drawing attention to the common aspects that do not rely on the nature of the constituents. This enables us to propose a mode of behavior applicable to a large range of materials. We will then discuss the possibility of relating the representative parameters of equivalent continuous medium to parameters representative of a discontinuous medium as well as the pertinent representation scales of this discontinuous medium. Our investigation is limited to monotonous axisymmetric compression loading on dry or water-saturated materials. Section 2.2 is devoted to remolded laboratory-prepared soils, considered as continuous materials. Section 2.3 studies the relationship between a discontinuous

Chapter written by Jean BIAREZ and Pierre-Yves HICHER.

and equivalent continuous medium. Section 2.4 develops an analysis of natural soils from all the preceding discussion.

2.2. Remolded soil behavior

It is possible in a laboratory to prepare, remolded clay samples from a mixture of dry clay powder and water. This slurry is afterwards progressively consolidated in order to obtain a saturated solid material whose mechanical properties can be studied (Figure 2.1). The advantage of this technique is that we can have at our disposal a large number of identical specimens with a reproducible and, under specifically prepared conditions, isotropic structure. The results of several triaxial tests presented in several normalized planes illustrate the mechanical behavior of such materials, normally called consolidated materials, which corresponds to the fact that the mean effective stress at the beginning of the loading test is equal to the maximum stress borne by the soil sample (Figure 2.2). These results, usually obtained from clays, are more difficult to obtain from sands, because it is almost impossible to prepare a dry or saturated sand sample under the same conditions. However, if we use slightly wet sand, we can prepare a sand sample with a sufficiently high initial void ratio in order to obtain behavior similar to that obtained previously from normally consolidated clay (Figure 2.3). These results clearly show a highly non-linear response from these materials as well as the influence of the mean stress, which in this case corresponds simply to a homothetic influence on the q-ε_1 curves for deformations larger than 10^{-2}. The final state, called the perfect plasticity state, is defined by a stress criterion $q/p' = M$, identical to a Mohr-Coulomb criterion in axisymmetric compression condition with $\sin\phi_{pp} = 3M/(6+M)$, and by a linear relation between the final void ratio and the logarithm of the mean effective stress. The materials appear in this case to be contractant, which means that they are characterized by an anelastic volume decrease under deviatoric stress loading.

A constant M value on stress paths different from the axisymmetric condition leads to a Drücker-Prager plastic criterion, which is not obtained experimentally. In order to generalize these results in true 3D condition, we have to consider a criterion of the type $q/p' = M(\theta)$, where θ is Lode's angle. Several expressions have been proposed, in particular by Lade and Matsuoka [HIC 85]. The Mohr-Coulomb criterion (ϕ = constant, independent of Lode's angle) remains the most popular. It gives conservative values of the maximum strength along stress paths other than the axisymmetric compression (Figure 2.4).

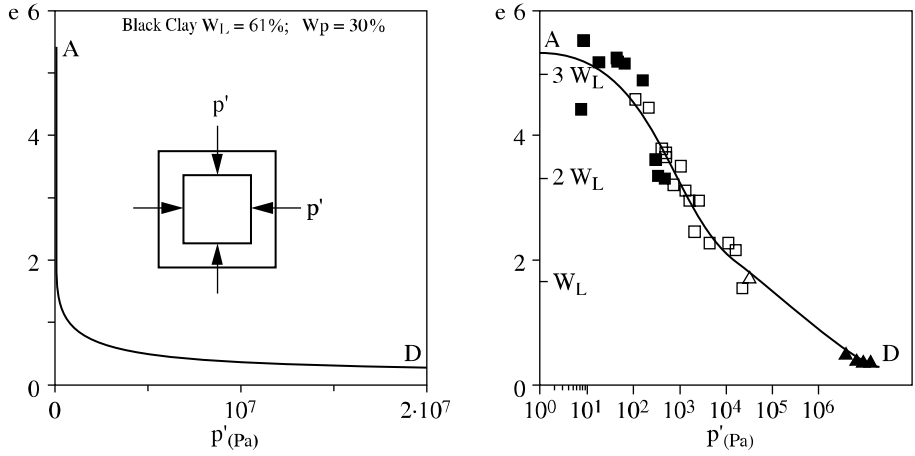

Figure 2.1. *Isotropic compression on clay*

The effect of an overconsolidated state on clay behavior – where the mean effective stress at the beginning of the test is smaller than the maximum effective stress borne by the specimen – can be observed in Figure 2.5 [HAT 95]. The material becomes dilatant (anelastic volume increases) and, at a given mean stress, its rigidity as well as its maximum strength are higher. Identical results are obtained on sands when the initial void ratio is decreased: the dilatancy increases with the initial density (Figure 2.6). The concept of perfect plasticity defined above in the plane e-log (p') helps to explain this change from contractant to dilatant behavior as a function of the initial state of stress and void ratio.

We must however note that this perfect plasticity state is difficult to obtain experimentally, since strain localization usually develops inside the specimens, especially the dilatant specimens. Putting together all these results obtained on reconstituted soils enables us to show a strong analogy between their mechanical behavior and the influence of the volume changes on the stress-strain relationship, independently of the nature of the particle constituents, as long as these particles can be considered elastic (Figure 2.7).

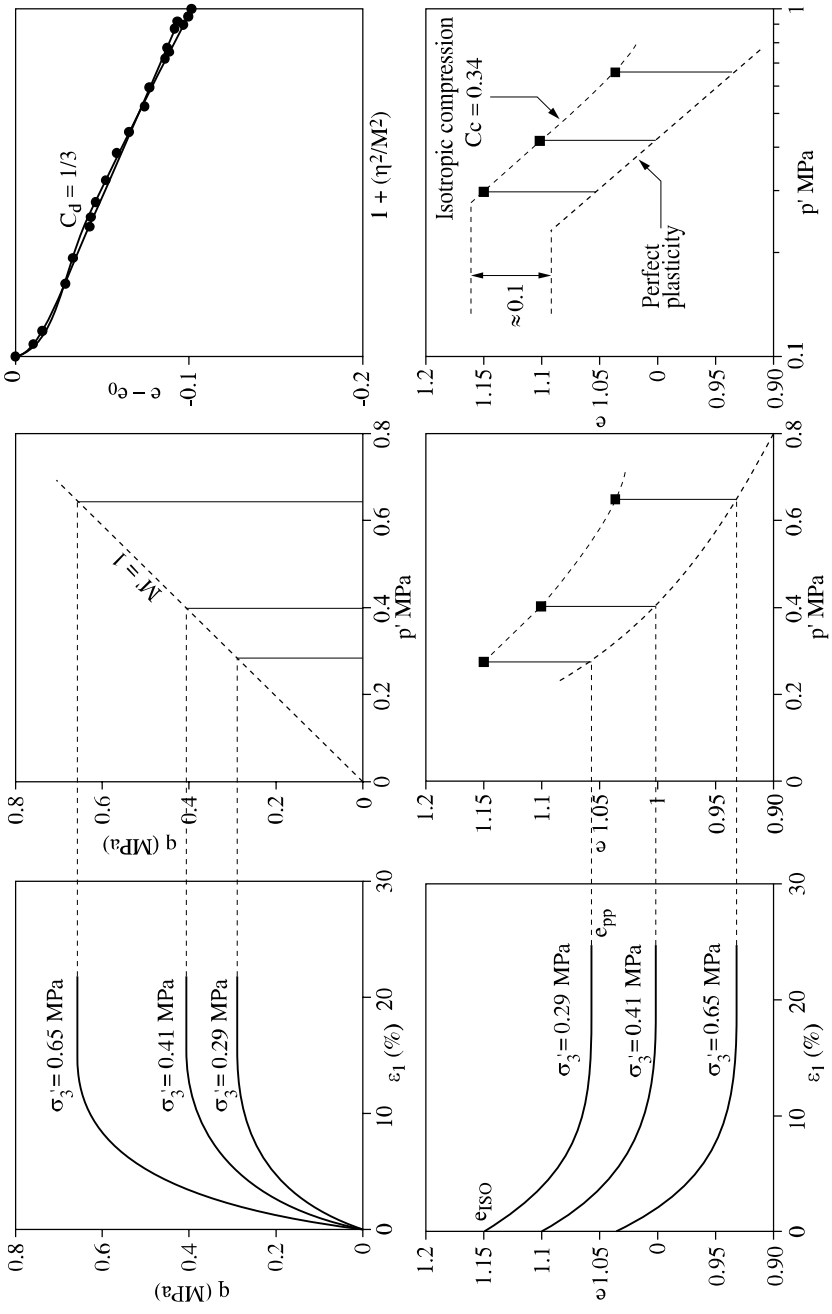

Figure 2.2. *Constant p' triaxial tests on normally consolidated clay*

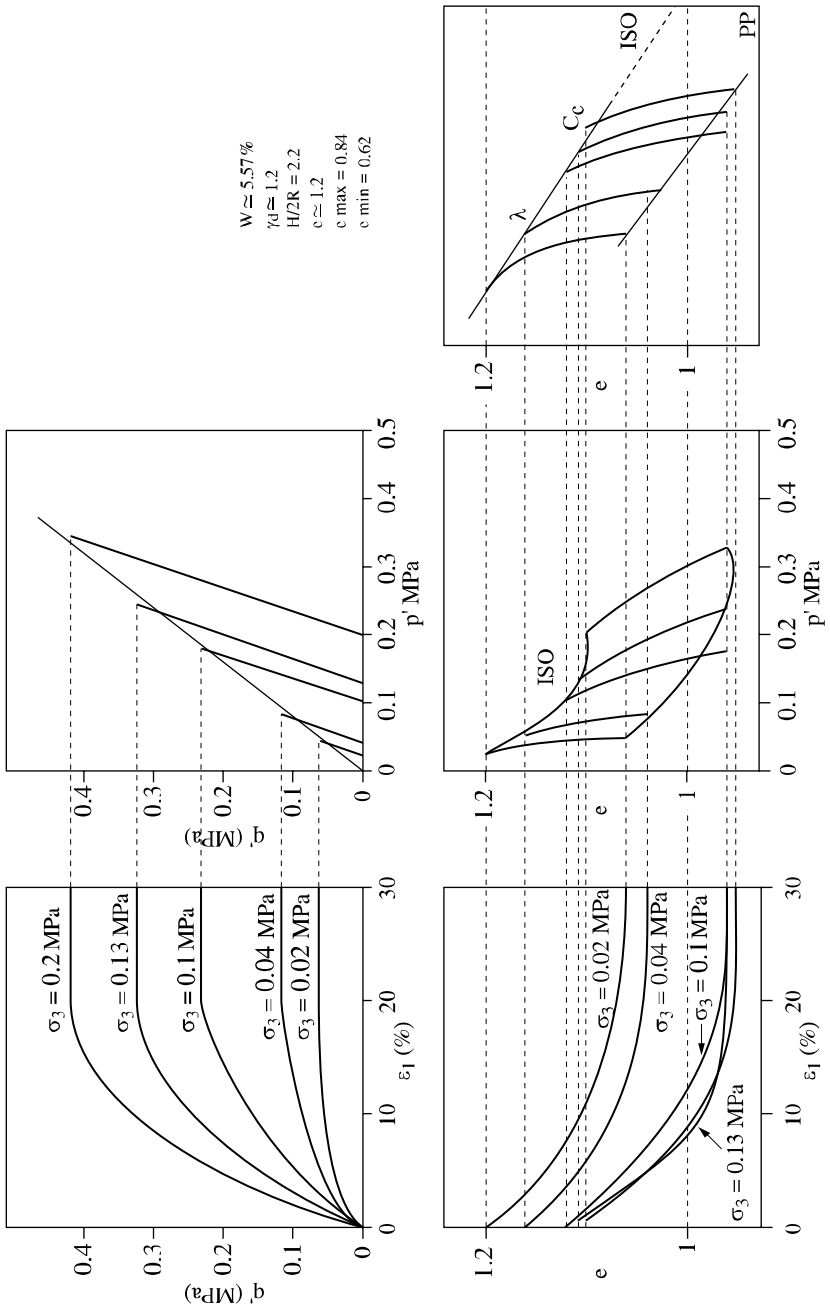

Figure 2.3. *Drained triaxial tests on very loose sand*

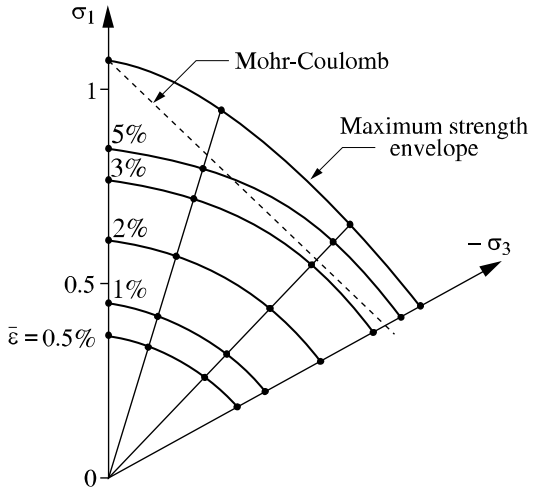

Figure 2.4. *3D tests on normally consolidated clay*

The volume change under deviatoric loading can be quantified from the following relation for normally consolidated soils:

$$e = e_0 - C_d \log (1+\eta^2/M^2) = e_0 - \lambda_d \mathrm{Ln}(1+\eta^2/M^2) \qquad \text{where } \eta = q/p'$$

or with a formulation close to that proposed by Roscoe *et al*. [ROS 58]:

$$e = e_0 - (\lambda - \kappa_p)\, \mathrm{Ln}\, (1+\eta^2/M^2)$$

where κ_p is different from k introduced by Roscoe, which corresponds to the slope of the isotropic or oedometric unloading curve corresponding to an elastic behavior. Parameter λ corresponds to the slope of a stress path at η constant in the e-Ln(p') plane. Therefore, the isotropic stress path ($\eta=0$), the oedometric stress path ($\varepsilon_2=\varepsilon_3=0$, $\sigma'_3/\sigma'_1=K_0$, which corresponds to $\eta=3(1-K_0)/(1+2K_0)$), and the perfect plasticity state are parallel in this plane.

For overconsolidated clays, the relation e- p' allows a pseudoelastic volumetric limit to be defined in the p', q plane. At first, the curve follows a path corresponding to an elastic recompression. It then moves away, either to follow a normally consolidated type of path until it reaches the perfect plastic state for OCR < 2, or to follow a dilatant path when the stress ratio q/p' moves close to M for OCR > 2. The size of this limit increases with the increase of the consolidation stress, all the different limits being homothetic, with the homothetic transformation being equal to the consolidation stress amplitude.

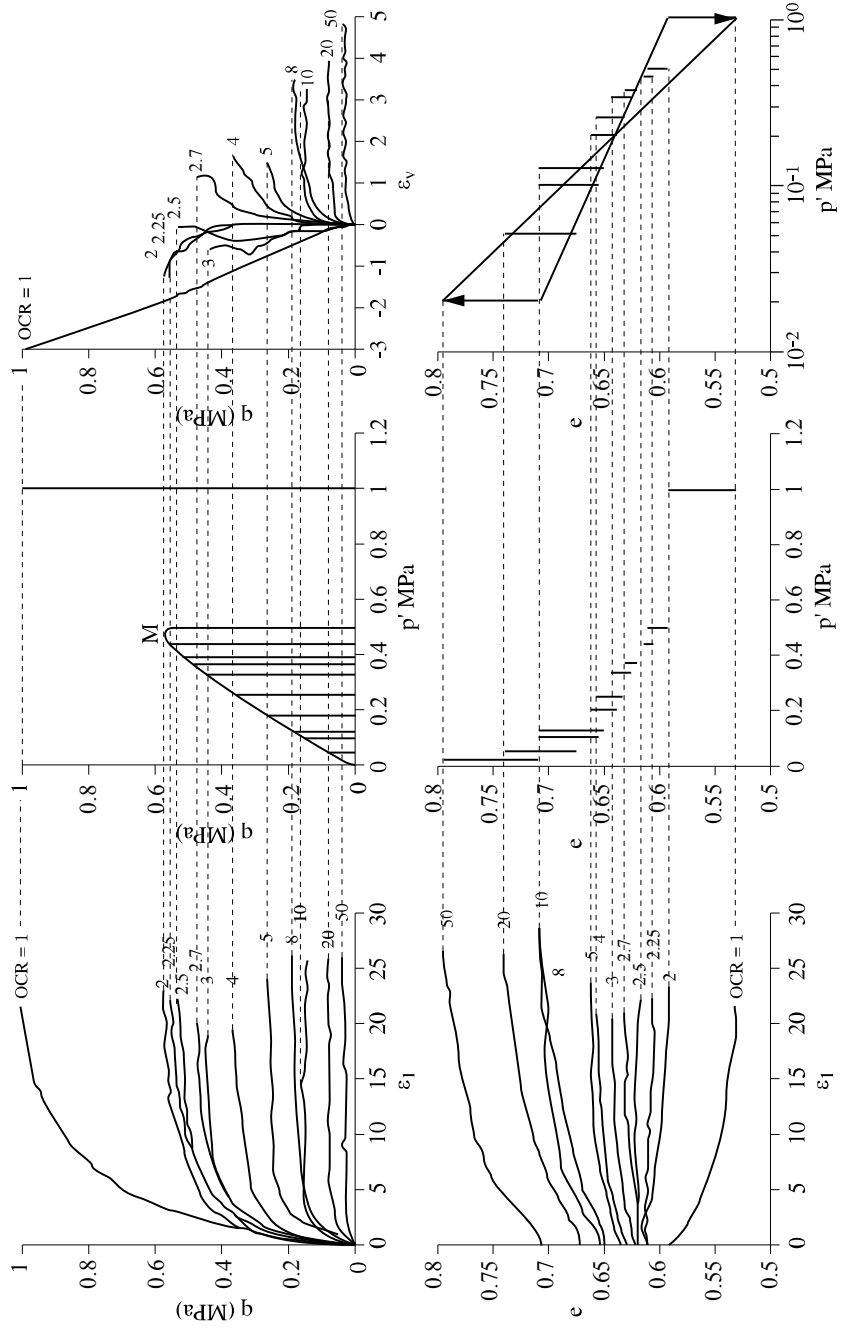

Figure 2.5. *Constant p' triaxial tests on overconsolidated clay*

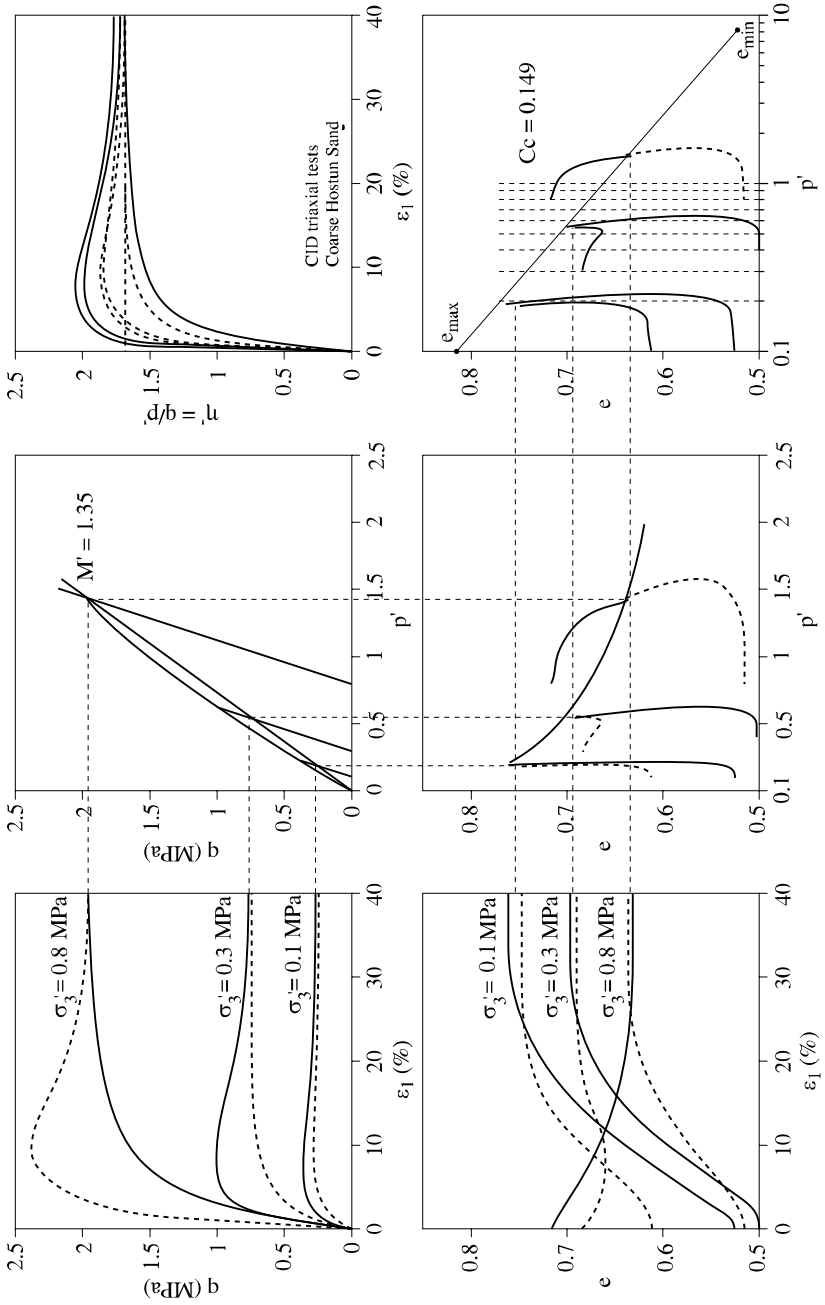

Figure 2.6. *Drained triaxial tests on sand with different initial densities (Bouvard (1982) reported in [BIA 94])*

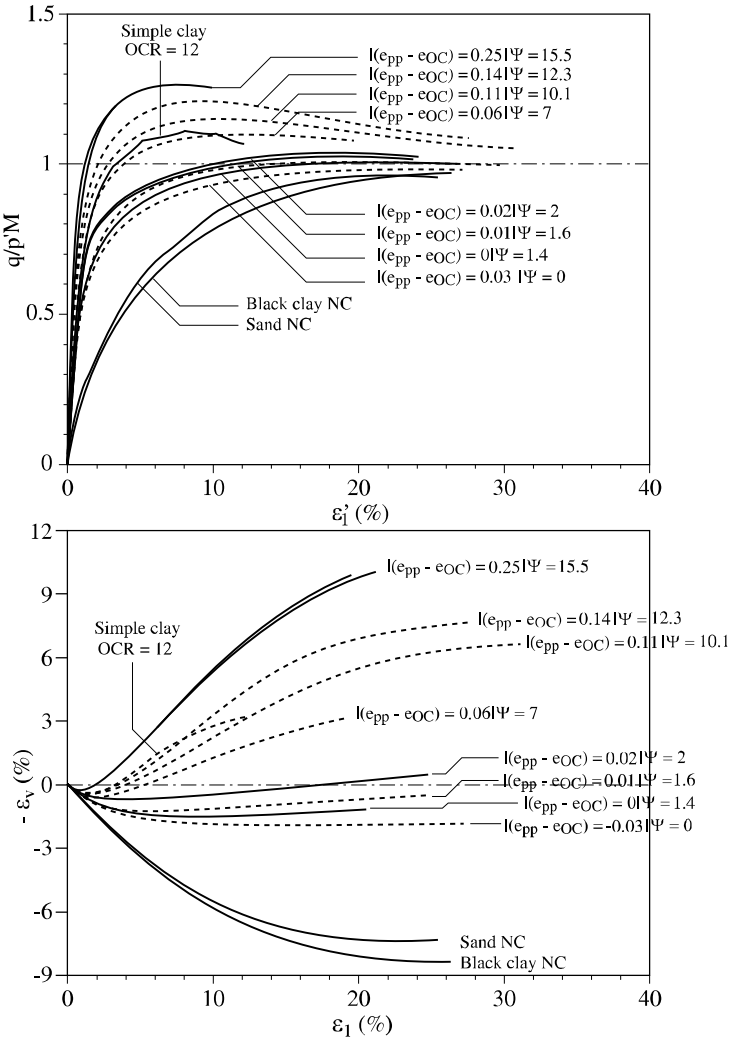

Figure 2.7. *General behavior of remolded soils*

Similar results are obtained on sands, especially in the dilatant domain. The shape of the pseudoelastic limit shows, however, that the junction with the isotropic stress path is reached only for elevated stresses (Figure 2.9), at which grain crushing occurs. The position of this junction point depends on the initial density of the material. In the p', q plane the regime change from contractant to dilatant can be represented by a straight line passing through the origin. This line is called the "phase transformation line" by Ishihara or "characteristic line" by Luong.

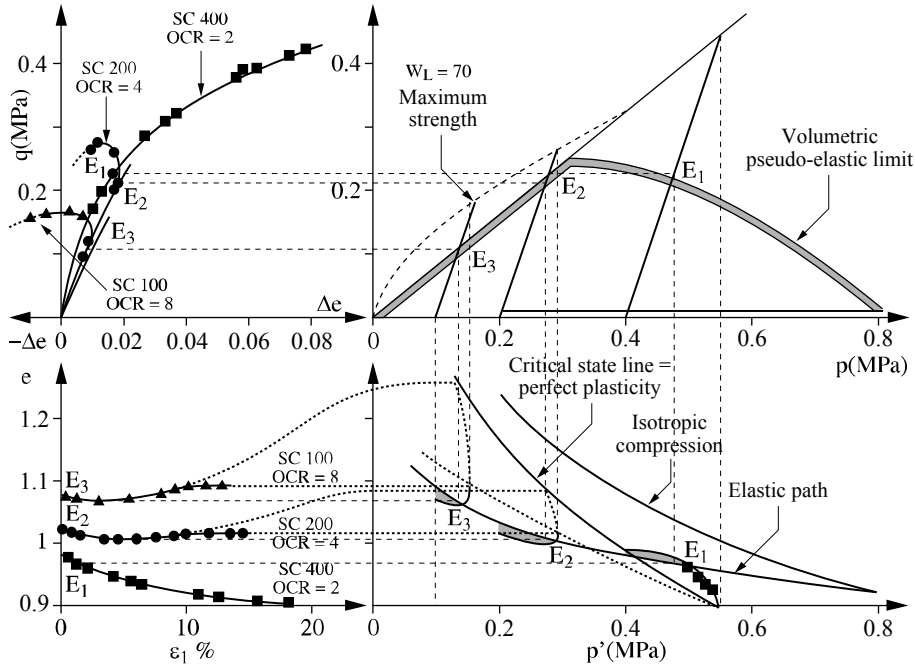

Figure 2.8. *Determination of the pseudo-elastic limit for overconsolidated clay*

Different expressions of the generalized overconsolidation can be proposed (Figure 2.10):

– $e_{NC} - e_{OC}$: for a clayey material, we can see that a given isotropic overconsolidation ratio p'ic/p'i, for different values of p'ic, corresponds to a straight line in the plane e, logp', parallel to the isotropic consolidation line. We can therefore express overconsolidation by the distance to this line, which can be the value of $e_{NC} - e_{OC}$ for a given p', where e_{NC} is the void ratio on the isotropic consolidation line for this value of p' and e_{OC} is the actual void ratio: $e_{NC} - e_{OC} = (C_c - C_s)\log(p'_{ic}/p')$;

– the "state parameter" $e_{SS} - e_{OC}$: we can also relate the initial point e, logp' to the distance to the perfect plastic line, which can be considered as parallel to the isotropic consolidation line at a distance $e_{NC} - e_{SS} = 0.1$. In these conditions, we can define overconsolidation by the state parameter $(e_{SS} - e_{OC}) = (e_{NC} - e_{SS}) - 0.1$;

– the dilatancy $\Psi - \beta$: we can also define the distance of the initial point e_{OC}, p' to the perfect plastic line along a triaxial path ($\sigma'_2 = \sigma'_3 =$ constant). This path

reaches the perfect plastic line at a point of void ratio e_{pp} and corresponds to a curve in the e1,ev plane with a maximum slope $tg\beta = d\varepsilon_v/d\varepsilon_1$, which can also be written: $tg\beta = 2\sin\Psi/(1 - \sin\Psi)$.

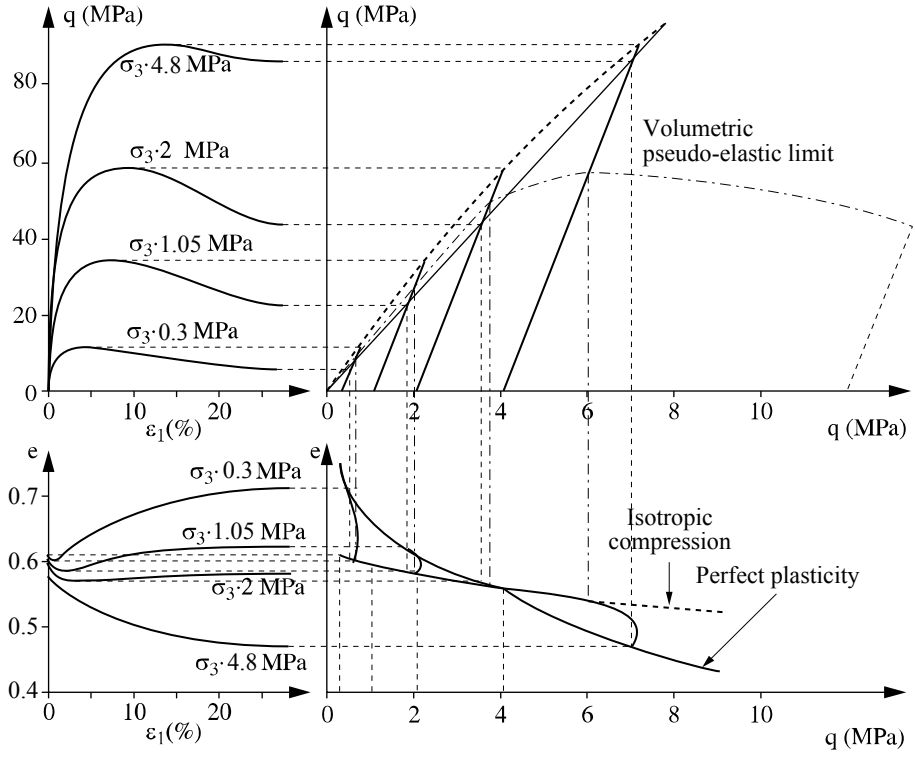

Figure 2.9. *Pseudo-elastic limit for sand*

The volume change due to the application of a deviatoric stress affects the entire stress-strain relationship. Rowe [ROW 62] has shown that the results of triaxial tests can be represented in a preliminary approximation by a linear relationship between σ'_1/σ'_3 and $(1 - d\varepsilon_v/d\varepsilon_1)$. This is independent of the initial void ratio. If the slope of this line is expressed as $tg^2(\pi/4 + \phi'/2)$, ϕ' can be approximated by the perfect plasticity friction angle ϕ_{pp}. Rowe's stress-dilatancy law can thus be written as follows:

$$\sigma'_1/\sigma'_3 = tg^2(\pi/4 + \phi_{pp}/2)(1 - d\varepsilon_v/d\varepsilon_1)$$

This relation implies that the characteristic line and perfect plasticity line correspond to the same mobilized friction angle. It also implies a relationship between the dilatancy angle defined by the maximum of $d\varepsilon_v/d\varepsilon_1$ and the maximum friction angle ϕ' which decreases if the mean stress decreases. For a given mean stress, ϕ' increases if the initial void ratio increases according to the approximation:

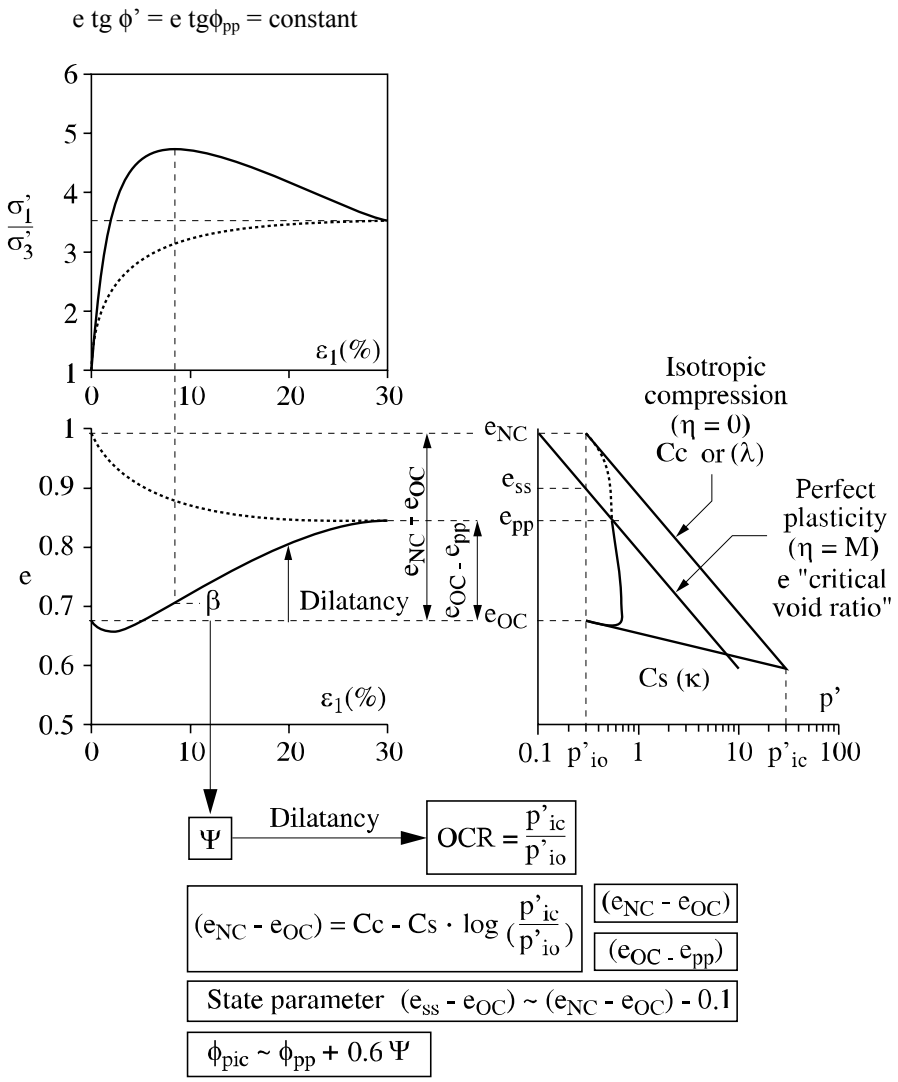

Figure 2.10. *Characterization of the generalized overconsolidation*

The pseudoelastic limit defined previously does not correspond to a perfectly reversible behavior. For remolded soils, the size of the real elastic domain is very small and can be studied only by measuring very small deformations using specific experimental devices, such as that shown in Figure 2.11. Figures 2.12 and 2.13 show, for clay and sand respectively, the evolution of the secant modulus during a triaxial loading test as a function of strain amplitude. We can see that a perfectly reversible behavior can be obtained only for strain amplitudes smaller than 10^{-5}.

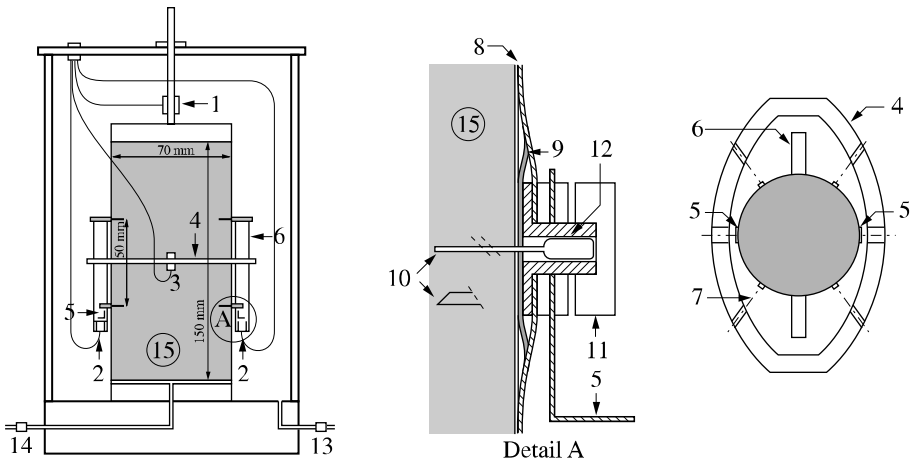

1. load cell
2. axial displacement sensor
3. radial displacement sensor
4. plexiglas ring for radial displacement sensor
5. metallic target for axial displacement measurement
6. support for vertical sensor
7. support for plexiglas ring
8. outer membrane
9. inner membrane
10. needle
11. sealing cap
12. valve
13. lateral pressure sensor
14. pore pressure sensor
15. specimen

Figure 2.11. *Triaxial test with small strain measurement device*

2.3. Relationships between discontinuous and continuous medium

The mechanical behavior of the equivalent continuous medium depends on the properties of the discontinuous medium. An example can be seen in the elastic law at very small strains as defined in the previous section. The elasticity is non-linear, the isotropic modulus depends on the mean stress, in agreement with a calculation that uses Hertz' theory for an assembly of identical spheres [BIA 94]:

$$E_{iso} = 3/2(4E_g/3(1 - \nu_g^2)G(e))^{2/3}p'^{1/3}$$

where E_g and ν_g are the elastic constant of linear elasticity for the spheres and G (e) is a function of the assembly void ratio.

For soils, Young's modulus E can be written in the general form:

$$E = kp_a(p'/p_a)^n$$

where k depends on the nature and density of the soil and p_a is the atmospheric pressure. n is close to 0.5 for all soils if the void ratio influence is completely taken into account in the value of k [HIC 96]. Several expressions of k as a function of the void ratio have been proposed, in particular by Hardin and Drnevitch [HAR 72]. From a wide collection of different soils, a simple relation can approximate the experimental results:

$$E = b/e\ (p')^{0.5}$$

where b depends on the nature of the soil, more precisely on the modulus of the grains or aggregates (see the next section).

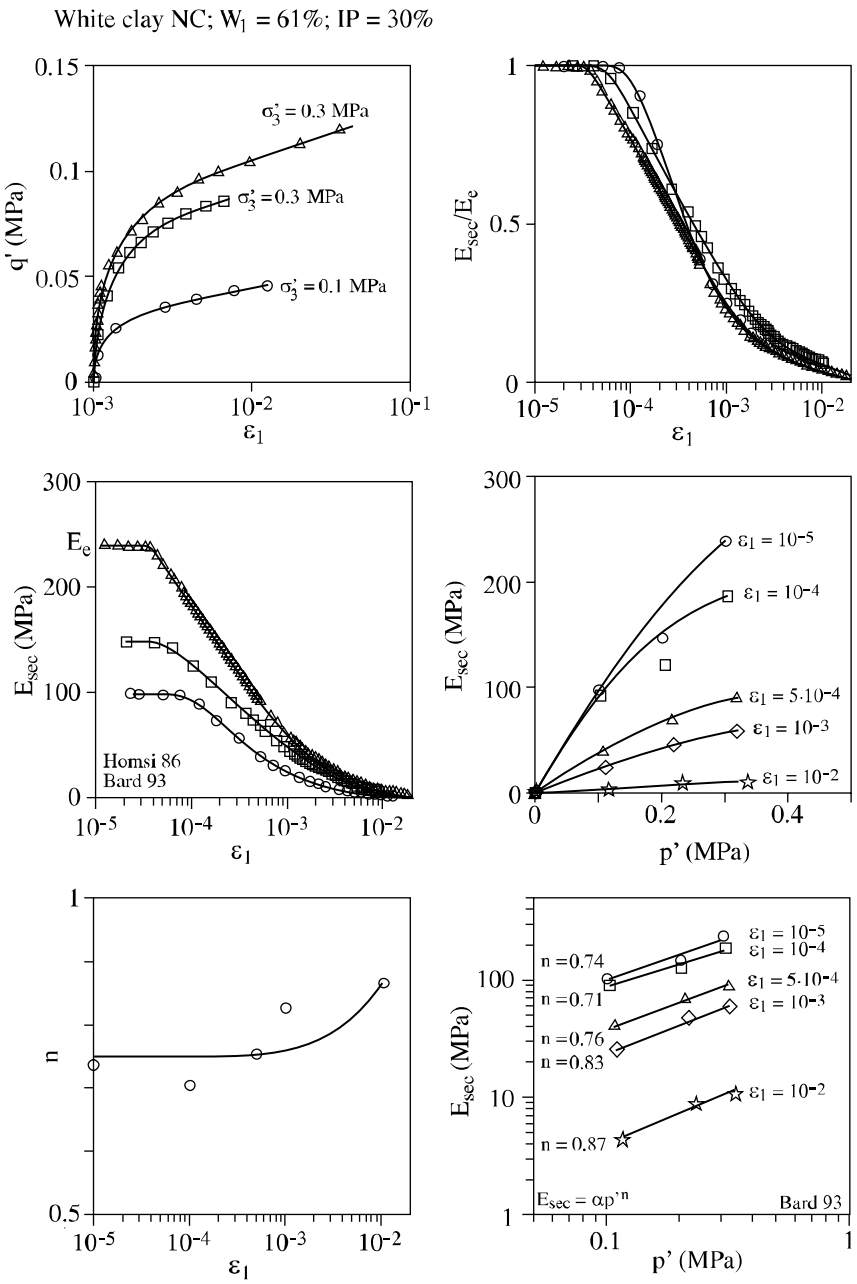

Figure 2.12. *Triaxial test with accurate strain measurement on normally consolidated clay*

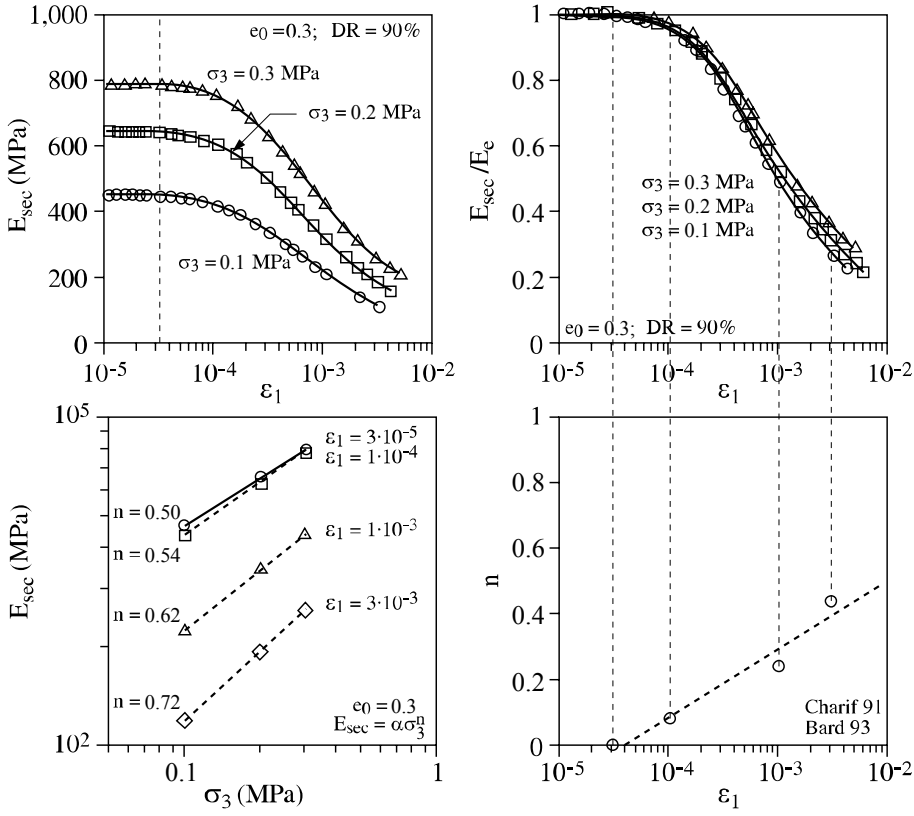

Figure 2.13. *Triaxial test with accurate strain measurement on dense sand*

The true elastic limit is thus a surface close to the hydrostatic axis in the principal stress space for an isotropic material, and therefore close to the p' axis in the p',q plane. The evolution of the secant modulus, for a given strain amplitude, is also a non-linear function of the mean stress, the coefficient of non-linearity n increasing from 0.5 at very small strains to 1 for $\varepsilon > 10^{-2}$. This last result is in agreement with the homothetic character of the q-ε curves, as presented in the previous section.

The discontinuous medium can be studied at different scales, more or less representative of the phenomena observed at the macroscopic scale, i.e. at the scale of the specimen, which corresponds to the equivalent continuous medium.

2.3.1. *Granular materials*

As for granular materials (sands, gravels, etc.), the representative scale appears to be that of the grain itself [DAR 95, HIC 98]. The relation between a discontinuous and an equivalent continuous medium can be established by trying to relate the parameters representative of the continuous medium behavior to the parameters representative of the grains. These latter can be divided into two groups:

– the mechanical properties of the grains and the local contact law. In most cases an elastic behavior can be retained for the grains;

– the geometrical conditions of the grain assembly. The geometry of the grains themselves can be defined by parameters representing the size, shape and grain size distribution, which can generally be considered as invariable. The geometry of the arrangement, which can vary, includes, on one hand, a parameter expressing the compacity (a scalar), and on the other hand, a parameter describing its anisotropy (a tensor).

The research for correlative links between the parameters of the continuous medium and those of the discontinuous medium has been the object of various studies in soil mechanics, and there are several expressions concerning the parameters used in foundation calculations in particular. As it is difficult to identify all the parameters of the grain geometry, the nature of the granular medium is often synthesized by a specific arrangement of the grains in response to suitable normalized tests. For sands and gravels, we use two specific void ratios called "maximal void ratio" e_{max} and "minimal void ratio" e_{min}. They give the interval of the natural void ratio variation for a given material. Their values depend on both the shape and surface roughness of the grains and on the grain size distribution.

Figure 2.14 gives an example of correlative links between the two nature parameters e_{max} and e_{min} and a mechanical property of the grain assembly, in this case the position of the perfect plasticity relation in the e, logp' plane. This approach can be extended to the determination of constitutive model parameters from correlations with parameters representative of the discontinuous granular medium [HIC 94]. These correlative links can give an initial set of parameters which is sufficiently precise so that it can be used as a starting point for an optimization procedure. This approach can be very useful in practical applications of a constitutive model in finite element calculations.

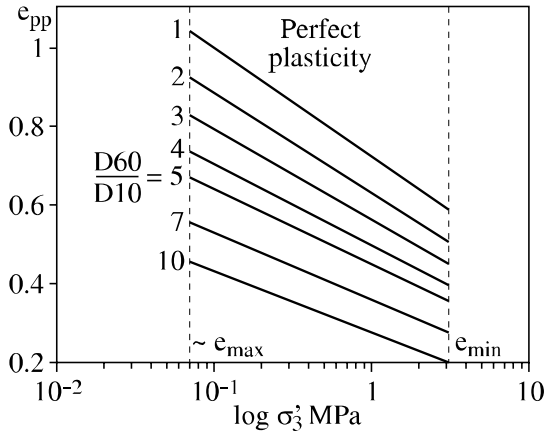

Figure 2.14. *Perfect plasticity relationship as a function of void ratios e_{max} and e_{min}*

2.3.2. *Remolded clayey materials*

The representative scale of the constitutive elements which affect the mechanical behavior of the equivalent continuous medium is less evident in this case. Several scales coexist in a clayey material:

– the basic clay layer, basic element of a clay particle;

– the clay particle made up of an assembly of layers, usually by organized stacks;

– the aggregate made up of particles, whose size and internal arrangement depend on the history of the material. The size of the aggregates can be measured by sedimentation.

A research study has been undertaken to relate the mechanical behavior of saturated remolded clays to their structural organization [HIC 00]. Two clays were studied: a kaolinite and a bentonite. The evolution of the shape, size, concentration and orientation of the elements which constitute the clay structure was examined by means of scanning and transmission electron microscopes, thanks to techniques which obviate possible disturbances of the micro-structure during observation. The results of this study show the main role played by the aggregates, similar to the role played by the grains in the mechanical behavior of granular materials. This explains the similar behavior of the equivalent continuous medium for the different nature of the constituents, as seen in the previous section. The difference in nature between grains and aggregates is however insufficient to explain quantitative differences in the stress-strain relationship. In particular, the deformability of the aggregates can play an important role. This deformability depends on the way the clay particles are

assembled, which is dependent on the mineralogy, adsorbed ions, etc. Photographs in Figures 2.15 and 2.16 show two different examples: the kaolinite is made of rigid small particles assembled in compact stacks; on the other hand, the bentonite is made of larger, more flexible particles creating less compact and therefore more deformable aggregates.

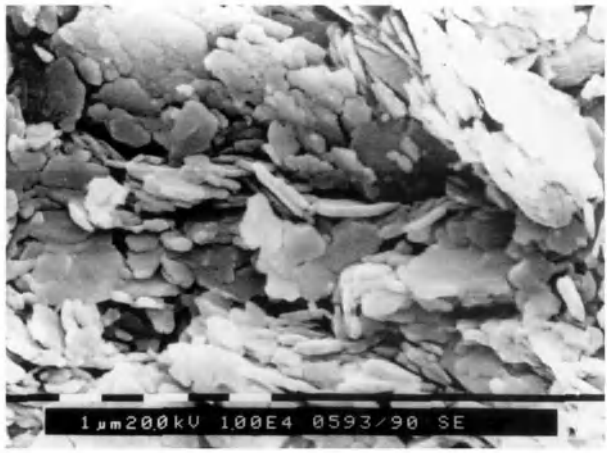

Figure 2.15. *SEM photos of Kaolinite P300*

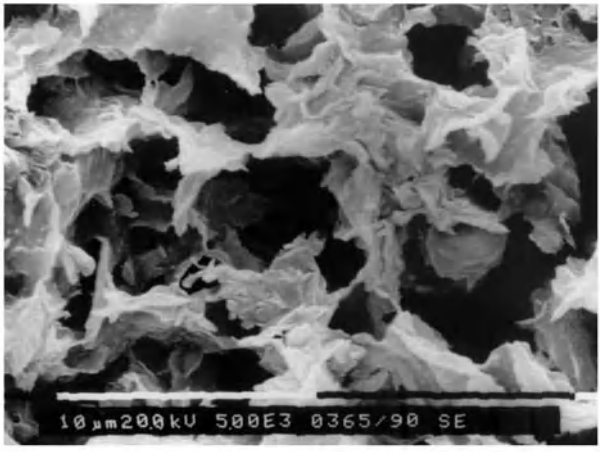

Figure 2.16. *SEM photos of Bentonite*

This study also showed significant evolution of the aggregate sizes during mechanical loading. As progressive division of the aggregates into smaller elements takes place, the bigger aggregates are the first to be affected by this breakage. This phenomenon induces a reduction in size of the elements which constitute the clayey material and also reduces the pore size. As long as the amount of breakage remains small, the mechanical properties of a normally consolidated clay can be considered as homothetic to the mean stress, as seen previously. It is no longer the case when the ruptures increase for high stresses. We can thus see an increase of the deformability under deviatoric stresses, as in the case of sands and gravels [BIA 94, BIA 97].

The links between the characteristics of the discontinuous medium and the parameters of the equivalent continuous medium are more difficult to define for clays rather than for sands. We can use, for example, two specific values of density called Atterberg's limits which are expressed in terms of water content w_l and w_p, obtained as for e_{max} and e_{min} using normalized tests. These two parameters are mainly dependent on the mineralogy of the constituents and adsorbed ions, and therefore on the particle arrangement, size and shape of the aggregates. Figure 2.17 presents an example of a link between the liquid limit w_l and the compressibility of clayey materials. It is also possible to obtain a correlation between Atterberg's limits and the perfect plasticity line in the e, logp' plane (Figure 2.18). In this last case, a similar correlation as that proposed for sands is obtained by substituting w_l and w_p to e_{max} and e_{min}.

The influence of the aggregate deformability is particularly pronounced on the elastic properties of clayey materials, since the elastic domain is restricted to very small strains (< 10-5), for which the relative displacements of the constituents are negligible. The deformation of the equivalent continuous medium is, therefore, mainly due to the deformation of the discontinuous medium constituents (Hertz's law). In these conditions the elastic moduli measured in sands and gravels are much higher than in clays. For clays, the more rigid aggregates of a kaolinite give elastic moduli higher than those of a bentonite (Figure 2.19 [LIU 99]).

The influence of the significant deformability of bentonite aggregates can also be seen at larger deformations, for example on the isotropic compressibility curve whose slope is much higher than the kaolinite one. Its value for the kaolinite is close to that obtained for sands, corresponding to a high rigidity of the aggregates which causes them to behave more like sand grains. In this last case, the major deformation mechanisms of the continuous medium are due to relative displacements of grains or aggregates.

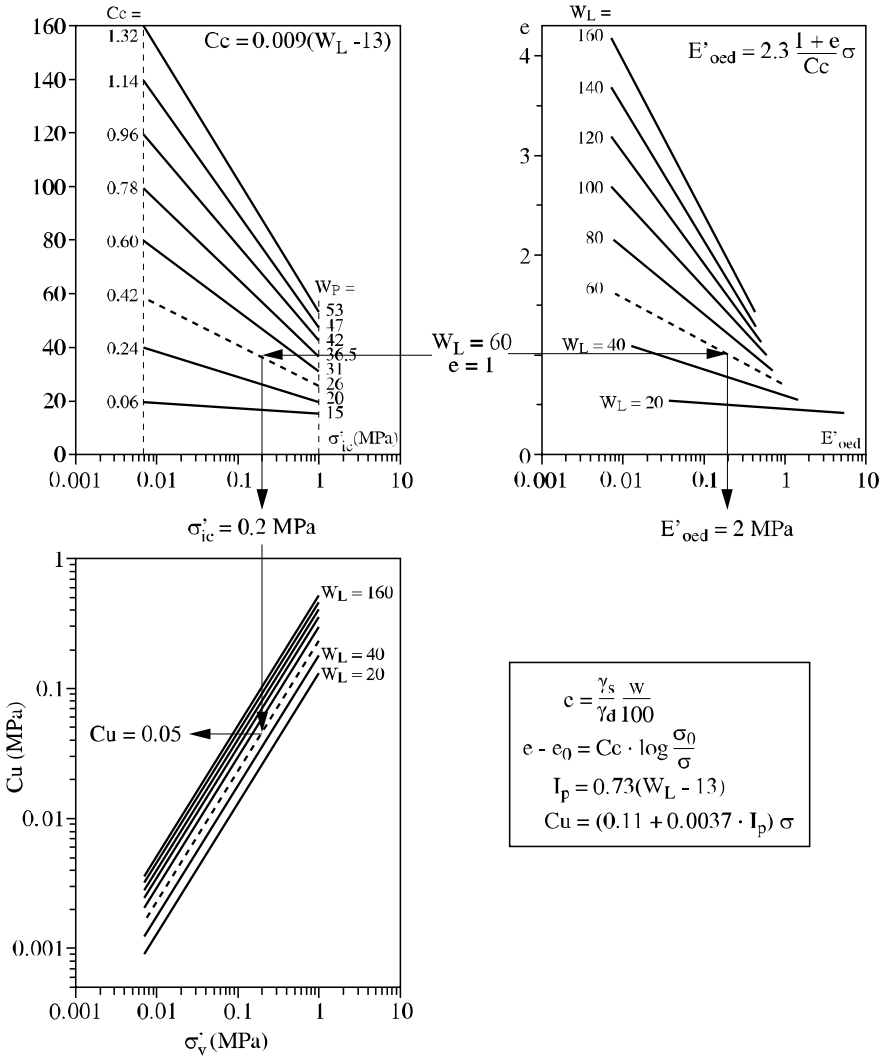

Figure 2.17. *Mechanical properties of normally consolidated clays correlated to Atterberg's limits*

2.3.3. *Granular materials with intergranular glue*

The previous results correspond to materials for which the contact law between two grains is reduced to solid friction. If two grains in contact are also "glued", the change in the contact law also produces a change in the mechanical properties of the

equivalent continuous medium. Its overall behavior depends on the glue behavior. The main visible change in the material behavior is the fact that the maximum strength envelope does not intercept the origin of the axes and that the material exhibits a non-zero strength in traction: this is usually expressed by the term "cohesion". However, the role of the intergranular glue cannot be reduced to a scalar representing this cohesion, experimental results show that the whole stress-strain relationship is affected by the glue properties. For example, in unsaturated granular materials, the capillary forces act as a glue with negligible stiffness. Therefore, the material will have a non-linear elastic behavior with a dependency on the mean stress. On the other hand, if the glue has a stiffness similar to that of the grains, there is a significant decrease of the role of mean stress on the elastic properties. At the same time, the force necessary to displace two grains in contact is proportional to the normal force in the case of a simple solid friction. If the two grains are glued, we have to add the strength of the glue; if this strength is constant, the role of the friction is negligible on the condition that the normal force is small and becomes preponderant at elevated normal forces. For the equivalent continuous material, this implies that its behavior is strongly dependant on the glue properties at small mean stresses, when c >> Mp', and much less at high mean stresses when c << Mp'. A progressive damage of the glue during a mechanical loading can modify the relative influence of the cohesion and friction. The two following examples illustrate these different aspects of the intergranular glue influence.

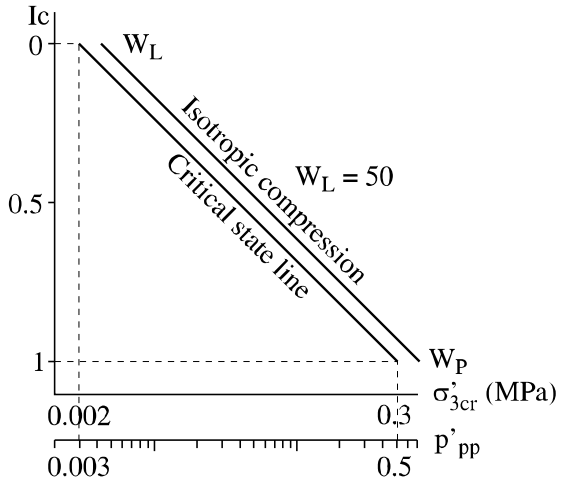

Figure 2.18. *Perfect plasticity relationship as a function of Atterberg's limits*

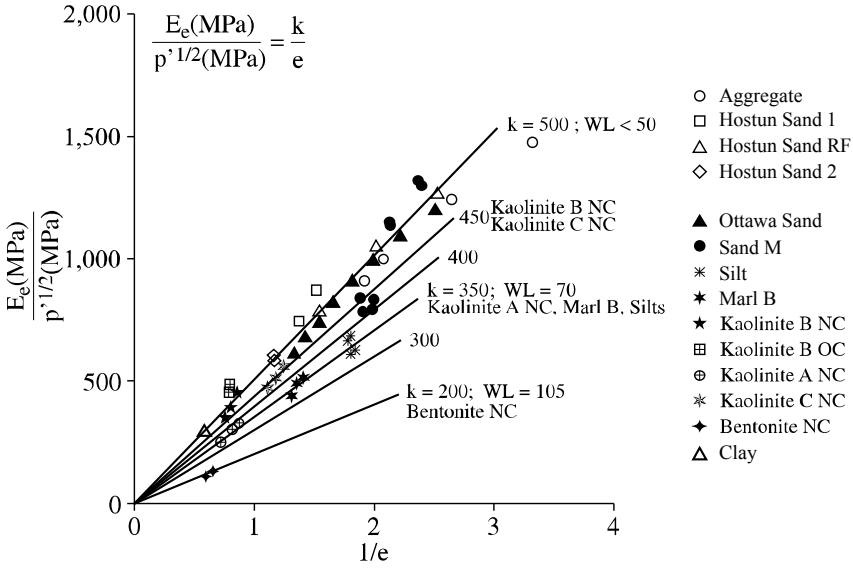

Figure 2.19. *Influence of soil nature on the elastic modulus*

The first example corresponds to experimental results obtained on sands injected by different grouts [TAI 98]. Each grout creates a specific type of glue between the grains. The mechanical strength of the injected sand is higher than that of the natural sand at the same confining stress. The maximum strength envelope in the p',q plane is a line that has the same slope as that of the natural sand, but translated from q_0 or c, which represents the cohesion due to the glue (Figure 2.20). The beginning of the stress-strain curves are almost independent of the mean stress, which corresponds to a constant stiffness. Afterwards, the curves become different when the dilatancy begins. Traction causes damage to the glue, which creates cracks inside the specimen with a frictional effect and, therefore, an influence of the mean stress.

The second example corresponds to the behavior of a bituminous concrete [BAR 93]. Here, the bitumen plays the role of the glue. It corresponds to a more ductile and, at the same time, viscous material, which transmits to the equivalent continuous material its viscous properties. As in the previous example, the stress-strain curves are almost independent of the mean stress for small deformations, which gives almost constant secant moduli for $\varepsilon < 10^{-2}$ (Figure 2.21). The maximum strength depends on the strain rate due to the viscous properties of the bitumen. At small strain rates, the maximum strength envelope is a straight line in the σ_3, qmax plane. The slope decreases with the strain rate increase. For high strain rates, the envelope is almost horizontal in that plane, which corresponds to a maximum strength independent of the mean stress. The increase of the strain rate increases the rigidity

of the glue, which, as a consequence, increases the cohesion and decreases the friction angle of the bituminous concrete. The peaks observed on the $q(\varepsilon_1)$ curves correspond to damage to the glue by traction when the granular material becomes dilatant. This damage is more accentuated at elevated strain rates because the bitumen becomes more rigid and less ductile. Cracks develop in bituminous concrete which behaves similarly to granular material without bitumen at large strains.

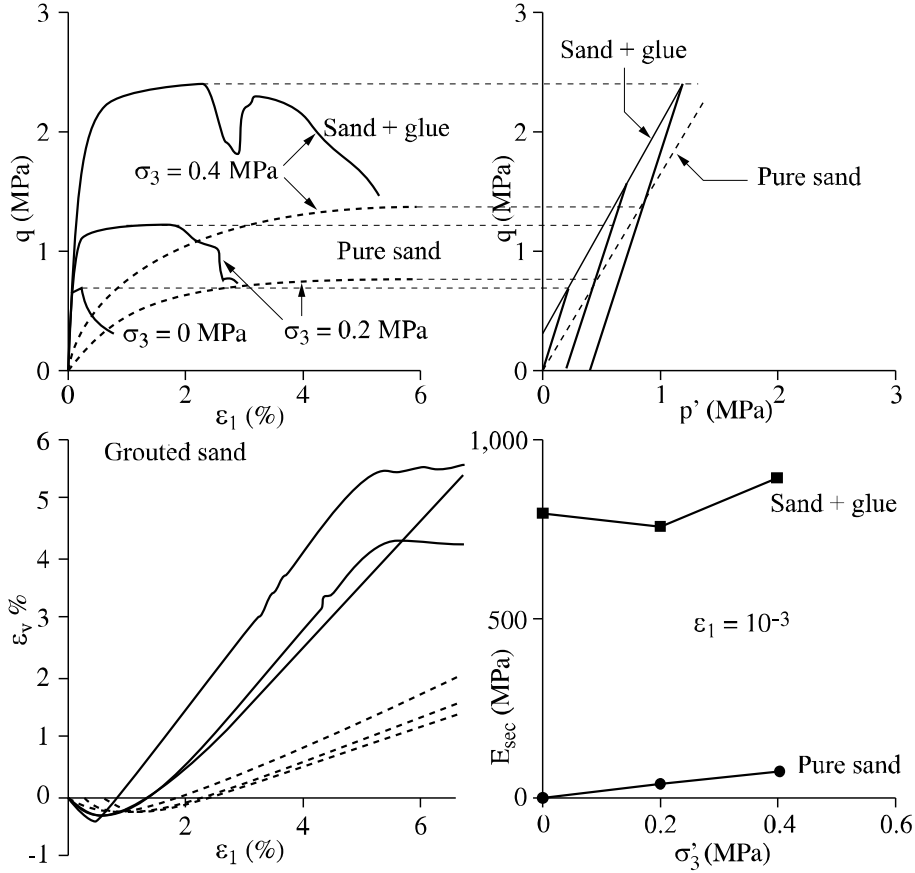

Figure 2.20. *Triaxial tests on grouted sand*

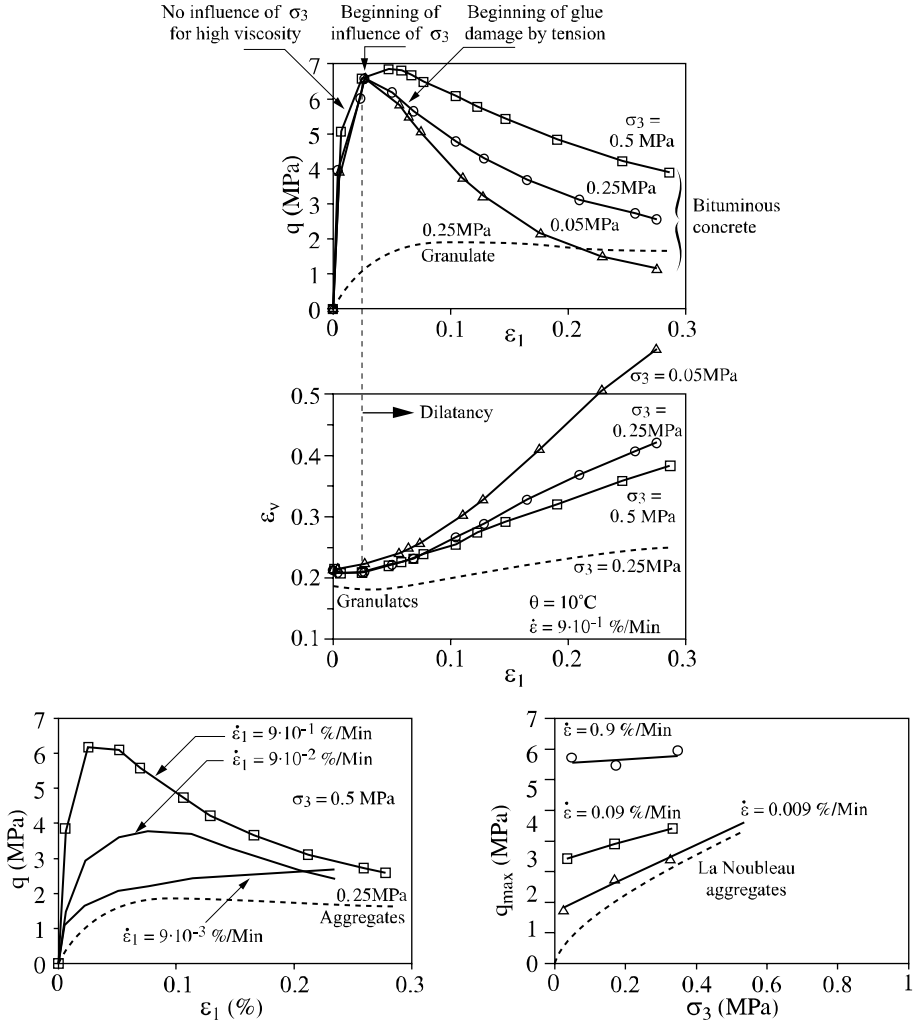

If the strain rate within the bituminous concrete is large, the cohesion C is large and the role of σ_3 is reduced

Figure 2.21. *Triaxial tests on bituminous concrete*

2.4. Natural soils

The geological history of sedimentary depositions has a significant impact on mechanical properties, in particular the maximum stress state borne by the material during its history, called the consolidation stress. We can roughly distinguish two large families: recent soils, which have been deposited since the last Ice Age and

which are normally or slightly overconsolidated; older soils, which are often strongly overconsolidated, at least in the superficial layers. Their mode of deposition as well as their evolution with time produces specific characteristics, which cannot be found in laboratory prepared soils, such as those examined above. First of all, their structure or the geometry of their particle arrangement is usually anisotropic due to their deposition in the gravity field. This creates mechanical properties higher in the vertical rather than the horizontal directions. This aspect will not be studied here. Another important characteristic is the existence of an intergranular "glue", mainly due to physicochemical evolutions at the particle contacts. The influence of this glue can be found in the mechanical properties of the equivalent continuous medium. It can significantly increase the initial stiffness as well as its maximum strength. Figure 2.22 presents an example of the behavior of a recent natural clay during oedometric and triaxial loading. We can see during the oedometric test a small deformability of the specimen at the beginning of the loading, which then increases strongly before decreasing again at elevated stresses. The correlations presented in the previous section and obtained from remolded clays are particularly helpful in explaining this peculiar behavior. We observe that the initial void ratio is higher than that expected from the correlations for a clay having a liquid limit w_l = 117%. The sudden strain increase allows it to progressively meet the compression curve corresponding to this liquid limit value and therefore to reach a traditional normally consolidated behavior. The material's initial behavior having been influenced by an intergranular glue which took place early in the history of the creation of the clay layer and, by reinforcement of the clay structure, led to a natural void ratio higher than that which would have been obtained for a material without this internal cohesion in the same consolidation conditions. This cohesion becomes progressively destroyed during the oedometric loading and the stress-strain relationship evolves to reach that corresponding to a material without cohesion.

Triaxial tests allow us to measure the effects of this intergranular glue on the material considered as the equivalent continuous medium. The post peak behavior corresponds to the destruction of the glue during a deviatoric loading. The stress-strain curves after the peak converge towards an envelope of maximum strength without cohesion identical to that obtained on the same remolded clay. However, we have to be careful in interpreting the post peak curves, since they are often the consequence of strain localization in shear bands inside the specimens.

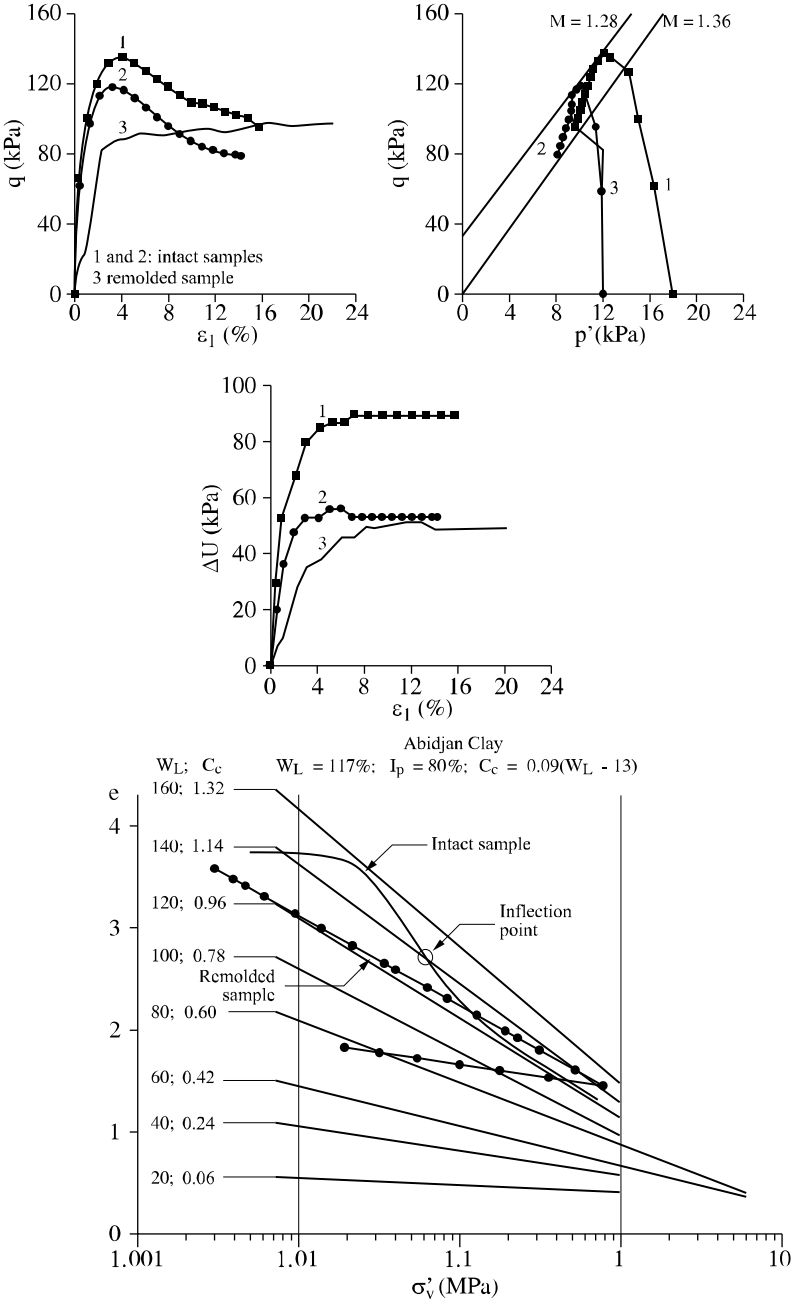

Figure 2.22. *Oedometric and triaxial tests on recently deposited intact and remolded clay*

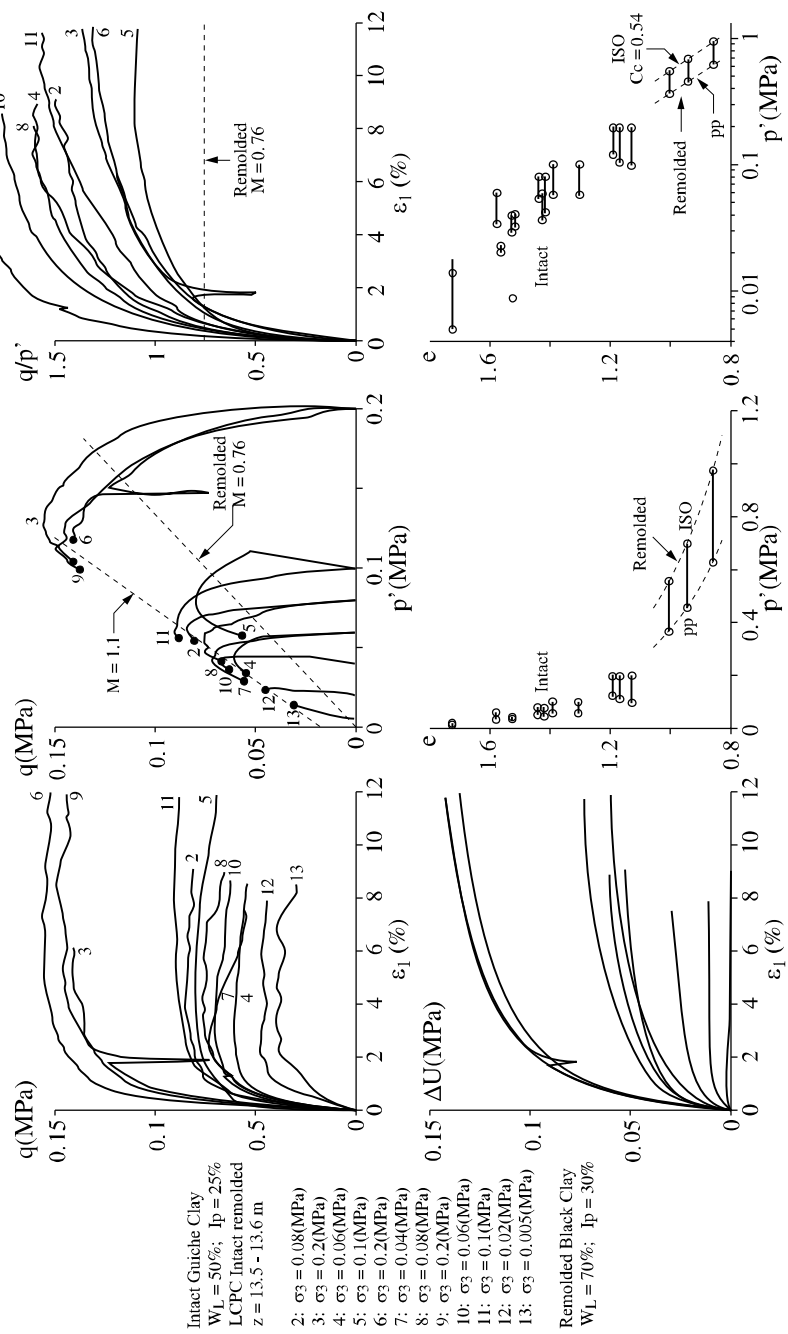

Figure 2.23. *Triaxial tests on recently deposited clay (Guiche Clay) [FAY 00]*

Generally, natural soils will present a higher mechanical strength than remolded soils, as confirmed by Figure 2.23 where several results obtained on a post last Ice Age clay are presented together with results on a remolded clay having similar mineralogical properties. The maximum strength envelopes are two straight lines on the p'-q plane with almost the same slope. The envelope corresponding to the intact clay is located above, the distance between the two lines $q_0 = 0.04$ Mpa represents the macroscopic cohesion of the intact clay. Sometimes, the intergranular glue is ductile enough to sustain macroscopic deformations of several percentage points. In these conditions, the maximum strength can remain constant after reaching the peak, which creates the equivalent of a perfectly plastic state for a cohesive material.

This intergranular glue is present in almost all the natural clayey soils and also, only less frequently, in sandy soils, especially in ancient deposits. Its importance is weak for "young" materials, such as the previous example. It can be significantly higher in "older" clays, in particular if they have been subjected to high consolidation. Figure 2.24 presents an example of the behavior of a deep clay (layer located at 400 m depth), with an initial void ratio $e_0 = 0.34$ and 20% of $CaCO_3$. Oedometric and triaxial tests were performed on both intact and remolded specimens at the same void ratio. The remolded samples were prepared by one dimensional consolidation from a powder obtained by the desegregation of natural samples (HEI 95]. The stiffness of the aggregates being much higher than that of the glue, only the intergranular glue was affected by the remolding. Analyses by means of scanning electron microscope and mercury porosimetry confirmed this hypothesis. The triaxial tests demonstrate that the natural clay samples have a much higher initial stiffness compared to the remolded ones, as well as a more fragile behavior with strain localization starting as early as with 1% axial deformation. The oedometer tests show an elevated consolidation stress for both materials. After this consolidation stress, the remolded clay follows a stress-strain relationship in accordance with the normally consolidated behavior as presented in Figure 2.17, while the natural clay has a steeper consolidation slope which corresponds, as in the previous example, to the progressive rupture of the intergranular glue. Its higher resistance in this case leads to a slower evolution: we cannot see a brusque change in the stress-strain relationship but a more gentle increase of the slope in the e, logσ'v plane.

In the case of overconsolidated clays, this internal cohesion will superimpose its effect on the overconsolidated one. A typical example is the London Clay which has been widely studied, in particular by Bishop *et al.* [BIS 65]. Between 20 m and 40 m depth in the clay layer, the liquid limit varies between 65% and 70%, and the plastic limit between 25% and 30%. The clay layer was subjected to an unloading corresponding to an erosion of 360 m of superficial sedimentary deposits. The maximum strength envelope from drained and undrained tests is represented by a curve with very little dispersion (Figure 2.25). Its shape is similar to that obtained

with a remolded clay having the same mineralogical properties (Figure 2.26), but its position is located above due to the effect of the intergranular glue. For remolded clays, the junction between this envelope and the straight line q = Mp' obtained for normally consolidated states corresponds to an overconsolidation ratio close to 2. For the London Clay, this junction is delayed: it occurs for a mean stress higher than the consolidation stress and can be associated with the creation of a damage of the intergranular glue during the initial isotropic loading.

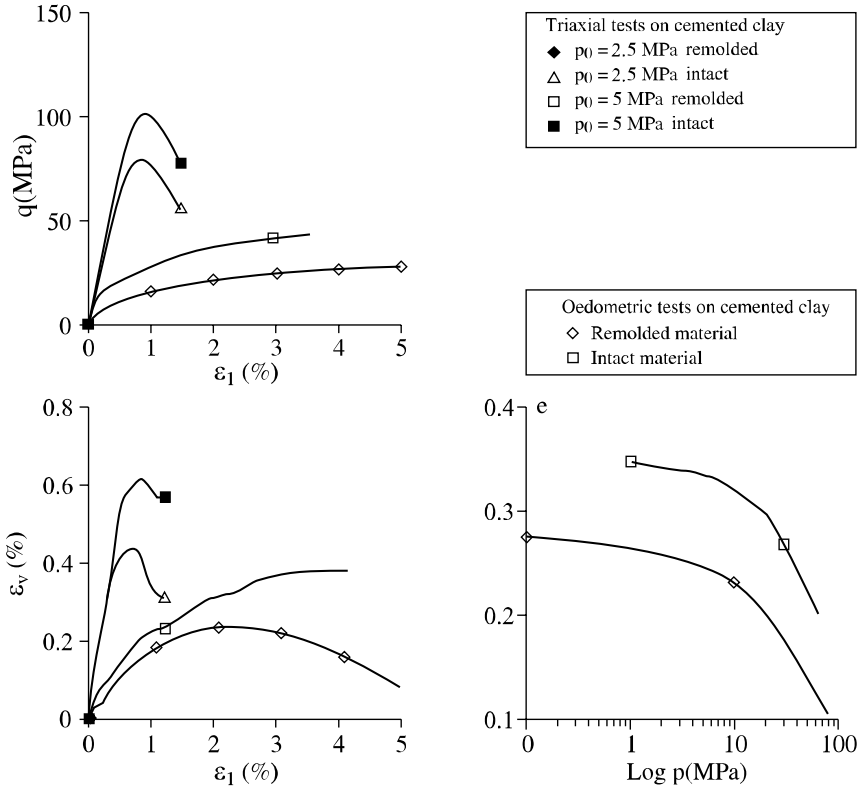

Figure 2.24. *Oedometric and triaxial tests on strongly overconsolidated clay*

As glue damage also occurs during a deviatoric loading, we can assume that the position of the maximum strength envelope depends on the role of overconsolidation, of the intergranular glue, and of its damage evolution during loading.

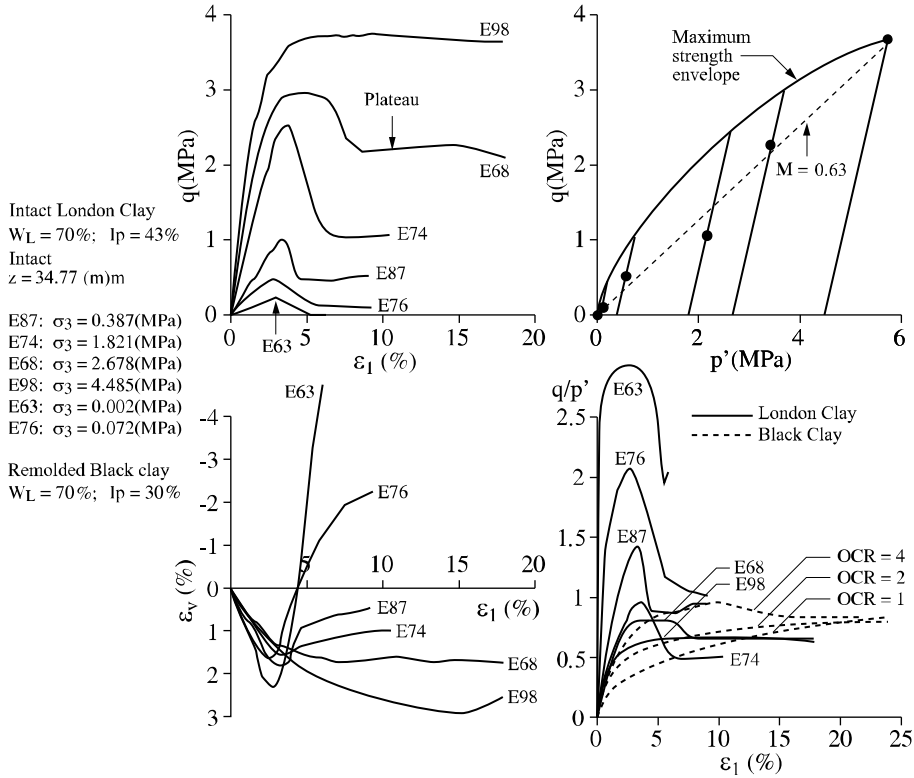

Figure 2.25. *Drained triaxial tests on the London Clay*

This damage can take place *in situ* when the decompression of a highly overconsolidated clay creates, in the upper part of the layer, vertical stresses sufficiently smaller than the horizontal stresses in order to reach the maximum strength envelope. Under theses conditions, cracks develop inside the clay layer. Afterwards, the influence of climatic changes and the circulation of water inside the cracks provoke, in the upper part of the clay layer, a physicochemical alteration, often characterized by an increase of Atterberg's limits. These phenomena increase the void ratio. For this type of material, we can schematically propose a profile with

a depth similar to that obtained on Cattenom Clay (Figure 2.27) for which oedometer tests show a vertical unloading higher than 5 Mpa:

– a first layer (1) of several meters in depth, with an increasing liquid limit wl, a decreasing density and mechanical properties also decreasing with very disperse values when we get closer to the surface;

– an intermediary layer (2) with almost constant values of wl and gd, but in which the unloading has created some fissuration;

– a third layer (3) with little disturbance from depths around 30 to 40 m.

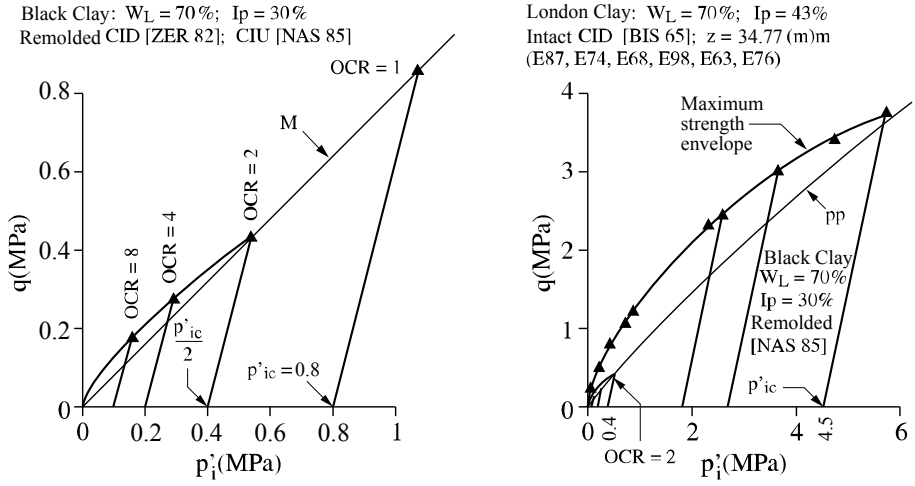

Figure 2.26. *Maximum strength envelopes for overconsolidated intact and remolded clay*

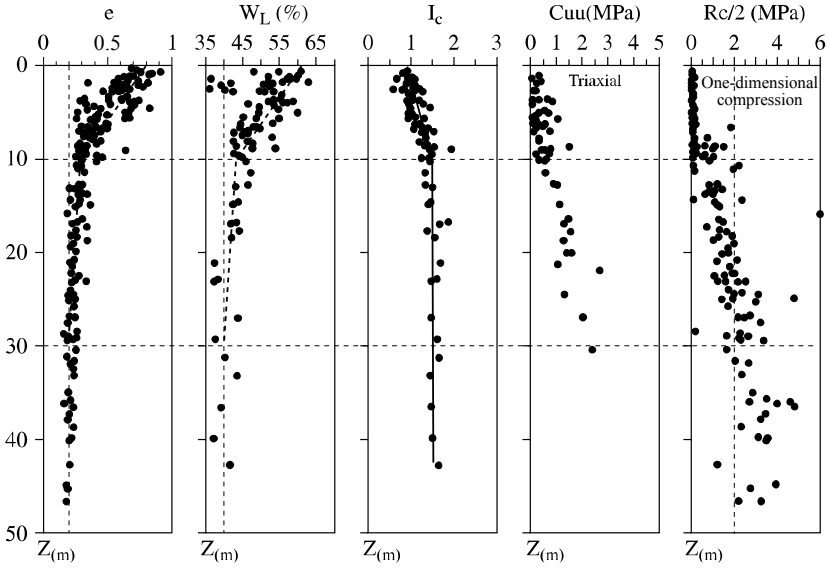

Figure 2.27. *Typical profile for a site made of strongly overconsolidated clayey soil*

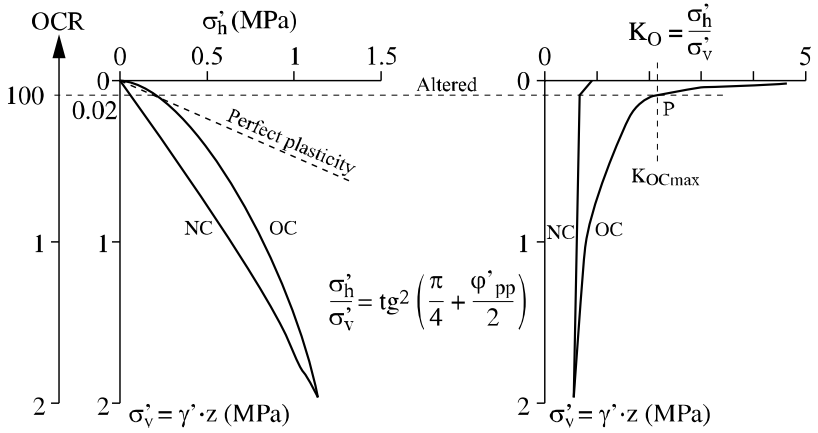

Figure 2.28. *Stress path during a geological unloading*

These mechanisms allow us also to explain the differences between the results obtained by Bishop *et al.* on the London Clay and those obtained by Josseaume [JOS 97] on the Flandrian Clay. These two clays, close in their mineralogy and geological histories, can be distinguished by the depth at which the tested samples were taken: 20 to 40 m for the London Clay, less than 10 m for the Flandrian Clay.

The latter is nowadays covered by a layer of silty sand, which prevents it being exposed at the surface as in the case of Cattenom Clay. It has not therefore been subjected to a physicochemical alteration and we can consider that it corresponds to a layer of type (2), while the London Clay, taken at greater depth, corresponds to a type (3) layer. This aspect affects the triaxial test results obtained for each material. The Flandrian Clay has lower as well as more scattered values of maximum strength, due to the fissuration induced by the decompression which helps the strain localization during the loading (Figure 2.29). The dispersion of the stiffness values measured for strains varying between 10^{-3} to 10^{-2} is less marked. This is due to the fact that the localization zones are not yet mobilized. It is therefore not always advisable to express the modulus as a function of the undrained shear resistance c_u.

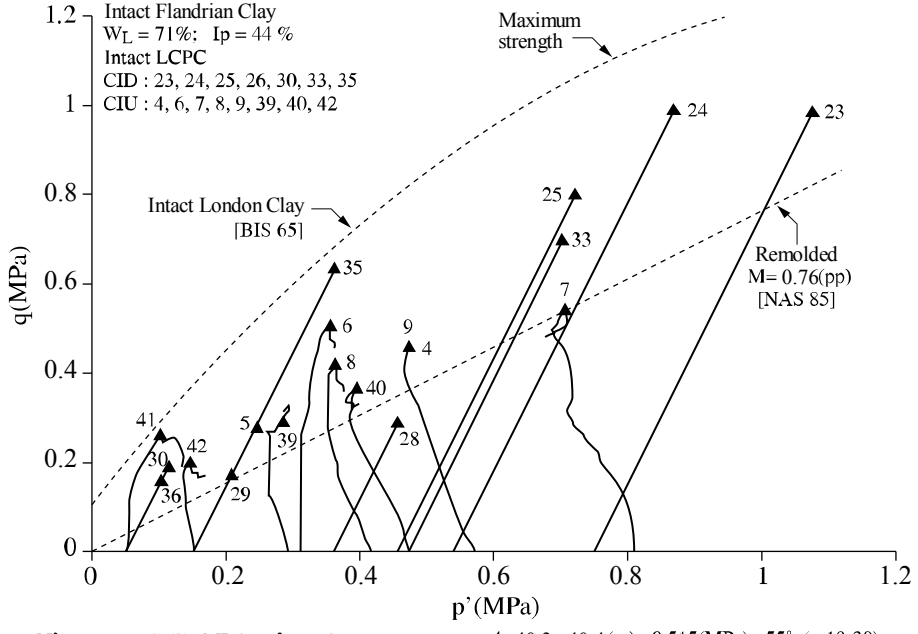

N°x: z(m); $\sigma'_3(0)$ (MPa); α°, (m10-x)
23: 41.4 - 41.5(m); 0.75(MPa); 55°, (m10-1)
24: 41.5 - 41.6(m); 0.54(MPa); 55°, (m10-2)
25: 41.6 - 41.7(m); 0.455(MPa); 41°, (m10-3)
26: 41.7 - 41.8(m); 0.36(MPa); 39°, (m10-4)
29: 41.8 - 41.9(m); 0.15(MPa); 58°, (m10-5)
30: 41.9 - 42(m); 0.05(MPa); 34°, (m10-6)
33: 42 - 42.1(m); 0.47(MPa); 62°, (m10-7)
35: 42.1 - 42.2(m); 0.15(MPa); 50°, (m10-8)
36: 42.2 - 42.3(m); 0.05(MPa); 57°, (m10-9)
4: 40.3 - 40.4(m); 0.515(MPa); 55°, (m10-20)
5: 40.4 - 40.5(m); 0.17(MPa); 30°, (m10-21)
6: 40.6 - 40.7(m); 0.308(MPa); 21°, (m10-22)
7: 40.2 - 40.3(m); 0.79(MPa); 26°, (m10-23)
8: 40.7 - 40.8(m); 0.41(MPa); 45°, (m10-24)
9: 40.9 - 41(m); 0.565(MPa); 20°, (m10-25)
39: 39.3 - 39.4(m); 0.3(MPa); 38°, (m10-26)
40: 39.4 - 39.5(m); 0.47(MPa); 52°, (m10-27)
41: 39.6 - 39.7(m); 0.05(MPa); 62°, (m10-28)
42: 39.5 - 39.6(m); 0.15(MPa); 18°, (m10-29)

Figure 2.29. *Drained and undrained triaxial tests on the Flandrian Clay*

The marine deposits usually contain a certain amount of $CaCO_3$, which plays an important role in the creation of the intergranular glue. We can see an example of this in Figure 2.30 where results of triaxial tests on four deep clay samples are presented, the percentage of $CaCO_3$ varying from 15% to 50% [HEI 95]. The test results clearly show that the macroscopic cohesion increases with the amount of $CaCO_3$ whose effect can be seen in the increase of the initial stiffness which increases from E = 740 MPa for $CaCO_3$ = 15% to E = 7900 MPa for $CaCO_3$ = 50%. This leads also to a strong increase of the maximum strength from 10 MPa ($CaCO_3$ = 15%) to 62 MPa ($CaCO_3$ = 50%) for a confining stress $\sigma'3 = 5$ MPa.

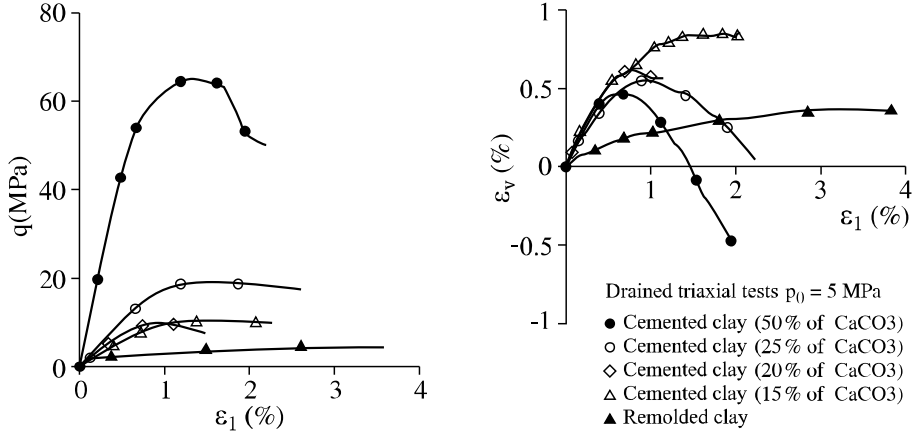

Figure 2.30. *Influence of calcium carbonate content on mechanical properties of a deep clay*

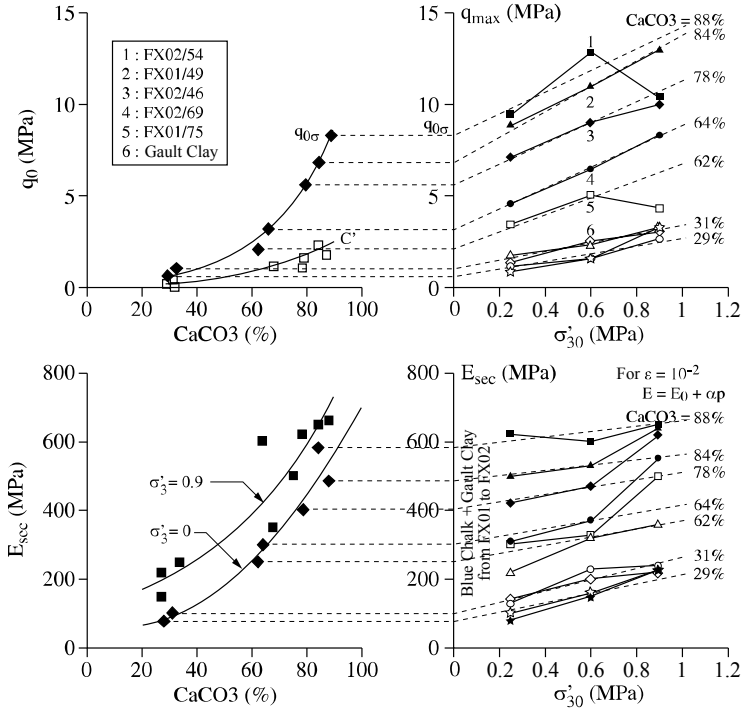

Figure 2.31. *Influence of calcium carbonate content on mechanical properties of clays and chalk at the Channel Tunnel site*

Similar results have been obtained on clay, marl and chalk at the site of the Channel Tunnel [FAY 00]. Along a depth of 100 m, we observe an increase of the $CaCO_3$ content from 10% in the first clay layer to 90% in the chalk. Triaxial tests on chalk show that maximum strength increases linearly with the confining stress p'_0 for a given $CaCO_3$ content: $qmax = q0 + \alpha p'_0$. q0 increases with the $CaCO_3$ content. The secant moduli, measured for $\varepsilon = 10\text{-}2$, also increase with the $CaCO_3$ content. These depend on the mean stress, but less and less with the increase of the $CaCO_3$ content in the investigated stress domain ($0.2<p'_0<1$MPa). These results clearly show the significant impact that cementation has on the chalk mechanical behavior.

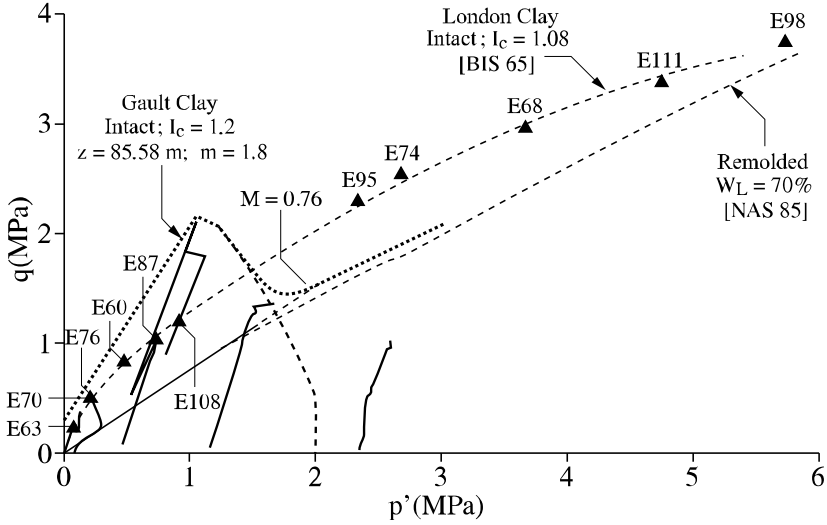

Figure 2.32. *Maximum strength envelope of the Gault Clay*

The results obtained on the Gault Clay, compared to those obtained on a remolded clay, confirm those obtained on the London Clay. The maximum strength of the Gault Clay is higher for p'_0, varying from 0.25 to 0.9 MPa (Figure 2.32). This is due to the fact that the Gault Clay is located deeper than the London Clay and that its consistency index Ic is bigger (1.2 instead of 1.08). However, the maximum stress envelope for the Gault Clay meets that corresponding to the remolded clay for p' = 3 MPa, compared to 6 MPa for the London Clay. This could be due to a higher overconsolidation which created weaker zones in the clay layer. The results obtained for elevated initial stresses show a decrease of the maximum strength. In Figure 2.33, we can see that the test performed at p'_0 = 2.5 MPa gives a stress-strain relationship identical to that obtained on a remolded normally consolidated clay. This phenomenon is usually observed in natural soils with internal cohesion when the strains induced by the loading are big enough to break the intergranular glue. As for maximum strength, the moduli measured in the Gault Clay are higher than those obtained for the London Clay. Their evolution shows a smaller dependency with mean stress, due to a stronger cementation of the Gault Clay. Figure 2.34 gathers secant modulus values obtained for $\varepsilon = 5\ 10^{-3}$ on different materials. Its shows the predominant influence of the intergranular glue on these values as well as the decrease of the mean stress influence when cohesion increases.

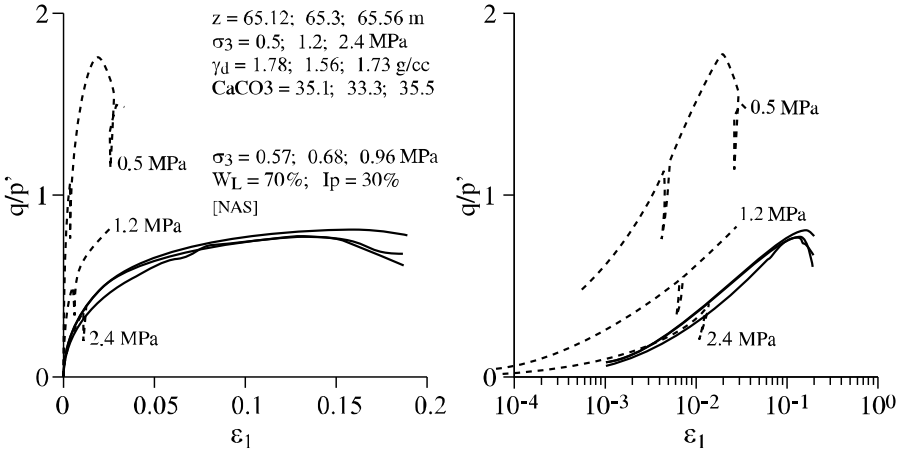

Figure 2.33. *Influence of mean stress on the Gault Clay behavior*

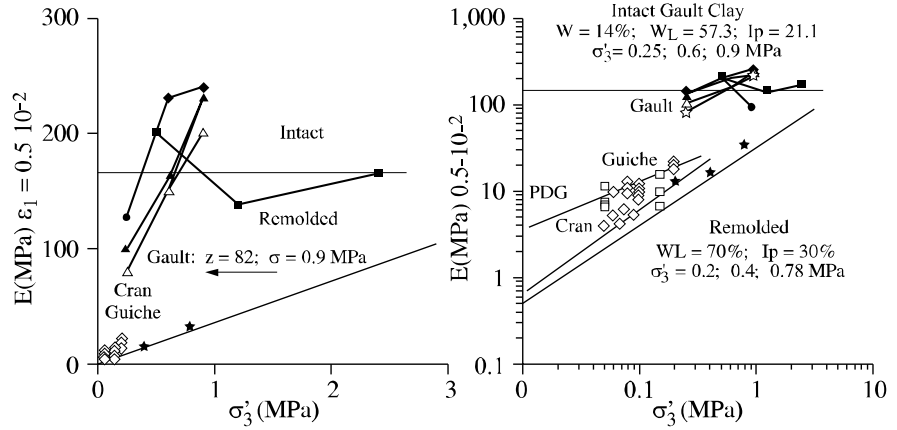

Figure 2.34. *Comparison of secant modulus values for different soils. A non-remolded soil has a secant modulus higher than a remolded one. Non-remolded soil modulus before peak is less dependent on mean stress*

For very high cohesion, this influence can even disappear completely as in the two examples presented in Figures 2.35 and 2.36 concerning Vosges sandstone [GUS 89] and a marble [WAW 70]. The stress-strain curves are similar for small mean stresses and then diverge for elevated mean stresses under the combined effect of damage, predominant under deviatoric stress at small mean stress, and plasticity. We have here results similar to those obtained on injected sands in section 2.2.

The pseudo-elastic limit defined in remolded soils has a different shape for natural clays. The shape depends on both the intergranular glue and the history of the *in situ* stresses, in particular the ratio $K_0 = \sigma'h/\sigma'v$. In the p',q plane, we can see that the axis of symmetry is no longer axis p' but is closer to the straight line with a slope equal to the *in situ* stress ratio $q/p' = 3(1-K_0)/(1+2K_0)$. Its determination can be achieved from several tests having different stress paths in the p',q plane. An example is given in Figure 2.37, concerning a post-last Ice Age clay, the Pornic Clay, which is lightly overconsolidated [MOU 88]. Each point of this pseudo-elastic limit corresponds to a threshold in the stress-strain curves, characteristic of a net increase of the plastic deformation amplitude (Figure 2.37). Similar results have been obtained by several other authors on slightly overconsolidated natural clays.

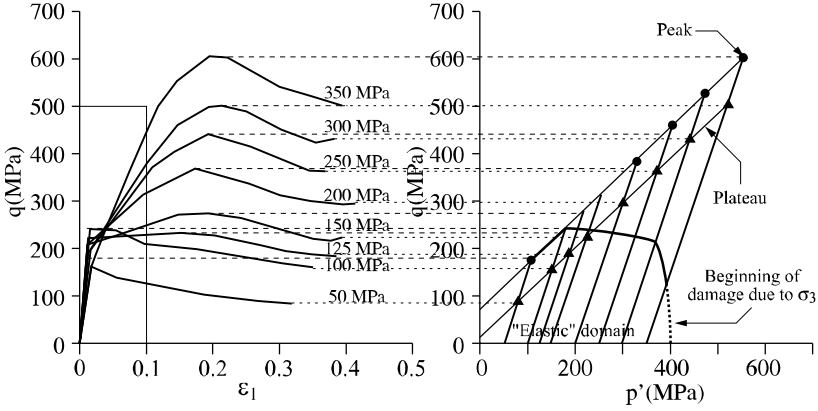

Figure 2.35. *Triaxial tests on red Vosges sandstone [GUS 89]*

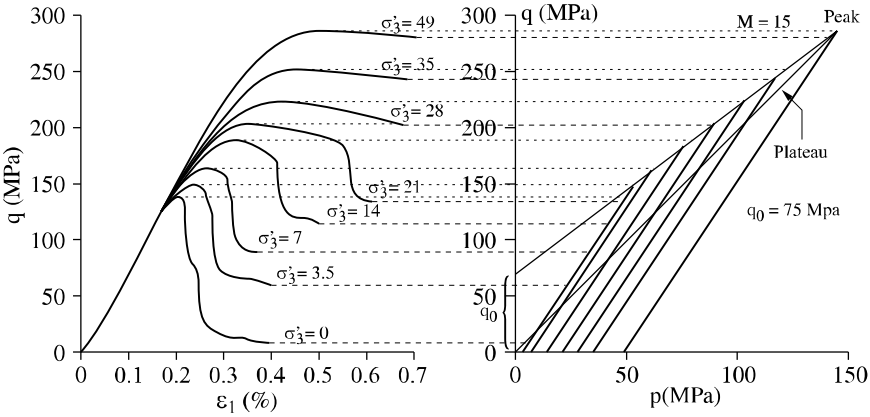

Figure 2.36. *Triaxial tests on Tenessee marble [WAW 70]*

The evolution of this pseudo-elastic limit by hardening is clearly established by its determination from different specimens of the same clay taken at different depths. In these conditions, the curves are homothetic with each other in the same ratio as the consolidation stresses (Figure 2.38). The evolution of this limit along stress paths different from those produced by oedometric consolidation remains to be understood.

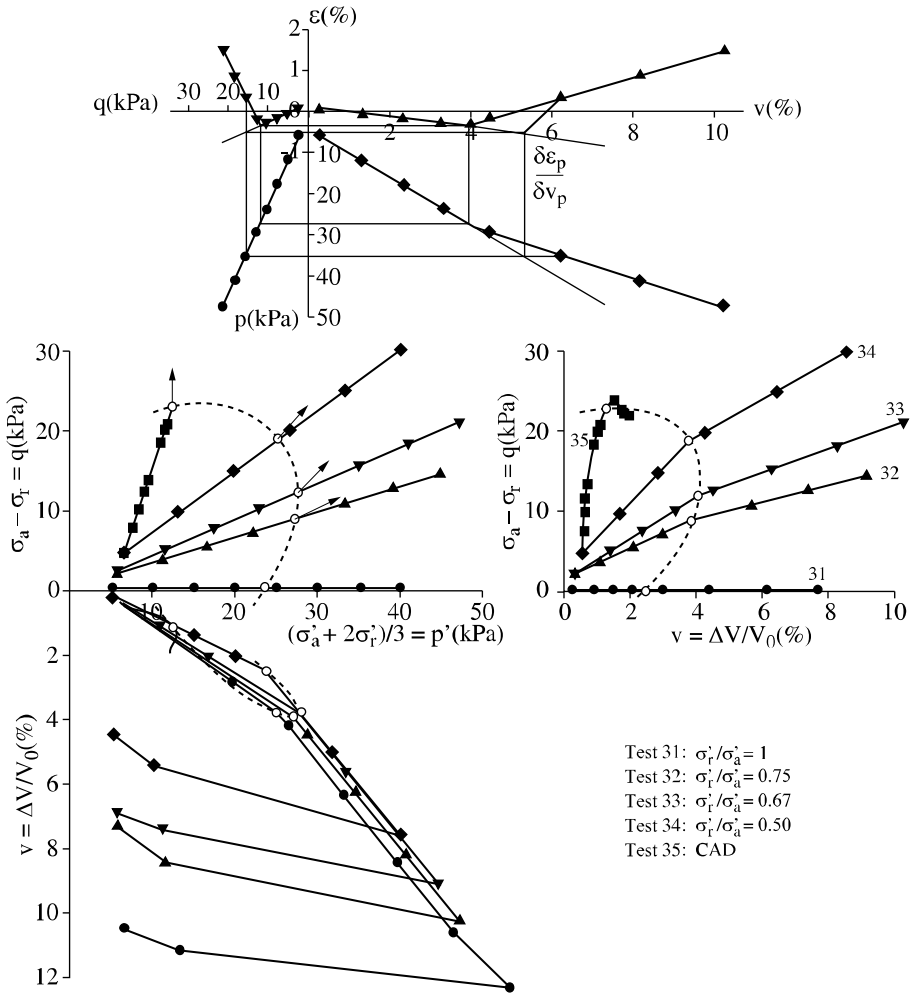

Figure 2.37. *Construction of the pseudo-elastic limit for a natural clay: the Pornic Clay [MOU 88]*

The existence of an intergranular glue induces a behavior of the equivalent continuous medium which is a function of the behavior of the glue itself. In several previous examples, its damage on various stress paths has been mentioned. High intensity isotropic or oedometric consolidation can produce a progressive homogenous breakage of the glue inside the specimen. The consequence is an increase, sometimes very accentuated, of the slope in the e – log(p') relationship. The damage material, when loaded afterwards along a deviatoric stress path, shows a significant decrease of the additional strength given by the intergranular glue and its behavior comes close to that of a remolded material having the same mineralogical characteristics (see for example the previous result obtained with the Gault Clay isotropically consolidated under an isotropic stress equal to 2.4 MPa). Damage can also occur during an oedometric unloading due to a strong increase of the ratio σ'_h/σ'_v when the overconsolidation ratio becomes very high. Under these conditions, cracks develop inside the material, as they do during a deviatoric triaxial test. They play a particularly marked role at small mean stresses. We can define a damage limit, corresponding to a given stress path to the beginning of the damage spread, which takes a specific shape such as that obtained for Vosges sandstone in Figure 2.35. The stress – strain relationship for the equivalent continuous medium after this damage limit depends on two types of mechanisms: relative displacements of the grains and damage of the intergranular glue. Constitutive models, coupling damage and plasticity, have been developed to take into account the simultaneous role of theses two mechanisms (see for example [CHA 98]).

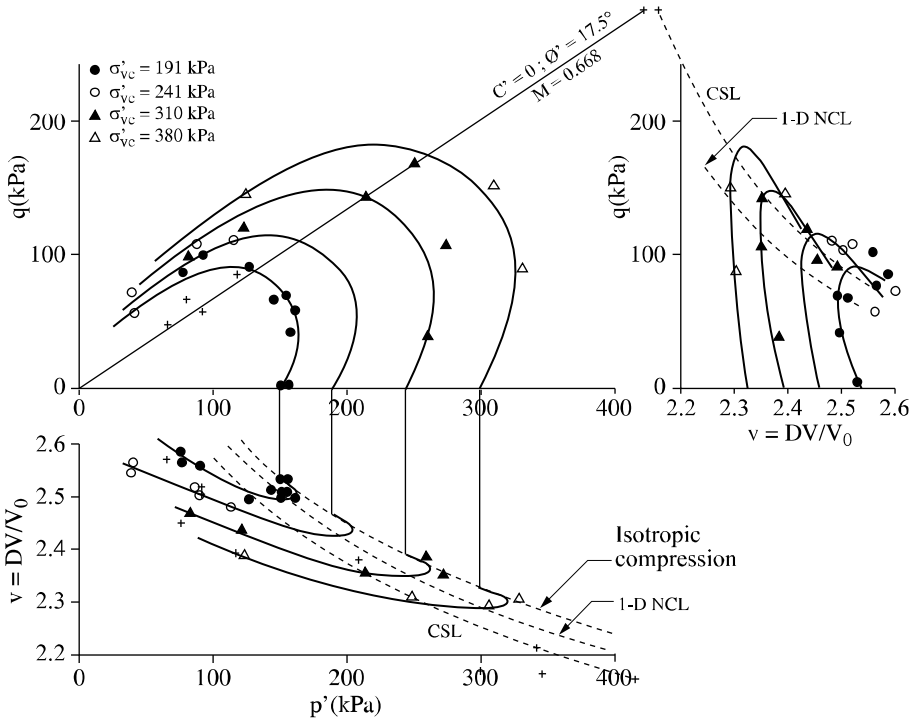

Figure 2.38. *Determination of the pseudo-elastic limit for different consolidation pressures [GRA 83]*

2.5. Conclusion

The mechanical behavior of remolded soils prepared in the laboratory show broad similarities between sandy and clayey materials. The analysis of the deformation mechanisms at the level of their structural constitutive elements enables us to explain these similarities and propose correlative relations between the parameters of the discontinuous medium and those of a constitutive model for the equivalent continuous medium. In sandy materials, the grain scale is the most appropriate; the mechanisms involved in the deformation of the continuous medium being essentially grain relative displacements. In the case of clayey materials, the appropriate scale is more difficult to estimate. We can assume that it corresponds to the aggregate scale for both natural and remolded clays, which explains the similarities observed with sandy materials. The differences between sand and remolded clay are mainly due to the deformability of the structural constituents, much larger for the aggregates than for the grains. The natural clay study showed the influence, sometimes very pronounced, of the intergranular glue, where nature and strength depend on the physicochemical and mechanical history of the soil. The intergranular glue can be taken into account in the constitutive model for the equivalent continuous medium. It is possible to model different behaviors for the glue, corresponding to different physical natures: fragile with damage, ductile, viscous, etc. The interest of this approach is to be able to take into account the different mechanisms which, at the scale of the discontinuous medium, influence the mechanical behavior of the equivalent continuous medium.

2.6. References

[BAR 93] E. BARD, "Comportement des matériaux granulaires secs et avec liant hydrocarboné", Doctoral thesis, Ecole Centrale de Paris.

[BIA 94] J. BIAREZ and P.-Y. HICHER, *Elementary Mechanics of Soil Behaviour: Saturated Remoulded Soils*, Balkema, 200 pp.

[BIA 97a] J. BIAREZ and P.-Y. HICHER "Influence de la granulométrie et de son évolution par ruptures de grains sur le comportement mécanique de matériaux granulaires", *Revue Française de Génie Civil*, vol. 1, no. 4, pp. 607-631.

[BIA 97b] J. BIAREZ, R. SAIM, S. TAIBI, H. LIU and B. RICHANE, "Analogie entre le comportement mécanique des sables et des argiles remaniées", *14th International Congress on Soil Mechanics and Geotechnics*, Hamburg, pp. 251-254.

[BIS 65] A.W. BISHOP, D.L. WEBB and P.I. LEWIN, "Undisturbed samples of London clay from Asford common shaft: Strength effective stress relationships", *Geotechnique*, vol. 15, no. 1, pp. 1-31.

[CHA 98] C. CHAZALLON and P.-Y. HICHER, "A constitutive model coupling elastoplasticity and damage for cohesive-frictional materials", *Mechanics of Cohesive-Frictional Materials*, vol. 3, pp. 41-63.

[DAR 95] F. DARVE, P.-Y. HICHER and J.M. REYNOUARD, *Les géomatériaux: théories, expériences et modèles*, Hermes, pp. 208.

[FAY 00] T. FAYAD, "Mécanique des grains avec et sans colle pour une comparaison avec des sols naturels et remaniés", Doctoral thesis, l'Ecole Centrale de Paris.

[GRA 83] J. GRAHAM, M.L. NOOMAN and K.V. LEW, "Yield states and stress-strain relationship in a natural plastic clay", *Can. Geotech. J.*, 20, pp. 502-516.

[GUS 89] J. GUSTKIEWICZ, "Synoptic view of mechanical behaviour of rock under triaxial compression", *Proc. Symp. Rock at Great Depth*, Pau (ed.), Balkema.

[HAR 72] B.O. HARDIN and V.P. DRNEVICH, "Shear modulus and damping in soil: design equations and curves", *J. SMFD. ASCE*, vol. 98; SM 6, pp. 667-692.

[HAT 95] M. HATTAB and P.-Y. HICHER, "Experimental study of the dilatancy in overconsolidated clay", *Int. Symp. on Compression and Consolidation on Clayed Soils*, Hiroshima.

[HEI 95] J.F. HEITZ, "Comportement des argiles profondes", ANTEA/BRGM report for ANDRA.

[HIC 85] P.-Y. HICHER, "Comportement mécanique des argiles saturées sur divers chemins de sollicitations monotones et cycliques. Application à une modélisation élastoplastique et viscoplastique", Doctoral thesis, Paris 6 University.

[HIC 94] P.-Y. HICHER and A. RAHMA, "Micro-macro correlations in granular media. Application to the modelling of sands", *European Journal of Mechanics – A:solids* 13, no. 6, pp.763-781.

[HIC 96] P.-Y. HICHER, "Elastic properties of soils", *Journal of Geotechnical Engineering*, ASCE, vol. 122, no. 8, pp. 641-648.

[HIC 98] P.-Y. HICHER, "Experimental behaviour of granular materials", in *Behaviour of Granular Materials*, B. Cambou (ed.), Springer-Wien New York, pp 1-97.

[HIC 00] P.-Y. HICHER, H. WAYUDI and D. TESSIER, "Microstructural analysis of inherent and induced anisotropy in clay", *Mechanics of Cohesive-frictional Materials*, vol. 5, pp. 341-371.

[HUJ 85] J.C. HUJEUX, "Une loi de comportement pour les chargements cycliques des sols", *Génie Parasismique*, Presses des Ponts et Chaussées, Paris, pp. 287-302.

[JOS 97] H. JOSSEAUME, "Propriétés mécaniques de l'argile des Flandres de Dunkerque à Calais", *Revue Française de Géotechnique*, no. 84.

[LIU 99] LIU HUA, "Étude des comportements de sols naturels et des sols reconstitués au laboratoire", Doctoral thesis, l'Ecole Centrale de Paris.

[MOU 88] G. MOULIN, "Etat limite d'une argile naturelle de Pornic", Doctoral thesis, Nantes University and ENSM.

[ROS 58] K.H. ROSCOE, A.N. SCHOFIELD and C.P. WROTH, “On the yielding of soils”, *Geotechnique*, 8:1, pp. 22-53.

[ROW 62] P.W. ROWE, “The stress dilatancy relations for static equilibrium of an assembly of particles in contact”, *Proc. Royal Society, London*, series A, vol. 269, pp. 500-527.

[TAI 98] S. TAILLIEZ, “Étude expérimentale du comportement mécanique des sols granulaires injectés”, Doctoral thesis, Ecole Centrale de Paris.

[WAW 70] WAWERSICK and FAIRHURST, “A study of brittle rock fracture in laboratory compression experiments”, *Int. J. Mech. Min. Sci.*, vol. 7, p. 561-575, Pergamon Press, 1970.

Constitutive Modeling of Soils and Rocks
Edited by Pierre-Yves Hicher & Jian-Fu Shao

Chapter 3

Elastoplastic Modeling of Soils: Monotonous Loadings

3.1. Introduction

A natural soil is a porous material made up of two phases: the solid phase, composed of mineral or organic particles, and the liquid phase. The effective stress principle formulated by Terzaghi allows for a satisfactory description of the behavior of both phases as well as their interaction. This description consists of the combination of Darcy's law ruling fluid flow across the solid skeleton, the continuity (or mass balance) equations of the phases, and the constitutive law of the solid skeleton, expressed by a relation between the effective stress and strain tensors.

The development of such a constitutive law for the solid skeleton is based on the theoretical concepts of continuum mechanics (elasticity, plasticity, viscosity and combinations) and on the results of experimental studies carried out in the laboratory or in the field. In practice, the complexity of the constitutive laws that can be developed depends very much on whether the aim is to describe precisely the whole range of results that can be obtained experimentally in the laboratory, or rather to build a robust tool, limited to the main features of soil behavior, but much easier to handle in practice for designing structures.

Constitutive laws can take very different forms, but elastoplasticity provides the most convenient and simple framework. The existence of a plateau on the stress-strain curve and the experimental observation that only one part of the strain is reversible, suggest that this framework should be used for constitutive modeling of

Chapter written by Philippe MESTAT, Emmanuel BOURGEOIS and Philippe REIFFSTECK.

soils. This approach proved to be extremely efficient; it was possible to build relatively satisfactory descriptions of the main features of the mechanical behavior of saturated soils subjected to monotonous loadings. In addition, this framework is well adapted to the introduction of constitutive models in computation software based on the finite element method. This made it possible to give quantitative results for a wide range of problems in geotechnical engineering, such as slope stability or the service and ultimate limit states of foundations, embankments, tunnels and retaining structures.

Elastoplastic constitutive models can be divided into three categories:

– models with no strain hardening, defined by a yield function, a plastic potential (with an associated or unassociated flow rule) and an elastic law that can be linear or non-linear;

– models with one plastic hardening mechanism and an elastic law that can be isotropic or anisotropic, linear or non-linear;

– models combining several plastic mechanisms and non-linear elasticity.

3.2. Elastoplasticity equations

3.2.1. *Basic concepts*

The fundamental elastoplastic model is characterized by the following basic concepts:

– the partition of strains, which splits the total strain tensor into the sum of the elastic strain tensor and the plastic strain tensor;

– the yield surface, which defines the boundary in the stress space beside which the behavior of a material becomes plastic (irreversible);

– the elastic domain, which is the domain of stress space interior to the yield surface; inside the elastic domain, strains remain reversible;

– the plastic flow rule, which describes the evolution of the plastic strains;

– the hardening represents the changes of the size and position of the yield surface in the stress space, depending on the applied loads;

– the plasticity criterion or failure criterion, that characterizes the stress states for which failure occurs, i.e. strains tend towards infinity. In the case of “perfect plasticity”, there is no hardening and no evolution of the yield surface, therefore the failure criterion is the same as the yield surface.

3.2.2. *Yield surface and elastic domain*

The elastic domain is defined in practice by a scalar function F of the stress tensor (σ_{ij}). F is called the yield function, and the sign defines the position of a given stress state with respect to the yield surface:

$F(\sigma_{ij}) < 0$ corresponds to the elastic domain;

$F(\sigma_{ij}) = 0$ defines the stress states located on the yield surface;

$F(\sigma_{ij}) > 0$ corresponds to stress states located outside the elastic domain.

In the case of perfect plasticity, neither the yield surface nor the elastic domain evolves. In the case of a strain hardening material, the elastic domain depends on additional variables describing the current hardening state, denoted by k and introduced in the expression of the yield function: $F(\sigma_{ij}, k)$. The hardening state variable k only changes if there is an evolution of the plastic strain tensor. The current yield surface is defined by the equation $F(\sigma_{ij}, k) = 0$. Several theories have been developed to describe the evolution of the hardening state. The two major theories are:

– the isotropic hardening theory developed by Taylor and Quincey, in which hardening is a function of one single scalar parameter (k), and the elastic domain is transformed homothetically with respect of the origin O of the stress space;

– the kinematic hardening theory, introduced by Prager, in which the successive positions of the yield surface are obtained by translating the initial boundary of the elastic domain in the stress space. In this context, it is necessary to introduce a tensorial variable to describe the hardening state: k becomes (k_{ij}).

We denote by (σ_{ij}, k) a stress and hardening state for a given loading step.

If this state is such that $F(\sigma_{ij}, k) < 0$, the stress tensor (σ_{ij}) is located inside the current elastic domain and the strain variation is reversible (elastic):

$$d\varepsilon_{ij} = d\varepsilon_{ij}^{e}$$

If, on the other hand $F(\sigma_{ij}, k) = 0$, stress tensor (σ_{ij}) belongs to the yield surface (i.e. the boundary of the elastic domain). In this case, the appropriate formulation of the equations describing strain evolution depends on whether the material point undergoes a loading process (the stress state moves towards the exterior of the elastic domain), or an unloading process (the stress state moves towards the inside of the yield surface).

The material point undergoes a loading process if and only if:

$$F(\sigma_{ij}, k) = dF(\sigma_{ij}, k) = 0$$

$$\frac{\partial F}{\partial \sigma_{ij}} d\sigma_{ij} > 0$$

$$d\varepsilon_{ij} = d\varepsilon_{ij}^{e} + d\varepsilon_{ij}^{p}$$

The material point undergoes an unloading process if and only if:

$$F(\sigma_{ij}, k) = 0$$

$$\frac{\partial F}{\partial \sigma_{ij}} d\sigma_{ij} < 0$$

$$d\varepsilon_{ij} = d\varepsilon_{ij}^{e}$$

(ε_{ij}^{p} are zero or remain constant)

(with the convention of implicit summation over repeated indices).

This makes it possible to know under what conditions plastic strains occur: it remains to be seen how they develop. The flow rule provides the necessary information to evaluate the plastic strain.

3.2.3. *Plastic flow rule*

The plastic flow rule gives the expression of the increment of plastic strain $(d\varepsilon_{ij}^{p})$ for a given state of stress (σ_{ij}) and a given stress increment ($d\sigma_{ij}$), and for the current value of the hardening variable (k), through the introduction of a new function denoted by G called "plastic potential", such that:

$$d\varepsilon_{ij}^{p} = d\lambda \frac{\partial G}{\partial \sigma_{ij}}$$

$d\lambda$ is a non-negative scalar, called a plastic multiplier. Note that generally G can be different from the yield function: if F and G are identical, the flow rule is said to be "associated"; if F and G are different, the flow rule is "unassociated".

In the case of strain hardening, it is convenient to introduce an additional scalar variable denoted by $H(\sigma_{ij}, k)$, called hardening modulus, and defined by:

$$H d\lambda = \frac{\partial F}{\partial \sigma_{ij}} d\sigma_{ij}$$

3.2.4. *Incremental relations for one plastic mechanism model*

The elastic strain increment $(d\varepsilon_{ij}^{e})$ and stress increment $(d\sigma_{ij})$ are related to each other by the elastic moduli tensor (E_{ijkl}), or its inverse (D_{ijkl}),

$$d\sigma_{ij} = E_{ijkl} d\varepsilon_{kl}^{e} \text{ or } d\varepsilon_{ij}^{e} = D_{ijkl} d\sigma_{kl}$$

If, moreover, (σ_{ij}, k) denotes the current stress and hardening state, located on the boundary of the current elastic domain, the following relationships hold:

$$F(\sigma_{ij}, k) = 0$$

$$d\varepsilon_{ij} = d\varepsilon_{ij}^{e} + d\varepsilon_{ij}^{p} = d\varepsilon_{ij}^{e} + \alpha\, d\lambda \frac{\partial G}{\partial \sigma_{ij}}$$

with $\alpha = 0$ in the case of unloading and $\alpha = 1$ in the case of loading.

In order to complete the formulation of the constitutive law, the value of the plastic multiplier remains to be discussed. This is given by the consistency condition $dF = 0$, which states that the stress state must remain on the yield surface when loading occurs $(F = 0)$. The consistency condition reads:

$$dF = \frac{\partial F}{\partial \sigma_{ij}} d\sigma_{ij} + \frac{\partial F}{\partial k} dk = 0$$

Eventually, the scalar variable k is, in turn, a function of the plastic strain (ε_{ij}^{p}). For instance, in the case of isotropic hardening, the model closure requires the definition of an appropriate hardening law such as:

$$k = k(\varepsilon_{ij}^{p})$$

The set of equations above makes it possible to calculate the hardening modulus H:

$$d\lambda\, H = \frac{\partial F}{\partial \sigma_{ij}} d\sigma_{ij} = -\frac{\partial F}{\partial k} dk = -\left(\frac{\partial F}{\partial k}\right)\left(\frac{\partial k}{\partial \varepsilon_{ij}^{p}}\right) d\varepsilon_{ij}^{p}$$

which yields, given the flow rule, if $d\lambda \neq 0$: $H = -\left(\frac{\partial F}{\partial k}\right)\left(\frac{\partial k}{\partial \varepsilon_{ij}^{p}}\right)\left(\frac{\partial G}{\partial \sigma_{ij}}\right)$.

The stress increment ($d\sigma_{ij}$) can therefore be expressed as:

$$d\sigma_{ij} = E_{ijkl} d\varepsilon^{e}_{kl} = E_{ijkl}(d\varepsilon_{kl} - d\varepsilon^{p}_{kl}) = E_{ijkl}(d\varepsilon_{kl} - d\lambda \frac{\partial G}{\partial \sigma_{kl}})$$

Multiplying each member of this equation by $\left(\frac{\partial F}{\partial \sigma_{ij}}\right)$, we obtain:

$$\left(\frac{\partial F}{\partial \sigma_{ij}}\right) d\sigma_{ij} = \left(\frac{\partial F}{\partial \sigma_{ij}}\right) E_{ijkl} d\varepsilon_{kl} - d\lambda \left(\frac{\partial F}{\partial \sigma_{ij}}\right) E_{ijkl} \left(\frac{\partial G}{\partial \sigma_{kl}}\right) = d\lambda \, H$$

and the plastic multiplier is thus given by: $d\lambda = \dfrac{\dfrac{\partial F}{\partial \sigma_{ij}} E_{ijkl} d\varepsilon_{kl}}{H + \dfrac{\partial F}{\partial \sigma_{ij}} E_{ijkl} \dfrac{\partial G}{\partial \sigma_{kl}}}$.

At this stage, we can establish the relationship between the strain and stress increments:

$$d\sigma_{ij} = \left\{ E_{ijkl} - \frac{\left(E_{ijnm} \dfrac{\partial G}{\partial \sigma_{nm}}\right)\left(\dfrac{\partial F}{\partial \sigma_{rs}} E_{rskl}\right)}{H + \dfrac{\partial F}{\partial \sigma_{nm}} E_{nmrs} \dfrac{\partial G}{\partial \sigma_{rs}}} \right\} d\varepsilon_{kl}$$

This makes it possible to define an elastoplastic behavior tensor (E^{p}_{ijkl}), or elastoplastic behavior matrix. The above increment relation remains true in the case of a perfectly-plastic material (in which no hardening takes place), i.e. for H = 0.

In the case of hardening, it is also possible to derive the inverse of the elastoplastic tensor. The elastic part of the strain is given by:

$$d\varepsilon^{e}_{ij} = D_{ijkl} d\sigma_{kl} = d\varepsilon_{ij} - d\varepsilon^{p}_{ij} = d\varepsilon_{ij} - d\lambda \frac{\partial G}{\partial \sigma_{ij}}$$

Replacing $d\lambda$ by its expression (taken from the definition of hardening modulus H), we obtain an alternative form of the constitutive law:

$$d\varepsilon_{ij} = \left[D_{ijkl} + \frac{1}{H}\left(\frac{\partial G}{\partial \sigma_{ij}}\right)\left(\frac{\partial F}{\partial \sigma_{kl}}\right)\right] d\sigma_{kl} .$$

3.2.5. *Incremental relationships for multi-mechanism elastoplasticity*

The traditional elastoplastic framework with one plastic mechanism has proved to be too limited to account for some of the phenomena which can be observed experimentally when geomaterials are submitted to a wide variety of stress paths. A larger theoretical framework was necessary. It was defined by introducing several sources of plasticity [KOÏ 60, MAN 65].

Dividing the strain tensor into the sum of the elastic and plastic strain tensors remains valid; but the flow rule adopts a more general form and becomes a linear combination of the contributions of several different plastic potentials, their number being dependent on the stress path. Each of the plastic potentials defines a plastic mechanism; the presence of a plastic potential in the flow rule indicates that the corresponding plastic mechanism is active.

If p is the number of admissible mechanisms for a given material, each mechanism, for instance that denoted by m, is characterized by a yield surface $F_m(\sigma_{ij}, k_m)$, a plastic potential G_m and a hardening variable k_m. The notion of activating a mechanism (or of several mechanisms simultaneously) replaces the notion of a loading process as defined in the traditional framework of a single mechanism.

By definition, we have:

– if $F_m < 0$ or $F_m = 0$ and $dF_m < 0$, the mechanism is inactive, and $d\lambda_m = 0$;

– $F_m = 0$ and $dF_m > 0$, the mechanism is active, and $d\lambda_m > 0$.

If q is the number of active mechanisms ($q < p$) at a given instant, the plastic strain increment is obtained as the sum of q terms,

$$d\varepsilon_{ij}^{p} = \sum_{m \le q} d\lambda_m \frac{\partial G_m}{\partial \sigma_{ij}}$$

The consistency condition $dF_m = 0$ yields:

$$\sum_{n\le q}\left[\left(\frac{\partial F_m}{\partial \sigma_{ij}}\right)E_{ijkl}\left(\frac{\partial G_n}{\partial \sigma_{kl}}\right)-\left(\frac{\partial F_m}{\partial k_m}\right)\left(\frac{\partial k_m}{\partial \varepsilon^p_{ls}}\right)\left(\frac{\partial G_n}{\partial \sigma_{ls}}\right)\right]d\lambda_n=\left(\frac{\partial F_m}{\partial \sigma_{ij}}\right)E_{ijkl}d\varepsilon_{kl}$$

The constitutive law can be expressed as a multilinear relation between the stress and strain increments. The equation above, written for all active mechanisms, leads to a system of q equations:

$$\sum_{n\le q}A_{mn}d\lambda_n=B_m$$

with

$$A_{mn}=\left(\frac{\partial F_m}{\partial \sigma_{ij}}\right)E_{ijkl}\left(\frac{\partial G_n}{\partial \sigma_{kl}}\right)-\left(\frac{\partial F_m}{\partial k_m}\right)\left(\frac{\partial k_m}{\partial \varepsilon^p_{ls}}\right)\left(\frac{\partial G_n}{\partial \sigma_{ls}}\right)$$

and

$$B_m=\left(\frac{\partial F_m}{\partial \sigma_{ij}}\right)E_{ijkl}d\varepsilon_{kl}\,.$$

The complexity of the system depends on the chosen flow rule (associated or unassociated), on the existence of a coupling between different mechanisms, i.e. on the choice of the hardening parameters for each mechanism. The hardening parameter k_m for mechanism m can depend on the plastification of all active mechanisms or only on the plastic strains developed in mechanism m (in which case the underlying physical phenomena associated with hardening are independent). Between the extreme situations there are numerous intermediate possibilities: in the end, only experimental results can provide a sound basis for the choice of one of these possibilities for a given geomaterial.

3.3. Constitutive laws and laboratory tests

Natural soils can be classified into two main categories: frictional soils (with high permeability, for example most sands and gravels) and cohesive soils (fine soils with low permeability, for example most clays and silt). The experimental techniques used to characterize the mechanical behavior of soils (size and preparation of the samples, testing devices, testing procedures) are adapted to these classes of materials. In particular, as it is practically impossible to obtain samples of sands and gravels in their natural state, the experimental identification of the

constitutive laws is generally carried out on reconstituted and remolded materials, and it is uncertain whether their mechanical behavior is identical or even similar to *in situ* materials.

According to the type of tests that are performed, a soil sample can exhibit very different features that do not necessarily seem to reflect a unique kind of behavior. The experimental results obtained by means of the different testing techniques are, however, different aspects of the same global constitutive law that describes the interaction between the deformability and the strength of the ground. The challenge is to create a constitutive law that takes into account and reproduces the main features of the observed behavior for a given soil. Equations relating the effective stresses and strains should therefore be written only after a detailed experimental programme of the deformability and strength properties of soil samples having been subjected to traditional or special triaxial tests, to shear tests on hollow cylinder samples, and to oedometer tests (Table 3.1).

These mechanical tests are carried out on homogenous soil samples. The homogenity of samples makes it possible to define an "average" behavior on the basis of measures made on their boundaries; the question of whether or not the sample is homogenous is a constant concern for researchers and technicians involved in experimental investigation.

Type of tests	Usual tests	Research tests
Triaxial tests on cylindrical samples	Isotropic or anisotropic consolidation + shearing stress path (generally in compression) (UU, CU, CD, CU+u)	Isotropic + anisotropic consolidation. For the shearing stress path, various possibilities: compression or extension; p' = constant; p'/q = constant; K_0 test (with no radial strain).
Tests on cubic samples	-	Same as for triaxial test, plus test for constant values of b ($b = (\sigma_2 - \sigma_1) / (\sigma_1 - \sigma_3)$)..
Plane strain tests	-	Compression test
Hollow cylinder tests	-	All tests above, + tests with rotation of the principal stresses (torsion).
Oedometer tests	Compression	Relaxation and creeping

UU = unconsolidated and undrained test
CU = consolidated and undrained test
CD = consolidated and drained test
CU+u = consolidated and undrained test with measure of pore pressure
K_0 = coefficient of earth pressure at rest

Table 3.1. *Types of mechanical tests performed in the laboratory on soil samples (monotonous loadings)*

For each type of test, the displacements and forces or pressures applied are measured and then converted into strains and stresses. The processing of the results is generally based on the assumption of small strains.

3.4. Characterization of natural cohesive soil behavior

3.4.1. *Analysis of triaxial test results*

The tests carried out on cohesive natural soils subjected to monotonous mechanical loadings (CU, CD and CU+u tests) made it possible to identify some features common to all these materials (see Chapter 2):

– independently of the type of test, the deformability of the soil increases after a given stress is reached, which corresponds to a strain of 1%. In failure tests (in drained or undrained conditions), this value of the stress is a threshold that corresponds either to a peak value of the shear strength or to an asymptote in the (q, ε_1) diagram. Generally, overconsolidated clays tend to show an increase in volume when shearing occurs, whereas normally consolidated clays show a decrease in volume (Figure 3.1);

– if we represent, for samples of the same soil tested from different initial stress states, the points corresponding to stress states for which strains start increasing rapidly, we can define a zone of the effective stress space, such that, for stresses inside this zone, the behavior of the ground is practically reversible, at least for a small number of unloading-reloading cycles. When the limit of this zone is breached, the soil sample exhibits irreversible strain (especially volumetric strains) and the threshold value changes;

– the position of the curve limiting the reversible domain in the effective stress plane depends on time and on the initial state of the soil (density, stresses and pore pressure). The experimental data show that curves associated with different initial states are deduced from one another by a homothetic transformation. The limit of the domain thus defined for the initial possible states of the clay is called the “limit state surface”;

– values of the stresses at failure, obtained for various tests, make it possible to build a failure envelope in (τ, σ) plane: it is composed of a curved line at small values of the mean stress, and of a straight line for larger values of the mean stress (Figure 3.2). Such behaviors correspond to overconsolidated or normally consolidated soils;

– the pore pressure has a predominant influence on the stress at failure. Shear strength of soils depends on drainage conditions and on the loading rate. It is necessary to distinguish between drained (CD and CU+u) and undrained (CU and UU) characteristics;

– irreversible strains associated with the viscosity of the soil are also included in the experimental results.

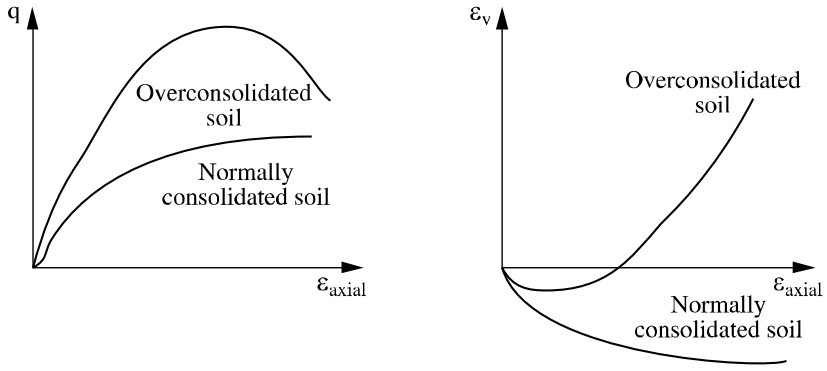

Figure 3.1. *Experimental results for cohesive natural soils: compression tests in drained condition (Magnan, 1989)*

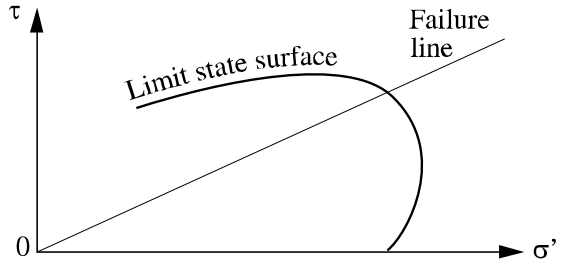

Figure 3.2. *Failure envelope typical for a cohesive soil*

3.4.2. *Analysis of oedometer tests*

Oedometer tests, being very simple, have always been used by geotechnical engineers as well as by researchers. This is the reason a large quantity of data relative to cohesive soils is available: their analysis confirms, on the whole, the main features of soil behavior already identified on the basis of triaxial tests:

– existence of a threshold value (overconsolidation pressure) above which compressibility increases;

– effect of time in terms of creeping and changes in the overconsolidation pressure when the strain rate increases.

3.4.3. *Elasto-viscoplasticity or elastoplasticity?*

To improve the interpretation in terms of strain, it is necessary to choose at first the role played by time in the mathematical formulation of the constitutive model. All experimental data on cohesive soils show that strains are not instantaneous, which leads to preferring visco-elastic or elasto-viscoplastic models. Data show that the constitutive law of clays depends on effective stress, strain and strain rate. However, the development of elastoplastic models is far beyond that of viscous models, mainly because, in practice, settlements of clayey soils are calculated on the basis of the oedometer compressibility curve and on the theory of 1D consolidation that do not take into account the time-dependent characteristics of soil behavior. This approach gives satisfactory results for relatively simple projects.

Observations made before also show that all the characteristics of the elastoplastic behavior can be found in the experimental results for cohesive soils: existence of irreversible strains, a yield surface in the stress space, and evolutions of the yield surface, failure surface and plastic flow plateau. The elastoplastic framework also made it possible to describe quantitatively elastic and plastic strains, and to provide analytical mathematical expressions.

3.5. Characterization of frictional soil behavior

3.5.1. *Analysis of triaxial test results*

Monotonous loadings on frictional soils carried out with triaxial apparatus (CU+u and CD) led to the following observations (see Chapter 2):

– even for small strains, the stress-strain relationship is different in loading and unloading. Macroscopic strains, mainly produced by the relative displacements of grains, are not reversible. The values of the strain for which the behavior is reversible is limited to very small values of the strain (smaller than 10^{-5}). However, as with natural clays, natural sands (i.e. *in situ*) show relatively small strains in a given domain surrounding their initial state. This small strain domain reflects their geological history, and the mechanical loads they have been subjected to in the past;

– in a general way, the drained behavior of a frictional soil is analogous to that of a cohesive soil: dense sands show a peak in shear strength (like overconsolidated clays) followed by a progressive softening, during which shearing is associated with a decrease in volume, then by a volume increase. On the other hand, loose sands show an asymptotic trend, and the volume decreases continuously, as in the case of normally consolidated clays or samples reconstituted in the laboratory (Figure 3.3);

– the failure envelope, i.e. the set of points of maximal shear strength in the Mohr plane (σ, τ), is a straight line passing through the origin, for loose as well as

dense sands. The shear strength depends not only on the nature and state (initial stress and density) of the soil, but also on the intensity of the loads and on the application procedure;

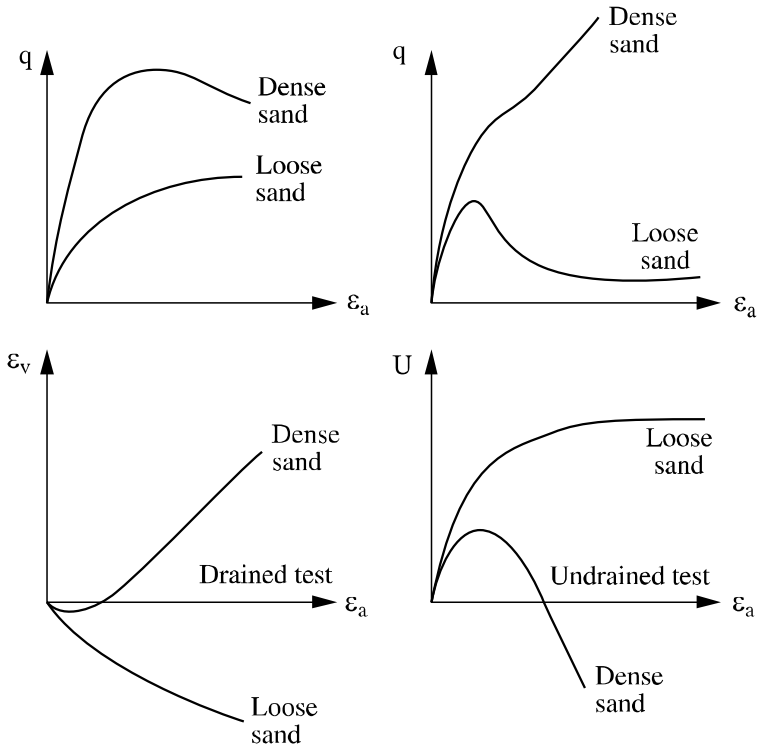

Figure 3.3. *Typical results of triaxial tests on a frictional soil: compression tests in drained and undrained conditions*

– for very large strains, the volumetric strain tends towards a limit, called the "critical state" (which corresponds to the condition $d\varepsilon_v = 0$);

– the state of the soil corresponding to the extremum of the volumetric strain vs, axial strain curve ($d\varepsilon_v = 0$) and to the change in the sign of $d\varepsilon_v$ is called the "characteristic state". The mechanical phenomenon, associated with the onset of irreversible changes of the volumetric strain is called "dilatancy". In the case of moderately dense or dense sands, the volumetric strain increases with the axial strain, in a rather linear way, after the characteristic state has been reached, and eventually the volumetric vs axial strain curve tends towards an asymptote corresponding to the critical state;

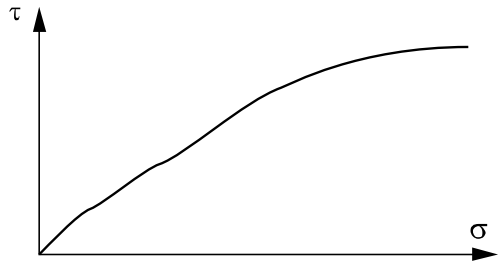

Figure 3.4. *Example of failure envelope for a frictional soil (sand)*

– for large values of the mean stress, we can observe a curvature of the failure envelope, oriented towards the axis of isotropic compressions (Figure 3.4). Actually, the behavior of a sand sample under high pressures is very different from its behavior when subjected to moderate stresses. The maximum shear strength decreases with the applied pressure. This decrease becomes slower and slower as the pressure increases, and we eventually obtain a limit value;

– tests carried out on a three-dimensional apparatus have shown that the intersection of the yield surface with the deviatoric plane is close to a succession of linear segments, but without angles (Figure 3.5);

– in the case of a humid or lightly cemented sand, the origin of the stress space is no longer a point of the failure envelope. The cohesion thus exhibited experimentally is created either by the mechanical bonding created by cementation, or by water meniscus located at the contact points between particles;

– in the case of undrained tests, the density has a very large influence on the behavior. For dense sands, the deviatoric stress increases continuously with strain and the pore pressure reaches first a peak, then decreases. On the other hand, for loose sands, the deviatoric stress exhibits a peak value, then decreases more or less rapidly to a relatively small asymptotic value; the pore pressure increases, then stabilizes at a value close to the preconsolidation pressure (Figure 3.3). Loose sand then loses a great part of its strength: this phenomenon is called static liquefaction [DUP 97].

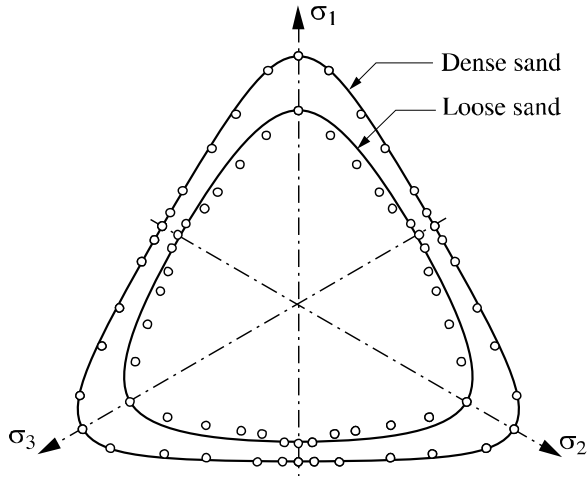

Figure 3.5. *Intersection of the yield surface with the deviatoric plane ([LAD 77])*

3.5.2. *Elastoplasticity framework for frictional soils*

As in the case of cohesive soils, it is not easy to build up a unique theoretical behavior formulation which accounts for all the observations obtained for various loadings in conditions of applied stress or strain paths. It has often been noted, however, that the drained behavior of a frictional soil is qualitatively analogous to that of a cohesive soil: dense sands exhibit volume increases during shearing, as do overconsolidated clays, whereas loose sands show volume decrease as do normally consolidated clays.

On the other hand, in many cases, the behavior of frictional soils can be considered as globally isotropic and it is generally accepted that strains change simultaneously with the stress states and that viscosity and ageing effects are negligible. The rate of loading has therefore little or no influence on the behavior of the material. These assumptions are in relatively good agreement with experimental results.

Apart from failure, the analysis of the tests brings to light several important features of the behavior of frictional soils that are consistent with the elastoplasticity framework. This makes it possible both to take advantage of the experimental curves to provide a sound basis for the concepts of critical state, characteristic state, and to provide a set of equations describing the dilatancy phenomenon.

3.6. Principles for the derivation of elastoplastic models

In order to build up an elastoplastic constitutive law, for instance for a model with one mechanism (for the sake of simplicity), "experience" shows that we must go through the following steps:

– definition of the initial elastic domain and of the elastic law;

– definition of the yield surface;

– choice of a plastic potential;

– description of the evolution of the yield surface and of the hardening law.

The following sections illustrate this process, show its complexity, and underline the interactions between the different parts of the model that must be clearly stated in order to obtain an acceptable model. The presented process is essentially based on drained tests and all stresses used are effective stresses, noted σ_{ij} and p for simplicity, and not σ'_{ij} or p'.

3.6.1. *Elastic behavior*

3.6.1.1. *Elasticity and unloading-reloading cycles*

When experimental results include tests with one or several unloading-reloading cycles, the hypothesis of an elastoplastic material leads us to consider that the strains measured during unloading and reloading up to the stress level reached when stress reversal occurred are elastic strains. Gathering these sets of points leads to analytical expressions between stresses and strains. Such expressions cannot be arbitrary, as they have to comply with certain physical laws, such as material stability. For this reason, a number of authors who have developed models tend to prefer the so-called hyperelastic approach, models for which the stresses are obtained by derivation of a scalar potential with respect to strains.

Furthermore, before any attempt to derive an elastic law from "elastic" data can be made, it must be decided whether the elastic behavior is isotropic or not. In the anisotropic case, the elastic behavior is generally assumed to be linear, given that the number of parameters that must be determined experimentally is so large that any other type of analysis is extremely difficult to achieve. In the isotropic case, the problem adds up to finding the variations of two scalar coefficients (K and G, or E and ν) when the stress state (or its invariants) changes. Table 3.2 presents some of the expressions that can be found in the literature. In tensorial form, the isotropic elasticity equation reads:

$$\Delta\varepsilon_{ij} = \frac{1+\nu}{E}\Delta\sigma_{ij} - \frac{3\nu}{E}\Delta p\delta_{ij} \text{ or } \Delta\sigma_{ij} = 2G\Delta\varepsilon_{ij} + \left(K - \frac{2G}{3}\right)\Delta\varepsilon_{kl}\delta_{kl}\delta_{ij}$$

References	K	G
Burland and Roscoe (1968)	$\frac{1+e_o}{\kappa}p$	G_o
Nelson and Baron (Desai *et al*., 1984)	$K_o + \alpha_1 p$	$G_o + \alpha_2 q$
Chen and Baladi (Desai *et al*., 1984)	$\frac{K_o}{1-K_1}(1-K_1 e^{-3K_2 p})$	$\frac{G_o}{1-G_1}(1-G_1 e^{-\sqrt{3}G_2 q})$
Boyce (1980) Cambou and Jafari (1988)	$\frac{K_o p_a \left(\frac{p}{p_a}\right)^{1-n}}{1-(1-n)\frac{K_o}{6G_o}\frac{q^2}{p^2}}$	$G_o p_a \left(\frac{p}{p_a}\right)^{1-n}$
Loret (1981) f is an arbitrary function	$3r_o f\left(p^2 + r_o q^2\right)$	$f\left(p^2 + r_o q^2\right)$
Loret (1981) Lade and Nelson (1987)	$\frac{3r_o E_o p_a}{2(1+\nu)}\left[\left(\frac{p}{p_a}\right)^2 + r_o\left(\frac{q}{p_a}\right)^2\right]$	$\frac{E_o p_a}{2(1+\nu)}\left[\left(\frac{p}{p_a}\right)^2 + r_o\left(\frac{q}{p_a}\right)^2\right]^n$
Vermeer (1982)	$\frac{2}{3}G$	$G_o\left[\frac{\sqrt{\sigma_1^2+\sigma_2^2+\sigma_3^2}}{3p_0}\right]^{1-\beta}$
p_a denotes the atmospheric pressure; $K_o, G_o, n, r_o, E_o, \nu, e_o, \kappa, \alpha_1, \alpha_2, K_1, K_2, G_1, G_2$ are constants.		

Table 3.2. *Expressions of the bulk modulus K and shear modulus G available in the literature*

If experimental tests do not include unloading-reloading tests, it is necessary in the first place to identify the initial elastic domain in order to make the difference between elastic and total strains.

3.6.1.2. *Initial elastic domain*

For natural clays, it is commonly assumed that there is an initial elastic domain, generally limited to small or very small strains [LER 85]. The search for the boundary of this domain is based on the analysis of monotonous triaxial tests and on the experimental identification of a clear change in the stress-strain curves: for instance, a sharp change in the curvature of the (q, ε_1) line, for a triaxial compression test (Figure 3.6). Taking into account the assumption of the linearity of the anisotropic elastic behavior, it is generally simple to identify this sharp change, as it is associated with a loss of linearity of the stress-strain relationship, and with the onset of larger plastic-strain. Each test provides one point of the boundary of the initial elastic domain, i.e. the yield surface. In the case of an anisotropic and non-linear elastic behavior, this procedure no longer holds.

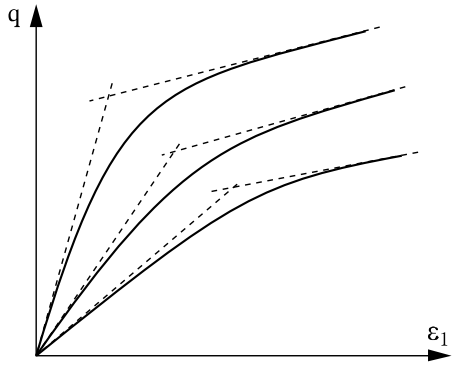

Figure 3.6. *Initial elastic domain for natural clays*

Interpretation of traditional tests on frictional soils is often implicitly based on the assumption that the soil sample becomes plastic at the first loading. In other words, the material has no initial elastic domain, but an elastic domain is created as loads increase. This assumption is justified by relative displacements of grains, with respect to one another, that explain why irreversible strains occur under the slightest applied stress. The elastic domain is thus defined by the yield function and the characterization of the elastic law can only be made through unloading-reloading cycles.

More sophisticated studies can be carried out with a triaxial apparatus specially equipped for the measure of very small strain. An initial domain is thus identified for frictional soils, but it is limited to strains smaller than 10^{-5} or 10^{-4}. The initial elastic domain can also be characterized in non-linear diagrams. For example, we can look for a loss of linearity in a $(\ln p, \varepsilon_v)$ diagram.

Another, more difficult to use, method consists of applying small variations of the applied stress starting from a given stress state, and to examine whether, once the variation of stress is removed, any irreversible strain has been generated or not. We can thus define locally a boundary separating the stress states belonging to the elastic domain from those lying outside. In order to be fruitful, this approach must be supplemented by the choice of an appropriate hardening variable, since this procedure leads to the identification of the current elastic domain which is associated with a given value of the hardening parameters. To continue along these lines, we have to choose a type of variable, and to determine experimentally a number of points of the yield surface for the same value of hardening variable, before the elastic domain for a given hardening state can be properly defined. The initial domain could also be obtained thanks to a thorough study of the evolution of the elastic domain as hardening parameters vary, and by extrapolating the results for small strains. This procedure, however simple and attractive it may seem, is extremely difficult to carry out, especially for natural soils. Moreover, the distinction between reversible and irreversible strains depends very much on the accuracy of the experimental setup.

3.6.1.3. *Anisotropy of natural clays*

Most natural clays exhibit a very anisotropic behavior: the same stress variation applied in two different directions produces very different strain increments. This is why it may be necessary, in order to obtain an approximate representation of their mechanical behavior, to use an elastoplastic model with an anisotropic linear elasticity. This anisotropy is often limited to the simplest case of transverse anisotropy. It is generally acceptable that there is a symmetry around the vertical axis (the direction of gravity) for horizontal ground layers, and that the behavior is isotropic in the plane perpendicular to this axis (isotropy plane or stratification plane). This is no longer the case if the ground layer is inclined or has been subjected to large tectonic forces. The elastic parameters are the following: a Young's modulus associated with the vertical direction E_v; a Young's modulus associated with the horizontal direction E_h; two Poisson's coefficients ν_{vh} and ν_{hh}, and an additional shear modulus G_{vh}, that characterizes the relation between shear stresses and strains in planes which contain the vertical axis. Measuring these five parameters can be achieved thanks to traditional triaxial tests performed on samples cut in different directions. The axes of the sample are thus no longer identical to those of the triaxial apparatus (Figure 3.7).

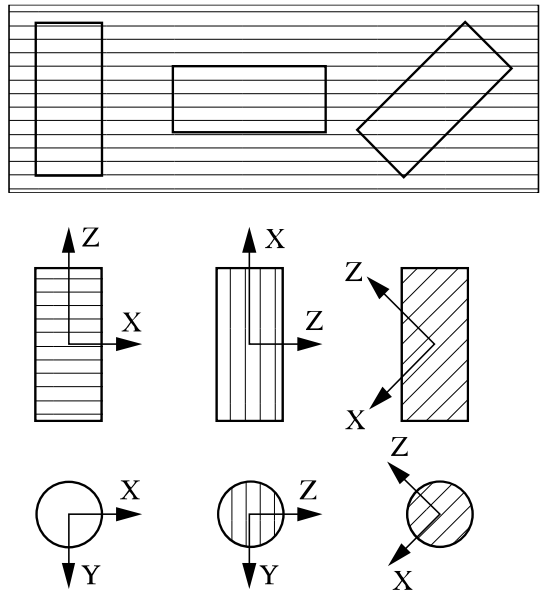

Figure 3.7. *Sampling in vertical, horizontal and inclined directions*

3.6.2. *Estimation of the plastic behavior*

The construction of the plastic part of the model is based on the interpretation of tests in terms of failure surface (or plasticity criterion), of strains and plastic potentials, of evolutions of the yield surface and of the hardening variables. This interpretation depends in turn on the type of elastoplastic model that is to be defined. For the sake of simplicity, and to present the various possible approaches, we retain here the framework of elastoplastic models with one plastic mechanism.

For traditional tests, and in a first step, the procedure can be identical to that which has been adopted for the characterization of elastic behavior. The components of the plastic model are searched for under the form of relationships between p, q, ε_v, ε_d, ε_v^p, ε_d^p and their increments. Results of triaxial axisymmetric tests in drained compression, for a constant value of the mean stress and a constant value of the q/p ratio are often chosen as the basis for analytical developments. The plastic strains ($\varepsilon_v^p, \varepsilon_d^p$) that appear, when the stress state is on the yield surface, can be deduced from measures of total strains by substracting the elastic strains calculated from the elastic law previously identified. However, being able to calculate the plastic strains is one thing, the question of knowing when they have to be calculated

is another question. In other words, we are brought back to the question of the initial elastic domain. If the determination of this domain cannot be carried out, we can assume, for stress states far from the origin of the stress space, that for loading processes, elastic strains can be neglected and experimental strains are equal to plastic strains. Even if such an approach can be criticized (and may give rise to some confusion in the model formulation), it is often the one that is used in constitutive modeling.

3.6.3. *Failure surface*

3.6.3.1. *Notion of critical state*

When a soil sample is subjected to a triaxial loading, it undergoes progressive volumetric strain (positive or negative), where upon the sample volume reaches a constant value as deviatoric strain develops. The final state is called the critical state [SCH 68] and can be defined as the ultimate state reached for large strains when monotonous shearing is carried out at constant volume. The experimental characterization is difficult and often needs an extrapolation procedure. Quantitatively, the critical state is defined by the following conditions:

– plastic flow occurs at constant volumetric strain $d\varepsilon_v^p = 0$;

– the void ratio depends only on the mean stress, according to a relationship such as $e = e_{cs} - \lambda \ln \frac{p}{p_1}$, where e_{cs} and λ are two parameters of the model and p_1, a reference pressure value (1 kPa, for instance);

– the stress ratio q/p is constant.

The notion of critical state has enabled significant advances in elastoplastic constitutive modeling of soil behavior, and is the source of the first hardening models.

3.6.3.2. *Failure surface in the (p, q) and (σ, τ) planes*

For any given soil, the maximum strength, reached under various loading conditions, defines a failure surface in the principal stress space. The search for the failure surface is relatively simple if test results are available for a wide array of loading paths. For example, triaxial tests on cylindrical samples make it possible to obtain the intersection of the failure surface with the (σ, τ) or (p, q) planes.

For cohesive soils, the intersection of the failure surface with the (τ, σ) plane is made up of a curved part for small values of the mean stress, and a straight line for higher values of the mean stress (Figure 3.8). These behaviors correspond,

respectively, to overconsolidated and normally consolidated soils. Usually, for the values of stress that are commonly encountered in practical projects, these curves are summed up as the combination of two straight lines, according to the stress state in the soil or to the values of the stresses. Line (a) does not include the origin, whereas line (b) does (Figure 3.8). Both lines are described by the same equation:

$$\tau = c + \sigma \tan\varphi$$

where c is the drained shear strength (or effective shear strength) and φ, the friction angle (or effective friction angle). These parameters depend on the nature of the material (chemical composition, shape and size of the grains), on the initial state (density and stresses) and on the testing conditions (intensity of the confining pressure, stress path).

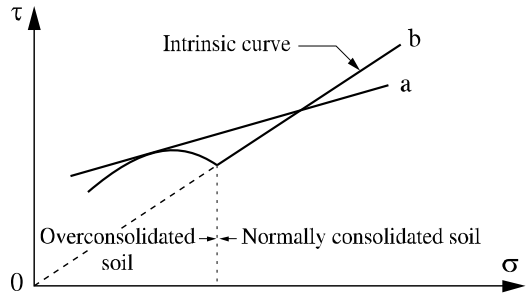

Figure 3.8. *Intersection of the failure surface with the (σ, τ) plane*

For frictional soils and reconstituted clays, the conventional approach is to assume that the intersection of the failure surface with the (σ, τ) or (p, q) planes is a straight line including the origin:

$$\tau = \sigma \tan\varphi$$

3.6.3.3. *Failure surface in the stress space*

As it is easier to carry out tests on frictional soils (sands), in-depth research has been undertaken to characterize the three-dimensional failure surface, by means of three-dimensional apparatus and hollow cylinder sample testing devices. Such sophisticated testing facilities make it possible to investigate the influence of the intermediate principal stress σ_2, otherwise impossible to assess with traditional triaxial tests ($\sigma_2 = \sigma_3$). In the first place, we can extend the expressions obtained for the intrinsic curve in the (p-q) space to the space of the principal stresses (σ_1, σ_2, σ_3), thus obtaining a cone with a revolution symmetry around the line of equation: $\sigma_1 = \sigma_2 = \sigma_3$. The shape of the section cannot be obtained by traditional

axisymmetric tests, but can be studied by means of true three-dimensional tests (true triaxial apparatus or hollow cylinder apparatus). The experimental results thus make it possible to state that, in the principal stress space, the failure surface has a conical shape, the summit being the origin and the section being not very different from a rounded triangle (Figure 3.9).

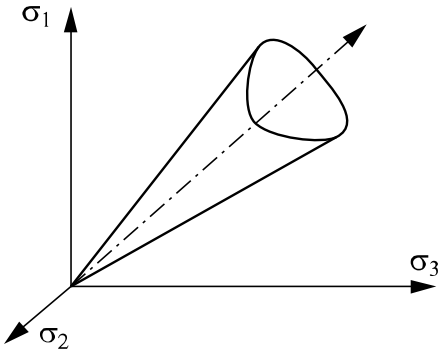

Figure 3.9. *Three-dimensional failure surface*

From a theoretical point of view, this adds up to introducing the third invariant of the stress tensor (the determinant or the Lode angle). Several authors have chosen to express the failure surface using the following form:

$$\frac{q}{p} = f(\theta, p)$$

where f is a homogenous function of degree zero with respect to its arguments and θ, the Lode angle defined by: $\sin\theta = -3\sqrt{3}J_3/(2J_2^{3/2})$.

3.6.3.4. *Analytical expressions of the failure surface*

According to the authors and the type of tests under discussion, several categories of failure surface (or plasticity criteria) have been proposed. Some of these are expressed in terms of principal stresses and others in terms of stress invariants. Table 3.3 shows the models most commonly used in geomechanics.

Type of criterion	Mathematical formulation	n*	Type of soil
Tresca	$\sigma_1 - \sigma_3 - 2c_u$	1	Clays and limestones (short term)
Mohr-Coulomb	$\sigma_1 - \sigma_3 - \sin\varphi\,(\sigma_1 + \sigma_3) - 2c\sin\varphi$	2	Most soils (long term)
Drücker-Prager	$\sqrt{J_2} - \alpha I_1 - k$	2	Sands and clays (long term)
Di Maggio and Sandler (1971)	$\sqrt{J_2} + \gamma \exp(-\beta I_1) - k$	3	Sands and clays (long term)
Matsuoka-Nakai (1974)	$\frac{I_1 I_2}{I_3} - k$	1	Sands
Lade-Duncan (1975)	$\frac{I_1^3}{I_3} - k$	1	Sands
Lade (1977)	$\left(\frac{I_1}{p_a}\right)^m \left(27 - \frac{I_1^3}{I_3}\right) - k$	2	Sands
Hoek and Brown (1980)	$\sigma_1 - \sigma_3 - \sqrt{m\sigma_3\sigma_c + s\sigma_c^2}$	3	Hard soils, soft rocks
Van Eekelen (1980)	$\sqrt{J_2} + a\left(1 + b\frac{I_3}{J_2^{3/2}}\right)^n (I_1 - k)$	4	Sands and clays (long term)
Desai and Siriwardane (1984)	$J_2 - \alpha I_1 - \beta I_1 I_3^{1/3} - k^2$	3	Sands and clays (long term)
Matsuoka *et al.* (1990)	$\sqrt{\frac{I_1 I_2}{9 I_3} - 1} - k$	1	Sands

* where n is the number of parameters of the criterion; p_a, a reference value for pressure.

Table 3.3. *Expressions of the failure surface for soils*

The stress invariants are defined by:

$$I_1 = \sigma_{xx} + \sigma_{yy} + \sigma_{zz};$$

$$I_2 = \sigma_{xx}\sigma_{yy} + \sigma_{xx}\sigma_{zz} + \sigma_{yy}\sigma_{zz} - \sigma_{xy}^2 - \sigma_{xz}^2 - \sigma_{yz}^2;$$

$$I_3 = \sigma_{xx}\sigma_{yy}\sigma_{zz} - \sigma_{xx}\sigma_{yz}^2 - \sigma_{yy}\sigma_{xz}^2 - \sigma_{zz}\sigma_{xy}^2 + 2\sigma_{yx}\sigma_{xz}\sigma_{yz} ;$$

$$J_2 = \frac{(\sigma_{xx} - \sigma_{yy})^2 + (\sigma_{xx} - \sigma_{zz})^2 + (\sigma_{yy} - \sigma_{zz})^2}{6} + (\sigma_{xy})^2 + (\sigma_{xz})^2 + (\sigma_{yz})^2 .$$

Lade's criterion [LAD 77] and Matsuoka-Nakai's criterion [MAT 74] have been validated by their authors for numerous experimental results and for different types of sands. Although the shape of the surfaces are relatively similar in the deviatoric plane (Figure 3.10), some differences can be pointed out:

– Matsuoka-Nakai's criterion, like Mohr-Coulomb's, corresponds to the same friction angles in triaxial extension and in triaxial compression;

– the criterion proposed by Lade associates different values of the friction angle with triaxial compression and triaxial extension conditions, which seems to be closer to the experimental results [ZIT 88];

– in the case of Lade's criterion, a second parameter, denoted by n, is necessary to take into account the influence of the mean stress on the peak value of the friction angle, which corresponds to experimental results observed over a large range of stress values.

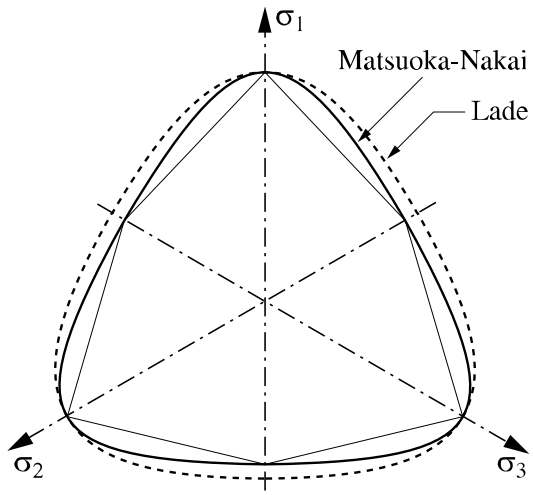

Figure 3.10. *Failure surfaces proposed by Lade and Matsuoka-Nakai*

3.6.4. *Total and plastic strains*

3.6.4.1. *Notions of characteristic state and dilatancy*

During a drained triaxial compression test, a frictional soil shows initially a decrease in volume, or a contractant phase. Then, as the deviatoric stress increases, the volumetric strain rate tends to decrease towards zero for loose soils. In the case of denser soils, the volumetric strain rate shifts sign, and the soil volume starts to increase before large strains occur (Figure 3.11). The "dilatancy" thus produced is greater if the material is initially in a denser state, and if the initial confining pressure is low.

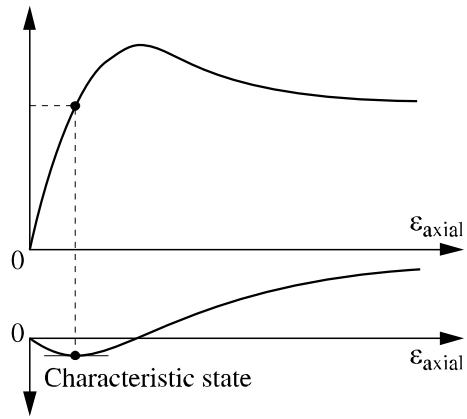

Figure 3.11. *Definition of the characteristic state*

The stress state associated with zero volumetric strain rate and with the change in the sign of volumetric strain variations is called the "characteristic state". It is defined by the following two conditions [LUO 80]:

– the volumetric strain rate is zero ($d\varepsilon_v = 0$);

– the Mohr circles for characteristic states reached for different isotropic initial stresses have a common tangent, called the "characteristic line", whose gradient is equal to tan φ_c.

The angle φ_c has been interpreted as the ability of the grains to become entangled. Its experimental determination is direct and easy: it is obtained for relatively small axial strains (typically 1 or 2%). Tests carried out on different sands show that φ_c is an intrinsic parameter, independent of the density, the grain size distribution, and the mean stress [LUO 80]. However, in spite of the fact that the existence of the characteristic state has been confirmed for other stress paths in the

triaxial plane, in drained as well as undrained conditions, it seems difficult to define uniquely the transition between contractant and dilatant behavior. For example, the value of the axial strain corresponding to the characteristic state is not smaller in extension than the value that can be observed in triaxial compression.

3.6.4.2. *Stress-dilatancy relationship*

Studying the experimental volumetric strain vs axial strain curves makes it possible to derive theoretical expressions for the plastic strain. For isotropic soils, the processing of the results is based on the use of invariants ε_v^p and ε_d^p and of their increments, and on the dilatancy rate δ, defined as the ratio between the volumetric and deviatoric plastic strain rates:

$$\delta(p,q) = \frac{d\varepsilon_v^p}{d\varepsilon_d^p}$$

Variations of this ratio when p and q vary, or when p and η (η=q/p) vary, makes it possible to derive a stress-dilatancy relationship. Combined with a simulation of the plastic part of the isotropic compression test [ε_v^p=g(p)], the following equations for the components of the plastic increments can be obtained:

$$d\varepsilon_v^p = \left(\frac{dg}{dp}\right)dp \text{ and } d\varepsilon_d^p = \frac{1}{\delta(p,q)}\left(\frac{dg}{dp}\right)dp .$$

It remains to be seen if the results are in reasonably good agreement with the direct estimation of the plastic strains obtained by subtracting the elastic strains from the total strains. If results are satisfactory, the stress-dilatancy relationship can also lead to the derivation of a plastic potential.

3.6.5. *Plastic potential*

3.6.5.1. *Analysis in the (p, q) plane*

Indications on the plastic potential can be supplied by the experimental results if we associate in the same figure the direction of the plastic strain increments ($\Delta\varepsilon_v^p$, $\Delta\varepsilon_d^p$) with the yield surface previously obtained in the (p, q) plane, or at least with the boundary of the initial elastic domain. It can thus be decided whether the flow rule is associated or not, with the restrictions due to the precision of the measures (Figure 3.12). In general, directions of the plastic strain increments are not strictly normal to the yield surface. The most difficult point is thus to choose an analytical

expression which matches the experimentally observed plastic flow directions. Two possibilities have been investigated: the first consists of expressing the gradient of the plastic potential as a linear combination of the normal to the yield surface and of a given vector of the (p, q) plane, defining a straight line including the origin or the center of the yield surface (case of natural clays); the other possibility consists of adopting an explicit analytical expression for the dilatancy ratio, and in integrating the differential equation thus obtained.

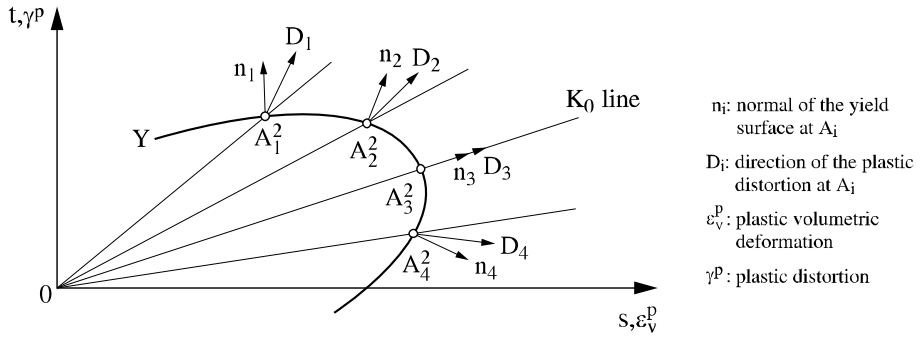

Figure 3.12. *Plastic flow directions on the yield surface*

3.6.5.2. *Plastic potential and stress-dilatancy relationship*

The dilatancy ratio previously defined gives access to a method making it possible to derive the plastic potential. In the case of traditional triaxial tests, we have, by definition:

$$\delta(p,q) = \frac{d\varepsilon_v^p}{d\varepsilon_d^p} = \frac{\dfrac{\partial G}{\partial p}}{\dfrac{\partial G}{\partial q}}.$$

For a given hardening state, the curve defined in the (p, q) plane by the plastic potential is defined by the equation G(p, q) = constant. A local differentiation of this relationship yields:

$$dG = \frac{\partial G}{\partial p}dp + \frac{\partial G}{\partial q}dq = 0$$

Introducing this expression in the dilatancy rate, we obtain the following differential equation:

$$\delta(p,q) = \frac{\dfrac{\partial G}{\partial p}}{\dfrac{\partial G}{\partial q}} = -\frac{dq}{dp}$$

This equation can be solved, provided that the dilatancy rate is given a suitable (relatively simple) expression $\delta(p, q)$. Two solutions can be considered:

– we can, in the first place, deduce the dilatancy rate directly from variations of the experimental quantities $\Delta\varepsilon_v^p$ and $\Delta\varepsilon_d^p$ along a test [NAM 70; STR 71; NOV 82; TOU 82];

– alternatively, we can choose a theoretical expression of the plastic dissipation rate $dW^p = \sigma_{ij} d\varepsilon_{ij}^p = p d\varepsilon_v^p + q d\varepsilon_d^p$ as a function of p and q [SCH 68].

From both approaches, we can derive an expression of the dilatancy rate $\delta(p, q)$ so that the differential equation can be solved and an expression of the plastic potential $G(p, q, p_0)$ can be proposed, where p_0 is an integration constant. Plastic potentials obtained by such a procedure are the basis of the Cam-Clay models [SCH 68] and the model proposed by Nova [NOV 82].

The plastic potential $G(p, q, p_0)$, built on the basis of triaxial tests, is thus extrapolated for the simulation of multiaxial stress situations. The assumption that the model gives reasonably good results when applied outside the experimental referential on which it is based must be checked by comparing simulations and results of other types of tests, especially with true three-dimensional tests. For example, a generalized definition of the dilatancy rate can be given by the following relation [DEG 83]:

$$\delta = \frac{-d\varepsilon_v^p}{\sqrt{d\varepsilon_{ij}^p d\varepsilon_{ij}^p}}.$$

This ratio represents relatively well the tendency of the sample volume to increase ($\delta > 0$) or to decrease ($\delta < 0$). The tests carried out on a true three-dimensional apparatus show that the plastic flow occurs for a roughly constant dilatancy ratio during a given test [ZIT 88]. These observations have been made for monotonous and relatively simple test conditions (in axisymmetric conditions and for a constant value of b; see Table 3.1). These interpretations remain to be confirmed by three-dimensional condition tests of a higher level of complexity.

3.6.5.3. *Plastic potential and plastic mechanism*

A closer examination of the experimental results tends to suggest that the flow rule itself is not well adapted to the description of frictional soil behavior. The definition of the flow rule implies that, regardless of the direction of the strain increment ($d\sigma_{ij}$) that induces plastic flow, the direction of the plastic strain increment is entirely defined by the current stress state (σ_{ij}); however, experimental results show that their direction also depends on the stress increment itself [POO 67; TAT 74; LOR 81; TOU 82; VER 82; TAN 90]. These authors have shown that the influence of the stress path on the dilatancy ratio is greater for small values of the stress ratio η and tends to vanish for values of η close to failure.

If we represent for different stress paths graphically the dilatancy ratio δ vs the stress ratio η, it appears that δ depends strongly on the stress path (Figure 3.13). The unicity of the plastic potential is therefore not proved, except in the vicinity of failure. The flow rule must be replaced by an incremental relationship such as:

$$d\varepsilon_{ij}^{p} = G_p(\sigma_{kl}, d\sigma_{mn})d\sigma_{rs}$$

where G_{ijkl} is a tensor whose components are functions of degree zero with respect to their second argument ($d\sigma_{ij}$). This non-linear relationship has been studied by Dafalias and Popov [DAF 76] and Mroz and Zienkiewicz [MRO 78]. In order to account for this dependency, another solution consists of adopting an elastoplastic model combining several plastic mechanisms. The use of several yield surfaces, each attached to a different plastic mechanism, introduces a loss of uniqueness in the plastic strain increment direction, which depends on the stress increment direction at any point where more than one plastic mechanism is activated. The higher the number of mechanisms, the higher the sensitivity to the stress increment direction. For instance, in the case of two mechanisms (one deviatoric and one volumetric), the relationship between ($d\varepsilon^{p}_{ij}$) and ($d\sigma_{ij}$) becomes quadrilinear. This improves the simulations notably, but we must be aware that the number of parameters increases, and that they may not be independent of one another. From a more fundamental point of view, we should also investigate the question of knowing whether the yield surfaces are independent or not: can the activation of one of the mechanisms change the shape of the other yield surfaces? The answer to this question remains open, and more research is necessary. Nevertheless, most researchers in the field of constitutive modeling think that one or two mechanisms (deviatoric and volumetric) provide a framework that should be wide enough to account for most physical phenomena observed experimentally in the case of monotonous loadings. This idea has been adopted by Lade [LAD 77], Vermeer [VER 82], Luong and Loret [LUO 82], Aubry *et al*. [AUB 82], Cambou and Jafari [CAM 88] or Tan [TAN 90]. In the case of cyclic loadings, however, it may be necessary to introduce two or three mechanisms.

Working with several plastic mechanisms also leads to more complex expressions of the dilatancy ratio:

$$\delta = \frac{d\varepsilon_v^p}{d\varepsilon_d^p} = \delta(p, q, dp, dq) .$$

From a qualitative point of view, this formulation seems to be closer to reality; but unfortunately extremely difficult to identify. Due to this, the models proposed are more based on mathematical constructions rather than on experimental data.

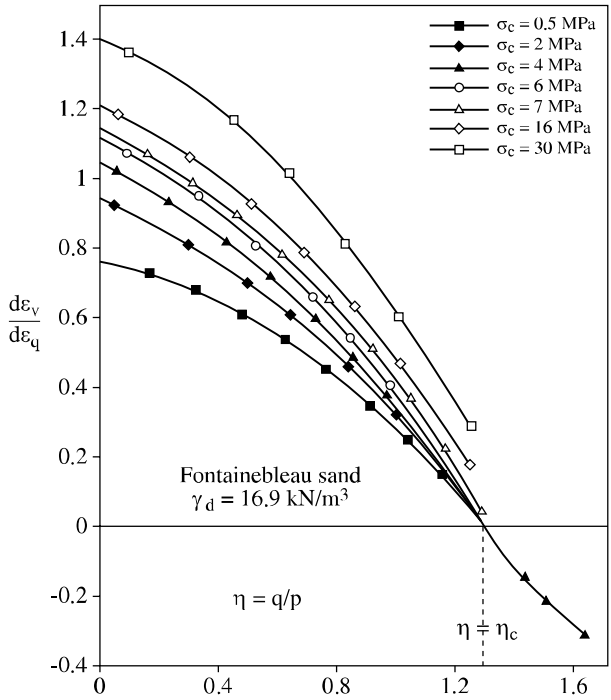

Figure 3.13. *Dilatancy ratio vs stress ratio (Luong and Touati, 1983)*

3.6.6. *Yield surface*

Elastoplasticity with hardening makes it possible to better describe the intermediate phases between the onset of the irreversible strains and the ultimate failure of the sample. Hardening changes the yield surface in the stress space. The changes of its shape have been extensively discussed in numerous research works, combining experimental observations and theoretical hypothesis.

3.6.6.1. *Principles of the mathematical formulation*

Even if its extreme positions are known (the initial elastic domain for very small strains and the failure surface reached for very large strains), finding an appropriate mathematical expression for the yield surface on the basis of experimental results can be quite difficult. We have to build the yield surface in the stress space, determine the internal variables describing the hardening phenomenon, and, finally, express the influence of the hardening variables on the evolution of the yield surface. During a loading path, this surface can undergo successively or simultaneously an expansion, a translation, a change in shape or even a rotation. Describing the changes of the yield surface requires us to look for its shape in many points of the loading path. Thus, it remains to define the influence of the applied stress path.

Given the complexity of the problem, we have to resort to simplifying assumptions about the nature of the internal variables which govern the changes of the yield surface. The construction of the yield surface is thus the result of more or less sophisticated combinations of experimental observations and theoretical opinions on the nature of hardening and on the shape of the failure and yield surfaces, or on the plastic potential. For example, the following observations make it possible to limit the scope of the possibilities:

– the yield surface is convex and contains the origin;

– after a given point on the stress-strain curve in isotropic compression, the unloading curve is different from the loading curve: this proves that irreversible strains exist, and that the stress path has crossed the yield surface. This result implies that the yield surface intersects the isotropic compression axis (p axis);

– tests carried out for a decreasing deviatoric stress combined with simultaneous increasing mean stress p show irreversible strains. This tends to indicate that the yield surface is perpendicular to the isotropic compression axis.

In practice, methods determining the yield surface are based on:

– the so-called normality rule (meaning that the flow rule is more often associated than not);

– a relatively good knowledge of the failure surface;

– a careful analysis of experimental results.

3.6.6.2. *Derivation based on the normality rule*

In this approach, it is assumed that the plastic flow is governed by an associated flow rule. In other words, the direction of the plastic strain increment is also the direction of the outer normal to the yield surface. The yield function is therefore also

the plastic potential. The problem thus consists of expressing the plastic potential. The first elastoplastic models with hardening were developed to describe the behavior of reconstituted soil samples. The shape of the yield surface was validated on remolded clay samples, isotropic and normally consolidated [SCH 68]. For natural soils, this approach is relatively less employed, since the flow rule is generally very far from being associated.

3.6.6.3. *Derivation based on the failure surface*

Numerous authors have used the shape of the failure surface to define the shape of the yield surface. The idea is simple. Once the failure surface equation has been obtained, for instance $f_r(\sigma_{ij}) = k$, where k denotes a constant and f_r a homogenous function of the invariants of the stress tensor, we use function f_r to define yield function f_c as:

$$f_c(\sigma_{ij}, \varepsilon_{ij}^p) = f_r(\sigma_{ij}) - p_0(\varepsilon^p) = 0$$

where ε^p represents the hardening variable associated with plastic strain and p_0, a function that tends towards the k constant as we get closer to failure. The problem is now to provide a suitable function $p_0(\varepsilon^p)$ that describes the shape, size, orientation of the yield surface and the way in which it tends towards the failure surface.

3.6.6.4. *Hardening variables and changes in the yield surface*

For an isotropic soil, the hardening variables are in most cases:

– the invariants of the plastic strain tensor (especially ε_v^p and ε_d^p) or their linear combination (for example, $\varepsilon_v^p + D\varepsilon_d^p$ where D is a constant);

– the plastic work W^p ($dW^p = \sigma_{ij}\, d\varepsilon^p{}_{ij}$);

– the plastic distortion γ^p ($d\gamma^p = \sqrt{\frac{3}{2} de_{ij}^p de_{ij}^p}$ with $e_{ij}^p = \varepsilon_{ij}^p - \varepsilon_{kk}^p \delta_{ij}$).

In any case, it is crucial that the hardening variable should be easily measurable. For instance, if plastic work W^p is chosen as the hardening variable, and if the function associated with the failure surface $f_r(\sigma_{ij})$ is known, the only thing to do is to place the experimental points in a (W^p, $f_r(\sigma_{ij})$) plot, which upon an appropriate mathematical processing of the data gives an approximate expression of $p_0(W^p)$. Here, the choice of the equations describing hardening should be dictated by simplicity.

Kinematic or anisotropic hardening laws have also been proposed to describe the changes of the yield surface inside the failure surface. From a mathematical point of view, these notions are expressed by the following equations:

– isotropic hardening: $f_c(\sigma_{ij}, \varepsilon^p) = 0$;

– kinematic hardening: $f_c(\sigma_{ij} - A_{ij}) = 0$;

– anisotropic hardening: $f_c(\sigma_{ij}, A_{ij}) = 0$;

where ε^p is a scalar hardening variable and (A_{ij}), a symmetric tensorial hardening variable. Kinematic hardening is also introduced to account for the influence of cycles on the yield surface. Anisotropic hardening makes it possible to take into account the anisotropy induced by the applied loads.

3.6.6.5. *Hardening modulus and changes in the yield surface*

Analyzing the experimental results in order to find the hardening modulus H also makes it possible to discuss the changes of the yield surface. Starting from the plastic potential G and from the assumption that the yield surface is such that:

$$f_c(\sigma_{ij}, \varepsilon_{ij}^p) = f_r(\sigma_{ij}) - p_0(\varepsilon^p) = 0$$

f_r denoting the function defining the failure surface, we can write the incremental relationships:

$$\Delta\varepsilon_{ij}^p = \frac{1}{H}\left(\frac{\partial f_r}{\partial \sigma_{kl}}\Delta\sigma_{kl}\right)\frac{\partial G}{\partial \sigma_{ij}}.$$

Using this relationship provides a way of deriving the variations of the hardening modulus, then of fitting an appropriate mathematical function $H(\varepsilon^p)$. It is thus possible (in theory) to obtain the hardening law through the following equation:

$$H = \frac{\partial p_0}{\partial \varepsilon^p}\frac{\Delta\varepsilon^p}{\Delta\lambda}$$

where $\Delta\lambda$ is the plastic multiplier that can be evaluated experimentally.

3.6.6.6. *Hardening and plastic mechanisms*

Theoretical analyses and simulations of tests have also led to some conclusions relating to the form of hardening laws. It has been shown that models in which hardening only depends on the volumetric plastic strain $[p_0(\varepsilon_v^p)]$ are not well adapted for undrained loadings [LOR 87]. This proves that, for the design of

geotechnical structures, the choice of a model also depends on the kind of computations that are to be carried out (drained or undrained for instance). To overcome this difficulty, some authors have proposed to take into account a hardening defined as the linear combination of the volumetric plastic strain and the deviatoric plastic strain. However, in the case of sands, comparisons between simulations and experimental results seem to show that the relationship between the strain and stress increments depends on the stress increment. This observation implies that more complex models should be designed, with at least two plastic mechanisms, and also two or more hardening variables [LOR 82; LOR 87]. Other theoretical models have been developed on the basis of the "incrementally non-linear approach" (see Chapter 6).

3.6.6.7. *Derivation of the yield surface on the basis of experimental results*

For a practical determination of the yield surface, several methods have been proposed, depending on the nature of the soil: natural cohesive soils, frictional soils or soils reconstituted in the laboratory.

A. Case of natural cohesive soils

Research works on reconstituted soils carried out at the University of Cambridge [ROS 58; SCH 68] have led to the first elastoplastic models with hardening and with a non-linear isotropic elastic law (Cam-Clay models). Later, at the Laval University in Quebec [TAV 79] and the Laboratoire Central des Ponts et Chaussées [MAG 86; LEP 90; AZI 88], a somewhat more realistic shape for the yield surface, or limit state line, in the (p, q) space was proposed. This research, carried out on samples extracted from ground at different depths, showed that the principles of the constitutive modeling that had been elaborated for reconstituted clays, remained qualitatively acceptable for natural anisotropic clays.

Crooks and Graham [CRO 76] proposed searching for the shape of the yield surface by means of a series of triaxial tests on reconsolidated samples, subjected to the same stress level as *in situ*. Each sample is subjected to a radial drained triaxial load (Figure 3.14). For any given test, the search for a clear change of the sample behavior provides a dot in the (p, q) plane that belongs to the initial plastic domain (initial position of the yield surface).

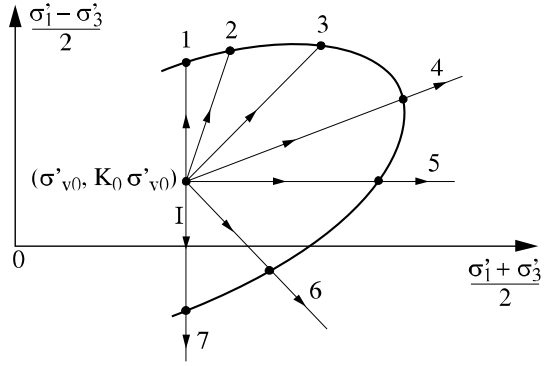

Figure 3.14. *Determination of the yield surface: principle of the method proposed by Crooks and Graham (1976)*

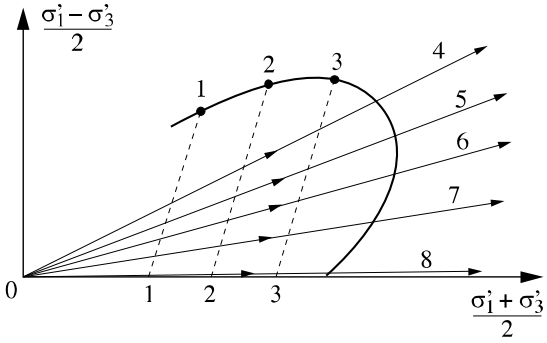

Figure 3.15. *Research of the yield surface: Tavenas and Leroueil method (1979)*

Another more simple method was described by Tavenas and Leroueil [TAV 79], which consisted of performing the whole set of traditional tests listed below:

– oedometer tests, conducted to obtain the preconsolidation pressure σ'_p; this value makes it possible to define one point of the initial position of the yield surface;

– triaxial undrained compression tests with a measurement of the pore pressure (CU+u) for confining pressures lower than 0.5 σ'_p (Figure 3.15). For each test, the peak of the (q, ε_1) curve is assumed to be associated with a point of the initial position of the yield surface;

– compression tests conducted with a constant value of the effective stress ratio, and during which volume variations are measured (Figure 3.15). Points of the initial yield surface are obtained using the same procedure as previously.

The plotting of the points characteristic of a clear change of behavior, in the (p, q) plane, shows that the initial shape of the yield surface is close to that of a more or less tilted ellipse compared to the mean pressure p axis (Figure 3.16) [LER 85]. An elastoplastic behavior law with isotropic hardening and anisotropic linear elasticity was developed, starting from these observations, to describe the behavior of natural clays [MOU 83; MAG 86; KAT 90]. The yield function suggested has the following general form:

$$f_c(\sigma_{ij}, \varepsilon_{ij}^p) = q^2 + ap^2 + bpq - pf_0(\varepsilon_v^p) - qf_1(\varepsilon_v^p) - f_2(\varepsilon_v^p) = 0$$

where a and b are two constants and f_0, f_1 and f_2 are three scalar functions.

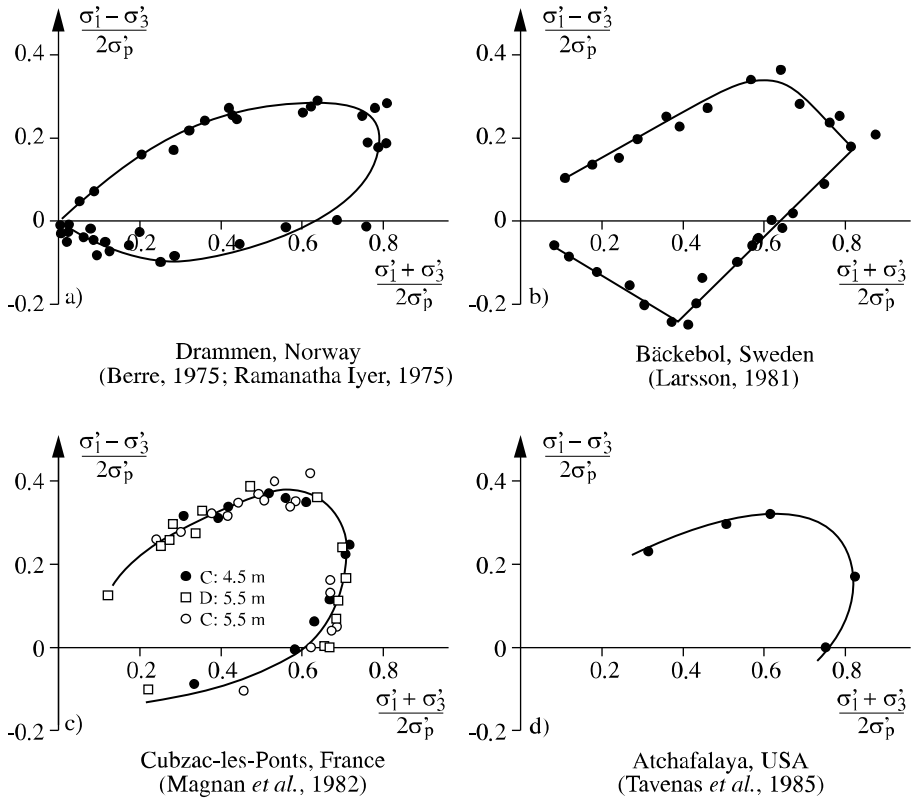

Figure 3.16. *Examples of the initial domain of elasticity for natural cohesive soils (or limit state curves)*

B. Case of frictional soils

Poorooshasb *et al*. [POO 66], then Tatsuoka and Ishihara [TAT 74], completed an important work that enabled the shape of the yield surface of sands in the (p, q) plane to be defined. They carried out, in this plane, a succession of conventional triaxial and constant deviatoric stress paths in drained condition. This approach rests on the assumption, in conformity with the principles of elastoplasticity, that the yield surface is convex and contains the origin. If a load increment brings the soil from point 1 to point 2, with the supposition that point 2 is plastic, and if the load increment is removed, this last followed path is located within the current elastic domain (Figure 3.17). A reloading up to point 6, supposed outside of the elastic domain, shows that there is necessarily a point 5, located on the yield surface defined by the value of the hardening variable of point 2 and, such as starting from this point 5, the strains increase in a notable way. This observation highlights a portion of the curve joining points 2 and 5 which belongs to the yield surface. The problem is thus to determine a function of the hardening variable "ε^p" which has the same value in points 2 and 5.

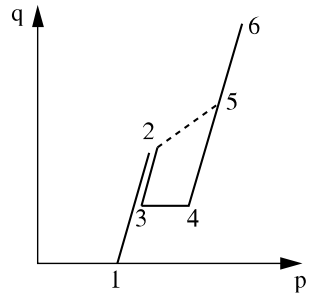

Figure 3.17. *Research of the boundary of the yield surface for frictional soils*

If the process is repeated, starting from point 5, several couples of points such as 2 and 5 will be obtained. By means of an adapted mathematical fitting, an equation of the type $f_c(\sigma_{ij}, \varepsilon^p) = 0$ or $f_c(p, q, \varepsilon^p) = 0$, can be given. Poorooshasb *et al.* (1966) established that the yield function could be approached by the equation:

$$f_c(p, q, \varepsilon^p) = \frac{q}{p} + m \ln p - f_0(\varepsilon_v^p) = 0$$

where the hardening variable ε^p is equal to the invariant ε^p_v; f_0 is a scalar function to be determined and m, a constant.

Tatsuoka and Ishihara [TAT 74] proposed introducing the plastic deviatoric strain like a hardening parameter, as well as the plastic volumetric deformation. The yield function is thus approached by the general equation

$$f_c(p,q,\varepsilon_v^p,\varepsilon_d^p) = \frac{q}{p} - f_1(p) - f_0(\varepsilon_v^p,\varepsilon_d^p) = 0$$

where f_1 is a scalar function to be determined. Figure 3.18 represents the boundary of these surfaces for various hardening states [TAT 74]. We should note that the curvature of these surfaces is all the larger, as the frictional soil is initially dense.

The trace of the yield surface has also been studied in the deviatoric plane (p = constant). The experiments on a true triaxial apparatus show that this boundary is not angular, that its form is convex, close to that of a triangle and that it is close to the shape of the yield surface (Figure 3.19) [LAD 73; ZIT 88].

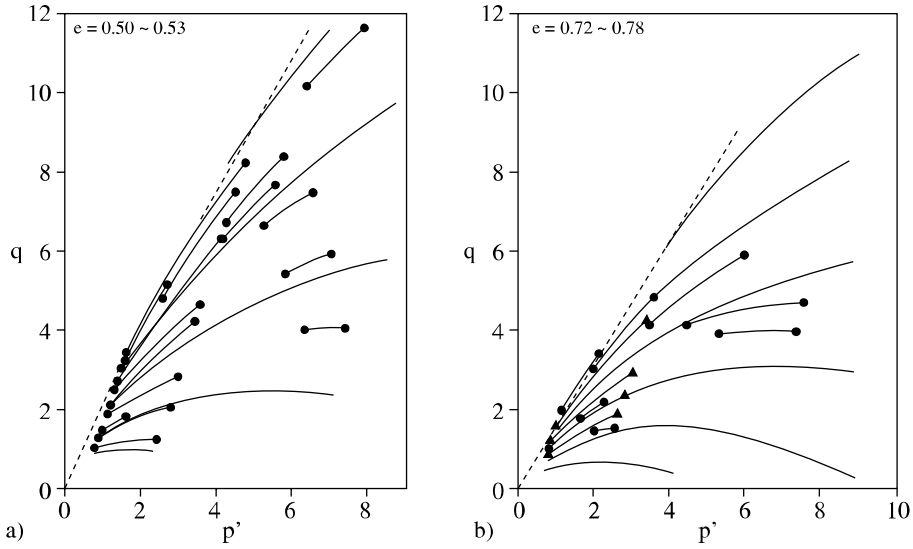

Figure 3.18. *Traces of the yield surface for various values of a hardening variable in the (p, q) plane: a) dense sand; b) loose sands (Tatsuoka and Ishihara, 1974)*

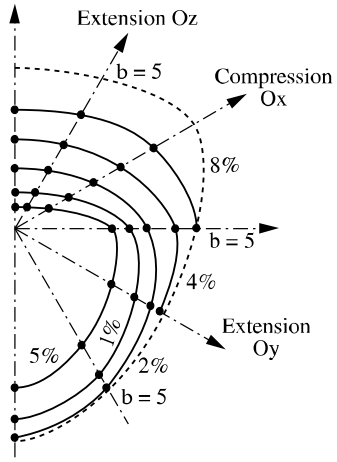

Figure 3.19. *Trace of an experimental yield surface in the deviatoric plane*

3.7. Three-dimensional aspect of the models and calculation of geotechnical works

The traditional method for constructing constitutive models prefers to use the long-established triaxial stress paths on cylindrical samples, in which the principal directions of stresses and strains remain fixed. Therefore, the models built are theoretically valid only on the paths used for their development and "fitting". Any generalization with other types of paths, or with the true three-dimensional case, remains an extrapolation to be checked.

Generalizing the three-dimensional case forces us to introduce into the equations the influence of the intermediate stress, which does not appear in the axisymmetric conditions of tests on cylindrical samples ($\sigma_2 = \sigma_3$). If the writing of the models according to invariants p and q allows a certain influence of the intermediate principal stress to be introduced, it cannot be experimentally justified when going from the cylindrical triaxial conditions ($p = \frac{\sigma_1 + 2\sigma_3}{3}$; $q = \sigma_1 - \sigma_3$) to the multiaxial conditions ($p = \frac{\sigma_1 + \sigma_2 + \sigma_3}{3}$; $q = \sqrt{3J_2}$). We can certainly always think that the conceptual model is "universal", and that, consequently, it is thus sufficient to characterize the equations on some specific tests. However, to be rigorous, it remains that this approach makes it possible to build only restrictions of the yield functions, potentials, etc. All attempts at generalizing require certain assumptions that must be confronted with the experimental reality, which only

validates or refutes a model. Ideally, we would reason directly on three-dimensional tests with three-dimensional variables. Unfortunately, the tests are both complex and expensive, thus rarely performed, in particular for cohesive soils. Their interpretation is also made difficult by the number of variables to be measured: three invariants of stresses and three invariants of strains.

In developing these models, the authors thus favored axisymmetric tests (available in great number) for setting up the constitutive equations. Thus, they tried to validate the models based on three-dimensional results and corrected the equations in order to take into account the effect of the intermediate stress, while keeping the model response as close as possible to the traditional tests results. The use of the models in finite element calculations of geotechnical works has also contributed to the evolution of their formulation, either to a certain simplification, or towards a greater complexity. The first tendency seems dominant at the present time, with a clear decrease of the number of model parameters. This is due to the fact that there is often very little geotechnical data available to estimate the parameters. Methodologies to determine the parameters must be adapted to the practice of the current studies and the interpretation of *in situ* tests.

Constant and long scientific effort has been required to the development of successive versions of a model. Only a few authors seem to have followed this path (essential in our opinion) with extended confrontations between theory, numerical method and validation. We can cite the work of Lade *et al*. ("Lade model"), Cambou *et al*. ("CJS model"), Hicher *et al*. ("Hujeux model"), Magnan *et al*. ("Melanie model") and Nova ("Nova model").

We understand that the simplest models (elastoplasticity without hardening) are still very much used by engineers in calculation of geotechnical works; this is all the more the case as they often provide satisfactory simulations, considering the uncertainties of the problem. On the other hand, if there is abundant data and if we have some measurements of the geotechnical works for an initial fitting, the models with hardening can give excellent estimated results.

3.8. Examples of perfect elastoplastic models

3.8.1. *The Mohr-Coulomb model*

3.8.1.1. *Description of the model*

This elastic, perfectly plastic constitutive law is used to describe in an approximate way the behavior of frictional (sands) and cohesive (clays and silts) soils under short and long-term conditions. In the principal stress space $(\sigma_1,\sigma_2,\sigma_3)$, the yield surface is a pyramid of hexagonal section of equation:

$$F(\sigma_{ij})=|\sigma_1-\sigma_3|-(\sigma_1+\sigma_3)\sin\varphi-2\,c\cos\varphi=0$$

where σ_1 and σ_3 represent the extreme principal stresses, ($\sigma_1\geq\sigma_2\geq\sigma_3$, with the following sign convention: compressions are counted positively). When $\varphi = 0°$ and $\psi = 0°$, the model is called the Tresca model and is used for studying cohesive soils under short term conditions; the pyramid thus degenerates into a cylinder.

The plastic potential is written: $G(\sigma_{ij})=|\sigma_1-\sigma_3|-(\sigma_1+\sigma_3)\sin\psi$.

When angles φ and ψ are equal, the flow rule is associated.

The elastic part of the behavior is defined by isotropic linear Hooke elasticity. On the whole, the model requires five parameters: E (Young's modulus), ν (Poisson's ratio), c (cohesion), φ (friction angle) and ψ (dilatancy angle). These parameters are usually obtained from laboratory test results (oedometer and triaxial apparatus). Figure 3.20 represents the modeling of a triaxial compression test of compression by the Mohr-Coulomb model. The value of the parameters results from an identification between this representation and the tangents and asymptotes obtained from the test curves represented on the same diagrams. This figure also shows that there are five unknown factors for four equations and that one needs at least two triaxial compression tests in order to determine all the parameters. In general, three tests are carried out with various confining pressures. Cohesion c and friction angle φ are also traditionally calculated in the Mohr plane (σ, τ) from the stress states at failure, estimated for each triaxial compression test.

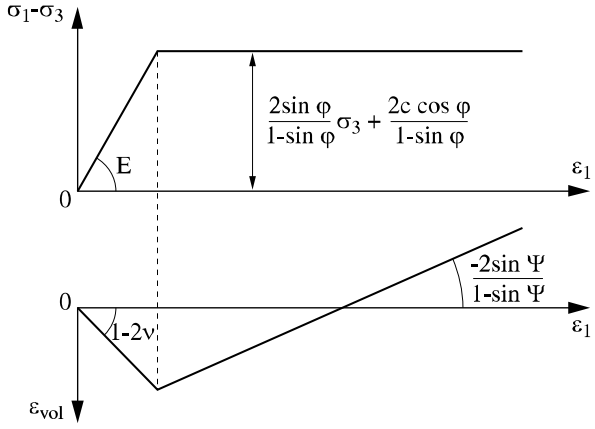

Figure 3.20. *Modeling of a triaxial compression test by the Mohr-Coulomb model*

3.8.1.2. *Typical values of the parameters of the Mohr-Coulomb model*

Several studies have been carried out concerning the influence of various factors on the value of the friction angle, in particular in the case of frictional soils (Table 3.4). The current values lie between 15 and 45 degrees. The lower values of around 30 degrees are typical for clays while higher values characterize sands (between 25 and 45 degrees). At a given density, the friction angle is practically independent of the water content of the ground, but it increases with the average diameter of the grains. The friction angle also depends on the form and the surface quality of the grains. This parameter is higher for soils with angular grains than for soils with round grains, and for a rough surface quality than for a smooth surface quality grains (Table 3.5). Cohesion c is more difficult to estimate. Nevertheless, we can note that the frictional soils practically have no cohesion ($c = 0$ or some kilopascals which are due to capillary forces or cementing) and that cohesive soils have a cohesion ranging between several and several hundred kilopascals. The value of the dilatancy angle ψ generally lies between 0 and 15 degrees. Loose sands and clays have very low values, being worth a few degrees, even zero. Generally, the friction angle is practically always higher than the dilatancy angle. A simple, generally well verified, empirical relation connecting the dilatancy angle to the natural angle of repose was proposed (P. Vermeer): $\psi = \varphi - 30°$. In addition, in the case of strongly contracting materials at rupture, the estimate of the dilatancy angle can lead to negative values.

The Young's modulus depends primarily on the strain level at which it is estimated and on the confining pressure. Table 3.6 provides orders of magnitude of Young's modulus and Poisson's ratio for sands. Table 3.7 provides some examples of parameter values deduced from the study of sands in a laboratory or adopted in calculations of geotechnical works by the finite element method. Indicative values for natural cohesive soils are provided in Tables 3.16 and 3.17, where the anisotropy is taken into account.

In addition, it is advisable to remember that the natural angle of repose obtained with tests in plane strain is 3 to 5 degrees higher than the friction angle determined by using triaxial compression tests on cylindrical samples (axisymmetric tests). Wise precautions must thus be taken before using the model in finite element calculations of geotechnical works with parameters deduced from tests made by the traditional triaxial apparatus.

Influence factor	Influence on the friction angle
Void ratio e	e ↑, φ ↓
Angularity A	A ↑, φ ↑
Uniformity coefficient C_U	C_U ↑, φ ↑
Surface roughness R	R ↑, φ ↑
Water content w	w ↑, φ ↓ slightly
Grain size	small influence if e is constant
Mean stress p	p ↑, φ ↓

Table 3.4. *Factors having an influence on the friction angle (Holtz and Kovacs, 1991).*

Nature of the ground	Compacity	φ (degrees) Rounded grains Uniform granulometry	φ (degrees) Angular grains well graded granulometry
Average sand	Very loose	28°–30°	32°–34°
	Moderately dense	32°–34°	36°–40°
	Very dense	35°–38°	44°–46°
Sand and gravel:			
65% gravel 35% sand	Loose		39°
65% gravel 35% sand	Moderately dense	37°	41°
80% gravel 20% sand	Dense		45°
80% gravel 20% sand	Loose	34°	

Table 3.5. *Orders of magnitude for the friction angle of frictional soils (Leonards, 1968)*

Type of sand	Young's modulus (MPa)	Poisson's ratio
	7–20	0.15–0.25
Loose sand	10–25	0.30–0.35
Dense sand	50–80	0.30–0.35
Very dense sand and gravel	100–200	0.30

Table 3.6. *Typical values of the elastic properties of sands*

Sand	References	γ (kN/m^3)	E (MPa)	ν	c (kPa)	φ (deg)	ψ (deg)
Hostun (loose)	Mounir (1992)	14	55	0.28	0	35	0.7
Hostun (medium dense)	Mounir (1992)	15.5	85	0.28	0	37	5.5
Hostun (dense)	Mounir (1992)	16.3	95	0.33	0	41	11
Fontainebleau	Ghorbanbeigi (1995)	15.5	40	0.33	0	39	14
Labenne	Mestat *et al*. (1999)	16	33.6	0.28	1	36.5	11.4
Karlsruhe	Arafati (1996)	16	30–45	0.25	0–3	41.6	11.6

Table 3.7. *Values of the Mohr-Coulomb parameters (sands)*

NOTE.– Improved versions of the Mohr-Coulomb model have been proposed in recent years, which incorporate linear anisotropic elasticity, modulus varying with depth, non-linear isotropic elasticity, or limitation of the plastic volumetric strain in order to describe the critical state properly.

3.8.2. *The Drücker-Prager model*

3.8.2.1. *Model formulation*

In the principal stress space $(\sigma_1,\sigma_2,\sigma_3)$, the failure surface is a cone with a circular cross section. Its equation is given by:

$$F(\sigma_{ij})=\sqrt{J_2(\sigma_{ij})}-\alpha I_1-k=0$$

where $J_2(\sigma_{ij})$ is the deviatoric stress and I_1 the trace of the stress tensor.

The plastic potential is defined by: $G(\sigma_{ij})=\sqrt{J_2(\sigma_{ij})}-\beta I_1$.

The elastic part of the constitutive relations is defined by Hooke's linear isotropic law. On the whole, the model requires five parameters: E (Young's modulus), ν (Poisson's ratio), α, β and k. When $\alpha = 0$ and $\beta = 0$, the model is reduced to that proposed by von Mises, and the cone becomes a cylinder in the principal stress space. The parameters are obtained relatively simply by means of traditional laboratory tests (oedometer and triaxial apparatus). Figure 3.21 represents the results of the simulation of a triaxial compression test for an ideal Drücker-Prager material. The value of the parameters can be deduced from the comparison of this representation and the results of tests plotted in the same axes. Like the Mohr-

Coulomb model, the Drücker-Prager model requires at least two triaxial tests for all parameters to be determined.

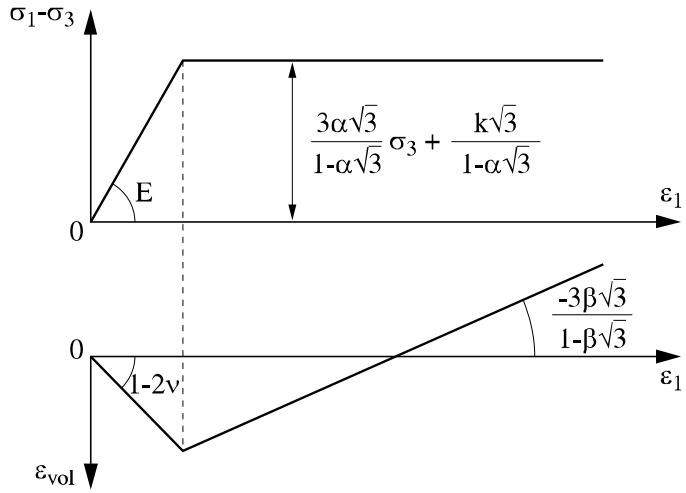

Figure 3.21. *Simulation of a triaxial compression test for an ideal Drücker-Prager material*

3.8.2.2. *Values of the parameters*

The parameters of Drücker-Prager model α, β and k are frequently expressed from those of Mohr-Coulomb c, φ and ψ. Different relations are obtained according to the test considered. For example, in the case of a triaxial compression ($\sigma_2 = \sigma_3$ and $\sigma_1 > \sigma_3$), the two criteria are written respectively:

$$\sigma_1 - \sigma_3 - (\sigma_1 + \sigma_3)\sin\varphi - 2\,c\cos\varphi = 0 \quad \text{and} \quad \frac{\sigma_1 - \sigma_3}{\sqrt{3}} - (\sigma_1 + 2\sigma_3)\,\alpha - k = 0 \,.$$

By supposing these equations verified for any stress field observing the conditions of the test, it is easy to deduce from them the relations existing between the parameters. We can proceed in the same way for other stress or strain paths (Tables 3.8 and 3.9). Particular attention was paid to the case of the plane strain condition.

Type of test	α	k	β
Triaxial compression: σ_1; $\sigma_2 = \sigma_3$ = contstant.	$\frac{2\sin\varphi}{\sqrt{3}(3-\sin\varphi)}$	$\frac{6c\cos\varphi}{\sqrt{3}(3-\sin\varphi)}$	$\frac{2\sin\psi}{\sqrt{3}(3-\sin\psi)}$
Triaxial extension: $\sigma_1 = \sigma_2$; σ_3 = contstant.	$\frac{2\sin\varphi}{\sqrt{3}(3+\sin\varphi)}$	$\frac{6c\cos\varphi}{\sqrt{3}(3+\sin\varphi)}$	$\frac{2\sin\psi}{\sqrt{3}(3+\sin\psi)}$
Plane strain: $\varepsilon_2 = 0$ (general case).	$\frac{\sin\varphi\sqrt{3+\sin^2\psi}}{\sqrt{3}(3+\sin\varphi\sin\psi)}$	$\frac{c\cos\varphi\sqrt{9+3\sin^2\psi}}{3+\sin\varphi\sin\psi}$	$\frac{\tan\psi}{\sqrt{9+12\tan^2\psi}}$
Plane strain: $\varepsilon_2 = 0$ (if $\varphi = \psi$).	$\frac{\tan\varphi}{\sqrt{9+12\tan^2\varphi}}$	$\frac{3c}{\sqrt{9+12\tan^2\varphi}}$	$\frac{\tan\psi}{\sqrt{9+12\tan^2\psi}}$

Table 3.8. *Parameters of the Drücker-Prager model according to those of the Mohr-Coulomb model*

Type of test	c	$\sin\varphi$	$\sin\psi$
Triaxial compression: σ_1; $\sigma_2 = \sigma_3$ = contstant.	$\frac{\sqrt{3}k}{2\sqrt{1+\sqrt{3}\alpha-6\alpha^2}}$	$\frac{3\sqrt{3}\alpha}{2+\sqrt{3}\alpha}$	$\frac{3\sqrt{3}\beta}{2+\sqrt{3}\beta}$
Triaxial extension: $\sigma_1 = \sigma_2$; σ_3 = contstant.	$\frac{\sqrt{3}k}{2\sqrt{1-\sqrt{3}\alpha-6\alpha^2}}$	$\frac{3\sqrt{3}\alpha}{2-\sqrt{3}\alpha}$	$\frac{3\sqrt{3}\beta}{2-\sqrt{3}\beta}$
Plane strain: $\varepsilon_2 = 0$ (general case).	$\frac{k}{\sqrt{1-12\alpha^2+\frac{3(\alpha-\beta)^2}{1-3\beta^2}}}$	$\frac{3\alpha\sqrt{1-3\beta^2}}{1-3\alpha\beta}$	$\frac{3\beta}{\sqrt{1-3\beta^2}}$

Table 3.9. *Parameters of the Mohr-Coulomb model according to those of the Drücker-Prager model*

The expression of the Drücker-Prager model also prompts the following comment: the friction angles in compression are limited to low values. In fact, the maximum friction angle that the material can have in extension is 90°, from where, while deferring in the equation of the criterion, the value of α and $\beta = 0$. Starting from these values, we can calculate the angle of maximum compression, i.e., approximately 37°. This means that the friction angle cannot exceed this value in

triaxial compression. However, particularly in the case of sands, many experimental results show the opposite. It is thus advisable to use this criterion with precaution.

3.9. Examples of elastoplastic models with hardening

Drücker, Gibson and Henkel [DRU 57] were the first to consider soils as elastoplastic materials with hardening. They assumed the existence of a yield surface similar to that of the Mohr-Coulomb model, but closed by a second surface called the "cap", able to move along the axis of isotropic compressions. This constitutive law brought about a family of models, known as "cap-models". Each was developed by introducing a fixed failure surface associated with a second variable surface (Figure 3.22). The volumetric plastic strain governs the evolution of the "cap" surface according to an empirical law. One of the main shortcomings of such models lies in the fact that they generally adopt an associated flow rule, which is generally not acceptable in view of experimental data.

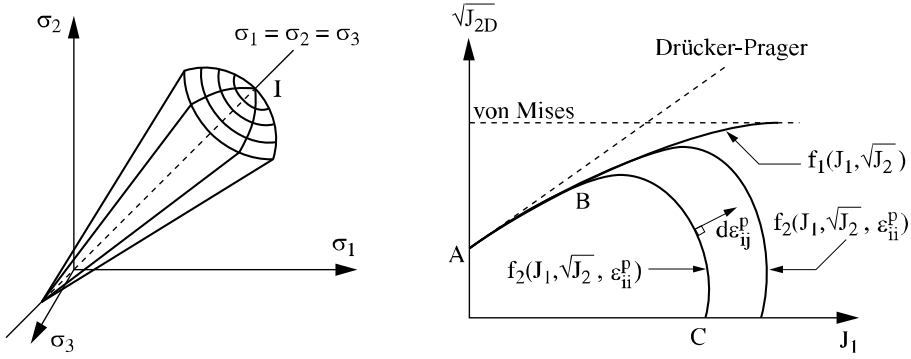

Figure 3.22. *Yield surface for a cap-model (Desai and Siriwardane, 1984)*

3.9.1. *University of Cambridge models (Cam-Clay models)*

Roscoe *et al.* [ROS 58] derived general elastoplastic constitutive relations for soils, based on the theory of hardening plasticity, and on the analysis of oedometric and triaxial tests. Such models belong to the family of "cap-models", and are known as "Cam-Clay models", or in short "Cam-Clay". They are basically oriented towards the description of the behavior of remolded clays. They are based on four main concepts: results of isotropic compression tests, the notion of critical state, the notion of a relationship between stress and dilatancy and the normality rule.

3.9.1.1. *Isotropic compression test*

In the (e, ln p) plane, [where e denotes the void ratio], the representation of the results of an isotropic compression test yields curves that can be assimilated to straight lines (Figure 3.23):

– one is the initial compression line, or λ-curve, which describes the elastoplastic phase of the test:

$$e = e_1 - \lambda \ln \frac{p}{p_1};$$

– the other is the unloading-reloading curve, or κ-curve, which represents a cycle during which the load is reduced then increased again. Within the framework of elastoplasticity, this curve is supposed to give the elastic non-linear response of the sample:

$$e = e^p - \kappa \ln \frac{p}{p_1};$$

where e_1 and e^p correspond to the values obtained for a given reference pressure denoted by p_1 (generally taken equal to 1 kPa); λ and κ are two parameters of the model.

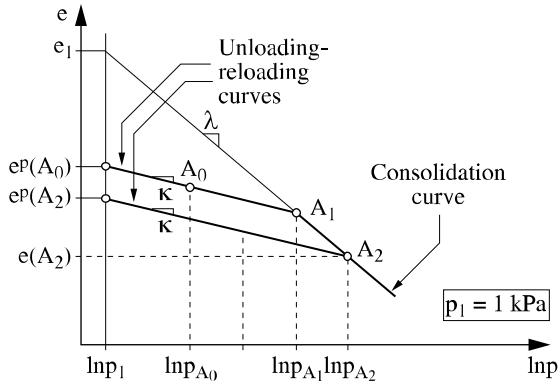

Figure 3.23. *Representation of a triaxial isotropic compression test (Cam-Clay model)*

Figure 3.23 shows that e^p (interpreted as the "plastic" void ratio: $e = e^e + e^p$) changes when the load increases, and is related to the boundary of the current elastic domain. It can therefore be used as a hardening parameter in the description of the isotropic compression test.

3.9.1.2. *Equations of the Cam-Clay models*

Plasticity is described by means of a stress-dilatancy relation derived from the analysis of triaxial compression tests such that (p = constant and q/p = constant) (Table 3.10). Integrating this differential relation makes it possible to derive the plastic potential $G(p,q,p_c)$, and, through the normality rule, the expression of the yield surface $F(p,q,p_c) = G(p,q,p_c)$.

Two versions of the Cam-Clay model have been proposed. The original model allowed us to reproduce qualitatively the main features of the experimental results. However, for some stress paths close to the isotropic compression axis, the model yields excessively large deviatoric strains. This is the reason the flow rule (or stress-dilatancy rule) was modified by Burland and Roscoe [BUR 68].

Cam-Clay model	Original version	Modified form
Stress-dilatancy rule	$\frac{d\varepsilon_v^p}{d\varepsilon_d^p} = M - \frac{q}{p}$	$\frac{d\varepsilon_v^p}{d\varepsilon_d^p} = \frac{M^2 - \left(\frac{q}{p}\right)^2}{2\frac{q}{p}}$
Yield surface	$\frac{q}{Mp} - \ln\left(\frac{p_c}{p}\right) = 0$	$\frac{q^2}{M^2p^2} + 1 - \frac{p_c}{p} = 0$
Non-linear elastic law	$d\varepsilon_v^e = \frac{\kappa}{1+e_o}\frac{dp}{p}$ $d\varepsilon_q^e = 0$	$d\varepsilon_v^e = \frac{\kappa}{1+e_o}\frac{dp}{p}$ $d\varepsilon_q^e = \frac{1}{3G}dq$

Table 3.10. *Stress-dilatancy rule, yield surface and non-linear elastic law for the Cam-Clay models*

where $\varepsilon_v^p = \varepsilon_{ij}^p \delta_{ij}$; $\varepsilon_d^p = \sqrt{\frac{2}{3} e_{ij}^p e_{ij}^p}$ and $e_{ij}^p = \varepsilon_{ij}^p - \frac{1}{3}\varepsilon_{ij}^p \delta_{ij}$.

G denotes the shear modulus and e_0 the initial void ratio.

The elastic part of the constitutive law can be formulated as follows in the elastic regime:

$$d\varepsilon_{ij}^{e} = \frac{1}{2G} d\sigma_{ij} + \left(\frac{\kappa}{3(1+e_0)p'} - \frac{1}{2G} \right) dp'.\delta_{ij}$$

The stress p_c is the "integration constant" resulting from the integration of the stress-dilatancy rule. p_c is also the coordinate of the point of the isotropic axis that is located at the intersection of the yield surface and of the isotropic compression axis, therefore on the boundary of the current elastic domain (Figure 3.24); this value can be seen as the variable governing the evolution of the yield surface, i.e., the hardening of the yield surface. The hardening law between the plastic void ratio e^p and the value of p_c can be obtained by combining the λ- and κ-curves at point p_c (Figure 3.25). We obtain the incremental relationship:

$$\frac{dp_c}{p_c} = \frac{1+e_o}{\lambda-\kappa} d\varepsilon_v^p .$$

Failure occurs when the critical state is reached: $d\varepsilon_v^p = 0$; q = M p and $e = e_{cs} - \lambda \ln \frac{p}{p_1}$.

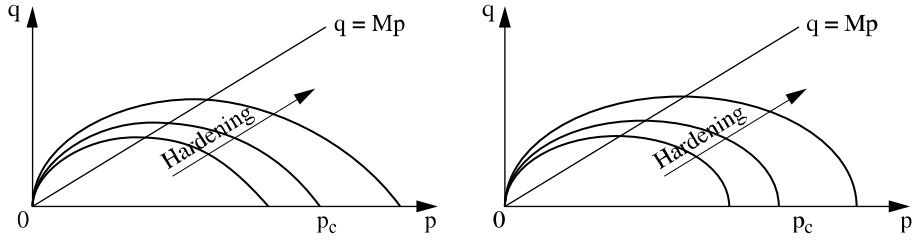

a) almond-shaped yield surface (original model)

b) elliptical surface of the modified model

Figure 3.24. *Yield surfaces of the Cam-Clay models in the (p, q) plane*

3.9.1.3. *Determination of the parameters of the modified Cam-Clay model*

The modified Cam-Clay model involves seven parameters: M, e_{cs}, λ, κ, e_1, p_1, G and three more parameters describing the initial state of the soil (e_0, p_0, q_0). The parameters can be derived from the results of triaxial tests (drained tests, or undrained tests with measurement of the pore pressure) and oedometer tests (Table 3.11).

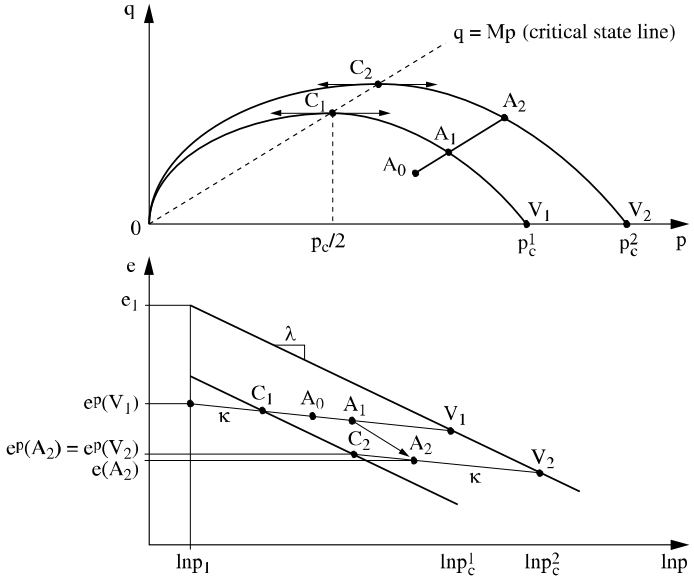

Figure 3.25. *Representation of the hardening law of the Cam-Clay models*

Parameters	Principle of the determination
e_0, p_0, q_0	Initial stress state *in situ*, or parameters estimated on the basis of isotropic compression tests or triaxial tests.
G (or E and ν)	Derivation from results of triaxial tests including unloading phases, after estimation of the initial elastic domain.
λ, κ, e_1, p_1	Interpretation of isotropic compression tests in the (e, ln p) plane, or oedometric tests. Pressure p_1 is a reference value, often taken equal to 1 kPa.
M, e_{cs}	Stress ratio at failure for shear tests in the (p, q) plane, and position of the critical state in the (e, ln p) plane.

Table 3.11. *Determination of the parameters of the Cam-Clay models*

3.9.1.4. *Examples of typical values of the parameters of the Cam-Clay model*

The state of the art report by Duncan [DUN 94] indicated that the modified Cam-Clay model remained the most used in numerical simulations of coherent soils. This stems from the fact that it is relatively simple to include in a finite element code, and from the reduced number of parameters, that can be derived from traditional soil mechanics tests. Table 3.12 gives indicative values of the parameters.

Soil	G (MPa)	ν	M	e_{cs}	λ	κ
London Clay	G(z)	0.15	0.9		0.08	0.008
Las Planas marl	150	0.3	1.18		0.04	0.007
Pescara Clay (Italy)		0.3	0.898	1.91	0.18	0.045
Clay (Rio de Janeiro)	G(z)		1.14		0.83	0.13
Clay (Muar, Malaysia)		0.3	1.19	3.07	0.13	0.05
Clay (San Francisco)			1.2	3.72	0.326	0.043

Table 3.12. *Examples of typical values of the parameters of the modified Cam-Clay model*

3.9.2. *Nova model (1982 version)*

3.9.2.1. *Description of the model*

The constitutive model proposed by Nova (version 1982) is an adaptation of the modified Cam-Clay model, devoted to the description of the sand behaviour [NOV 82]. It combines a non-linear elastic law with a hardening plastic law, with a flow rule that is associated or not, depending on the value of the stress ratio q/p (Table 3.13).

In the elastic domain, the following isotropic non-linear relation holds:

$$d\varepsilon_{ij} = L_0 d\eta_{ij} + B_0 \frac{dp}{3p}\delta_{ij}$$

where $\eta_{ij} = \dfrac{\sigma_{ij} - p\delta_{ij}}{p}$; B_0 and L_0 are two material parameters.

Stress ratio	Stress-dilatancy rule	Yield surface $F(p,q,p_c)$ and plastic potential $G(p,q,p_c)$
$\dfrac{q}{p} \le \dfrac{M}{2}$	$\dfrac{d\varepsilon_v^p}{d\varepsilon_d^p} = \dfrac{4\mu}{M^2}\dfrac{p}{q}$	$F(p,q,p_c) = G(p,q,p_c)$ $G(p,q,p_c) = \dfrac{4\mu}{M^2}\dfrac{q^2}{p^2} + 1 - \dfrac{p_c^2}{p^2} = 0$
$\dfrac{q}{p} \ge \dfrac{M}{2}$	$\dfrac{d\varepsilon_v^p}{d\varepsilon_d^p} = \dfrac{M}{\mu} - \dfrac{q}{\mu p}$	$F(p,q,p_c) = \dfrac{q}{p} - \dfrac{M}{2} + m\ \ln\left(\sqrt{1+\mu}\,\dfrac{p}{p_c}\right) = 0$ $G(p,q,p_c) = \dfrac{q}{p} - \dfrac{M}{1-\mu}\left[1 - \mu\left(\dfrac{p}{p_{cg}}\right)^{\frac{1-\mu}{\mu}}\right] = 0$

Table 3.13. *Expressions of the yield surface and of the plastic potential (according to the value of the stress ratio) for the Nova model [NOV 82]*

The evolution of the hardening parameter is governed by a linear combination of the first two invariants of the plastic strain tensor ε_v^p and ε_d^p:

$$p_c = p_{co} \exp\left(\frac{\varepsilon_v^p + D\varepsilon_d^p}{\ell - B_o} \right).$$

The hardening parameter p_c is therefore given by a relation very similar to that adopted in the Cam-Clay models; the difference lies in the introduction of the deviatoric term ε_d^p that makes it possible to account for the dilatant behavior of sands. The variable p_{cg} represents the intersection of the plastic potential with the isotropic compression axis and is linked to the hardening variable p_c.

3.9.2.2. *Determination of the parameters of the Nova model (1982 version)*

The model has eight parameters, seven of which are non-dimensional and can be derived from fitting the results of traditional drained triaxial tests ([NOV 82]; [MES 00]). Table 3.14 describes the procedure.

Parameter	Determination
B_o	Analysis of the (ε_v^e , p) curve (unloading-reloading)
L_o	Analysis of the (ε_d^e , q) curve (unloading-reloading)
M	Parameter related to the characteristic state (of sand) and to failure
μ	Parameter associated with the failure (q/p tends towards M+μD)
D	Slope of the dilatancy curve at failure
ℓ	Analysis of the (ε_v , p) curve (first loading)
m	Parameter associated with the characteristic state and with the curvature of the (q, ε_1) curve

Table 3.14. *Determination of the parameters of the Nova model (1982 version)*

The last parameter p_{co} is a reference pressure, which can be evaluated in either of the following ways:

– by assuming that the initial stress state belongs to the yield surface, p_{co} being solution to the equation $F(p_o, q_o, p_{co}) = 0$;

– by fitting tests results: this method should be avoided, since it leads to overestimation of the mechanical meaning of this parameter (which should only reflect the initial state of the soil).

3.9.3. *Mélanie model*

3.9.3.1. *Description of the model*

Works by Tavenas and Leroueil [TAV 79] on the clay of Saint-Alban (Québec) and by Magnan *et al.* [MAG 82] on the clay of Cubzac-les-Ponts (France) confirmed the applicability of the concepts developed at the University of Cambridge, with appropriate corrections to take into account the anisotropy of natural clays. These works have led to the so-called Mélanie model, developed by the French Public Works Laboratory (Laboratoire Central des Ponts et et Chaussées: [MOU 83]; [LEP 90]; [KAT 90]). The model was built according to the principles underlying the University of Cambridge models. A first version was elaborated in the ($s = \frac{\sigma_1 + \sigma_3}{2}$, $t = \frac{\sigma_1 - \sigma_3}{2}$, e) space, then adapted to the (p, q, e) space. The model is based on the following experimental observations and assumptions:

– the yield surface has en elliptical shape in the (p, q) plane (Figure 3.26);

– the yield surfaces corresponding to different preconsolidation states are deduced from one another by a homothety with respect to the origin;

– the flow rule is unassociated. The direction of the plastic strain increment is given by the bissector of the normal to the yield surface and the radial direction.

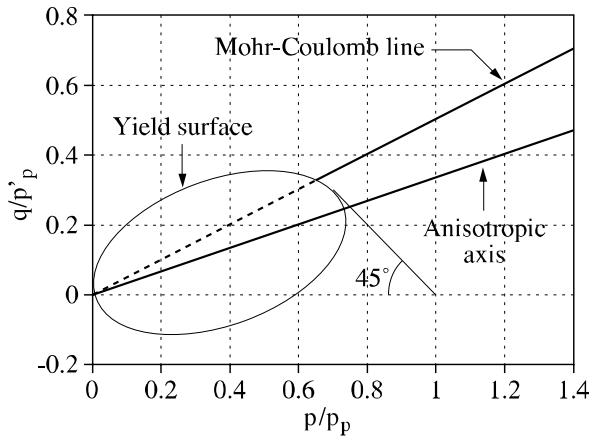

Figure 3.26. *Yield surface or limit state line of the Mélanie model*

The yield surface is an ellipse inclined with an angle θ with respect to the horizontal axis:

$$A^2\left(p\cos\theta+\frac{q}{2}\left[\sin\theta+\frac{1}{3}\cos\theta\right]-\frac{p_p}{AC}\right)^2+B^2\left(\frac{q}{2}\left[\cos\theta-\frac{1}{3}\sin\theta\right]-p\sin\theta\right)^2-\left(\frac{p_p}{C}\right)^2=0$$

where $A = 2(\cos\theta+\sin\theta)$; $B^2=\frac{A^2\cos\theta}{C\sin^2\theta}\left(\frac{2}{A}-\cos\theta\right)$; $C=0.6$ and $\theta=\arctan\left(\frac{1-K_o}{1+K_o}\right)$, and K_o denotes the coefficient of earth pressure at rest (for a normally consolidated state).

The plastic flow rule in point A of the (p, q) plane reads:

$$d\varepsilon_{ij}^p=d\lambda\frac{\partial G}{\partial\sigma_{ij}}\ \text{with}\ \frac{\partial G}{\partial\sigma_{ij}}=\frac{\dfrac{\partial F}{\partial\sigma_{ij}}}{\left\|\dfrac{\partial F}{\partial\sigma_{ij}}\right\|}+\frac{OA}{\|OA\|},$$

where $\|OA\|$ represents the Euclidean norm of vector OA.

The elastic part of the law is linear, and transversely isotropic:

$$\begin{bmatrix}\varepsilon_{xx}\\ \varepsilon_{yy}\\ \varepsilon_{zz}\\ \varepsilon_{yz}\\ \varepsilon_{xz}\\ \varepsilon_{xy}\end{bmatrix}=\begin{bmatrix}\frac{1}{nE_v} & \frac{-\nu_{hh}}{nE_v} & \frac{-\nu_{vh}}{E_v} & 0 & 0 & 0\\ \frac{-\nu_{hh}}{nE_v} & \frac{1}{nE_v} & \frac{-\nu_{vh}}{E_v} & 0 & 0 & 0\\ \frac{-\nu_{vh}}{E_v} & \frac{-\nu_{vh}}{nE_v} & \frac{1}{E_v} & 0 & 0 & 0\\ 0 & 0 & 0 & \frac{1}{G_{vh}} & 0 & 0\\ 0 & 0 & 0 & 0 & \frac{1}{G_{vh}} & 0\\ 0 & 0 & 0 & 0 & 0 & \frac{2(1+\nu_{hh})}{E_h}\end{bmatrix}\begin{bmatrix}\sigma_{xx}\\ \sigma_{yy}\\ \sigma_{zz}\\ \sigma_{yz}\\ \sigma_{xz}\\ \sigma_{xy}\end{bmatrix}$$

where $n = \frac{E_h}{E_v}$; E_v and E_h denote the elastic moduli in the vertical and horizontal directions; ν_{vh}, the Poisson's ratio in the vertical direction under a vertical stress; ν_{hh}, Poisson's ratio in the horizontal direction under a horizontal stress and G_{vh}, the shear modulus between the vertical and horizontal directions.

The constitutive law can be expressed as follows:

$$\begin{bmatrix} \sigma_{xx} \\ \sigma_{yy} \\ \sigma_{zz} \\ \sigma_{yz} \\ \sigma_{xz} \\ \sigma_{xy} \end{bmatrix} = \begin{bmatrix} c(1-n(\nu_{vh})^2) & c(\nu_{hh}+n(\nu_{vh})^2) & c(1+\nu_{hh})\nu_{vh} & 0 & 0 & 0 \\ c(\nu_{hh}+n(\nu_{vh})^2) & c(1-n(\nu_{vh})^2) & c(1+\nu_{hh})\nu_{vh} & 0 & 0 & 0 \\ c(1+\nu_{hh})\nu_{vh} & c(1+\nu_{hh})\nu_{vh} & \frac{c}{n}(1-(\nu_{hh})^2) & 0 & 0 & 0 \\ 0 & 0 & 0 & G_{vh} & 0 & 0 \\ 0 & 0 & 0 & 0 & G_{vh} & 0 \\ 0 & 0 & 0 & 0 & 0 & \frac{E_h}{2(1+\nu_{hh})} \end{bmatrix} \begin{bmatrix} \varepsilon_{xx} \\ \varepsilon_{yy} \\ \varepsilon_{zz} \\ \varepsilon_{yz} \\ \varepsilon_{xz} \\ \varepsilon_{xy} \end{bmatrix}$$

with $c = \frac{nE_v}{(1+\nu_{hh})(1-\nu_{hh}-2n(\nu_{hh})^2)}$.

The hardening parameter p_p is determined by the intersection of the isotropic original compression and of the line of isotropic reversible behavior in the (e, p) plane (Figure 3.27). The relation between e^p and p_p reads:

$$e^p = e_1 - \lambda \ln \frac{p_p}{p_1} + \alpha(p_p - p_1),$$

where e_1 denotes the void ratio corresponding to the reference pressure p_1 (generally taken as equal to 1 kPa). Slope α of the reversible isotropic strains depends on the elastic characteristics:

$$\alpha = (1+e_o)\frac{2(1-\nu_{hh})+n(1-4\nu_{hh})}{nE_v}.$$

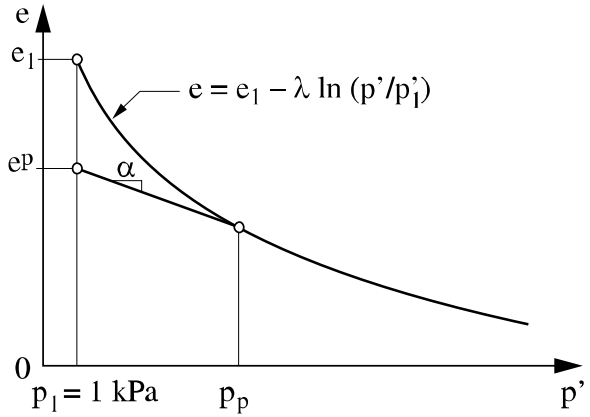

Figure 3.27. *Definition of hardening parameter p_p*

3.9.3.2. *Determination of the parameters of the Mélanie model*

The parameters can be obtained by taking advantage of the results of drained triaxial tests, undrained triaxial tests during which the pore pressure is measured, and oedometric tests (Table 3.15).

3.9.3.3. *Examples of typical values of the Mélanie model*

The Young's moduli in the horizontal direction are lower than the moduli in the vertical direction for soft clays, and larger in the case of stiff clays. In addition, it seems that the ratio of the shear modulus G_{vh} to the vertical modulus varies in the range 0.3 – 0.5. The values of the Poisson ratios lie in the range 0 – 0.40. Note that, unlike the models presented before, the elastic law is not isotropic: it must be recalled that the complete determination of the five elastic parameters of an ideally orthotropic material by means of standard tests is not common practice and remains out of reach in most cases. Indicative values are given in Table 3.16. Table 3.17 provides examples of values for the other parameters of the model.

Parameters	Principle of the determination
e_o, K_o^{nc}, K_o^{oc}, σ'_{vo}	Initial stress state, and results of tests *in situ* or in the laboratory. The coefficients of earth pressure at rest K_o^{nc} (normally consolidated state) and K_o^{oc} (overconsolidated state) are given by $K_o^{nc} = 1 - \sin\varphi$ and $K_o^{oc} = K_o^{nc}\sqrt{\frac{\sigma'_p}{\sigma'_{vo}}}$, where φ is the internal friction angle. The preconsolidation pressure σ'_p is derived from the oedometric test.
E_v, E_h, ν_{vh}, ν_{hh}, G_{vh}	Results of triaxial tests with anisotropic consolidation on samples of different orientations. In practice, the values of $\frac{E_h}{E_v}$, $\frac{G_{vh}}{E_v}$, ν_{hh} and ν_{vh} are assumed to be fixed, chosen according to values obtained on reference sites. It remains to choose E'_v. Using the oedometric tests results, we obtain $E_v = \frac{(1+e_o)(\sigma'_p - \sigma'_{vo})}{C_s \ln\frac{\sigma'_p}{\sigma'_{vo}}}\left(1 - 2\frac{E_h \nu_{vh}^2}{E_v(1-\nu_{hh})}\right)$, where C_s is the oedometric swelling index.
e_1, p_1, λ	The void ratio e_1 can be obtained experimentally by means of an oedometric test or thanks to the following relationship: $e_1 = e_0 - \alpha(p_1 - p_p) + \lambda \ln\frac{p_p}{p_1}$ where p_p defines the initial position of the yield surface. The reference pressure p_1 is equal to 1 kPa. Parameter λ is linked to the compression index C_c derived from the oedometric test ($\lambda = C_c / \ln 10$).

Table 3.15. *Determination of the parameters of the Mélanie model*

Site	E_v (MPa)	E_h (MPa)	G_{vh} (MPa)	ν_{hh}	ν_{vh}
Cubzac	3.6	2.285	1.65	0.10	0.25
Lake Agassiz	4.95	9.34	2.7	0.23	0.17
London	11	22		0.00	0.19
Léda	9.5	6.5	3.5	0.30	0.30
Lias	14	6.58		-0.38	0.19
St-Louis de Bonsecours	6.9	4.3		0.20	0.35
Romainville	22.2	24.6		0.38	0.40

Table 3.16. *Values of the elastic parameters for some natural clays*

depth	σ'_{vo} (kPa)	σ'_p (kPa)	γ (kN/m^3)	e_o	C_c	C_s	E_v (kPa)	E_h (kPa)	ν_{hh}	ν_{vh}	G_{vh} (kPa)
0–1 m	6.5	55	16	1.16	0.30	0.04	2,490	1,550	0.1	0.25	1,120
1–2 m	11	40	13.8	2.55	1.23	0.10	1,680	1,050	0.1	0.26	755
2–3 m	15	30	14.3	2.40	1.16	0.13	1,120	700	0.1	0.25	505
3–4 m	20	37	14.9	2.01	0.79	0.10	1,950	1,220	0.1	0.25	880
4–6 m	27.5	45	15	1.95	0.88	0.09	2,475	1,550	0.1	0.25	1,115
6–7 m	35	55	14.8	2.07	0.98	0.10	2,510	1,570	0.1	0.25	1,130
7–8 m	39	60	14.8	2.07	1.14	0.11	2,680	1,675	0.1	0.25	1,205
8–9 m	44	70	14.8	2.15	1.07	0.11	3,215	2,010	0.1	0.25	1,450

Table 3.17. *Examples of typical values of the plastic parameters of the Mélanie model (site of Cubzac les Ponts) (with $K_o^{nc} = 0.5$)*

3.10. Conclusions

The mechanical behavior of the solid skeleton of soils can be described satisfactorily by an elastoplastic model including hardening. Table 3.18 sums up, for different situations (nature and state of soils), the main features of the behavior and the models generally used in the finite element modeling of saturated grounds.

Nature and state of the soil	Behavior	Models generally adopted
Hard soils and soft rocks (stiff clays, marls, limestone, chalk, etc.).	Small strains, linear, depending on time (through permeability and viscosity). Failure is often brittle.	Linear or non-linear elasticity combined with consolidation and creep.
Soft soils and organic soils (soft clays, silt, mud, peat, etc.).	Large and highly non-linear strains, dependent on time (permeability and viscosity).	Elastoplasticity (with anisotropic properties when needed). Consolidation and creep.
Frictional soils (sands, gravels, etc.).	Instantaneous strains strongly dependent on the initial density (controlling dilatant or contractant behavior).	Elastoplasticity (with unassociated flow rule).

Table 3.18. *Behavior of saturated soils and simulation of structures by the finite element method*

The validation of a model by comparison with laboratory tests does not ensure its efficiency for the simulation of real structures. Testing constitutive models at the scale of the geotechnical structures requires that the model is introduced in finite element software.

In addition, the use of advanced elastoplastic models in engineering practice remains a challenge, because the models involve a large number of parameters that cannot be determined unless a large number of complex laboratory tests are carried out, and with a physical meaning that is not necessarily clear, because of the traditional difficulty of knowing the initial stress state (which has a considerably larger influence on the results than in the case of the simple usual models), and because of the heterogenity of natural or urban soils. Engineers often prefer to use the traditional Mohr-Coulomb model or the modified Cam-Clay model. More advanced models often combine features that are not well understood by the users, and the interpretation of the results (if attempted) may give rise to difficult questions.

However, advanced constitutive models, with complex hardening laws, provide an indispensable aid to getting more realistic deformation mechanisms, and more efficient design. The main difficulty lies in the determination of parameters, generally far too complex to be achieved with the data contained in a standard geotechnical survey. The lack of expertise in this field may lead to very inaccurate results and is the main reason why the use of such models remains relatively rare in day-to-day practice.

3.11. Notations

Mean stress: $p = \dfrac{\sigma_1 + \sigma_2 + \sigma_3}{3}$

Deviatoric stress: $q = \sqrt{\dfrac{(\sigma_1 - \sigma_2)^2 + (\sigma_1 - \sigma_3)^2 + (\sigma_2 - \sigma_3)^2}{6}}$.

Volumetric strain: $\varepsilon_v = \varepsilon_1 + \varepsilon_2 + \varepsilon_3$

Deviatoric strain: $\varepsilon_d = \dfrac{3}{2}\sqrt{\dfrac{(\varepsilon_1 - \varepsilon_2)^2 + (\varepsilon_1 - \varepsilon_3)^2 + (\varepsilon_2 - \varepsilon_3)^2}{2}}$.

3.12. References

[ARA 96] ARAFATI N. “Contribution à la modélisation du déchargement des massifs de sol”, Doctoral thesis, Ecole Nationale des Ponts et Chaussées, 1996.

[AUB 82] AUBRY D., HUJEUX J.C., LASSOUDIERE F. and MEIMON Y. “A double memory model with multiple mechanisms for cyclic soil behaviour”. *Proc. International Symposium on Numerical Models in Geomechanics*, Zürich, p. 3-13, 1982.

[AZI 88] AZIZI F. and JOSSEAUME H., “Loi de comportement des sols raides, Détermination de la courbe d'état limite de l'argile verte de Romainville”, Laboratoire Central des Ponts et Chaussées, Laboratory report, Série Géotechnique no. GT 33, 1988.

[BOY 80] BOYCE H.R., “A non linear model for the elastic behaviour of granular materials under repeated loading”. *Int. Symp. on Soils under Cyclic and Transient Loading,* Swansea, vol. 1, p. 285-294, 1980.

[BUR 68] BURLAND J.B. and ROSCOE K.H., “On the generalized stress-strain behaviour of wet clay”, in *Engineering Plasticity*. Heyman-Leckie, Cambridge, 1968.

[CAM 88] CAMBOU B. and JAFARI K., “Modèle de comportement des sols non cohérents”, *Revue Française de Géotechnique*, vol. 44, p. 43-55, 1988.

[CRO 76] CROOKS J.H.A. and GRAHAM J. “Geotechnical properties of the Belfast estuarine deposits”, *Géotechnique*, vol. 26, no. 2, p. 293-315, 1976.

[DAF 76] DAFALIAS Y.F. and POPOV E.P., “Plastic internal variables formalism of cyclic plasticity”, *Jour. Appl. Mech*., vol. 43, p. 645-650, 1976.

[DEG 83] DEGNY E., “Etude du comportement d'un sable dense à l'aide d'une presse tridimensionnelle”, Doctoral thesis, Institut National Polytechnique de Grenoble, Grenoble, 1983.

[DES 84] DESAI C.S. and SIRIWARDANE H.J., *Constitutive Laws for Engineering Materials with Emphasis on Geologic Materials*, Prentice Hall, 1984.

[DIM 71] Di MAGGIO F.L. and SANDLER I.S., "Material model for granular soil", *Journal of Engineering Mechanics Division*, ASCE, vol. 97, EM3, p. 935-950, 1971.

[DRU 57] DRUCKER D.C., GIBSON R.E. and HENKEL D.J., "Soil mechanics and work-hardening theories of plasticity", *Transactions of the ASCE 122*, p. 338-346, 1957.

[DUN 94] DUNCAN J.M., "The role of advanced constitutive relations in practical applications", *Proc. 13th International Conf. on Soil Mechanics and Foundation Engineering*, New-Delhi, vol. 5, p. 31-48, 1994.

[DUP 97] DUPLA J.C. and CANOU J., "Sollicitation pressiométrique cyclique et propriétés de liquéfaction d'un sable", *14ème Congrès International de Mécanique des Sols et des Travaux de Fondation*, Balkema, p. 473-476, 1997.

[GHO 95] GHORBANBEIGI S., "Développement et validation d'un programme tridimensionnel pour le calcul des ouvrages souterrains : application aux tunnels peu profonds", Doctoral thesis, Université des Sciences et Technologies de Lille, 1995.

[HIC 85] HICHER P.Y., "Comportement mécanique des argiles saturées sur divers chemins de sollicitations monotones et cycliques. Application à une modélisation élastoplastique et viscoplastique", Doctoral thesis, Pierre and Marie Curie University, 1985.

[HOE 80] HOEK E. and BROWN E.T., "Empirical strength criterion for rock masses", *Journal of the Geotechnical Engineering Division*, ASCE, vol. 106, GT9, p. 1013-1035, 1980.

[HOL 91] HOLTZ R.D. and KOVACS W.D., *Introduction à la géotechnique*. Editions de l'Ecole Polytechnique de Montréal, translated by Jean Lafleur, 1991.

[HUJ 79] HUJEUX J.C., "Calcul numérique de problèmes de consolidation élastoplastique", Doctoral thesis, École Centrale de Paris, 1979.

[KAT 90] KATTAN A., "Fluage et consolidation des sols saturés et quasi-saturés. Analyse Numérique", Doctoral thesis, École Nationale des Ponts et Chaussées, Paris, 1990.

[KOÏ 60] KOÏTER J., "General theorems for elastoplastic solids", in *Progress in Solid Mechanics*, North-Holland Pub., vol. 1, p. 165-221, 1960.

[LAD 73] LADE P.V. and DUNCAN J.M., "Cubical triaxial tests on cohesionless soil", *J. Soil Mech. Found. Div.*, ASCE, vol. 99, no. 7, p. 793-812, 1973.

[LAD 75] LADE P.V. and DUNCAN J.M., "Elastoplastic stress-strain theory for cohesionless soil", *J. Geotec. Eng. Div.*, vol. 101, no. GT10, p. 1037-1053, 1975.

[LAD 77] LADE P.V., "Elastoplastic stress-strain theory for cohesionless soil with curved yield surface", *Int. Jour. Solids and Structures*, vol. 13, no. 7, p 1019-1035, 1977.

[LAD 87] LADE P.V. and NELSON R.B., "Modelling the elastic behaviour of granular materials", *Int. J. for Num. and Analy. Methods in Geomechanics*, vol. 11, p. 521-542, 1987.

[LAD 89] LADE P.V., "Double hardening constitutive model for soils, parameter determination and predictions for two sands", in *Constitutive Equations for Granular Non-cohesive Soils*, A. Saada and G. Bianchini Ed., A.A. Balkema, Rotterdam, p. 367-382, 1989.

[LEO 68] LEONARDS G.A., *Les fondations*, Dunod, Paris, 1968.

[LEP 90] LÉPIDAS I. and MAGNAN J.-P., "Fluage et consolidation des sols argileux : modélisation numérique", Laboratoire Central des Ponts et Chaussées, Laboratory report, LPC no. 157, 1990.

[LER 85] LEROUEIL S., MAGNAN J.-P. and TAVENAS F., *Remblais sur argiles molles*, Éditions Lavoisier, Paris, 1985.

[LOR 81] LORET B., "Formulation d'une loi de comportement élastoplastique des milieux granulaires", Doctoral thesis, Ecole Nationale des Ponts et Chaussées, Paris, 1981.

[LOR 82] LORET B. and LUONG M.P. "A double deformation mechanism model for sand", *Proc. of the Fourth Int. Conf. on Num. Methods in Geomech*., Edmonton, p. 197-205, 1982.

[LOR 87] LORET B. "Application de la théorie des multimécanismes à l'étude du comportement des sols", in *Manuel de Rhéologie des Géomatériaux*, Presses de l'ENPC, Paris, p. 189-214, 1987.

[LUO 80] LUONG M. T., "Phénomènes cycliques dans les sols pulvérulents", *Revue Française de Géotechnique*, no. 10, p. 39-53, 1980.

[LUO 83] LUONG M.P. and TOUATI A., "Sols grenus sous fortes contraintes", *Revue Française de Géotechnique*, no. 24, p. 51-63, 1983.

[MAG 86] MAGNAN J.-P., "Modélisation numérique du comportement des argiles molles naturelles", Laboratoire Central des Ponts et Chaussées, Laboratory report, LPC, no. 141, 1986.

[MAG 89] MAGNAN J.P., "Validation des méthodes de calcul des déformations des sols mous par comparaison avec le comportement des ouvrages", *Symposium franco-soviétique VNIIOSP-LCPC*, Moscou, avril 1989, Laboratoire Central des Ponts et Chaussées, Laboratory report, GT 39, p. 47-84, 1989.

[MAG 82] MAGNAN J.P., SHAHANGUIAN S. and JOSSEAUME H., "Etude en laboratoire des états limites d'une argile molle organique", *Revue Française de Géotechnique*, no. 20, p. 13-19, 1982.

[MAG 84] MAGNAN J.P. and PIYAL M., "Mesure des paramètres d'élasticité anisotrope de l'argile molle organique de Cubzac-les-Ponts dans le domaine surconsolidé", *Revue Française de Géotechnique*, no. 33, p. 5-18, 1984.

[MAN 65] MANDEL J., "Généralisation de la théorie de la plasticité de W.T. Koïter", *Int. Jour. of Solids and Structures* 1, p. 273-295, 1965.

[MAT 74] MATSUOKA H. and NAKAI T., "Stress-strain and strength characteristics of soil under three different principal stresses", *Proc. Japanese Society of Civil Engineers*, no. 232, p. 59-70, 1974.

[MAT 90] MATSUOKA H., HOSHIKAWA T. and UENO K., "A general failure criterion and stress-strain relation for granular materials to metals", *Soils and Foundations*, vol. 30, no. 2, p. 119-127, 1990.

[MES 98] MESTAT P. and ARAFATI N., "Modélisation par éléments finis du comportement du rideau de palplanches expérimental de Hochstetten", *Bulletin des Laboratoires des Ponts et Chaussées*, no. 216, p. 19-39, 1998.

[MES 00] MESTAT P. and ARAFATI N., "Modélisation des sables avec la loi de Nova : détermination des paramètres et influence sur les simulations", *Bulletin des Laboratoires des Ponts et Chaussées*, no. 225, March-April, p. 21-40, 2000.

[MOU 83] MOURATIDIS A. and MAGNAN J.P., "Modèle élastoplastique anisotrope avec écrouissage pour le calcul des ouvrages sur sols compressibles. Laboratoire Central des Ponts et Chaussées, Paris, Laboratory report, LPC no. 121, 1983.

[MRO 78] MROZ Z., NORRIS V.A. and ZIENKIEWICZ O.C., "An anisotropic hardening model for soils and its application to cyclic loading", *Int. J. Num. Anal. Meth. in Geom.*, vol. 2, p. 203-222, 1978.

[NAM 70] NAMY E., "An investigation of certain aspects of stress-strain deformation for clay soils", PhD Thesis, Cornell University, 1970.

[NOV 82] NOVA R., "A model of soil behaviour in plastic and hysteretic ranges", *International Workshop on Constitutive Behaviour of Soils*, Grenoble, p. 289-309, 1982.

[POO 66] POOROOSHASB H.B., HOLUBEC I. and SHERBOURNE A.N., "Yielding and flow of sand in triaxial compression", *Canadian Geotechnical Journal*, Part 1 (1966), vol. 4, no. 3, p. 179-190; Part 2 and 3 (1967), vol. 4, no. 4, p. 376-397.

[ROS 58] ROSCOE K.H., SCHOFIELD A.N. and WROTH C.P. "On the yielding of soils", *Géotechnique*, vol. 8, no. 1, p. 22-53, 1958.

[SCH 68] SCHOFIELD A.N. and WROTH C.P., *Critical State Soil Mechanics*, McGraw-Hill, New York, 1968.

[STR 71] STROUD M. A., "The behaviour of sand at low stress levels in the simple shear apparatus", PhD Thesis, Cambridge University, UK, 1971.

[TAN 90] TAN C. H., "Développement d'un modèle élastoplastique pour le comportement des matériaux granulaires sous sollicitations non monotones complexes", Doctoral thesis, Université des Sciences et techniques de Lille, 1990.

[TAT 74] TATSUOKA F. and ISHIHARA K., "Yielding of sand in triaxial compression", *Soils and Foundations*, vol. 14, no. 2, p. 63-76, 1974.

[TAV 79] TAVENAS F. and LEROUEIL S., "Les concepts d'état limite et d'état critique et leurs applications à l'étude des argiles", *Revue Française de Géotechnique*, no. 6, p. 27-49, 1979.

[TOU 82] TOUATI A. "Comportement mécanique des sols pulvérulents sous fortes contraintes", Doctoral thesis, Ecole Nationale des Ponts et Chaussées, Paris, 1982.

[VAN 80] VAN EEKELEN H.A.M., "Isotropic yield surfaces in three dimensions for use in soil mechanics", *International Journal for Numerical and Analytical Methods in Geomechanics*, vol. 4, p. 89-101, 1980.

[VER 82] VERMEER P., "A five constant model unifying well established concepts", *International Workshop on Constitutive Behaviour of Soils*, Grenoble, p. 175-197, 1982.

[ZIT 88] ZITOUNI Z., "Comportement tridimensionnel des sables", Doctoral thesis, Joseph Fourier University, Grenoble, 1988.

Constitutive Modeling of Soils and Rocks
Edited by Pierre-Yves Hicher & Jian-Fu Shao

Chapter 4

Elastoplastic Modeling of Soils: Cyclic Loading

Cyclic loading applied to soils occur for different reasons. It can result from an intentionally applied procedure, such as compaction, in order to improve the soil's mechanical behavior for the building of roads, embankments, backfills, etc. It can be the consequence of natural hazards such as earthquakes, waves, wind, etc. We therefore need to develop constitutive models which can be used in construction projects.

4.1. Soil behavior under drained loading

4.1.1. *Isotropic and oedometric cyclic loading*

A succession of isotropic loading and unloading creates a progressive compaction of granular materials. For a given number of cycles, compaction increases with the stress amplitude. The cycles become more and more reversible but a complete stabilization can be achieved only for very high numbers of cycles (Figure 4.1) [LUO 80]. Similar results are obtained along "radial" stress paths: q/p' = constant, including the oedometric loading.

Chapter written by Bernard CAMBOU and Pierre-Yves HICHER.

4.1.2. *Cyclic triaxial loading*

4.1.2.1. *One-way cyclic tests*

One-way tests, in which q is cycled between zero and q_c, show a significant plastic strain during the first cycle. The cycles retain practically the same shape as they move along the ε_1 axis (Figure 4.2) [FRA 79].

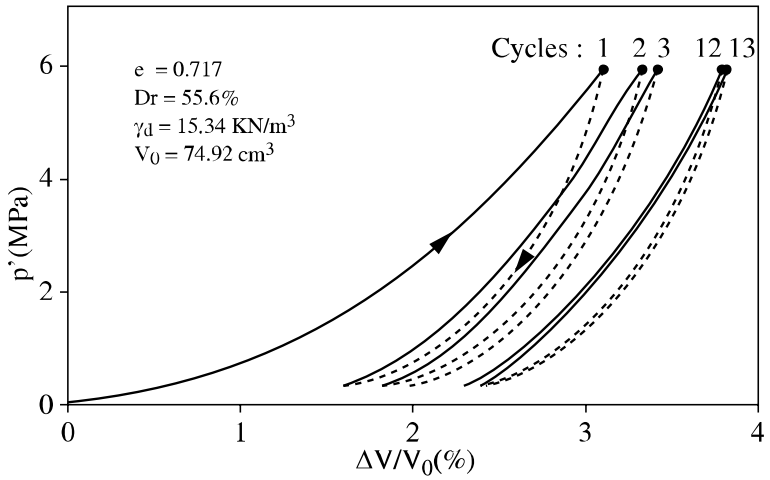

Figure 4.1. *Cyclic isotropic loading on Fontainebleau Sand [LUO 80]*

The plastic strain during the first loading is important. It is clearly less so for the following cycles even though the plastic deformations continue. If after one or several cycles up to the same stress amplitude, the maximum stress amplitude is increased, a "bend" in the stress-strain curve appears. There is a clear reduction in the gradient when the stress passes the maximum reached in preceding cycles. However, the following cycles are more regular and are straighter at the top of the cycle.

There is therefore a "memory phenomenon" which can be characterized by the maximum value of the cyclic stress amplitude. This becomes a memory parameter analogous to p'_{ic} and this mechanism plays the role of a loading surface. Its increase is associated with significant plastic deformations. Inside the surface there is also plastic strain but of lower amplitude.

Volume changes depend on the position of the stress path with respect to the contractant domain (in general $q'/p' < M$) defined by monotonic tests. If the stress path is situated entirely within this region, the cycles will produce a progressive

compaction even for initially dense materials. If it crosses the boundary of the region during each cycle, there will be a period of compaction and a period of dilation. If the average level of the cycle lies within the contractant domain, cyclic loading produces a compaction; otherwise it produces a dilation [LUO 80].

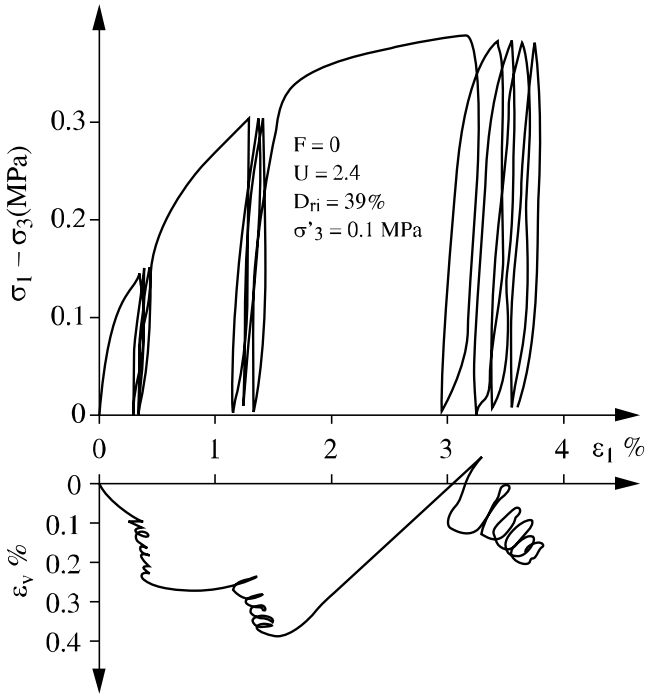

Figure 4.2. *One-way cyclic triaxial test on Granville Sand [FRA 79]*

Figure 4.3 presents results on a normally consolidated clay [DOA 84]. In this case, the material always contracts and the additional compaction caused by cyclic loading compared to monotonic loading can be seen. A monotonic loading after the cycles shows that this additional compaction gives to the material an overconsolidated behavior.

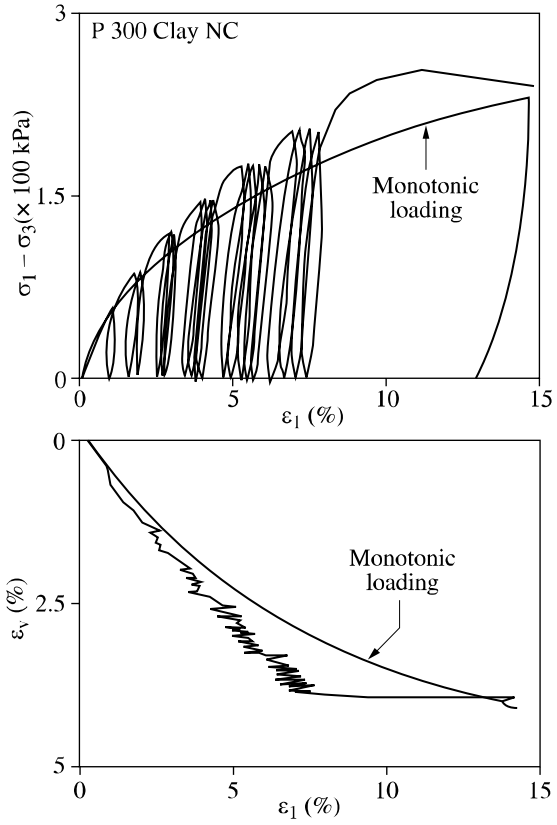

Figure 4.3. *One-way cyclic triaxial test on normally consolidated clay [DOA 84]*

4.1.2.2. *Two-way cyclic triaxial tests*

In this type of test each cycle, which consists of alternating axisymmetric compression and extension, involves a sudden 90° change in the directions of the major and minor principal stresses as they interchange. The results showing the influence of a rotation of the principal stress (Chapter 3) reveal that considerable rotation tends to cause compaction when the stress is close to the isotropic state and therefore well inside the contractant domain. The results of two-way cyclic tests confirm this analysis and progressive compaction is always observed irrespective of the amplitude and the average level of the cycles. Figures 4.4 and 4.5 show the results obtained on sand which can be compared with the previous graphs. For the same number of cycles at the same amplitude, the final density is always higher for two-way tests. In the case of normally consolidated clay, the variation in volume for a two-way cyclic test is twice that for a one-way test.

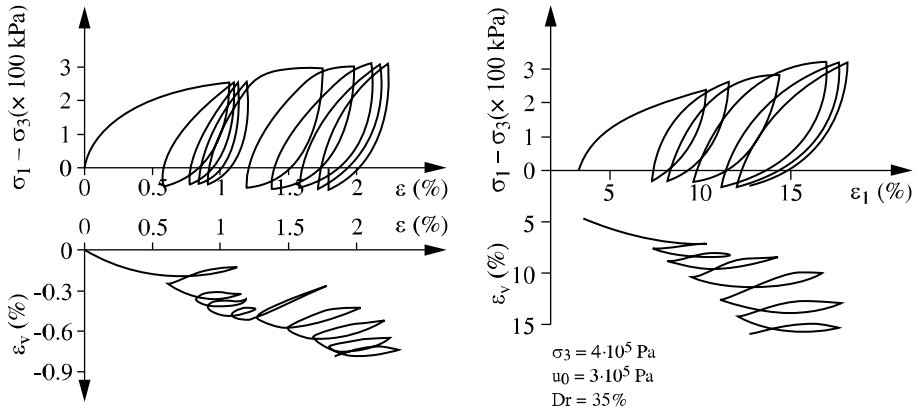

Figure 4.4. *Two-ways cyclic triaxial test on Granville Sand [FRA 79]*

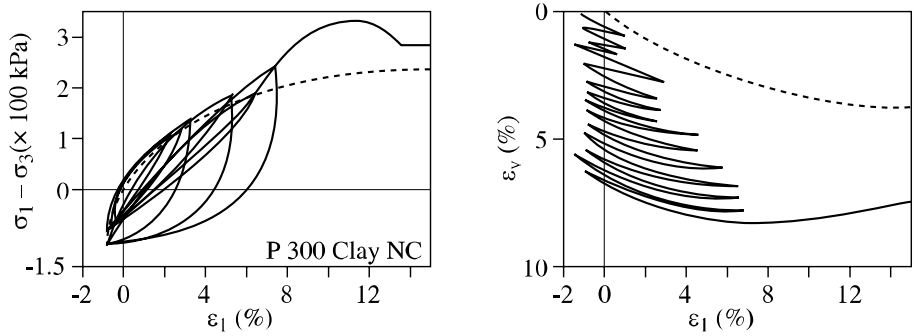

Figure 4.5. *Two-ways cyclic triaxial test on normally consolidated clay [DOA 84]*

The shape of the stress-strain cycles may alter. We no longer see a simple translation of the loop for each cycle along the ε_1 axis, but instead a modification of its slope. Tests with fixed strain amplitudes lead to analogous results. Due to the increasing density of the material with each cycle, the value of the maximum stresses in compression or in tension increases with each cycle. The variation in volume clearly shows a region of contraction bounded (in compression as for extension) by a limiting value of q'/p' beyond which dilation occurs (Figure 4.6).

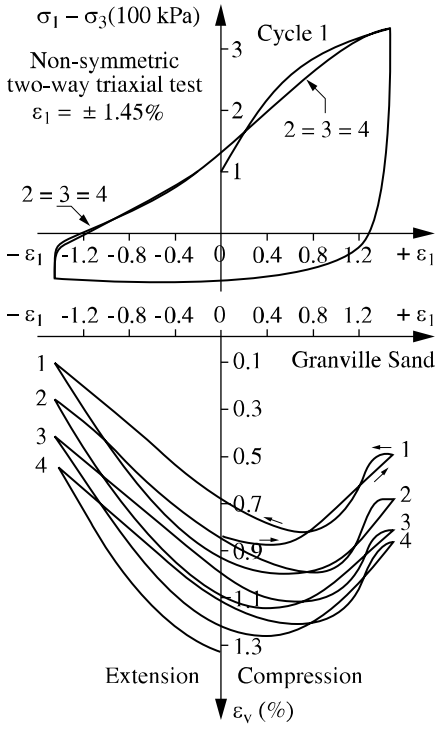

Figure 4.6. *Two-ways cyclic triaxial test at constant strain amplitude [FRA 79]*

4.1.3. *Influence of rotating principal axes*

Wong and Arthur [WON 86], using the directional shear, carried out tests on loose sand, keeping the ratio σ'_1/σ'_3 constant and cyclically turning the axis of σ'_1 and σ'_3 through a constant amplitude of rotation (θ). Figure 4.7 shows the volume variations obtained. For an amplitude of $\theta = 30°$, no significant variation occurs; for $\theta = 55°$ and 70° they obtained considerable contraction during the cycles. These results can be explained by the influence of induced anisotropy. Monotonic tests with the same apparatus have shown a decrease in the gradient of q-ε_1 curves when the direction of the major principal stress deviates from the direction of anisotropy created by a preceding loading. This phenomenon is accompanied by an increase in compaction and is particularly marked for angles > 50°. This limit angle corresponds approximately to the orientation of the lines with no extension during the initial loading. This could be explained by the fact that, during a loading, the number of intergranular contacts increases in the compression zones and decreases in the extension zone. During the rotation, the contacts re-orient themselves. This becomes more significant when the direction of σ_1 is found to correspond to a

previous line of extension, leading to a reduction in modulus and an increase in compaction.

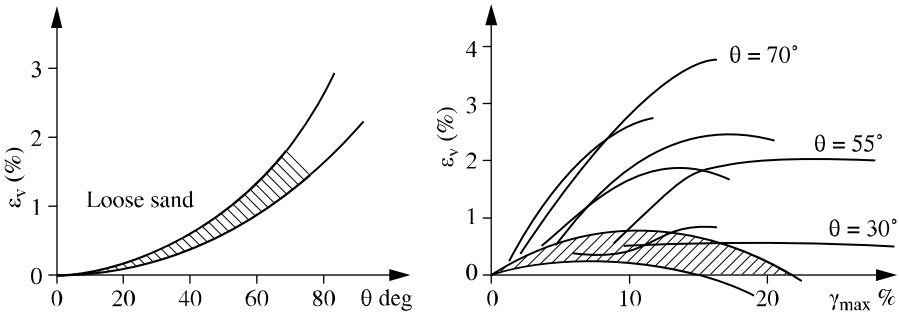

Figure 4.7. *Volume changes due to cyclic rotation of principal stress directions [WON 86]*

This effect of stress rotation was confirmed by tests carried out by Joer [JOE 91] on a two-dimensional material (PVC rods) in a plane strain device called "1γ2ε". Tests with constant principal stresses and continuous rotation of the principal axes were performed. The cyclic effect of the rotation induced a compaction of the specimen (Figure 4.8). Along the circular stress path, incremental strain vectors were super-imposed, showing that the principal incremental strain axes do not coincide with the principal stress axes. A cyclic rotation of principal directions could therefore produce significant variations of volume in the material which would be accompanied by a modification of the stress-strain relationships during the cycles.

4.2. Isochoric triaxial tests

Isochoric tests correspond in particular to undrained tests on saturated soils. In the isochoric test, variations of mean stress will depend on the tendency of the soil to contract or dilate. We have seen in the preceding paragraphs that cyclic tests generally lead to an increase in the density of granular materials. In the isochoric test, this will translate into a decrease in mean stress. The decrease could, in certain cases, be large enough to cause complete loss of stress: this is the phenomenon of liquefaction, also called cyclic mobility.

Liquefaction only occurs with two-way cyclic tests. One way tests also produce decreases in mean stress, but these tend to stabilize before liquefaction occurs.

Many factors determine whether a granular material will or will not liquefy:

– relative density (Dr): the higher Dr is, the more cycles are required for liquefaction to occur;

– mean stress;

– cyclic stress amplitude;

– particle size distribution: a uniform particle size facilitates liquefaction.

Figure 4.10 shows the behavior of a granular material during a liquefaction test. This process can be broken down into three stages:

(a) small cyclic deformation, constant decrease of mean stress;

(b) the stress path reaches the intrinsic line. The mean stress continues to decrease, the cyclic strain accelerates and the cycle develops a “stepped” like shape;

(c) the stress path becomes stable. It passes the point of zero effective stress twice per cycle. The mean stress varies periodically. Strains become large and continue to increase.

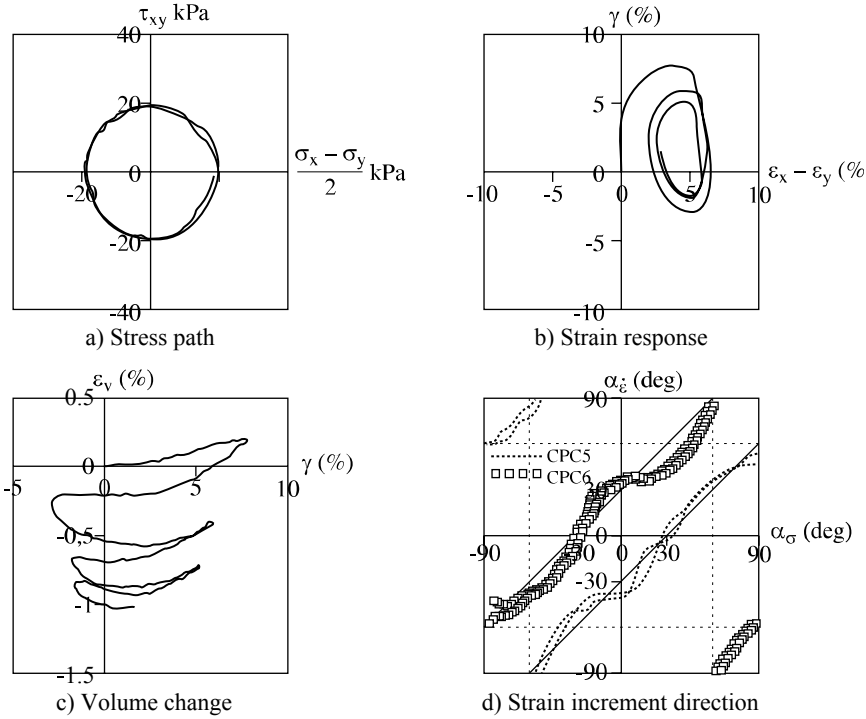

Figure 4.8. *Cyclic compaction due to cyclic rotation of principal stress directions [JOE 91]*

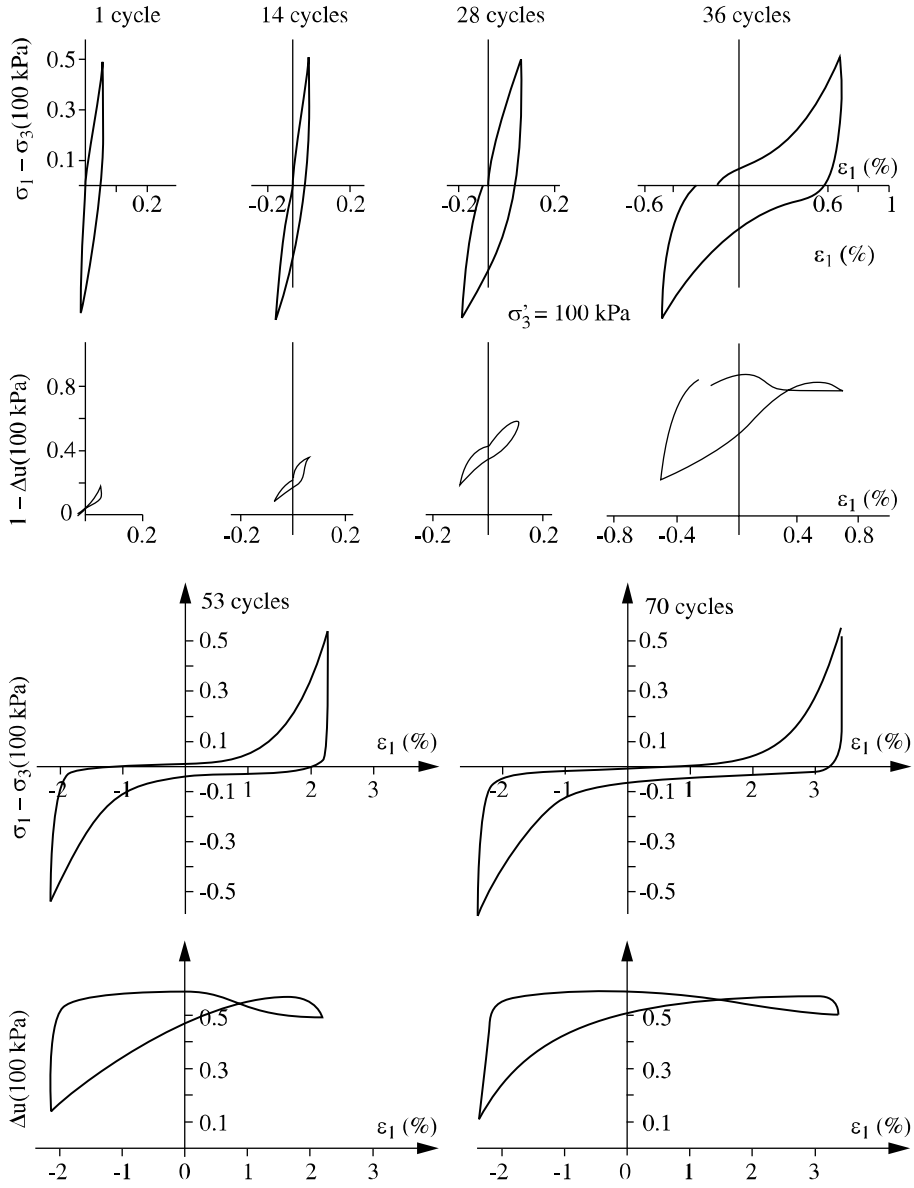

Figure 4.9. *Undrained cyclic triaxial test on Granville Sand [FRA 79]*

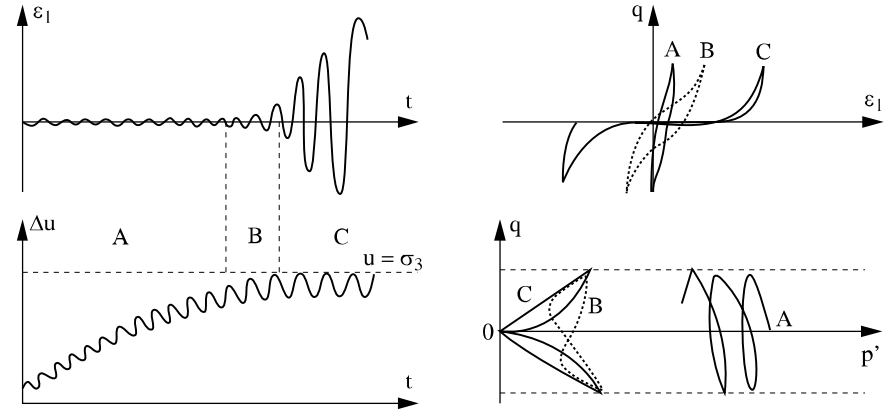

Figure 4.10. *Schematic representation of cyclic liquefaction*

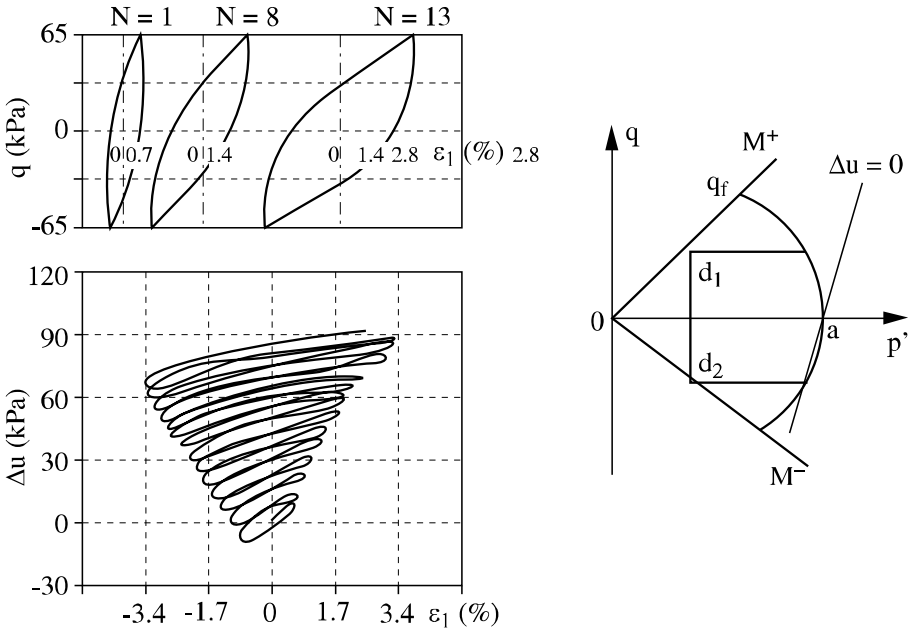

Figure 4.11. *Undrained cyclic triaxial test on normally consolidated clay*

There is therefore a liquefaction region in which deformations are associated with near-zero stress. This explains the long "flat" portion of the q'-ε_1 curves on either side of the origin during which the material has very little rigidity. Beyond a

certain strain however, depending on the shape of the cycle, the mean stress increases and the material stiffens. If monotonic loading is continued beyond the value of the cyclic stress amplitude, the same strength values are obtained after liquefaction as before.

In the case of clay the pore pressure increases until the stress cycle meets the line of perfect plasticity q = Mp'. At this point there is a large increase in the strain and a general rupturing of the material (Figure 4.11).

The effect of the principal axis rotation can also be observed in isochoric tests. Figure 4.12 presents results obtained by Joer [JOE 91] in the 1γ2ε device. Continuous rotations of principal strain axes were imposed at constant volume. In the deviatoric stress plane (τ_{xy}, $(\sigma'_x - \sigma'_y)/2$) the path takes the form of a spiral towards the origin. The mean effective stress $(\sigma'_x + \sigma'_y)/2$ increases at the beginning of the tests, then decreases continuously to zero. The state of stress tends to move to the origin and a liquefaction state occurs due to the cyclic rotation of the principal strain axes.

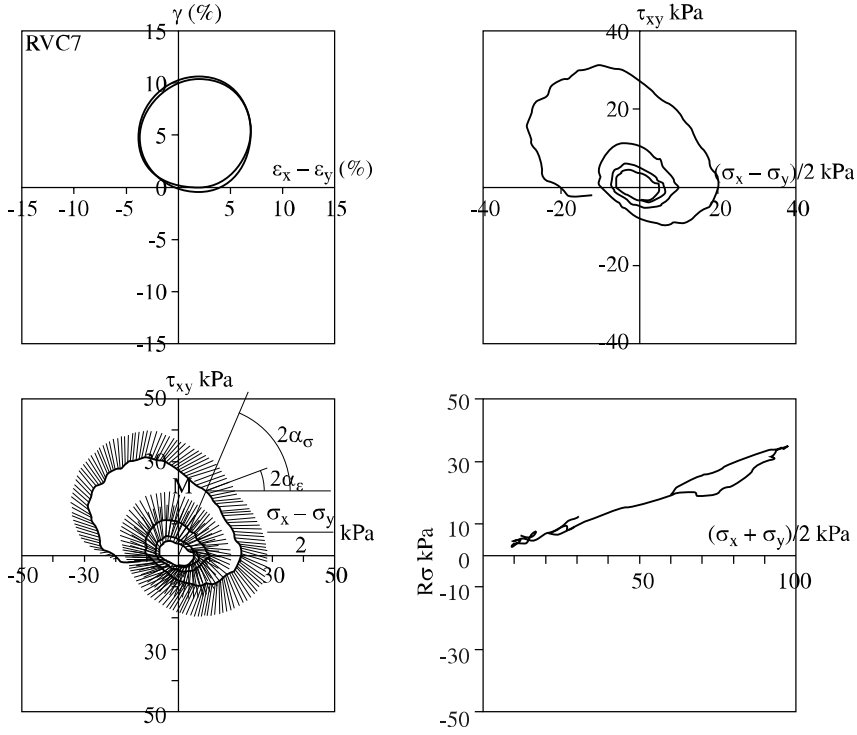

Figure 4.12. *Cyclic liquefaction by rotating principal strain directions [JOE 91]*

The influence of a rotation of the principal stresses in undrained condition has also been studied on clay. Hicher and Lade [HIC 87] have carried out tests on an anisotropic K_0-consolidated clay with and without rotation of the principal stress with respect to the axis of anisotropy. The same cyclic stress amplitude has been applied in three-dimensional triaxial tests and on hollow cylinders, with a rotation of the major and minor principal stresses in the latter case. The pore pressure was found to be sensitive to the rotation in that a rotation caused a larger increase in the pore pressure. In addition, the strains were larger in the presence of rotation (Figure 4.13).

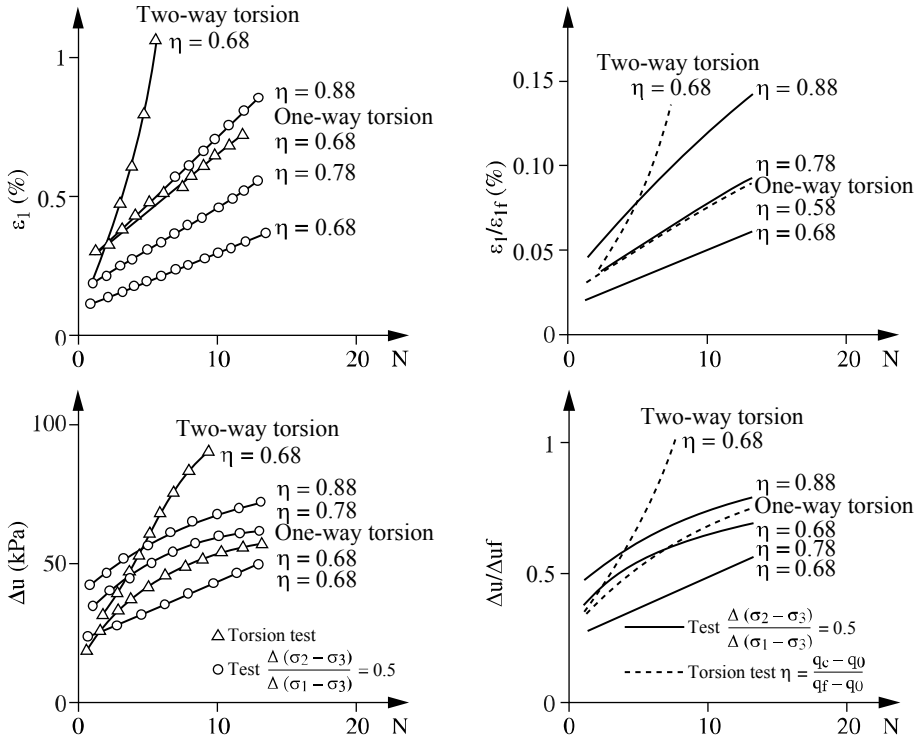

Figure 4.13. *Influence of principal stress axes rotation in undrained condition on normally consolidated clay*

4.3. Modeling soil cyclic behavior

The experimental results presented in the previous section show on one hand the influence of the stress loading history, which affects mainly the deviatoric response, and on the other hand the influence of the volume change, which leads to a density

increase in a drained condition and a decrease of the mean stress in an undrained condition. The first aspect corresponds to an evolution of the stress induced anisotropy with the loading history, which is similar to what can be observed on other different materials. We can take this into account in the framework of plasticity theory by means of a kinematic hardening, with respect to a hardening tensorial variable whose evolution can be continuous or discrete. The second aspect needs the introduction of a second hardening variable, which can be a scalar related to the density change.

4.3.1. *Difficulties involved in the modeling of the soil cyclic behavior in the framework of elastoplasticity*

The simplest elastoplastic models are based on one yield surface without hardening (for example the elastic plastic Mohr Coulomb model) or with isotropic hardening (such as the Cam-Clay model), or on two yield surfaces, one for isotropic loading and the other for deviatoric loading, both presenting isotropic hardening (such as Lade's model) (see Chapter 3). These models can reproduce the soil behavior along monotonic loading but appear not to be adapted for a realistic description of the cyclic behavior.

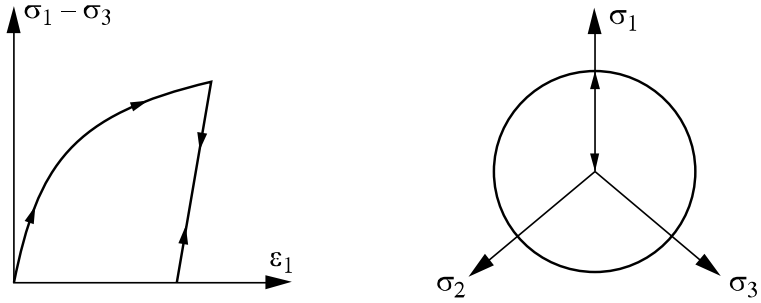

Figure 4.14. *Modeling the cyclic behavior by means of an elastoplastic Drücker-Prager model with isotropic hardening*

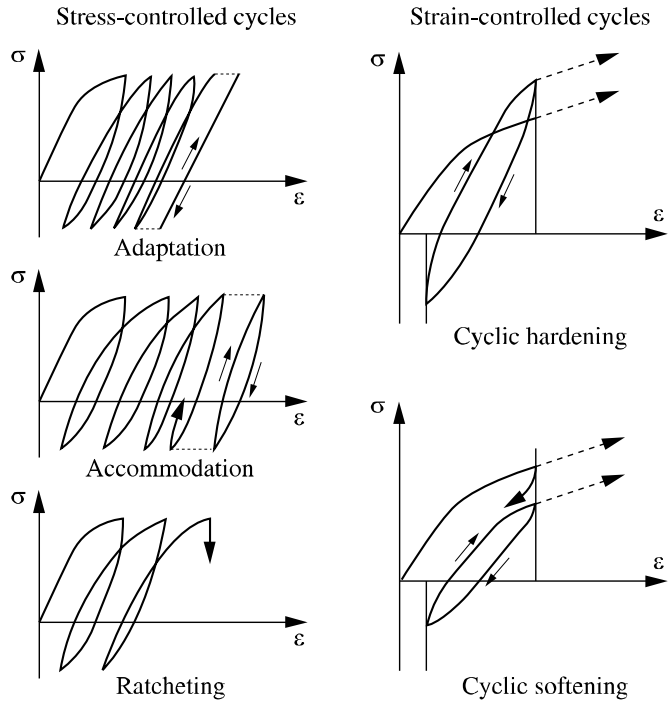

Figure 4.15. *Several types of cyclic behaviors*

In fact, with this type of model, the yield surface is activated and plastic deformation occurs during the initial loading. However, unloading and reloading up to the maximum stress during the first loading do not activate the plasticity mechanism and the cyclic loading is modeled by an elastic behavior (Figure 4.14), whereas experimental results show that irreversible deformations take place during successive cycles.

The different plastic phenomena which can occur during cyclic loading are characterized in Figure 4.15. If we consider a constant stress amplitude loading, three types of behavior can be found. The "adaptation" corresponds to cycles, initially open with energy dissipation, which converge towards a purely non-dissipative elastic cycle. The "accommodation" corresponds to an open cycle, with energy dissipation and irreversible cumulative deformation, which evolve progressively towards a stabilized cycle with a hysteresis loop showing energy dissipation. Experimentally, this phenomenon is found during drained, one-way cyclic tests, with small or moderate amplitude and a large number of cycles. The

"ratchet" phenomenon corresponds to open cycles with irreversible strain accumulation, keeping the same shape (Figure 4.15).

For cyclic loading at constant strain amplitude, types of behavior can be defined. The cyclic hardening corresponds to an increase in the cyclic stress amplitude, as for example during drained cyclic tests with density increase. The cyclic softening corresponds to the opposite phenomenon, as in undrained tests with pore pressure increase.

These behaviors cannot be reproduced by a simple model such as that presented in Figure 4.14. Modeling the soil cyclic behavior requires more complex models, which are capable of producing plastic deformations during the whole sequence of cycles. Different approaches have been proposed and the main ones are presented in the following sections.

4.3.2. *The Masing model*

The Masing model was originally developed for the modeling of metallic material behavior. It has become the basic model for cyclic plasticity. In a simple 1D version, it can be considered as a generalization of the Prager model, which can be defined by the rheological model in Figure 4.16.

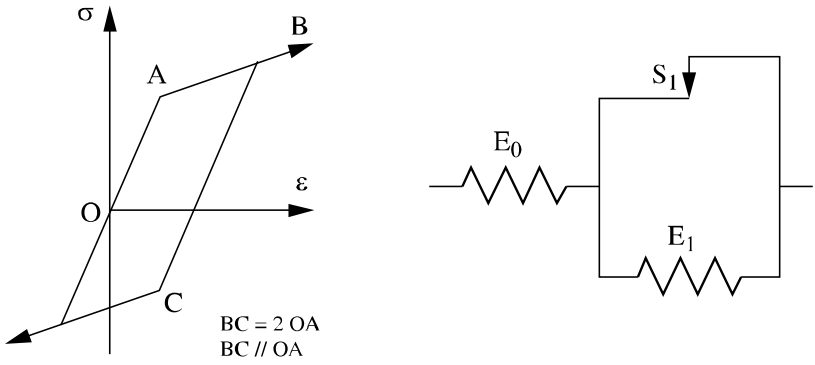

Figure 4.16. *Prager's model response in cyclic loading*

The elastoplastic Prager model corresponds to: $\varepsilon=\varepsilon^e+\varepsilon^p$

The elastic part is given by:

$\sigma=E_0\varepsilon^e$, $\dot{\varepsilon}^p=0$, $\left|\hat{\sigma}_1\right|<s_1$

The plastic part is given by:

$f = \left|\sigma - E_1\varepsilon^p\right| - s_1 \le 0$ (elastic limit), $\dot{\varepsilon}^p \neq 0$, $\left|\hat{\sigma}_1\right| = s_1$

$\hat{\sigma}_1$: stress transmitted by the frictional pad s_1 with $|\hat{\sigma}_1| \le s_1$

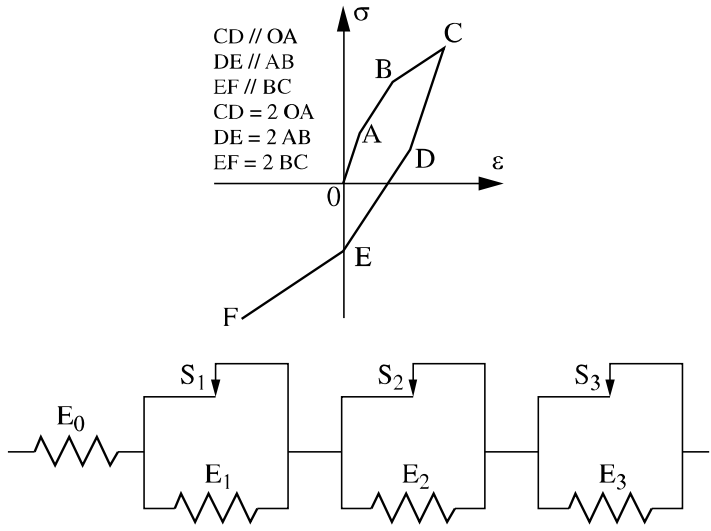

Figure 4.17. *Extended Prager's model response in cyclic loading*

The model has a plasticity criterion which depends on the internal variable ε^p. It corresponds therefore to a hardening plasticity model. We can show that, during a cyclic loading, the center $E_1\varepsilon^p$ of the elastic domain evolves, but its size remains constant, equal to $2s_1$, which corresponds to a kinematic hardening. Since the plastic part of the deformation is linearly linked to the stress in spring E_1, the model is defined as an elastoplastic model with linear kinematic hardening.

A possible extension of this model consists of associating several Prager's models as shown in Figure 4.17. The resulting model is piecewise linear. We can obtain a non-linear continuous model by generalizing it to an infinite number of Prager's elements, which corresponds to the behavior of the Masing model.

Each element of the continuous serial model is defined by:

– a frictional pad k;

– a spring of elastic compliance J''_1 (k) dk.

$\hat{\sigma}$ (k) is the stress transmitted by pad k. The stress-strain relationship can be written:

$$\varepsilon = J_0\sigma + \int_0^{\infty} J_1''(k)\left(\sigma - \hat{\sigma}(k)\right)dk$$

with $|\hat{\sigma}(k)| \leq k$.

The state of the system can be described by the function $\hat{\sigma}$ (k).

Loading condition:

$\hat{\sigma}$ (k) = σ if $\sigma < k$

$\hat{\sigma}$ (k) = k if $\sigma \geq k$

thus:

$$\varepsilon = J_0\sigma + \int_0^{\sigma} J_1''(k)(\sigma - k)dk$$

The integration of the integral function leads to:

$$\varepsilon = J_0\sigma + J_1(\sigma) = J(\sigma)$$

$J_1(\sigma)$ is the double integral of $J''_1(\sigma)$ with $J_1(0) = 0$ and $J_1'(0) = 0$

Unloading condition: during an unloading from σ equal to σ_0, with $\Delta\sigma = \sigma - \sigma_0$, the relationship becomes:

$$\Delta\varepsilon = J_0\Delta\sigma + 2\int_0^{\frac{\Delta\sigma}{2}} J_1''(k)(\Delta\sigma - k)dk$$

The integration of this equation leads to:

$$\Delta\varepsilon = J_0\Delta\sigma + J_1\left(\frac{\Delta\sigma}{2}\right)$$

If elastic deformations are negligible compared to plastic deformations, we can see that the previous equation gives a stress-strain curve homothetic to the loading curve with a homothetic ratio equal to 2, which can be expressed by the following relations:

– initial loading:

$$\varepsilon^p = f(\sigma)$$

– unloading – reloading from the reversal point (σ_0, ε_0):

$$\frac{\varepsilon_0^p - \varepsilon^p}{2} = f\left(\frac{\sigma_0 - \sigma}{2}\right)$$

The Masing model can produce plastic deformations during unloading and reloading. The stiffness increase in the unloading curve compared to the initial loading curve is called *Masing's effect*. The scaling coefficient is called Masing's coefficient. In some other models, this coefficient can be different from 2, but corresponds to a value determined from experimental results and is usually between 1 and 2. We can note that the Masing model leads to a hysteresis loop which remains constant with successive cycles of the same amplitude, the ratcheting phenomenon cannot be obtained.

4.4. Models based on one or several independent yield surfaces

The preceding section demonstrated how a kinematic hardening produces plastic deformation during unloading. It has been introduced in tridimensional models such as Hujeux or CJS model. Usually, kinematic hardening is defined by a tensorial variable X_{ij}, called *back stress*, which is introduced in the yield function by the following term:

$$f(\sigma_{ij} - X_{ij}) \leq 0$$

X_{ij} corresponds to a thermodynamic force which is function of a hardening variable α_{ij} also defined in a tensorial form. For example, plastic deformation ε^p_{ij} can be used as a hardening variable. The evolution of X_{ij} is therefore controlled linearly or non-linearly by the evolution of α_{ij}.

As an example, we can consider the Von Mises model with kinematic hardening defined by:

$$f = q_{II} - R \leq 0 \text{ with } q_{ij} = s_{ij} - X_{ij}\,(\varepsilon_{ij}^p)$$

where q_{II} is the second invariant of q_{ij}.

The yield surface is a cylinder in the principal stress space and its axis is defined by X_{ij} whose value is a function of ε_{ij}^{p}: X_{ij} (ε_{ij}^{p}) (Figure 4.18).

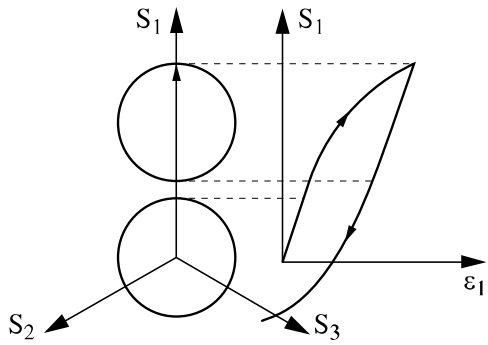

Figure 4.18. *Von Mises' model with kinematic hardening*

4.4.1. *The CJS model*

Different versions of the CJS model have been developed; version CJS 3 was the first version developed for the modeling of cyclic loadings.

This model takes into account one mechanism of elasticity and two mechanisms of plasticity, so the increment of strain can be written:

$$\dot{\varepsilon}_{ij} = \dot{\varepsilon}_{ij}^{e} + \dot{\varepsilon}_{ij}^{ip} + \varepsilon_{ij}^{dp}$$

The first term of the right side of this equation corresponds to the elastic strain, the second to the plastic strain linked with the isotropic plastic mechanism and the last to the plastic strain linked with the deviatoric plastic mechanism.

– The elastic strain is obtained using a non-linear incremental formulation. The considered shear and bulk moduli depend on the effective mean stress.

– The isotropic plastic mechanism is defined from the following yield function:

$$f^{i}(I_1, Q) = \frac{I_1}{3} - Q = 0$$

Its evolution is defined by an isotropic hardening mechanism which is defined by:

$$\dot{Q} = K_0^p \left(\frac{Q}{P_a} \right)^n \dot{\varepsilon}_v^{ip}$$

ε_v^{ip} is the volumetric plastic strain linked with this plastic mechanism, P_a is equal to 100 kPa and K_0^p and n are two constants of the model.

The deviatoric plastic mechanism is defined from the following yield function:

$$f^d(\sigma_{ij}, R, X_{kl}) = q_{II} h(\theta) - R I_1 = 0$$

with: $q_{II} = \sqrt{q_{ij} q_{ij}}$ $\qquad q_{ij} = s_{ij} - I_1 X_{ij}$ $\qquad s_{ij} = \sigma_{ij} - \delta_{ij} \frac{\sigma_{kk}}{3}$

$$h(\theta) = (1 - \gamma \cos 3\theta)^{\frac{1}{6}} = \left[1 - \sqrt{54\gamma} \frac{\det(q_{ij})}{q_{II}^3} \right]^{\frac{1}{6}}$$

The geometrical representation of this yield function is a cone whose angle is linked with the value of R and the location of the axis with the value of X_{ij}. Figure 4.19 shows this surface. s_{ij}, q_{ij}, X_{ij} are deviatoric tensors. Parameter γ characterizes the observed asymmetry of this yield surface. θ is the Lode angle.

The evolution of this yield function is linked with two hardening mechanisms, one is isotropic, the other is kinematic.

Isotropic mechanism

This mechanism governs the evolution of R which is expressed by:

$$\dot{R} = \frac{A R_m^2}{(R_m + Ap)^2} \dot{p}$$

with $\dot{p} = \lambda^d \frac{\partial f^d}{\partial R} \left(\frac{I_1}{3P_a} \right)^{-1.5} = \lambda^d I_1 \left(\frac{I_1}{3P_a} \right)^{-1.5}$

A and R_m are two constants of the model, R_m is in particular the value of R at failure.

λ^d is the plastic multiplier of this deviatoric mechanism; it can be calculated from the consistency equation.

Kinematic hardening

This hardening governs the evolution of parameter X_{ij}. This evolution is non-linear and can be expressed by:

$$\dot{X}_{ij} = \frac{1}{b}\lambda^d I_1 (Q_{ij} - \Phi X_{ij}) \left(\frac{I_1}{3P_a} \right)^{-1.5}$$

with $$Q_{ij} = dev\left(\frac{\partial f^d}{\partial q_{ij}} \right)$$

and $$\Phi = \Phi_0 h(\theta) Q_{II}$$

b is a constant and Q_{ij} is the normal to the yield surface. Φ is a function which allows the evolution of X_{ij} to be bounded. Φ_0 is defined from the characteristics obtained at failure.

Plastic potential

The deviatoric plastic mechanism is unassociated. The flow rule is defined by:

$$\dot{\varepsilon}_v^{dp} = \beta \frac{s_{II}}{s_{II}^c} \frac{\left| s_{ij} \dot{e}_{ij}^{dp} \right|}{s_{II}}$$

β is a parameter of the model and s_{II}^c is the second invariant of the characteristic deviatoric stress. We recall that in the stress space the characteristic surface corresponds to the boundary between contractant states and dilatant states. This surface is defined from the following equation:

$$f^c = s_{II}^c h(\theta) - R_c I_1 = 0$$

R_c is a parameter linked to the angle of the cone corresponding to the characteristic surface.

Failure surface

The failure state is directly linked with the non-linearity of the hardening laws and corresponds to the limit value of hardening parameters. The limit value of R, written R_m, is reached when p becomes infinite. The limit value of X_{ij} is reached when $\dot{X}_{ij} = 0$. Considering these conditions and the yield function, it is possible to define the equation of the limit envelope for the yielding surfaces.

$$f^f = s_{II} h(\theta) - R_m I_1 = 0$$

The surface defined by this equation is considered as the failure surface, its geometrical shape is similar to that of the yielding surface.

The concept of critical state is introduced considering the following relation:

$$R_m - R_c = \Delta R = \mu \ln \frac{3 p_{cr}}{I_1}$$

p_{cr} is the mean stress which corresponds to the case where the peak stress is equal to the critical state ($R_m = R_c$). This value p_{cr} depends on the relative density of the considered material.

R_c is a constant of the model corresponding to the critical state which is supposed to be identical to the characteristic state.

μ is a constant of the model.

The evolution of p_{cr} depends on the evolution of the density of the material:

$$p_{cr} = p_{c0} \exp(c\, \varepsilon_v^p)$$

p_{c0} in this relation corresponds to the value of p_{cr} in the initial state.

This relation allows the coupling between the two mechanisms of plasticity to be considered.

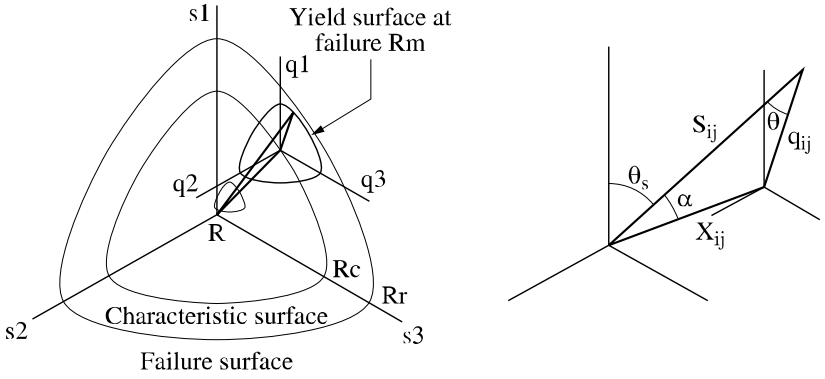

Figure 4.19. *CJS model: plastic limit, characteristic and current loading surfaces in the deviatoric plane*

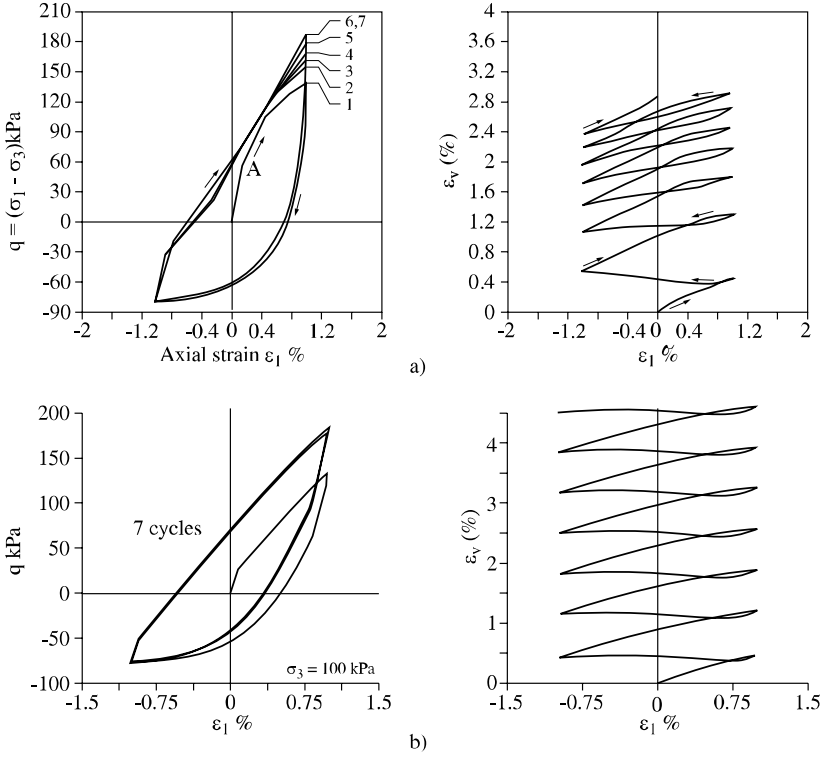

Figure 4.20. *Drained cyclic triaxial test at constant strain amplitude: a) experimental results b) numerical simulation by CJS 3 model*

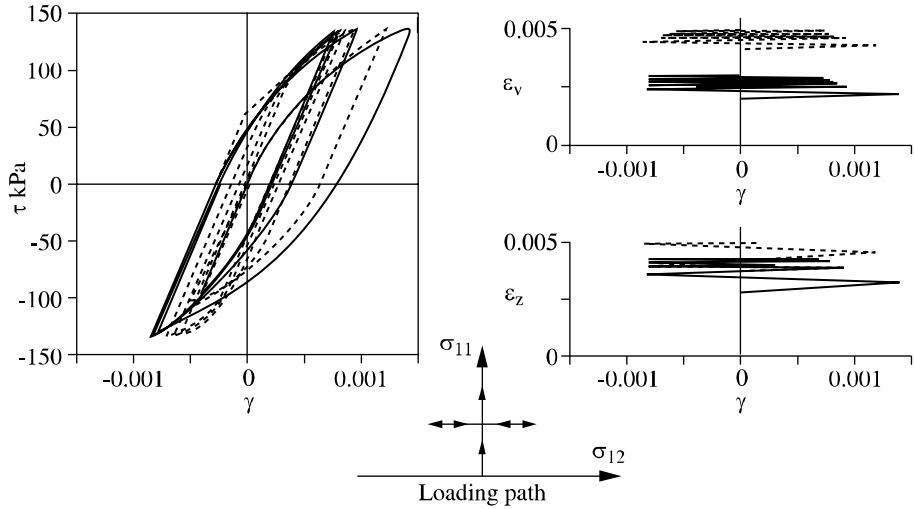

Figure 4.21. *Drained cyclic triaxial test followed by cyclic torsion shear test simulated by the CJS 3 model*

This model is able to give reasonable modeling g of a small number of cycles. However, it can be noted in Figure 4.20 that the cyclic hardening which appears in the experimental results is underestimated by this model.

Results shown in Figure 4.21 correspond to an axisymmetric triaxial loading path, then five cyclic torsions, then an axisymmetric triaxial loading until failure. This rather complex loading is well described by this model CJS3.

4.5. Models based on nested yield surfaces

Most of the models for cyclic plasticity are defined by means of several nested yield surfaces. Usually, we distinguish one particular surface, corresponding to the maximum stress ratio experienced by the material, named differently by various authors, such as bounding surface [DAF 75] or normal yield surface [HAS 93]. The models of this type are mainly differentiated by the number of nested surfaces defined inside this surface.

The Mroz model corresponds to the first model of this type. It was originally designed for metallic materials. It has thus been adapted by different authors to be applied to soil behavior.

4.5.1. *Models with nested yield surfaces: the Mroz model*

The Mroz model is based on the following hypotheses. The yield surfaces are cylindrical akin to the Von Mises type, initially centered on the isotropic stress axis. The nested inner surfaces have different radii. Each nested surface has a fixed radius and its center moves when the state of stress reaches the corresponding limit. The plastic modulus of a given yield surface is a function of the size of this surface (Figure 4.22).

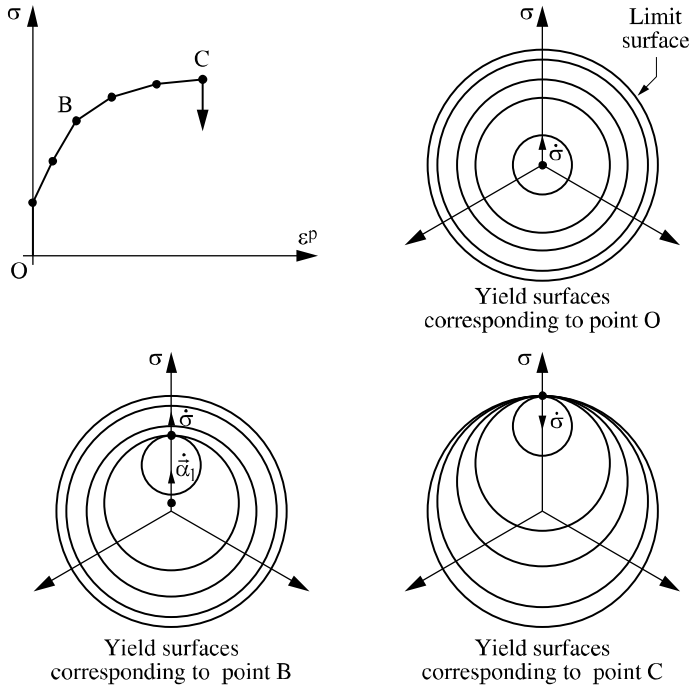

Figure 4.22. *Modeling of the soil behavior by a multiple yield surface model*

This type of model corresponds to a three-dimensional generalization of the Masing model. The same scaling factor can be obtained, equal to 2, between the loading and unloading curves. However, even though it has the advantage of being able to give plastic deformations during an unloading phase, it is not capable of simulating a ratcheting behavior for a constant stress amplitude cyclic loading. In addition, it is difficult to use, because it requires us to store the position of all the nested surfaces at each loading step and compare the position of the actual stress state with all the nested surfaces.

4.5.2. *Model with infinite yield surfaces: the Hujeux model*

In this type of model only the maximum yield surface and the surfaces corresponding to the change of stress direction are stored. The advantage is that this gives a continuous stress-strain relationship for a continuous stress path. The Hujeux model is based on this principle and introduces, in addition to this peculiar kinematic hardening, an isotropic hardening which allows us to take into account the change in density during cyclic loading. The hardening variable is a function of the initial density and the plastic volume change during loading. The kinematic hardening allows us to take into account a discrete memory linked, on one hand, to the highest deviatoric stress and, on the other hand, to the different points of loading – unloading or unloading – reloading.

The Hujeux model is comprised of four plastic mechanisms: three deviatoric mechanisms corresponding to three plane-strain mechanisms in three orthogonal planes and an isotropic mechanism which generates only pure volumetric strains. The state of stress of mechanism k contained in the (i,j) plane is defined by the center of Mohr circle p_k and by vector S_k whose norm q_k corresponds to the radius of the circle.

$$P_k = \frac{(\sigma_{ii})_k + (\sigma_{jj})_k}{2} \qquad q_k = \left[\frac{(\sigma_{ii} - \sigma_{jj})^2}{4} + \sigma_{ij}^2 \right]^{1/2} = \left\| \overline{S}_k \right\|$$

S_{k1} and S_{k2} are the components of vector S_k

$$S_{k1} = \frac{(\sigma_{ii})_k - (\sigma_{jj})_k}{2} \qquad S_{k2} = (\sigma_{ij})_k$$

The state of plastic strain of mechanism k is defined by plastic volumetric strain ε_v^p and by deviatoric plastic strain vector e_k^p whose components e_{k1}^p and e_{k2}^p are:

$$e_{k1}^p = \varepsilon_{ii}^p - \varepsilon_{jj}^p \qquad \textit{and} \qquad e_{k2}^p = 2\varepsilon_{ij}^p$$

$$(\varepsilon_v)_k = (\varepsilon_{ii})_k + (\varepsilon_{jj})_k \qquad \gamma_k = \left[(\varepsilon_{ii} - \varepsilon_{jj})^2 + 4\varepsilon_{ij}^2 \right]^{1/2}$$

Deviatoric mechanisms (k = 1, 2, 3)

The equations of each mechanism are identical. In primary loading the yield surface for mechanism k is given by the equation:

$$f_k = \left\| \overline{S}_k \right\| - r_k^m \quad \text{normalized function-threshold}$$

where $\overline{S}_k = S_k / F_{pk}$

F_{pk} is a factor of normalization given by:

$$F_{pk} = \sin\varphi . P_k \left(1 - b \log {P'}/{P_c} \right),$$

φ is the friction angle in perfect plasticity, p' is the mean stress and p_c is the critical pressure.

p_c is related to the plastic volumetric strain ε_v^p by the following equation:

$$P_c = P_{co} \exp \beta . \varepsilon_v{}^p$$

where p_{c0} is the initial value of p_c which depends on the material initial void ratio and $1/\beta$ is the slope of the perfect plasticity line in the plane ε_v^p, logp'.

In the deviatoric plane $(\sigma_{ii} - \sigma_{jj})/2$, σ_{ij} of each mechanism normalized by the function F_{pk}, the yield surface is a circle with a radius equal to r_k^m which is a hardening variable that allows mechanism k to be progressively mobilized.

$$r_k^m = r_k^e + {\gamma_k^p} \Big/ \left(a + \gamma_k^p \right)$$

Its evolution law is given by:

$$dr_k = \lambda_k . l(\sigma, r_k)$$

so that the plastic modulus H_k^r depends only on r_k:

$$H_k^r = -\frac{\partial f_k}{\partial r_k} . l_k = \frac{(1 - r_k)^2}{a}$$

λ_k is the plastic multiplier of the mechanism k.

In the k plane, the plastic deviatoric strain rate tensor and the plastic volumetric strain rate are defined as:

$$\text{for i and j} \neq \text{k} \quad \partial e_k^p = \lambda_k \left(\Psi_k^d \right) \begin{cases} \partial e_{k1}^d = \lambda_k \Psi_{k1}^d \\ \partial e_{k2}^d = \lambda_k \Psi_{k2}^d \end{cases}$$

$$\text{for i} = \text{j} = \text{k} \begin{cases} \left(\partial_t e_k^p \right)_k = 0 \\ \left(\partial_t \varepsilon_v^p \right)_k = \lambda_k \Psi_k^n \end{cases}$$

The hypothesis of associated law in the normalized deviatoric plane defines:

$$\Psi_k^d \begin{pmatrix} \Psi_{k1}^d \\ \Psi_{k2}^d \end{pmatrix}$$

$$de_k^p = \begin{bmatrix} e_{k1}^p \\ e_{k2}^p \end{bmatrix} = \lambda_k \begin{bmatrix} \Psi_{k1}^d \\ \Psi_{k2}^d \end{bmatrix} = \lambda_k \begin{bmatrix} \dfrac{\Psi_{ii} - \Psi_{jj}}{2} \\ \Psi_{ij} \end{bmatrix} = \lambda_k \begin{bmatrix} S_{k1} / q_k \\ S_{k2} / q_k \end{bmatrix}$$

$$\left[d\varepsilon_v^p \right]_k = \lambda_k \left[\Psi_k^v \right] = \lambda_k \left[\frac{\Psi_{ii} + \Psi_{jj}}{2} \right] = \lambda_k \left[\sin\varphi - \frac{\left(S_k . \Psi_k^d \right)}{P_k} \right] \alpha.\alpha(r_k)$$

$$= \lambda_k \left[\sin\varphi - \sin(\varphi_{mob})_k \right] . \alpha.\alpha(r_k)$$

This last expression is a generalization of the equation of the Cam-Clay model which controls the condition of plastic contractancy and dilatancy, where α is a dilatancy factor and $\alpha(r_k)$ is the mobilized friction in the k plane.

The perfect plastic state is defined by:

$$\begin{cases} r_k = 1 \; and \; P = P_c \\ q_{k = \sin\phi . P_k} \\ \left(\phi_{mob} \right)_k = \phi \end{cases}$$

This corresponds to a Mohr-Coulomb failure criterion in each plane.

In the normalized deviatoric plane of mechanism k, the yield surfaces in primary loading are concentric circles. In cyclic loading, the circles become tangent to each other at point D_k which represents the stress state at stress reversal (Figure 4.23), n_k being the normal vector to the yield surface at point D_k:

$$f_k\left(P_k, S_k, \varepsilon_v^p, r_k^c, D_k, n_k\right) = \left\| \bar{S}_k - \left(D_k - n_k r_k^c\right) \right\| - r_k^c$$

In the deviatoric plane of mechanism k, the equation becomes:

$$f_k^c = \frac{q_k}{F_{pk}} - r_k^c$$

The loading memory of the material is expressed by D_k which corresponds to the normalized deviatoric stress at the last stress reversal, n_k which is the normal vector to the yield surface at the point D_k and r_k^c which represent the length of the unloading path from the reversal point D_k.

D_k, n_k and r_k^c are reinitialized at each stress reversal and also when the cyclic yield surface becomes tangent to the primary loading surface. The model generalizes in a continuous way Mroz's discrete nested surface theory.

Each mechanism therefore keeps in its memory:

– the maximum degree of mobilization r_k^m: this corresponds to the historical memory;

– the last stress reversal, D_k and n_k: this corresponds to the instant memory.

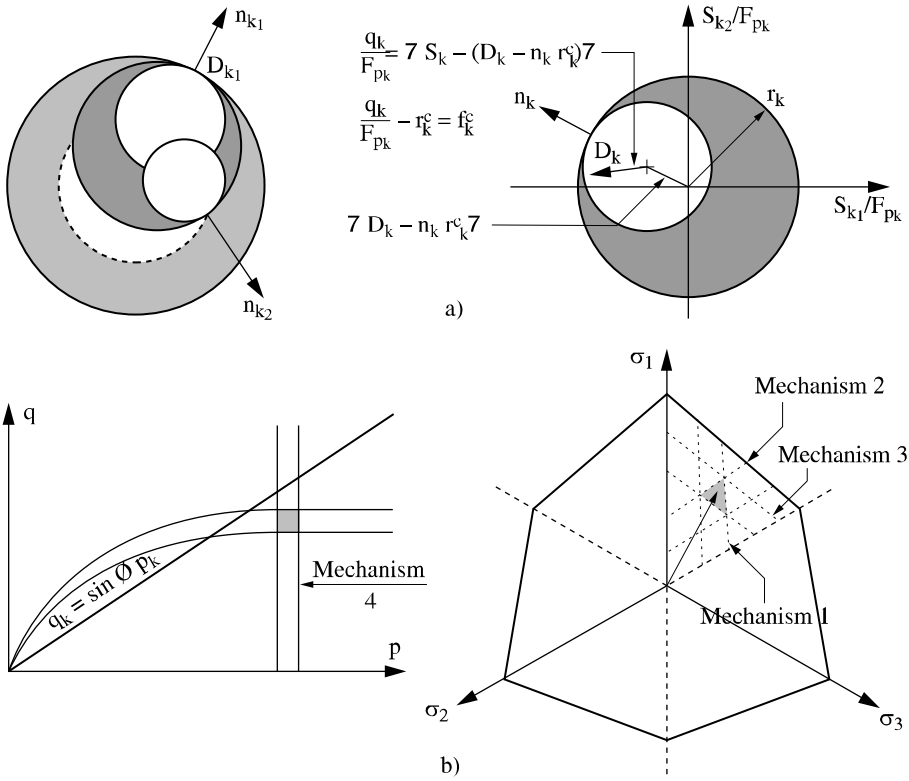

Figure 4.23. *a) Evolution of the yield surface in the deviatoric plane of mechanism k during cyclic loading; b) elastic domain at the intersection of the plastic mechanisms*

The hardening parameter keeps the same expression as for the primary loading, with the possibility for parameter a to have a different value a_m in primary loading and a_c in cyclic loading:

$$r_k^c = r_k^e + \gamma_k^p \Big/ \left(a + \gamma_k^p\right) \leq 1$$

The evolution law is given by:

$$dr_k^c = \lambda_k . l\left(S_k', r_k^c, D_k', n_k\right)$$

$$dr_k^c = \lambda_k \frac{\left(1 - r_k^c\right)^2}{\left[a_{cyc} + \left(a_m - a_{cyc}\right)\alpha\left(r_k^c\right)\right]}$$

so that plastic modulus H_k^r depends only on r_k^c:

$$H_k^r = -\frac{\partial f_k}{\partial r_k^c}.l_k = \frac{\left(1 - r_k^c\right)^2}{a\left(r_k\right)}$$

The choice of function $\alpha(r_k)$ allows us to reproduce the evolution of the stress-strain cycles observed during cyclic loading, by fixing several behavior domains :

$$a\left(r_k\right) = a_c + \left(a_m - a_c\right)\alpha\left(r_k\right)$$

$$If \qquad r \le r_{hys} \qquad \alpha\left(r_k\right) = 0 \qquad \varepsilon < 10^{-5}$$

$$If \qquad r_{hys} \le r \le r_{mbl} \qquad \alpha\left(r_k\right) = \left(\frac{r - r_{hys}}{r_{mbl} - r_{hys}}\right)^m \qquad 10^{-5} < \varepsilon < 10^{-4}$$

$$If \qquad r_{mbl} \qquad \alpha\left(r_k\right) = 1 \qquad \varepsilon > 10^{-4}$$

Isotropic mechanism (k = 4)

Experimental results exhibit plastic strain during an isotropic compression. As they are not activated during this stress path, the three deviatoric mechanisms cannot generate purely volumetric strains. An isotropic mechanism is thus introduced. The yield surface is a plane perpendicular to the hydrostatic axis:

$$f_4(p, p_c, r_4) = \left|\tilde{p}\right| - r_4$$

where $\tilde{p} = \dfrac{p}{F_4(p_c)}$

and $F_4(pc)$ is a normalization factor given by:

$$F_4(pc) = dp_c$$

r_4 is the degree of mobilization of the mechanism. Its value increases from r_4^{el} (elastic domain) to 1 and its evolution law is in the hyperbolic form:

$$r_4^m = r_4^e + \varepsilon_v^p \Big/ c + \varepsilon_v^p$$

$$d.r_4 = \frac{(1 - r_4)^2}{c.P_c} P_a d\varepsilon_{v4}^p$$

The mechanism generates purely volumetric plastic strains:

$$\partial_t \varepsilon_4^v = \lambda_4 . \Psi_4^v$$

λ_4 is the plastic multiplier:

$$\begin{cases} \left(\partial_t \varepsilon_{ii}^p\right)_4 = \lambda_4 . \partial_{\sigma ii} f / 3 = \pm \lambda_4 / 3 \\ \left(\partial_t \varepsilon_v^p\right)_4 = \lambda_4 . \Psi_4^v = \lambda_4 \sum_{i=1}^{3} \partial_{\sigma ii} f_4 = \pm \lambda_4 \end{cases}$$

The plastic modulus H_4^r is written:

$$H_4^r = \frac{(1 - r_4)^2}{c.P_c} . Pa$$

where p_a is the atmospheric pressure.

In cyclic loading, the equation of the yield surface takes the following form:

$$f_4^c = \left| \tilde{P} - \left(D_4 - n_4 r_4^c \right) \right| - r_4^c$$

The hardening variable r_4^c is given by:

$$r_4^c = r_4^e + \varepsilon_v^p \Big/ c_{cyc} + \varepsilon_v^p$$

Its evolution has a hyperbolic form:

$$d.r_4^c = \lambda_4 \frac{\left(1 - r_4^c\right)^2}{c_{cyc}}$$

During loading, the four mechanisms can be activated and are coupled by the density hardening p_c as follows:

$$\varepsilon_v^p = \sum_{k=1}^{4} \left(\varepsilon_v^p \right)_k$$

Figures 4.24 and 4.25 show examples of numerical simulations using the Hujeux model, for drained and undrained cyclic loading on sand. The results agree reasonably well with the experiments. We can see in particular that the model is capable of simulating cyclic mobility during undrained cyclic loading.

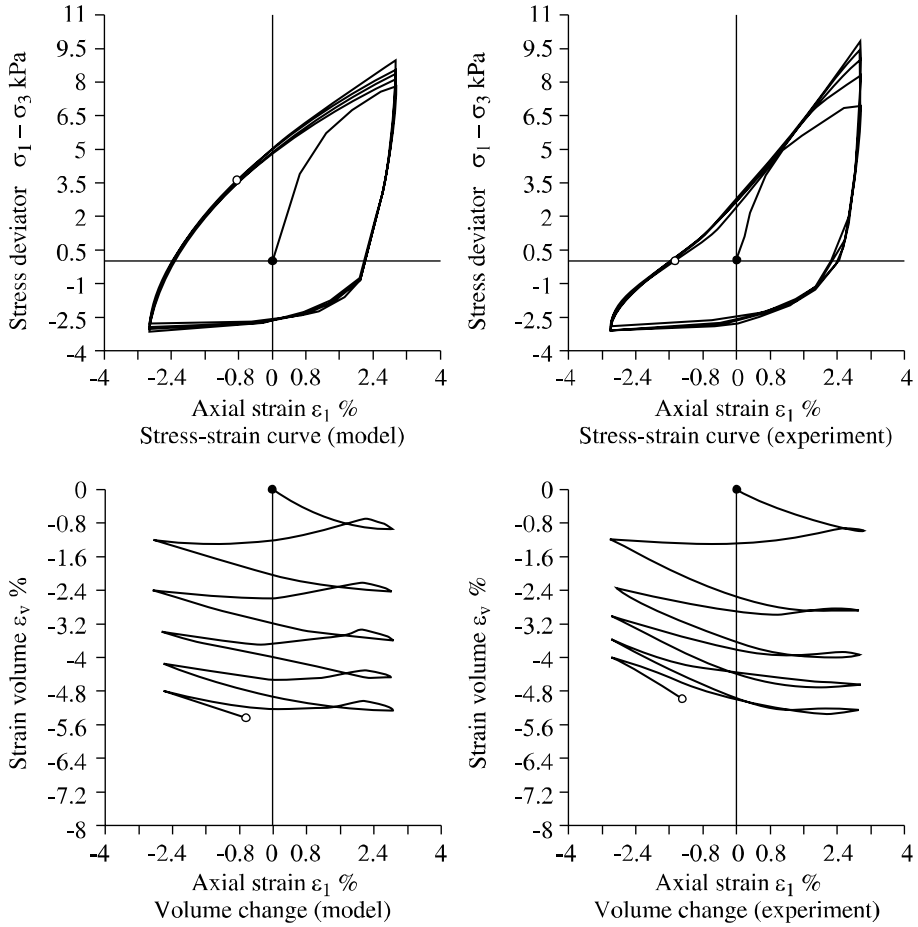

Figure 4.24. *Modeling of a drained cyclic triaxial test using the Hujeux model*

4.5.3. *Models with two yield surfaces: the Dafalias model*

In this model two yield surfaces are considered: the limit surface called the bounding surface and an inner surface [DAF 75]. They are of identical shape and fixed dimensions. The interior of the inner surface corresponds to the elastic domain. The plastic modulus is defined by monotonous increasing function of the distance between the actual stress point and the conjugated point on the bounding surface. For both points, the normal vectors to the two surfaces have the same direction.

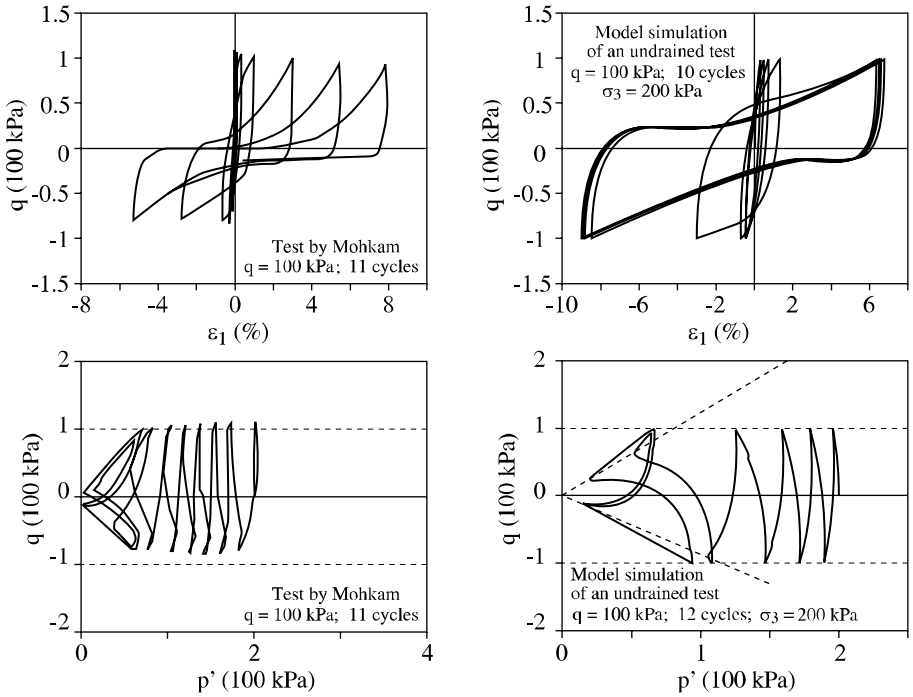

Figure 4.25. *Cyclic liquefaction of a saturated sand: comparison of experimental results and numerical simulations by Hujeux's model*

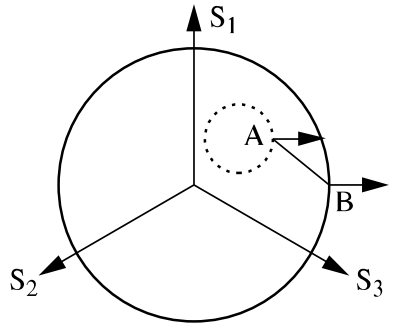

Figure 4.26. *Limit surface and yield surface in the deviatoric plane for Dafalias' model with two yield surfaces*

This model produces plastic deformation during unloading. The ratcheting effect can be reproduced by this type of model, but its effect is usually overestimated. The model can be reduced to a single yield surface [DAF 77]. It is similar to the two yield surfaces model with an elastic domain reduced to a point. It does not produce Masing's effect, the unloading curve is identical to the loading curve, and the ratcheting effect is also overestimated.

4.5.4. *Models with two yield surfaces: the Hashigushi model*

The model takes into account two yield surfaces: a limit surface called the normal yield surface and an inner surface called the subloading surface. The normal yield surface has an isotropic hardening connected to the material density. The essential difference with the previous model is only that the size of the inner surface evolves during loading. The plastic modulus is a monotonic decreasing function of the size ratio between the two surfaces. This ratio increases during a plastic loading. When the state of stress reaches the normal yield surface, the two surfaces become identical [HAS 80].

The two surfaces have a similar shape, in a ratio R, the center of similitude being a point in the stress space (for example the origin), this point being fixed in a given version of the model. During loading, the actual stress point always belongs to the subloading surface. Therefore, during unloading, the stress vector is directed towards the inside of this surface, creating elastic deformation. The surface follows the stress point, its size will thus decrease and become a single point when the stress state meets the center defined above.

The model allows for a continuous behavior to be ensured when the stress point reaches the normal yield surface, a continuity that previous models could not ensure. It does however have certain limitations, in particular that an elastic behavior is produced during unloading until the stress state reaches the center of similitude, which does not correspond to the real behavior of the soil. Furthermore, the ratcheting effect is over predicted. Hashigushi modified the model [HAS 93] so that it corresponds to an extension of the previous model in which the center of similitude evolves in the stress space as a function of the plastic strains. During a plastic loading, the size of the inner surface as well as the center of similitude evolves. During unloading, the strain is purely elastic and therefore the center of similitude remains fixed. The extended model gives better responses than the initial model does, particularly in simulating the ratcheting effect more realistically.

4.5.5. *Models with two yield surfaces: CJS 4 model*

An improvement to CJS 3 has been proposed to provide a better modeling of a large number of cycles. For this purpose two types of behavior are considered: the monotonic and the cyclic behavior. The monotonic behavior will be considered when the yield surface is tangent to the "memory surface", and the cyclic behavior when these two surfaces have no contact.

For this, two values of parameter b are considered (b_{mon}, b_{cyc}). Parameter b appears in the evolution law of the kinematic hardening. A new expression of b is thus proposed:

$$b = b_{mon} + z(b_{cyc} - b_{mon})$$

Variable z takes values between 0 and 1. This is evaluated from measuring the distance between the actual stress state and the maximal stress state.

$$z = \frac{R_{mem} - R_{ac}}{R_{mem} - R_{cyc}}$$

R_{mem} corresponds to the angle of the cone of the yield surface characterized by the maximal loading.

R_{ac} corresponds to the angle of the cone of a similar surface passing through the actual stress state.

R_{cyc} corresponds to the angle of the cone of a similar surface. If the stress state is in the domain bounded by this surface, z = 1. R_{cyc} has been taken as equal to 0.9 R_{mem}.

It can be noted that if $R_{ac} > R_{mem}$ z = 0, and if $R_{ac} < R_{cyc}$ z = 1

The expression of the memory surface is similar to the expression of the failure surface defined in CJS 3:

$$s_{II} h(\theta) - R_{mem} I_1 \log(\frac{3p_c}{I_1}) = 0$$

p_c is the mean stress corresponding to the intersection of the memory surface and the hydrostatic axis in the stress space.

$$p_c = p_{cr} \exp(\frac{R_c}{\mu})$$

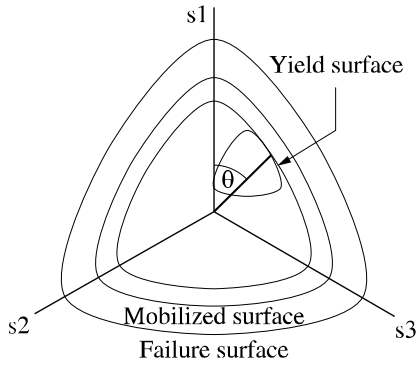

Figure 4.27. *Representation of the "memory" surface in the deviatoric plane (CJS 4 model)*

The analysis of the cyclic behavior of granular material leads to the necessity of taking into account an evolution of the plastic modulus all along the cycles.

Two variables have been considered, the plastic volume change and a variable d_1* linked with the plastic deviatoric strain. Parameter b_{cyc} is thus defined by:

$$b_{cyc} = (b_{\max} - (b_{\max} - b_{\min}) \exp(-d_1^* k) \exp(-d_2 \left|\varepsilon_v^p\right|)$$

The dependency of b_{cyc} with respect the volume change allows for the densification of the medium to be correctly taken into account.

At each change in direction of the loading, the value of variable k is changed to 0. The evolution of k is governed by:

$$\dot{k} = \frac{1}{2}\left(1 - \frac{q_{ij} X_{ij}}{\left|q_{kl} X_{kl}\right|}\right) \dot{e}_{II}^p$$

$$\text{with } \dot{e}_{II}^p = \sqrt{\dot{e}_{ij}^p \dot{e}_{ij}^p} \quad \text{and} \quad d_1^* = d_1 \left(\frac{R_{mem} \ln(\frac{3p_c}{I_1})}{R_f} \right)^m$$

Parameter m is considered to be a constant equal to 2.

To define the change in direction of the loading which leads to the change in value of k, variables x and x_M are considered:

$$x = \sqrt{(X_{ij} - X_{ij}^c)(X_{ij} - X_{ij}^c)}$$

$$x_M = x \quad \text{if} \quad x > x_M$$

During the loading, the direction of the loading is assumed to be changed if $x < x_M$; in such a case we consider the following changes:

$$K = 0,\ x = 0 \text{ and } X_{ij}^c = X_{ij}$$

This new version of the CJS model, called CJS 4, improves the simulation of cyclic loading of granular soils. It can be seen in Figure 4.28 that in a drained triaxial test the ratcheting effect is correctly described; furthermore, the evolution of the cycle shape all along the loading is greatly improved.

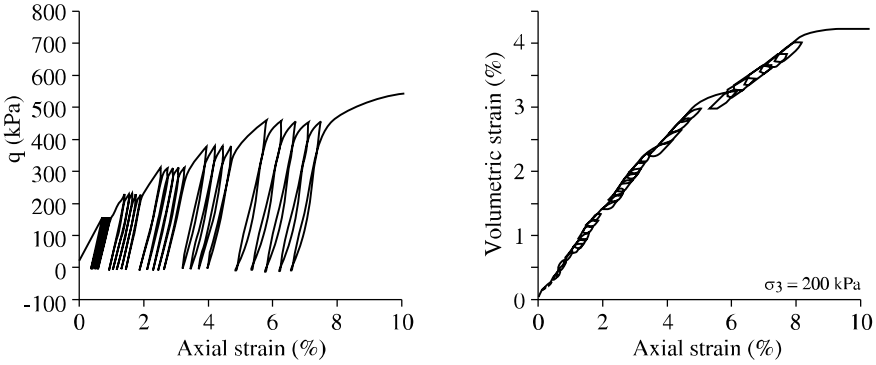

Figure 4.28. *Simulation of a drained cyclic triaxial test by CJS 4 model*

4.6. Generalized plasticity models

The generalized theory of plasticity was introduced by Zienkiewicz and Mroz in 1985 [ZIE 85] and later extended by Pastor and Zienkiewicz [PAS 90]. The basic assumption of this theory is to assume that the strain increment can be written as:

$$d\varepsilon_L = C_L : d\sigma \text{ for } n : d\sigma^e > 0 \text{: loading}$$

$$d\varepsilon_U = C_U : d\sigma \text{ for } n : d\sigma^e < 0 \text{: unloading}$$

where $d\sigma^e = D_e : d\varepsilon$ is the stress increment produced if the behavior is elastic.

By imposing the condition of continuity between loading and unloading states, we obtain:

$$C_L = C^e + (1/H_L)n_{gL}*n$$

$$C_U = C^e + (1/H_U)n_{gU}*n$$

where n_{gL} and n_{gU} are arbitrary unit tensors and H_L and H_U two scalar functions corresponding to loading and unloading plastic moduli.

The previous equations lead to the decomposition of the strain increment in elastic and plastic parts such that:

$$d\varepsilon = d\varepsilon^e + d\varepsilon^p$$

with

$$d\varepsilon^e = C^e{:}d\sigma$$

and

$$d\varepsilon^p = (1/H_L)(n_{gL}*n){:}\, d\sigma \text{ in loading}$$

$$d\varepsilon^p = (1/H_U)(n_{gU}*n){:}\, d\sigma \text{ in unloading}$$

The advantage of the generalized plasticity framework is that it does not require the introduction of any yield or plastic potential surface. The model can be constructed by giving the directions of plastic flow n_{gL} and n_{gU} and the plastic moduli H_L and H_U, while using suitable interpolation laws for simulating the cyclic behavior of soils [PAS 90].

4.7. Parameter identification for cyclic plasticity models

Generally, the parameters of models developed for simulating cyclic loading can be divided into two groups of parameters: the first group contains parameters which essentially control the first loading response, the second group contains parameters whose effect is visible only during cyclic loading. The latter can be identified only by using cyclic laboratory tests, which require specific experimentation and high quality measurement techniques.

4.8. Conclusion

The cyclic behavior of soils is strongly affected by the volume changes induced by loading. These volume changes correspond generally to a progressive density increase with the cycles, which leads to an increase of the mechanical properties in drained condition. The application of this property concerns in particular the compaction of soil masses used as foundation support. However, when this density increase is prevented (fast loading on saturated sand for example), it leads to a decrease of effective stresses, eventually down to zero: this phenomenon, called liquefaction or cyclic mobility, has been the cause of numerous disasters in seismic areas.

The modeling of cyclic behavior is a difficult task, because it requires taking into account with high accuracy the plastic deformations which occur all along the cycles and whose amplitude evolves with the internal state of the material. In the framework of elastoplasticity, a double hardening, which is kinematic and isotropic, allows a significant amount of the observed phenomena to be reproduced. Some progress is still necessary, particularly in cases of a large rotation of principal stress directions, which require a very accurate modeling of induced anisotropy.

4.9. References

[BIA 94] BIAREZ J. and HICHER P.-Y., *Elementary Mechanics of Soil Behaviour. Saturated Remoulded Soils*, Balkema, 1994.

[CAM 88] CAMBOU B., JAFARI K., "Modèle de comportement des sols non cohérents", *Revue Française de géotechnique*, no. 44, pp. 43-55, 1998.

[CHA 77] CHABOCHE J.L., "Viscoplastic constitutive equations for the description of cyclic and anisotropic behavior of metals", *Bull. Acad. Polon. Sci. Ser. Sci. Tech,* 25, 1977.

[CHA 83] CHABOCHE J.L. and ROUSSELIER G., "On the plastic and viscoplastic constitutive equations", *J. Pressure Vessel Tech*. ASME, 105, pp. 153-164, 1983.

[DAF 75] DAFALIAS Y.F. and POPOV E.P., "A model of nonlinearly hardening materials for complex loading", *Acta Mech*, 23, pp. 173-192, 1975.

[DAF 77] DAFALIAS Y.F. and POPOV E.P., "Cyclic loading for materials with a vanishing elastic domain", *Nucl. Engng. Des.*, 41, pp. 293-302, 1977.

[DAF 80] DAFALIAS Y.F. and HERRMANN L.R., "A bounding surface soil plasticity model", in G.N. Pande and O.C. Zienkiewicz (eds.), *Proc. Int. Symp. Soils under Cyclic Trans. Load,* Swansea, A.A. Balkema, Rotterdam, pp. 335-345. 1980.

[DAR 95] DARVE F., HICHER P.-Y. and REYNOUARD J.M., *Les géomatériaux: théories, expériences et modèles*, Hermes, 1995.

[GHA 82] GHABOUSSI J. and MOMEN H., "Modelling and analysis of cyclic behaviour of sand", in G.N. Pande and O.C. Zienkiewicz (eds.), *Soil Mechanics-Transient and Cyclic Loads,* Wiley, New York, pp. 313-342, 1982.

[HAS 80] HASHIGUCHI K., "Constitutive equations of elastoplastic materials with elastic-plastic transition", *J. Appl. Mech.* ASME, 47, pp. 266-272, 1980.

[HAS 89] HASHIGUCHI K., "Subloading surface model in unconventional plasticity", *Int. J. Solids Struct.,* 25, pp. 917-945, 1989.

[HAS 93] HASHIGUCHI K., "Fundamental requirements and formulation of elastroplastic constitutive equations with tangential plasticity", *Int. J. Plasticity,* 9, pp. 525-549, 1993.

[HAS 93] HASHIGUCHI K., "Mechanical requirements and structures of cyclic plasticity model", *Int. J. Plastcity,* 9, pp. 721-748, 1993.

[HIC 85] HICHER P.-Y., "Comportement mécanique des argiles saturées sur différents chemins de sollicitation monotone et cyclique. Application à une modélisation élastoplastique et viscoplastique", Doctoral thesis, Paris VI, 1985.

[HUJ 85] HUJEUX J.C., "Une loi de comportement pour le chargement cyclique des sols", in *Génie Parasismique*, (ed.) Davidovici, publ. Presses des Ponts et Chaussées, pp. 287-301, 1985.

[ISH 75] ISHIHARA K., TATSUOKA F. and YASUDA S., "Undrained deformation and liquefaction of sand under cyclic stresses", *Soils Found*., 15, pp. 29-44, 1975.

[KOL 92] KOLYMBAS D. (ed.), *Modern Approaches to Plasticity,* Elsevier, Amsterdam, 1992.

[JOE 91] JOER H.A., "1γ2ε: une nouvelle machine de cisaillement pour l'étude du comportement des milieux granulaires", Doctoral thesis, Joseph Fourier University, Grenoble I, 1991.

[LUO 80] LUONG M.P., "Stress-strain aspects of cohesionless soils under cyclic and transient loading", *Int. Symp. on Soils under Cyclic and Transient Loading*, Swansea, pp. 353-376, 1980.

[MAL 98] MALEKI M., "Modélisation hiérarchisée du comportement des sols", Doctoral thesis, Ecole Centrale de Lyon, 1998.

[MOH 83] MOHKAM M., "Contribution à l'étude expérimentale et théorique du comportement des sables sous chargement cyclique", Doctoral thesis, INP Grenoble, 1983.

[MRO 67.] MROZ Z., "On the description of anisotropic hardening", *J. Mech. Phys. Solids*, 15, pp. 163-175, 1967.

[MRO 81] MROZ Z., NORRIS V.A. and ZIENKIEWICZ O.C., "An anisotropic, critical state model for soils subjected to cyclic loading", *Géotechnique*, 31, pp. 451-469, 1981.

[PAS 90] PASTOR M., ZIENKIEWICZ O.C. and CHAN A.H.C., "Generalized plasticity and the modelling of soil behaviour", *Int. J. Num. Anal. Methods in Geomech.*, 14, pp. 151-190, 1990.

[PREV 82] PREVOST J.H., "Two-surface versus multi-surface plasticity", *Int. J. Numer. Analyt. Meth. Geomech.*, 6, pp. 323-328, 1982.

[SAA 89] SAADA A.S. and BIANCHINI G. (eds.), *Proc. Int. Workshop on Constitutive Equations for Granular Non-cohesive Soils,* Cleveland, Balkema, Rotterdam, 1989.

[WON 86] WONG R.K.S. and ARTHUR J.R.F., "Sand sheared by stresses with cyclic variations in direction", *Geotechnique 36*, no. 2, pp. 215, 226.

[ZIE 85] ZIENKIEWICZ O.C. and MROZ Z., "Generalised plasticity formulation and application to geomechanics", *Mechanics of Engineering Materials*, C.S. Desai and R.H. Gallaher (eds.), John Wiley and Sons, 1985.

Constitutive Modeling of Soils and Rocks
Edited by Pierre-Yves Hicher & Jian-Fu Shao

Chapter 5

Elastoplastic Behavior of Ductile Porous Rocks

5.1. Introduction

This chapter addresses the elastoplastic modeling of porous rocks, highlighting especially the ductile plastic behavior under high compressive stresses. Damage modeling of brittle behavior of rocks under low compressive stresses or tensile stresses will be discussed in Chapter 8.

Modeling of the mechanical behavior of rocks such as chalk, sandstone and limestone is of great interest for various applications in mining engineering, tunnel construction and the petroleum industry. For instance, the evaluation of subsidence due to pore compaction of porous rocks is an important feature for off-shore reservoir engineering. Porous rocks present a complex mechanical behavior if only because various features such as low material cohesion, strong pressure sensitivity, plastic pore collapse, time-dependent strain, and dependency on porosity and mineralogical compositions are involved. Generally speaking, two plastic mechanisms can be identified: plastic pore collapse leading to significant volumetric deformation and plastic shearing leading to material failure. The volumetric compaction is a specific feature of porous materials, which is related to the microstructure of the material. In granular and powder materials, the volumetric compaction is generally generated by the rearrangement of grains reducing the pore space. In porous cohesive rocks, the volumetric compaction is generated in general by inelastic pore collapse through the contact force breaking between grains.

Chapter written by Jian-Fu SHAO and Shou-Yi XIE.

Two families of constitutive models have been developed for modeling geological materials which exhibit two plastic mechanisms. In the first family, two distinct yield surfaces are introduced: a cap surface for volumetric compaction and a cone surface for plastic shearing [LAD 77]; [DES 80]; [DES 84]; [GEN 93]; [DES 01] and others. In the second family of models whose aim is to avoid a singularity point at the intersection between two surfaces, plastic models with a single yield surface incorporating cap and cone are proposed [LAD 95]; [AUB 99]; [AUB 04] and others. Generally, models with two distinct yield surfaces provide more flexibility in the description of volumetric and deviatoric hardening in complex loading conditions, whereas models with a single yield surface have the advantage of mathematical regularity for numerical implementation.

Based on experimental data obtained from a porous chalk, we will first outline the basic features of the mechanical behavior of porous rocks under compressive stresses. An example of an elastoplastic model with two yield surfaces will be presented. In the second part, a short review of modeling the effects of water saturation and time-dependent behavior will be given.

5.2. Review of typical mechanical behavior of porous rocks

Hydrostatic triaxial compression tests are performed basically to characterize the mechanical behavior of rock materials. In this section, we summarize the basic mechanical behavior of porous rocks based on experimental data obtained from so-called "Lixhe chalk" drilled in the CBR quarry near Liège (Belgium). It is composed of more than 98% $CaCO_3$, and its average porosity is about 43%. A series of experimental studies have been performed on different chalks, including a microstructure analysis and mechanical behavior investigation [ELL 85]; [HAL 90]; [BRI 94]; [AND 92]; [RIS 98]; [RIS 01]; [MON 95]; [SCH 98]; [HOM 00]; [SCH 03a]; [CHE 03]; [DEG 04].

Typical hydrostatic stress versus volumetric strain curves are shown in Figure 5.1. Typically, the material response can be decomposed into three phases. In the first phase, a quasilinear and reversible stress strain relation is obtained, representing the elastic compressibility of the chalk skeleton. The elastic bulk modulus can be determined from the slope of the stress strain curve during this phase. When the hydrostatic stress reaches a limit value, called the pore collapse yield stress, an abrupt accelerated and irreversible volumetric strain is produced, corresponding to the phase of the plastic collapse of the pore structure. The pore collapse induces an increase in the contact surface between grains, leading to the decrease of the volumetric strain rate. This third phase resembles the plastic consolidation in soil materials.

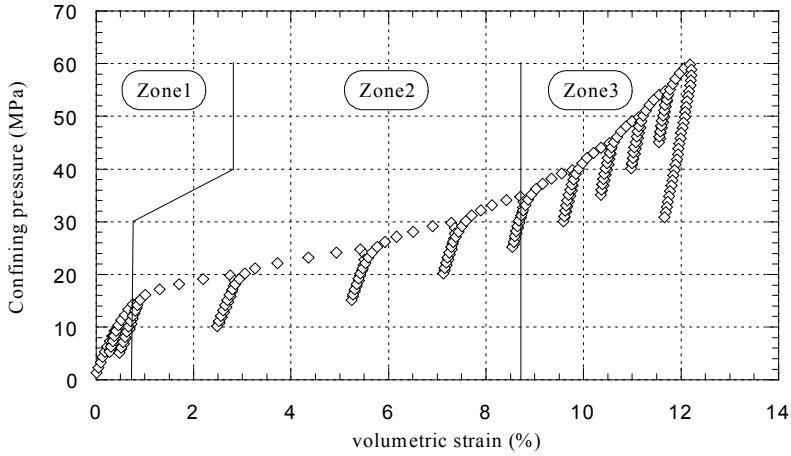

Figure 5.1. *Volumetric strain curve of a porous chalk in hydrostatic compression tests ([HOM 00])*

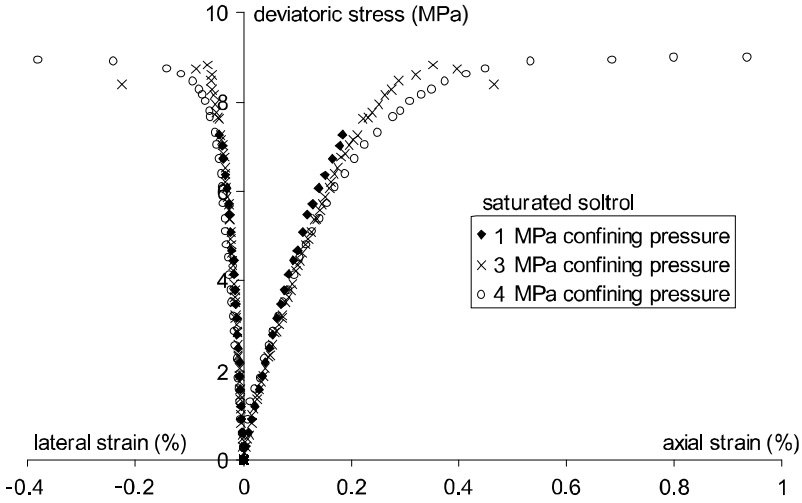

Figure 5.2. *Typical stress strain curves of chalk in triaxial compression tests with low confining pressures ([HOM 00])*

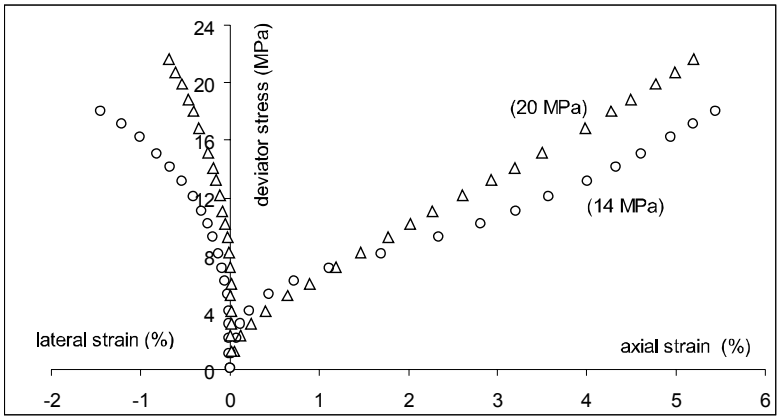

Figure 5.3. *Typical stress strain curves of chalk in triaxial compression tests with high confining pressures ([HOM 00])*

Conventional triaxial compression tests are then conducted with different confining pressures in order to study the mechanical behavior of chalk subjected to deviatoric stress. Typical stress strain curves are shown in Figures 5.2 and 5.3 for oil saturated samples. We can see that the mechanical behavior of chalk is strongly dependent on confining pressure. Under low confining pressures, i.e. when the maximal mean stress is lower than the pore collapse stress, the basic behavior of chalk is elastic-brittle or elastoplastic-brittle. The failure state may be characterized by a peak stress. At very low confining pressures close to uniaxial compression, the brittle failure occurs with material softening. Sample failure is traditionally produced by the formation of localized shear bands. The orientation of shear bands depends on the value of the confining pressure. The mechanical response changes substantially when the confining pressure increases. At high confining pressures, i.e. when the mean stress is close to the plastic pore collapse stress, no peak stress can be found up to very large values of the axial strain. The slope of the stress-strain curve increases continuously with a concave form similar to that in a hydrostatic compression test. This means that the applied deviatoric stress under high confining pressures enhances the pore collapse process, producing plastic hardening due to the increase in contact area. Accordingly, an important volumetric contraction is obtained due to the pore collapse. One of the specific features is that, due to the pore collapse, the lateral strain at the first stage of a triaxial test is smaller than that which should be obtained in a linear elastic material. At very high confining pressures, the lateral strain may even be compressive during the first stage of a triaxial test (see Figure 5.3). Material failure is characterized by the destruction of the pore structure, transforming the cohesive material into a compacted powder assembly after significant volumetric deformation.

In light of the above results, it seems appropriate to formulate a constitutive model with two plastic mechanisms. At low hydrostatic stresses, the plastic shear mechanism dominates with a plastic hardening process from the initial elastic limit to the ultimate failure state (peak stress), eventually followed by a softening phase. A non-associated flow rule is generally needed to describe plastic volumetric compressibility and dilatancy. On the other hand, at high hydrostatic stresses, the pore collapse mechanism becomes the main process with a continuously positive hardening process producing volumetric compressibility.

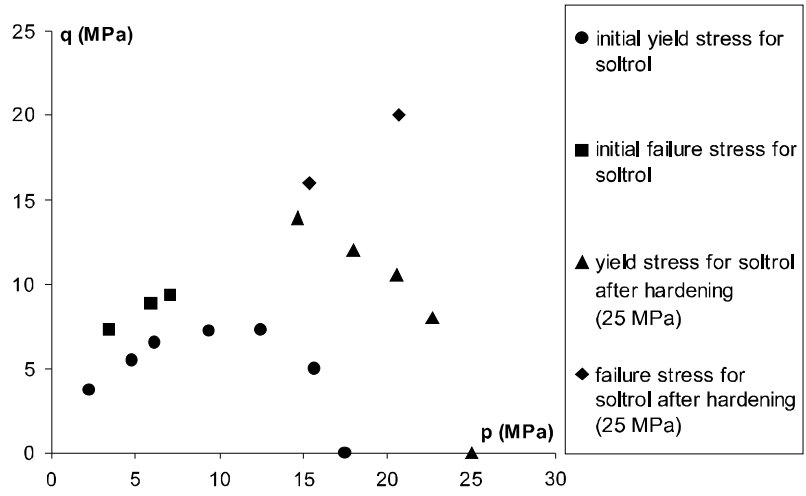

Figure 5.4. *Evolution of yield surface during plastic hardening in the $p-q$ plane ([HOM 00])*

Some specific tests have been performed by Homand and Shao ([HOM 00]) to characterize the evolution of yield surfaces during plastic hardening. The loading path is composed of two phases in the conventional $p-q$ plane. The sample is first subjected to a hydrostatic compression up to 25 MPa, which is higher than the initial pore collapse stress. Plastic hardening is then generated in the sample during this preliminary phase. Afterwards, the hydrostatic stress is unloaded to a given value (i.e. 10, 14, 17 and 20 MPa). From this point on, the sample is subjected to a triaxial compression test through an increase of the axial stress. Yielding stress and possibly failure stress are determined during the triaxial phase. The yielding surface obtained after the hydrostatic preloading is compared with the initial surface (Figure 5.4). The evolution of the yield surface due to plastic hardening can probably be characterized by an isotropic expansion of the elastic domain. Therefore, an isotropic plastic hardening law can be used for this material, at least for the plastic collapse

mechanism. Another interesting feature of these results is that the failure stresses due to plastic shearing are not affected by the preliminary plastic hardening in the pore collapse process. In fact, the failure stresses obtained from two triaxial tests performed on preliminary plastically deformed samples with 10 and 14 MPa confining pressure are lined up with the failure stresses obtained from virgin samples. This result would suggest that the two plastic mechanisms could be considered as independent of each other; the plastic hardening (expansion) of the cap surface does not necessarily affect the cone surface.

5.3. Formulation of the constitutive model

According to the above review, two plastic deformation mechanisms have to be taken into account: plastic shearing and pore collapse. Plastic shearing is a common mechanism for frictional materials. Plastic models based on traditional and extended Mohr-Coulomb or Drücker-Prager failure criteria have been widely developed. However, one particular feature of porous rocks is the strong pressure dependency, which must be taken into account. Pore collapse, on the other hand, is specifically related to the high porosity of materials. This mechanism plays an essential role in many engineering applications such as subsidence analysis of oil reservoirs. Therefore, particular attention is paid here to the modeling of pore collapse in porous rocks.

The microstructure of porous rocks is generally complex. However, as a first approximation of typical porous chalk in view of macroscopic modeling, an idealized schematization can be adopted. Chalk can roughly be seen as an assembly of solid grains with different types of contacts and a connected macroscopic porosity [XIE 06] (Figure 5.5). For example, three types of contacts can be identified: cemented solid contact, frictional point contact and liquid contact due to capillary water. Inter-connected pores constitute the macroscopic porosity for fluid flow. After a first homogenization phase, it is assumed that the assembly of solid grains, together with their contacts, can be replaced by an equivalent cohesive-frictional solid matrix. Closed porosity can eventually be included in this equivalent solid matrix. Thus, the macroscopic mechanical behavior of the material is essentially controlled by the mechanical properties of the solid matrix and the macroscopic porosity, denoted by ϕ. The mechanical properties of the equivalent solid matrix are related to the evolution of contacts during its deformation history. The increase of frictional point contacts will result in a plastic hardening behavior while the destruction of these contacts leads to a weakening of the mechanical strength.

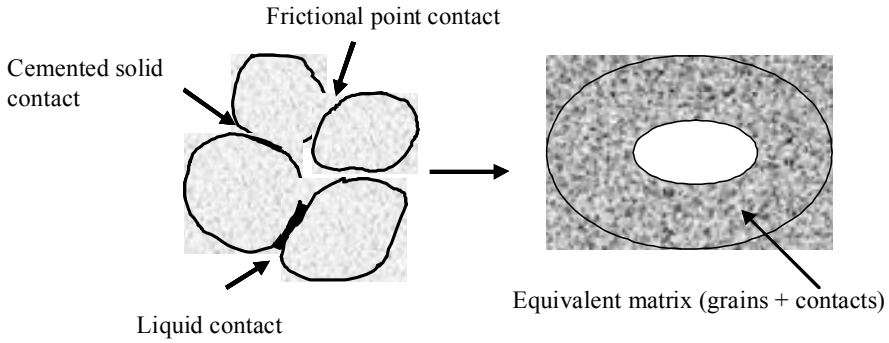

Figure 5.5. *Simplified schematization of porous chalk as an equivalent homogenous porous medium*

Based on the previous analysis, an elastoplastic model with two flow mechanisms is thus proposed [XIE 06]. The formulation of this constitutive model has to satisfy the standard requirements in irreversible thermodynamics (Lemaitre and Chaboche 1998; Khan and Huang 1995). Small strains are assumed. The total incremental strain $d\varepsilon_{ij}$ is composed of an elastic part $d\varepsilon_{ij}^{e}$ and a plastic part $d\varepsilon_{ij}^{p}$. The plastic strain is further divided into a collapse component $d\varepsilon_{ij}^{c}$ and a shear component $d\varepsilon_{ij}^{s}$.

$$d\varepsilon_{ij} = d\varepsilon_{ij}^{e} + d\varepsilon_{ij}^{p},\ d\varepsilon_{ij}^{p} = d\varepsilon_{ij}^{c} + d\varepsilon_{ij}^{s} \tag{5.1}$$

The elastic strains are given by the linear Hook's law:

$$d\varepsilon_{ij}^{e} = \frac{1}{2\mu_0} d\sigma_{ij}^{d} + \frac{1}{3k_0} d\sigma_m \delta_{ij} \tag{5.2a}$$

$$\sigma_{ij}^{d} = \sigma_{ij} - \sigma_m \delta_{ij},\ \sigma_m = \frac{1}{3}\sigma_{kk} \tag{5.2b}$$

where σ_{ij} are the components of the Cauchy stress tensor, σ_{ij}^{d} the components of the deviatoric stress tensor and μ_0 and k_0 the initial shear modulus and the bulk modulus of the intact material respectively.

5.3.1. *Plastic pore collapse model*

Based on an energy consideration, Gurson ([GUR 77]) proposed a general macroscopic yield criterion for porous materials with a homogenous solid matrix. The plastic behavior of the solid matrix is described by the von Mises perfect plastic criterion. This criterion has been widely used and extended by many authors for modeling ductile rupture of porous metals including the nucleation and expansion of pores ([TVE 90]). Using a rigorous limit analysis, Perrin and Leblond ([PER 90]) and Leblond and Perrin ([LEB 96]) studied the micromechanic features of Gurson's criterion. It has been shown that this criterion represents the analytical solution of the macroscopic yield function of a porous material with a solid matrix verifying the von Mises perfect plastic criterion which contains spherical pores. The macroscopic yield function depends on the yield stress of the solid matrix and the macroscopic porosity. Heuristic extensions may be proposed to introduce a plastic hardening law of the solid matrix. Considering the idealized representation adopted here for porous rocks, Gurson's criterion is used as the basic yield function for the pore collapse mechanism. Therefore, the plastic yield function is expressed by the following form:

$$f_c = \frac{\sigma_{eq}^2}{\bar{\sigma}^2} + 2\phi\cosh\left(q_2 \frac{3\sigma_m}{2\bar{\sigma}}\right) - 1 - \phi^2 = 0\ ,\ \sigma_{eq} = \sqrt{\tfrac{3}{2}\sigma_{ij}^d \sigma_{ij}^d} \tag{5.3}$$

where σ_{eq} denotes the equivalent deviatoric stress. Parameter q_2 is introduced to control the geometrical form of the yield surface ([TVE 90]). $\bar{\sigma}$ denotes the yield stress of the solid matrix. The value of $\bar{\sigma}$ depends on plastic deformation and is affected by the evolution of contacts. The variation of $\bar{\sigma}$ as a hardening law of the solid matrix is issued from a heuristic extension of the original Gurson's model. Based on the experimental data from hydrostatic compression, the following hardening function is proposed [XIE 06]:

$$\bar{\sigma} = \bar{\sigma}_0 \left[1 + a(-\varepsilon_{kk}^c)^n e^{b(-\varepsilon_{kk}^c)}\right] \tag{5.4}$$

where ε_{kk}^c is the plastic volumetric strain due to the pore collapse process, taken as the internal hardening variable. $\bar{\sigma}_0$ denotes the initial yield stress of the solid matrix. a, n and b are three parameters of the hardening law, which can be identified from a hydrostatic compression test. Moreover, according to equation (5.3), the macroscopic yield stress of a porous medium depends on the porosity. By assuming that the plastic compressibility of solid grains may be neglected, the porosity change is related to the plastic volumetric strain:

$$d\phi = (1-\phi)\, d\varepsilon_{kk}^{p} \tag{5.5}$$

In most geomaterials, an unassociated plastic flow rule is generally needed to describe the volumetric deformation more accurately. By adopting a similar form as the yield function, the plastic potential takes the following form:

$$Q_c = \frac{\sigma_{eq}^2}{\bar{\sigma}} + 2\phi \cosh\left(q_2^* \frac{3\sigma_{eq}}{2\sigma_m}\right) \tag{5.6}$$

where q_2^* is a parameter controlling the orientation of the plastic flow. However, based on the experimental data obtained from triaxial compression tests at high confining pressures, it seems that an associated flow rule describes the pore collapse process accurately enough. Therefore, for the sake of simplicity, we have taken $q_2^* = q_2$.

For a loading history, where only the pore collapse mechanism is activated, the plastic flow rule is written as:

$$\dot{\varepsilon}_{ij}^{c} = \lambda_c \frac{\partial Q_c}{\partial \sigma_{ij}} \tag{5.7}$$

Plastic multiplier λ_c is determined by the plastic consistency condition:

$$d\lambda_c = \frac{\dfrac{\partial f_c}{\partial \boldsymbol{\sigma}} : \mathbb{C}^0 : d\boldsymbol{\varepsilon}}{\dfrac{\partial f_c}{\partial \boldsymbol{\sigma}} : \mathbb{C}^0 : \dfrac{\partial Q_c}{\partial \boldsymbol{\sigma}} - H_c} \tag{5.8}$$

$$H_c = \frac{\partial f_c}{\partial \bar{\sigma}} \frac{d\bar{\sigma}}{d\varepsilon_{kk}^{c}} \frac{\partial Q_c}{\partial \sigma_m} + \frac{\partial f_c}{\partial \phi}(1-\phi) \frac{\partial Q_c}{\partial \sigma_m} \tag{5.9}$$

The fourth order tensor $\mathbb{C}^0$ denotes the elastic stiffness tensor of intact material.

5.3.2. *Plastic shearing model*

As previously mentioned, plastic shearing is a common mechanism for frictional rocks, leading to the macroscopic failure of material by the formation of shear bands and crack coalescence. However, in materials with high porosity, the shear

mechanism is dominant only under low confining pressures. Furthermore, this plastic mechanism significantly depends on the confining pressure. A curved yield surface is necessary. Based on the failure surface proposed by Pietruszczak *et al.* ([PIE 88]), the following quadratic yield function is proposed:

$$f_s = \left(\frac{\sigma_{eq}}{p_r}\right)^2 + \alpha_p A\, g(\theta)\left(\frac{\sigma_m}{p_r} - C_s\right) = 0 \tag{5.10}$$

Parameter C_s denotes the material cohesion. The normalizing parameter $p_r = 1MPa$ is taken to render parameter A dimensionless. Function $g(\theta)$ describes the influence of Lode's angle. Different forms can be found in the literature. However, since relevant data is not available for the material studied here, we take for the sake of simplicity $g(\theta) = 1$. Function α_p defines the plastic hardening law for the plastic shearing process. Since strain softening in porous rocks is observed only at very low confining pressures, it is then neglected. Only a positive plastic hardening law will be used. Material failure is reached when $\alpha_p \to 1$. Based on the experimental data from triaxial compression tests at low confining pressures, the following hyperbolic law is proposed [XIE 06]:

$$\alpha_p = \alpha_p^0 + (1 - \alpha_p^0)\frac{\gamma_s}{B + \gamma_s} \tag{5.11}$$

Parameter α_p^0 denotes the initial yield threshold of the plastic shearing mechanism; parameter B controls the hardening kinetics. Variable γ_s is the generalized plastic distortion used as a hardening variable:

$$d\gamma^s = \sqrt{\frac{2}{3} de_{ij}^s de_{ij}^s} \Big/ \chi_p \,,\; e_{ij}^s = \varepsilon_{ij}^s - \frac{1}{3}\varepsilon_{kk}^s \delta_{ij} \tag{5.12}$$

$$\chi_p = \left(\frac{\langle \sigma_m - p_{atm} \rangle + p_{atm}}{p_r}\right)^{\beta_1} \tag{5.13}$$

The normalizing coefficient, χ_p, is introduced to take into account the influence of the confining pressure on the deviatoric plastic hardening. Bracket $\langle x \rangle$ denotes $\langle x \rangle = (|x| + x)/2$ and p_{atm} is the atmospheric pressure.

In most cohesive-frictional geomaterials, the plastic shearing process can generate volumetric compressibility and dilatancy. The volumetric plastic strain rate depends on the level of applied stresses. There is usually a transition from compressibility to dilatancy during plastic shearing. Therefore, an unassociated flow rule is needed. Based on the experimental data from triaxial compression tests under low confining pressures, and the adapted plastic potential as proposed by Pietruszczak *et al*. ([PIE 88]), the following function is used for the plastic shear model:

$$Q_s = \sigma_{eq} + \eta_c \left(\sigma_m - p_r C_0\right) \ln\left(\frac{\sigma_m - p_r C_0}{I_0}\right) = 0 \tag{5.14}$$

Variable I_0 defines the intersection point between the potential surface and axis σ_m. The transition from plastic compressibility to dilatancy occurs on the boundary defined by the condition, $\partial Q_s / \partial \sigma_m = 0$. In this model, it is assumed that this transition boundary can be described by a linear function:

$$\bar{f}_{cd} = \sigma_{eq} - \eta_c (\sigma_m - p_r C_0) = 0 \tag{5.15}$$

Parameter η_c defines the slope of the transition boundary in the $\sigma_{eq} - \sigma_m$ plane.

For the loading history where only the plastic shear mechanism is activated, the plastic flow rule is written as:

$$d\varepsilon_{ij}^s = d\lambda_s \frac{\partial Q_s}{\partial \sigma_{ij}} \tag{5.16}$$

Plastic multiplier $d\lambda_s$ can be determined by the plastic consistency condition.

$$d\lambda_s = \frac{\dfrac{\partial f_s}{\partial \boldsymbol{\sigma}} : \mathbb{C}^0 : d\boldsymbol{\varepsilon}}{\dfrac{\partial f_s}{\partial \boldsymbol{\sigma}} : \mathbb{C}^0 : \dfrac{\partial Q_s}{\partial \boldsymbol{\sigma}} - H_s} \tag{5.17}$$

$$H_s = \frac{\partial f_s}{\partial \alpha_p} \frac{d\alpha_p}{d\gamma_p} \frac{1}{\chi_p} \sqrt{\frac{2}{3} \left(\mathbb{K} : \frac{\partial Q_s}{\partial \boldsymbol{\sigma}}\right) : \left(\mathbb{K} : \frac{\partial Q_s}{\partial \boldsymbol{\sigma}}\right)},$$

$$\mathrm{K}_{ijkl} = \frac{1}{2}(\delta_{ik}\delta_{jl} + \delta_{il}\delta_{jk}) - \frac{1}{3}\delta_{ij}\delta_{kl} \tag{5.18}$$

The fourth order tensor $\mathbb{K}$ defines the deviatoric part of a second order tensor.

In general loading conditions, two plastic mechanisms may be activated simultaneously. In such a case, two plastic multipliers $d\lambda_c, d\lambda_s$ can be determined from the consistency conditions of two plastic yield functions; $df_c = 0 \cup df_c = 0$. Appropriate integration algorithms should be used ([SIM 98], [XIE 06]).

5.4. Examples of numerical simulations

The proposed model contains 12 parameters which can be determined from conventional laboratory tests. As an example, the initial yield surfaces are shown in Figure 5.6 for porous chalk. The detailed procedure for determining the model's parameters and typical values for porous chalks are given in [XIE 06].

The simulation of a hydrostatic compression test is shown in Figure 5.6. We can see that the plastic deformation due to pore collapse and the plastic hardening process due to increasing frictional contact force are well described by the model. In Figures 5.7 and 5.8, two triaxial compression tests with different confining pressures are simulated (14 and 20 MPa). Again, a good agreement between the numerical simulations and experimental data is obtained. The deviatoric stress enhanced pore collapse is correctly predicted by the proposed model.

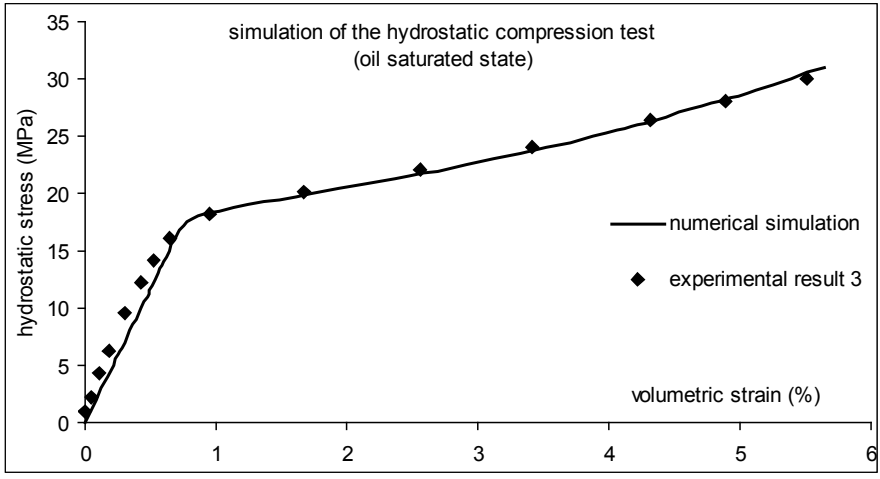

Figure 5.6. *Simulation of a hydrostatic compression test on oil-saturated Lixhe chalk (after [XIE 06])*

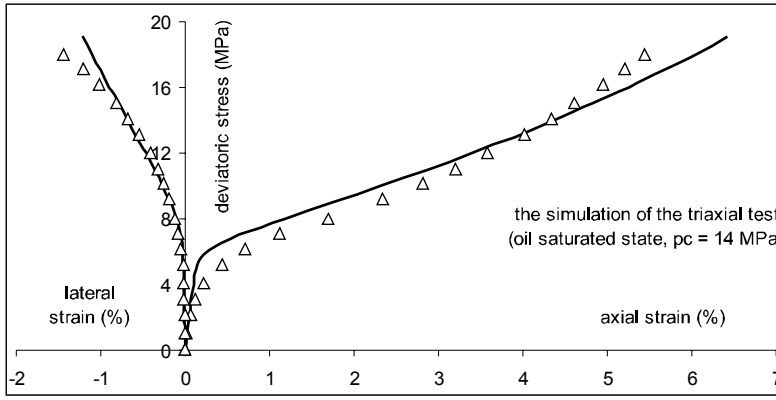

Figure 5.7. *Simulation of a triaxial compression test on oil-saturated Lixhe chalk with 14 MPa confining pressure (after [XIE 06])*

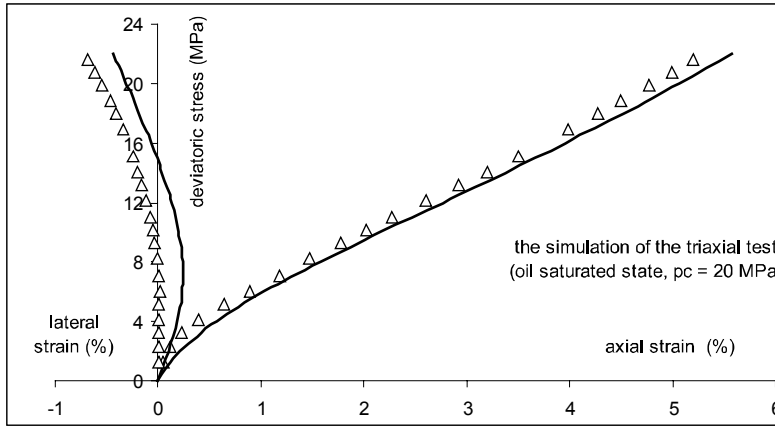

Figure 5.8. *Simulation of a triaxial compression test on oil-saturated Lixhe chalk with 20 MPa confining pressure (after [XIE 06])*

In Figures 5.9 and 5.10, we present the simulations of three triaxial compression tests at low confining pressures. In these tests, the plastic deformation is dominated by the plastic shearing mechanism. Again, it seems that the proposed model is able to describe the chalk mechanical behavior for the whole range of confining pressures. Note that material softening and strain localization are not discussed in this chapter. These features need to be completed in order to describe the progressive failure process in geomaterials.

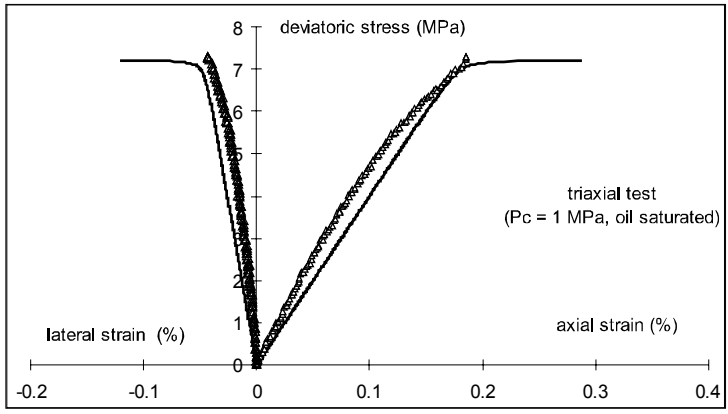

Figure 5.9. *Simulation of a triaxial compression test on oil-saturated chalk with 1 MPa confining pressure (after [XIE 06])*

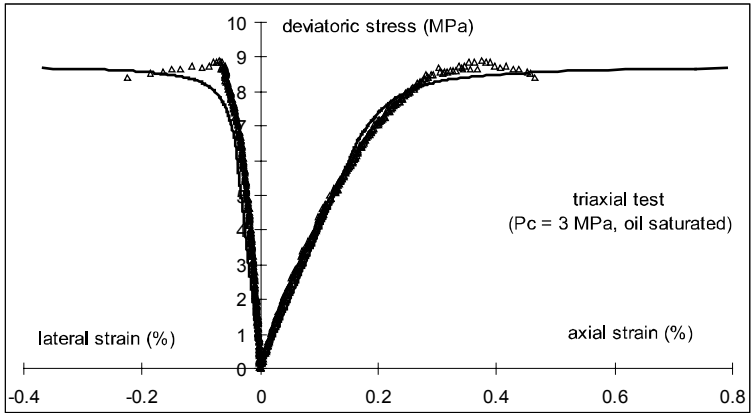

Figure 5.10. *Simulation of a triaxial compression test on oil-saturated chalk with 3 MPa confining pressure (after [XIE 06])*

5.5. Influence of water saturation

In some engineering applications, modifying the nature of pore fluids in porous rocks generates physical and chemical reactions. In the oil industry, for example, porous chalk is initially saturated by oil-like fluids. In order to maintain pore pressure during hydrocarbon production leading to pressure depletion, a large amount of water is injected, which induces a significant change in the water content

of porous chalk. In order to study the influence of saturating fluids on mechanical behavior, laboratory tests have been performed on water saturated and oil saturated samples. In Figure 5.11, yield and failure surfaces for two groups of samples are shown. It is clear that the mechanical behavior of chalk strongly depends on the nature of pore fluids. Typically, the elastic domain in water saturated samples compared with oil saturated samples is largely reduced. Given that the pore collapse stress decreases with water saturation, the transition from brittle to ductile behavior occurs at lower confining pressure. The cohesion and failure strength are also reduced. However, it was found that elastic properties are only slightly affected by water saturation. Figure 5.12 shows that the pore collapse yield stress decreases continuously with the degree of water saturation, but this quick decrease at low degrees of water saturation tends towards a stationary value when the degree of water saturation reaches a limit value. Schroeder ([SCH 03b]) performed a series of hydrostatic compression tests on samples saturated with fluids of different viscosities and showed that the mechanical behavior is quasi-independent of the viscosity of the fluids. Therefore, the degree of water saturation is the key factor which influences the mechanical behavior of pure chalk. It was also found that the effects of water saturation are related to several factors such as pore structure, water wettability and water activity ([RIS 01]; [RIS 03]).

With regard to water saturation effects in porous chalk, different constitutive models have been proposed. For example, an empirical model has been constructed in which a fictitious stress tensor was introduced to produce enhanced deformation of chalk due to water injection ([PIA 98]). Such an approach is neither based on sound analysis of physical mechanisms nor in agreement with a thermodynamic framework. Based on the mechanics of partially saturated soils [ALO 90] the influence of water saturation has been interpreted using the generalized suction concept ([PAP 97], [COL 02]). A suction stress is introduced depending on the degree of water saturation. Then, the Bishop's effective stress concept ([BIS 63]) is extended to take into account the effect of suction. On the other hand, suction is used as an independent force which affects the plastic yield surface. These two approaches are directly developed by extending the basic concepts used in unsaturated soil mechanics. However, the microstructure and chemical nature of porous chalk may be different from those of most soils. Therefore, the validity of the suction concept is still debatable. In addition, this concept cannot directly explain the fact that creep deformation is enhanced by water saturation.

Based on experimental data by Hellemann *et al*. ([HEL 02a]) and inspired by the notion of pressure solution in porous media, a chemoplastic model has been proposed by Pietruszczak *et al*. ([PIE 06]). The effect of water saturation is interpreted as a consequence of a chemical degradation in the contacts between grains by a pressure solution process. An internal variable is introduced to describe the state of chemical degradation. The kinetics of chemical degradation are

controlled by the rate of dissolution of the contacts betweens grains and the diffusion process of dissolved solids in the pore space. Rigorous micromechanical analyses have been performed in order to determine the evolution of the internal variable for chemical degradation ([LYD 07]). It was found that the evolution of the chemical degradation variable covers a large time scale range from seconds to the geological scale. At the first stage, very fast dissolution of solid contacts may occur leading to a spontaneous degradation of mechanical properties of chalk as observed in the water saturated sample. Its mechanical properties are defined as those of sound material. The influence of the degree of water saturation may be taken into account through a solubility coefficient. For instance, the completely oil saturated sample is seen as the reference state without chemical degradation. The solubility increases with the water saturation degree and reaches the maximal value in completely water saturated samples. The residual mechanical properties of fully saturated samples are defined as the properties of a completely degraded material.

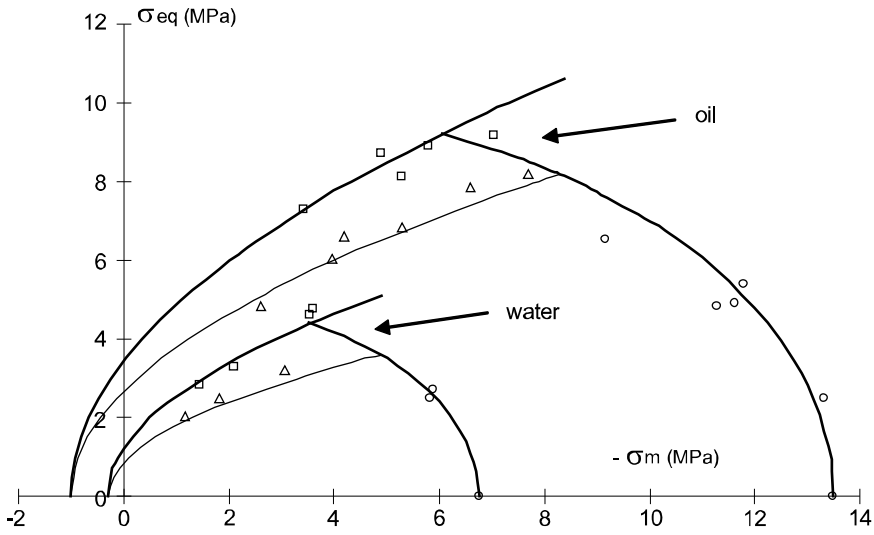

Figure 5.11. *Initial yield surfaces, failure surfaces and pore collapse yield surface for a porous rock in oil and water saturated conditions (after [XIE 06])*

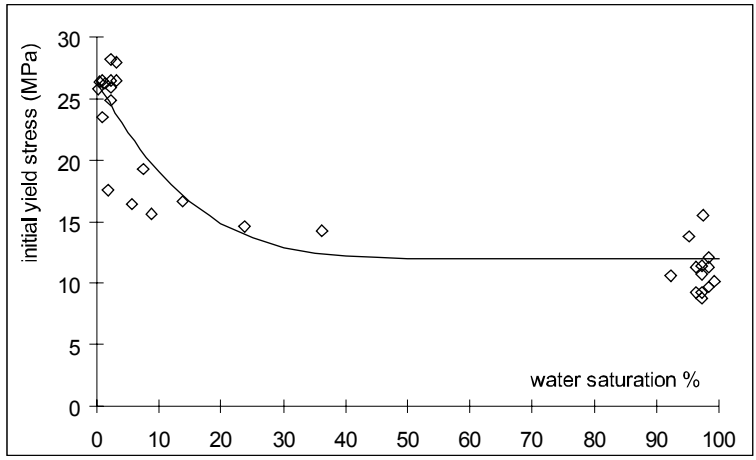

Figure 5.12. *Variation of the initial yield stress of the equivalent matrix depending on the water saturation degree (according to data from [COL 02])*

The above concept of chemical degradation has been used in the elastoplastic modeling of porous chalk ([XIE 06]). In Figure 5.13 the simulation of a triaxial compression test under a confining pressure of 1 MPa is shown. Compared with the mechanical responses of an oil saturated material (see Figure 5.9), it is clear that the mechanical strength is significantly affected by water saturation.

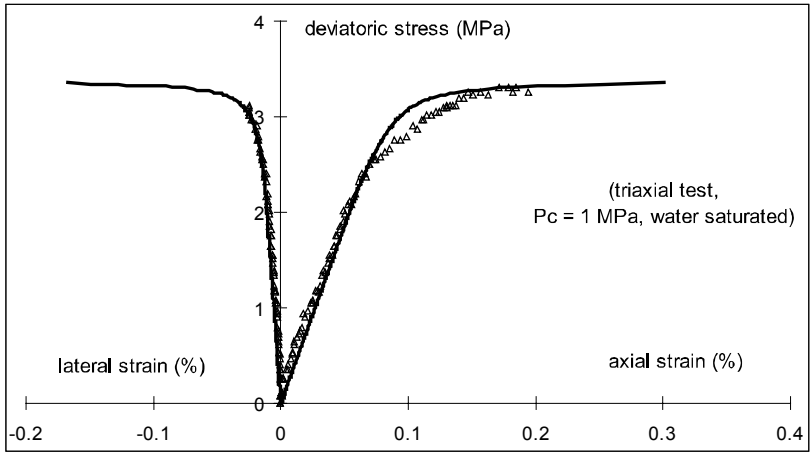

Figure 5.13. *Simulation of a triaxial compression test on water-saturated Lixhe chalk with 1 MPa confining pressure (after [XIE 06])*

5.6. Creep deformation

Under traditional approaches, creep deformation of material is generally described by viscoplastic theory. Various viscoplastic models have been proposed ([PER 66]; [CRI 86], [CRI 94]; [MAR 01]; [COL 02]; [DEG 03], [DEG 04]; [SHA 95], [SHA 03], just to name a few related to porous rocks). All these models are based on a mathematical formulation for modeling creep deformation. The physical mechanisms involved in creep deformation are not clearly interpreted. For instance, in rock materials, it is known that time-dependent deformation may be related to physical and chemical degradation processes, such as a sub-critical propagation of microcracks and chemical dissolution of solid grains and contacts. Therefore, more physically based constitutive models should be developed. In the case of porous chalk, it is now recognized that the creep deformation is essentially related to two mechanisms. The first involves a viscous mechanism generating progressive compaction of a solid skeleton. In addition, the second mechanism is related to pressure dissolution of contacts between grains ([HEL 02b]). The two mechanisms involve two different time scales. The viscous compaction is predominant in the short-term while the pressure solution process controls creep deformation over the long term on a geological timescale.

Based on these analyses, Lydzba *et al*. ([LYD 07]) proposed a phenomenological approach including the two mechanisms leading to a time-dependent behavior of porous chalk. The detailed presentation of the model can be found in the related reference. In a general way, the total strain rate may be expressed as follows:

$$\dot{\boldsymbol{\varepsilon}} = [C]\dot{\boldsymbol{\sigma}} + \boldsymbol{b}\dot{\zeta} + [\Gamma]\boldsymbol{\sigma} \tag{5.19}$$

$$[C]=[C^e]+\frac{1}{H}\left\{\frac{\partial Q}{\partial \boldsymbol{\sigma}}\left(\frac{\partial f}{\partial \boldsymbol{\sigma}}\right)^T\right\}; \quad \boldsymbol{b}=\frac{\partial}{\partial \zeta}[C^e]\boldsymbol{\sigma}+\frac{1}{H}\frac{\partial f}{\partial \zeta}\frac{\partial Q}{\partial \boldsymbol{\sigma}} \tag{5.20}$$

The first term corresponds to the time-independent elastic/plastic strain rate due to the applied stress rate; $[C]$ denotes the elastoplastic stiffness matrix with H being the plastic hardening modulus. The second term describes the time-dependent strain rate due to a pressure solution process, which affects elastic properties and plastic behaviour respectively. The internal variable ζ represents the state of chemical degradation. Finally, the last term is related to the viscous mechanism leading to a time-dependent compaction of the solid skeleton. The kinetics of viscous deformation are determined by the evolution of the internal variable $\xi \in [0,1]$. The viscous strain rates are given by:

$$\dot{\varepsilon}_{ij} = \Gamma_{ijkl}\,\sigma_{kl}\ ; \quad \Gamma_{ijkl} = \dot{\xi}(a_1\delta_{ij}\delta_{kl} + a_2\delta_{ik}\delta_{jl})\ , \ \dot{\xi} = B_3(1-\xi) \tag{5.21}$$

B_3, a_1, and a_2 are three parameters of the model ([LYD 07]). In Figure 5.14, a simulation of a triaxial creep test with 5 MPa confining pressure is presented. Note that in this example, the time scale involved is about a day. Therefore, the creep deformation is dominated by the viscous mechanism. The numerical predictions are in good agreement with the experimental data. In Figure 5.15, triaxial creep tests with a confining pressure of 2 MPa and three different values of the deviatoric stress are shown. Basically, when the applied deviatoric stress is lower than the failure strength of a fully degraded material (water saturated sample), a stationary state is obtained. On the other hand, a spontaneous failure is produced for a higher deviatoric stress. Again, the numerical simulations reproduce the experimental data quite accurately.

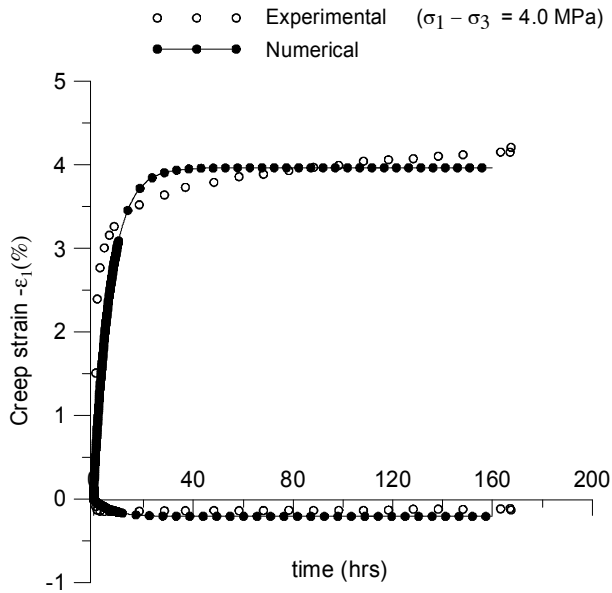

Figure 5.14. *Simulation of triaxial creep test under 5 MPa confining pressure and 4 MPa deviatoric stress on a water saturated sample (after [PIE 06])*

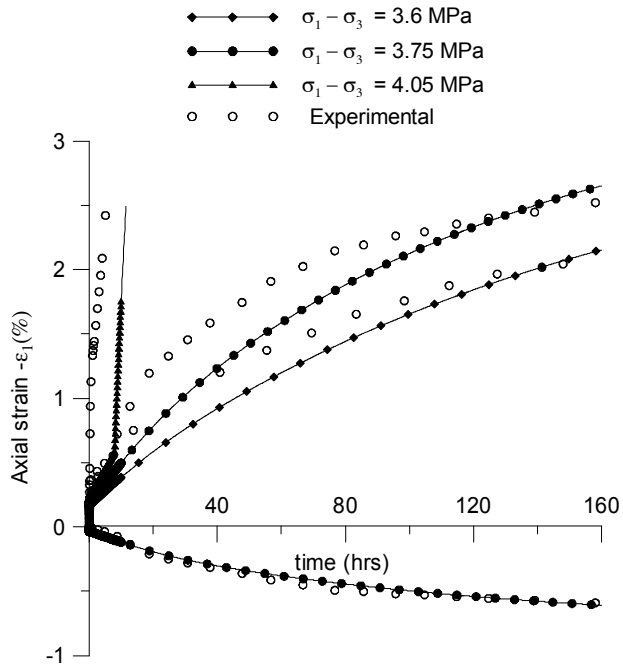

Figure 5.15. *Simulation of a creep tests under 2 MPa confining pressure and four values of the deviatoric stress on water saturated sample (after [PIE 06])*

5.7. Conclusion

In this chapter, we addressed the plastic modeling of the ductile behavior of porous rock subject to compressive stresses. An important specific feature of this class of materials comes from the fact that two plastic flow mechanisms are observed: pore collapse and deviatoric shearing. An example of a constitutive model with two yield surfaces is illustrated. Furthermore, the mechanical behavior of these materials is sensitive to water saturation. A fully phenomenological approach is presented. Finally, the time-dependent deformation is also discussed. Based on micromechanical analysis, the creep deformation is seen as a consequence of a chemical degradation process. A simple phenomenological formulation has also been presented. More detailed discussions on the chemical dissolution process as well as on water sensitivity may be found in a number of indicated references.

5.8. References

[ALO 90] Alonso E.E., Gens A. and Josa A., "A constitutive model for partially saturated soils", *Géotechnique*, 40 (3), 405–430, 1990.

[AND 92] Andersen M.A., Foged N. and Pedersen H.F., "The rate-type compaction of a weak North Sea chalk", *Proc. of 33rd US Rock Mechanics Symposium*, Santa Fe, New Mexico, June 1992.

[AUB 99] Aubertin M., Yahya O.M.L. and Julien M., "Modeling mixed hardening of alkali halides with a modified version of an internal state variables model", *Int. J. Plasticity 15*, 1067-1088, 1999.

[AUB 04] Aubertin M. and Li L., "A porosity-dependent inelastic criterion for engineering materials", *International Journal of Plasticity* 20, 2179–2208, 2004.

[BIO 55] Biot M.A., "Theory of elasticity and consolidation for a porous anisotropic solid", *J. Appl. Phys*, 26, 182–185, 1955.

[BIO 73] Biot M.A., "Non linear and semilinear rheology of porous solids", *J. of Geophy. Res.*, vol. 78, no. 23, 4924–4937, 1973.

[BIS 63] Bishop A.W. and Blight G.E., "Some aspects of effective stress in saturated and partly saturated soils", *Géotechnique*, 13 (3), 177–197, 1963.

[BRI 94] Brignoli M., Santarelli F.J. and Righetti C., "Capillary Phenomena in Impure Chalk", *SPE/ISRM paper 28135, Proc. of Eurock'94 – Rock Mechanics in Petroleum Engineering*, Delft, Balkema, 837–843, 1994.

[CHE 03] Chen H. and Hu Z. Y., "Some factors affecting the uniaxial strength of weak sandstones", *Bull. Eng. Geol. Env.* 62(4), 323-332, 2003.

[COL 02] Collin F., Cui Y.J., Schroeder C. and Charlier R., "Mechanical behaviour of Lixhe chalk partly saturated by oil and water: experimental and modelling", *International Journal for Numerical and Analytical Methods in Geomechanics*, 26, 897–924, 2002.

[COU 95] Coussy O., *Mechanics of Porous Continua,* John Wiley & Sons, UK, 1995.

[CRI 86] Cristescu N., "Damage and failure of viscoplastic rock-like materials", *International Journal of Plasticity*, 2(2), 189–204, 1986.

[CRI 94] Cristescu N., "A procedure to determine non-associated constitutive equations for geomaterials", *International Journal of Plasticity*, 10(2), 103–131, 1994.

[DAS 85] Da Silva F., Sarda J.P. and Schroeder C., "Mechanical behavior of chalks", *Second North Sea Chalk Symposium*, Volume II, Stavanger, Norway, 1985.

[DEG 03] De Gennaro V., Delage P., Cui Y.J., Schroeder C. and Collin F., "Time dependent behaviour of oil reservoir chalk: a multiphase approach", *Soils and Foundations*, 43(4), 131–148, 2003.

[DEG 04] De Gennaro V., Delage P., Priol G., Collin F. and Cui Y.J., "On the collapse behaviour of oil reservoir chalk", *Géotechnique*, 54(6), 415–420, 2004.

[DES 80] Desai C.S., "A general basis for yield, failure and potential functions in plasticity", *Int. J. Num. Anal. Meth. Geomech.*, 4, 361–375, 1980.

[DES 84] Desai C.S. and Siriwardane H.J., *Constitutive Laws for Engineering Materials with Emphasis on Geological Materials*, Prentice Hall, Englewood Cliffs, NJ, 1984.

[DES 01] Desai C.S., *Mechanics of Materials and Interfaces: The Disturbed State Concept*, CRC Press, Boca Raton, 2001.

[DIM 71] DiMaggio F.L. and Sandler I.S., "Material model for granular soils", *ASCE J. Eng. Mech. Div*, 97(EM3), 935–950, 1971.

[ELL 85] Elliott G.M. and Brown E.T., "Yield of a soft, high porosity rock", *Geotechnique*, 35(4), 413–423, 1985.

[GEN 93] Gens A. and Nova R., "Conceptual bases for a constitutive model for bonded soils and weak rocks", *Proc. Symp. on Geotechnical Engineering of Hard Soils – Soft Rocks*, A. Agagnostopoulos *et al*. (eds.), Balkema, 485-493, 1993.

[GUR 77] Gurson A.L., "Continuum theory of ductile rupture by void nucleation and growth: Part I- yield criterion and flow rules for porous ductile media", *Transactions of the ASME*, 99, 2–15, 1977.

[HAL 90] Halleux L., Detiege C., Poot B., Schroeder C., Monjoie A., Debande G. and Da Silva, F., Mechanical Behavior of Chalks", *Proceedings of the 3rd North Sea Chalk Symposium*, Copenhagen, 1990.

[HEL 02a] Hellemann R., Renders P.J.N., Gratier J.P. and Guiguet R., "Experimental pressure solution compaction of chalk in aqueous solutions, Part 1: Deformation behaviour and chemistry, water-rock interactions", *The Geochemical Society, special publication*, no. 7, R. Hellmann and S.A. Wood (eds.), 129–152, 2002.

[HEL 02b] Hellemann R., Renders P.J.N., Gratier J.P. and Guiguet R., "Experimental pressure solution compaction of chalk in aqueous solutions, Part 2: Deformation examined by SEM, porosimetry, synthetic permeability and X-ray computerized tomography, water-rock interactions", *The Geochemical Society, special publication*, no. 7, R. Hellmann and S.A. Wood (eds.), 129–152, 2002.

[HOM 00] Homand S. and Shao J.F., "Mechanical behavior of a porous chalk and water/chalk interaction, Part I: Experimental study", *Oil & Gas Science and Technology*, 55(6), 591–598, 2000.

[HOU 97] Houlsby G.T., "The work input to an unsaturated granular material", *Géotechnique*, 47(1), 193–196, 1997.

[JIN 98] Jin J. and Cristescu N., "An elastic viscoplastic model for transient creep of rock salt", *International Journal of Plasticity*, 14, 85–107, 1998.

[LAD 77] Lade P.V., "Elastic-plastic stress-strain theory for cohesionless soil with curved yield surfaces", *Int. J. Solids Structures*, 13, 1019–1035, 1977.

[LAD 95] Lade P.V. and Kim M.K., "Single hardening constitutive model for soil, rock and concrete", *Int. J. Solids Structures*, 32(14), 1963–1978, 1995.

[LEB 96] Leblond J.B. and Perrin G., "Introduction à la mécanique de la rupture ductile des métaux", Lecture notes (in French), Ecole Polytechnique, Paris, 1996.

[LOR 98] Lord C.J., Rhett D.W. and Johlman C.L., "Is capillary suction a viable cohesive mechanism in chalk", *Proc. Eurock'98*, 367–375, Trondheim, Norway, 1998.

[LYD 07] Lydzba D., Pietruszczak S. and Shao J.F., "Intergranular pressure solution in chalk; A multiscale approach", accepted for publication by *Computers & Geotechnics*, 2007.

[MAR 01] Maranini E. and Yamaguchi T., "A non-associated viscoplastic model for the behaviour of granite in triaxial compression", *Mechanics of Materials*, 33, 283–293, 2001.

[MON 95] Monjoie A., Schroeder Ch. and Da Silva, F., "Mechanical behaviour of chalks", *Proceedings of the 3rd North Sea Chalk Symposium*, Stavanger, Norway, 1995.

[PAP 97] Papamichos E., Brignoli M. and Santarelli F.J., "An experimental and theoretical study partially saturated collapsible rock", *Int. J. of Mechanics of Cohesive-Frictional Materials*, 2, 251–278, 1997.

[PER 66] Perzyna P., "Fundamental problems in viscoplasticity", *Advances Application Mech*, 9, 243–377, 1966.

[PER 90] Perrin G. and Leblond J.B., "Analytical study of a hollow sphere made of plastic porous material and subjected to hydrostatic tension- application to some problems in ductile fracture of metals", *International Journal of Plasticity*, 6(6), 677–699, 1990.

[PIA 94] Piau J.M. and Maury V., "Mechanical effects of water injection on chalk reservoirs", *SPE/ISRM paper 28133, Proc. Eurock'94 – Rock Mechanics in Petroleum Engineering*, Delft, Balkema, 837–843, 1994.

[PIA 98] Piau J.M., Bois A.P., Atahan C., Maury V. and Hallé G., "Water chalk interaction, Part I: Comprehensive evaluation of strain and stress jumps at the waterfront", *Proc. Eurock'98 – Rock Mechanics in Petroleum Engineering*, SPE INC. 419–428, Trondheim, 1998.

[PIE 88] Pietruszczak S., Jiang J. and Mirza F.A., "An elastoplastic constitutive model for concrete", *Int. J. Solids & Structures* 24 (7), 705–722, 1988.

[PIE 04] Pietruszczak S., Lydzba D. and Shao J.F., "Description of creep in frictional materials in terms of microstructure evolution", *Journal of Engineering Mechanics*, ASCE, 130(6), 681–690, 2004.

[PIE 06] Pietruszczak S., Lydzba D. and Shao J.F., "Modeling of deformation response and chemo-mechanical coupling in chalk", *Int. J. for numerical and analytical methods in geomechanics*, 30, 997–1018, 2006.

[RIS 98] Risnes, R. and Garspestad, O.J., "Strain hardening and extensional failure in high porosity chalk", *SPE/ISRM 47581, Proc. Eurock'98 – Rock Mechanics in Petroleum Engineering*, SPE INC. 475–484, Trondheim, 1998.

[RIS 99a] Risnes R., Korsnes R.K. and Vatne T.A., "Tensional strength of soft chalks measured in direct and Brazilian tests", *Proc. 9th ISRM Congress on Rock Mechanics, Paris 1999*, vol. 2, 667–672, Balkema, Rotterdam, 1999.

[RIS 99b] Risnes R. and Flaageng O., "Mechanical properties of chalk with emphasis on chalk-fluid interactions and micromechanical aspects", *Oil & Gas Science and Technology – Revue IFP*, Vol. 54, no. 6, 751–758, 1999.

[RIS 00] Risnes R., Berg T., Furuvald A. and Paulsen T., "Tensional failure and solid-fluid interactions in high porosity chalk", *Proc. 4th North American Rock Mechanics Symposium*, 205–212, Balkema, Rotterdam, 2000.

[RIS 01] Risnes R., "Deformation and yield in high porosity outcrop chalk", *Phys. Chem. Earth (A)*, vol. 26, no. 1–2, 53–57, Elsevier, 2001.

[RIS 03] Risnes R., Haghighi H., Korsnes R.I. and Natvik O., "Chalk – water interactions with glycol and brines", *Tectonophysics*, 370, 213–226, 2003.

[SCH 98] Schroeder C., Bois A.P., Maury V. and Hallé G., "Water/chalk (or collapsible soil) interaction, Part II: Results of tests performed in laboratory on lixhe chalk to calibrate water/chalk models", *SPE/ISRM 47587, Proc. Eurock'98-Rock Mechanics in Petroleum Engineering*, SPE INC., 505–514, Trondheim, 1998.

[SCH 03a] Schroeder, Ch., "Du coccolithe au réservoir pétrolier; approche phénoménologique du comportement mécanique de la craie en vue de sa modélisation à différentes échelles", Doctoral Thesis (in French), University of Liège, 2003.

[SCH 03b] Schroeder C. (Coordinator), "Mechanical behaviour of partially and multiphase saturated chalks and fluid-skeleton interaction: Main factor of chalk oil reservoirs compaction and related subsidence", Final report of the EU project (PASACHALK2), 2003.

[SHA 95] Shao J.F., Dahou A. and Bederiat M., "Experimental and numerical investigations on transient creep of porous chalk", *Mechanics of Materials*, 21, 147–158, 1995.

[SHA 03] Shao J.F., Zhu Q.Z. and Su K., "Description of creep in rock materials in terms of material degradation", *Computer and Geotechnics* 30, 549-555, 2003.

[SIM 98] Simo J.C. and Hughes T.J.R., *Computational Inelasticity*, Springer-Verlag, New York, Inc., 1998.

[TVE 90] Tvergaard V., "Material failure by void growth to coalescence", *Adv. Appl. Mech*., 27, 83–151, 1990.

[WON 92] Wong T.F., Szeto H. and Zhang J., "Effect of loading path and porosity on the failure mode of porous rocks", *Appl. Mech. Rev*., 45(8), 281–293, 1992.

[XIE 06] Xie S.Y. and Shao J.F., "Elastoplastic deformation of a porous rock and water interaction", *International Journal of Plasticity*, 22, 2195–2225, 2006.

Constitutive Modeling of Soils and Rocks
Edited by Pierre-Yves Hicher & Jian-Fu Shao

Chapter 6

Incremental Constitutive Relations for Soils

6.1. Incremental nature of constitutive relations

The notion of constitutive modeling is recent. Generally, it represents, with all the possible problems linked to it, the whole of physics at small scales of a median considered as continuous, which means without an internal scale. From a practical point of view, we can say that it is indispensable for any modeling calculation. The choice of a specific model allows us to express, in a mathematical form, that different media "do not behave" in the same way (for example, sands and concretes have different behaviors). From explicative or taxonomic models in the 1960s, the constitutive models, due to the use of finite element calculus, have taken the form of equations which relate the state of stress to the functional of the kinematic history:

$$\sigma(t) = \underset{s=0}{\overset{s=t}{\mathfrak{F}}}[\nabla u(s)] \tag{6.1}$$

Obviously, this functional has to be objective. From this theoretical description, a very significant simplification can be made by assuming that the history can be expressed by the actual state. This leads to an elastic model, which becomes hyperelastic if we add the assumption that the energy lost outside the medium during a cycle cannot be positive. We can use this type of model if we want to describe the behavior along a monotonic loading path. This is currently done for applications on metallic materials when the deformation theory of plasticity is used. However, in order to be able to use the model along more complicated loading paths, especially loading-unloading paths, a more complicated constitutive model is needed. An

Chapter written by René CHAMBON, Félix DARVE and Farid LAOUAFA.

incremental or rate formulation is indispensable. Since we will consider only non-viscous behaviors, the two formulations are equivalent.

Assuming the state E of a given material to be known, it is possible to find a relationship between an objective derivative of the stress – in what follows, Jaumann's derivative $\dot{\sigma}$ will be considered – and a spatial description of the kinematics – in what follows, strain rate $\dot{D}$, which is the symmetric part of the rate gradient, will be considered. An implicit relation can be written:

$$F(\dot{\sigma}, \dot{D}, E) = 0 \tag{6.2}$$

Due to the hypothesis of non-viscous behavior, function F has to be positive and homogenous in $\dot{\sigma}$ and $\dot{D}$. If equation (6.2) can be solved in $\dot{\sigma}$ and/or $\dot{D}$, we can have:

$$\dot{\sigma} = f(\dot{D}, E) \tag{6.3}$$

$$\dot{D} = g(\dot{\sigma}, E) \tag{6.4}$$

f and g are also positive and homogenous of degree 1 in $\dot{D}$ and $\dot{\sigma}$, respectively. These two dual forms are not completely equivalent. Equation (6.3) is completely inside the framework defined by equation (6.1). In fact, from equation (1.3), we can deduce:

$$\sigma(t) = \int_{s=0}^{s=t} \dot{\sigma} ds = \int_{s=0}^{s=t} f(\dot{D}, E) ds \tag{6.5}$$

if we have an evolution law for the state of the material. Equation (6.4) requires solving the problem of the inversion, which is not always a simple problem.

Often, the problem can be simplified by assuming that f and g are linear functions of their first argument. In that case, we obtain a reversible behavior, as:

$$\dot{\sigma}(\dot{D}, E) = f(\dot{D}, E) = -f(-\dot{D}, E) = -\dot{\sigma}(-\dot{D}, E) \tag{6.6}$$

This hypothesis can be partially justified for a given class of strain rates, using a rigorous reasoning in several simple cases. For example in the case of metal plasticity, if we assume that the plastic deformation is due to a unique microscopic sliding mechanism in a direction well defined by the metal structure, we can demonstrate that function f is linear when this mechanism is active. If we assume that the behavior is elastic when the mechanism is inactive, relation (6.3)

corresponds to two linear relations, one for plastic loading, and the other for elastic unloading. Of course, a consistency condition between these two relations is necessary, so that the model gives the same result at the boundary between the domains (neutral loading). Ignoring this condition leads to calculation results which depend on the computer used to obtain them [NEL 78]: this has been known for a long time, but tends to be forgotten.

As just seen, the bilinearity can be justified only if a plastic mechanism can be well identified. Many reasons can be cited to show that this is not the case in geomaterials. Already, in many cases, the recent plasticity models for metals have several (sometimes many) mechanisms. Concerning geomaterials, the microscopic study of the deformations does not show a specific mechanism capable of justifying the hypothesis of bilinearity and experimental results on soils have demonstrated the non-validity of this hypothesis [TAT 74]. We should not conclude that the incrementally bilinear models are insignificant, but rather that the *in situ* observed phenomena will be better described by models which are not based on this simple hypothesis.

In this chapter we will show two different ways of overcoming the bilinearity and even the polylinearity of elastoplastic models with several plastic mechanisms by using completely non-linear relations. The first part is devoted to hypoplastic models in general and CloE models in particular, which have been specially constructed to describe in a realistic manner the localized failure in geomaterials, even if they are also capable of describing various other geomaterials characteristics. The second part is devoted to incrementally non-linear constitutive models which constitute a more general framework than the hypoplasticity, and can give more realistic responses for cyclic loading and treat different classes of instability and bifurcation.

6.2. Hypoplastic CloE models

Hypoplastic models have been independently developed by Kolymbas and co-workers [KOL 87] and the authors [CHA 85, CHA 89]. A complete historical presentation can be seen in [TAM 00a]. A common characteristic of the hypoplastic models is to write equation (6.3) in the form of the following non-linear relation in order to describe irreversibility:

$$\dot{\sigma} = A : \dot{D} + b\left\|\dot{D}\right\| \qquad\qquad \dot{\sigma}_{ij} = A_{ijkl}\dot{D}_{kl} + b_{ij}\left\|\dot{D}\right\| \tag{6.7}$$

The fourth order tensor A and the second order tensor b are both functions of the material state. This dependency needs of course to be expressed. We will develop all

the theoretical consequences of equation (6.7), after which we will give several examples of applications of these models.

6.2.1. *Irreversibility in hypoplasticity*

By using equation (6.7), the model is clearly irreversible. Contrary to what can be seen in equation (6.6), we can see that, for a given material state:

$$\dot{\sigma}(\dot{D}) = A : \dot{D} + b\left\|\dot{D}\right\| \neq \dot{\sigma}(-\dot{D}) = -A : \dot{D} + b\left\|\dot{D}\right\| \tag{6.8}$$

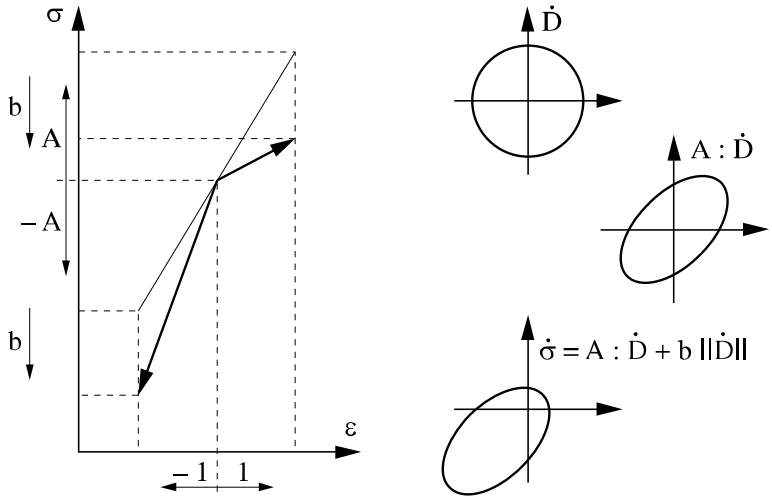

Figure 6.1. *Irreversibility in 1D and 2D hypoplasticity*

It is interesting to reproduce this fundamental mathematical property graphically. Figure 6.1 illustrates the irreversibility in 1D and 2D. The left part of the figure corresponds to the 1D case. In such a case, $\dot{\sigma}$, $\dot{D}$, A and b are scalars and the norm becomes an absolute value. We obtain:

$$\dot{\sigma} = A\dot{D} + b\left|\dot{D}\right| \tag{6.9}$$

If we give to $\dot{D}$ the values +1 and –1, we obtain for $\dot{\sigma}$, $A + b$ in the first case and $–A + b$ in the second case, which is illustrated in Figure 6.1 for a negative value of b. We can clearly see that the irreversibility does not necessarily have to be

modeled by two different linear relations, one for loading and one for unloading. A single non-linear relation can be sufficient.

The 1D example is however insufficient to understand completely the incremental non-linearity of the hypoplastic models. Let us now consider the 2D scheme on the right side of Figure 6.1. Due to the positive homogenity of degree 1 in time, it is sufficient to consider only the solutions of equation (6.7) obtained for strain rates with a norm equal to 1 in all the directions. In Figure 6.1, this corresponds to a circle centered at the origin of the axes in the strain rate plane. Multiplying by A transforms the circle into an ellipse in the stress rate plane, and adding b, which is a vector in the 2D case, translates the ellipse in the same plane. It appears clearly again that the additional term linked to the norm controls the irreversibility.

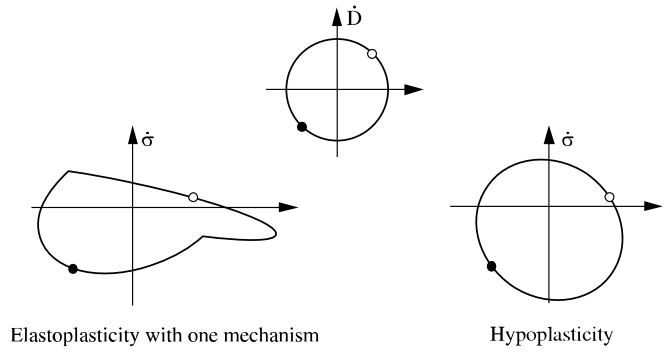

Figure 6.2. *Comparison of incremental constitutive relations in traditional elastoplasticty and in hypoplasticity*

In order to see even more clearly that the 1D representation is meaningful but insufficient, let us now consider two different ways of expressing the irreversibility along a given loading path. For this purpose, we have in Figure 6.2 the responses in $\dot{\sigma}$ for two cases. The case of the hypoplastic response has been previously studied and it has been shown that we obtain a non-centered ellipse as shown on the right part of Figure 6.2. On this ellipse, we have identified two specific points corresponding to two opposite strain rates. On the left part, we present the same representation for a bilinear model, for example an elastoplastic model with one mechanism. In that case, the response envelop consists of two half-ellipses, both centered but of different sizes and connected to each other due to the consistency condition mentioned in section 6.1. The difference between the two ellipses describes the irreversibility. In the two cases, hypoplasticity and elastoplasticity, the responses $\dot{\sigma}$ for the two specific values of $\dot{D}$ are the same, which illustrates that the

knowledge of the response along a given loading-unloading path is not enough to determine the incremental relation.

To conclude this study of the irreversibility, it is interesting to note that, for $b = 0$, the hypoplastic model degenerates into a reversible incrementally linear model, and is therefore potentially elastic.

6.2.2. *Limit states*

One of the big advantages presented by equation (6.7) is that it is possible to deduce easily several model properties, or, in other words, that it is easy to establish mathematically some properties which can allow us to test numerical software in which the model has been implemented.

6.2.2.1. *Dual model*

An interesting question to ask may be: under what conditions can equation (6.7) be inverted? It is easy to demonstrate that a necessary condition is that A can indeed be inverted. We called A^{-1} its inverse. Owing to the homogenity of the model, we can assume that response $\dot{D}$ with a norm equal to 1 is obtained for $\dot{\sigma}$, defined by its direction s and its norm λ. Under these conditions, equation (6.7) becomes:

$$\lambda s = A : \dot{D} + b \tag{6.10}$$

thus:

$$\dot{D} = A^{-1} : (\lambda s - b) \tag{6.11}$$

which always has a solution if s and λ exist. Since the norm of $\dot{D}$ must be equal to 1, we obtain:

$$\lambda^2[(A^{-1} : s) : (A^{-1} : s)] - 2\lambda[(A^{-1} : s) : (A^{-1} : b)] + (A^{-1} : b) : (A^{-1} : b) = 1 \tag{6.12}$$

which is a second degree equation in λ, that must have only one positive root. Therefore, if $(A^{-1} : b) : (A^{-1} : b) - 1 < 0$, equation (6.7) can be inverted, the solution being obtained from equation (6.11), with λ as the unique positive solution of equation (6.12). In a physical way, the possibility of inversion means that the material is able to deform homogenously for any state of stress. It can be worthwhile to introduce a new expression of the constitutive equation:

$$B = A^{-1} : b \tag{6.13}$$

$$\dot{\sigma} = A : (\dot{D} + B\left\|\dot{D}\right\|) \tag{6.14}$$

From this new relation, we can deduce the previous result. The relationship between $\dot{D}$ and $\dot{\sigma}$ can be decomposed into a relation which allows us to go from $\dot{D}$ to $\dot{D} + B\left\|\dot{D}\right\|$, followed by multiplying by A, which can be inverted according to our hypothesis. Therefore, the condition for the existence of the dual model corresponds to: $B : B - 1 < 0$

6.2.2.2. *Plasticity and flow rule*

We will now see if it is possible to find values of $\dot{D}$ different from zero corresponding to the condition $\dot{\sigma}$ = 0. In other words, we have to find conditions for tensors A and b, which lead to a perfectly plastic flow. By using the previous developments, a necessary condition is that one of the solutions of equation (6.12) is $\lambda = 0$. Therefore, we obtain the following relation:

$$(A^{-1} : b) : (A^{-1} : b) = B : B = 1 \tag{6.15}$$

If A and b are functions of the stress state, equation (6.15) represents in fact the equation of the perfect plasticity surface. If equation (6.15) is satisfied, $\lambda = 0$ and:

$$\dot{D} = -A^{-1} : b = -B \tag{6.16}$$

which thus represents the flow rule, meaning the strain rate, different from zero, for which the stress remains constant, something which is easy to verify by inserting equation (6.11) into equation (6.7).

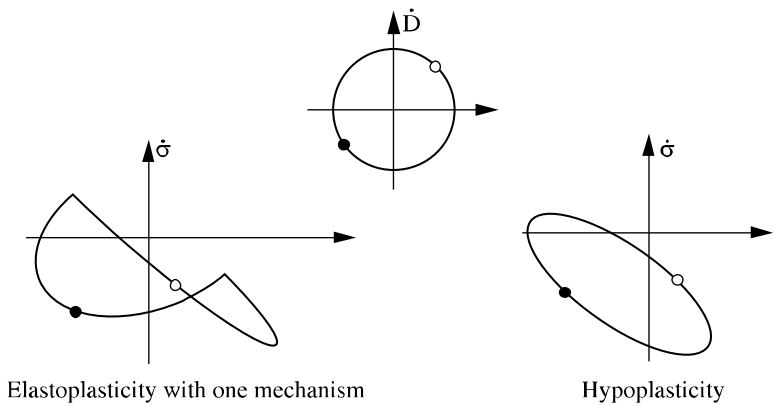

Figure 6.3. *Softening in elastoplasticity and in hypoplasticity*

6.2.2.3. *Softening*

We have seen the implication of the condition $(A^{-1} : b) : (A^{-1} : b) < 1$ for the model. Having just demonstrated that the condition $(A^{-1} : b) : (A^{-1} : b) = 1$ corresponds to perfect plasticity, we will now study the implication of the condition $(A^{-1} : b) : (A^{-1} : b) > 1$, which can also be written $B : B > 1$. If we go back to the calculation made in section 6.2.2.1, the model can no longer be inverted, which corresponds to the case of elastoplastic models with negative hardening. This is why we will call this particular case *softening*. Figure 6.3 illustrates in the 2D case how the softening is treated in elastoplasticity and hypoplasticity. In elastoplasticity, the plastic half-ellipse is located on the same side as the elastic half-ellipse, which implies that half the plane of the strain rate is not accessible to the model, as in perfect plasticity. In hypoplasticity, the ellipse is shifted in such a way that the plane origin is located outside the ellipse, which implies that, by extension in 3D, a cone in the strain rate space is inaccessible. The drawing was made, as previously, by assuming that the two classes of models gave the same responses for a given strain rate in one direction, and also in the opposite direction.

6.2.2.4. *Consistency relation at the limit state*

We have seen in section 6.2.2.2 how perfect plasticity was modeled in the framework of hypoplasticity. Without more constraint (in the mathematical sense), we can obtain a surface, for example in the stress space, which can be crossed over towards softening states. This is not necessarily a desirable situation. It could be preferable that the plastic surface was also a limit surface, making the states of stress located outside this surface inaccessible. In that case, in the presence of softening, the equation of the plastic surface cannot be dependent only on the stress. This need for the stress states to belong to a well identified domain is often useful. In practice, it allows us to better control the model use.

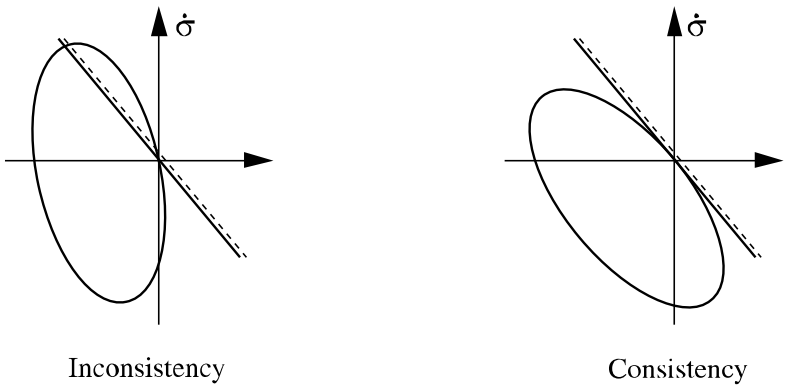

Figure 6.4. *Principle of the consistency relation in hypoplasticity*

Once more, it is easier to understand this aspect by drawing a diagram in 2D. For a potentially perfectly plastic state, the limit surface appears – if assumed to be regular – as a straight line passing through the origin in the stress space. On the left side of Figure 6.4, we can see clearly that there are stress rates which can cross the limit surface, while on the right side, no stress rate can be directed towards the forbidden zone. We say, in the second case, that the model verifies the consistency relation given in equation (6.17). We can see the details of the calculation in [CHA 89]:

$$n : A = -\lambda B \tag{6.17}$$

where n is the outer normal to the limit surface in the stress space and λ is a positive scalar. This relation is one of the aspects characterizing CLoE models.

In elastoplasticity, with or without hardening, the consistency relation expresses the condition that a stress state cannot be located outside the yield surface. In hypoplasticity, it is possible to force the stress state to stay inside a limit surface. This explains why we adopted the same expression. The fundamental difference is that the relation applies only in an asymptotic state, when the state of stress tends towards the limit state surface.

6.2.3. *A simple example: the 2D Mohr-Coulomb model*

In order to illustrate our theoretical developments, we will present a simple application of these concepts for a 2D medium [CHA 98]. Such a 2D model is simpler to study, and at the same time interesting enough, since many practical problems are treated in 2D conditions. The model is written in the principal stress axes. We have:

$$\sigma = \begin{bmatrix} \sigma_{11} & 0 \\ 0 & \sigma_{22} \end{bmatrix} \tag{6.18}$$

Where σ_{11} is the minor principal stress. Without cohesion, the plastic surface also considered as the limit surface is defined by:

$$\frac{\sigma_{22} - \sigma_{11}}{2} + \frac{\sigma_{22} + \sigma_{11}}{2} \sin\phi = 0 \tag{6.19}$$

where ϕ is the friction angle. In the same way, by assuming dilatancy in perfect plasticity, the flow rule is written:

$$\frac{\dot{D}_{22}+\dot{D}_{11}}{2}+\frac{\dot{D}_{22}-\dot{D}_{11}}{2}\sin\psi=0 \tag{6.20}$$

where ψ is the dilatancy angle. Starting from these relations, we will give the expressions of A and B as functions of the stress state; more precisely here, depending on the mobilized friction angle, which will give us the constitutive relation from equation (6.14). In what follows, we will write A and B in the form of 3*3 and 3*1 matrices by using the usual convention, since we are developing a constitutive model. Equation (6.20) gives us the value of the transpose of B^{lim}, which represents the value of B at the limit state:

$$\left[B^{\lim}\right]^T=\begin{bmatrix}\dfrac{1}{\sqrt{1+(\dfrac{1+\sin\phi}{1-\sin\phi})^2}} & \dfrac{1}{\sqrt{1+(\dfrac{1-\sin\phi}{1+\sin\phi})^2}} & 0\end{bmatrix} \tag{6.21}$$

For intermediate states, we take:

$$B=B^{\lim}\frac{\sin\phi_{mob}}{\sin\phi} \tag{6.22}$$

where ϕ_{mob} is the mobilized friction angle. We can note that, for isotropic states of stress, $B=0$, which means that the model gives reversible behavior. It is therefore natural to assume that, in this condition, A is the isotropic elastic matrix. In respect to the consistency relation, the solution adopted in what follows consists of multiplying this isotropic matrix by a rotation matrix dependent on an angle θ, whose limit value $\theta^{\lim}$ is calculated from equation (6.17). We can take for example:

$$\theta=\theta^{\lim}\frac{\sin\phi_{mob}}{\sin\phi} \tag{6.23}$$

We can finally write A as follows:

$$A=\begin{bmatrix}\cos\theta & \sin\theta & 0\\ -\sin\theta & \cos\theta & 0\\ 0 & 0 & 1\end{bmatrix}\begin{bmatrix}\dfrac{E(1-\nu)}{(1+\nu)(1-2\nu)} & \dfrac{E\nu}{(1+\nu)(1-2\nu)} & 0\\ \dfrac{E\nu}{(1+\nu)(1-2\nu)} & \dfrac{E(1-\nu)}{(1+\nu)(1-2\nu)} & 0\\ 0 & 0 & \dfrac{2E}{(1+\nu)}\end{bmatrix} \tag{6.24}$$

where E and ν are respectively a Young's modulus and a Poisson's ratio, which can be interpreted as elastic parameters in isotropic stress states only, the only states for which the model degenerates in an elastic model. Finally, we easily constructed a model with four parameters: Young's modulus E, Poisson's ratio ν, friction angle ϕ and dilatancy angle ψ.

Obviously, the previous model is very simple. We can construct more elaborated 3D CLoE models using interpolations between experimentally known behaviors, in particular along triaxial loading paths. We do not have the room here to present a more detailed application of this approach, which gives very precise models. For more detailed studies and applications on specific geomaterials with comparison to experimental results, see [CHA 94a, ELH 96, VIG 99].

6.2.4. *Use in boundary value problems*

The non-linear modeling of material behavior is not straightforward. In particular, it is very difficult to know if a particular model leads to mathematically well-written problems. In a book like this, it is indispensable to know if the presented models are effectively usable in finite elements calculations. The story reported in [NEL 76] about the computer dependence of some numerical results is quite old but exemplary. It is very probable that all the models lead to mathematical difficulties which cannot be overcome (we will discuss this point in section 6.2.5). It is therefore interesting to possess some well assessed results concerning the mathematical problem associated with a given model, as well as some precise numerical experiments, with quantification of the accuracy of the integration schemes.

Concerning CLoE models, we demonstrated that the positivity condition of the second order work (equation (6.25)) in each point of the soil volume concerned by a small deformation calculus, was a sufficient condition of existence and uniqueness of the problem solution expressed in terms of the strain rate [CHA 99]:

$$\Delta W = \dot{\sigma} : \dot{D} = \dot{\sigma}_{ij} \dot{D}_{ij} > 0 \tag{6.25}$$

This condition is no longer verified when we get close to the limit surface, and we will see that we have to examine carefully the states close to failure, as for all the other models, because the models based on a continuous medium assumption do not apply anymore.

In all cases for which we can reasonably assume that the mathematical problem is well posed, CLoE models are easy to integrate. A Crank-Nicolson method for

local integration [TAM 00b], associated with a Newton-Raphson method for the global problem, allows us to integrate these models efficiently.

6.2.5. *Explicit criterion of localization*

Failure of geomaterials happens in most cases in a localized mode. It is therefore indispensable that modern modeling is able to take into account this phenomenon. The name CLoE accounts for the fact that, even if the model is non-linear, it allows us to conduct a complete analysis of localization and to obtain an explicit form for it. This is very important, considering that numerous localization analyses are only partially treated. CLoE stands for consistence and explicit localization (*Consistance et Localization Explicite* in French).

Localization calculus is based on the following. Guided by experimental observations and also by some theoretical considerations which are not discussed here, we are looking for the existence, within a homogenous infinite medium subjected to a homogenous strain rate, of a band of undetermined width, subjected also to a homogenous deformation, albeit different from the rest of the medium. We can then write the kinematic compatibility condition between the two zones:

$$\dot{F}^i = \dot{F}^e + g \otimes n \qquad \dot{F}^i_{kl} = \dot{F}^e_{kl} + g_k n_l \tag{6.26}$$

where $\dot{F}^i$ is the strain rate gradient inside the normal band n, $\dot{F}^e$ the strain rate gradient outside the band, and n a possibly unknown vector. We can also write the condition of equilibrium at the band boundary:

$$\hat{\sigma}^i.n = \hat{\sigma}^e.n \qquad \hat{\sigma}^i_{ij} n_j = \hat{\sigma}^e_{ij} n_j \tag{6.27}$$

where $\hat{\sigma}$ is the stress derivative in fixed axes. These equations, combined with the constitutive relations, give, when available, the shear band localization criterion. CLoE and the hypoplastic models, generally expressed by equation (6.7) or equation (6.14), which are equivalent, allow us to obtain an explicit localization criterion:

$$\begin{aligned} &M_{ijkl} = A_{ijkl} + \frac{1}{2}(\sigma_{il}\delta_{jk} - \sigma_{ik}\delta_{jl} + \sigma_{jl}\delta_{ik} - \sigma_{jk}\delta_{il}) \quad P_{ik} = M_{ijkl} n_l n_j \\ &\left\| \frac{1}{2}(P^{-1}_{il} b_{lk} n_k n_j + P^{-1}_{jl} b_{lk} n_k n_i) \right\| \geq 1 \end{aligned} \tag{6.28}$$

When the band is located within a specific plane, which is the case for a simple model such as the one presented in section 6.2.3, this criterion can be expressed by a

polynomial form of degree 4 in tan α, where α is the angle between the normal direction to the band and the x axis for example.

At the present stage, some observations have to be made.

The localization criterion for hypoplastics models, obtained by a completely rigorous calculation (see equation (6.25)), has nothing to do with a determinant of the acoustic tensor. In addition, in order to determine an acoustic tensor, we first have to linearize the non-linear model rigorously, which is easy to do for the hypoplastic models, but is of interest only for solving strain rate boundary problems. A localization calculation made with the linear model corresponding to the linearization of the model in the vicinity of the strain rate gradient $\dot{F}^e$ gives a result which sometimes overestimates the medium's resistance to localization [CHA 85, TAM 00c].

We can demonstrate that, if the localization condition is fulfilled for the small strain hypothesis ($M_{ijkl} = A_{ijkl}$ in equation (6.25)), the second order work is no longer positive. This result is not surprising, since the fulfilment of the localization condition in fact means that there are several solutions to a given boundary problem.

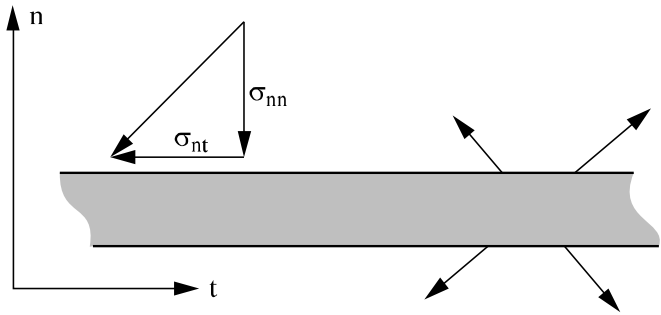

Figure 6.5. *Physical interpretation of the localization*

Finally, it is important to have a more physical view on this localization criterion. It can be proved that, for a given material state represented in Figure 6.5 in principal axes, the localization will take place in a band having a direction *t* and a normal *n*, if this band can be sheared with a stress increment at the boundary equal to zero: $\dot{\sigma}_{nn} = \dot{\sigma}_{nt} = 0$. This result can be proved, rigorously again in a small strain condition, in order to be equivalent to the criterion given by equation (6.25) [CHA 98a]. It is important to understand that this result does not mean that the model is in the plasticity condition as presented in section 6.2.2.2. The important difference is

that $\dot{\sigma}_{tt} \neq 0$ in the case of localization. However, since the band width is not specified because of the absence of material internal scale, the fact that $\dot{\sigma}_{tt} \neq 0$ does not allow the global problem to maintain the uniqueness of the solution.

6.2.6. *Induced anisotropy*

The last observation in the previous section clearly shows that, for a localization to be possible, the existence of a weak zone in a given direction is necessary. The localization phenomenon is thus clearly directed. In other words, following Vardoulakis' conclusion [VAR 80], we can say that the appearance of a localization in laboratory tests should not be considered as an undesirable effect, but rather as a added piece of information on the incremental anisotropy of the material when the localization takes place. Based on these general principles, we developed a means to integrate this information in our hypoplastic models. This is the main aspect which characterizes CloE models among other hypoplastic models.

In laboratory homogenous testing (direct simple shear is thus excluded), the strain and stress directions remain fixed if the material is initially isotropic. For the model studied in section 6.2.3, this means that the term A_{33} in matrix A, which will be called the shear modulus in the loading axes, does not play any role in this type of test. Except for the isotropic state, where it is fixed and equal to $G = \dfrac{2E}{(1+\nu)}$, this term is undetermined, while it plays an important role in the equation of the localization criterion. Therefore, we chose to vary the shear modulus from its value at the isotropic state to a value which gives the localization in the same conditions as observed in the experimental tests, i.e. orientation and mechanical state, defined in the simplified case by the mobilized friction angle ϕ_{mob}. An interpolation is thereafter made between the initial isotropic and the localized states:

$$G = \frac{2E}{(1+\nu)}\left[1 - \omega \frac{\sin \phi_{mob}}{\sin \phi}\right] \tag{6.29}$$

Matrix A is therefore modified by taking for term A_{33} the expression in equation (6.29). We can verify that consistency is verified at the isotropic state, which is fundamental for the model's use in numerical calculations, in order to prevent the problems mentioned in section 6.1. Finally, we have introduced in our 2D model a new parameter ω which can be viewed as the one controlling the anisotropy induced by a loading from the initial isotropic state to the actual state. ω can also be viewed as the parameter controlling the appearance of the plastic strain localization.

Generalizing this concept in 3D does not imply a particular problem. In fact, this concept has first been applied to a general 3D model before being applied to the simplified 2D model chosen here as an example. In the 3D model, we must note, however, that there are three shear moduli and that it is necessary to verify the consistency condition more precisely. In addition to the relation at the isotropic state for the three moduli, there are also relations for each of them for axisymmetric states. For more details, see [CHA 94b].

Hypoplasticity thus offers a great flexibility for introducing this induced anisotropy. The effects are different but similar to those obtained in the plasticity framework by using vertex models, providing that they correspond to complete constitutive models, which is rarely the case, or by using non-coaxial models, such as models with kinematic hardening.

6.2.7. *Extension to media with internal length*

Traditional constitutive models, based on the description of the displacement gradient tensor, have no internal length. Geomaterials, however, are clearly materials with internal length: grain sizes for soils or concretes, spatial distribution of pre-existing discontinuities for rocks. If, in numerous cases, the absence of internal length in the models used can be ignored, this is no longer possible in the case of localized failure. It has been proved experimentally that the dimension and the width of localized bands in sands depend on the grain size distribution and mainly on the mean grain size. If the traditional models can predict without difficulty the apparition of a localized zone, it is illusionary to think that they can also correctly predict the post-localized regime, even if this assumption is very often made. Numerically, the results are computer independent, but depend strongly on the size of the spatial discretizing in finite elements. We are not going to present an exhaustive list of possible solutions, but rather concentrate on two specific solutions, without too many details, since it is a field which is constantly evolving [CHA 98a].

An important class of models with internal length concerns the models with microstructure. Their kinematics are no longer only described by the displacement field, which, by spatial derivation, gives the gradient, rotation and the usual deformation, but also by a micro-gradient field, which considers strains and rotations at the grain level and gives by derivation a gradient of the micro-gradient. This enriched kinematic requires taking into account, by duality, additional stress tensors. The energy variables, or the virtual or real works, contain these kinematics and static enrichments. By adding mathematical constraints, we can develop these models into Cosserat's models, second gradient models, etc. We will not develop these theories, which have demonstrated their ability to take into account an internal length within the studied material, especially in post-localization problems.

Another possible way consists of introducing localized zones, whose behavior differs from the rest of the medium. For example, experiments have shown that the significant dilatancy obtained in dense sands leads asymptotically to a limit density called the *critical void ratio*. Well instrumented experiments have shown that this phenomenon was concentrated within shear bands [DES 96]. It is therefore understandable to enter this behavior within a localized band rather than in the whole volume. For this purpose, we can construct a specific model representative of the band's behavior, consistent with the CloE model, from which it is built, and leading to a critical void ratio inside the band. In this kind of model, the width of the model is explicitly introduced and corresponds to an additional parameter to be determined. For more details on this topic, see [CHA 98a].

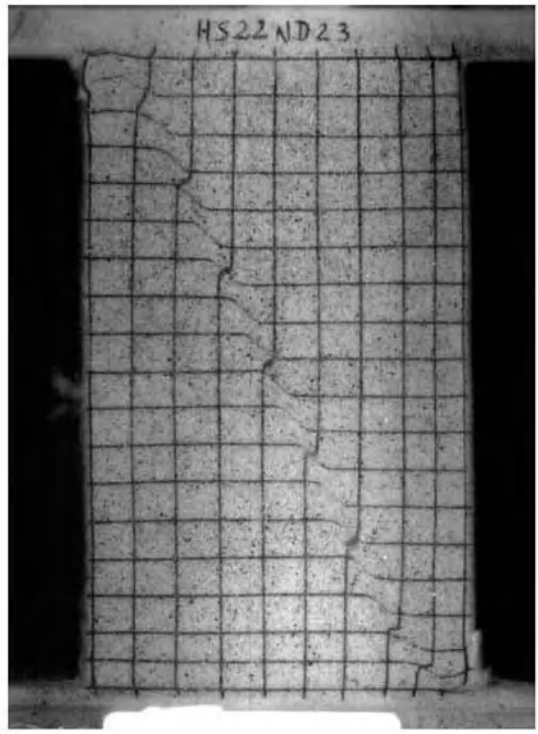

Figure 6.6. *Photo of a biaxial test with localization*

6.2.8. *Examples of application*

We cannot develop too many examples of CloE model applications. We chose to present here some results of integration in a finite elements code by selecting two

different cases: one concerning an homogenous loading, the other a boundary value problem.

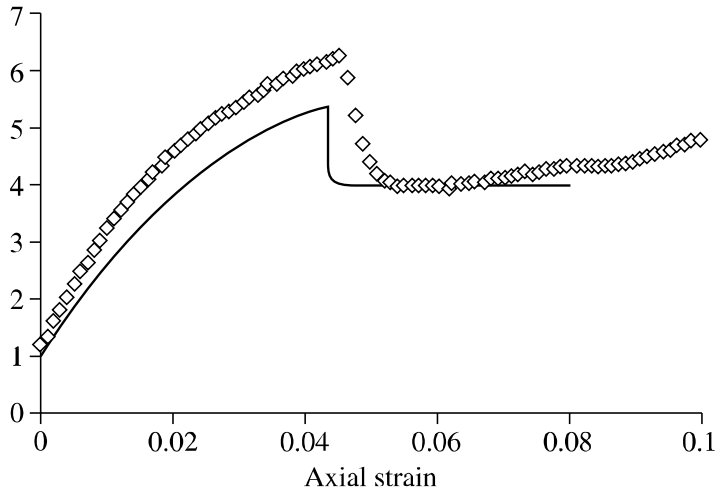

Figure 6.7. *Comparison between experimental results and numerical modeling with Daphnis and CLoE model of a biaxial test*

6.2.8.1. *Modeling of biaxial test*

We first present the modeling by Daphnis-CloE of a biaxial test in plane strain conditions, imposed by a glass wall, which allows us to show the tested specimen. Figure 6.6 shows the specimen after localization. The CloE model used in this study is the one presented in section 6.2.3. The numerical modeling was performed with the following parameters: E = 30,000 kPa, ν = 0.32, ω = 0.6, ϕ = 45°, ψ = 25°. The confining stress was equal to 200 kPa. The specimen's initial dimensions were: 338.5 mm x 102.5 mm. The initial void ratio was 0.66, the critical void ratio within the band was taken equal to 0.8, in agreement with the value of 0.85 given in [DES 96] at a smaller mean stress, and the width of the band was taken as equal to 7 mm.

The modeling was not refined in order to best fit the experimental results. Figure 6.7 presents the relationship between the stress ratio and axial strain. We can see that the model reproduces correctly not only the initial phase of the localization, but also the post-peak plateau. For more details on this calculation, see [CHA 98a].

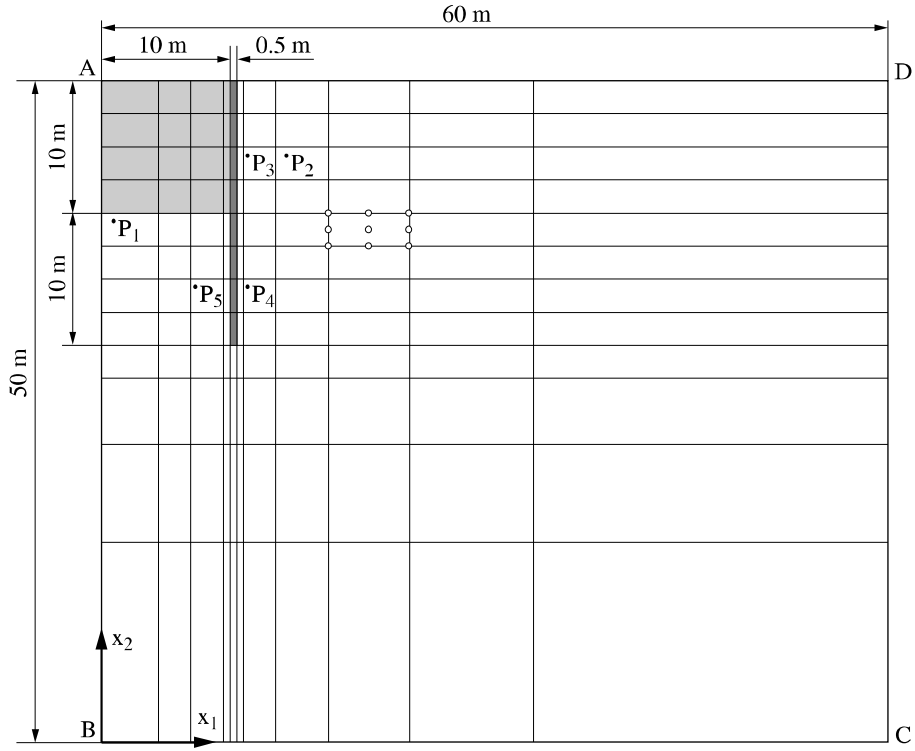

Figure 6.8. *Geometry and discretization of the trench*

6.2.8.2. *Modeling of a trench excavation with a retaining wall*

The modeling of a trench excavation with a retaining wall was performed by using the 3D CloE model presented in [CHA 94a]. The calculation was made assuming plane strain conditions. A comparison was made with the results of the same type of calculation obtained by commercial software. Detailed results can be found in [VIG 99]. Figure 6.8 presents the trench geometry. The grey zone corresponds to the excavated soil.

Figure 6.9 presents a map of the volumetric deformations in the upper part and the deviatoric strains in the lower part, using the CloE model (left part) and the Hard Soil Model (incrementally bilinear consistent model) (right part). Details of the choices made to perform this numerical comparison can be found in [VIG 99]. In the case presented in Figure 6.9, corresponding to a rigid wall, the predictions of the CloE model are more realistic, especially concerning the soil displacements in the vicinity of the retaining wall. This result has significant practical interest.

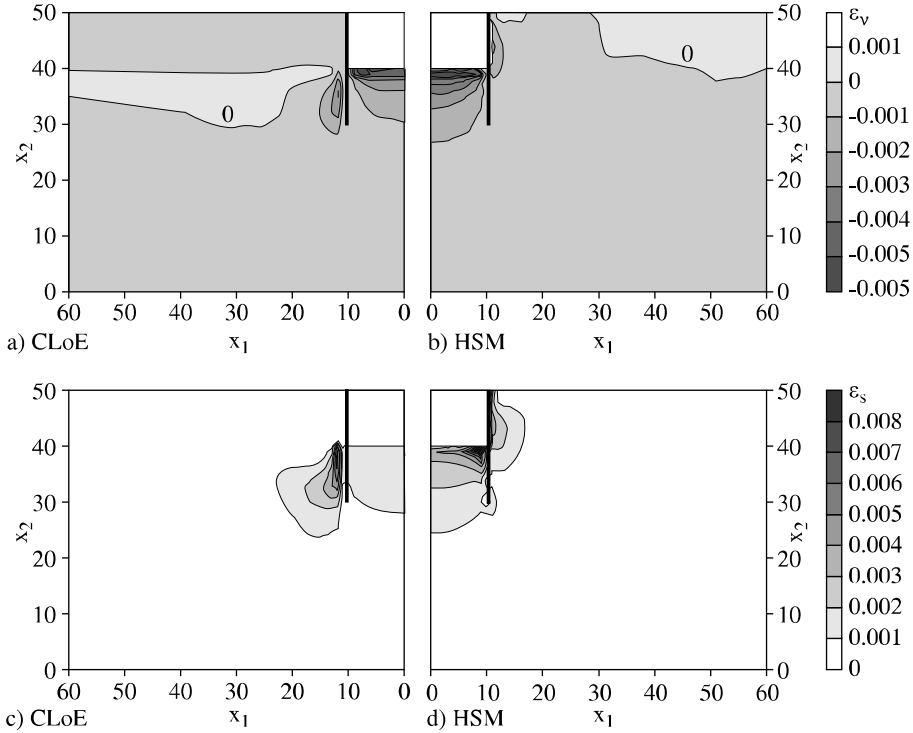

Figure 6.9. *Iso-values of volumetric and deviatoric strains: comparison of numerical simulations obtained with CLoE and HSM*

6.3. Incrementally non-linear constitutive relations

6.3.1. *Formalism*

We have shown in Chapter 1 that the general relations for non-viscous behavior could be written:

$$\mathrm{d}\varepsilon_\alpha = \mathbf{M}_{\alpha\beta}(u_\gamma)\,\mathrm{d}\sigma_\beta, \qquad \alpha,\beta,\gamma \in \{1,2,\cdots,6\}^3 \tag{6.30}$$

or in the dual form:

$$\mathrm{d}\sigma_\alpha = \mathbf{N}_{\alpha\beta}(v_\gamma)\,\mathrm{d}\varepsilon_\beta, \qquad \alpha,\beta,\gamma \in \{1,2,\cdots,6\}^3 \tag{6.31}$$

where u_γ represents the direction of the incremental stress $\mathrm{d}\sigma_\gamma$:

$$u_\gamma = \frac{\mathrm{d}\sigma_\gamma}{\|\mathrm{d}\sigma\|}, \quad \gamma \in \{1,2,\cdots,6\}, \qquad \text{with} \qquad \|\mathrm{d}\sigma\| = \sqrt{\mathrm{d}\sigma \cdot \mathrm{d}\sigma} \tag{6.32}$$

and where v_γ represents the direction of the incremental strain $\mathrm{d}\varepsilon_\gamma$:

$$v_\gamma = \frac{\mathrm{d}\varepsilon_\gamma}{\|\mathrm{d}\varepsilon\|}, \quad \gamma \in \{1,2,\cdots,6\}, \qquad \text{with} \qquad \|\mathrm{d}\varepsilon\| = \sqrt{\mathrm{d}\varepsilon \cdot \mathrm{d}\varepsilon}$$

We will now specify the structure of **M**(u) and **N**(v). For this purpose, we will consider the developments in polynomial series of the elements of these two matrices:

$$\mathrm{M}_{\alpha\beta}(u_\gamma) = \mathrm{M}^1_{\alpha\beta} + \mathrm{M}^2_{\alpha\beta\gamma} u_\gamma + \mathrm{M}^3_{\alpha\beta\gamma\delta} u_\gamma u_\delta + \cdots, \qquad \alpha\beta\gamma\delta \in \{1,\cdots,6\}^4 \tag{6.33}$$

$$\mathrm{N}_{\alpha\beta}(v_\gamma) = \mathrm{N}^1_{\alpha\beta} + \mathrm{N}^2_{\alpha\beta\gamma} v_\gamma + \mathrm{N}^3_{\alpha\beta\gamma\delta} v_\gamma v_\delta + \cdots, \qquad \alpha\beta\gamma\delta \in \{1,\cdots,6\}^4 \tag{6.34}$$

From equations (6.30) and (6.31), it follows that:

$$\mathrm{d}\varepsilon_\alpha = \mathrm{M}^1_{\alpha\beta}\, \mathrm{d}\sigma_\beta + \frac{1}{\|\mathrm{d}\sigma\|} \mathrm{M}^2_{\alpha\beta\gamma}\, \mathrm{d}\sigma_\beta\, \mathrm{d}\sigma_\gamma + \cdots, \qquad \alpha\beta\gamma \in \{1,\cdots,6\}^3 \tag{6.35}$$

$$\mathrm{d}\sigma_\alpha = \mathrm{N}^1_{\alpha\beta}\, \mathrm{d}\varepsilon_\beta + \frac{1}{\|\mathrm{d}\varepsilon\|} \mathrm{N}^2_{\alpha\beta\gamma}\, \mathrm{d}\varepsilon_\beta\, \mathrm{d}\varepsilon_\gamma + \cdots, \qquad \alpha\beta\gamma \in \{1,\cdots,6\}^3 \tag{6.36}$$

The first terms of equations (6.35) and (6.36) describe the incrementally linear elastic behavior. The two first terms give the general representation of incrementally non-linear second order constitutive relations:

$$\mathrm{d}\varepsilon_{ij} = \mathrm{M}^1_{ijkl}\, \mathrm{d}\sigma_{kl} + \frac{1}{\|\mathrm{d}\sigma\|} \mathrm{M}^2_{ijklmn}\, \mathrm{d}\sigma_{kl}\, \mathrm{d}\sigma_{mn}, \qquad ijklmn \in \{1,\cdots,3\}^6 \tag{6.37}$$

$$\mathrm{d}\sigma_{ij} = \mathrm{N}^1_{ijkl}\, \mathrm{d}\varepsilon_{kl} + \frac{1}{\|\mathrm{d}\varepsilon\|} \mathrm{N}^2_{ijklmn}\, \mathrm{d}\varepsilon_{kl}\, \mathrm{d}\varepsilon_{mn}, \qquad ijklmn \in \{1,\cdots,3\}^6 \tag{6.38}$$

We can verify that expressions (6.37) and (6.38) are non-linear and homogenous of degree 1 with respect to $\mathrm{d}\sigma$ and $\mathrm{d}\varepsilon$, respectively.

In order to determine more precisely tensors $\mathbf{M}^1$, $\mathbf{M}^2$, $\mathbf{N}^1$, $\mathbf{N}^2$, we have to define their general form. For this purpose, three hypotheses are in order:

– the incremental relation is orthotropic;

– when expressed in the orthotropy axes:
$\forall \alpha, \beta \in \{1,2,3\}$, $\alpha \neq \beta$, $\mathrm{M}^2_{\alpha\beta\gamma} = 0$ and $\mathrm{N}^2_{\alpha\beta\gamma} = 0$;

– the "shear" part of the relation is incrementally linear in the orthotropy axes:
$\forall \beta \in \{4,5,6\}$, or $\gamma \in \{4,5,6\}$, $\mathrm{M}^2_{\alpha\beta\gamma} = 0$ and $\mathrm{N}^2_{\alpha\beta\gamma} = 0$.

In the orthotropy axes, equations (6.37) and (6.38) are then reduced to the following simplified form:

$$\begin{pmatrix} \mathrm{d}\varepsilon_{11} \\ \mathrm{d}\varepsilon_{22} \\ \mathrm{d}\varepsilon_{33} \end{pmatrix} = \mathbf{A} \begin{pmatrix} \mathrm{d}\sigma_{11} \\ \mathrm{d}\sigma_{22} \\ \mathrm{d}\sigma_{33} \end{pmatrix} + \frac{1}{\|\mathrm{d}\sigma\|} \mathbf{B} \begin{pmatrix} (\mathrm{d}\sigma_{11})^2 \\ (\mathrm{d}\sigma_{22})^2 \\ (\mathrm{d}\sigma_{33})^2 \end{pmatrix} \tag{6.39}$$

$$\begin{pmatrix} \mathrm{d}\sigma_{11} \\ \mathrm{d}\sigma_{22} \\ \mathrm{d}\sigma_{33} \end{pmatrix} = \mathbf{C} \begin{pmatrix} \mathrm{d}\varepsilon_{11} \\ \mathrm{d}\varepsilon_{22} \\ \mathrm{d}\varepsilon_{33} \end{pmatrix} + \frac{1}{\|\mathrm{d}\varepsilon\|} \mathbf{D} \begin{pmatrix} (\mathrm{d}\varepsilon_{11})^2 \\ (\mathrm{d}\varepsilon_{22})^2 \\ (\mathrm{d}\varepsilon_{33})^2 \end{pmatrix} \tag{6.40}$$

and:

$$\begin{pmatrix} \mathrm{d}\sigma_{23} \\ \mathrm{d}\sigma_{31} \\ \mathrm{d}\sigma_{12} \end{pmatrix} = 2 \begin{bmatrix} G_1 & & \\ & G_2 & \\ & & G_3 \end{bmatrix} \begin{pmatrix} \mathrm{d}\varepsilon_{23} \\ \mathrm{d}\varepsilon_{31} \\ \mathrm{d}\varepsilon_{12} \end{pmatrix} \tag{6.41}$$

We have therefore to determine matrices of dimension 3x3: **A**, **B** , **C**, **D** and functions G_1, G_2 , G_3. The idea is to identify the constitutive relations in equations (6.39) to (6.41) by specific behaviors which can be experimentally determined. For the model given by equation (6.39), they correspond to "generalized triaxial paths" and for the dual model given by equation (6.40), they correspond to "generalized oedometric paths". Their definitions are, respectively, as follows:

– a path is called a "generalized triaxial path" if the stress and strain principal axes are identical to a constant given direction, and if the two lateral stresses are maintained constant along the stress path;

– a path is called a "generalized oedometric path" if the stress and strain principal axes are identical to a constant given direction, and the two lateral strains are maintained constant along the strain path;

We will call triaxial compression, respectively triaxial extension, a loading path with positive, respectively negative, axial stress rate. In a dual manner, we will call oedometric compression, respectively oedometric extension, a loading path with positive, respectively negative, axial strain rate. The case of softening materials is not considered here.

We thus define:

– the generalized tangent Young's modulus (E_i) : $E_i = \left(\dfrac{\partial \sigma_i}{\partial \varepsilon_i} \right)_{\sigma_j \sigma_k}$

– the generalized tangent Poisson's ratio (ν_i^j) : $\nu_i^j = -\left(\dfrac{\partial \varepsilon_j}{\partial \varepsilon_i} \right)_{\sigma_j \sigma_k}$

– the generalized tangent oedometric modulus (O_i) : $O_i = \left(\dfrac{\partial \sigma_i}{\partial \varepsilon_i} \right)_{\varepsilon_j \varepsilon_k}$

– the generalized tangent stress ratio (K_i^j) : $K_i^j = \left(\dfrac{\partial \sigma_j}{\partial \sigma_i} \right)_{\varepsilon_j \varepsilon_k}$

By denoting "+" for the compression and "-" for the extension, we define:

$$\mathbf{N}^+ = \begin{bmatrix} \dfrac{1}{\mathrm{E}_1^+} & -\dfrac{\nu_2^{1+}}{\mathrm{E}_2^+} & -\dfrac{\nu_3^{1+}}{\mathrm{E}_3^+} \\ -\dfrac{\nu_1^{2+}}{\mathrm{E}_1^+} & \dfrac{1}{\mathrm{E}_2^+} & -\dfrac{\nu_3^{2+}}{\mathrm{E}_3^+} \\ -\dfrac{\nu_1^{3+}}{\mathrm{E}_1^+} & -\dfrac{\nu_2^{3+}}{\mathrm{E}_2^+} & \dfrac{1}{\mathrm{E}_3^+} \end{bmatrix} \text{ and } \mathbf{N}^- = \begin{bmatrix} \dfrac{1}{\mathrm{E}_1^-} & -\dfrac{\nu_2^{1-}}{\mathrm{E}_2^-} & -\dfrac{\nu_3^{1-}}{\mathrm{E}_3^-} \\ -\dfrac{\nu_1^{2-}}{\mathrm{E}_1^-} & \dfrac{1}{\mathrm{E}_2^-} & -\dfrac{\nu_3^{2-}}{\mathrm{E}_3^-} \\ -\dfrac{\nu_1^{3-}}{\mathrm{E}_1^-} & -\dfrac{\nu_2^{3-}}{\mathrm{E}_2^-} & \dfrac{1}{\mathrm{E}_3^-} \end{bmatrix}$$

$$\mathbf{P}^+ = \begin{bmatrix} O_1^+ & K_2^{1+} O_2^+ & K_3^{1+} O_3^+ \\ K_1^{2+} O_1^+ & O_2^+ & K_3^{2+} O_3^+ \\ K_1^{3+} O_1^+ & K_2^{3+} O_2^+ & O_3^+ \end{bmatrix} \text{ and } \mathbf{P}^- = \begin{bmatrix} O_1^- & K_2^{1-} O_2^- & K_3^{1-} O_3^- \\ K_1^{2-} O_1^- & O_2^- & K_3^{2-} O_3^- \\ K_1^{3-} O_1^- & K_2^{3-} O_2^- & O_3^- \end{bmatrix}$$

By identification of the behaviors along generalized triaxial paths and, respectively, oedometric paths, we obtain:

$$\mathbf{A} + \mathbf{B} = \mathbf{N}^{+} \text{ and } \mathbf{A} - \mathbf{B} = \mathbf{N}^{-}$$

$$\mathbf{C} + \mathbf{D} = \mathbf{P}^{+} \text{ and } \mathbf{C} - \mathbf{D} = \mathbf{P}^{-}$$

We thus obtain the expressions of **A**, **B**, **C** and **D**:

$$\begin{cases} \mathbf{A} = \dfrac{\mathbf{N}^{+} + \mathbf{N}^{-}}{2} \\ \mathbf{B} = \dfrac{\mathbf{N}^{+} - \mathbf{N}^{-}}{2} \end{cases} \quad \text{and} \quad \begin{cases} \mathbf{C} = \dfrac{\mathbf{P}^{+} + \mathbf{P}^{-}}{2} \\ \mathbf{D} = \dfrac{\mathbf{P}^{+} - \mathbf{P}^{-}}{2} \end{cases} \tag{6.42}$$

Equations (6.39) to (6.42) can be interpreted as a quadratic non-linear interpolation between material behaviors known along particular loading paths, generalized triaxial and oedometric paths. Other types of interpolation are possible. The simplest one is linear interpolation, which leads to incrementally piecewise linear constitutive relations, consisting of eight tensorial zones where the relation is incrementally linear, called the octo-linear model. The linear interpolation model can be written:

$$\begin{pmatrix} \mathrm{d}\varepsilon_1 \\ \mathrm{d}\varepsilon_2 \\ \mathrm{d}\varepsilon_3 \end{pmatrix} = \frac{1}{2}\left[\mathbf{N}^{+} + \mathbf{N}^{-}\right] \begin{pmatrix} \mathrm{d}\sigma_1 \\ \mathrm{d}\sigma_2 \\ \mathrm{d}\sigma_3 \end{pmatrix} + \frac{1}{2}\left[\mathbf{N}^{+} - \mathbf{N}^{-}\right] \begin{pmatrix} |\mathrm{d}\sigma_1| \\ |\mathrm{d}\sigma_2| \\ |\mathrm{d}\sigma_3| \end{pmatrix} \tag{6.43}$$

and for the dual model:

$$\begin{pmatrix} \mathrm{d}\sigma_1 \\ \mathrm{d}\sigma_2 \\ \mathrm{d}\sigma_3 \end{pmatrix} = \frac{1}{2}\left[\mathbf{P}^{+} + \mathbf{P}^{-}\right] \begin{pmatrix} \mathrm{d}\varepsilon_1 \\ \mathrm{d}\varepsilon_2 \\ \mathrm{d}\varepsilon_3 \end{pmatrix} + \frac{1}{2}\left[\mathbf{P}^{+} - \mathbf{P}^{-}\right] \begin{pmatrix} |\mathrm{d}\varepsilon_1| \\ |\mathrm{d}\varepsilon_2| \\ |\mathrm{d}\varepsilon_3| \end{pmatrix} \tag{6.44}$$

Royis [ROY 98] has given a general expression for these interpolation type models in the following form:

$$\mathrm{d}\varepsilon = \left\|\mathrm{d}\sigma\right\| \left[\mathbf{N}^{+}\phi(u)^{+} + \mathbf{N}^{-}\phi(u)^{-}\right]$$

with ${}^{t}\phi(u)^{+} = \left\{\varphi(u_1)^{+}, \varphi(u_2)^{+}, \varphi(u_3)^{+}\right\}$ and ${}^{t}\phi(u)^{-} = \left\{\varphi(u_1)^{-}, \varphi(u_2)^{-}, \varphi(u_3)^{-}\right\}$ and has proposed the following table:

	$\varphi(u_i)^+$	$\varphi(u_i)^-$
octo-linear model	$\frac{\lvert u_i\rvert + u_i}{2}$	$\frac{\lvert u_i\rvert - u_i}{2}$
second order non-linear model	$\frac{u_i^2 + u_i}{2}$	$\frac{u_i^2 - u_i}{2}$
Chambon's interpolation	$\frac{\lvert u_i\rvert^3 + u_i}{2}$	$\frac{\lvert u_i\rvert^3 - u_i}{2}$
Doanh's model	$u_i(1+u_i)^2/4$	$-u_i(1-u_i)^2/4$

Table 6.1. *Some directional interpolations*

Another interpolation has also been proposed, by Robinet [ROB 82], Di Benedetto [DIB 87] and Royis [ROY 89]. A comparison of these different models and experimental results has been made by Royis and Doanh [ROY 98], by using the construction of the response envelopes as proposed by Gudehus [GUD 79]. Figures 6.10 to 6.12 show the results obtained by the octo-linear and the non-linear second order models. In the following section, we will also present such comparisons for the model proposed by Laouafa [DAR 99], who has combined the two previous models.

6.3.2. *Continuous transition between non-linear and octo-linear interpolations*

The octo-linear and non-linear interpolations proposed by Darve have shown their capabilities in predicting the soil behavior in international benchmarks [GUD 84, SAA 88], as presented in Figures 6.10 to 6.12. They raise, however, the problem of the choice of the nature of the interpolation, for material behavior as well as for the use in boundary problem analysis (for instance, in finite element calculations). These interpolations have been studied from both a mathematical point of view [ROY 89, ROY 98] and a physical point of view [ROY 98]. In the description of the observed mechanisms, no fundamental distinction can be made between the two interpolations. Mathematical study has shown that the non-linear interpolation leads to a loss of biunivocity (existence of bifurcation states) along given loading paths, which is less the case for the octo-linear interpolation. The latter, however, belongs to the class C^0.

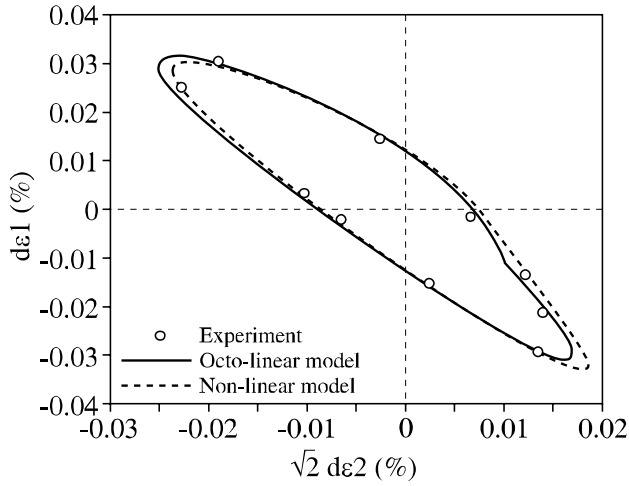

Figure 6.10. *Experimental and numerical response envelopes at a confining stress equal to 100 kPa and an axial stress equal to 100 kPa [ROY 86]*

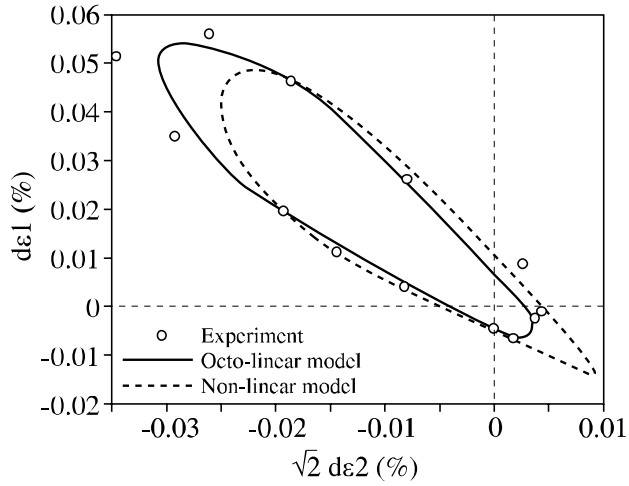

Figure 6.11. *Experimental and numerical response envelopes at a confining stress equal to 100 kPa and an axial stress equal to 200 kPa [ROY 86]*

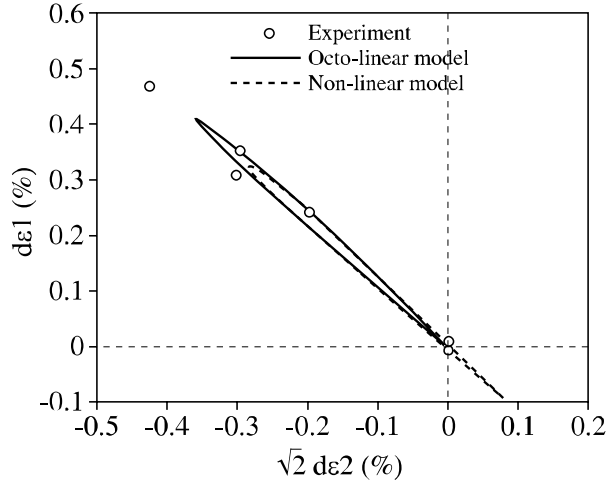

Figure 6.12. *Experimental and numerical response envelopes at a confining stress equal to 100 kPa and an axial stress equal to 400 kPa [ROY 86]*

The interpolation proposed by Laouafa [DAR 99] allows for the two interpolations to be described in a continuous way. The non-linear and the octo-linear interpolation in Darve's models become two particular cases of interpolation used in Laouafa's model, which depends on a real and positive scalar parameter ρ. Its expression in the principal axes is as follows:

$$\begin{pmatrix} d\varepsilon_1 \\ d\varepsilon_2 \\ d\varepsilon_3 \end{pmatrix} = \frac{1}{2}\left[\mathbf{N}^+ + \mathbf{N}^-\right]\begin{pmatrix} d\sigma_1 \\ d\sigma_2 \\ d\sigma_3 \end{pmatrix} + \frac{1}{2}\left[\mathbf{N}^+ - \mathbf{N}^-\right]\left(\sqrt{1+\rho}\right)\begin{pmatrix} \dfrac{d\sigma_1^2}{\sqrt{d\sigma_1^2 + \rho\|d\sigma\|^2}} \\ \dfrac{d\sigma_2^2}{\sqrt{d\sigma_2^2 + \rho\|d\sigma\|^2}} \\ \dfrac{d\sigma_3^2}{\sqrt{d\sigma_3^2 + \rho\|d\sigma\|^2}} \end{pmatrix}$$

When $\rho \to 0$, the above expression converges toward the octo-linear formulation, and when $\rho \to \infty$, this same expression converges toward the non-linear formulation. Figures 6.13 to 6.15 show the response envelopes for different values of ρ (ρ = 0.005, 0.05, 1, 100).

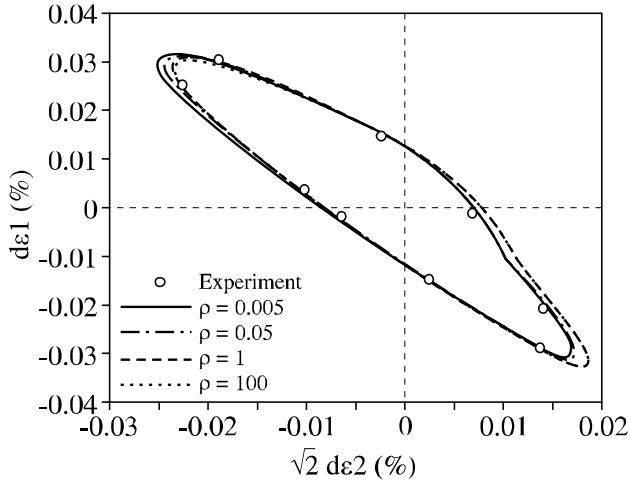

Figure 6.13. *Experimental and numerical response envelopes at a confining stress equal to 100 kPa and an axial stress equal to 100 kPa for different values of* $\rho = 0.005, 0.05, 1.1$

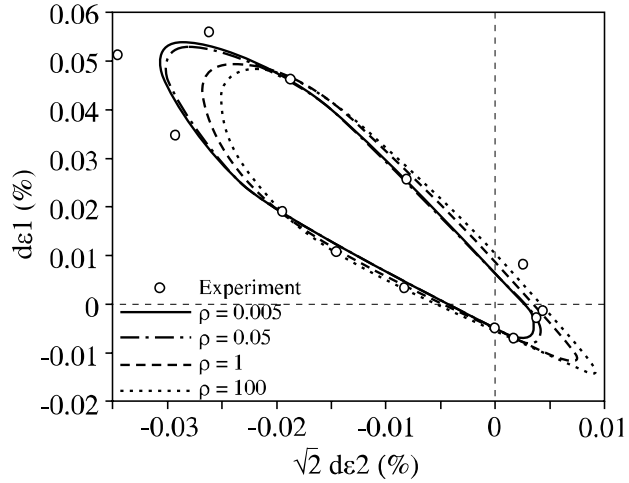

Figure 6.14. *Experimental and numerical response envelopes at a confining stress equal to 100 kPa and an axial stress equal to 200 kPa for different values of* $\rho = 0.005, 0.05, 1.1$

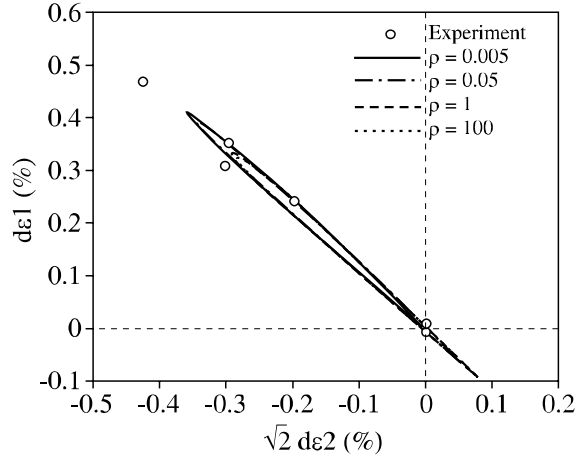

Figure 6.15. *Experimental and numerical response envelopes at a confining stress equal to 100 kPa and an axial stress equal to 400 kPa for different values of ρ = 0.005, 0.05, 1.1*

The value of parameter ρ is arbitrarily defined as a continuous function of some given memory parameters, excluding any variable dependent on stress and strain increments.

6.3.3. *Significant degenerations*

In order to understand better the possibilities and limits of these models, it is interesting to consider several significant cases of degeneration: the one-dimensional, the elastic and the perfectly plastic cases. These will be analyzed successively.

One-dimensional degeneration

The octo-linear and non-linear models degenerate into the same expression in the case of a one-dimensional material, for which the incremental stress and strain are two scalars:

$$\mathrm{d}\varepsilon = \frac{1}{2}\left(\frac{1}{E^+} + \frac{1}{E^-}\right)\mathrm{d}\sigma + \frac{1}{2}\left(\frac{1}{E^+} - \frac{1}{E^-}\right)\left|\mathrm{d}\sigma\right| \tag{6.45}$$

$$\mathrm{d}\sigma = \frac{1}{2}\left(E^+ + E^-\right)\mathrm{d}\varepsilon + \frac{1}{2}\left(E^+ - E^-\right)\left|\mathrm{d}\varepsilon\right| \tag{6.46}$$

E^+ represents the tangent modulus during loading and E^- the tangent modulus during unloading. E^+ and E^- depend, through scalar variables, on the loading history. Any one-dimensional elastoplastic behavior can be reproduced by equations (6.45) and (6.46).

It is interesting to note on this very simple example that a single non-linear incremental relation is strictly equivalent to a double elastoplastic relation with a loading-unloading criterion:

$$\begin{cases} \mathrm{d}\varepsilon = \dfrac{1}{E^+}\mathrm{d}\sigma, & \text{if } \mathrm{d}\sigma \geq 0 \text{ (loading)} \\ \mathrm{d}\varepsilon = \dfrac{1}{E^-}\mathrm{d}\sigma, & \text{if } \mathrm{d}\sigma \leq 0 \text{ (unloading)} \end{cases}$$

We can also note that the octo-linear model can be seen as a direct tridimensional generalization of equations (6.45) and (6.46).

Elastic degeneration

If the mechanical behavior is elastic, the responses on basic paths (generalized triaxial and oedometric paths) are identical in loading and unloading. We thus obtain the following relations:

$$\begin{cases} \mathbf{N}^- \equiv \mathbf{N}^+ \text{ (called } \mathbf{N}\text{)} \\ \mathbf{P}^- \equiv \mathbf{P}^+ \text{ (called } \mathbf{P} = \mathbf{N}^{-1}\text{)} \end{cases}$$

The two models, octo-linear and non-linear, subsequently degenerate into an identical relation:

$$\begin{pmatrix} \mathrm{d}\varepsilon_1 \\ \mathrm{d}\varepsilon_2 \\ \mathrm{d}\varepsilon_3 \end{pmatrix} = \mathbf{N} \begin{pmatrix} \mathrm{d}\sigma_1 \\ \mathrm{d}\sigma_2 \\ \mathrm{d}\sigma_3 \end{pmatrix}$$

where **N** corresponds to the general non-linear orthotropic elastic tensor. If no other symmetry hypothesis is made on **N**, it will correspond to a hypo-elastic model. If the existence of an elastic potential is assumed, this hypothesis will impose the symmetry of **N** and the model will become hyperelastic.

Perfectly plastic degeneration

This type of degeneration can be conveniently studied by considering the constitutive relation in the following form:

$$\mathrm{d}\sigma = \mathbf{M}^{-1}(u)\,\mathrm{d}\varepsilon \tag{6.47}$$

A perfectly plastic behavior – if it exists – can be obtained by looking for solutions corresponding to an indefinite strain under a state of constant stress:

$$\left\| \mathrm{d}\varepsilon \right\| \neq 0 \text{ with } \left\| \mathrm{d}\sigma \right\| = 0 \text{ (in the case of small strains)}$$

A necessary and sufficient condition for the existence of such solutions in the case of incrementally piecewise linear relations is given by:

$$\det \mathbf{M}^{-1}(u) = 0$$

which corresponds to the plastic criterion. For the octo-linear model, this condition can be obtained by the nullity of one of the six tangent moduli:

$$E_1^+ E_2^+ E_3^+ E_1^- E_2^- E_3^- = 0$$

The solutions for the strains are given by the relation:

$$\mathbf{M}^{-1}(u)\,\mathrm{d}\varepsilon = 0 \tag{6.48}$$

An infinite number of solutions can be obtained. They differ by their norm, the direction of $\mathrm{d}\varepsilon$ (being in general imposed by equation (6.48)). Equation (6.48) can then be seen as a plastic flow rule. We can note that it is a singular flow rule as the directions of $\mathrm{d}\varepsilon$, solutions of equation (6.48), generally depend on the direction of $\mathrm{d}\sigma$ (existence of a vertex). In the case of the octo-linear model, this local singularity of the flow rule is of pyramidal type [DAR 05a].

6.3.4. *Applications*

In order to study the predictive capabilities of a given constitutive model, we can examine its responses on various classes of loading paths. The following section is devoted to this purpose.

Non-proportional loading paths

Two examples will be considered. The first concerns the modeling of a circular stress path in the deviatoric plane. This type of loading can be found in practice (for example, in the case of vehicles passing on a road) when repeated loads induce within the soil almost closed stress paths. In addition, a circular stress path loading was chosen as one of the tests to be modeled during the International Workshop in Cleveland [SAA 87]. Figure 6.16 presents the results in the deviatoric strain plane and Figure 6.17 shows the evolutions of the three principal strains and the volume change. Due to successive increases and decreases of the principal stresses, these evolutions present complex oscillations for the experimental results as well as for the numerical simulations.

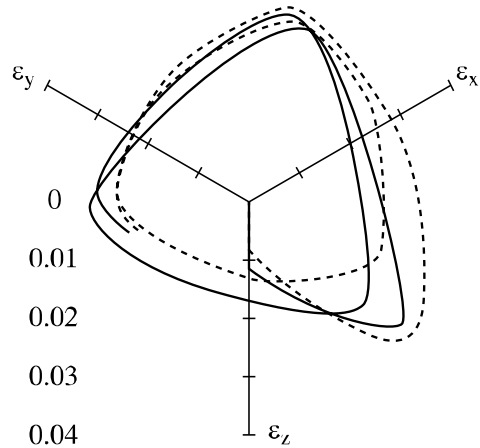

Figure 6.16. *Prediction of the incrementally non-linear model of second order for a circular strain path in the deviatoric plane [SAA 87]. Continuous lines: experimental results, dashed lines: numerical results*

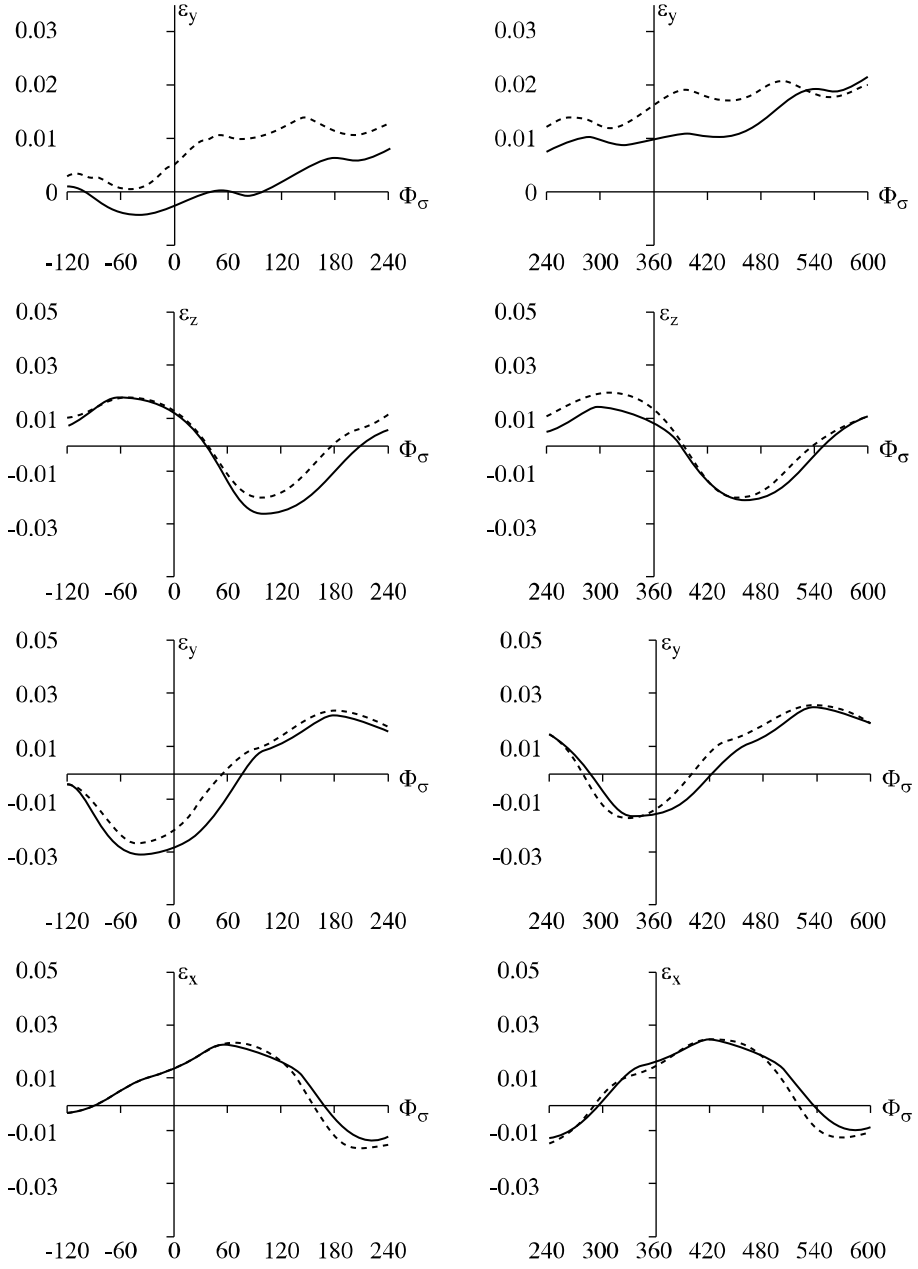

Figure 6.17. *Evolution of the principal strains and the volumetric strain. Continuous lines: experimental results, dashed lines: numerical results*

A second example concerns step-wise loading paths. A given proportional loading path is approached by means of a small increment sequence. Experimentally, it is known that servo-controlled machines are not able to follow the required loading path exactly but must approach it by successive approximations. The experimental responses are considered to be satisfactory as soon as the difference between the desired and the real loading paths is "small enough". This experimental procedure introduces a systematic error which has to be quantified. In addition, the superposition principle for incremental loading is valid only in the case of incrementally linear relations. The condition:

$$\forall\ \mathrm{d}\sigma^{(1)}, \mathrm{d}\sigma^{(2)} : \mathbf{G}(\mathrm{d}\sigma^{(1)}) + \mathbf{G}(\mathrm{d}\sigma^{(2)}) = \mathbf{G}(\mathrm{d}\sigma^{(1)} + \mathrm{d}\sigma^{(2)})$$

is valid only if **G** is linear.

Here we should ask: what happens in the case of incrementally non-linear relations for which the principle does not apply at all as **G** is non-linear?

Figure 6.18 presents one of these examples. A drained triaxial stress path is approached by successive loading steps decomposed into two parts: an isotropic incremental loading ($\Delta\sigma_1 = \Delta\sigma_2 = \Delta\sigma_3$) followed by a constant mean stress loading ($\Delta\sigma_1 + 2\Delta\sigma_3 = 0$).

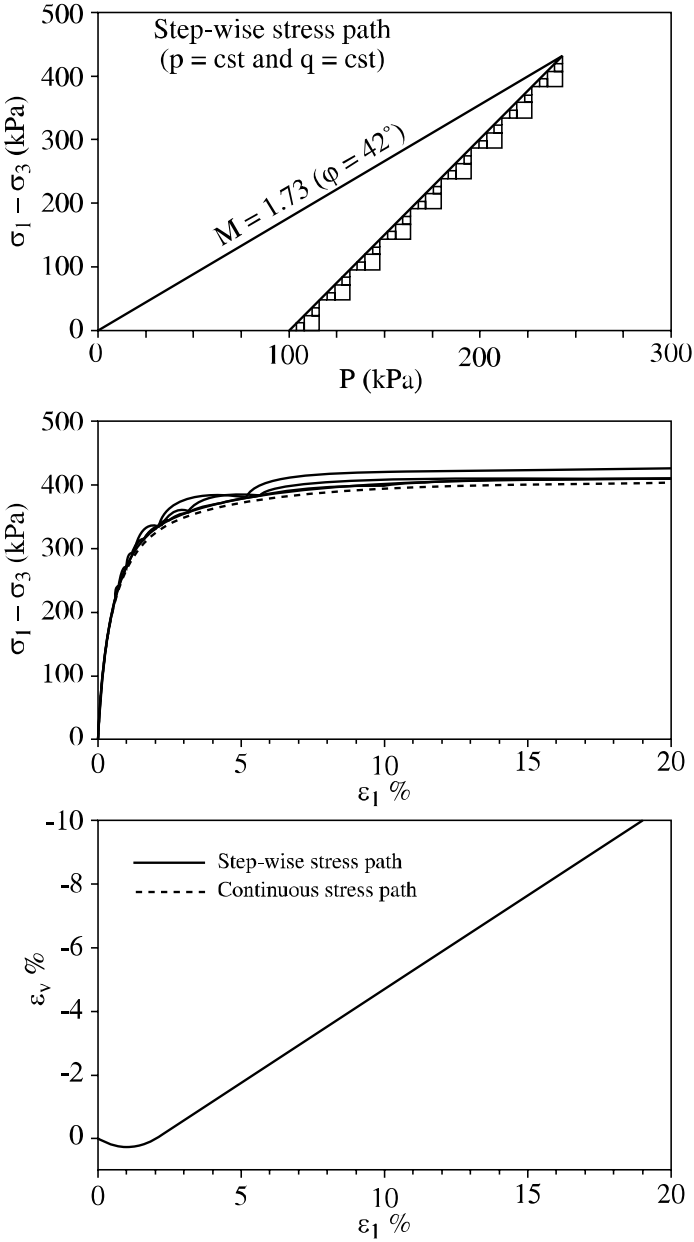

Figure 6.18. *Comparison of numerical simulations obtained by the incrementally non-linear model for a drained triaxial test (dashed line) and a step-wise loading path with various step amplitudes (continuous lines) [DAR 95]*

Figures 6.19 to 6.21 present another example in the case of an undrained triaxial test approached by successive steps of effective stresses:

$$\begin{cases} \Delta\sigma_1 / \Delta\sigma_3 = cons\,tan\,t \\ \Delta\sigma_1 + 2\Delta\sigma_3 = 0 \\ \Delta\varepsilon_1 < 0 \end{cases} \quad \text{and} \quad \begin{cases} \Delta\sigma_1 / \Delta\sigma_3 = cons\,tan\,t \\ \Delta\sigma_3 = 0 \\ \Delta\varepsilon_1 < 0 \end{cases}$$

applied in such a way that the negative volume variation induced by the first loading condition is compensated for by an opposite volume change during the following loading step.

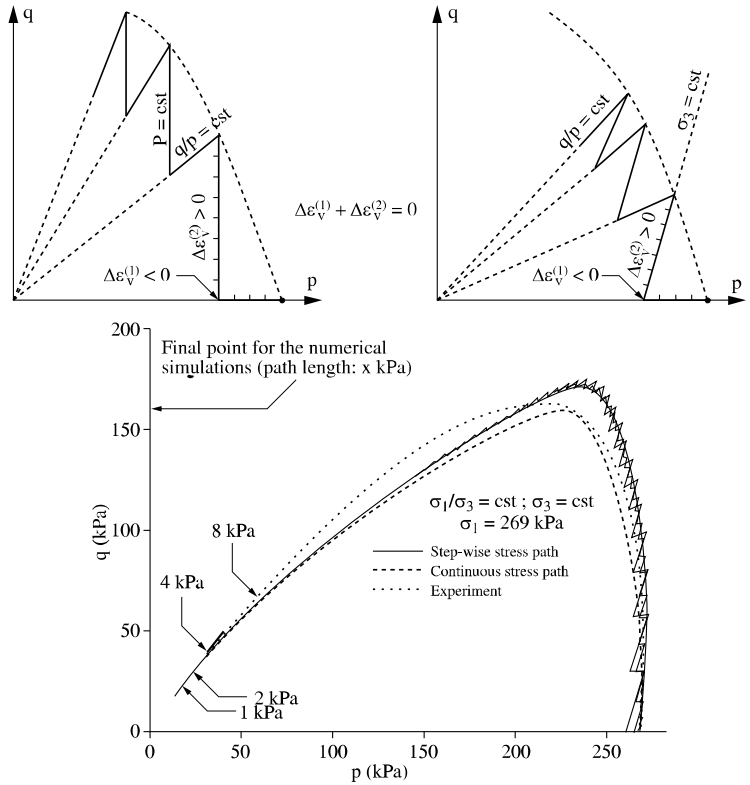

Figure 6.19. *Undrained triaxial test. Upper figure: modeling of the isochoric condition by means of two different paths: constant q/p and constant mean stress or constant q/p and constant lateral stress [DAR 95]. Lower figure: influence of the step amplitudes: four different amplitudes are considered. The numerical simulations (continuous lines) converge when the amplitude decreases toward a single asymptote, different from the response obtained for the undrained triaxial test (dashed line)*

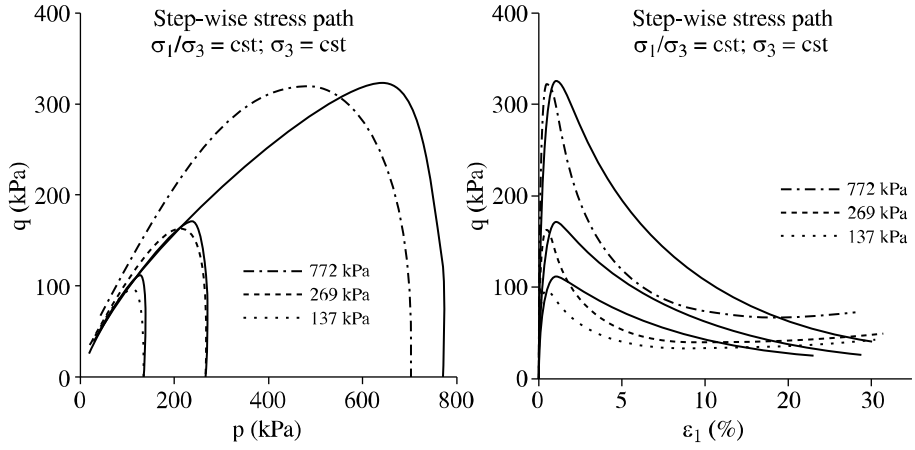

Figure 6.20. *Numerical simulation of an undrained triaxial test on loose Hostun Sand along a stress path decomposed in steps at σ'_1/σ'_3 constant and σ'_3 constant [DAR 95]*

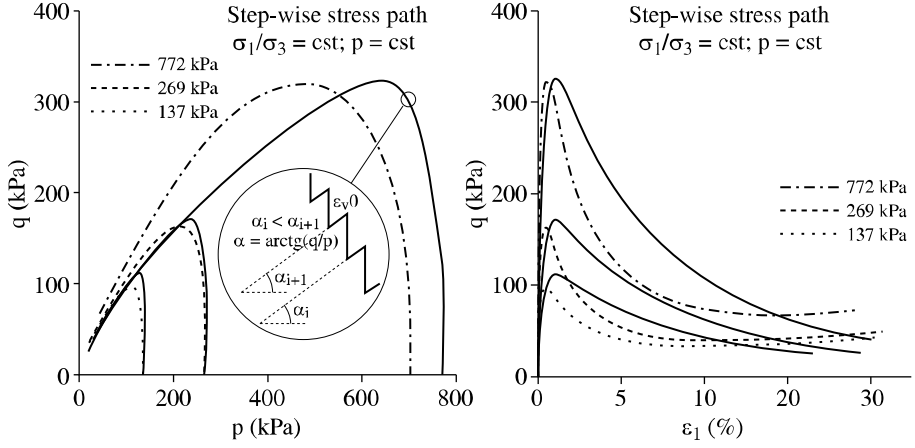

Figure 6.21. *Numerical simulation of an undrained triaxial test on loose Hostun Sand along a stress path decomposed in steps at σ'_1/σ'_3 constant and p' constant [DAR 95]*

The results show that, when the length of the steps decreases, the numerical responses converge toward a given asymptotic behavior. The asymptotic responses are not identical to the responses along the proportional loading path but remain close enough to justify the use of servo-controlled machines.

Simulations of elastic limit surfaces

The elastic limit surfaces have been studied experimentally for a long time, especially in metals. The usual experimental procedure consists of applying a given loading condition and then unloading to a given load value in the same direction. All the stress directions are tested in the same way from this last stress-strain state and the intensity of the strain responses is controlled by a given strain amplitude. The elastic limit surface is then defined by the locus of all the corresponding stress points. In the incrementally non-linear model, the notion of elastic limit does not exist: any loading creates plastic deformation, which can eventually become negligible. It is therefore interesting to follow numerically the same procedure in order to analyze the possibility of defining the elastic limit concept from a model which does not include it. Figures 6.22 and 6.23 show such simulations in the cases of a loose, respectively dense, sand in the bisector plane of the stress space (the so-called Rendulic plane). Figure 6.24 presents the simulation results in the deviatoric stress plane. From these figures, the following conclusions can be drawn: the main mechanism which influences the evolution of the elastic limit is a kinematic hardening, the isotropic hardening remains small. Even if this analysis of the numerical results is made in the framework of elastoplasticity theory, we must recall that the model does not include either hardening variables or yield surfaces. Even if the isotropic hardening remains small, the shape of the elastic limit evolves during loading to approach the shape of the plastic limit at elevated stress levels.

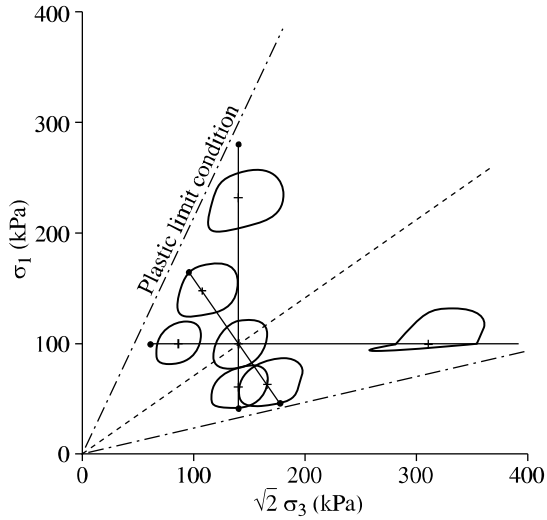

Figure 6.22. *Numerical simulations of elastic limit surfaces in the Rendulic stress plane for loose Hostun Sand. The sand is loaded up to stress states defined by a black dot, then unloaded to the states defined by a cross, before the determination of the elastic limit [DAR 95]*

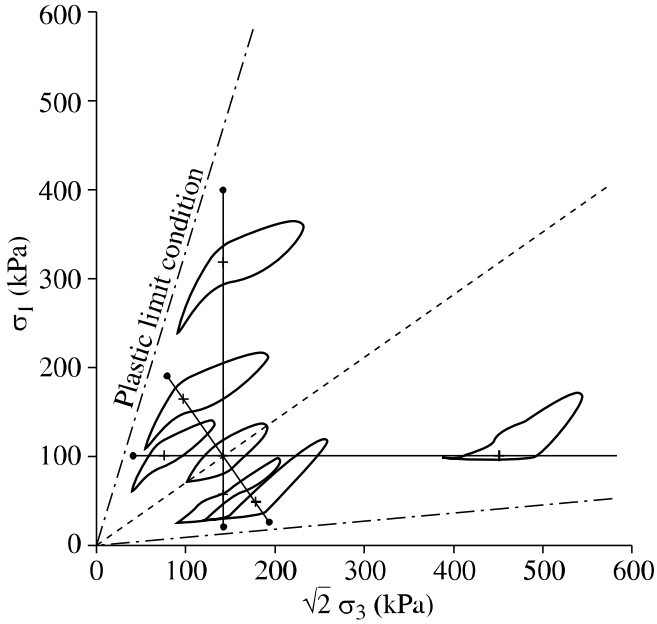

Figure 6.23. *Numerical simulations of elastic limit surfaces in the Rendulic stress plane for dense Hostun Sand. The sand is loaded up to stress states defined by a black dot, then unloaded to the states defined by a cross, before the determination of the elastic limit [DAR 95]*

Liquefaction

Liquefaction of saturated loose sands for a long time remained a little understood phenomenon, mainly because it was analyzed as intrinsically linked to the undrained condition and to the small density of the liquefiable sands. Experimental results [LAN 89] have shown that it is possible to liquefy dry sands if, by using servo-controlled machines, we can apply isochoric loading paths. In addition, even this condition is not necessary since it appears possible to liquefy dense sands by applying a sufficiently dilatant proportional strain path. Figure 6.25 presents numerical simulations on loose Hostun sand using the incrementally non-linear model; they show that liquefaction is a very common phenomenon in granular materials: even a contractant strain path can lead to the liquefaction of a loose sand (results corresponding to R = 0.45 and R = 0.425). In fact, we have presented [DAR 96] a general static liquefaction criterion by comparing the volume change rate induced by the flow rule corresponding to the tested material with the volume change rate imposed by the strain controlled loading path. If these two rates are equal, the sand will undergo a perfectly plastic flow. If the first is higher than the

second (with the sign convention: dilatancy is positive, contractancy is negative) the stresses will decrease and eventually reach a zero value for the liquefied state.

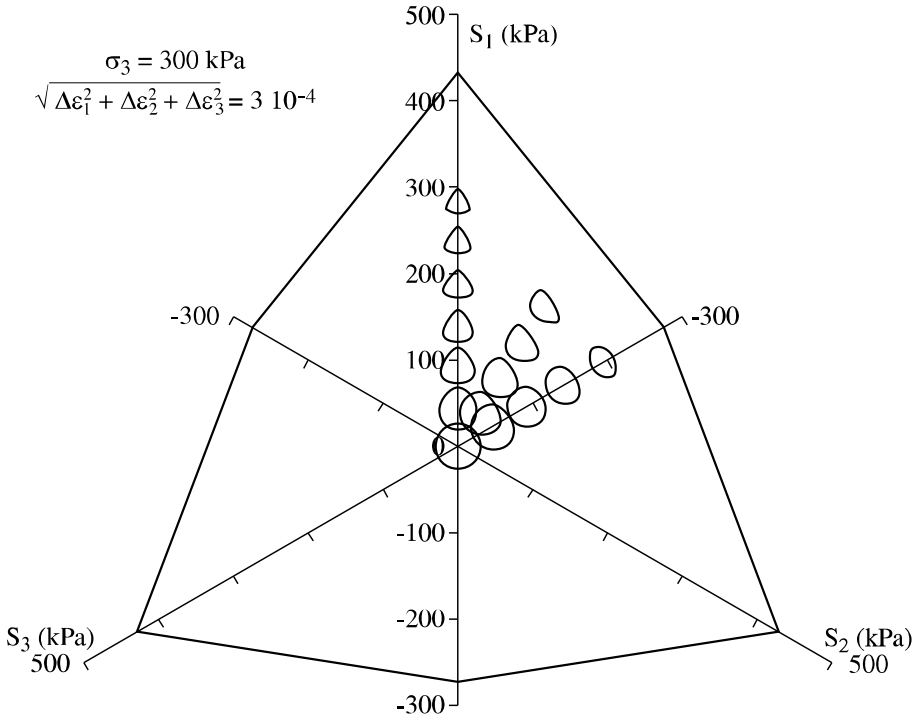

Figure 6.24. *Numerical simulations of elastic limit surfaces in the deviatoric stress plane for loose Hostun Sand. The sand is loaded up to stress states defined by a black dot, then unloaded to the states defined by a cross, before the determination of the elastic limit [DAR 95]*

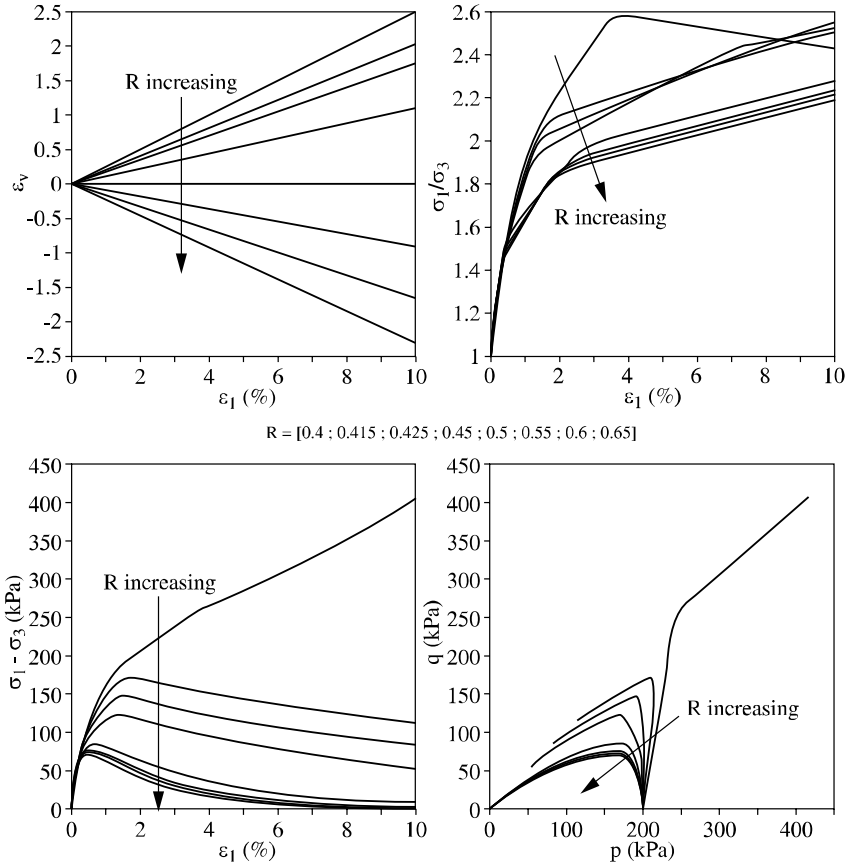

Figure 6.25. *Modeling of proportional axisymmetric strain paths defined by:* $d\varepsilon_2 = d\varepsilon_3 = -Rd\varepsilon_1$ *on loose Hostun Sand*

This general criterion is illustrated, for example, by Figure 6.26 where we can see that, by decreasing the initial void ratio, the sand behavior changes from contractant to dilatant, which induces a change from a liquefying behavior to a behavior corresponding to an effective stress increase in the undrained condition. For an intermediate void ratio, the critical state is obtained (the volume change rate imposed by the flow rule is equal to zero in this case) and a perfectly plastic behavior will develop.

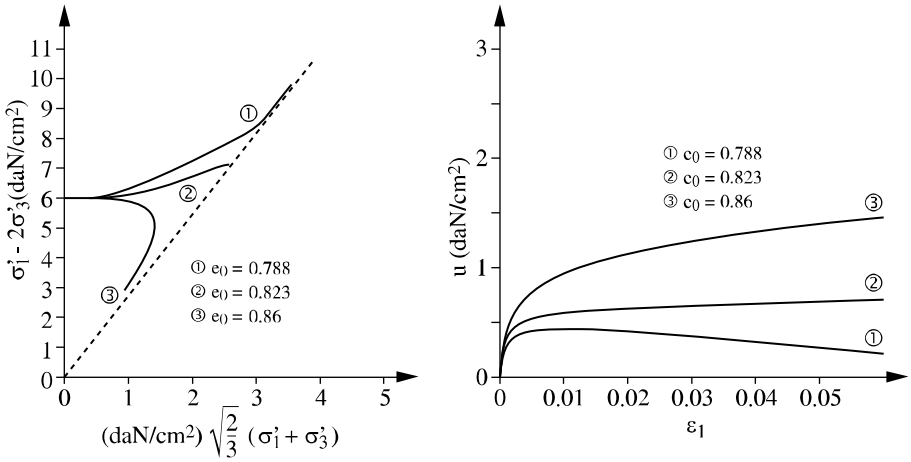

Figure 6.26. *Modeling of the liquefaction of loose Monterey Sand. Three different void ratios are considered; only the highest one, corresponding to a drained contractant behavior, leads to liquefaction*

Instability in granular materials

The experimental evidence of the existence of instability in granular materials is not recent, even if all the consequences have not yet been drawn. In fact, if we consider liquefiable loose sand, the deviatoric stress $q = \sigma_1 - \sigma_3$ presents necessarily an extremum (a maximum in compression). If, from this state during an undrained triaxial compression, we increase by a very small value the applied axial force, a brutal collapse of the specimen occurs while the plastic failure criterion has not been reached. Considering the notion of stability as defined by Lyapunov [LYA 07], this material behavior corresponds to the existence of an unstable state strictly inside the plasticity criterion.

Furthermore, the existence of instability and bifurcation before the plastic failure are predicted by elastoplasticity theory for unassociated materials, which is precisely the case for geomaterials. The reasoning is based on the fact that plastic failure is linked to the nullity of the determinant of the constitutive matrix, whereas instability is linked to the nullity of the determinant of the symmetric part of this matrix. In the case of unassociated flow rule, the constitutive matrix is not symmetric and it is known (from linear algebra) that, along a given loading path, the determinant of the symmetric part becomes equal to zero before the determinant of the whole matrix.

We have systematically studied the condition of stability in granular materials with the octo-linear and the non-linear models, by considering the sufficient condition of stability proposed by Hill [HIL 58]. For a given material, a state of

stress and strain, produced by a given loading history, is considered stable if, for any stress and strain increments linked by the constitutive relation, the second order work is strictly positive:

$$\forall \mathrm{d}\sigma : \mathrm{d}^2 W = \mathrm{d}\sigma : \mathrm{d}\varepsilon > 0 \tag{6.49}$$

The sign of the normalized second order work $\mathrm{t} = \mathrm{d}^2 W / \|\mathrm{d}\sigma\| / \|\mathrm{d}\varepsilon\|$ has therefore been studied in a systematic manner for loose and dense sand in axisymmetric and plane strain conditions, by using a polar diagram [DAR 99]. Figure 6.27 presents the most significant results in the axisymmetric condition and Figure 6.28 in the plane strain condition. For the non-linear model, the first stress level at which a potential instability is detected in a given stress direction corresponds to $q/p = 0.45$ for loose sand and to 0.83 for dense sand in the axisymmetric condition (Figure 6.27) [DAR 04b]. In the plane strain condition (Figure 6.28), the minimum mobilized friction angle corresponding to the first appearance of instability was found to be equal to 13° [KHO 06]. All the results demonstrate the existence of a large domain of potential instability in the stress space ("potential", since the boundary conditions must allow – or not – the instability to develop toward a kinematically admissible failure mode).

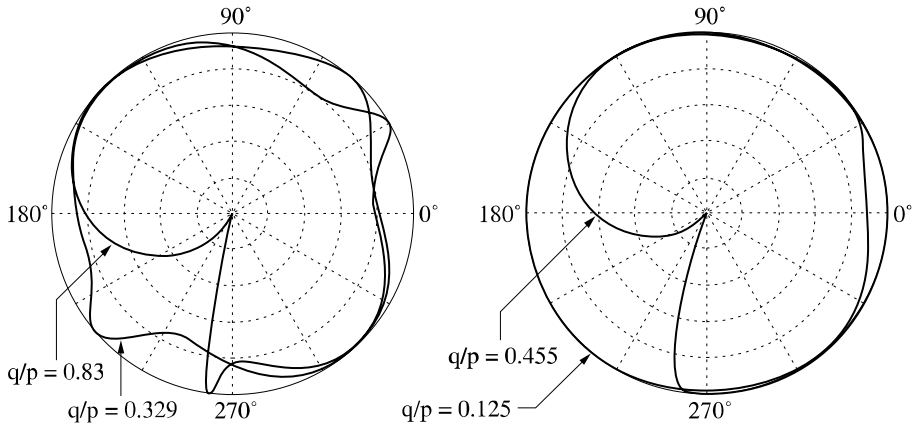

Figure 6.27. *Polar representation of the normalized second order work for different stress ratios q/p. Dense Hostun Sand on the left side, loose Hostun Sand on the right side. The first instabilities are detected where the curve reaches the axis origin*

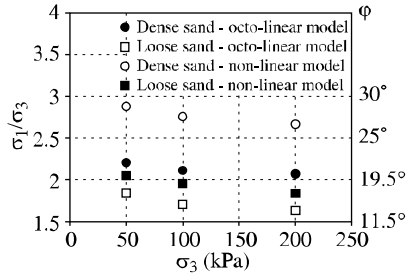

Figure 6.28. *Stress states corresponding to the first detected instabilities in plane strain conditions for dense and loose Hostun Sand*

The existence of such an instability domain, probably has various applications in geotechnics. One of these could be the analysis of slope failure mechanisms. Some failures taking place for small (smaller than 14°) to very small (smaller than 8°) slope angles cannot be explained by traditional plasticity theory, but by instability analysis [DAR 99].

Inverse analysis in geomechanics

Determining mechanical parameters from laboratory testing is a long, costly and imprecise procedure due to the remolding of the samples. In the future, *in situ* testing will probably become more developed and more widely used to calibrate constitutive models. They will require specific rigorous methods for this purpose, based on inverse analysis. However, due to rheological non-linearity, the uniqueness of the solution is not guaranteed, and it is therefore necessary to develop specific constitutive models, which have a limited number of independent parameters.

In this way, two dual constitutive models have been developed, each of them having five parameters. The constitutive relations are incrementally second order non-linear and the two models correspond to equations (6.39) to (6.41). The methodology adopted to construct the models comprises two independent phases: at first, the selection of the basic loading path: triaxial or oedometric; secondly, the choice of the interpolation, linear or non-linear, between the responses along the basic paths. Here, in the framework of inverse analysis, the same interpolations as previously are kept, but the choice is made of modeling the basic loading paths in the simplest manner by means of only five model parameters: for the "direct" model $E,\upsilon,C,\varphi,\psi$ and for the dual model $E_{oedom},K_o,C,\varphi,\alpha$ [DAR 98b]. All these parameters are ordinary soil parameters, except for α, which is used to indirectly control the contractancy or the dilatancy during drained deviatoric loading. Figures 6.29 and 6.30 present the predictions of the dual model, calibrated on oedometric paths, for drained and undrained triaxial paths in compression and extension, for loose and dense sand.

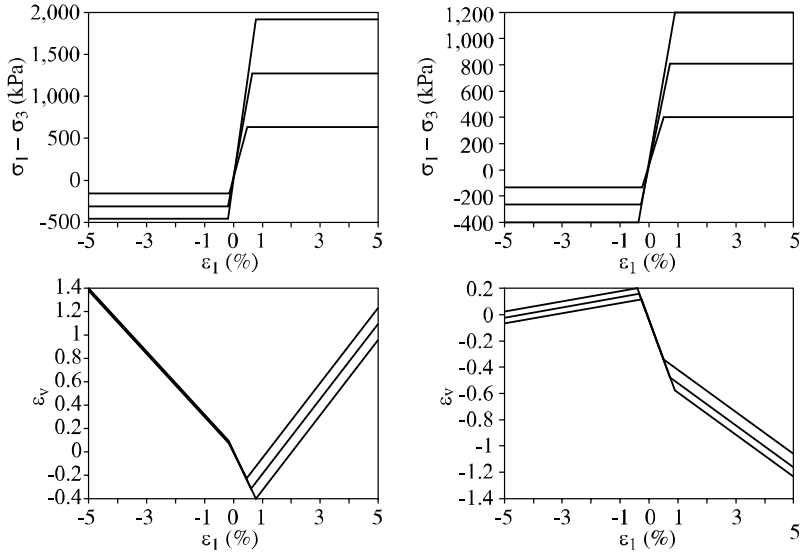

Figure 6.29. *Modeling of drained triaxial tests with the incrementally non-linear model with five parameters calibrated along an oedometer path on dense sand (left side) and loose sand (right side)*

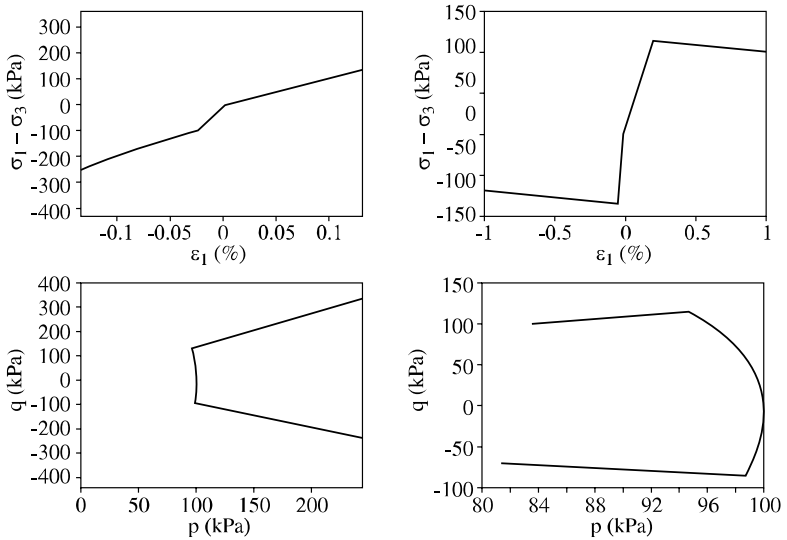

Figure 6.30. *Modeling of undrained triaxial tests with the incrementally non-linear model with five parameters calibrated along an oedometer path on dense sand (left side) and loose sand (right side)*

6.3.5. *Conclusions*

In comparison with the elastoplastic models, the incrementally non-linear models present the advantage of having to introduce neither an elastic limit nor a flow rule, whose experimental determination is difficult in the case of geomaterials. They are based on the explicit choice of a non-linear relation between incremental stresses and strains [DAR 05b].

In order to construct this relation, we proposed the following procedure, composed of two independent steps: at first, the choice of the basic loading paths (triaxial or oedometric) and the description of the material responses along these paths; secondly, the choice of the interpolations – linear or non-linear – between these responses. Based on this method, it is possible to construct in a flexible way a robust model which, due to the interpolation procedure, provides realistic responses for various loading paths.

Then, we illustrated the predictive capabilities of these models for different classes of problems: non-proportional loading paths, elastic limit locus, liquefaction, material instability in granular media and inverse analysis. Others problems have not been addressed here, such as the modeling of plastic strain localization in shear bands in granular materials [DAR 80a] and structured clays [DAR 98, DAR 04], a failure mode which corresponds to a non-homogenous bifurcation of the strain field (so-called "localized failure" [KHO 06]). Homogenous bifurcation modes can also develop due to a loss of uniqueness of the constitutive response [DAR 98] (so-called "diffuse failure"). All these different cases show that our models allow us to analyze, in a coherent manner, various complex aspects of the geomaterial's behavior.

6.4. General conclusion

The first conclusive note is that, nowadays, almost all the constitutive models implemented in finite elements codes are written in an incremental form, whatever the formalism used to construct the model. This "incremental" denomination was originally given to this family of models in order to distinguish their incremental formulation, as presented in Chapter 1, from the expression of constitutive relations by means of rheological fonctionals.

The second point concerns the following question: can experimental results provide the means to make a distinction between incrementally non-linear and incrementally piecewise linear constitutive models, such as elastoplastic models? The response envelopes as defined by Gudehus [GUD 79] are good indicators for answering this question. However, the discussion opened hereby remains

controversial [ROY 98]. If we consider any phenomenological characteristics of the geomaterial's behavior, it always seems possible to find an elastoplastic formulation suitable to describe it. We can also refer to the initial demonstration made by Hill [HIL 67], who linked the incrementally piecewise linear formulations to microstructural considerations, associated with the existence of a finite number of particular micro-sliding planes in the case of metallic monocrystals. It is obvious that, for granular materials, these particular sliding directions are *a priori* not determined, thus leading to an incrementally non-linear structure for constitutive relations. [DAR 80b, DAR 05b]

Benchmarking is another way of comparing the validity domains of different constitutive models. The two benchmarks in Genoble in 1982 [GUD 84] and in Cleveland in 1987 [SAA 88] have shown that the different models gave reasonably close results along proportional loading paths (linear paths in the stress or strain space), whereas the results could be very different for non-proportional loading paths, some incrementally non-linear models giving good predictions. It is, in fact, quite clear that a constitutive matrix with a continuous dependency on the direction of the incremental loading is more likely to give a better response along a non-proportional loading path than a constitutive matrix which can have only two expressions: elastic or plastic. The influence of the structure of the constitutive model can also be seen in the analysis of the bifurcation and instability conditions. It is well know that associated plasticity can describe bifurcation or instability only when the plastic limit criterion is reached, which is not experimentally verified. The incrementally non-linear models are able to describe "discontinuous bifurcations" leading to localized failure in shear bands as well as "homogenous bifurcations" leading to diffuse failure inside the plastic limit criterion [DAR 04a, DAR 04b, KHO 06].

The last observation concerns the different classes of incrementally non-linear models. Endochronic [VAL 71] and hypoplastic (as defined by Chambon in the first part of this chapter or by Kolymbas [KOL 88]) models have the common property of describing the incremental non-linearity by means of a scalar, always positive for any direction of the incremental loading. Chambon's model, CloE, has the advantage of considering in a rigorous manner the condition of limit states and of allowing an analytical explicit determination of the bifurcation condition by strain localization. It also has the advantage of allowing theorems concerning the existence and uniqueness of solutions for boundary problems to be demonstrated. The importance of these theorems consists of the confidence that we can have in the numerical solutions obtained by the finite element method. Incremental models of the interpolation type (in the sense given by Darve in the second part of this chapter, or given by Di Benedetto [DIB 87] or Royis [ROY 89]) express the incremental non-linearity in a more general manner by means of a quadratic tensorial form. Darve's incrementally non-linear model of second order can describe certain cyclic

behaviors and various classes of bifurcations and instabilities [DAR 80b, DAR 84, DAR 04b]. Moreover the octo-linear model enables simple analytical calculations when necessary. Finally, Dafalias' model [DAF 86] is an incrementally non-linear generalization of his bounding surface model.

In the future, micromechanical models will probably help us to develop constitutive relations closer to the essence of granular physics ([NIC 05]) and to understand more intimately failure mechanisms ([NIC 06, SIB 07, NIC 07a, NIC 07b, NIC 07c]).

6.5. References

[CHA 84] CHAMBON R., "Une loi rhéologique incrémentale non-linéaire pour les sols non-visqueux", *J. Meca. Théorique et Appl.*, vol. 3, 521-544, 1984.

[CHA 85] CHAMBON R., DESRUES J., *Bifurcation par Localization et non Linéarité Incrémentale, un Exemple Heuristique d'Analyse Complète,* Proc. Plastic Instability Presse E.N.P.C., 101-103, 1985.

[CHA 89] CHAMBON R., *Une classe de loi de comportement incrémentalement non linéaire pour les sols non visqueux: résolution de quelques problèmes de cohérence,* C. R. Acad. Sci. 308 II, 1571-1576, 1989.

[CHA 94a] CHAMBON R., DESRUES J., HAMMAD W., CHARLIER R., "CLoE a new rate model for geomaterials, theoretical basis and implementation", *Int. J. Numer Anal Meth Geom.*, 18, 4, 253-278, 1994.

[CHA 94b] CHAMBON R., DESRUES J., TILLARD D., *Shear modulus identification versus experimental localization data*, 3rd International Workshop on Localization and Bifurcation Theory for Soils and Rocks, R. CHAMBON, J. DESRUES, I. VARDOULAKIS (eds.), A.A. BALKEMA, Rotterdam, 101-109, 1994.

[CHA 98a] CHAMBON R., CROCHEPEYRE S., "Daphnis a new model for the description of post localization behavior", *Mech. Cohesive Frictional Materials*, 3, 2, 128-153, 1998.

[CHA 98b] CHAMBON R., CAILLERIE D., EL HASSAN N., "One dimensional localization studied with a second grade model", *Eur. J. of Mechanics A/Solids*, 4, 637-656, 1988.

[CHA 99] CHAMBON R., CAILLERIE D., "Existence and uniqueness theorems for boundary value problems involving incrementally non-linear models", *Int. J. Solids and Strutures*, 364, 5089-5099, 1999.

[DAF 86] DAFALIAS Y. F., "Bounding surface plasticity. I. Mathematical foundation and hypoplasticity", *J. Eng. Mech.*, vol. 112, no. 9, 966-987, 1986.

[DAR 80a] DARVE F., LABANIEH S., "Comportement mécanique des milieux granulaires en liaison avec leur structure", *Compte-rendus du XV Colloque du Groupe Français de Rhéologie*, Paris, 329-341, 1980.

[DAR 80b] DARVE F., DESRUES J., JACQUET M., "Les surfaces de ruptures en mécanique des sols en tant qu'instabilité de déformation", *Cahier du Groupe Français de Rhéologie*, vol. 5, no. 3, 93-106, 1980.

[DAR 82] DARVE F., LABANIEH S., "Incremental constitutive law for sands and clay. Simulations of monotonic and cyclic test", *Int. J. Numer Anal Meth Geom.*, 6, 243-275, 1982.

[DAR 84] DARVE F., "An incrementally non-linear constitutive law of second order and its application to localization", *Mechanics of Engineering Materials*, Desai & Gallagher (eds.), Wiley, Chapter 9, 179-196, 1984.

[DAR 93] DARVE F., FLAVIGNY E., MÉGHACHOU M., "Yield surfaces and principle of superposition revisited by incrementally non-linear constitutive relations", *Int. J. of Plasticity*, vol. 11, no. 8, 927-948, 1993.

[DAR 96] DARVE F., "Liquefaction phenomenon of granular materials and constitutive instability", *Int. J. Eng. Comput.*, vol. 13, no. 7, 5-28, 1996.

[DAR 97a] DARVE F., PAL O ROGUIEZ X., "Material instabilities and bifurcations in granular media", *6th Int. Symp. Numerical Models in Geomechanics*, Pande and Pietruszczak (eds.), A.A. Balkema, pp. 167-173, 1997.

[DAR 97b] DARVE F., "Liquefaction. A Phenomenon Specific to Granular Media", in *Powders and Grains*, Behringer & Jenkins (eds.), Balkema, 167-173, 1997.

[DAR 97c] DARVE F., ROGUIEZ X., "Instabilities in Granular Materials", in *Computational Plasticity*, Owen, Onate, Hinton (eds.), CIMNE, 720-727, 1997.

[DAR 98a] DARVE F., ROGUIEZ X., "Homogeneous Bifurcations", in *Localization and Bifurcation Theory for Soils and Rocks*, ADACHI, OKA & YASHIMA (eds.), Balkema, 43-50, 1998.

[DAR 98b] DARVE F., PAL O., "A new incrementally non-linear constitutive relation with 5 material constant", in *Computer Methods and Advances in Geomechanics*, Yuan (ed.), Rotterdam. Balkema, 2445-2454, 1998.

[DAR 99] DARVE F., LAOUAFA F., "Plane strain instabilities in soil. Application to slopes stability", *Numerical Models in Geomechanics*, Pande Pietruszczak and Schweiger (eds.), A.A. Balkema, pp. 85-90, 1999.

[DAR 00] DARVE F., LAOUAFA F., "Instabilities in granular materials and application to landslides", *Int. J. Mech. of Cohes. Fric. Mat.*, vol. 5, no. 8, 627-652, 2000.

[DAR 04a] DARVE F., VARDOULAKIS I., *Degradations and Instabilities in Geomaterials*, Springer, 2004.

[DAR 04b] DARVE F., SERVANT G., LAOUAFA F., KHOA H.D.V., "Failure in geomaterials, continuous and discrete analyses", *Comput. Meth. Applied Mech. and Eng.*, vol. 193, no. 27-29, 3057-3085, 2004.

[DAR 05a] DARVE F., NICOT F., "On flow rule in granular media. Phenomenological and multiscale views", *Int. J. Num. Anal. Meth. Geomech.*, vol. 29, no. 14, 1411-1432, 2005.

[DAR 05b] DARVE F., NICOT F., "On incremental non-linearity in granular media", *Int. J. Num. Anal. Meth. Geomech.*, vol. 29, no. 14, 1387-1410, 2005.

[DES 96] DESRUES J., CHAMBON R., MOKNI M., MHAZEROLLE F., "Void ration evolution inside shear band studied by computerized tomography", *Géotechnique*, 46, 3, 529-546, 1996.

[DIB 87] DI BENEDETTO H., "Modélisation du comportement des géomatériaux. Application aux enrobés et aux bitumes", Doctoral Thesis, University of Grenoble, 1987.

[DOA 89] DOANH T., DI BENEDETTO H., GOLCHEH G., KHARCHAFI K., "Non linear incremental constitutive equation: application to sands", *Constitutive Equations for Granular Soils*, Saada & Bianchini (eds.), Balkema, 255-276, 1989.

[ELH 96] EL HASSAN N., DESRUES J., CHAMBON R., "Modelling a deep borehole excavation in marls using an advanced constitutive model", in *Eurock '96*, G. Barla (ed.), Balkema, 777-784, 1996.

[GUD 84] GUDEHUS G., DARVE F., VARDOULAKIS I., *Constitutive Relations for Soils*, A. A. Balkema, 1984.

[GUD 79] GUDEHUS G., "A comparison of some constitutive laws for soils under radially symmetric loading and unloading", *3rd Int. Conf. Num. Mech. in Geomech.*, ed. Wittke, Balkema, vol. 4, 1309-1323, 1979.

[HIL 58] HILL R., "A general theory of uniqueness and stability in elastic-plastic solids", *J. of the Mech. and Phys. of Solids*, 6, pp. 236-249, 1958.

[KHO 06] KHOA H. D. V., GEORGOPOULOS I. O., DARVE F., LAOUAFA F., "Diffuse failure in geomaterials, experiments and modeling", *Comput. and Geotechn.*, vol. 33, 1-14, 2006.

[KOL 87] KOLYMBAS D., "A novel constitutive law for soils", *Proc. 2nd Int. Conf. on Constitutive Laws for Engineering Materials*, Elsevier 1., 319-326, 1987.

[KOL 88] KOLYMBAS D., "Generalized hypoplastic constitutive equation", *Constitutive Equations for Granular Soils*, Saada & Bianchini (eds.), A. A. Balkema, 349-366, 1988.

[LAN 89] LANIER J., BLOCK J. F., *Essais à volume constant réalisés sur presse tridimensionnelle*, Greco Geomaterials report, 240-243, 1989.

[LYA 07] LYAPUNOV A. M., *Problème général de la stabilité de mouvement*, Reports from the Toulouse Faculty of Science, 9. pp. 203-474, 1907.

[NEL 78] NELSON I., "Constitutive models for use in numerical computation", in *Plastic and Long Term Effects Insoils 2*, G. Gudehus (ed.), Balkema, 1978.

[NIC 05], NICOT F., DARVE F., "A multi-scale approach to granular materials", *Mech. Mat.*, vol. 37, 980-1006, 2005.

[NIC 06] NICOT F., DARVE F., "Micro-mechanical investigation of material instability in granular assemblies", *Int. J. Solids and Struct.*, vol. 43, 3569-3595, 2006.

[NIC 07a] NICOT F., DARVE F., KHOA H.D.V., "Bifurcations and second order work in geomaterials", *Int. J. Num. Anal. Meth. Geomech.*, vol. 31, no. 8, 1007-1032, 2007.

[NIC 07b] NICOT F., SIBILLE L., DONZE F., DARVE F., "From microscopic to macroscopic second order work in granular assemblies", *Mech. Mat.*, vol. 39, no. 7, 664-684, 2007.

[NIC 07c] NICOT F., DARVE F., "A micromechanical investigation of bifurcation in granular materials", *Int. J. Solids and Struct.*, vol. 44, 6630-6652, 2007.

[ROB 82] ROBINET J. C., MOHKAM M., Doanh T., Deffayet M., "A non-linear constitutive law for soil", *Constitutive Relations for Soils*, Gudehus, Darve & Vardoulakis (eds.), Balkema, 405-418, 1982.

[ROY 89] ROYIS P., "Interpolation and one-to-one properties of incremental constitutive laws. A family of incrementally non linear constitutive laws", *Eur. J. Mech. A/Solids*, vol. 8, 385-411, 1989.

[ROY 98] ROYIS P., DOANH T., "Theoretical analysis of strain response envelopes using incrementally non-linear constitutive equations", *Int. J. Numer Anal Meth Geom.*, 22, 97-132, 1998.

[SAA 88] SAADA A. S., BIANCHINI G., *Constitutive Equations for Granular Soils*, A. A. Balkema, 1988.

[SIB 07] SIBILLE L., NICOT F., DONZE F.V., DARVE F., "Material instability in granular assemblies from fundamentally different models", *Int. J. Num. Anal. Meth. Geomech.*, vol. 31, no. 3, 457-482, 2007.

[TAM 00a] TAMAGNINI C., VIGGIANI C., CHAMBON R., "A review of two differnt approaches to hypoplasticity", *Constitutive Modeling including Development in Hypoplasticity*, Chapter A, Elsevier, 2000.

[TAM 00b] TAMAGNINI C., VIGGIANI C., CHAMBON R., "Evaluation of different strategies for the integration of hypoplastic constitutive equations, Application to the CLoE model", *Mech. Cohesive Frictional Materials*, 2000.

[TAM 00c] TAMAGNINI C., VIGGIANI C., CHAMBON R., "Some remarks on shear band analysis in hypoplasticity", *5th International on Localization and Bifurcation Theory for Soils and Rocks*, H.B MUHLHAUS (ed.), A.A. BALKEMA, Rotterdam, 2000.

[TAT 74] TATSUOKA F., ISHIARA K., "Yielding on sand in triaxial compression", *Soils and Foundations*, 4, 2, 1974.

[VAL 71] VALANIS K. C., "A theory of viscoplasticity without a yield surface", *Archives of Mechanics*, vol. 23, 517-551, 1971.

[VAR 80] VARDOULAKIS I., "Shear band inclination and shear modulus of sands in biaxial tests", *Int. J. Numer Anal Meth Geom.*, 4, 103-119, 1980.

[VIG 99] VIGGIANI C., TAMAGNINI C. "Hypoplasticity for modelling soil non linearity in excavation problems", *Prefailure Deformation Characteristics of Geomaterials*, M. JAMIOLKOWSKI, R. LANCELLOTA, D. LO PRESTI (eds.), A.A. BALKEMA Rotterdam, vol. 1, 581-588, 1999.

Constitutive Modeling of Soils and Rocks
Edited by Pierre-Yves Hicher & Jian-Fu Shao

Chapter 7

Viscoplastic Behavior of Soils

7.1. Introduction

Various laboratory testing and *in situ* observations show the time-dependent behavior of soils, especially fine soils. If we neglect the ageing effects here due to physicochemical reactions at the level of the particles, we could say that this characteristic has two origins: the pore pressure dissipation during consolidation [BIO 41, SAN 69] and the viscous properties of the material constituents. These two phenomena act together and their effects are not easy to separate. It is usually assumed that the pore pressure dissipation is the main factor controlling the initial consolidation phase, called the primary consolidation, and the viscous effects are predominant in the second phase, called the secondary consolidation.

The viscous behavior of fine soils is mainly linked to their internal structure, especially to adsorbed water. When an external load is applied to a soil element, there is a progressive transmission of viscous contacts to frictional contacts, which manifests itself at a macroscopic level by a time-dependent response. Considering the importance of this phenomenon for the stiffness and the strength of clayey soils, it is necessary to take it accurately into account in the modeling of constructions.

The viscous behavior of fine soils has been the subject of numerous experimental and numerical works [ADA 82, AUB 86, BJE 67, BOR 85, DES 87, FOD 97, GRA 83, HIC 85, JAM 79, KAT 84, MES 77, SHI 69, SIN 68, TAV 78, VAI 77, YIN 99,

Chapter written by Pierre-Yves HICHER and Isam SHAHROUR.

YIN 06, ZIE 74, ZIE 75]. Laboratory testing consists mainly of triaxial and oedometer tests. The modeling is based on different concepts, mainly in the viscoplasticity framework.

In this chapter, we present first a synthesis of experimental results showing the time-dependent behavior of soils and then the modeling concepts. For the latter, the attention will be focused on viscoplastic models developed in the framework of the overstress theory developed by Perzyna [PER 63, PER 66], which is mostly used in soil modeling. The implementation of these models in finite element programs will also be presented.

7.2. Laboratory testing

7.2.1. *Strain rate influence*

Figure 7.1 presents the results of undrained triaxial tests produced on a bentonite clay at three different strain rates: $1.5 10^{-4}$/s, $6 10^{-6}$/s, $6 10^{-7}$/s [HIC 85]. We can see that the strain rate increase induces a deviatoric stress increase at any strain level. These results, presented in a ε_1, q/q_{max} diagram, give a single curve, demonstrating that the strain rate influence is quantitatively the same at any strain level. The relationship between q_{max} and log ε_1 is linear in the interval 10^{-3}%/mn < ε_1 < 10^{2}%/mn (Figure 7.2). For smaller strain rate values, the maximum strength q_{max} converges towards a constant value which represents the long term resistance of the clayey material. The maximum strength increase, for a ten-fold strain rate increase, varies between 4% to 12% for remolded clays and 6% to 16% for intact clays.

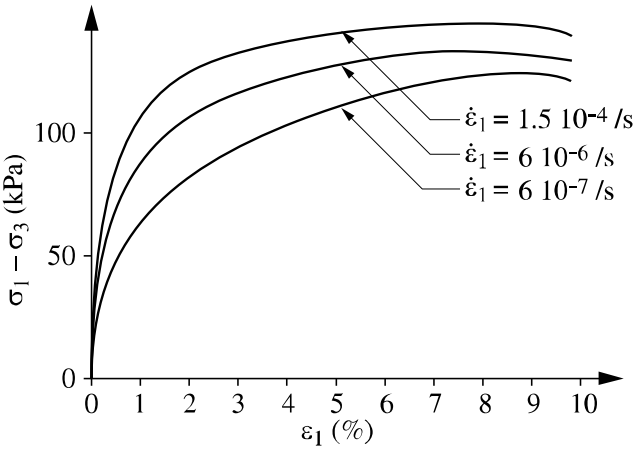

Figure 7.1. *Undrained triaxial tests on bentonite*

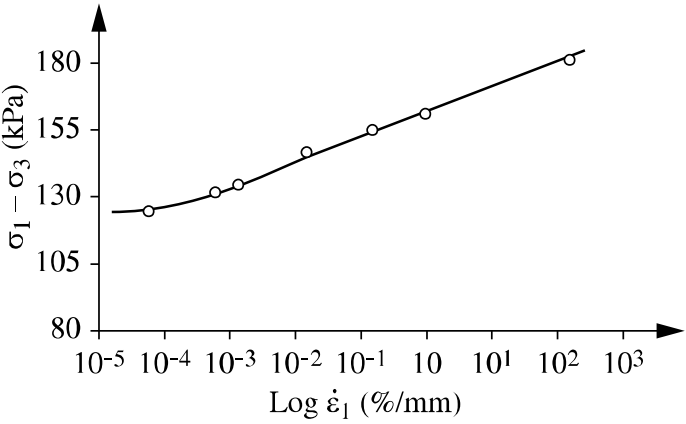

Figure 7.2. *Strain rate influence on undrained maximum strength of normally consolidated bentonite (NC 200)*

The strain rate effect can also be highlighted by triaxial tests with strain rate changes. Figure 7.3 shows results obtained by Graham *et al*. [GRA 83] on a natural clay. A sudden change in the strain rate induces a change in the material stress-strain relationship which converges gradually toward the curve corresponding to a loading at a constant strain rate equal to the last value and applied from the beginning of the test. This type of test allows the strain rate influence to be measured for a given soil, without the interference of any discrepancy in natural properties, as is the case when comparing test results obtained from several different specimens.

The effective stress paths are also affected by the strain rate (Figure 7.4). However, the failure criterion q_{max} = Mp' appears to be independent of the strain rate. Other researchers have also come to the conclusion of the independence of the friction angle with the strain rate in a drained or undrained condition. In the case of drained conditions, we have to recall that only a small number of test results exploring the strain rate effect are available due to a duration which is too long in this type of testing. In undrained conditions, the strain rate has to remain small enough in order not to generate pore pressure gradients inside the specimens. These experimental difficulties can sometimes lead to contradictory results, but we can admit that, with a first approximation, the friction angle is independent of the strain rate.

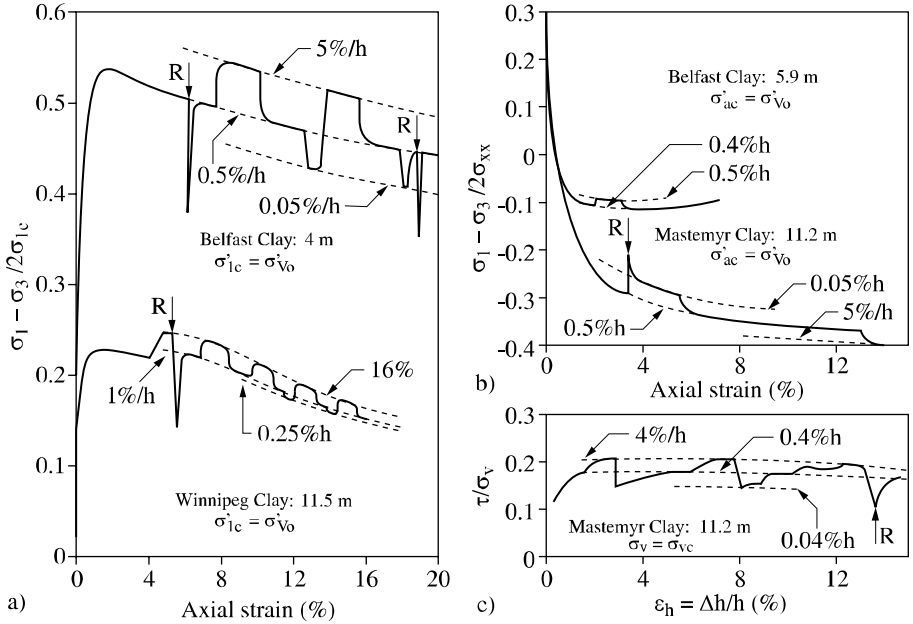

Figure 7.3. *Strain rate influence on the behavior of a natural clay along triaxial and simple shear tests [GRA 83]*

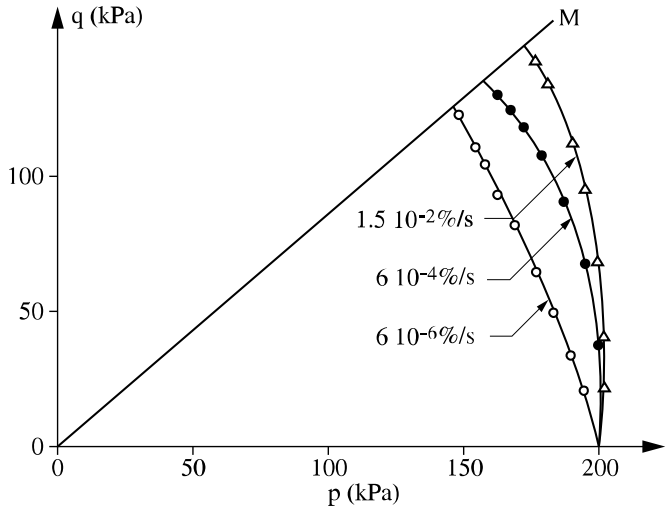

Figure 7.4. *Strain rate influence on the effective stress path during undrained triaxial tests on normally consolidated bentonite (NC 200)*

7.2.2. *Creep tests*

7.2.2.1. *Creep during consolidation tests*

The test results show that the creep strain amplitude during isotropic secondary consolidation, i.e. at constant effective pressure, is usually small. Under anisotropic consolidation, the creep strains are bigger and increase with the deviatoric stress level. Oedometric tests show a linear relationship between the variation of the void ratio and the logarithm of time during secondary consolidation. The slope of the relation is called c_α. Jamiolowsky [JAM 79] considers that this coefficient is independent of time, loading increment and specimen size. Mesri *et al*. [MES 77] have shown that c_α is a function of the loading history and in particular of the overconsolidation degree (Figure 7.5). In the normal consolidation domain, ratio c_α/c_c can be considered constant and comprise between 0.03 and 0.05 for mineral clays [MES 84].

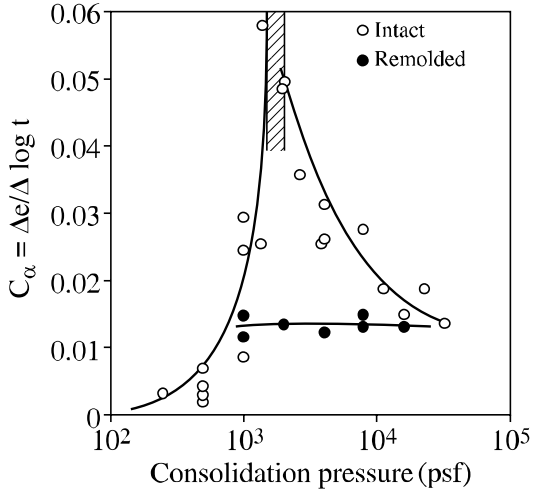

Figure 7.5. *Influence of the consolidation stress on the secondary compression coefficient*

Compression index c_c has been found to be independent of time; this is not the case for consolidation stress σ'_p which increases with the strain rate (Figure 7.6 [GRA 83]). The dependency can be written in the following form:

$$(\sigma'_p)_t/(\sigma'_p)_{t0} = (t_0/t)^{c\alpha/cc} \text{ or } (\sigma'_p)_\varepsilon/(\sigma'_p)_{\varepsilon 0} = (\varepsilon/\varepsilon_0)^{c\alpha/cc}$$

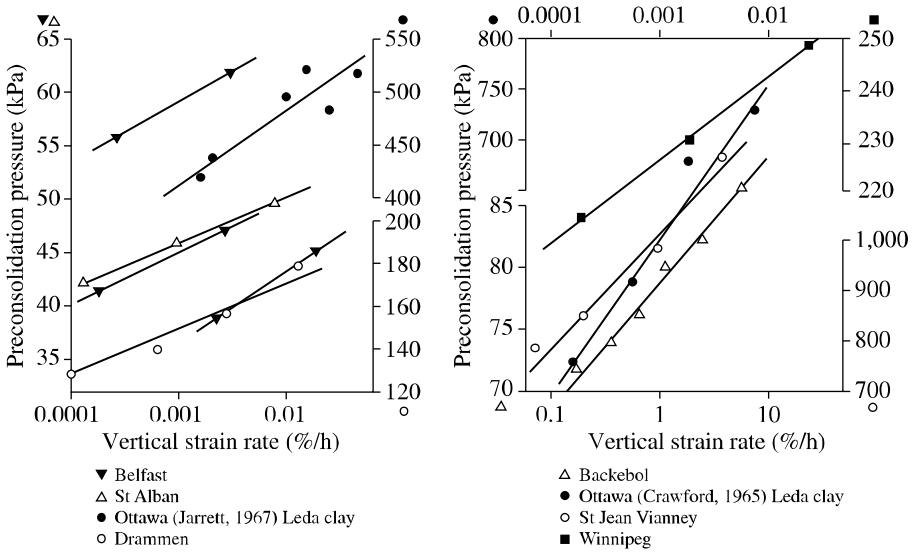

Figure 7.6. *Strain rate influence on the determination of the consolidation stress*

We can directly link these results to Bjerrum's diagram in Figure 7.7 [BJE 67]. The void ratio decrease during secondary consolidation gives the material an overconsolidated behavior when subjected to a stress increment. The density increase provokes a hardening of the material and a shift of the elastic limit during the creep phase.

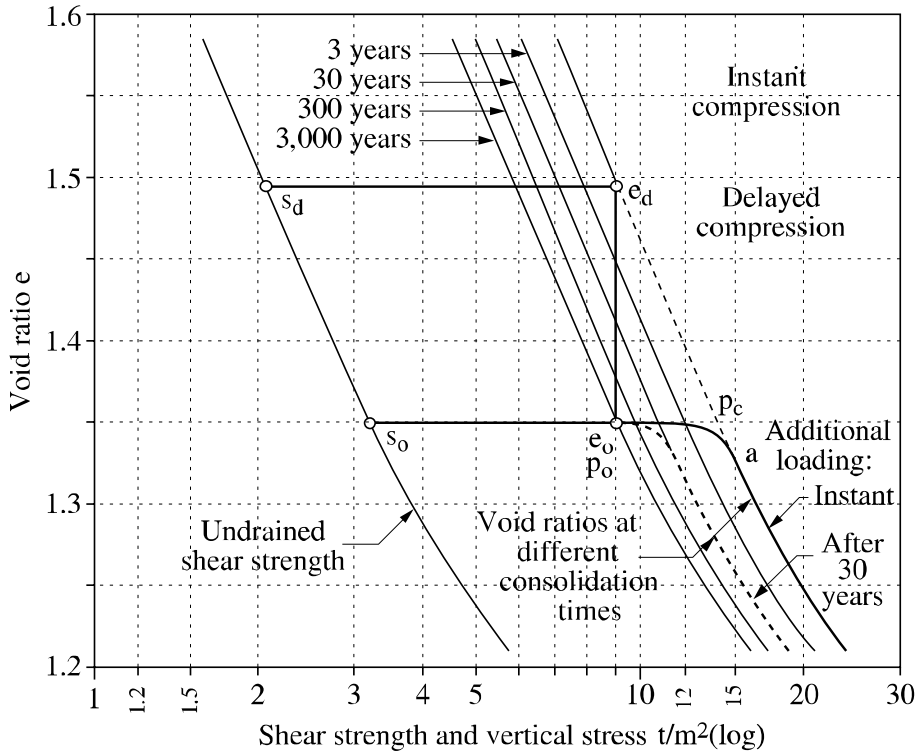

Figure 7.7. *Void ratio evolution with the consolidation time [BJE 67]*

7.2.2.2. *Drained triaxial creep*

Drained triaxial creep tests show the evolution of the volumetric and deviatoric strains with time. Normally consolidated clays have a contractant volume change during creep (Figure 7.8) [SHI 69] while strongly overconsolidated clays can exhibit dilation with time (Figure 7.9) [AKA].

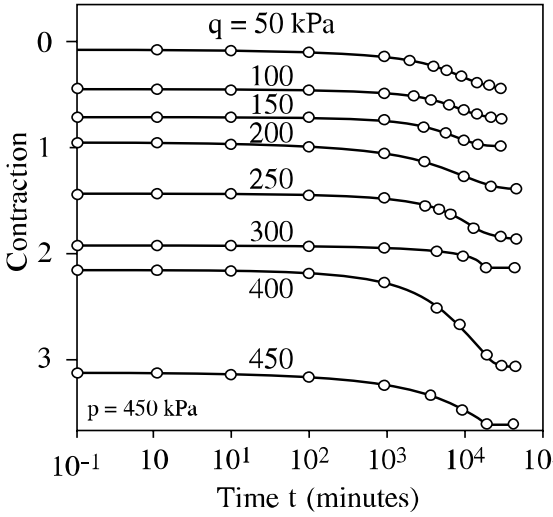

Figure 7.8. *Triaxial creep tests at constant mean stress [SHI 69]*

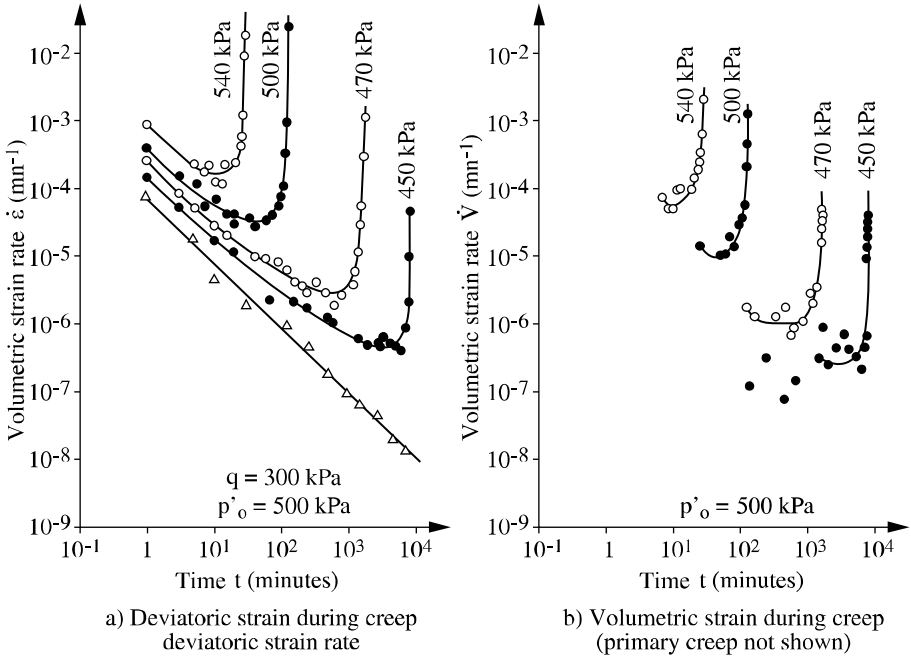

Figure 7.9. *Drained triaxial creep tests [AKA 77]*

During creep tests, three phases in strain evolution with time can be observed:

– a primary creep at decreasing strain rate;

– a secondary creep at constant strain rate;

– a tertiary creep at increasing strain rate.

The primary creep phase always exists during a given period of time immediately following the application of the constant stress. The tertiary creep phase exists only for elevated applied stresses leading to the failure of the specimen. In drained creep tests, it appears only for stress values close to the maximum strength of the material (Figure 7.10: creep tests on London Clay performed by Bishop and Lovenburry [BIS 69]). The existence of the secondary creep phase depends on the nature of the material and on the loading amplitude. Most of the tests leading to failure show a direct change from primary to tertiary creep without a secondary creep phase [TAV 78].

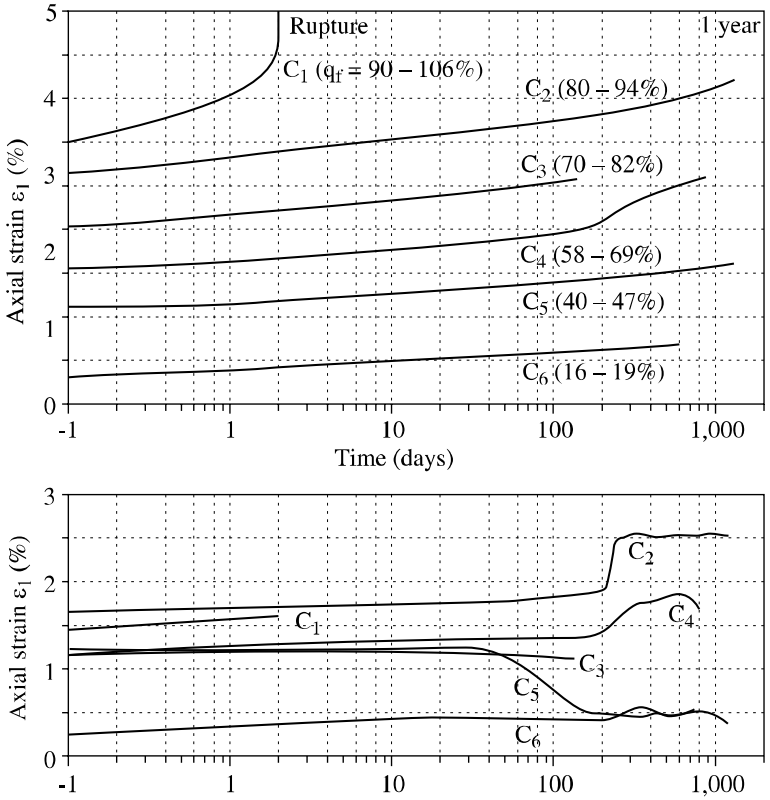

Figure 7.10. *Drained triaxial creep tests on London Clay [BIS 69]*

Singh and Mitchell [SIN 68] have proposed the following relation between axial deformation and elapsed time during drained or undrained triaxial creep tests:

$$\dot{\varepsilon}_1 = Ae^{\alpha q}\left(\frac{t_i}{t}\right)^m$$

where α, m and A are soil parameters. They are not intrinsic parameters but depend on the stress path. This relation can be used to describe only the primary creep phase. Tavenas *et al*. [TAV 78] have generalized Singh-Mitchell's relation by separating volumetric and deviatoric strains. They propose the following relations:

$$\dot{\varepsilon}_v = f(\sigma')\left(\frac{t_i}{t}\right)^m$$

$$\dot{\varepsilon}_d = g(\sigma')\left(\frac{t_i}{t}\right)^m$$

From these two equations, we can derive the plastic flow rule:

$$\frac{\dot{\varepsilon}_v}{\dot{\varepsilon}_d} = \frac{f(\sigma')}{g(\sigma')}$$

We can see that the flow rule is independent of time. This result has been obtained by other researchers, such as Fodil *et al*. [FOD 98] and Walker [WAL 69] on normally consolidated clays (Figure 7.11). Aka *et al*. [AKA 75] have obtained similar results from tuff samples. They proposed a viscoplastic flow rule which can be written:

$$\varepsilon_v/\varepsilon_d = 1/\eta\ (M\text{-}q/p)$$

This is similar to the flow rule proposed by Nova in his elastoplastic model (see Chapter 3). Dilatancy is also obtained during creep tests for $q/p > M$.

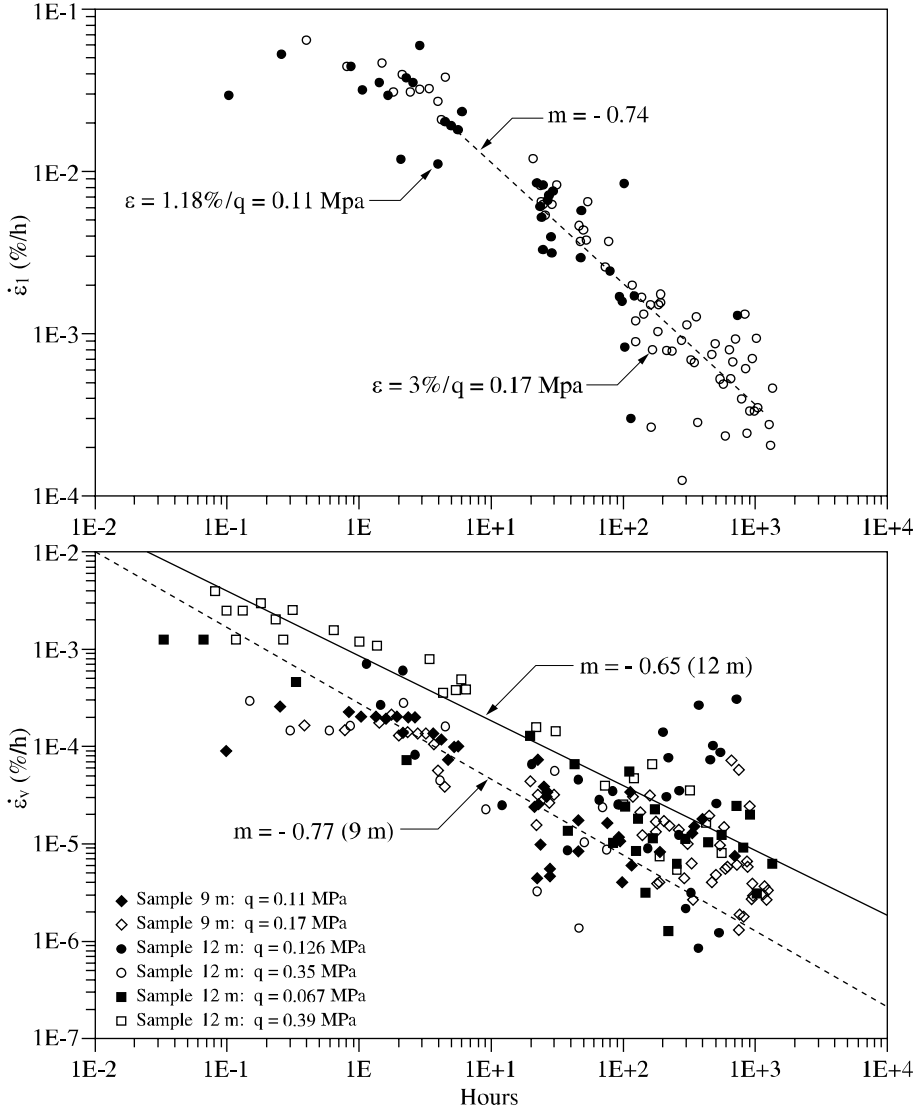

Figure 7.11. *Drained triaxial creep tests on normally consolidated clay [FOD 98]*

7.2.2.3. *Undrained triaxial creep*

The term *undrained creep* is applied to tests for which a deviatoric stress is applied and kept constant with time in undrained conditions. As pore pressure evolves with time, an evolution of the effective stress tensor is provoked. The term *creep* is therefore incorrect in the strict sense, since the state of effective stress does not stay constant, but numerous results for this kind of test are available and also show a viscous behavior of the soils. Figures 7.12 to 7.15 present results obtained from a normally consolidated bentonite [ELG 82, HIC 88]. They show the existence of a primary creep phase which can be adequately represented by Singh-Mitchell's equation, and a tertiary creep phase for elevated values of the applied deviatoric stress. The pore pressure increases with time, creating a decrease of the mean effective stress. Large deformations develop when the effective stress state reaches the condition q = Mp', which confirms that the failure condition expressed in effective stresses is time-independent.

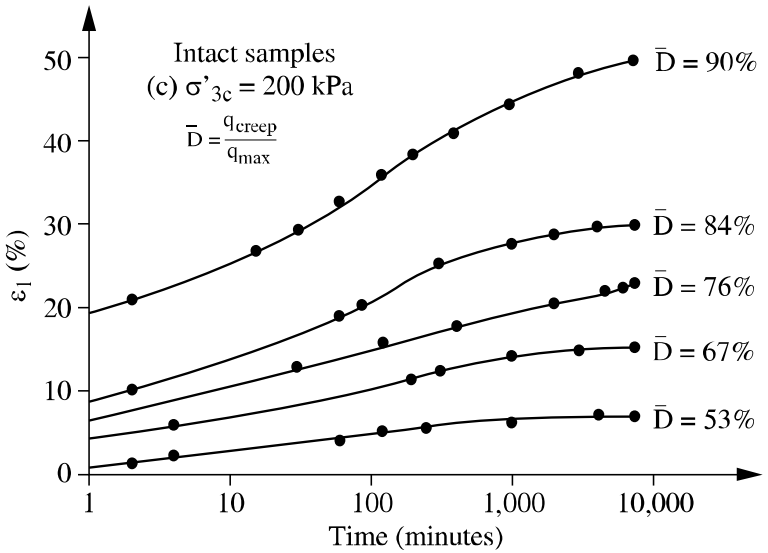

Figure 7.12. *Undrained triaxial creep tests on normally consolidated bentonite (NC 200)*

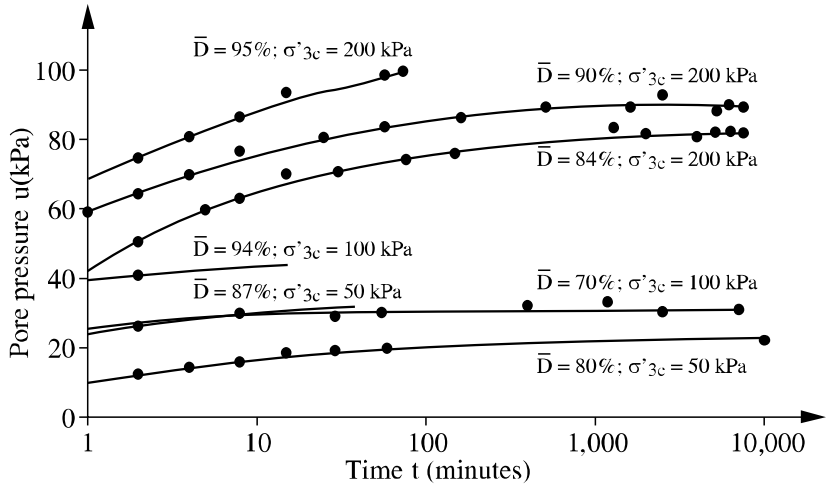

Figure 7.13. *Undrained triaxial creep tests on normally consolidated bentonite (NC 200). Pore pressure evolution*

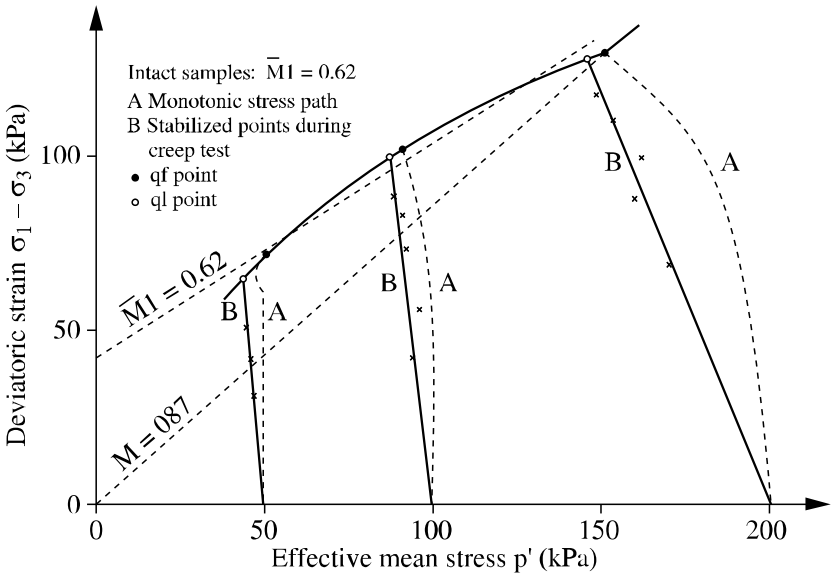

Figure 7.14. *Undrained triaxial creep tests on bentonite. Effective stress paths*

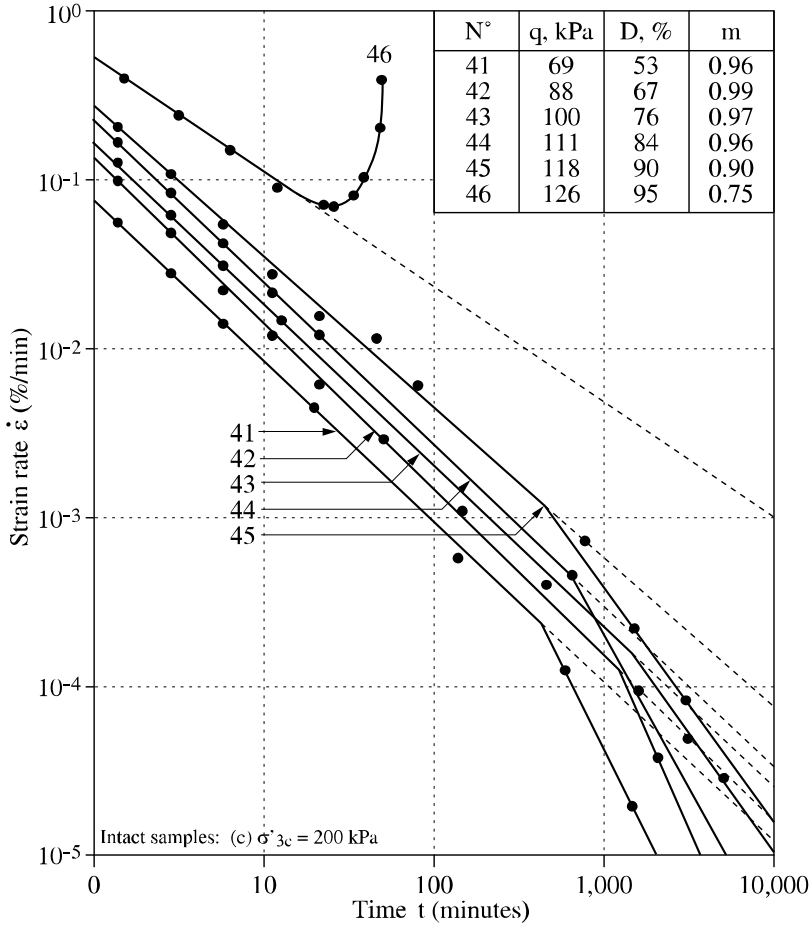

Figure 7.15. *Axial strain rate evolution during an undrained creep test on normally consolidated bentonite (NC 200)*

7.2.2.4. *Stress relaxation tests*

Fewer results are available for this type of test than for creep tests. Figure 7.16 presents results obtained from a bentonite [HIC 85]. In the three tests, an axial deformation was first imposed in undrained condition and at a strain rate equal to 6.10^{-6}/s and then maintained as constant. We can observe a decrease in the deviatoric stress with time. The decrease appears to be at first proportional to log(t) and then becomes smaller for elapsed time higher than 700 mn. These results are similar to those presented by Murayama *et al*. [MUR 64], Lacerda *et al*. [LAC 73], Tjong Kie

[TJO 85] who also obtained a linear relationship between the deviatoric stress change and log(t). More recently, Fodil *et al*. [FOD 97, FOD 98] reached the same conclusion from drained stress relaxation on a normally consolidated natural clay. They showed that the deviatoric stress decrease Δq/q was higher for a higher strain rate during initial loading and independent of the applied strain (Figure 7.17). This last result confirms that the viscosity influence is independent of the stress and strain level.

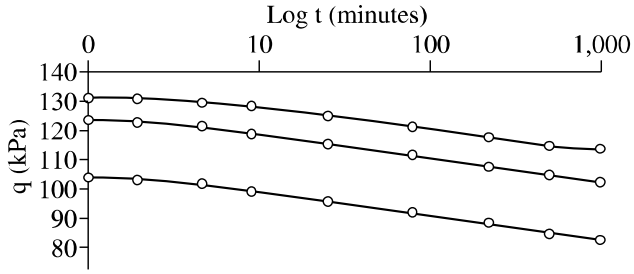

Figure 7.16. *Stress relaxation test on normally consolidated bentonite (NC 200)*

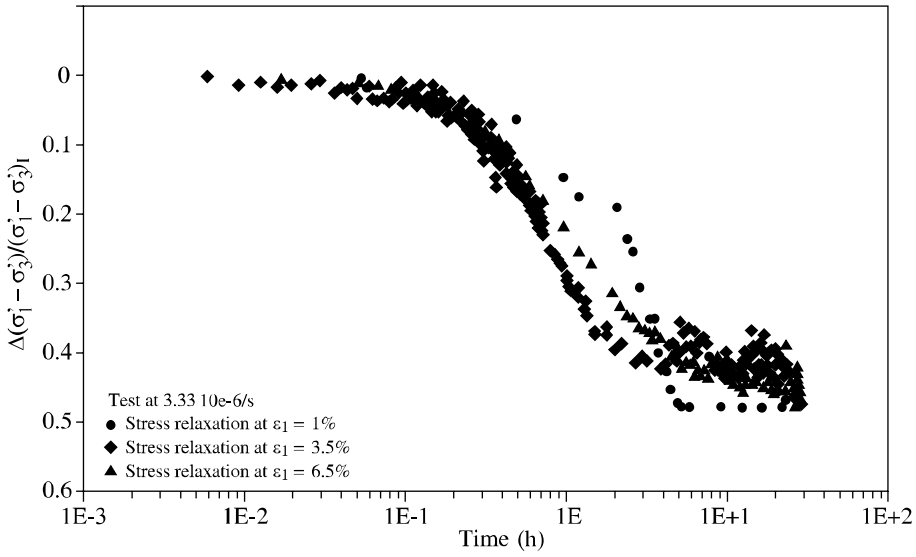

Figure 7.17. *Stress relaxation test on a natural clay [FOD 98]*

7.2.2.5. *Synthesis of time-dependent behavior*

All the test results obtained from the bentonite are gathered in the plane p',q, considering the different effective stress paths (Figure 7.18) [HIC 85, HIC 88]. All the stabilized stress states during creep and stress relaxation tests give a single curve, similar in shape to those obtained for undrained constant strain rate loading tests and located to the left of all of them. We can assume that this curve represents the long term behavior of the clay in undrained conditions. Its junction with the line q = Mp' gives the long term maximum strength. Similar results obtained from undrained creep tests have been presented by Roscoe *et al*. [ROS 63].

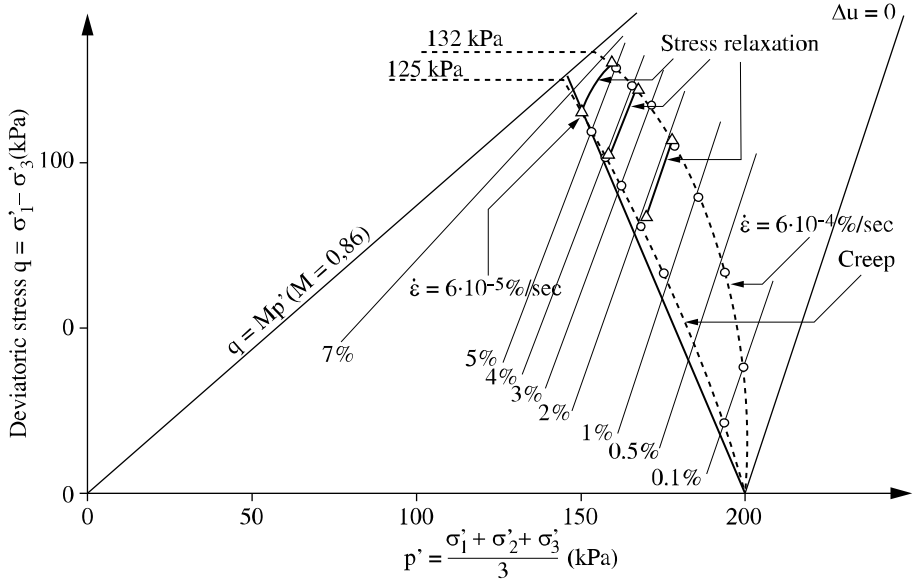

Figure 7.18. *Effective stress paths during undrained creep and stress relaxation tests on normally consolidated bentonite (NC 200)*

Furthermore, a single relation $q - \varepsilon_1$ for a given strain rate has been found. These results have been confirmed by the work by Vaid [VAI 88] on the Haney Clay. If the results are plotted in the $q/q_{max} - \varepsilon_1$ diagram where q_{max} is the maximum strength for a given strain rate, all the results lead to a single curve, independent of time, which allows us to characterize the elastoplastic behavior independently of the viscous properties. The latter can then be measured by comparison to this time-independent reference behavior. The number of available results in drained condition is not sufficient for the analysis to be extended to the intrinsic

characteristics of clayey materials. This division of the stress-strain relationship in two parts, dependent and independent of time, is useful from the perspective of developing constitutive models for viscous materials.

7.3. Constitutive models

7.3.1. *Modeling framework*

Several theories have been developed in order to represent the time-dependent behavior of fine soils. Some of the models introduce time explicitly in the formulation [MAT 86, SEK 84], but most of them consider it implicitly through the hardening parameter evolution. Generally, the deformations are decomposed in two parts: elastic and anelastic. The anelastic deformations are mostly strain dependent (viscoplastic), but some authors assume that a part of them are time-independent (plastic) [BOR 85, KAL 85].

Most of the models assume the existence of an elastic domain, but some others assume that anelastic deformations take place immediately at the beginning of the loading [KUT 92]. The elastic part can be time-dependent [MUR 64], but for simplicity's sake, it is mostly assumed to be time-independent, since the viscous effects are more marked in the plastic domain.

Numerous models have been developed in the framework of viscoplasticity theory. The strain tensor is decomposed into two parts: elastic and viscoplastic [ADA 82, DES 87, KUT 92, ZIE 74]. The viscoplastic part is governed by a function which controls the magnitude of the viscoplastic strain rate tensor *S* and a potential which gives the direction of this tensor:

$$\dot{\varepsilon}_{vp} = S\frac{\partial g}{\partial \sigma}$$

Function *S* is determined in most of the models for soils by Perzyna's formulation [PER 63, PER 66], but some authors use the concept of the time equivalence [YIN 99] or the "time line" [BOR 85, KUT 92].

7.3.2. *Perzyna's formulation*

Perzyna's formulation is widely used in the development of viscoplastic models for soils in order to model monotonous as well as cyclic loading, as for example [ADA 82, AUB 86, BOR 85, DES 87, KAT 84, KOD 83, MAT 86, OKA 88, YIN 99, YIN 07, ZIE 75].

The success of this theory is due to several factors:

– the definition of a yield surface is easy, and is often derived from elastoplastic, time-independent models;

– it allows us to reproduce the time-dependent soil behavior along a large variety of loading paths;

– the mathematical formulation is well adapted to the numerical modeling and its implementation in finite elements programs;

– the parameter identification from laboratory testing is usually straightforward.

Perzyna assumes that the strain increment tensor can be decomposed into an elastic and a viscoplastic part:

$$\dot{\varepsilon} = \dot{\varepsilon}^{e} + \dot{\varepsilon}^{vp}$$

where *e* and *vp* correspond respectively to the elastic and the viscoplastic strain increment tensors.

The stress increment tensor is linked to the elastic strain increment tensor by the elastic matrix D:

$$\dot{\sigma} = D\dot{\varepsilon}^{e}$$

Viscoplastic strains are created when the state of stress goes beyond a given limit, defined by the yield function f which depends on the stress tensor $\boldsymbol{\sigma}$ and hardening parameters α.

$$f(\sigma, \alpha) = 0$$

The hardening parameters are assumed to depend on the viscoplastic strains ε^{vp}. The viscoplastic strain increment tensor is determined in the following way:

$$\dot{\varepsilon}^{vp} = \frac{\phi(F)}{\eta}\frac{\partial g}{\partial \sigma}$$

where $\phi(F)$ is the viscous nucleus and η a viscosity parameter. The direction of the viscoplastic strain increment tensor is given by the plastic potential g. F is a scalar which represents the overstress corresponding to a measure of the distance between the current state of stress and the current yield surface. In the case of associated flow rule, the plastic potential is the same as the yield function: g = f; in most cases, the two functions are different and the model is non-associated.

The viscous nuclear ϕ is a monotonous increasing positive function of F and is equal to zero when F becomes negative or zero. This means that the plastic yield surface f defines a limit surface between the elastic domain for $f < 0$ and the viscoplastic domain for $f > 0$. F is often chosen as being the value of $f(\sigma,\alpha)$, σ being the current state of stress at time t and α the current values of the hardening variables at the same time t. F is therefore positive when the state of stress is located beyond the limit yield locus and viscoplastic strains can develop.

Function ϕ take different forms in the existing viscoplastic models. For soils, the usual expressions are the following:

$$\phi(F) = \left(\frac{F}{F_0}\right)^N$$

$$\phi(F) = \mathrm{Exp}\left(\frac{F}{F_0}\right)^N - 1$$

N is a constitutive parameter, and F_0 is a constant with the same dimension as F.

Therefore, the extension of an elastoplastic model to a viscoplastic model requires only the definition of function f.

The evolution law of the hardening variables is written:

$$d\alpha = l(\sigma, \alpha)$$

Usually, the following form is chosen:

$$l(\sigma, \alpha) = h(\alpha) \langle f(\sigma, \alpha) \rangle$$

which allows us to assure that the hardening variables vary if and only if there are viscoplastic deformations. When the state of stress is outside the yield locus, the hardening will develop and the yield locus will evolve according to the dependency of the viscous nucleus to the hardening variables. For example, in the case of a creep test, the state of stress remains fixed, while the yield surface evolves with time and comes closer to the stress point in the stress state. There is therefore a progressive decrease of the distance F between the yield locus and the stress point and, as a

consequence, a progressive decrease of the viscoplastic strain increment with time. This corresponds to the primary creep behavior. After a long period of time, the yield surface will eventually reach the stress point and the viscoplastic deformation will stabilize. If the stress point is located on or outside the limit surface corresponding to the failure condition, the viscoplastic deformation will continuously increase with time, and no stabilization can be obtained.

7.4. Numerical integration of viscoplastic models

Zienkiewicz *et al*. [ZIE 74] have proposed an explicit scheme for the integration of viscoplastic models. The scheme is simple, requiring only the elastic stiffness matrix, the non-linearity being put in the second member. The main problem with this scheme is that it requires very small time steps in order to assure stability conditions. Hughes *et al*. [HUG 78] have proposed an implicit scheme which depends on only one parameter in order to avoid numerical instability. The disadvantage of this method, however, is that it requires us to solve a non-linear problem at each time step.

The integration of viscoplastic models may be performed from the following equations:

$$\Delta\sigma = D(\Delta\varepsilon - \Delta\varepsilon^{vp})$$

$$\Delta\varepsilon^{vp} = \Delta t[(1-\theta)\dot{\varepsilon}_n^{vp} + \theta\dot{\varepsilon}_{n+1}^{vp}]$$

$\theta = 0$ corresponds to an explicit scheme and requires a small time step Δt in order to avoid any problem of instability. An implicit scheme is obtained for $\theta > 0$. Since the solution depends on the strain increment at time t_{n+1}, it is necessary to use an iterative calculation. For $\theta > 0.5$ the scheme is unconditionally stable, the choice of Δt depends only on the required precision.

The two equations lead to:

$$D^{-1}\sigma_{n+1} + \theta\Delta t\dot{\varepsilon}_{n+1}^{vp} = \Delta\varepsilon - \Delta t(1-\theta)\dot{\varepsilon}_n^{vp} + D^{-1}\sigma_n$$

which can be written:

$$F(\sigma_{n+1}, \dot{\varepsilon}_{n+1}^{vp}) = q_n$$

The resolution of the equation is carried out by using an iterative Newton-Raphson scheme, with the following algorithm:

– determination of $\Delta\sigma^i$ from the relation:

$$\frac{\partial F}{\partial \sigma}\Delta\sigma^i = q_n - P^i$$

– actualization:

$$\sigma^{i+1} = \sigma_n + \Delta\sigma^{i+1}$$
$$\varepsilon^{vp(i+1)} = \varepsilon^{n+1} - D^{-1}\sigma^{i+1}$$
$$f^{i+1} = f(\sigma^{i+1}, \varepsilon^{vp(i+1)})$$
$$\dot{\varepsilon}^{vp(i+1)} = \frac{1}{\eta}\phi(f^{i+1})\frac{\partial g^{i+1}}{\partial \sigma}$$

– back to the first step until the condition of convergence is obtained for a requisite small value of $\Delta\sigma^i$.

7.5. Viscoplastic models for clays

7.5.1. *Choice of the viscoplastic mechanisms*

The central idea here is to choose a yield surface which provides the same response as an elastoplastic model for very small viscosity values or for very low strain rate loading. For this purpose, the expression of $f(\sigma, \alpha)$ is kept similar to that corresponding to an elastoplastic model. Tavenas *et al.* [TAV 78] present the results of drained creep tests by plotting isovolumetric and deviatoric strain rate curves in the p',q plane (Figure 7.19). We can see that the volumetric strain rate lines maintain a similar shape as the yield surface defined in elastoplasticity for this type of material (see Chapter 2) and that the inner domain reduces in size when the strain rate decreases.

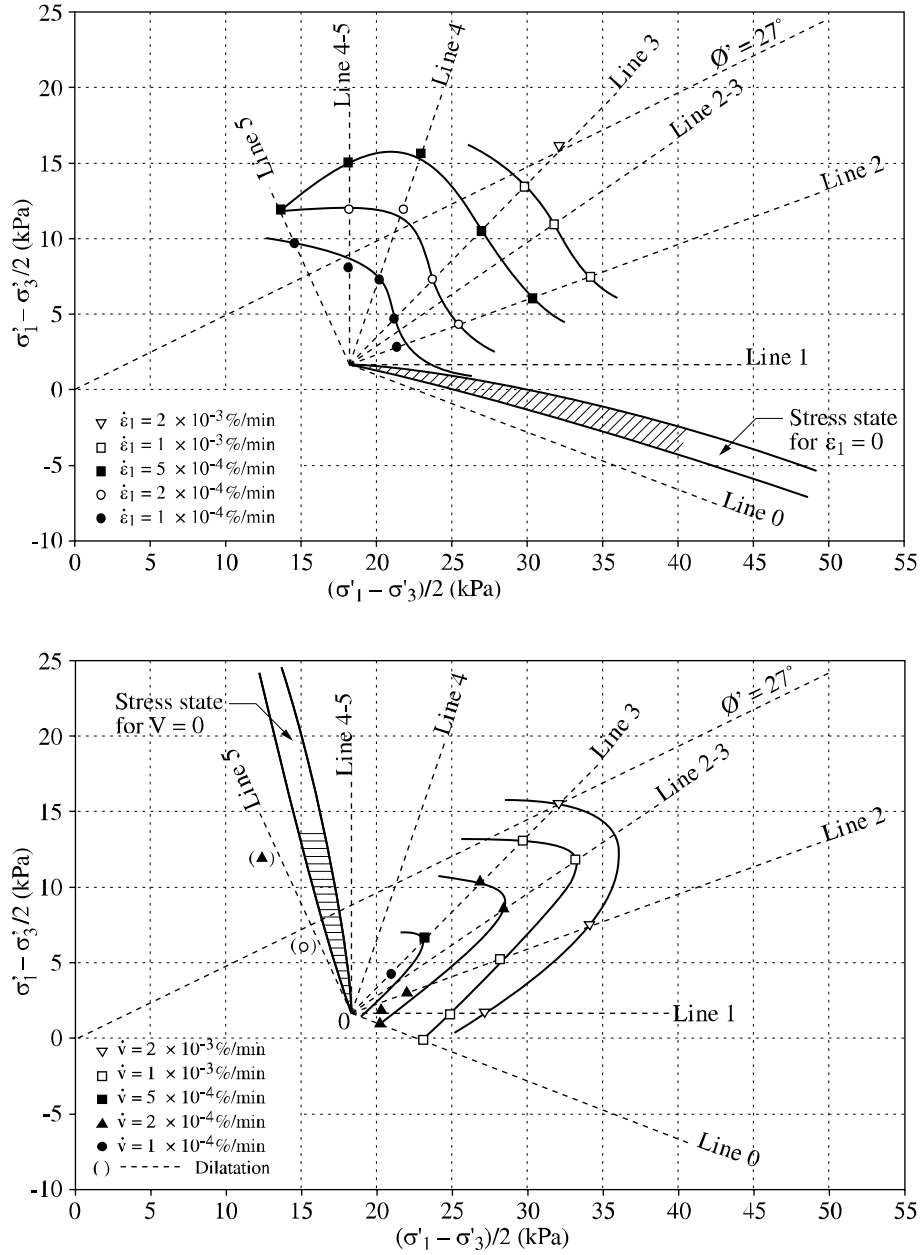

Figure 7.19. *Triaxial creep tests. Iso-strain rate contours*

As for the flow rule, experimental works, as presented previously, have shown that it could be considered as independent of time and dependent only on the state of stress. Several authors consider that flow rules proposed in elastoplasticity and derived most of the time from the Cam-Clay model can also be applied in viscoplasticity.

7.5.2. *Viscoplastic models derived from the elastoplastic Cam-Clay model*

Several researchers have developed viscoplastic models for clay based on the concepts of the Cam-Clay model. Thus, Adachi *et al*. [ADA 82] developed a viscoplastic version of the initial Cam-Clay model, keeping the expressions of the yield surface and the plastic potential, as well as the hardening variable ε_v^p. They assumed an associated flow rule and considered an exponential function for the viscous nucleus ϕ:

$$\phi(F) = c_0 \exp(m'F)$$

$$m' = (\lambda - \kappa)/c_\alpha(1 + e)$$

Figure 7.20 shows simulations given by the model for undrained triaxial creep tests.

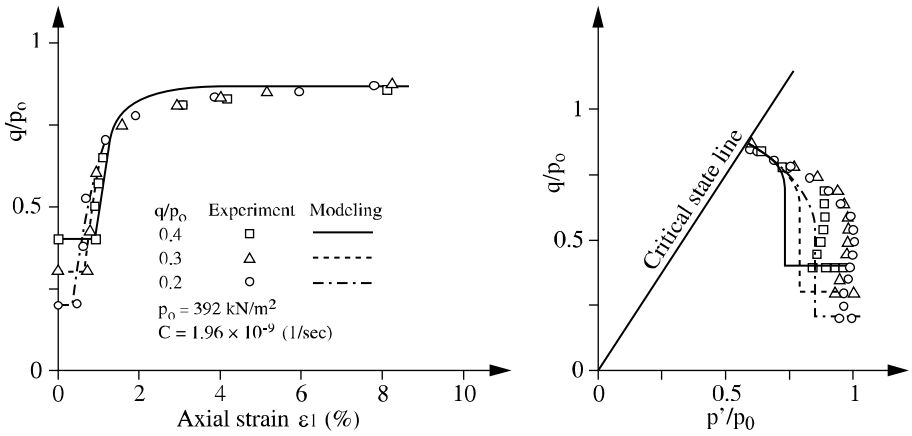

Figure 7.20. *Comparison between experimental data and numerical simulations by Adachi et al. model [ADA 82]*

Recently, Yin *et al*. [YIN 06, YIN 07] developed a viscoplastic version of the modified Cam-Clay model with the purpose of developing inverse methods for *in situ* identification of soil viscous parameters (see Chapter 11). The authors define a static yield criterion "f_s" which represents a reference yield surface for the material. Its initial shape depends on the consolidation pressure "p_c^s". The expansion of the static yield surface, which represents the hardening of the material, is expressed by the variation of the consolidation pressure due to the inelastic volumetric strain "ε_v^{vp}":

$$\partial p_c^s = p_c^s \cdot \frac{1+e_0}{\lambda-\kappa} \cdot \partial \varepsilon_v^{vp}$$

or

$$p_c^s = p_{c0} \cdot \exp\left(\frac{1+e_0}{\lambda-\kappa}\varepsilon_v^{vp}\right) = p_{c0} \cdot \exp\left(\frac{1}{\beta^*}\varepsilon_v^{vp}\right)$$

A dynamic yield criterion "f_d" is defined to represent the current state of stress and is expressed as follows:

$$f_d = \frac{q^2}{M^2} + p' \cdot (p' - p_c^d) = 0$$

Based on the values of "p_c^s" and "p_c^d", the scaling function "μΦ(F)", which controls the amplitude of the viscoplastic strain rate, is taken as a power form or exponential form as follows:

$$\mu \cdot \phi(F) = \mu \cdot \left(\frac{p_c^d}{p_c^s} - 1\right)^N$$

or

$$\mu \cdot \phi(F) = \mu \cdot \left(\exp\left[N \cdot \left(\frac{p_c^d}{p_c^s} - 1\right)\right] - 1\right)$$

where, "μ" and "N" are the viscous parameters of the model. The exponential type of function is closer to the test results which show that the stress evolution for a given deformation is quite proportional to the logarithmic strain rate Furthermore, it allows us to limit the increase of the deviatoric stress with the strain rate, which therefore enlarges the domain of application of the viscoplastic model, as already pointed out by Fodil *et al*. [FOD97].

The flow rule for the viscoplastic strain rate, in a simple case of infinitesimal strain field, follows the form proposed by Perzyna:

$$\dot{\varepsilon}_{ij}^{vp} = \mu\langle\phi(F)\rangle\frac{\partial f_d}{\partial\sigma'_{ij}}$$

where the MacCauley function is: $\langle F\rangle = \begin{cases} 0 \cdot for \cdot F \le 0 \\ F \cdot for \cdot F > 0 \end{cases}$.

The principles of the model are illustrated by the effective stress path of an undrained triaxial test presented in Figure 7.21. The stress state "A" represents an initially normally K'$_0$ consolidation state. Along the loading stress path "A-B-C", viscoplastic volumetric strains occur during loading and cause the static yield surface to expand in the stress space. As point C approaches C', corresponding to the critical state, the soil is subjected to a constant amount of overstress which provokes an increase of the deviatoric strain at constant strain rate, without any volumetric strain.

As for the creep stress path "B-D", the static yield surface expands with the time-dependent plastic volumetric strain, function of the amount of overstress. If the static yield surface can reach the actual stress point, an equilibrium is obtained and the strain will stabilize with time. If not, the effective stress will continue to evolve until it reaches the critical state at point D' where it will stop because no plastic volumetric strain will develop, but deviatoric strain will continue to increase.

Taking into account the elastic stress-strain relations, the constitutive equations of the viscoplastic model for normally consolidated clays are derived as follows:

$$\dot{\varepsilon}_{ij} = \frac{\dot{s}'_{ij}}{2G} + \frac{\dot{p}'}{3K} + \mu\langle\phi(F)\rangle\left(\frac{3s'_{ij}}{M^2} + \left(2p' - p_c^d\right)\frac{\delta_{ij}}{3}\right)$$

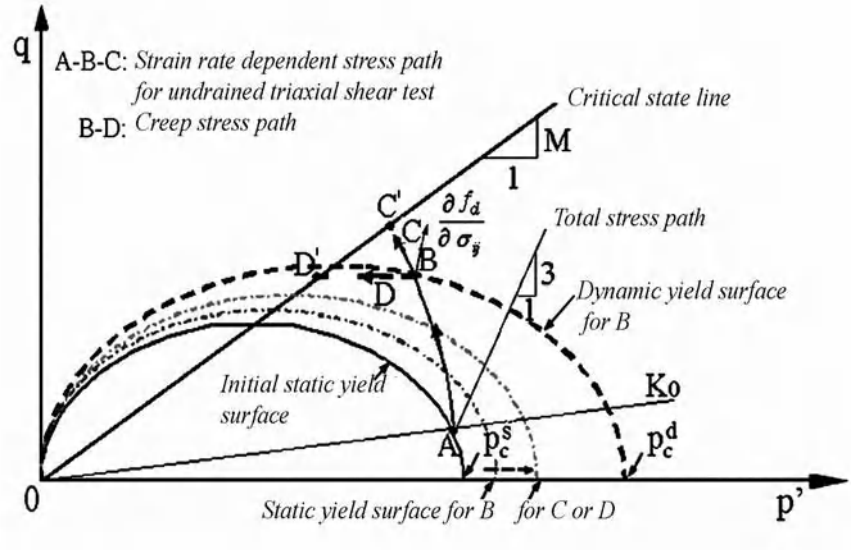

Figure 7.21. *Schematic behavior of the elasto-viscoplastic modified Cam-Clay model during CAU triaxial compression and triaxial creep tests*

The comparison between experimental [HIN 96] and numerical results, presented in Figure 7.22, shows a good agreement in the evolution of the deviatoric stress as well as in the excess pore pressure response during undrained triaxial tests at different strain rates.

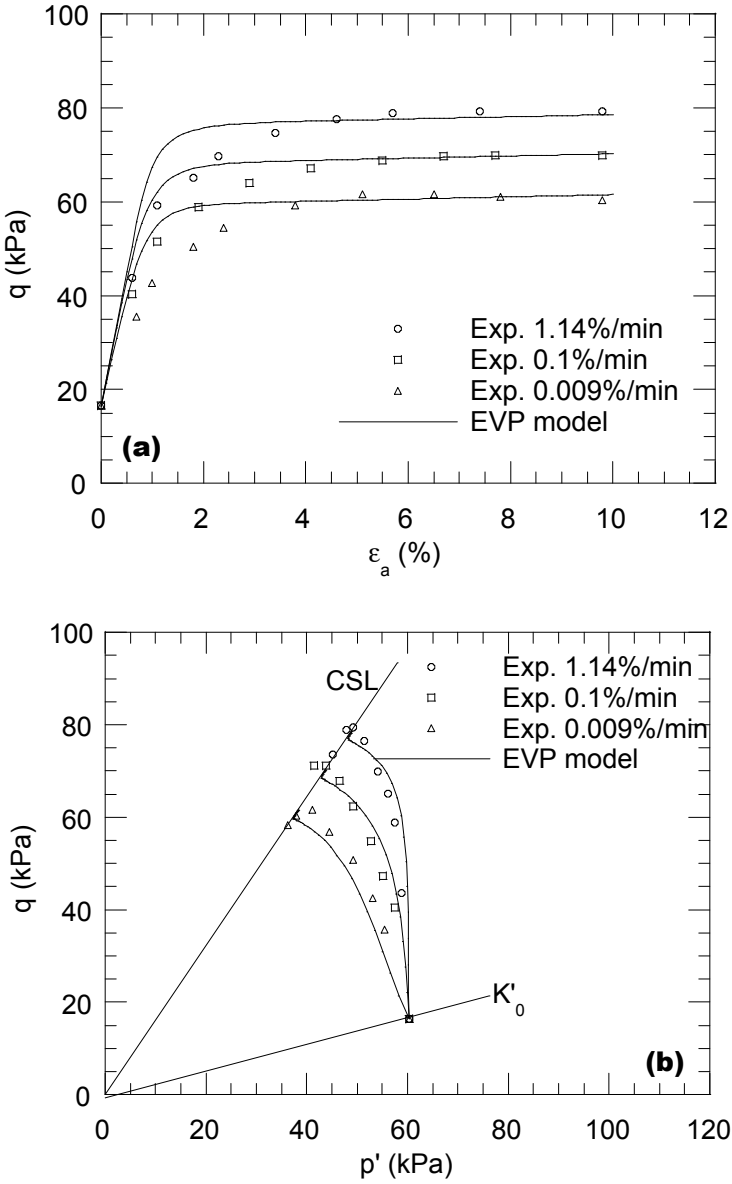

Figure 7.22. *Comparison between predicted and experimental results for constant strain rate triaxial tests on Sackville clay*

The evolution of the normalized maximal deviatoric stress q_{max}* (maximal deviatoric stress for each rate divided by the one corresponding to the greatest strain rate) as a function of the strain rate, presented in Figure 7.23, shows the effect of the strain rate on the undrained shear strength. The experimental results correspond to constant strain rate tests on remolded Haney clay under strain rates varying from 0.0001 to 10%/min [VAI 77] and on undisturbed Osaka alluvial clay under strain rates of 1, 0.021 and 0.00078%/min [ADA 85]. For tests with medium-sized strain rates, the strain rate effect can be represented by the relationship proposed by Sheahan *et al*. [SHE 96]:

$$\frac{q_{f,a}}{q_{f,a0}} = 1 + \rho_{a0} \cdot \log\left(\frac{\dot{\varepsilon}_a}{\dot{\varepsilon}_{a0}}\right)$$

where the indexes a and a_0 represent two values corresponding to two different strain rates; q_f, the undrained shear strength and ρ_{a0}, a strain rate parameter.

As shown in Figures 7.22 and 7.23, the model can take into account the strain rate effect on the undrained shear strength in a large range of strain rate, as well as the decrease of this effect for small values of the strain rate (Haney clay samples).

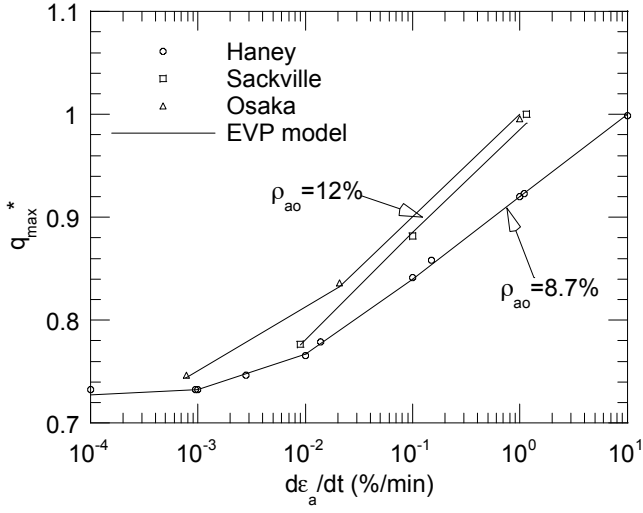

Figure 7.23. *Comparison between predicted and experimental results for constant strain rate triaxial tests*

Figure 7.24 shows numerical simulations of undrained creep tests on Sackville clay. For low applied stress, the strain increases slowly and seems to converge toward a stabilized value, as for a higher applied stress the strain rate is higher and the strain continues to increase with time. Pore pressure increases with time and converges toward a stabilized value, dependent on the applied deviatoric creep stress.

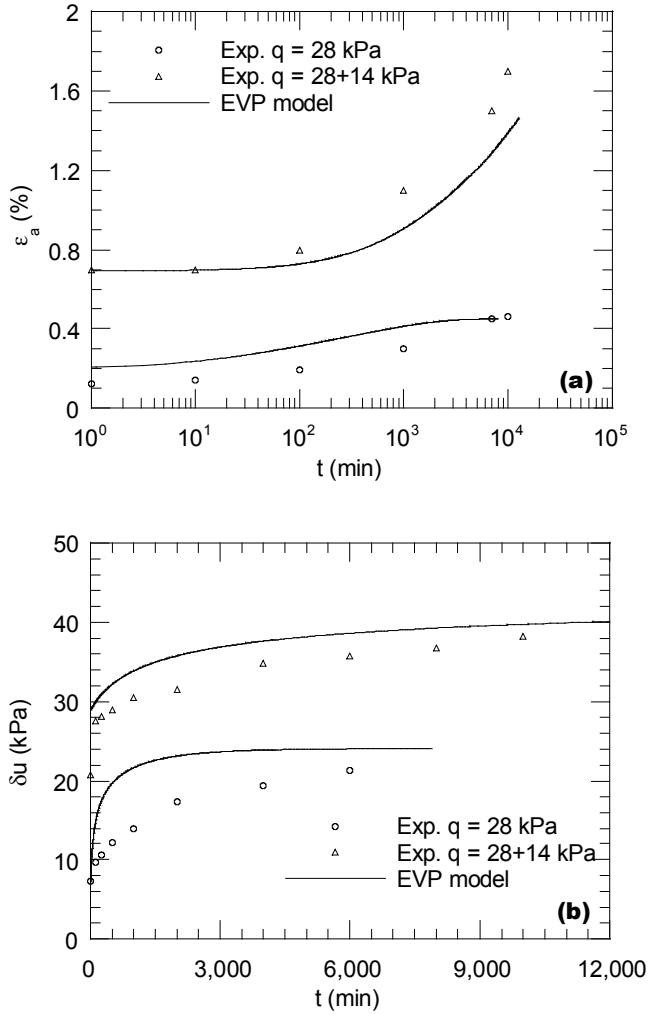

Figure 7.24. *Comparison between predicted and experimental results for creep triaxial tests on Sackville clay*

Results of stress-relaxation tests on Flumet clay in a triaxial apparatus are provided by Fodil *et al*. [FOD 97]. An initial loading with an axial strain rate of 0.15%/h was applied. The stress-relaxation tests were then performed on the same sample for each test at about 1%, 3.5% and 6.7% of axial strain and lasted at least 24 h. The viscoplastic model predicts the results of the stress-relaxation tests reasonably well in terms of deviatoric stress decrease versus time, as shown in Figure 7.25.

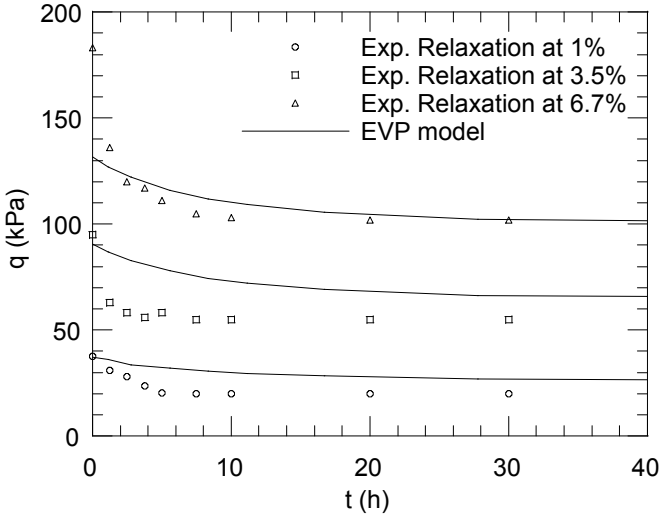

Figure 7.25. *Comparison between predicted and experimental results for stress relaxation tests on Flumet clay*

Kodaissi [KOD 83] has developed a viscoplastic model based on the elastoplastic Hujeux's model, which has introduced a second hardening variable linked to the deviatoric plastic strain ε_d^p in the yield function of the Cam-Clay model:

$$f(\sigma,\alpha) = q - Mp\,(1 - b\,\mathrm{Ln}\,p/p_c)\,\varepsilon_d^p\,/(a + \varepsilon_d^p)$$

The plastic potential function is the same as in the Cam-Clay model:

$$g(p,q) = q/Mp + \mathrm{Ln}\,p$$

The direction of the plastic strain increment is given by the normal to the plastic potential surface at the actual stress state. The overstress F is equal to the value of $f(\sigma, \alpha)$ where σ is the actual state of stress. ϕ is a power function of F:

$$\phi(F) = (f(\sigma,\alpha)/f_0)^n$$

The evolution laws of the two hardening variables are:

$$d\alpha_v = d\varepsilon_v^p - H_v/\eta_2 \, \alpha_v$$

$$d\alpha_d = d\varepsilon_d^p - H_d/\eta_2 \, \alpha_d$$

with $H_v = \partial f/\partial \varepsilon_v^p = \beta \, Mp \, \varepsilon_d^p/(a + \varepsilon_d^p)$

and $H_d = \partial f/\partial \varepsilon_d^p = a \, Mp \, (1 - Ln \, p/p_c)/(a + \varepsilon_d^p)^2$

The viscoplastic strain increment takes the following form:

$$d\varepsilon^{vp} = 1/\eta_1 < (f(\sigma, \alpha_v, \alpha_d)/f_0)^n > \psi(\sigma, \alpha_v, \alpha_d)$$

where $\psi(\sigma, \alpha_v, \alpha_d)$ is the plastic potential gradient.

Therefore, the viscosity is controlled by three parameters: n, η_1 and η_2. The parameter determination is carried out in two steps: firstly, the determination of the parameters common to the elastoplastic and viscoplastic models from triaxial and oedometer tests performed at small strain rate; secondly, the determination of the viscous parameters by curve fitting from test results which allow us to isolate the viscous behavior, such as in drained creep tests.

Figures 7.26 and 7.27 show some examples of simulations. We can see that the model can represent reasonably well drained and undrained creep tests, leading to strain and pore pressure stabilization.

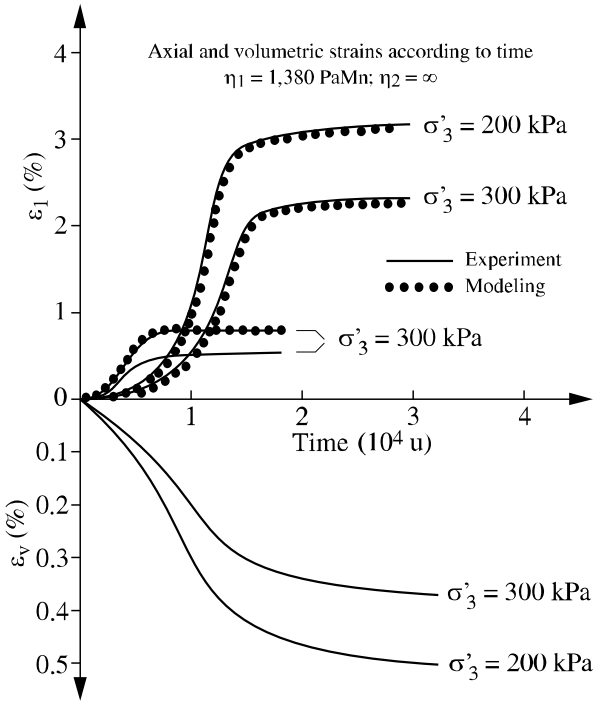

Figure 7.26. *Comparison between experimental data and numerical simulations of a drained creep test by Kodaissi model [KOD 93]*

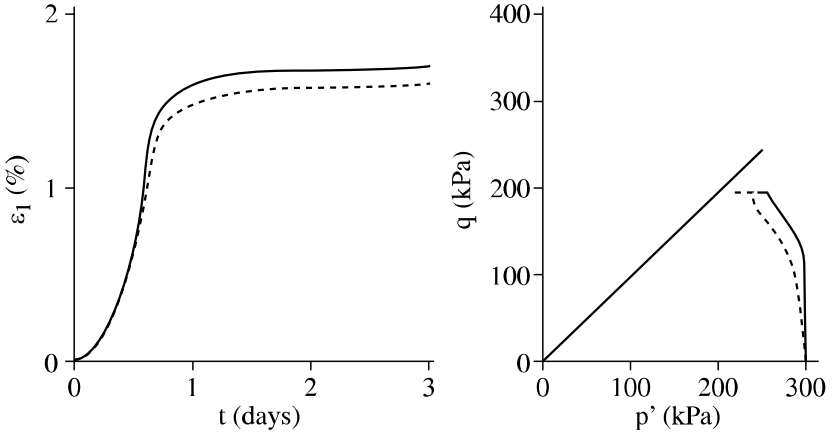

Figure 7.27. *Comparison between experimental data and numerical simulations of an undrained creep test by Kodaissi model [KOD 93]*

7.5.3. *Cyclic viscoplastic modeling*

A viscoplastic version of Hujeux's multimechanism elastoplastic model (see Chapter 4) has been developed by Aubry *et al*. [AUB 86] in order to reproduce time-dependent behavior during cyclic loading. The viscoplastic strain increments corresponding to each deviatoric mechanism *k* are written:

$$d\varepsilon_{dk}^{vp} = < (f_k/f_0)^n > \psi_k^d$$

$$d\varepsilon_{vk}^{vp} = < (f_k/f_0)^n > \psi_k^v$$

The evolution law of the hardening variable r_k linked to the deviatoric plastic deformations of each mechanism *k* is given by:

$$dr_k = < (f_k/f_0)^n / \mu_d > (1 - r_k)^2/a$$

The isotropic mechanism produces purely isotropic viscoplastic deformations:

$$d\varepsilon_v^{vp} = < (f_4/f_0)^n / \mu_v > p/3dp_c$$

The viscous properties are introduced by means of the three parameters n, μ_d and μ_v. Figure 7.28 shows the modeling of the strain rate influence during undrained triaxial testing. Figures 7.29 and 7.30 present simulations of cyclic tests performed by the model.

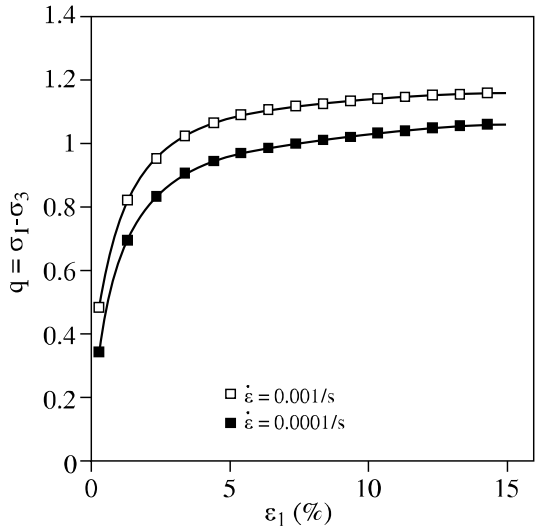

Figure 7.28. *Strain rate influence during an undrained triaxial test [AUB 86]*

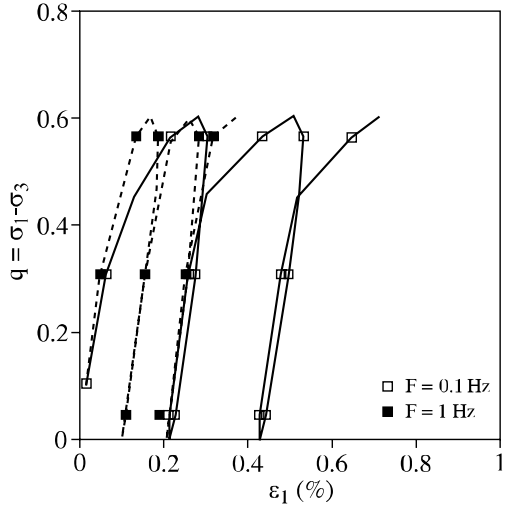

Figure 7.29. *Undrained cyclic triaxial tests: influence of the cycle frequency [AUB 86]*

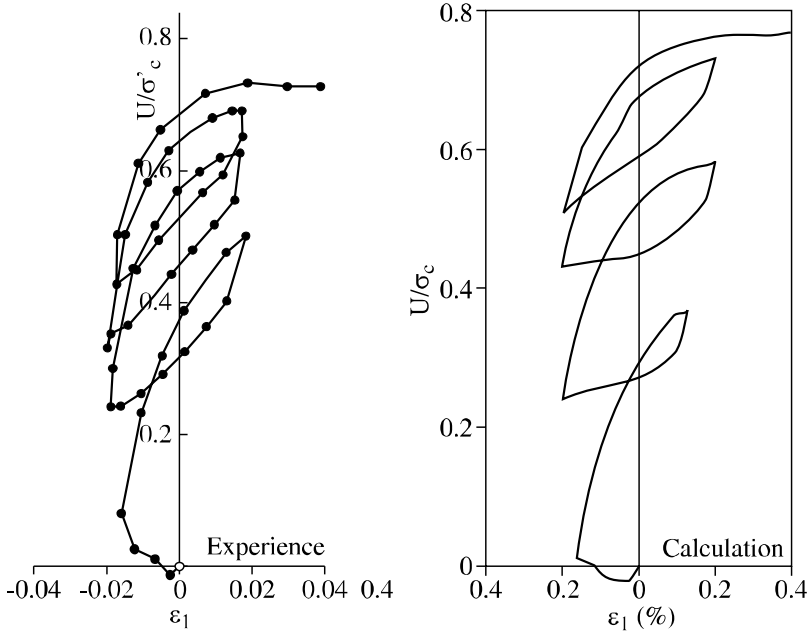

Figure 7.30. *Undrained cyclic triaxial test on Karlsruhe Clay: relation between axial strain and pore pressure [AUB 86]*

7.6. Conclusion

Laboratory and *in situ* testing have shown the viscous behavior of fine soils. More recent works [TAT DIB] have also demonstrated that granular materials, such as sands, also have a time-dependent behavior, even if the amplitude of the strain evolution with time is less marked than in clay. Most of the developed models adapted for describing the clay's viscous behavior use an implicit formulation of the time-dependency through the evolution of the hardening variables. Among them, models using Perzyna's overstress theory are the more numerous, since this approach links in a straightforward manner elastoplasticity and viscoplasticity through the definition of a yield surface and a plastic potential function, and can also be easily implemented in finite elements codes. The examples presented here have shown that these models can reproduce in a satisfactory way monotonic as well as cyclic loading. However, their use for modeling real civil engineering structures still remains limited, mainly due to the necessary calibration of the model which requires additional parameters in comparison to a similar elastoplastic model.

7.7. References

[ADA 82] Adachi T., Oka F. "Constitutive equations for normally consolidated clay based on elasto-viscoplasticity", *Soils and Foundations*, vol. 22, pp. 57-70, 1982.

[ADA 85] Adachi T., Mimura M., Oka F. "Descriptive accuracy of several existing constitutive models for normally consolidated clays", *Proceedings of the Fifth International Conference on Numerical Methods in Geomechanics*, Nagoya, vol. 1, p 259-266.

[AKA 75] Akai K., Adachi T., Ando N., "Existence of a unique stress-strain-time relation for clays", *Soils and Foundations*, 15, pp. 1-16, 1975.

[AKA 77] Akai K., Adachi T., Nishi K., "Mechanical properties of soft rocks", *Proc., IX ICSMFE*, Tokyo, pp. 7-10, 1977.

[AUB 86] Aubry D, Kodaissi E., Meimon Y., "A cyclic viscoplastic constitutive equation for soils with kinematical hardening", *2nd International Symposium on Numerical Models in Geomechanics*, Ghent, Belgium, 1986.

[BIO 41] Biot M. A., "General theory of three dimensional consolidation", *Journal of Applied Physics*, 12, pp. 155-164, 1941.

[BIS 69] Bishop A. W., Lovenburry H. T., "Creep characteristics of two undisturbed clays", *VII ICSMFE*, Mexico 1969.

[BOR 85] Borja R. I., Kavazanjian E., "A constitutive model for the stress-strain behavior of wet clays", *Géotechnique*, vol. 35, pp. 283-298, 1985.

[BJE 67] Bjerrum L., "Engineering geology of Norwegian normally consolidated marine clays as related to the settlement of buildings", *Géotechnique*, vol. 17, pp. 83-118, 1967.

[DES 87] Desai C. S., Zhang S., "Viscoplastic model for geologic materials with generalized flow rule", *Inter. J. for Num. and Anal. Meth. in Geomechanics*, vol. 11, no. 6, pp. 603-620, 1987.

[FOD 97] Fodil A., Aloulou W., Hicher P.-Y. "Viscoplastic behaviour of soft clay", *Geotechnique*, 47, no. 3, pp. 581-591, 1997.

[FOD 98] Fodil A., Etude du comportement mécanique d'argiles naturelles, de l'expérience à la modélisation, Doctoral thesis, Ecole Centrale de Paris, 1998.

[GRA 83] Graham J., Crooks J. H. A., Bell A. L., "Time effects on stress-strain behavior of natural soft clays", *Géotechnique*, vol. 33, pp. 327-340, 1983.

[HIC 85] Hicher P.-Y., Comportement Mécanique des argiles saturées sur divers chemins de sollicitations monotones et cycliques. Application à une modélisation élastoplastique et viscoplastique, Doctoral thesis, University of Paris 6, Paris, 1985.

[HIC 88] Hicher P.-Y., "The viscoplastic behaviour of Bentonite", *Int. Conf. on Rheology and Soil Mechanics*, Coventry, Ed. Elsevier, pp. 89-107, 1988.

[HIN 96] Hinchberger S. D., The behaviour of reinforced and unreinforced embankments on rate sensitive clayey foundations, PhD Thesis, University of Western Ontario, Canada, 1996.

[HUG 78] Huges T. R., Taylor R. L., "Unconditionally stable algorithms for quasi static elastoplastic finite element analysis", *Computer and Structures*, vol. 8, pp. 169-173, 1978.

[JAM 79] Jamiolkowski M. "Design parameters for soft clay", *Proc. VII European CSFE*, Brighton, vol. 5, 1979.

[KAL 85] Kaliakin V. N., Bounding surface elastoplasticity viscoplasticity for soils, PhD dissertation, University of California, 1985.

[KAT 84] Katona M. G., "Evaluation of viscoplastic cap model", *Journal of Geotechnical Engineering*, vol. 110, no. 8, pp. 1106-1125, 1984.

[KOD 83] Kodaissi E., Un modèle de loi de comportement viscoplastique appliqué à la mécanique des sols, Doctoral thesis, Ecole Centrale de Paris, 1983.

[KUT 92] Kutter B. L., Sathialingam N., "Elastic-viscoplastic modeling of the rate-dependent behavior", *Géotechnique*, no. 3, 427-441, 1992.

[LAI 92] Laigle F., Modèles de comportement viscoplastique de l'Ecole Centrale de Paris, report EDF-CNEH, 1992.

[MAT 86] Matsui T., Abe N., "Flow surface model of viscoplasticity for normally consolidated clay", *2nd Int. Symp. on Numerical Models in Geomechanics*, Ghent, pp. 157-164, 1986.

[MES 77] Mesri G., Goldewski P.M., "Time and stress-compressibility interrelationship", *ASCE*, 103, pp. 417-430, 1977.

[MUR 64] Murayama S. and Shibata T., "Flow and stress relaxation of clays", *IUTAM Symp. Rheology and Soil Mechanics*, Grenoble, pp. 99-129, 1964.

[OKA 88] Oka F., "A cyclic viscoplastic constitutive model for clay", *6th Int. Conf. on Numerical Methods in Geomechanics*, Balkema, pp. 293-298, 1988.

[PER 63] Perzyna P., "The constitutive equations for rate sensitive plastic materials", *Q. App. Math*., 20, pp. 321-332, 1963.

[PER 66] Perzyna P., "Fundamental problems in viscoplasticity", *Advances in Applied Mechanics*, vol. 9, pp. 243-377, 1966.

[RUN 99] Runesson K., Ristinmaa M., Mahler L., "A comparison of viscoplasticity formats and algorithms", *Mechanics of Cohesive-frictional Materials*, 4, pp. 75-98, 1999.

[SAN 69] Sandhu R.S., Wilson E.L., "Finite element analysis of flow in saturated porous media", *Proc, Am. Soc. Civ. Eng. 95, EM3*, pp. 641-652, 1969.

[SEK 84] Sekiguchi H. "Theory of undrained creep rupture of normally consolidated clays based on elasto-viscoplasticity", *Soils and Foundations*, 24, no. 1, pp. 129-147, 1984.

[SHE 96] Sheahan T. C., Ladd C. C., Germaine J. T., "Rate-dependent undrained shear behaviour of saturated clay", *ASCE, Journal of the Geotechnical Engineering*, vol. 122, no. 2, pp. 99-108, 1996.

[SHI 69] Shibata T., Karube D., "Creep rate and creep strength of clays", *Proc. VII ICSMFE*, Mexico, pp. 361-367, 1969.

[TAV 78] Tavenas F., Leroueil S., "Creep behavior of an undisturbed lightly overconsolidated clay", Research report, University of Sheerbrocke, 1978.

[VAI 77] Vaid Y. P., Campanella R. G., "Time-dependent behavior of undisturbed clay", *ASCE, Journal of the Geotechnical Engineering*, vol. 103, no. 7, pp. 693-709, 1977.

[VAI 88] Vaid Y. P., "Time dependent shear deformation of clay", *Int. Conf. On Rheology and Soil Mechanics*, Coventry, Ed. Elsevier, pp. 123-138, 1988.

[VAL 71] Valanis K. C., "A theory of viscoplasticity without a yield surface", *Archives of Mechanics*, no. 23, pp. 517-555, 1971.

[WAL 69] Walker L. K., "Secondary compression in the shear of clays", *ASCE, 95, SM1*, pp. 167-188, 1969.

[YIN 99] Yin J. H., Graham J., "Elastic viscoplastic modeling of the time-dependent stress-strain behavior of soils", *Canadian Geotechnical Journal*, 36, pp. 736-745, 1999.

[YIN 06] Yin Z. Y., Modélisation viscoplastique des argiles naturelles et application au calcul de remblais sur sols compressibles, Thesis, l'Ecole Centrale de Nantes and University of Nantes.

[YIN 07] Yin Z. Y., Hicher P.-Y., "Identifying parameters controlling soil delayed behaviour from laboratory and in situ pressuremeter testing", *International Journal for Numerical and Analytical Methods in Geomechanics*, 2007.

[ZIE 74] Zienkiewicz O. C., Cormeau I. C., "Viscoplasticity, plasticity and creep in elastic solids – a unified numerical approach", *International Journal for numerical methods in Engineering*, vol. 8, pp. 821-845, 1974.

[ZIE 75] Zienkiewicz O. C., Humpheson C, Lewis R. W., "Associated and non associated viscoplasticity and plasticity in soil mechanics", *Géotechnique*, vol. 25, no. 4, pp. 671-689, 1975.

Constitutive Modeling of Soils and Rocks
Edited by Pierre-Yves Hicher & Jian-Fu Shao

Chapter 8

Damage Modeling of Rock Materials

8.1. Introduction

In quasi-brittle rock materials exhibiting fracturing [DAR 95], non-linear mechanical behavior can be determined from the kinetics of pre-existent and/or loading initiated mesocracks. The term "meso", traditionally used to designate the intermediate scale between "macro" and "micro", is currently used to indicate that the scale of defects and the related representative volume are accessible to the naked eye. However, this term should be handled rather carefully. In fact, among sandstone, limestone and granite, which could be classed in the family of quasi-brittle rocks, and also different concretes which are considered mechanically similar, there are a number of discriminating factors related to the geological formation in the case of rocks and to the manufacturing process in the case of concrete. This implies that there are different types of microcracks from one material to another and that various physico-chemical mechanisms play a role in deformation and microcracking.

Selecting either "macro" and "meso" scales depends also on the nature of the engineering problem which needs to be solved. In the context of constitutive laws including damage effects, a representative volume (a material point of structure body) is generally measured in centimeters whereas the size of heterogenities (grains, defects) is in millimeters. This situation corresponds to laboratory testing conditions and generally used sample sizes. Transposing laboratory results and their derived constitutive models to the scale of rock massifs measured in kilometers involves not only a rigorous scale analysis but also the fine art of engineers. In its

Chapter written by André DRAGON.

basic equations, continuum mechanics does not explicitly invoke the notion of scale, but the scale analysis has become essential today whenever constitutive modeling of heterogenous real materials, such as natural rocks or man-made concrete, is concerned.

Furthermore, the word “damage” which invokes volumetric or surface meso and micro defects inside the representative volume of a considered material acquires particular methodological significance in the field of damage mechanics, a discipline which has been developed since the 1960s whose objective is to include the phenomena of progressive deterioration in the description of the thermomechanical state of a medium and its evolution.

This discipline is based on the thermodynamics of irreversible processes where the dissipative evolutions (such as viscoplasticity with its hardening mechanisms, and the deterioration which is of interest here) are described with so-called internal variables; their values at time t summarize, condense and characterize the inelastic response of the medium. Readers interested in a greater description of this methodology, widely dominant in the fields of plasticity, viscoplasticity, and extended to certain domains of fracture mechanics, can refer to the papers by [BAT 75], [GER 83]. The internal state variables are involved only in constitutive relations; they are not involved in equilibrium relations or in boundary conditions. These internal variables are generally not controllable in standard laboratory tests; in most cases, they represent quantities related to the endured phenomena. Internal variables may possibly be characterized quantitatively, but the corresponding microstructures must be deeply examined, which means that the phenomenon to be studied must be captured in a fixed configuration by the use of pertinent instruments.

For example, we can observe with a scanning electron microscope (SEM) inter- and intragranular phenomena in crystalline materials (configurations of dislocations, microcracks) for a given state of plastic hardening after unloading and a careful sample preparation. Today, it is even possible to perform mechanical tests inside the SEM so that we can observe the mechanisms in evolution.

For a given mesofissuration state within a brittle material, we can approach the *in situ* damage by examining the mesostructure and by counting the number of cracks in a part of the specimen. This provides a better evaluation of the applied theoretical scheme as compared to the existing mechanisms. The choice of internal variables is very crucial; it always represents a compromise between the existing physical phenomena and the degree of complexity of the model. Internal variables are also called “hidden variables”, because they are not directly accessible under a phenomenological approach. They are assumed to express the material evolution at the meso- and microstructural scales during the evolution of a dissipative process.

Damage mechanics, as part of the non-linear mechanics of materials and structures, has undergone several stages of development, some successful and others not. Nowadays, the purely phenomenological approach seems less popular. At the same time, the purely micromechanical approach, using homogenization techniques for the transition from microscale to macroscale, leads to models which appear interesting but are frequently limited to specific loading paths. Furthermore, they are usually not applicable for modeling large geotechnical structures without adaptations which take them too far from their initial microstructural hypotheses.

Another problem is identifying their parameters as well as their validation in a context different from the one used for their formulation.

This chapter is devoted to an approach to modeling non-linear phenomena specific to pseudo-brittle geomaterials and linked to the development of mesocracks. This approach will be formulated in the framework of damage mechanics with internal variables, in order to propose a three-dimensional rigorous description of the irreversible evolutions and to include micromechanical knowledge within a relatively simple description, identifiable and applicable to the calculation of geotechnical structures for the petroleum industry, energy disposals, civil engineering, etc. The main idea is to propose an intermediary direction and a synthesis between, on the one hand, entirely phenomenological approaches and, on the other hand, entirely micromechanical approaches. Furthermore, knowing that the difficulty of modeling the behavior of quasi-brittle materials resides in the large number of phenomena involved, such as volumetric dilatancy, induced anisotropy, irreversible deformations, hysteretic effects due to the closing of the mesocracks and the friction along the closed mesocracks, we will propose here a modeling with an architecture that includes three levels of complexity as follows:

– a first level describing, in the framework of an internal variables approach, the progressive degradation through mesofissuration of quasi-brittle geomaterials, inducing an anisotropic behavior, a volumetric dilatancy and macroscopic effects such as irreversible deformations;

– a second level adding a rigorous analysis of the phenomenon which restores certain initial properties, such as the elastic moduli in directions perpendicular to the closed mesocracks, due to the closing of the defects. We can say that this level corresponds to the modeling of a “unilateral normal” behavior;

– a third level accounting for the modeling of the behavior linked to frictional effects (blocking and dissipative sliding) that concern the two sides of the closed mesocracks. At this level, the constitutive equations are similar to formulating anisotropic plasticity and are coupled to the two first levels in order to link sliding to damage.

The whole model forms a 3D theory, coupling plasticity and damage. It can be seen as a particular expression of the general non-linear theory proposed by Lubarda and Krajcinovic [LUB 95] for a large class of engineering materials.

The first level of modeling will be presented in section 8.2 and the second and third levels in section 8.3. Section 8.4 will present some aspects of the mathematical formulation of each level and of the coupled model, as well as some applications in geomechanics. The formulation at each level will be compared to experimental data corresponding to physical problems in relation to the considered level.

Throughout the chapter, the normal components of the stress and strain tensors, corresponding respectively to the tension and the extension, are considered to be positive. The hypothesis of small deformations is assumed and is considered acceptable in the context of pseudo-brittle materials, even if their deformability is much higher under compressive loading, especially for high confinements, rather than under tension.

8.2. Modeling of damage by mesocracks and induced anisotropy

Cohesive pseudo brittle geomaterials are characterized by a specific inelastic deformation mechanism resulting from nucleation and growth of mesocracks under mechanical loading. Its orientation-dependent character leads to the apparition of induced anisotropy if the material is initially isotropic. Otherwise, initial anisotropy (formation, manufacture) interacts with induced anisotropy, which produces a complex superimposed and possibly evolving anisotropy.

In the following section, we will consider an initially isotropic material. Anisotropy will be induced by a set of parallel mesocracks under loading. The induced anisotropy can evolve with damage progress. Particular care is needed in choosing the internal damage variables in order to take into account the induced anisotropy.

8.2.1. Preliminaries: damage variables and some micromechanical bases

The damage variable in question must reflect, in its mathematical form, the essential features of the damage mechanism considered, particularly the orientations and the density of mesocracks. It has been proven [DRA 94] that a reasonable approximation can be obtained by using a second order damage tensor. A set of parallel plane cracks is generally characterized by its orientation (unit normal vector $\underline{n}$) and the discontinuity surface area inside the representative volume. Based on the dimensionless assumption of defect density, which is necessary, among

others reasons, for assuring geometrical and mechanical similarity between samples and structures of different sizes, and in relation to certain micromechanical analyses [KAC 80], the following scalar quantity is proposed:

$$d(S) = \eta \frac{\sum_{k=1}^{N} S_{(k)}^{3/2}}{|V|} \tag{8.1}$$

where $S_{(k)}$ represents the area of the kth crack, $|V|$ a measure of representative volume and η a proportionality factor. For penny-shaped cracks with radius $a_{(k)}$, density $d(S)$ coincides with the standard crack density r^c:

$$d(S) = r^c = \frac{\sum_{k=1}^{N} a_{(k)}^3}{|V|} \tag{8.2}$$

with $S_{(k)} = \pi\, a_{(k)}^2$ and $\eta = \left(\pi\sqrt{\pi}\right)^{-1}$.

The preceding postulates lead to the following form of damage variable $\underline{\underline{D}}$, respectively, for one or several sets of mesocracks:

$$\underline{\underline{D}} = d(S)\, \underline{n} \otimes \underline{n} \qquad (j = 1) \tag{8.3}$$

$$\underline{\underline{D}} = \sum_{j} d^{(j)}(S)\, \underline{n}^{(j)} \otimes \underline{n}^{(j)} \tag{8.4}$$

Symbol "$\otimes$" denotes a dyadic tensor product: $n \otimes n$ corresponds to $n_i n_j$ in index notation.

Expression (8.4) signifies that $\underline{\underline{D}}$ is a second order tensor with real components. Accordingly, there exists a system of orthogonal eigenvectors $(\underline{v}^{(1)}, \underline{v}^{(2)}, \underline{v}^{(3)})$ associated with three positive eigenvalues $D_{(1)}, D_{(2)}, D_{(3)}$. In this coordinate system, the damage tensor is expressed by:

$$\underline{\underline{D}} = \sum_{k=1}^{3} D_{(k)}\, \underline{v}^{(k)} \otimes \underline{v}^{(k)} \tag{8.5}$$

This form can be interpreted – with respect to that of (8.4) – in the following way: any configuration of mesocracks is equivalent, when condensed in a damage variable of the (8.4) type, to a set of three orthogonal systems of parallel mesocracks.

Form (8.4) is thus restrictive (see also the analyses by Onat and Leckie, [ONA 88] and by Lubarda et Krajcinovic, [LUB 93]). It is nevertheless also physical as it is issued from micromechanical analyses. We briefly summarize as follows some elements of such analyses.

Consider a representative elementary volume (REV) in which mesocracks are embedded. The characteristic length of mesocracks is much smaller than that of the REV. The overall (macroscopic) strain of the REV is the sum of the strain of the intact solid matrix $\underline{\underline{\varepsilon}}^{o}$ (assumed here to be elastic with the stiffness tensor $\mathbb{C}^{O}$) and that contributed by mesocracks $\underline{\underline{\varepsilon}}^{c}$:

$$\underline{\underline{\varepsilon}} = \mathbb{C}^{o^{-1}} : \underline{\underline{\sigma}} + \frac{1}{2|V|}\sum_{i}\left(<\underline{b}>\otimes \underline{n} + \underline{n}\otimes<\underline{b}>\right)^{(i)} S_{(i)} = \underline{\underline{\varepsilon}}^{o} + \underline{\underline{\varepsilon}}^{c} \tag{8.6}$$

The symbols ":" and "." denote the contraction products between two tensors or between tensor and vector. Vector $\underline{b}^{(i)}$ represents a displacement discontinuity along the surfaces of the ith mesocracks: $\underline{b} = [\underline{u}]^{(i)}$. Bracket $<\underline{b}>^{i}$ denotes the average of $\underline{b}$ for the meso-surface of discontinuity S^{i}. The value of $<\underline{b}>$ may be related to macroscopic stresses as follows [KAC 92]:

$$<\underline{b}>^{(i)} = \underline{\underline{B}}^{(i)} . \underline{\underline{\sigma}} . \underline{n}^{(i)} \tag{8.7}$$

where $\underline{\underline{B}}^{(i)}$ is the compliance tensor of ith cracks. Its components can be obtained in some specific 2D and 3D cases.

By contracting (8.6) with $\underline{\underline{\sigma}}$, and after expressing $<\underline{b}>^{(i)}$ with the help of (8.7), we obtain the very useful expression of elastic energy (here the free enthalpy u) of a cracked elastic solid. Consider the penny-shaped cracks for which the expression of $\underline{\underline{B}}$ can be obtained in a 3D elastic solid (see [KAC 92]), we can then explicitly calculate the change of elastic energy contributed by mesocracks:

$$\Delta u = \Delta u\left(\underline{\underline{\sigma}}, \underline{\underline{D}}, \overline{\mathbb{D}}\right) = \frac{8\ \left(1-\nu_o^2\right)}{3E_o\left(1-\nu_o/2\right)}\left[\underline{\underline{D}}:\left(\underline{\underline{\sigma}}.\underline{\underline{\sigma}}\right)-\frac{\nu_o}{2}\underline{\underline{\sigma}}:\overline{\mathbb{D}}:\underline{\underline{\sigma}}\right]$$

$$= \Delta u^1\left(\underline{\underline{\sigma}}, \underline{\underline{D}}\right) + \Delta u^2\left(\underline{\underline{\sigma}}, \overline{\mathbb{D}}\right) \tag{8.8}$$

with $\underline{\underline{D}}$ defined by (8.4) and $\overline{\mathbb{D}}$ in the following form:

$$\overline{\mathbb{D}} = \sum_i d^{(i)}(S)\,\underline{n}^{(i)} \otimes \underline{n}^{(i)} \otimes \underline{n}^{(i)} \otimes \underline{n}^{(i)} \quad ; \quad d^{(i)} = \frac{1}{\pi\sqrt{\pi}}\frac{S_{(i)}^{3/2}}{|V|} \tag{8.9}$$

where E_o and ν_o are, respectively, Young's modulus and Poisson's ratio for the intact material.

We can see that the rigorous description of mesocrack effects on mechanical behavior requires two internal variables to be introduced in the elastic energy function, a second order tensor and a fourth order tensor. Note that, in the general 3D case where mesocracks are free to open, an energy approach using only the second order tensor $\underline{\underline{D}}$, without being rigorous, can provide a satisfactory approximation of the effective properties of cracked materials. However, when the case of closed cracks is considered, such as the case under compression-dominant stresses where mesocracks in certain orientations are forced to remain closed, the previous conclusion is no longer valid. In fact, when the opening component of $<\underline{b}>$ vanishes, only the tangential component remains. The expression of Δu becomes:

$$\Delta u = \Delta u\left(\underline{\underline{\sigma}}, \underline{\underline{D}}, \overline{\mathbb{D}}\right) = \frac{8\left(1-\nu_o^2\right)}{3E_o\left(1-\nu_o/2\right)}\left[\underline{\underline{D}}:(\underline{\underline{\sigma}}.\underline{\underline{\sigma}})-\underline{\underline{\sigma}}:\overline{\mathbb{D}}:\underline{\underline{\sigma}}\right] \tag{8.10}$$

Note the absence of the factor $\nu_o/2$ before the term $\sigma:\overline{\mathbb{D}}:\sigma$. As a consequence, and differently from case (8.8), the contribution of the term in $\overline{\mathbb{D}}$ to the effective compliance can no longer be neglected. Extended description is thus needed to take into account the unilateral effects due to the closure of mesocracks. This aspect, an important contribution of micromechanics as a guideline for phenomenological modeling, will be discussed in section 8.3.

The preceding analysis invokes a particular representation of elastic energy, which is a function of stress tensor $\underline{\underline{\sigma}}$ (free enthalpy *u*), while in the constitutive model to be developed in the next section, a strain-based formulation will be

adopted using the free energy function w. The relation between the two formulations is obtained by Legendre's transform:

$$w\left(\underline{\underline{\varepsilon}}, \underline{\underline{D}}, \overline{\mathbb{D}}\right) = -u\left(\underline{\underline{\sigma}}, \underline{\underline{D}}, \overline{\mathbb{D}}\right) + \underline{\underline{\sigma}} : \underline{\underline{\varepsilon}} \tag{8.11}$$

Parameters $\underline{\underline{D}}$ and $\overline{\mathbb{D}}$ being passive variables regarding this transformation, the previous conclusions can be extended to models derived from the thermodynamic potential w, which is the free energy per unit volume.

It is worth noting that the constitutive model, once formulated, will reveal the components of $\underline{\underline{D}}$ through an evolution law. However, we should not interpret these in terms of microscopic density and orientation, (which can cover several morphological configurations at the mesoscale). The definition of $\underline{\underline{D}}$ is justified by micromechanics, but it will be used in a quasi-phenomenological theory. However, the theory constructed in this way presents some advantages with respect to some damage models such as those proposed by Ju [JU 89], Govindjee *et al.* [GOV 95]. In their models, the effective stiffness tensor itself is used as a damage variable, since the damage affects the equivalent elastic stiffness of the material. It seems to be preferable to identify the influence of mesocracks precisely through a micromechanics-based damage variable such as $\underline{\underline{D}}$, rather than to deal with the black box of overall stiffness.

8.2.2. *Anisotropic damage model (basic model – level (i))*

Let us postulate the existence of a thermodynamic potential, formulated as the free energy w, a polynomial function of its arguments $(\underline{\underline{\varepsilon}}, \underline{\underline{D}})$. The following assumptions allow us to specify the particular form of $w(\underline{\underline{\varepsilon}}, \underline{\underline{D}})$:

– without damage, the solid matrix represents isotropic linear elastic behavior. Only as damage evolves, does anisotropic behavior appear with the association matrix-mesocracks. Related to decomposition (8.5) of damage tensor $\underline{\underline{D}}$ into three orthogonal systems, the induced anisotropy has an orthotropic form whose axes coincide with the principal axes of $\underline{\underline{D}}$;

– any simultaneous rotation of the principal directions of $\underline{\underline{\varepsilon}}$ and $\underline{\underline{D}}$ does not affect the expression of the free energy $w(\underline{\underline{\varepsilon}}, \underline{\underline{D}})$, which can be seen as an isotropic invariant. This justifies the use of tensor representation theory in terms of

independent invariants for each of the arguments as well as of the mixed invariants such as $tr(\underline{\underline{\varepsilon}}.\underline{\underline{D}}), tr(\underline{\underline{\varepsilon}}^2.\underline{\underline{D}}), tr(\underline{\underline{\varepsilon}}.\underline{\underline{D}}^2), tr(\underline{\underline{\varepsilon}}^2.\underline{\underline{D}}^2)$ (see [BOE 78] for more details);

– for any given state of damage, the behavior of material with cracks is linear elastic; $\underline{\underline{w}}(\underline{\underline{\varepsilon}}, \underline{\underline{D}})$ is thus at maximum quadratic in $\underline{\underline{\varepsilon}}$. It is assumed that there is no interaction between mesocracks; this implies the linearity of w in $\underline{\underline{D}}$. These two assumptions allow us to eliminate the last two mixed invariants which were previously mentioned;

– the damage itself can produce, according to preferential orientations of mesocracks, residual strains after unloading at $\underline{\underline{\sigma}} = \underline{\underline{0}}$ (and in a dual form residual stresses when $\underline{\underline{\varepsilon}} = \underline{\underline{0}}$). Thus, the expression of free energy w should contain a linear term in $\underline{\underline{\varepsilon}}$ and $\underline{\underline{D}}$: $g\, tr(\underline{\underline{\varepsilon}}.\underline{\underline{D}})$.

According to the preceding assumptions, the free energy function is expressed as follows [DRA 94]:

$$\begin{aligned} w\left(\underline{\underline{\varepsilon}}, \underline{\underline{D}}\right) &= g\, tr\left(\underline{\underline{\varepsilon}}, \underline{\underline{D}}\right) \\ &+ \frac{1}{2}\lambda\left(tr\,\underline{\underline{\varepsilon}}\right)^2 + \mu\, tr\,\underline{\underline{\varepsilon}}^2 \\ &+ \alpha\, tr\left(\underline{\underline{\varepsilon}}.\underline{\underline{D}}\right) tr\,\underline{\underline{\varepsilon}} + 2\beta\, tr\left(\underline{\underline{\varepsilon}}^2.\underline{\underline{D}}\right) \end{aligned} \tag{8.12}$$

Note that for $\underline{\underline{D}} = \underline{\underline{0}}$, expression (8.12) coincides with the free energy function of an isotropic linear solid (λ and μ being Lamé's constants). Constants α and β, introducing the two retained mixed invariants, are related to the degradation of elastic moduli with damage. We will see later (section 8.2.3) that β has a very clear physical meaning related to the diminution of shear modulus in the cracked orthotropic material. Modulus g controls residual effects: during a cycle of tension-compression along the axis x_3 the value of σ_3 for $\varepsilon_3 = 0$ is $\sigma_3 = g\, D_3$, as illustrated in Figure 8.1 and given by the relation $\underline{\underline{\sigma}}(\underline{\underline{\varepsilon}}, \underline{\underline{D}})$ in equation (8.13). Constant α is related to the degradation of Poisson's ratio in some loading paths such as tension with damage evolution.

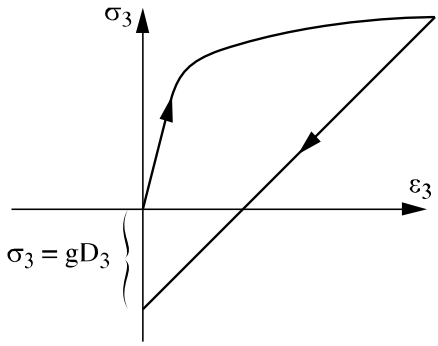

Figure 8.1. *Residual effect during a tension-compression cycle along axis*

By standard derivation of thermodynamic potential (8.12), the state laws which characterize, for $\underline{\underline{D}} \neq \underline{\underline{0}}$, the orthotropic elastic behavior of cracked material and the driving (thermodynamic) force $\underline{\underline{F}}^{D}$ associated with damage can be obtained as follows:

$$\underline{\underline{\sigma}} = \frac{\partial w}{\partial \underline{\underline{\varepsilon}}} = g\,\underline{\underline{D}} + \lambda\left(tr\,\underline{\underline{\varepsilon}}\right)\underline{\underline{1}} + 2\,\mu\,\underline{\underline{\varepsilon}} + \alpha\left[\left(tr\,\underline{\underline{\varepsilon}}\right)\underline{\underline{D}} + tr\left(\underline{\underline{\varepsilon}}.\underline{\underline{D}}\right)\underline{\underline{1}}\right] + 2\beta\left(\underline{\underline{\varepsilon}}.\underline{\underline{D}} + \underline{\underline{D}}.\underline{\underline{\varepsilon}}\right) \quad (8.13)$$

$$\underline{\underline{F}}^{D} = -\frac{\partial w}{\partial \underline{\underline{\varepsilon}}} = -g\,\underline{\underline{\varepsilon}} - \alpha\left(tr\,\underline{\underline{\varepsilon}}\right)\underline{\underline{\varepsilon}} - 2\beta\,\underline{\underline{\varepsilon}}.\underline{\underline{\varepsilon}} \quad (8.14)$$

The damage force $\underline{\underline{F}}^{D}$ physically represents the energy release rate due to mesocrack propagation. Two components can be distinguished; one related to the release rate concerning the residual effects $\underline{\underline{F}}^{D1} = -g\,\underline{\underline{\varepsilon}}$, and the other to the release rate associated with reversible effects $\underline{\underline{F}}^{D2} = -\alpha\,(tr\,\underline{\underline{\varepsilon}})\,\underline{\underline{\varepsilon}} - 2\,\beta\,\underline{\underline{\varepsilon}}.\underline{\underline{\varepsilon}}$.

As in classical plasticity theory and generally for any constitutive models for dissipative phenomena using internal variables, it is necessary to complete state laws (8.12)–(8.14) by complementary relations, which, in the present case, have to respond to the following questions:

"When does the damage evolve?" (→ criterion).

"How does this evolution take place?" (→ evolution law, to determine the form of damage kinetics).

Quasi-brittle materials are characterized by the dominant mechanism of mesocracking as illustrated in Figure 8.2. This so-called "splitting" mechanism is extensively observed even under compressive stresses with moderate confining pressure. Under compressive loading, the crack density is usually quite high compared to tensile loading, for which only a small number of mesocracks are developed and for which instability phenomena occur leading to the sample fracture. However, specific devices have been designed for tensile testing in order to delay bifurcation and better control diffused damage evolution; see Mazars and Berthaud [MAZ 89].

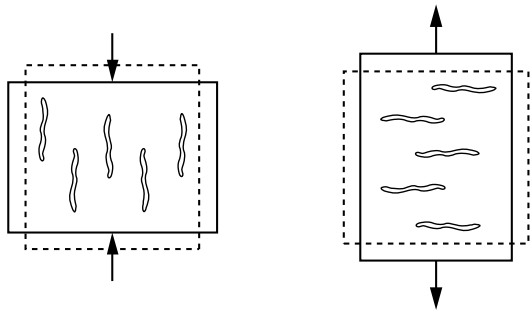

Figure 8.2. *Illustration of kinetics for brittle damage in uniaxial compression (a) and uniaxial tension (b)*

The splitting type kinetics can be defined by the mechanism characterized by formation and propagation of mesocracks in the direction perpendicular to those of tensile strains. This phenomenon motivated several authors to construct a pseudotensor of positive strains $\underline{\underline{\varepsilon}}^{+}$ by extracting positive eigenvalues of the total strain tensor $\underline{\underline{\varepsilon}}$. Consult for example Lubarda *et al.* [LUB 94] for a detailed construction procedure. For this purpose, we introduce the fourth order projector $\mathbb{P}^{+}$. Let $\varepsilon_{(n)}$, n = 1, 2, 3 be the three eigenvalues and $\underline{q}^{(n)}$ eigenvectors of $\underline{\underline{\varepsilon}}$. The projection $\mathbb{P}^{+}$ and the extraction of $\underline{\underline{\varepsilon}}^{+}$ are defined as follows:

$$
\begin{aligned}
&P^{+}_{ijkl} = Q^{+}_{ik}\, Q^{+}_{jl} \qquad with \qquad \underline{\underline{Q}}^{+} = \sum_{n=1}^{3} H\left(\varepsilon_{(n)}\right) \underline{q}^{(n)} \otimes \underline{q}^{(n)} \\
&\underline{\underline{\varepsilon}}^{+} = \mathbb{P}^{+} : \underline{\underline{\varepsilon}} = \sum_{n=1}^{3} H\left(\varepsilon_{(n)}\right) \varepsilon_{(n)}\, \underline{q}^{(n)} \otimes \underline{q}^{(n)}
\end{aligned}
\tag{8.15}
$$

with $H(\,)$ as the Heaviside function: $H(x) = 1 if\ x > 0$, $H(x) = 0$ otherwise.

In the current model, projector $\mathbb{P}^+$ is applied in order to decompose the energy release rate, associated with the residual effects $\underline{\underline{F}}^{D1}$, into one part $\underline{\underline{F}}^{D1+}$, related to positive strains and another part F^{D1-} such as:

$$\underline{\underline{F}}^{D1} = \underline{\underline{F}}^{D1+} + \underline{\underline{F}}^{D1-} = -g\underline{\underline{\varepsilon}}^{+} - g\left(\underline{\underline{\varepsilon}} - \underline{\underline{\varepsilon}}^{+}\right) \tag{8.16}$$

This decomposition is performed for a precise objective. It is stated that the damage criterion is mainly controlled by the part $\underline{\underline{F}}^{D1+}$ of the energy release rate, i.e. by the contribution of positive strains to residual effects:

$$f\left(\underline{\underline{F}}^{D} - \underline{\underline{F}}^{D1-} - \underline{\underline{F}}^{D2}, \underline{\underline{D}}\right) \leq 0 \tag{8.17}$$

Moreover, as we can see in (8.17), the damage variable $\underline{\underline{D}}$ is itself a parameter of damage criterion. The fact that only one part of the damage force is used in expressing the damage criterion can be seen as analogous to plasticity theory for which only one part of the stress tensor is used. For example, only the deviatoric stress $\underline{\underline{s}} = \underline{\underline{\sigma}} - \frac{1}{3}\underline{\underline{1}}\, tr\, \underline{\underline{\sigma}}$ is used in the Von Mises criterion. Furthermore, when kinematic hardening is being studied, the driving force is modified again by the backstress $\underline{\underline{X}}$ in the definition of the reduced second invariant, $\left[\frac{1}{2}\left(\underline{\underline{s}} - \underline{\underline{X}}\right) : \left(\underline{\underline{s}} - \underline{\underline{X}}\right)\right]^{1/2}$.

The damage criterion $C_D = \left\{\underline{\underline{F}}^{D} \,/\, f\left(\underline{\underline{F}}^{D}, \underline{\underline{D}}\right) \leq 0\right\}$ written in the space of thermodynamic forces associated with the damage variable $\underline{\underline{D}}$ is now proposed in the following form using three invariants $\frac{1}{2} tr\left(\underline{\underline{F}}^{D1+} . \underline{\underline{F}}^{D1+}\right)$, $tr\left(\underline{\underline{F}}^{D1+} . \underline{\underline{D}}\right)$ and $tr\, \underline{\underline{D}}$:

$$f\left(\underline{\underline{F}}^{D} - \underline{\underline{F}}^{D1-} - \underline{\underline{F}}^{D2}, \underline{\underline{D}}\right) = \sqrt{\frac{1}{2} tr\left(\underline{\underline{F}}^{D1+} . \underline{\underline{F}}^{D1+}\right)}$$

$$+ B\left|tr\left(\underline{\underline{F}}^{D1+} . \underline{\underline{D}}\right)\right| - \left(C_o + C_1 tr\, \underline{\underline{D}}\right) \leq 0 \tag{8.18}$$

The damage mechanism considered is assumed to be evolving and time-independent (non-viscous). The damage progressivity is assured by the fact that the

convex reversibility domain C_D in the space of components $\underline{\underline{F}}^D$ is controlled by $\underline{\underline{D}}$ (this is similar to a hardening mechanism in plasticity). Without this progressivity, brutal damage is produced, formally analogous to perfect plasticity, but corresponding to the opposite physical phenomenon: the corresponding curve $\underline{\underline{\sigma}} - \underline{\underline{\varepsilon}}$ exhibits a negative slope towards $-\infty$ after the peak value of σ related to the damage threshold C_o. Parameter C_1 which controls the effect of $\underline{\underline{D}}$ thus represents the degree of progression of material degradation: the lower the value of C_1, the more brittle the behavior of the material will be; the higher it is, the more ductile the behavior will be (curve $\underline{\underline{\sigma}} - \underline{\underline{\varepsilon}}$). The role of parameter B is to take into account the sensitivity of the damage criterion with respect to the directional factors of damage.

Since component $\underline{\underline{F}}^{D1+}$ is a function of $\underline{\underline{\varepsilon}}$, it appears natural to write the damage criterion $f = 0$ in the strain space. With (8.13) it can also be drawn in the stress space. The conventional (axisymmetric) triaxial compression test being one of the basic tests in geomechanics, it is instructive to represent criterion (8.18) in the strain and stress spaces under axisymmetric conditions. An illustration is given in Figure 8.3 corresponding to the initial damage surface (for $\underline{\underline{D}} = \underline{\underline{0}}$).

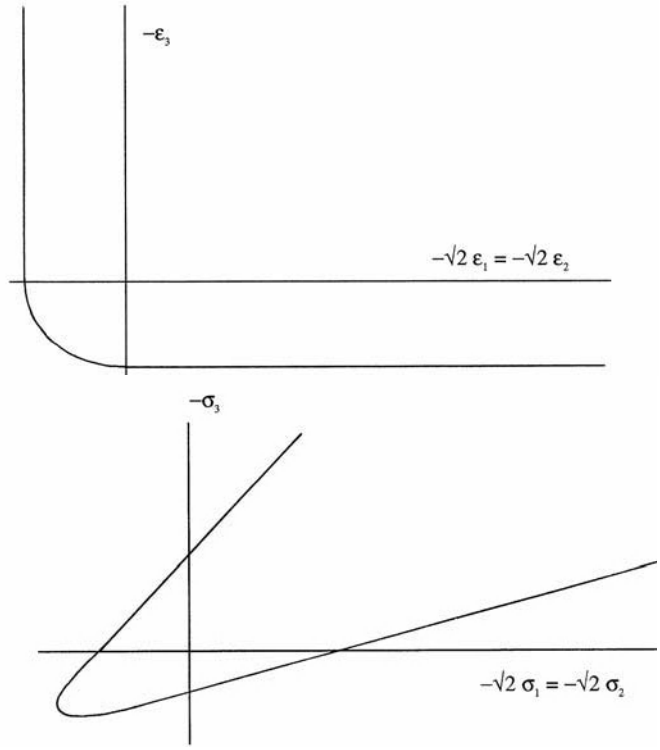

Figure 8.3. *Simulation of initial damage threshold in the space of principal axisymmetric strains (stresses respectively)*

The normality rule applied to the evolution of damage allows us to show the essential factors related to the splitting type damage mechanism. In fact, by writing:

$$\dot{\underline{\underline{D}}} = \Lambda_D \frac{\partial f\left(\underline{\underline{F}}^D - \underline{\underline{F}}^{D1-} - \underline{\underline{F}}^{D2}, \underline{\underline{D}}\right)}{\partial \underline{\underline{F}}^D} \quad , \quad \Lambda_D \geq 0 \tag{8.19}$$

and, by taking into account form (8.18) of f, we obtain:

$$\dot{\underline{\underline{D}}} = \begin{cases} \underline{\underline{0}} & \text{if } f < 0 \text{ or } f = 0 \text{ and } \dot{f}_{tot} < 0 \\ \Lambda_D \left[\dfrac{\underline{\underline{\varepsilon}}^+}{\sqrt{2\,tr\left(\underline{\underline{\varepsilon}}^+ . \underline{\underline{\varepsilon}}^+\right)}} + B\,\underline{\underline{D}} \right] & \text{if } f = 0 \text{ and } \dot{f}_{tot} = 0 \end{cases} \tag{8.20}$$

We can see that the first term indicates the orientation of damage in the direction of positive strains (brittle type kinetics). The second term, $B\,\underline{\underline{D}}$, induces the effect of existing damage on the current evolution of damage. In the case of non-proportional loading with rotation of principal directions of $\underline{\underline{\varepsilon}}^{+}$, this corrective term avoids the overly strong bifurcation of mesocracks.

The damage multiplier Λ_D is determined from the consistency condition $\dot{f}_{(tot)} = 0$ (as in plasticity theory). This condition implies that the current loading point must be and remain on the yield surface $f = 0$. Λ_D is given as follows:

$$\Lambda_D = \frac{|g|\,tr\left(\underline{\underline{\varepsilon}}^{+}.\dot{\underline{\underline{\varepsilon}}}^{+}\right) - B\,g\,tr\left(\dot{\underline{\underline{\varepsilon}}}^{+}.\underline{\underline{D}}\right)\sqrt{2\,tr\left(\underline{\underline{\varepsilon}}^{+}.\underline{\underline{\varepsilon}}^{+}\right)}}{Bg\,tr\left(\underline{\underline{\varepsilon}}^{+}.\underline{\underline{\varepsilon}}^{+}\right) + B^2 g\,tr\left(\underline{\underline{\varepsilon}}^{+}.\underline{\underline{D}}\right)\sqrt{2\,tr\left(\underline{\underline{\varepsilon}}^{+}.\underline{\underline{\varepsilon}}^{+}\right)} + C_1\,tr\,\underline{\underline{\varepsilon}}^{+} + C_1\,B\,tr\,\underline{\underline{D}}\sqrt{2\,tr\left(\underline{\underline{\varepsilon}}^{+}.\underline{\underline{\varepsilon}}^{+}\right)}} \tag{8.21}$$

Without giving a detailed presentation of the algorithm for the local integration of the constitutive model at stake, it is useful to note that the calculation of the damage multiplier Λ_D, using an implicit scheme, implies the resolution of a linear system without an iterative procedure contrary to the procedure applied to plastic models.

In this basic version of the model, damage is the only dissipation mechanism. The second law of thermodynamics implying non-negative intrinsic dissipation is reduced to the simple form:

$$\phi^D = \underline{\underline{F}}^D : \dot{\underline{\underline{D}}} \geq 0 \tag{8.22}$$

For normal dissipation systems, as is the case here, the condition $\phi^D \geq 0$ can be verified if the dissipation potential is convex, non-negative, and if the reversibility domain (C_D) contains the space origin. This last point has to be examined in the current model because the use of part $\underline{\underline{F}}^D - \underline{\underline{F}}^{D1-} - \underline{\underline{F}}^{D2}$ in (8.18), instead of the total quantity $\underline{\underline{F}}^D$, induces a translation of the damage surface in the space of F_{ij}^D, as in plasticity with kinematic hardening of the Prager type. In an extreme case, this can lead to configurations in which the loading surface does not contain the origin. It will then be necessary, in view of the integration algorithm, to control the sign of ϕ^D at each loading step and for each integration point.

8.2.3. Comments on the identification of the model's parameters and on its prediction capability

A number of simple loading paths show the physical significance of the model's parameters. Two cases are considered below: tension or compression inducing damage followed by shearing. Tension and compression are applied along the axis x_3; the shearing induces a distortion along this same axis. In the brittle splitting mechanism of mesocracks, we have in the first case one non-zero component of damage D_3 of $\underline{\underline{D}}$ and in the second case $D_1 = D_2 \neq 0$. The effective elastic properties which are relevant in these loading paths, such as the axial Young's modulus E_3, Poisson's ratio ν_{31} and the shear modulus μ_{31}, are given as follows:

(i) *tension-shearing*

$$E_3 = \lambda + 2\mu + 2(\alpha + 2\beta)D_3 - \frac{(\lambda + \alpha D_3)^2}{\lambda + \mu} \tag{8.23}$$

$$\nu_{31} = \frac{\lambda + \alpha D_3}{2(\lambda + \mu)} \tag{8.24}$$

$$\mu_{31} = \mu + \beta D_3 \tag{8.25}$$

(ii) *compression-shearing*

$$E_3 = \lambda + 2\mu - \frac{(\lambda + \alpha D_1)^2}{\lambda + \mu + 2(\alpha + \beta)D_1} \tag{8.26}$$

$$\nu_{31} = \frac{\lambda + \alpha D_1}{2[\lambda + \mu + 2(\alpha + \beta)D_1]} \tag{8.27}$$

$$\mu_{31} = \mu + \beta D_1 \tag{8.28}$$

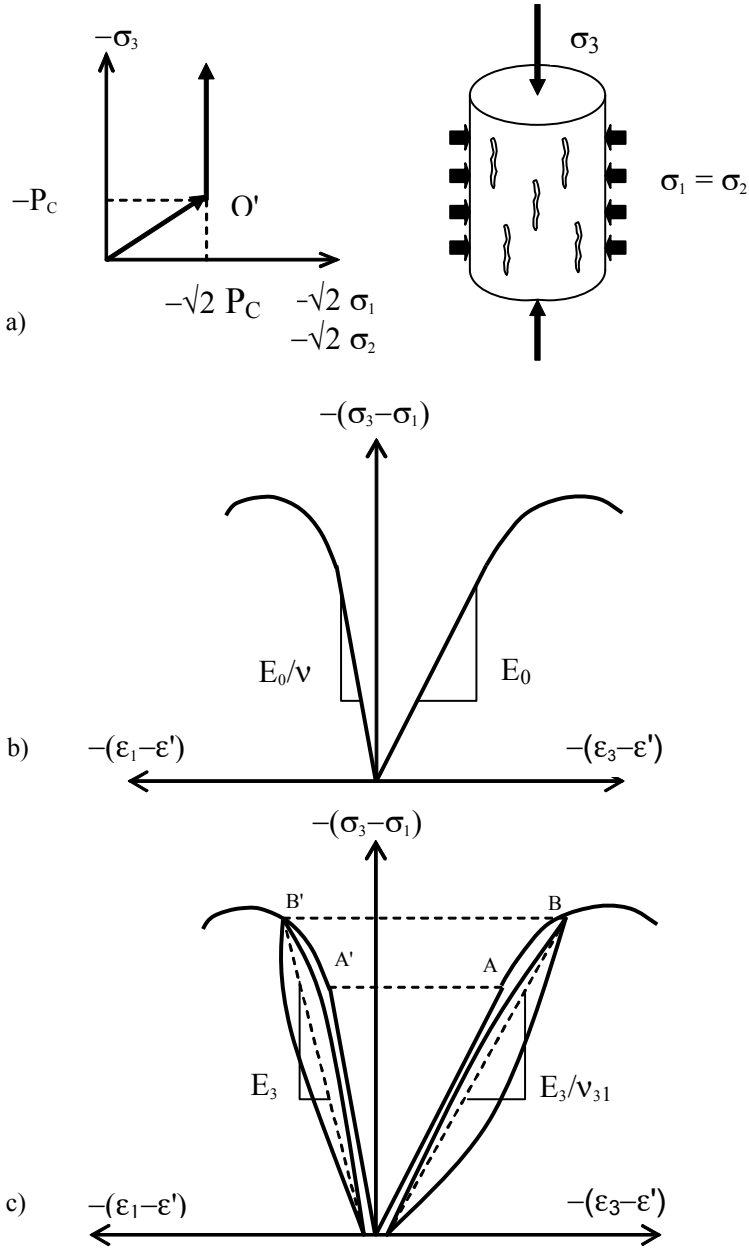

Figure 8.4. *Determination of parameters E_0, ν_0, E_3 and ν_{31} from triaxial compression test (P_c – confining pressure)*

The interpretation of β, which defines the degradation of the effective shear modulus, as mentioned in the previous section, is confirmed using relations (8.25) and (8.28) with $\beta < 0$.

The present damage model has been initially proposed in view of application in petroleum engineering. Identifying the model's parameters was our major concern. Given the fact that axisymmetric triaxial compression tests are widely used in geomechanics and the testing procedure is well established, a procedure for identifying parameters based on this test is proposed. It is to be noted that the proposed model predicts non-linear damage/elastic orthotropic behavior, and involves only eight parameters (λ, μ, α, β, g, C_o, C_1, B) whereas the linear orthotropic elasticity requires as many as nine parameters. For the present model, seven of the eight parameters can be determined from triaxial compression tests (all except B) including loading-unloading cycles. Typical loading path and schematic interpretations of stress-strain curves in terms of the given parameters are shown in Figure 8.4. This purely phenomenological scheme may be completed by relevant mesostructural analyses showing, for example, the morphology of mesocracks.

The initial sample state is assumed to be intact and isotropic. Possible initial cracks, which do not generate anisotropic behavior, may be taken into account by translating the initial concave curve towards a non-linear domain, as shown in Figure 8.5.

The initial (quasi-linear) slopes of curves $\sigma_3 - \sigma_1$ with ε_3 and ε_1 allow us to determine E_o and E_o / ν_o; see Figure 8.4. Lamé's constants λ and μ are thus calculated by:

$$\lambda = \frac{E_o \nu_o}{(1+\nu_o)(1-2\nu_o)} \quad , \quad \mu = \frac{E_o}{2(1+\nu_o)} \tag{8.29}$$

Parameters α, β and g are determined from the non-linear part of the stress strain curves affected by damage and unloading paths which are assumed to be described by an orthotropic linear elastic behavior. Points B and B' (Figure 8.4) have to be chosen sufficiently far from the initial point of the non-linear response, so that damage effects become significant ($D_1 = D_2 > 0$); however, these points should not be too close to the peak stress in order to avoid interference with the bifurcation phenomena. The effective properties involved in unloading paths are expressed as functions of quantities αD_1 and βD_1:

$$E_3 = \lambda + 2\mu - \frac{L_2^2}{L_1}, \quad \nu_{31} = \frac{L_2}{2L_1} \tag{8.30}$$

with $L_1 = \lambda + \mu + 2(\alpha + \beta)D_1$, $L_2 = \lambda + \alpha D_1$.

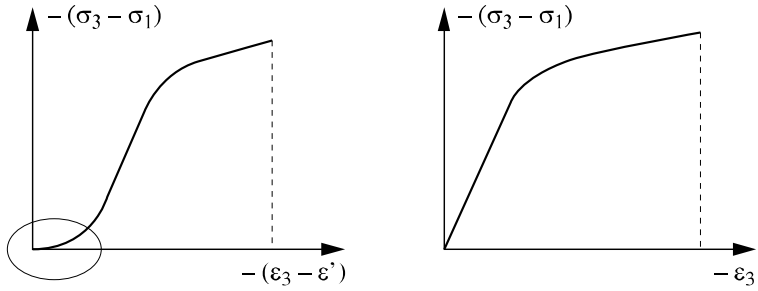

Figure 8.5. *Translation of initial porosity effect towards non-linear domain*

From (8.13) we can write:

$$g\,D_1 = \frac{E_3\,\varepsilon_3 - \sigma_3 + 2\nu_{31}\,\sigma_1}{2\nu_{31}} \tag{8.31}$$

At points A and A', representing the initial damage threshold, we have:

$$|g|\,\varepsilon_1^A - C_o = 0 \tag{8.32}$$

The verification of criterion (8.18) at B (corresponding to damage value D_1) leads to:

$$|g|\,\varepsilon_1^B - (C_o + 2C_1D_1) = 0 \tag{8.33}$$

For a given value of D_1, the five parameters α, β, g, C_o and C_1 can be obtained from the system of four equations (8.30)–(8.33). Therefore, the phenomenological fitting requires an iterative procedure starting from an arbitrary value of D_1. After having determined the values of the five parameters, we can draw the curves $\sigma_3 - \sigma_1$ as functions of ε_3 and ε_1. When a good agreement between experimental curves and numerical predictions is obtained, the determination procedure is completed. If not, a new iterative loop is performed, starting with a new value for D_1.

In principle, a single triaxial test is needed to determine seven parameters. In practice, due to natural scattering of experimental data obtained for rock materials, it is preferable to proceed with several confining pressures and to determine "average" values of material parameters.

Among the eight parameters involved in the model, only the determination of parameter B needs more complex laboratory testing. We have to perform tests on samples cut in an off-axis direction for pre-damaged material, in order to study the effects of existing damage on the current evolution of damage, according to (8.18). Further, the convexity of the yield function $f(\underline{\underline{F}}^D, \underline{\underline{D}})$ (and of the dissipation potential) imposes $|B| \leq \frac{\sqrt{2}}{2}$.

Using the procedure presented above, the model's parameters have been determined from experimental data obtained (except B taken to be zero) for Vosges sandstone [PEC 95] and for Vienne granite [HOX 98]. An implicit integration scheme is then used for the local integration of the model [COR 94]. Predicted theoretical curves are compared with the experimental curves for some loading paths, which are not used in the parameter determination procedure. Figure 8.6 shows triaxial compression tests on sandstone and, in particular, the curves of deviatoric stress with volumetric strain. The effect of dilatancy in the non-linear domain related to damage evolution is well described. We can observe a good correlation between the experiment and the simulation for different strains (axial, lateral and volumetric) for two different confining pressures.

In Figure 8.7, we present a quite discriminating path called lateral extension on Vienne granite. It appears that the model's prediction is also robust in this case.

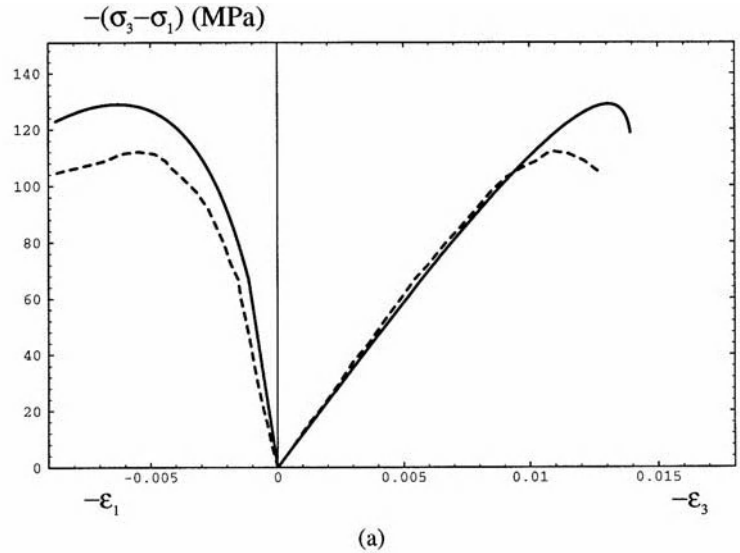

(a)

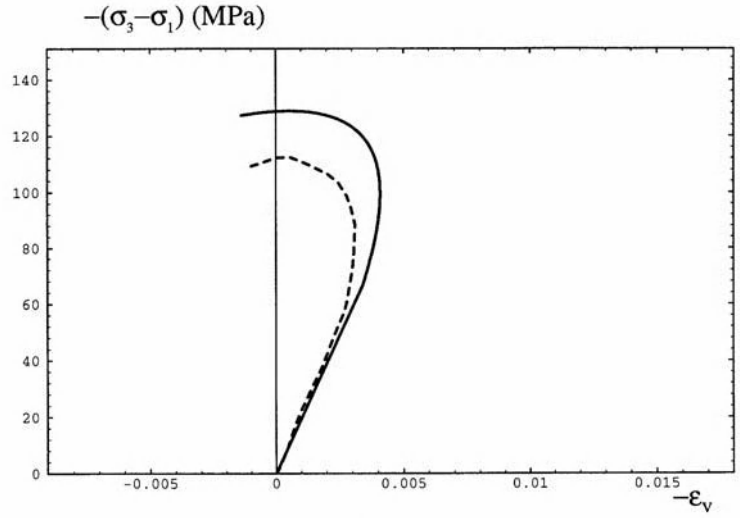

(b)

λ (MPa)	μ (MPa)	α (MPa)	β (MPa)	g (MPa)	C_0 (MPa)	C_1 (MPa)	B
3250	4875	9925	-11180	-32	0.02	0.27	0

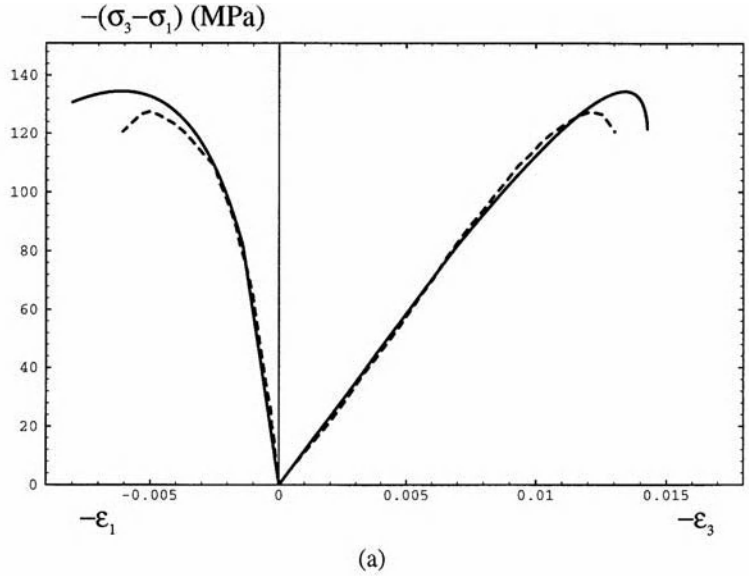

(a)

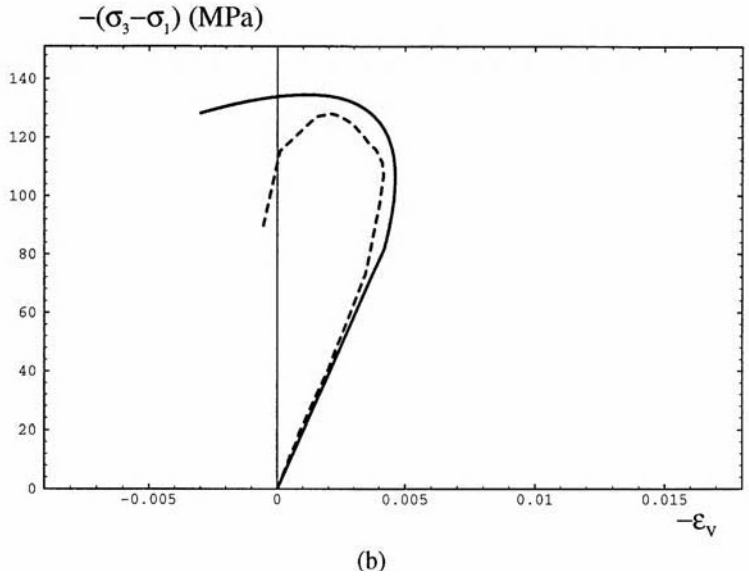

(b)

Figure 8.6. *Comparison simulations (——) – experiment (- - - -) in triaxial compression with two confining pressures10 MPa (respectively 15 MPa) (Vosges sandstone [PEC 95])*
(a) deviatoric stress versus axial and lateral strains
(b) deviatoric stress versus volumetric strain

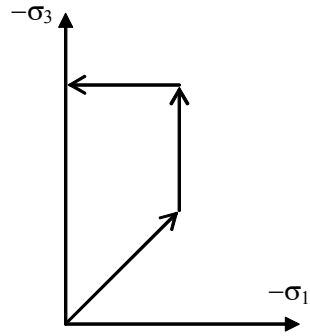

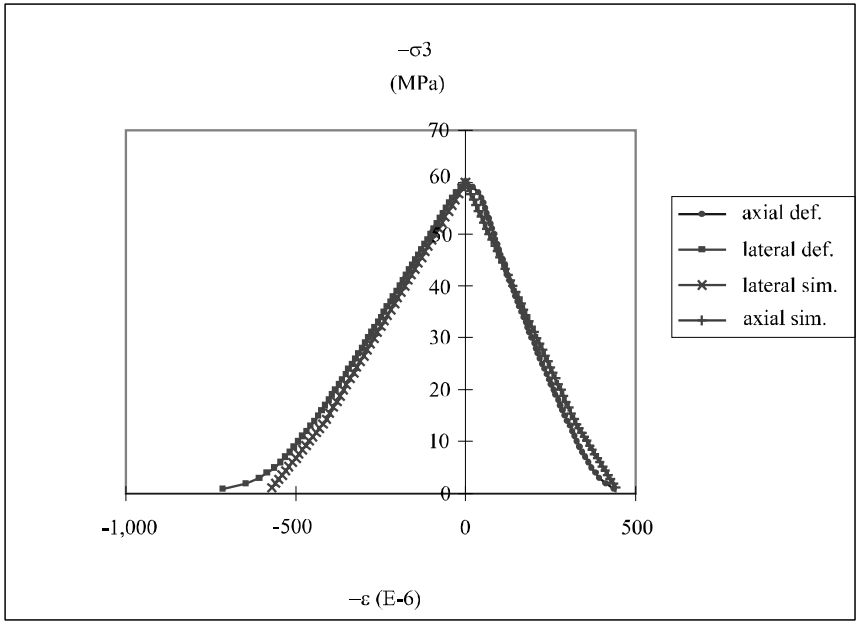

λ (MPa)	μ (MPa)	α (MPa)	β (MPa)	g (MPa)	C_0(MPa)	C_1(MPa)	B
39,850	31,300	-16,000	-31,000	-330	0.11	2.20	0

Figure 8.7. *Comparison simulation – experiment for a lateral extension test on Vienne granite (data from [HOM 99])*

As a conclusion for this basic version of the damage model, the following points can be made:

– although a phenomenological formulation is used, the proposed model is based on a micromechanical background, in particular on the choice of the damage variable $\underline{\underline{D}}$;

– the expression of the thermodynamic potential (free energy) predicts an orthotropic elasticity for a given state of damage (given $\underline{\underline{D}}$) as well as significant residual effects. The evolution of $\underline{\underline{D}}$, by a pseudo-standard scheme, describes a brittle type of damage kinetics, largely observed in the class of materials studied;

– the proposed model contains a small number of parameters (eight), and most of them can be easily determined from conventional triaxial compression tests with unloading paths;

– the stability of the integration algorithm is obtained by a natural implicit scheme.

The formulation makes it possible to introduce coupling with other dissipative mechanisms. This coupling is necessary in the view of extending the model to describe significant features related to cyclic loading paths involving mesocracks closure effects and restoring certain elastic constants. The crack closure effect will need to take into account coupling between damage and frictional sliding along crack surfaces. These features will be discussed in the next section.

8.3. Taking into account mesocrack closure effects: restitution of moduli and complex hysteretic phenomena

8.3.1. *Normal unilateral effect*

The progressive degradation of mechanical properties (moduli, mechanical strength, material symmetry) is more complex in nature than that described by the basic version of the model presented in the previous section. The nature of damage considered here implies open and closed defects, and the loading paths inducing the transition opening – closure of mesocracks lead to a material behavior similar to bi-linear elasticity. It concerns the unilateral effect at the mesoscale for a considered set of cracks; the macroscopic consequence of this effect is the restitution of elastic moduli in the direction normal to the set of cracks. In the following sections, we will briefly discuss the extended restitution phenomena including friction effects in closed cracks and how this restitution also affects shearing moduli.

In this section, only the "normal" unilateral effect is discussed. This effect can be illustrated by a simple cyclic tension-compression test as shown in Figure 10.8. The tension phase inducing a significant damage state, is followed by a compression phase in which the axial elastic stiffness is partially recovered.

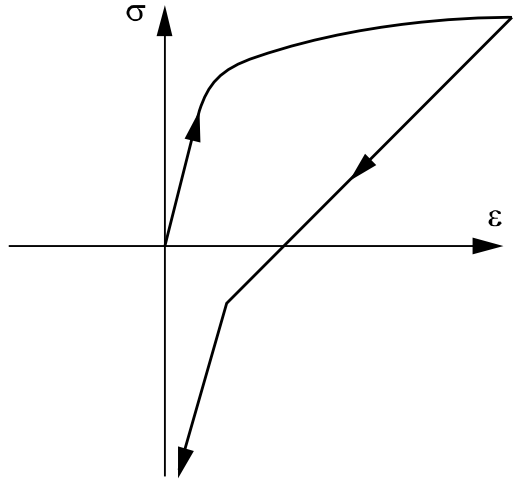

Figure 8.8. *Schematization of unilateral effect in tension-compression test*

The objective and also the main difficulty are to associate the description of activation/deactivation of damage with anisotropic behavior (induced or structural) by ensuring the continuity of the stress-strain response. This feature was the principal problem for a long time, until the middle of the 1990s, even if several approaches have been proposed:

– based on a relevant analysis of the unilateral contact at the mesocrack scale, ([AND 86], [GAM 93]) have proposed pertinent modeling schemes, but, by using quantities that were difficult to measure, efficient macroscopic models could not be formulated;

– some models have been devoted to the description of particular forms of damage (for example [JU 89], [LAD 94] for composites), by using the decomposition of the stress tensor into positive and negative parts. These models may exhibit some singularities (for example, dissymmetry of stiffness tensor) in taking into account the process of degradation – restitution in the general multiaxial case;

– Chaboche [CHA 93] has proposed an *a posteriori* modification of the stiffness tensor in the principal system of damage.

In what follows, the unilateral condition proposed by Halm and Dragon [HAL 96] is presented, based on the microscopic behavior of the mesocracks mentioned in section 8.2.1 and specifying a macroscopic opening/closure control term. This condition was introduced in the damage model presented in section 8.2 with emphasis put on the continuity of the stress-strain response during the transition between activation/deactivation of defects.

It was shown (section 8.2.1, relation (8.10)) that a fourth order tensor has a non-negligible contribution, in association with the second order damage tensor $\underline{\underline{D}}$, to the alteration of energy induced by a displacement field of closed cracks. In order to avoid the introduction of a new damage variable which will render the model more complex, we propose to use the fourth order quantity $\hat{\mathbb{D}}$ by extension of $\underline{\underline{D}}$ from its eigenelements:

$$\hat{\mathbb{D}} = \sum_{k=1}^{3} D_{(k)}\ \underline{\nu}^{(k)} \otimes \underline{\nu}^{(k)} \otimes \underline{\nu}^{(k)} \otimes \underline{\nu}^{(k)} \tag{8.34}$$

Note that this formulation conserves the orthotropic nature generated by (8.5) and cannot therefore describe greater general anisotropy. The analysis of the integrity bases associated with arguments $\underline{\underline{\varepsilon}}$ and $\hat{\mathbb{D}}$ can show that only one mixed invariant ($\underline{\underline{\varepsilon}} : \hat{\mathbb{D}} : \underline{\underline{\varepsilon}}$) is actually relevant for the fourth order quantity (the others can be reduced to the invariants of $\underline{\underline{D}}$). The term with this invariant will then be used as a control parameter of opening/closure of mesocracks; i.e. this term is absent in the thermodynamic potential when the damage is activated (fully opened cracks) and present if the damage is inactive. A new form of the thermodynamic potential (8.12) is then proposed. For the sake of clarity, only one family of cracks is considered, here ($\underline{\underline{D}} = d(s)\ \underline{\nu} \otimes \underline{\nu}$), in order to show the pertinence of the modified form:

– state 1: opened cracks, negligible effects of the term $\underline{\underline{\varepsilon}} : \hat{\mathbb{D}} : \overleftarrow{\underline{\underline{\varepsilon}}}$:

$$w^1\left(\underline{\underline{\varepsilon}}, \underline{\underline{D}}\right) = w^0\left(\underline{\underline{\varepsilon}}\right) + g\ tr\left(\underline{\underline{\varepsilon}} . \underline{\underline{D}}\right) + \alpha_1\ tr\ \underline{\underline{\varepsilon}}\ tr\left(\underline{\underline{\varepsilon}} . \underline{\underline{D}}\right) + 2\ \beta_1\ tr\left(\underline{\underline{\varepsilon}} . \underline{\underline{\varepsilon}} . \underline{\underline{D}}\right) + O\left(\underline{\underline{\varepsilon}} : \hat{\mathbb{D}} : \underline{\underline{\varepsilon}}\right) \tag{8.35}$$

where $w^0 = (1/2)\lambda\left(tr\ \underline{\underline{\varepsilon}}\right)^2 + \mu\ tr\left(\underline{\underline{\varepsilon}} . \underline{\underline{\varepsilon}}\right)$; $O(.)$ being a zero order term;

– state 2: closed cracks, the term $\underline{\underline{\varepsilon}} : \hat{\mathbb{D}} : \underline{\underline{\varepsilon}}$ is not negligible:

$$w^2\left(\underline{\underline{\varepsilon}}, \underline{\underline{D}}\right) = w^0\left(\underline{\underline{\varepsilon}}\right) + g\ tr\left(\underline{\underline{\varepsilon}} . \underline{\underline{D}}\right) + \underbrace{\alpha_2\ tr\ \underline{\underline{\varepsilon}}\ tr\left(\underline{\underline{\varepsilon}} . \underline{\underline{D}}\right) + 2\ \beta_2\ tr\left(\underline{\underline{\varepsilon}} . \underline{\underline{\varepsilon}} . \underline{\underline{D}}\right)}_{\Delta w'} + \underbrace{\gamma \underline{\underline{\varepsilon}} : \hat{\mathbb{D}} : \underline{\underline{\varepsilon}}}_{\Delta w''} \tag{8.36}$$

Modulus γ is determined by assuming that the stiffness in the direction perpendicular to closed mesocracks is equal to the initial stiffness; this means that the presence of the term $\Delta w''$ cancels out the degradation of stiffness induced by the term $\Delta w'$. In the reference system connected to the crack set, this condition may be written as follows (here axis x_1 is normal to mesocracks):

$$\frac{\partial^2 \Delta w'}{\partial \varepsilon_{11}\, \partial \varepsilon_{11}} + \frac{\partial^2 \Delta w''}{\partial \varepsilon_{11}\, \partial \varepsilon_{11}} = 0 \tag{8.37}$$

This leads to the following relation between α_2, β_2 and γ:

$$\gamma = -\alpha_2 - 2\beta_2 \tag{8.38}$$

The unilateral behavior of cracked materials is characterized by a stiffness discontinuity at the transition from the open to the closed state. The strain space is divided into two sub-domains separated by the boundary S. However, it is required that the continuity of the thermodynamic potential and that of the stress-strain response must be conserved, i.e.:

$$\left[\mathbb{C}\right] : \underline{\underline{\varepsilon}} = 0 \ \text{ on } S \ \Gamma \ \text{ with } \left[\mathbb{C}\right] = \frac{\partial^2 w^1}{\partial \underline{\underline{\varepsilon}}\, \partial \underline{\underline{\varepsilon}}} - \frac{\partial^2 w^2}{\partial \underline{\underline{\varepsilon}}\, \partial \underline{\underline{\varepsilon}}} \tag{8.39}$$

According to the theory of multi-linear functions (see in particular [WES 69] and [CUR 95]), as S is a hyper-surface of dimension 5, $\left[\mathbb{C}\right]$ must be singular and in particular of order 1 in the sense of the dimension of its image: dim Im $\left[\mathbb{C}\right] = 1$. It is sufficient for this that all the second order determinants of $\left[\mathbb{C}\right]$ are equal to zero. This is verified by the following relations:

$$\begin{cases} \alpha_1 = \alpha_2 \\ \beta_1 = \beta_2 \end{cases} \tag{8.40}$$

This also leads to the opening/closure condition:

$$\underline{\nu} \,.\, \underline{\underline{\varepsilon}} \,.\, \underline{\nu} = 0 \tag{8.41}$$

For convenience, we will use the notation defined in the basic version of the model; i.e. $\alpha = \alpha_1 = \alpha_2$, $\beta = \beta_1 = \beta_2$. The proposed approach, based on the consideration of meso-structural mechanisms (see [HAL 97] for a detailed presentation), leads to the formulation of a macroscopic criterion (8.41) which is similar to that proposed by Chaboche [CHA 93]. This approach developed for one set of mesocracks can easily be extended to any damage distribution. Since any distribution of mesocracks is equivalent to three equivalent independent systems, relation (8.41) can be generalized as follows:

$$\underline{\nu}^{(k)} \,.\, \underline{\underline{\varepsilon}} \,.\, \underline{\nu}^{(k)} = 0 \text{ , } k = 1,2,3 \tag{8.42}$$

The equivalent system of normal $\underline{\nu}^{(k)}$ becomes inactive (respectively active) when the normal component of the strain tensor $\underline{\nu}^{(k)} \,.\, \underline{\underline{\varepsilon}} \,.\, \underline{\nu}^{(k)}$ becomes negative (respectively positive). Parallel to that, term $\underline{\underline{\varepsilon}} : \hat{\mathbb{D}} : \underline{\underline{\varepsilon}}$ related to system k appears in the thermodynamic potential, so that the restitution of stiffness occurs in direction $\underline{\nu}^{(k)}$.

Let us now summarize the constitutive equations including normal unilateral effects (recall that *H* denotes the Heaviside function). Evolution law (8.20) remains valid and is not cited: the supplementary quantity $\hat{\mathbb{D}}$ is not a new internal variable but is constructed from $\underline{\underline{D}}$ and does not need an evolution law. The potential *w*, the expression of $\underline{\underline{\sigma}}$ and that of $\underline{\underline{F}}^D$ are written as:

$$w\left(\underline{\underline{\varepsilon}}, \underline{\underline{D}}\right) = w^0\left(\underline{\underline{\varepsilon}}\right) + g\, tr\left(\underline{\underline{\varepsilon}} \,.\, \underline{\underline{D}}\right) + \alpha\, tr\, \underline{\underline{\varepsilon}}\, tr\left(\underline{\underline{\varepsilon}} \,.\, \underline{\underline{D}}\right) + 2\beta\, tr\left(\underline{\underline{\varepsilon}} \,.\, \underline{\underline{\varepsilon}} \,.\, \underline{\underline{D}}\right)$$

$$-\left(\alpha + 2\beta\right) \underline{\underline{\varepsilon}} : \left[\sum_{k=1}^{3} H\left(-\underline{\nu}^{(k)} \,.\, \underline{\underline{\varepsilon}} \,.\, \underline{\nu}^{(k)}\right) D_{(k)}\, \underline{\nu}^{(k)} \otimes \underline{\nu}^{(k)} \otimes \underline{\nu}^{(k)} \otimes \underline{\nu}^{(k)} \right] : \underline{\underline{\varepsilon}} \tag{8.43}$$

$$\underline{\underline{\sigma}} = \frac{\partial w}{\partial \underline{\underline{\varepsilon}}} = \lambda\left(tr\,\underline{\underline{\varepsilon}}\right)\underline{\underline{1}} + 2\mu\,\underline{\underline{\varepsilon}} + g\,\underline{\underline{D}} + \alpha\left[tr\left(\underline{\underline{\varepsilon}}.\underline{\underline{D}}\right)\underline{\underline{1}} + \left(tr\,\underline{\underline{\varepsilon}}\right)\underline{\underline{D}}\right] + 2\beta\left(\underline{\underline{\varepsilon}}.\underline{\underline{D}} + \underline{\underline{D}}.\underline{\underline{\varepsilon}}\right)$$

$$-2\left(\alpha+2\beta\right)\sum_{k=1}^{3} H\left(-\underline{\nu}^{(k)}.\underline{\underline{\varepsilon}}.\underline{\nu}^{(k)}\right) D_{(k)}\left(\underline{\nu}^{(k)}.\underline{\underline{\varepsilon}}.\underline{\nu}^{(k)}\right)\underline{\nu}^{(k)} \otimes \underline{\nu}^{(k)} \tag{8.44}$$

$$\underline{\underline{F}}^{D} = -\frac{\partial w}{\partial \underline{\underline{D}}} = -g\,\underline{\underline{\varepsilon}} - \alpha\left(tr\,\underline{\underline{\varepsilon}}\right)\underline{\underline{\varepsilon}} - 2\beta\,\underline{\underline{\varepsilon}}.\underline{\underline{\varepsilon}}$$

$$+ \quad \left(\alpha+2\beta\right)\sum_{k=1}^{3} H\left(-\underline{\nu}^{(k)}.\underline{\underline{\varepsilon}}.\underline{\nu}^{(k)}\right)\left(\underline{\nu}^{(k)}.\underline{\underline{\varepsilon}}.\underline{\nu}^{(k)}\right)^{2}\underline{\nu}^{(k)} \otimes \underline{\nu}^{(k)} \tag{8.45}$$

Note that even if $H(.)$ is a discontinuous function in nature, the expressions of w, $\underline{\underline{\sigma}}$ and $\underline{\underline{F}}^{D}$ remain continuous, because the discontinuity of H occurs only when the quantity $(\underline{\nu}^{(k)}.\underline{\underline{\varepsilon}}.\underline{\nu}^{(k)})$ reaches zero. Relation (8.45) is given only for a given configuration of principal directions of $\underline{\underline{D}}$. The corresponding loading path is called $\underline{\underline{D}}$-proportional loading. All loading paths, which are not $\underline{\underline{D}}$-proportional, may be decomposed into a series of $\underline{\underline{D}}$-proportional sub-paths.

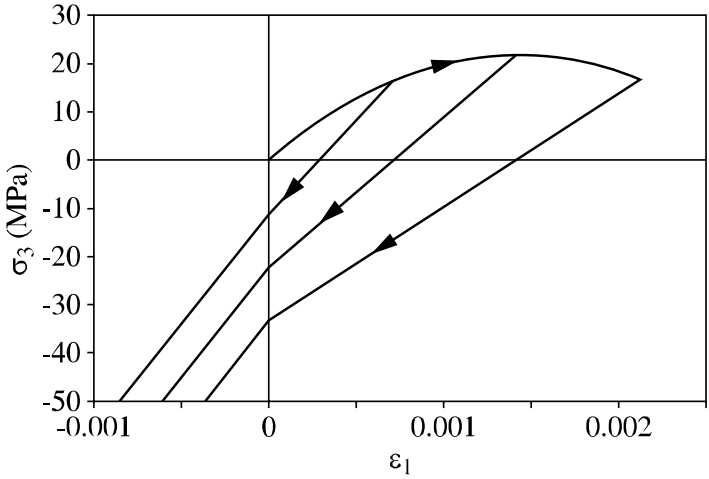

Figure 8.9. *Simulation of a tension-compression test on Fontainebleau sandstone*

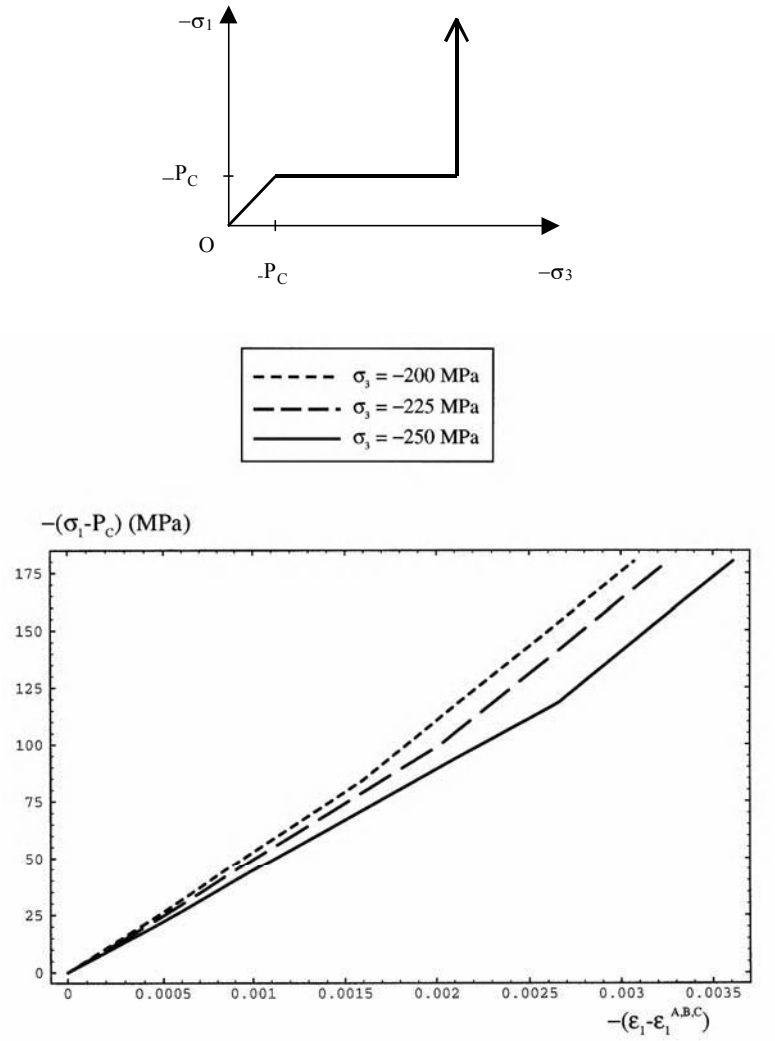

Figure 8.10. *Simulation of lateral stress strain responses during triaxial compression test with lateral overloading*

The modeling presented above successively associates the crack deactivation phenomenon with a particular mesocracking mechanism which induces an anisotropic behavior. Based on a meso-structural analysis of damage mechanisms, this approach leads to a three-dimensional macroscopic formulation with the same set of parameters as that involved in the basic version. The continuity of stress-strain

responses is verified. A series of simulations of laboratory tests (tension-compression Figure 8.9; triaxial compression with lateral confining followed by overloading Figure 8.10) have shown the pertinence of the proposed model. It predicts a full restitution of the elastic modulus; see [HAL 97]. Moreover, the proposed approach is open to be coupled with another dissipation mechanism, for instance the frictional sliding. The friction is involved in the deactivation of damage by locking the crack surface followed by possible sliding. We can consider the case where the sliding is the unique dissipation mechanism with $\underline{\underline{D}} = \text{cte}$. A more complex case can also be studied: the frictional sliding is coupled with damage growth. This is a dissipative coupling. It is possible to have a different configuration of dissipation for each equivalent system $(D_{(k)}, \underline{\nu}^{(k)})$. The main features of the third level of modeling including dissipative coupling are outlined in the next section.

8.3.2. *Introduction of friction*

The modeling of unilateral behavior previously presented is related to the restitution of the elastic modulus in the direction perpendicular to closed mesocracks. The restitution of the shear modulus implies a frictional phenomenon; and one of the consequences is the blockage of crack lips. For example, in compression tests on specimens with inclined closed mesocracks with respect to the axial direction, we can observe alternative states of blockage and sliding. This leads to hysteretic loops of the pseudo multi-linear type (the linear lines in the space $\underline{\underline{\sigma}} - \underline{\underline{\varepsilon}}$ obtained during sliding do not correspond to linear material behavior). An example of the hysteretic type is shown in Figure 8.11 for a constant damage state. Curves similar to that shown in Figure 8.11 have been obtained in a number of micromechanical studies, for instance [WAL 65], [AND 81], [KAC 82], [HOR 83], [NEM 88], [GAM 93], [FON 95], [LAW 98]; this list is probably not exhaustive. Some experimental data, for example, that obtained by Pecqueur on chalk has been reported. This data, simulated by Halm [HAL 98], confirms the scheme shown in Figure 8.11. However, the form of the curve may be more complex during loading when the propagation of mesocracks occurs simultaneously.

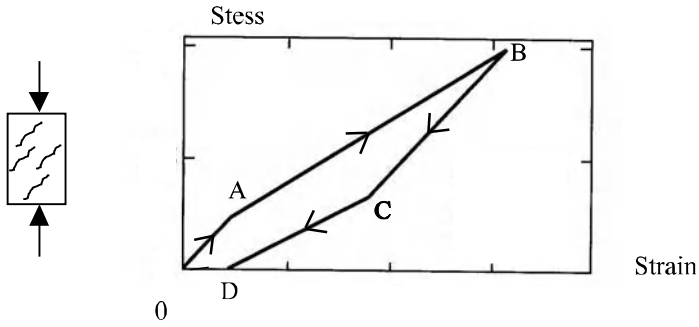

Figure 8.11. *Hysteretic loops during uniaxial compression: illustration of blockage and sliding effects of parallel closed cracks. Segments AB (loading) and CD (unloading) correspond to opposite sliding states*

Most micromechanical models are limited to the determination of effective elastic properties and do not involve the evolution sliding law. When it is studied (for instance [GAM 93]), only one class of particular loading paths is considered. Therefore, we propose here an operational formulation, mainly based on micromechanical considerations, which can be applied to complex 3D loading conditions. However, only the main features are briefly outlined here. Readers can refer to [HAL 98], [DRA 00] and [HAL 97] for more details.

Frictional sliding and its consequences may be considered as a form of plasticity (see for example, the unifying view of inelastic behavior of crystalline materials and of brittle materials, for which the propagation of mesocracks is the principal dissipation mechanism [LUB 95]). Therefore, the modeling of friction-damage coupling can be considered as a particular form of damage and plasticity coupling.

Let us introduce an internal variable $\underline{\underline{\gamma}}$ to characterize sliding between crack surfaces; its physical significance in the mesoscopic scale reflects the contributions of all mesocracks for an overall deformation of cracked representative volume (REV). It is similar to that defined by (8.6) with $<\underline{b}> \perp \underline{n}$. Considering, in the context introduced in this work, three equivalent systems of mesocracks $\underline{\nu}^{(k)}$, $k = 1,2,3$, sliding in direction $\underline{g}^{(k)}$, the corresponding sliding quantity being $\xi^{(k)}$, we can define:

$$\underline{\underline{\gamma}} = \sum_{k=1}^{3} \xi^{(k)} \left(\underline{\nu} \otimes \underline{g}\right)_{sym}^{(k)} = \sum_{k=1}^{3} \underline{\underline{\gamma}}^{(k)} \tag{8.46}$$

In order to simplify the notations and before generalizing them to any distribution of mesocracks, let us consider one set of mesocracks with normal $\underline{\nu}$. The thermodynamic potential for a closed state of cracks with frictional sliding is completed with invariants of $\underline{\underline{\varepsilon}}, \underline{\underline{\gamma}}$ and $\underline{\underline{D}}$:

$$w^3\left(\underline{\underline{\varepsilon}}, \underline{\underline{\gamma}}, \underline{\underline{D}}\right) = w^0\left(\underline{\underline{\varepsilon}}\right) + g\ tr\left(\underline{\underline{\varepsilon}} \,.\, \underline{\underline{D}}\right) + \alpha\ tr\ \underline{\underline{\varepsilon}}\ tr\left(\underline{\underline{\varepsilon}} \,.\, \underline{\underline{D}}\right) + 2\beta\ tr\left(\underline{\underline{\varepsilon}} \,.\, \underline{\underline{\varepsilon}} \,.\, \underline{\underline{D}}\right) - (\alpha + 2\beta)\,\underline{\underline{\varepsilon}} : \hat{\mathbb{D}} : \underline{\underline{\varepsilon}}$$

$$+2\beta\ \underline{\underline{\varepsilon}} \,.\, \hat{\mathbb{D}} \,.\, \underline{\underline{\varepsilon}} - 2\beta\ tr\left(\underline{\underline{\varepsilon}} \,.\, \underline{\underline{\varepsilon}} \,.\, \underline{\underline{D}}\right) + \eta_1\ tr\left(\underline{\underline{\varepsilon}} \,.\, \underline{\underline{\gamma}} \,.\, \underline{\underline{D}}\right) + 2\eta_2\left(\underline{\underline{\gamma}} \,.\, \underline{\underline{\gamma}} \,.\, \underline{\underline{D}}\right) \tag{8.47}$$

We can see that the first two terms of the second line of (8.47) remove the contribution of the two terms with parameter β in the first line of (8.47). In fact, as mentioned in section 8.2.2 and section 8.2.3 (equations (8.25) and (8.28)), the term $2\beta\ tr(\underline{\underline{\varepsilon}} \,.\, \underline{\underline{\varepsilon}} \,.\, \underline{\underline{D}})$ is alone responsible for the degradation of the shear modulus. This degradation is cancelled in the presence of friction due to the effect of a blockage.

The relationship between the thermodynamic potential for the state of opened/closed mesocracks (expression (8.43)) and potential w^3 given above, can be established by formulating the continuity of w and $\underline{\underline{\sigma}}$ during the closing of cracks. This leads once again to multi-linear function theory in the case of bi-linear elasticity for a given configuration of $(\underline{\underline{D}}, \underline{\underline{\gamma}})$ and implies the following relations:

$$\eta_1 = 4\beta \quad , \quad \eta_2 = -\beta \tag{8.48}$$

Also, at the opening /closure transition the continuity requires:

$$\begin{cases} \underline{\underline{\varepsilon}} \,.\, \underline{\underline{D}} = \underline{\underline{\gamma}} \,.\, \underline{\underline{D}} \\ \underline{\underline{D}} \,.\, \underline{\underline{\varepsilon}} = \underline{\underline{D}} \,.\, \underline{\underline{\gamma}} \end{cases} \tag{8.49}$$

System (8.49) states that at the point of the opening/closure transition, $\underline{\underline{\varepsilon}}$ and $\underline{\underline{\gamma}}$ have the same components in the plane of cracks. This can be expressed as follows:

$$\gamma_{ij} = sym\left(\varepsilon_{ik}\ \nu_k\ \nu_j\right) (\text{at the closure}) \tag{8.50}$$

and considered as the initiation condition of $\underline{\underline{\gamma}}$. The definite expression of $w\left(\underline{\underline{\varepsilon}}, \underline{\underline{D}}, \underline{\underline{\gamma}}\right)$ for all opening/closure configurations is given by:

$$w\left(\underline{\underline{\varepsilon}},\underline{\underline{D}},\underline{\underline{\gamma}}\right)=w^0\left(\underline{\underline{\varepsilon}}\right)+g\ tr\left(\underline{\underline{\varepsilon}}.\underline{\underline{D}}\right)+\alpha\ tr\ \underline{\underline{\varepsilon}}\ tr\left(\underline{\underline{\varepsilon}}.\underline{\underline{D}}\right)+2\beta\ tr\left(\underline{\underline{\varepsilon}}.\underline{\underline{\varepsilon}}.\underline{\underline{D}}\right)$$

$$+H\left(-\underline{\nu}.\underline{\underline{\varepsilon}}.\underline{\nu}\right)\left[-2\beta\ tr\left(\underline{\underline{\varepsilon}}.\underline{\underline{\varepsilon}}.\underline{\underline{D}}\right)-\alpha\ \underline{\underline{\varepsilon}}:\hat{\mathbb{P}}:\underline{\underline{\varepsilon}}+4\beta\ tr\left(\underline{\underline{\varepsilon}}.\underline{\underline{\gamma}}.\underline{\underline{D}}\right)-2\beta\ tr\left(\underline{\underline{\gamma}}.\underline{\underline{\gamma}}.\underline{\underline{D}}\right)\right] \tag{8.51}$$

The stress tensor $\underline{\underline{\sigma}}$ is classically derived from the thermodynamic potential with respect to $\underline{\underline{\varepsilon}}$. Similarly, by derivating with respect to $\underline{\underline{D}}$ and $\underline{\underline{\gamma}}$, we obtain the thermodynamic forces associated with damage and sliding.

The last one is written as:

$$\underline{\underline{F}}^{\gamma}=-\frac{\partial w}{\partial\underline{\underline{\gamma}}}=-2\beta\left(\underline{\underline{\varepsilon}}.\underline{\underline{D}}+\underline{\underline{D}}.\underline{\underline{\varepsilon}}\right)+2\beta\left(\underline{\underline{\gamma}}.\underline{\underline{D}}+\underline{\underline{D}}.\underline{\underline{\gamma}}\right) \tag{8.52}$$

$\underline{\underline{F}}^{\gamma}$ may be decomposed into a tangential force $\underline{\underline{F}}^{\gamma T}$ and a normal force $\underline{\underline{F}}^{\gamma N}$ with respect to the mesocrack plane:

$$\underline{\underline{F}}^{\gamma}=\underline{\underline{F}}^{\gamma T}+\underline{\underline{F}}^{\gamma N}\ \text{with}\ \underline{\underline{F}}^{\gamma T}=\underline{\underline{F}}^{\gamma}-\left(\underline{\nu}.\underline{\underline{F}}^{\gamma}.\underline{\nu}\right)\underline{\nu}\otimes\underline{\nu}$$

$$\underline{\underline{F}}^{\gamma N}=\left(\underline{\nu}.\underline{\underline{F}}^{\gamma}.\underline{\nu}\right)\underline{\nu}\otimes\underline{\nu} \tag{8.53}$$

We assume that the reversible domain for sliding is defined by a criterion of the form h = 0, which is based on the following assumptions:

– function h explicitly depends on the norm of the tangential force $\underline{\underline{F}}^{\gamma T}$;

– the sliding threshold is expressed in terms of the normal strain on mesocracks $\underline{\nu}.\underline{\underline{\varepsilon}}.\underline{\nu}$ (instead of normal stress as in the Coulomb criterion; we conserve the strain based formulation for all parts of the model). We write:

$$h\left(\underline{\underline{F}}^{\gamma}-\underline{\underline{F}}^{\gamma N},\underline{\nu}.\underline{\underline{\varepsilon}}.\underline{\nu}\right)=\sqrt{\frac{1}{2}tr\left[\left(\underline{\underline{F}}^{\gamma}-\underline{\underline{F}}^{\gamma N}\right).\left(\underline{\underline{F}}^{\gamma}-\underline{\underline{F}}^{\gamma N}\right)\right]}+\rho\underline{\nu}.\underline{\underline{\varepsilon}}.\underline{\nu}\le 0$$

$$\text{if}\ \underline{\nu}.\underline{\underline{\varepsilon}}.\underline{\nu}\le 0 \tag{8.54}$$

where ρ is a model's parameter to be determined, which plays a similar role as that of a friction coefficient; see [HAL 98] for details. Transformed in stress sub-space,

criterion (8.54) has some similar geometrical features as the Coulomb criterion. However, it is here expressed in terms of macroscopic quantities. Even when it is expressed in terms of stress, it does not, due to its definition, correspond to the local stresses applied to the crack surfaces. Moreover, it can be proven (see [HAL 97]) that an associated flow rule of the form

$$\underline{\underline{\dot{\gamma}}} = \Lambda_\gamma \frac{\partial h}{\partial \underline{\underline{F}}^\gamma} = \Lambda_\gamma \frac{\underline{\underline{F}}^{\gamma T}}{\sqrt{2tr\left(\underline{\underline{F}}^{\gamma T} \cdot \underline{\underline{F}}^{\gamma T}\right)}} \quad , \quad \Lambda_\gamma \geq 0 \tag{8.55}$$

is consistent with $\underline{\underline{D}}$-proportional loading paths (without rotation of the principal directions of $\underline{\underline{D}}$). Flow rule (8.55) means that evolution $\underline{\underline{\gamma}}$ is coaxial to $\underline{\underline{F}}^{\gamma T}$; i.e., the crack propagates along its own plane. There is no risk of crack surface separation and no contradiction related to the evolution law associated with the standard Coulomb criterion.

In particular, if the damage state remains constant as in the case of the uniaxial compression test mentioned at the beginning of this section, the proposed model predicts multi-linear hysteretic loops. This is illustrated in Figure 8.12 for the case of a shearing cycle in the mesocrack plane. The difference with the prediction given by the model without friction effects (dotted lines) is significant.

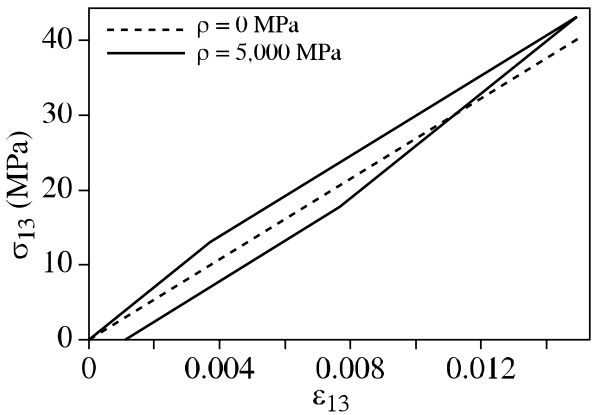

Figure 8.12. *Influence of friction on shearing behavior*

To simplify the presentation, some limitations have been introduced (one system of mesocracks, $\underline{\underline{D}}$-proportional loading or no evolution of $\underline{\underline{D}}$). These cases do not correspond to real situations. We can consider more general loading paths with simultaneous damage evolution and sliding by taking into account the rotation of principal directions of $\underline{\underline{D}}$. Halm and Dragon [HAL 98] proved that a partition of $\underline{\underline{F}}^{\gamma}$ more general than that given by (8.53) is possible and valid in the case of non-conservation of the sliding planes. Such a new partition includes, in the particular case without rotation of the $\underline{\underline{D}}$ axes, that mentioned above. We can write:

$$\underline{\underline{F}}^{\gamma} = \underline{\underline{F}}^{\gamma T} + 4\beta\left(\underline{\underline{\gamma}} : \underline{\underline{D}}\right)\underline{\nu} \otimes \underline{\nu} \quad - 4\beta\left(\underline{\underline{\varepsilon}} : \underline{\underline{D}}\right)\underline{\nu} \otimes \underline{\nu}$$

$$= \quad \underline{\underline{F}} \quad - 4\beta\left(\underline{\underline{\varepsilon}} : \underline{\underline{D}}\right)\underline{\nu} \otimes \underline{\nu} \tag{8.56}$$

where, for all the cases corresponding to $\underline{\underline{\gamma}} : \underline{\underline{D}} = 0$ ($\underline{\underline{D}}$-proportional or $\underline{\underline{D}}$ = cte), $\underline{\underline{F}} = \underline{\underline{F}}^{\gamma T}$.

We can now define the criterion h ≤ 0 and the evolution law in terms of $\underline{\underline{F}}$ and consider the assembly of equivalent systems, k = 1,2,3. The equations of the model can be represented with respect to the three systems by selecting them, one by one, with the help of the following operator $\mathbb{L}^{(k)}$:

$$\mathbb{L}^{(k)} = \underline{\nu}^{(k)} \otimes \underline{\nu}^{(k)} \otimes \underline{\nu}^{(k)} \otimes \underline{\nu}^{(k)} \tag{8.57}$$

We can write:

$$\underline{\underline{D}}^{(k)} = D_{(k)}\, \underline{\nu}^{(k)} \otimes \underline{\nu}^{(k)} = \mathbb{L}^{(k)} : \underline{\underline{D}} \tag{8.58}$$

The potential $w\left(\underline{\underline{\varepsilon}}, \underline{\underline{\gamma}}, \underline{\underline{D}}\right)$ and the state laws become:

$$w\left(\underline{\underline{\varepsilon}}, \underline{\underline{\gamma}}, \underline{\underline{D}}\right) = w^0\left(\underline{\underline{\varepsilon}}\right) + g\ tr\left(\underline{\underline{\varepsilon}} \,.\, \underline{\underline{D}}\right) + \alpha\ tr\ \underline{\underline{\varepsilon}}\ tr\left(\underline{\underline{\varepsilon}} \,.\, \underline{\underline{D}}\right) + 2\beta\ tr\left(\underline{\underline{\varepsilon}} \,.\, \underline{\underline{\varepsilon}} \,.\, \underline{\underline{D}}\right)$$

$$+ \sum_{k=1}^{3} H\left(-\underline{\nu}^{(k)} \,.\, \underline{\underline{\varepsilon}} \,.\, \underline{\nu}^{(k)}\right)\left[-\alpha\ \underline{\underline{\varepsilon}} : (D_{(k)}\, \mathbb{L}^{(k)}) : \underline{\underline{\varepsilon}} - 2\beta\ tr\left(\underline{\underline{\varepsilon}} \,.\, \underline{\underline{\varepsilon}} \,.\, \underline{\underline{D}}^{(k)}\right)\right.$$

$$+\ 4\beta\, tr\left(\underline{\underline{\varepsilon}}\cdot\underline{\underline{\gamma}}^{(k)}\cdot\underline{\underline{D}}^{(k)}\right)-2\beta\, tr\left(\underline{\underline{\gamma}}^{(k)}\cdot\underline{\underline{\gamma}}^{(k)}\cdot\underline{\underline{D}}^{(k)}\right)] \tag{8.59}$$

$$\underline{\underline{\sigma}}=\frac{\partial w}{\partial\underline{\underline{\varepsilon}}}=\lambda\left(tr\ \underline{\underline{\varepsilon}}\right)\underline{\underline{1}}+2\mu\,\underline{\underline{\varepsilon}}+g\,\underline{\underline{D}}+\alpha\left[tr\left(\underline{\underline{\varepsilon}}\cdot\underline{\underline{D}}\right)\underline{\underline{1}}+\left(tr\ \underline{\underline{\varepsilon}}\right)\underline{\underline{D}}\right]+2\beta\left(\underline{\underline{\varepsilon}}\cdot\underline{\underline{D}}+\underline{\underline{D}}\cdot\underline{\underline{\varepsilon}}\right)$$

$$+\sum_{k=1}^{3}H\left(-\underline{\nu}^{(k)}\cdot\underline{\underline{\varepsilon}}\cdot\underline{\nu}^{(k)}\right)\left[-2\alpha\, D_k\left(\underline{\nu}^{(k)}\cdot\underline{\underline{\varepsilon}}\cdot\underline{\nu}^{(k)}\right)\underline{\nu}^{(k)}\otimes\underline{\nu}^{(k)}-2\beta\left(\underline{\underline{\varepsilon}}\cdot\underline{\underline{D}}^{(k)}+\underline{\underline{D}}^{(k)}\cdot\underline{\underline{\varepsilon}}\right)\right.$$

$$\left.+2\beta\left(\underline{\underline{\gamma}}^{(k)}\cdot\underline{\underline{D}}^{(k)}+\underline{\underline{D}}^{(k)}\cdot\underline{\underline{\gamma}}^{(k)}\right)\right] \tag{8.60}$$

$$\underline{\underline{F}}^{D}=-\frac{\partial w}{\partial\underline{\underline{D}}}=-g\,\underline{\underline{\varepsilon}}-\alpha\left(tr\,\underline{\underline{\varepsilon}}\right)\underline{\underline{\varepsilon}}-2\beta\left(\underline{\underline{\varepsilon}}\cdot\underline{\underline{\varepsilon}}\right)+\sum_{k=1}^{3}H\left(-\underline{\nu}^{(k)}\cdot\underline{\underline{\varepsilon}}\cdot\underline{\nu}^{(k)}\right)\left[\alpha\left(\underline{\nu}^{(k)}\cdot\underline{\underline{\varepsilon}}\cdot\underline{\nu}^{(k)}\right)^{2}\right.$$

$$\left.\underline{\nu}^{(k)}\otimes\underline{\nu}^{(k)}+2\beta\ \underline{\underline{\mathbb{I}}}^{(k)}:\left(\underline{\underline{\varepsilon}}\cdot\underline{\underline{\varepsilon}}\right)-4\beta\ \underline{\underline{\mathbb{I}}}^{(k)}:\left(\underline{\underline{\varepsilon}}\cdot\underline{\underline{\gamma}}^{(k)}\right)+2\beta\ \underline{\underline{\mathbb{I}}}^{(k)}:\left(\underline{\underline{\gamma}}^{(k)}\cdot\underline{\underline{\gamma}}^{(k)}\right)\right] \tag{8.61}$$

$$\underline{\underline{F}}^{\gamma k}=-\frac{\partial w}{\partial\underline{\underline{\gamma}}^{(k)}}=H\left(-\underline{\nu}^{(k)}\cdot\underline{\underline{\varepsilon}}\cdot\underline{\nu}^{(k)}\right)\left[-2\beta\left(\underline{\underline{\varepsilon}}\cdot\underline{\underline{D}}^{(k)}+\underline{\underline{D}}^{(k)}\cdot\underline{\underline{\varepsilon}}\right)\right.$$

$$\left.+2\beta\left(\underline{\underline{\gamma}}^{(k)}\cdot\underline{\underline{D}}^{(k)}+\underline{\underline{D}}^{(k)}\cdot\underline{\underline{\gamma}}^{(k)}\right)\right] \tag{8.62}$$

$$\underline{\underline{F}}^{\gamma k}=\underline{\underline{F}}^{\gamma T(k)}+\underline{\underline{F}}^{\gamma N(k)}=\underline{\underline{F}}^{\gamma T(k)}+4\beta\left(\underline{\underline{\gamma}}^{(k)}:\underline{\underline{D}}^{(k)}\right)\underline{\nu}^{(k)}\otimes\underline{\nu}^{(k)}$$

$$-4\beta\left(\underline{\underline{\varepsilon}}:\underline{\underline{D}}^{(k)}\right)\underline{\nu}^{(k)}\otimes\underline{\nu}^{(k)}$$

$$=\underline{\underline{F}}^{(k)}-4\beta\left(\underline{\underline{\varepsilon}}:\underline{\underline{D}}^{(k)}\right)\underline{\nu}^{(k)}\otimes\underline{\nu}^{(k)} \tag{8.63}$$

The complementary law concerning the sliding $\underline{\underline{\gamma}}^{(k)}$ on three independent systems is expressed as:

$$h^{(k)}\left(\underline{\underline{F}}^{\gamma(k)},\underline{\nu}^{(k)}\cdot\underline{\underline{\varepsilon}}\cdot\underline{\nu}^{(k)}\right)=h^{(k)}\left(\underline{\underline{F}}^{(k)},\underline{\nu}^{(k)}\cdot\underline{\underline{\varepsilon}}\cdot\underline{\nu}^{(k)}\right)=\sqrt{\frac{1}{2}tr\left(\underline{\underline{F}}^{(k)}\cdot\underline{\underline{F}}^{(k)}\right)}$$

$$+\rho\,\underline{\nu}^{(k)}\cdot\underline{\underline{\varepsilon}}\cdot\underline{\nu}^{(k)}\le 0 \tag{8.64}$$

$$\dot{\underline{\underline{\gamma}}}^{(k)} = \Lambda_{\gamma}^{(k)} \frac{\partial\, h^{(k)}\left(\underline{\underline{F}}^{(k)}, \underline{\nu}^{(k)} \cdot \underline{\underline{\varepsilon}} . \underline{\nu}^{(k)}\right)}{\partial \underline{\underline{F}}^{\gamma(k)}} = \begin{cases} \underline{\underline{O}} \text{ if } h^{(k)} \le 0 \text{ or } h^{(k)} = 0 \,,\ \dot{h}^{(k)} < 0 \\ \Lambda_{\gamma}^{(k)} \dfrac{\underline{\underline{F}}^{(k)}}{\sqrt{2\ tr\left(\underline{\underline{F}}^{(k)} . \underline{\underline{F}}^{(k)}\right)}} \text{ if } h^{(k)} = 0 \text{ and} \\ \qquad\qquad\qquad\qquad\qquad\qquad \dot{h}^{(k)} = 0 \end{cases} \tag{8.65}$$

Physically, the directional term in evolution law (8.65) means that the sliding rate contains not only a component in the crack plane but also a normal component which can catch the rotation of the direction of equivalent mesocracks.

The advantage of the general model proposed here, beyond its three-dimensional and anisotropic features, resides in its modular construction. The introduction of friction requires only one parameter to be determined (frictional parameter ρ). The complete version of the model includes two dissipation mechanisms with nine material parameters. The energy dissipation is expressed by:

$$D = \underline{\underline{F}}^{D} : \dot{\underline{\underline{D}}} + \sum_{k=1}^{3} \underline{\underline{F}}^{\gamma(k)} : \dot{\underline{\underline{\gamma}}}^{(k)} \tag{8.66}$$

In the next section, we will give some indications on the numerical implementation algorithm and applications of the model to geomechanics.

8.4. Numerical integration and application examples – concluding notes

At the end of section 8.2.2, a few synthetic notes were made about the numerical integration of the basic version of the model. In particular, it was shown that the damage multiplier Λ_D could be determined without an iterative procedure in the context of the implicit integration of the model. Therefore, the numerical integration aspect of the proposed model has certain advantages with respect to classical plasticity. The reader can find a detailed algorithm in [DRA 00]. Particular features related to the frictional effects in closed cracks have also been discussed. The key point concerns the incremental procedure applied to (8.65) for the evolution of $\underline{\underline{\gamma}}$. The implicit procedure was used. An iterative procedure of the Newton-Raphson type is necessary to solve the non-linear system of equations.

When a joint evolution of damage and sliding takes place, it is necessary to determine the incremental values $\Delta \underline{\underline{D}}$ and $\Delta \underline{\underline{\gamma}}$ which are simultaneously produced. The integration procedure is facilitated due to the weak coupling between loading

function $f(\underline{\underline{F}}^D, \underline{\underline{D}})$ and function $h^k(\underline{\underline{F}}^{\gamma(k)}, \underline{\underline{\varepsilon}})$. The choice of the "active" part of $\underline{\underline{F}}^D$ involved in f as defined in the basic version of the model, and of the "active" form of f itself (see (8.18)) lead to the conclusion that function f varies with $\underline{\underline{D}}$ only, while h^k varies with $\underline{\underline{\gamma}}$ and $\underline{\underline{D}}$. This allows us to resolve first the equation governing $\Delta\underline{\underline{D}}$, without referring to sliding. The equation governing $\Delta\underline{\underline{\gamma}}$ is then solved; this takes into account the consequences of coupling.

N.B.: The algorithmic properties mentioned above can be modified by another choice of the thermodynamic potential and damage criterion. Some recent works suggest an alternative choice of the active part of $\underline{\underline{F}}^D$ such as:

$$\underline{\underline{F}}^{D+} = -\alpha\left(tr\ \underline{\underline{\varepsilon}}\right)\underline{\underline{\varepsilon}}^+ - 2\beta\,\underline{\underline{\varepsilon}}^+ . \underline{\underline{\varepsilon}}^+ \tag{8.67}$$

This choice neglects the irreversible effects (term $g\,\underline{\underline{\varepsilon}} : \underline{\underline{D}}$ in w is cancelled), leading to the form of criterion $f \le 0$, physically consistent with the behavior of certain brittle materials. This criterion, when expressed in the strain and/or stress space, appears to be quite close to that given by (8.18); see [HAL 02]. This means that deeper investigations, comparable to numerous studies performed on various plastic criteria and hardening laws, must also be performed for damage theories. This is particularly needed in the context of anisotropic effects as is the case in this chapter.

The choice of hierarchical modeling, including successively the basic version of the model, extended to include the normal unilateral effect, and finally completed by an elastoplastic form related to frictional effects, appears reasonable for a large class of brittle geomaterials. To demonstrate this, a number of laboratory tests and boundary value problems have been successfully simulated and studied. For example, the so-called "Sanford beam", a test-problem in rock mechanics introduced by Jaeger and Cook [JAE 79] was studied with the basic version of the model in the research project "GEOFRAC" (TOTAL-IFP) in 1994 [CHA 94]. The mechanical fields generated by the model appeared to be physically realistic.

Among geomechanical problems, we can cite situations more or less close to those related to petroleum engineering investigated by Pham [PHA 94]. Again, only the basic version of the model was tested and the results obtained appeared promising.

In the following, we summarize an application briefly presented in [DRA 94] and further detailed in [COR 94]. It consists of studying the boundary-value problem of a cubic body containing a central hole and subjected to prescribed displacements, as shown in Figure 8.13. The calculations using the finite element method are not limited to the determination of mechanical fields including the evolving damaged zone. We have also determined the bifurcation surface in the localized mode in 3D conditions. The strain localization corresponded here to the loss of ellipticity of the problem at a material point (actually one of the integration points). The phenomenon of strain and damage localization is seen as a precursor of fracture – transition from diffused volumetric damage to surface failure. The question is the following: does the basic model applied to the studied structure generate a (several) macroscopic failure mechanism(s)? In a surprising manner, the localization occured at point B inside the damage zone which is much more reduced than that developed around the top and bottom of the opening. This trend was confirmed by experimental observations obtained by Onaisi [ONA 89] from a series of blocks, tests including observations of macroscopic cracks (initiation and propagation). The example shown in Figure 8.13 corresponds to one of the tests performed by Onaisi. It is interesting to note that the induced anisotropy seems to play an important role in the failure mechanism in localized mode. Comparative calculations performed with an isotropic damage model showed that localization occured from the bore hole at the vertical axis (point A) inside the extended damage zone. For the block tested, this result is not in agreement with the initiation mechanism of macroscopic failure observed by Onaisi.

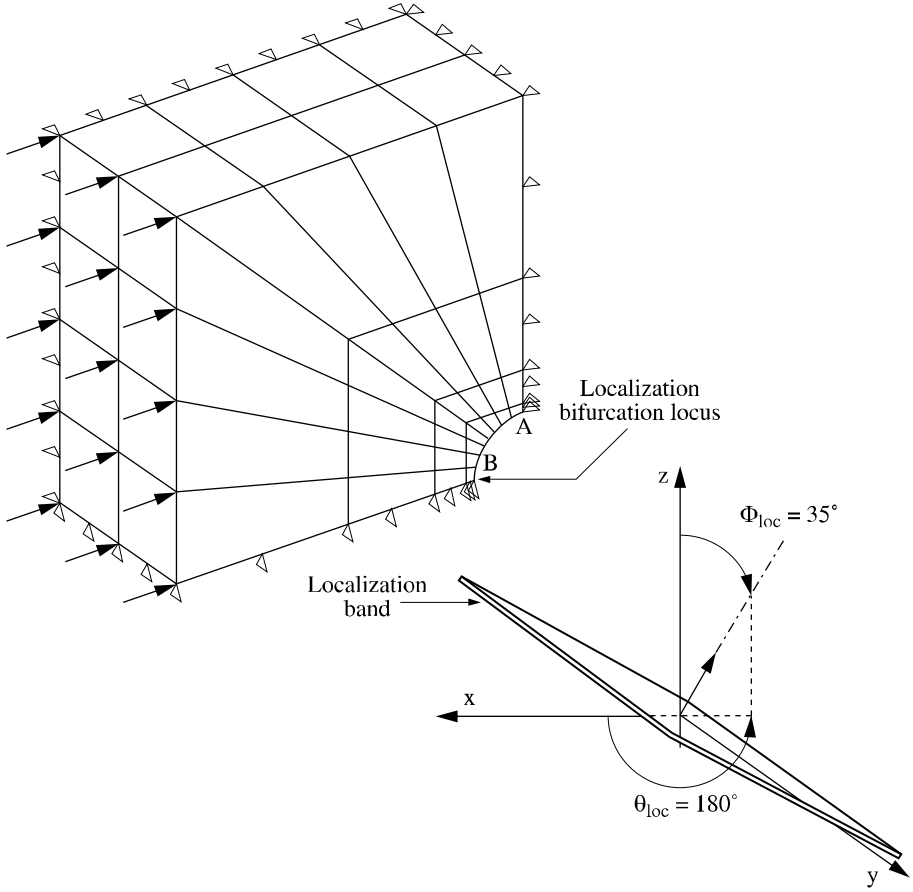

Figure 8.13. *Finite element analysis of rock structure with central hole: discretization and boundary conditions for a quarter of the block. Localization of damage and initiation of macroscopic failure*

The aforementioned examples concern the basic version of the model presented in section 8.2. The results obtained appear highly interesting and the proposed model can be applied to other structures with more complex loading conditions, for example, the anchoring problem mentioned by Berthaud and El Dalati [ELD 99]. This problem may imply a strong rotation of the damage directions in the support material (rock and concrete), due to loads applied to the anchor base.

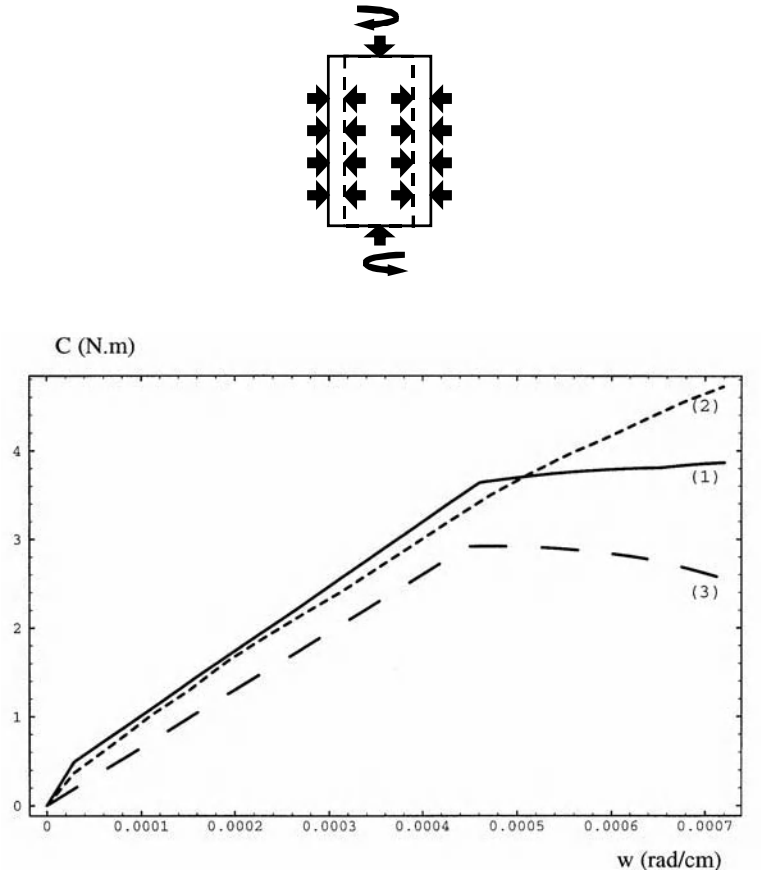

Figure 8.14. *Comparison simulation – experiment in hydrostatic compression – torsion on hollow cylinder of Vosges sandstone (P_c = 10 MPa). (1) extended model, (2) experiment [PEC 95], (3) model without friction*

To conclude without being limited to applications regarding the first level modeling introduced in this chapter, we shall present another example. A hollow cylinder sample (Vosges sandstone) is subjected to compression and torsion [PEC 95]. Figure 8.14 shows the torsion couple as a function of angular deformation of the central part of the cylinder, where the state of stress and strain is quasi-uniform. Let us recall that the cylinder is subjected to strong compression, so that most mesocracks are in a closed state. Only the model with frictional effects is able to reproduce the stiffness jump observed at the beginning of loading, corresponding to sliding along crack surfaces. The last loading phase shown in the figure corresponds to coupled damage and sliding evolution. The proposed coupled model seems to

overestimate the kinetics of damage evolution. The basic version of the model (without friction) systematically leads to an underestimation of the applied torque with respect to experimental data.

This example is a clear illustration of how more sophisticated features of the proposed model (taking into account normal unilateral effects and frictional effects) can be applied to engineering. It concerns loading conditions including cycles or phases of closure of various systems of mesocracks, non-proportional local evolutions and rotation of principal directions of the damage tensor.

As is indicated in section 8.2.1, the damage modeling and notably the modeling of damage activation/deactivation related to the normal unilateral effect is based on spectral decomposition (8.5) for the second-order tensor $\underline{\underline{D}}$ and the extrapolation of the latter leading to the restrictive fourth-order entity $\hat{\mathbb{D}}$ in (8.34). The corresponding hypotheses involve maintaining the form of damage-induced orthotropy of the effective elastic properties (to the detriment of more general anisotropy) and the relevant equivalence postulate stipulating that any system of mesocracks can be reduced to three commensurate orthogonal sets. The latter are embodied by eigendensities $D_{(k)}$ of $\underline{\underline{D}}$ and its eigenvectors $\underline{\nu}^{(k)}$. Maintaining orthotropy was arguably justified on some micromechanical bases by Kachanov [KAC 80], [KAC 92]. The equivalence postulate is an important component of the theory proposed in sections 8.2 and 8.3, as it concerns not only the damage segment of the coupled model but is also reconducted for the mesocrack friction plasticity model.

The damage description including a unilateral effect based on the spectral decomposition of a second-order damage (or strain) tensor was earlier postulated by Chaboche [CHA 93], cited in section 8.3.1.

In this regard, Cormery and Welemane [COR 02] have put forward critical analyses regarding the spectral decomposition-based damage models. As we could expect, difficulties appear for the damage configurations involving multiple principal bases characterizing purely isotropic spatial damage distribution $\underline{\underline{D}} = d_0 \underline{\underline{I}}$ and the like subspace, partial symmetries of $\underline{\underline{D}}$ like transverse planar isotropic distribution, i.e. $\underline{\underline{D}} = d_0(\underline{e}_1 \otimes \underline{e}_1 + \underline{e}_2 \otimes \underline{e}_2)$, $\underline{e}_1$ and $\underline{e}_2$ representing orthogonal unit vectors. For such configurations involving an infinity of principal bases (non-uniqueness), the choice of a particular set of eigenvectors leads to a form of the energy function different from a form obtained for another licit system. We thus observe, in general, non-uniqueness of the energy and of the resulting response (e.g.

stiffness $\mathbb{C}(\underline{\underline{D}})$) for specific (sub)spatially uniform damage distribution. This has been shown in detail for this model, as well as for the model by Chaboche [CHA 93]. Furthermore, such a non-uniqueness may produce the loss of continuity of the energy function with respect to $\underline{\underline{D}}$ and thus brings into question the very definition of $\underline{\underline{F}}^0$ (thermodynamic force) and corresponding evolution laws. It should thus be stressed that the aforesaid isotropic and the like damage configurations involving the multiplicity of principal bases should be tentatively excluded from the operational domain of any spectral decomposition-based damage model. More fundamentally, some topological safeguards should be searched for to assure the energy uniqueness (i.e. the existence of the thermodynamic potential) in the close neighborhood of such configurations.

An alternative method based on the so-called "discrete approach" of damage has recently been advanced by Bargellini *et al*. [BAR 06]. This approach introduces a finite number of crack densities associated with an equal number of directions in space. It enables us to represent essential phenomena related to anisotropic damage, including unilateral effects. Most of all, this approach avoids the disadvantages cited above and related to models employing the unique second-order tensor variable $\underline{\underline{D}}$ and its spectral decomposition (non-uniqueness of the free energy for particular configurations of damage and decomposition of the strain tensor into the positive and negative parts).

8.5. References

[AND 81] ANDRIEUX S., "Un modèle de matériau microfissuré avec frottement", *C.R. Acad. Sci. Paris*, vol. 293, series 2, no. 5, p. 329-332, 1981.

[AND 86] ANDRIEUX S., BAMBERGER Y. and MARIGO J.J., "Un modèle de matériau microfissuré pour les bétons et les roches", *J. Mécanique Théor. Appl.*, vol. 5, p. 471-513, 1986.

[BAR 06] BARGELLINI R., HALM D. and DRAGON A. "Modelling of anisotropic damage by microcracks: toward a discrete approach", *Arch. Mech.*, vol. 58, p. 93-123, 2006.

[BAT 75] BATAILLE J. and KESTIN J., "L'interprétation physique de la thermodynamique rationnelle", *J. Mécanique*, vol. 14, no. 2, p. 365-384, 1975.

[BOE 78] BOEHLER J.P., "Lois de comportement anisotrope des milieux continus", *J. Mécanique*, vol. 17, no. 2, p. 153-190, 1978.

[CHA 93] CHABOCHE J.L., "Development of continuum damage mechanics for elastic solids sustaining anisotropic and unilateral damage", *Int. J. Damage Mech*., vol. 2, p. 311-329, 1993.

[CHA 94] CHARLEZ Ph., FRANÇOIS O. and BATHELLIER E., GEOFRAC, Activity report 1994, TOTAL Paris, 1994.

[COR 94] CORMERY F., Contribution à la modélisation de l'endommagement par mésofissuration et du phénomène de localisation associé, Thesis, Poitiers, 1994.

[COR 02] CORMERY K. and WELEMANE H., "A critical review of some damage models with unilateral effect", *Mech. Res. Comm.*, vol. 29, p. 391-395, 2002.

[CUR 95] CURNIER A., HE Q. and ZYSSET P., "Conewise linear elastic materials", *J. Elasticity*, vol. 37, p. 1-38, 1995.

[DAR 95] DARVE F., HICHER P.Y. and REYNOUARD J.M. [coordinators], *Les géomatériaux. Théories, expériences et modèles*, vol. I, Hermes editions, 1995.

[DRA 94] DRAGON A., CORMERY F., DESOYER T. and HALM D., "Localised failure analysis using damage models", *Localisation and Bifurcation Theory for Soils and Rocks, Proc. 3rd Internat. Workshop*, R. Chambon, J. Desrues, I. Vardoulakis (eds.), A.A. Balkema, Rotterdam, p. 127-140, 1994.

[DRA 00] DRAGON A., HALM D. and DESOYER T., "Anisotropic damage in quasi-brittle solids: modelling, computational issues and applications", *Comput. Methods Appl. Mech. Engrg*., vol. 183, p. 331-352, 2000.

[ELD 99], EL DALATI R., Modélisation numérique du comportement à la rupture des ancrages soumis à des efforts de cisaillement, ENPC Thesis, Marne-le-Vallée, 1999.

[FON 95] FOND C. and BERTHAUD Y., "Extensions of the pseudo-tractions technique for friction in cracks, circular cavities and external boundaries; effect of the interactions on the homogenised stiffness", *Int. J. Fracture*, vol. 74, p. 1-28, 1995.

[GAM 93] GAMBAROTTA L. and LAGOMARSINO S., "A microcrack damage model for brittle materials", *Int. J. Solids Structures*, vol. 30, no. 2, p. 177-198, 1993.

[GER 83] GERMAIN P., NGUYEN Q.S. and SUQUET P., "Continuum thermodynamics", *Trans. ASME, J. Appl. Mechanics*, vol. 50, p. 1010-1020, 1983.

[GOV 95] GOVINDJEE S., KAY G.J. and SIMO J.C., "Anisotropic modelling and numerical simulation of brittle damage in concrete", *Int. J. Num. Meth. Engrng*., vol. 38, p. 3611-3633, 1995.

[HAL 96] HALM D. and DRAGON A., "A model of anisotropic damage by mesocrack growth; unilateral effect", *Int. J. Damage Mech*., vol. 5, p. 384-402, 1996.

[HAL 97] HALM D., Contribution à la modélisation du comportement unilatéral et du frottement dans les matériaux mésofissurés, Thesis, Poitiers, 1997.

[HAL 98] HALM D. and DRAGON A., "An anisotropic model of damage and frictional sliding for brittle materials", *Eur. J. Mech., A/Solids*, vol. 17, no. 3, p. 439-460, 1998.

[HAL 02] HALM D., DRAGON A. and CHARLES Y., "A modular damage model for quasi-brittle solids: extension to initially anisotropic materials", *Archive of Appl. Mechanics*, vol. 72, p. 498-510, 2002.

[HOM 99] HOMAND F., HOXHA D., HALM D., DRAGON A. and SHAO J.F., Modélisation phénoménologique de l'endommagement du granite, GdR FORPRO-Géomécanique, Report, La Grande Motte, 1999.

[HOR 83] HORII M. and NEMAT-NASSER S., "Overall moduli of solids with microcracks: load-induced anisotropy", *J. Mech. Phys. Solids*, vol. 31, no. 2, p. 151-171, 1983.

[HOX 98] HOXHA D., Modélisation de l'endommagement des massifs rocheux, Thesis, Nancy, 1998.

[JAE 79] JAEGER J.C. and COOK N.G.W. *Fundamentals of Rock Mechanics* (3rd edition), Chapman and Hall, 1979.

[JU 89] JU J.W., "On energy-based coupled elastoplastic damage theories: constitutive modeling and computational aspects", *Int. J. Solids Structures*, vol. 25, p. 803-833, 1989.

[KAC 80] KACHANOV M., "Continuum model of medium with cracks", *J. Eng. Mechanics Div., ASCE*, vol. 106, no. EM5, p. 1039-1051, 1980.

[KAC 82] KACHANOV M., "A microcrack model of rock inelasticity; part I: frictional sliding on microcracks", *Mechanics of Materials*, vol. 1, no. 1, p. 19-27, 1982.

[KAC 92] KACHANOV M., "Effective elastic properties of cracked solids: cristal review of some basic concepts", *Appl. Mech. Rev*., vol. 45, no. 8, p. 261-335, 1992.

[LAD 94] LADEVEZE P., GASSER A. and ALLIX O., "Damage mechanics modeling for ceramic composites", *Trans. ASME, J. Eng. Mater. Techn*., vol. 116, p. 331-336, 1994.

[LAW 98] LAWN B.R. and MARSHALL D.B., "Nonlinear stress-strain curves for solids containing closed cracks with friction", *J. Mech. Phys. Solids*, vol. 46, no. 1, p. 85-113, 1998.

[LUB 93] LUBARDA V.A. and KRAJCINOVIC D., "Damage tensors and the crack density distribution", *Int. J. Solids Structures*, vol. 30, no. 20, p. 2859-2877, 1993.

[LUB 94] LUBARDA V.A., KRAJCINOVIC D. and MASTILOVIC S., "Damage model for brittle elastic solids with unequal tensile and compressive strengths", *Engng. Fracture Mech*., vol. 49, no. 5, p. 681-697, 1994.

[LUB 95] LUBARDA V.A. and KRAJCINOVIC D., "Some fundamental issues in rate theory of damage-elastoplasticity", *Int. J. Plasticity*, vol. 11, p. 763-797, 1995.

[MAZ 89] MAZARS J. and BERTHAUD Y., "Une technique expérimentale appliquée au béton pour créer un endommagement diffus et mettre en évidence son caractère unilatéral", *C.R. Acad. Sci. Paris*, vol. 308, series II, p. 579-584, 1989.

[NEM 88] NEMAT-NASSER S. and OBATA M., "A microcrack model of dilatancy in brittle materials", *Trans. ASME, J. Appl. Mechanics*, vol. 55, p. 24-35, 1988.

[ONA 89] ONAISI A., Mécanismes de rupture d'un bloc percé en mécanique des roches en relation avec la rupture en parois d'un forage pétrolier, ECP Thesis, Paris, 1989.

[ONA 89] ONAT E.T. and LECKIE F.A., "Representation of mechanical behavior in the presence of changing internal structure", *Trans. ASME, J. Appl. Mechanics*, vol. 55, p. 1-10, 1988.

[PEC 95] PECQUEUR G., Etude expérimentale et modélisation du comportement d'une craie et d'un grès en torsion, Thesis, Lille, 1995.

[PHA 94] PHAM D., Suivi numérique des bandes de localisation dans les structures endommageables (endommagement par mésofissuration, anisotropie induite) – applications en géomécanique, Thesis, Poitiers, 1994.

[WAL 65] WALSH J.B., "The effect of cracks on the uniaxal elastic compression of rocks", *J. Geoph. Res*., vol. 70, p. 399-411, 1965.

[WES 69] WESOLOWSKI Z., "Elastic material with different elastic constants in two regions of variability of deformation", *Arch. Mechanics*, vol. 21, no. 4, p. 449-468, 1969.

Constitutive Modeling of Soils and Rocks
Edited by Pierre-Yves Hicher & Jian-Fu Shao

Chapter 9

Multiscale Modeling of Anisotropic Unilateral Damage in Quasi-brittle Geomaterials: Formulation and Numerical Applications

9.1. Introduction

Inelastic behavior and the failure process in quasi-brittle geomaterials such as concrete and most rocks, are commonly considered to be the consequence of the nucleation and growth of microcracks. A number of experimental investigations have shown that there are different ways in which microcracks initiate and grow in rock materials [1-8]. In general, we shall take into account two dissipation mechanisms, related to the microcrack size evolution and the dissipative frictional sliding in closed microcracks respectively, in order to model the resulting damage. The main consequences of damage caused by microcracks growth are non-linear stress – strain relations, deterioration of elastic properties, induced anisotropy, irreversible deformation after unloading, volumetric dilatancy, hysteretic response and the effects of microcrack closure on the material macroscopic response. Moreover, induced anisotropic damage can also affect transport and diffusion properties, in particular permeability. Rock permeability can indeed increase significantly due to the propagation of microcracks and the associated volumetric dilatancy [9-14]. In this chapter, however, only mechanical modeling of anisotropic damage will be addressed.

The modeling of induced anisotropic damage is traditionally performed by means of macroscopic continuum damage models (CDM). In these models, internal

Chapter written by Djimédo KONDO, Qizhi ZHU, Jian-Fu SHAO and Vincent PENSEE.

variables (scalar, vector, second order tensor and even higher rank tensors) are used to describe the state of damage. A damage evolution law is commonly formulated as a function of stress or strain, using the standard framework of irreversible thermodynamics or some fracture mechanics principles; see for instance [15-22]. Uses of CDM have the ability of providing macroscopic constitutive equations which can be easily implemented in computer codes and applied to engineering analysis. Nevertheless, some assumptions used in these models are not clearly linked to physical mechanisms involved in the microcracking process, for instance, the so-called effective stress concept. Despite the numerical efficiency of this approach, some critical issues still remain open. For example, the purely macroscopic description of unilateral effects related to microcrack closure and of coupling between damage and frictional sliding still requires more careful physical and mathematical investigations which could be quite complex.

On the other hand, significant advances have recently been made in the field of multiscale damage modeling of quasi-brittle materials, which offers a new way to obtain a more physically based description of anisotropic damage related to the progressive evolution of materials microstructure [23-24]. In fact, various homogenization models have been proposed for concrete and rocks, see for example [25-27]. Most of these models are limited to dilute microcrack concentration and do not use an Eshelby type homogenization procedure to define the macroscopic elastic behavior. As a consequence, the effects of microcrack interaction and spatial distribution cannot be properly described [28]. Another aspect, which is important for damage modeling in brittle rocks, is the coupling between damage and frictional sliding on closed microcrack faces. This generally leads to volumetric dilatancy which was not properly considered in previous models.

In the current chapter, we formulate a multiscale model for anisotropic damage coupled with frictional sliding for quasi-brittle rocks. This model, based on Eshelby-like techniques, is then numerically implemented for structural analysis. The basic idea is to integrate the Eshelby solution-based homogenization techniques into the standard thermodynamics framework for the description of damage by microcracking. This provides a general micromechanics background for damage modeling in which the microcrack interaction [29] and spatial distribution [30] can also be described. A great emphasis will be put on the microcrack closure and on the coupling between damage and frictional phenomena which allows us to explain the salient features of quasi-brittle behaviors of rocks under compressive loadings. It comes from the micromechanical analysis that the crack density parameter [31] in each space orientation and two kinematic variables (sliding and opening along the crack surface) can represent inelastic deformations induced by the presence of microcracks. Furthermore, a damage criterion based on the energy release rate is proposed to describe the evolution of the crack density parameter. The condition for microcrack opening/closure transition will also be discussed. Comparisons of the

model's predictions with experimental data are performed on both conventional and true triaxial compression paths, respectively, for two granites. Applying the proposed multiscale model, implemented in the finite element software Abaqus with UMAT facility, to an underground excavation problem shows a good agreement between numerical results and *in situ* data concerning radial displacements and the evolution of the damaged zone.

Throughout the paper, the following notations for the product of second-order tensors A and B will be used: $\left(\mathbf{A}\otimes\mathbf{B}\right)_{ijkl}=A_{ij}B_{kl}$, $\left(\mathbf{A}\underline{\overline{\otimes}}\mathbf{B}\right)_{ijkl}=A_{ik}B_{jl}+A_{il}B_{jk}$. The tensor product of two vectors $\underline{a}$ and $\underline{b}$ is denoted $\left(\underline{a}\otimes\underline{b}\right)_{ij}=a_ib_j$ and its symmetric part $(\underline{a}\overset{s}{\otimes}\underline{b})_{ij}=\frac{1}{2}\left(a_ib_j+a_jb_i\right)$. With the second rank identity tensor δ, the usually used fourth order isotropic tensors $\mathbb{I}$ and $\mathbb{J}$ are expressed as $\mathbb{I}_{ijkl}=\frac{1}{2}\left(\delta_{ik}\delta_{jl}+\delta_{il}\delta_{jk}\right)$ and $\mathbb{J}_{ijkl}=\frac{1}{3}\delta_{ij}\delta_{kl}$, respectively.

9.2. Homogenization of microcracked materials: basic principles and macroscopic energy

The general purpose of multiscale methods is to establish the effective properties of the studied material from the knowledge of the material microstructure. For this purpose, the microcracked material is considered as a multiphase composite with a matrix phase weakened by a set of microcracks. In this framework, it is convenient to introduce a representative elementary volume (REV), denoted by Ω (with boundary $\partial\Omega$), as shown in Figure 9.1.

This REV is composed of an isotropic linear elastic matrix whose stiffness tensor is noted $\mathbb{C}^s$ and a distribution of microcracks with the elasticity tensor $\mathbb{C}^c$ ($\mathbb{C}^c=0$ for opened microcracks in order to account for the cancelation of the local stress $\boldsymbol{\sigma}^c$ on crack faces). Thus, the REV may be considered as a matrix-inclusion system; this allows us to use the fundamental Eshelby solution [32-33].

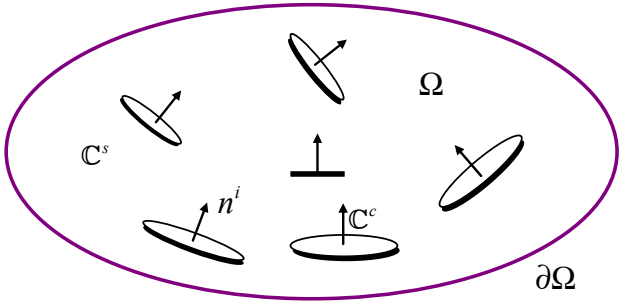

Figure 9.1. *Representative elementary volume (REV) of microcracked materials*

We assume that microcracks are the penny-shaped type. A family of cracks is identified by its normal $\underline{n}$, radius a and the half opening c (see Figure 9.2). The aspect ratio $\epsilon = c/a$ of such a penny-shaped crack is such that $\epsilon \ll 1$ (Figure 9.2). The volume fraction of cracks φ^c is expressed as:

$$\varphi^c = \frac{4}{3}\pi a^2 c \mathcal{N} = \frac{4}{3}\pi \epsilon d \tag{9.1}$$

where $\mathcal{N}$ denotes the crack density (number of cracks per unit volume) of the considered family of cracks and $d = \mathcal{N}a^3$ is the crack density parameter as initially introduced by Budiansky and O'Connell [31], and widely used as an internal damage variable in micromechanical analysis [34].

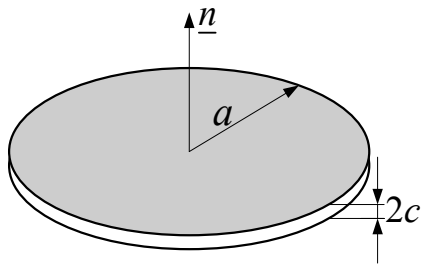

Figure 9.2. *Schematic representation of a penny-shaped crack*

The related displacement jump between the faces of two cracks is denoted by $[\underline{u}]$. The unilateral contact on the crack faces is then described by:

$$\left[u_n\right] \geq 0,\ \sigma_n^c \leq 0,\ \left[u_n\right] \cdot \sigma_n^c = 0 \tag{9.2}$$

where σ_n^c is the normal component of the local stress field and $\left[u_n\right]$ the normal component of the displacement jump $\left[\underline{u}\right]$.

We consider now a macroscopic uniform stress, Σ, applied to boundary $\partial\Omega$. The problem to be solved is the determination of local stress, strain and displacement fields inside the REV. According to [25] and [27], this problem may be decomposed into two sub-problems in terms of the displacement field, as shown in Figure 9.3. Accordingly, the macroscopic strain $\mathbf{E}$ of the cracked medium is written as the sum of two terms:

$$\mathbf{E} = \mathbf{E}^s + \mathbf{E}^c \tag{9.3}$$

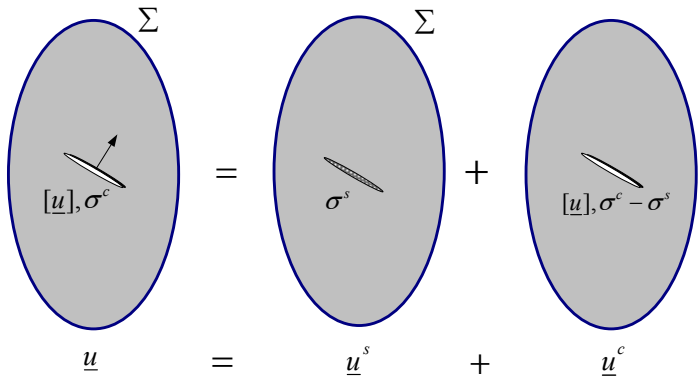

Figure 9.3. *Decomposition of the basic homogenization problem in terms of the displacement field*

The first term corresponds to the solid matrix strain $\mathbf{E}^s$ and the second term $\mathbf{E}^c$ is related to the contribution of microcracks, more precisely, to the microcrack displacement discontinuities, which read:

$$\mathbf{E}^c = \mathcal{N} \int_{\omega^+} \underline{n} \overset{s}{\otimes} \left[\underline{u}\right] dS = \beta\left(\underline{n} \otimes \underline{n}\right) + \underline{\gamma} \overset{s}{\otimes} \underline{n} \tag{9.4}$$

with β and $\underline{\gamma}$ as two kinematic variables characterizing the microcrack opening/closure state and the sliding in the crack plane, respectively, which are defined as:

$$\beta = \mathcal{N}\int_{\omega^+}[u_n]dS; \quad \underline{\gamma} = \mathcal{N}\int_{\omega^+}[\underline{u}_t]dS \tag{9.5}$$

Note that $[\underline{u}_t] = [\underline{u}] - [u_n]\underline{n}$. ω^+ denotes the crack surface with the unit normal $\vec{n}$.

The microscopic stress field $\boldsymbol{\sigma}^s$ is uniform which implies the relation: $\boldsymbol{\sigma}^s = \langle \boldsymbol{\sigma}^s \rangle_\Omega = \Sigma$ and the local stress $\left(\boldsymbol{\sigma}^c - \boldsymbol{\sigma}^s\right)$ on cracks is self balancing. Finally, the free energy W is expressed as the sum of an elastic energy corresponding to the solid matrix and of the stored energy due to the local stress field:

$$W = \frac{1}{2}\left(\mathbf{E} - \mathbf{E}^c\right) : \mathbb{C}^s : \left(\mathbf{E} - \mathbf{E}^c\right) - \frac{1}{2}\mathcal{N}\int_{\omega^+}\begin{Bmatrix}\left(\boldsymbol{\sigma}^c - \Sigma\right) : (\underline{n}\otimes\underline{n})[u_n] \\ +\underline{n}.\left(\boldsymbol{\sigma}^c - \Sigma\right).[\underline{u}_t]\end{Bmatrix}dS \tag{9.6}$$

In order to establish the relation between the deformation $\mathbf{E}^c$ and the local stress field $\boldsymbol{\sigma}^c$ in the cracks, inspired by the work of Barthelemy [35], the initial problem is decomposed into two sub-problems, as shown in Figure 9.4.

The solution of the sub-problem P^I is obtained through the homogenization procedure with the uniform macroscopic strain $\left(\mathbf{E} - \mathbb{S}^s : \boldsymbol{\sigma}^c\right)$ on the boundary $\partial\Omega$:

$$\mathbf{E}^I = \varphi^c \mathbb{A}^c : \left(\mathbf{E} - \mathbb{S}^s : \boldsymbol{\sigma}^c\right), \quad \mathbb{S}^s = \left(\mathbb{C}^s\right)^{-1} \tag{9.7}$$

where $\mathbb{A}^c$ is the concentration tensor associated with the considered family of microcracks. In the case of opening cracks ($\boldsymbol{\sigma}^c = 0$), the above expression (9.7) returns to that obtained in the traditional homogenization procedure:

$$\mathbf{E}^I = \varphi^c \mathbb{A}^c : \mathbf{E} \tag{9.8}$$

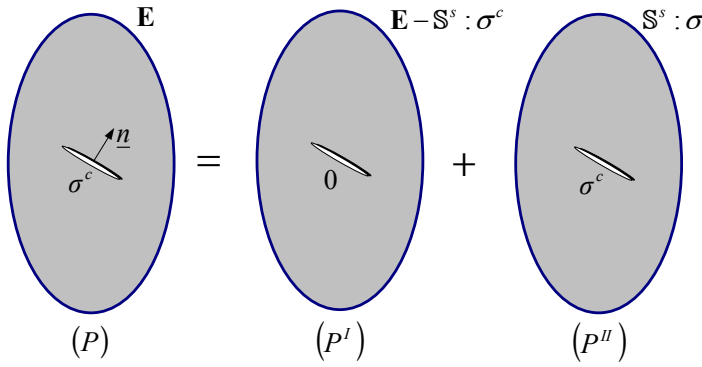

Figure 9.4. *Homogenization-based problem decomposition*

The corresponding macroscopic stress is determined with the help of the macroscopic stiffness tensor $\mathbb{C}^{\text{hom}}$:

$$\Sigma^I = \mathbb{C}^{\text{hom}} : \left(\mathbf{E} - \mathbb{S}^s : \boldsymbol{\sigma}^c\right) \tag{9.9}$$

for which we recall the general effective stiffness tensor $\mathbb{C}^{\text{hom}} = \mathbb{C}^s + \varphi^c(\mathbb{C}^c - \mathbb{C}^s) : \mathbb{A}^c$ in the case of open cracks ($\mathbb{C}^c = 0$) and frictionless closed cracks ($\mathbb{C}^c = 3k^s\mathbb{J}$). The uniformity of the sub-problem P^{II} gives:

$$\Sigma = \Sigma^I + \boldsymbol{\sigma}^c \tag{9.10}$$

The coherence between expressions (9.7) and (9.3) leads to the equality $\mathbf{E}^I = \mathbf{E}^c$, i.e.:

$$\beta\left(\underline{n} \otimes \underline{n}\right) + \underset{\sim}{\gamma}^s \otimes \underline{n} = \varphi^c \mathbb{A}^c : \left(\mathbf{E} - \mathbb{S}^s : \boldsymbol{\sigma}^c\right) \tag{9.11}$$

which allows us to simplify the notation by replacing $\mathbf{E}^c$ and $\mathbf{E}^I$ by $\mathbf{E}^{pl}$ [1]. The combination of (9.7), (9.9) and (9.10) allows us to express the local stress field $\boldsymbol{\sigma}^c$ according to the macroscopic stress Σ of the crack induced inelastic deformation $\mathbf{E}^{pl}$:

1 In fact, the strain due to closed microcracks is also referred to as "friction-induced plasticity" [20]. Its evolution can then be determined in the framework of classic plasticity theory.

$$\sigma^c = \sum - \mathbb{C}^{pl} : \mathbf{E}^{pl} \tag{9.12}$$

with

$$\mathbb{C}^{pl} = \left[\varphi^c \mathbb{A}^c : \left(\mathbb{I} - \varphi^c \mathbb{A}^c \right)^{-1} : \mathbb{S}^s \right]^{-1} \tag{9.13}$$

Equation (9.12) can also be rewritten in the form:

$$\sigma^c - \sum = -\mathbb{C}^{pl} : \mathbf{E}^{pl} \tag{9.14}$$

The insertion of (9.14) into (9.6) and using (9.4) gives the free energy function of the cracked material:

$$W = \frac{1}{2}\left(\mathbf{E} - \mathbf{E}^{pl} \right) : \mathbb{C}^s : \left(\mathbf{E} - \mathbf{E}^{pl} \right) + \frac{1}{2} \mathbf{E}^{pl} : \mathbb{C}^{pl} : \mathbf{E}^{pl} \tag{9.15}$$

9.3. Formulation of the multiscale anisotropic unilateral damage model

9.3.1. *Constitutive equations*

Profiting from the background previously defined, our aim is to formulate a micromechanical anisotropic damage model that accounts for microcrack closure. To this end, and thanks to the matrix-inclusion morphology of the microcracked materials, we implement the Mori-Tanaka estimate for which the following strain concentration tensor is available [28, 36, 37]:

$$\mathbb{A}^c = \left(\mathbb{I} - \mathbb{S}_\epsilon \right)^{-1} : \left[\varphi^s \mathbb{I} + \varphi^c \left(\mathbb{I} - \mathbb{S}_\epsilon \right) \right]^{-1} \tag{9.16}$$

where $\mathbb{S}_\epsilon$ is the Eshelby tensor corresponding to the penny-shaped crack inclusion (the components of $\mathbb{S}_\epsilon$ can be found in [23, 24]).

It is shown that for a unique family of microcracks, the macroscopic free enthalpy W^*, obtained by the means of the Legendre transform of the free energy W, can be expressed in the form:

$$W^* = \frac{1}{2}\Sigma : \mathbb{S}^s : \Sigma + \beta\,\Sigma : \left(\underline{n}\otimes\underline{n}\right) + \underline{\gamma}.\Sigma.\underline{n} - \frac{1}{2d}\left[H_0\beta^2 + H_1\underline{\gamma}.\underline{\gamma}\right] \tag{9.17}$$

with $H_0 = \dfrac{3E^s}{16\left[1-(\nu^s)^2\right]}$ and $H_1 = H_0\left(1-\dfrac{\nu^s}{2}\right)$.

Accordingly, the macroscopic Gibbs free energy, denoted Ψ^*, is obtained by integrating W^* over the unit sphere $\mathcal{S}^2 = \left\{\underline{n},\ |\underline{n}| = 1\right\}$:

$$\begin{aligned}\Psi^* = {} & \frac{1}{2}\Sigma : \mathbb{S}^s : \Sigma \\ & + \Sigma : \frac{1}{4\pi}\int_{\mathcal{S}^2}\left[\beta\left(\underline{n}\right)\left(\underline{n}\otimes\underline{n}\right) + \underline{\gamma}\left(\underline{n}\right)\overset{s}{\otimes}\underline{n}\right]dS \\ & - \frac{1}{8\pi}\int_{\mathcal{S}^2}\frac{1}{d\left(\underline{n}\right)}\left[H_0\beta^2\left(\underline{n}\right) + H_1\underline{\gamma}^2\left(\underline{n}\right)\right]dS\end{aligned} \tag{9.18}$$

Since distributions $\beta\left(\underline{n}\right)$, $\underline{\gamma}\left(\underline{n}\right)$ and $d\left(\underline{n}\right)$ are generally unknown for an arbitrary loading path, the closed-form expression of Ψ^* is not available. Thus, the Gauss type numerical integration formula with N points is adopted in this study, similarly to [38]. Therefore, integral form (9.18) is approximated as:

$$\begin{aligned}\Psi^* = {} & \frac{1}{2}\Sigma : \mathbb{S}^s : \Sigma + \Sigma : \sum_{r=1}^{N} w^r\left[\beta^r\left(\underline{n}^r\otimes\underline{n}^r\right) + \underline{\gamma}^r\overset{s}{\otimes}\underline{n}^r\right] \\ & - \frac{1}{2}\sum_{r=1}^{N}\frac{w^r}{d^r}\left[H_0\left(\beta^r\right)^2 + H_1\underline{\gamma}^r.\underline{\gamma}^r\right]\end{aligned} \tag{9.19}$$

where w^r is the weighting coefficient associated with the r^{th} microcrack family characterized by unit vector $\underline{n}^r$.

We shall now attempt to derive the expression of the macroscopic energy by taking into account the microcrack closure. First we determine from (9.15) the thermodynamic force associated with internal variable $\mathbf{E}^{pl}$:

$$\mathbf{F}^{pl} = -\frac{\partial W}{\partial \mathbf{E}^{pl}} = \sum -\mathbb{C}^{pl} : \mathbf{E}^{pl} = \boldsymbol{\sigma}^{c} \tag{9.20}$$

In a similar way, F^{β} and $\underline{F}^{\gamma}$ associated forces, with the forces associated with β and $\underline{\gamma}$ respectively, are given by:

$$F^{\beta} = -\frac{\partial W}{\partial \beta} = \boldsymbol{\sigma}^{c} : \left(\underline{n} \otimes \underline{n}\right) \tag{9.21}$$

$$\underline{F}^{\gamma} = -\frac{\partial W}{\partial \underline{\gamma}} = \boldsymbol{\sigma}^{c} . \underline{n} . \left(\delta - \underline{n} \otimes \underline{n}\right) \tag{9.22}$$

In agreement with (2), the crack opening/closure transition condition is defined by:

$$\boldsymbol{\sigma}^{c} : \left(\underline{n} \otimes \underline{n}\right) = 0, \text{ or } F^{\beta} = 0 \text{ (reversible process)} \tag{9.23}$$

which leads to the following relation for the Mori-Tanaka scheme:

$$\beta = \frac{d}{H_0} \sum : \left(\underline{n} \otimes \underline{n}\right) \tag{9.24}$$

Moreover, using condition $\underline{F}^{\gamma} = \underline{0}$ provides the following expression:

$$\underline{\gamma} = \frac{d}{H_1} \sum . \underline{n} . \left(\delta - \underline{n} \otimes \underline{n}\right) \tag{9.25}$$

Taking into account the unilateral condition, we need to make a clear distinction (in the energy contribution) between the opened crack families, numbered N_o, and the closed crack families, N_c with $N_c + N_0 = N$. The substitution of (9.24) and (9.25) into (9.19) yields the general expression:

$$\Psi^* = \frac{1}{2}\Sigma : \mathbb{S}^s : \Sigma + \frac{1}{2}\Sigma : \sum_{r=1}^{N_o} w^r d^r \left(\frac{1}{H_0}\mathbb{E}^{2,r} + \frac{1}{2H_1}\mathbb{E}^{4,r} \right) : \Sigma$$
$$+ \Sigma : \sum_{r=1}^{N_c} w^r \left[\beta^r \left(\underline{n}^r \otimes \underline{n}^r \right) + \underline{\gamma}^r \overset{s}{\otimes} \underline{n}^r \right] - \frac{1}{2}\sum_{r=1}^{N_c} \frac{w^r}{d^r} \left[H_0 \left(\beta^r \right)^2 + H_1 \underline{\gamma}^r . \underline{\gamma}^r \right]$$

(9.26)

with the notation $\Delta^r = \underline{n}^r \otimes \underline{n}^r$, $\mathbb{E}^{2,r} = \Delta^r \otimes \Delta^r$ and $\mathbb{E}^{4,r} = \frac{1}{2}\left[\Delta^r \underline{\overline{\otimes}} \left(\delta - \Delta^r \right) + \left(\delta - \Delta^r \right) \underline{\overline{\otimes}} \Delta^r \right] \cdot$

It is now possible to derive the first state law which defines the macroscopic stress-strain relations. We see from (9.26) that:

$$\mathbf{E} = \mathbb{S}^s : \Sigma + \sum_{r=1}^{N_o} w^r d^r \left(\frac{1}{H_0}\mathbb{E}^{2,r} + \frac{1}{2H_1}\mathbb{E}^{4,r} \right) : \Sigma + \sum_{r=1}^{N_c} w^r \left[\beta^r \left(\underline{n}^r \otimes \underline{n}^r \right) + \underline{\gamma}^r \overset{s}{\otimes} \underline{n}^r \right]$$

(9.27)

The second state law defining the thermodynamic force $F^{d^r} = \partial \Psi^* / \partial d^r$ associated with any internal damage variable d^r reads for a family of opened microcracks:

$$F^{d^r} = \frac{1}{2}\Sigma : \left(\frac{1}{H_0}\mathbb{E}^{2,r} + \frac{1}{2H_1}\mathbb{E}^{4,r} \right) : \Sigma \tag{9.28}$$

and equivalently:

$$F^{d^r} = \frac{1}{2\left(d^r \right)^2} \left[H_0 \left(\beta^r \right)^2 + H_1 \underline{\gamma}^r . \underline{\gamma}^r \right] \tag{9.29}$$

for a family of closed cracks. It is readily seen that $F^{d^r} = \partial \Psi^* / \partial d^r$ depends on the internal variables associated with each family of microcracks, namely $\beta^r, \underline{\gamma}^r, d^r$.

9.3.2. *Friction-damage coupling and evolution laws*

To complete the formulation of the damage model and its coupling with friction phenomena, we need to determine the evolution laws of damage and frictional sliding. It is assumed that the closed frictional microcracks obey the traditional Coulomb criterion at the local scale and that the saturation of the criterion is uniform on the microcrack faces. At the microscopic scale, the Coulomb criterion $g\left(\sigma^c\right)=0$ reads, as standard (in terms of normal and tangential components of the local stress σ^c applied on the microcracks faces):

$$g=\left|\sigma^c.\underline{n}.\left(\delta-\underline{n}\otimes\underline{n}\right)\right|+\mu_c\sigma^c:\left(\underline{n}\otimes\underline{n}\right)=0 \tag{9.30}$$

where μ_c is the friction coefficient on the microcrack faces. In terms of thermodynamic forces F^β and $\underline{F}^\gamma$, this criterion also reads:

$$g\left(\sigma^c\right)=\left|\underline{F}^\gamma\right|+\mu_c F^\beta=0 \tag{9.31}$$

It must be emphasized that the pressure sensitivity of geomaterial behavior is taken into account through the effect of normal stress on the crack $\sigma^c:\left(\underline{n}\otimes\underline{n}\right)$ (which explicitly appears in (9.30)).

Concerning the damage evolution law, the following general form, based on the energy-release rate, is adopted for the damage criterion of each family of microcracks:

$$f\left(F^d,d\right)=F^d-\mathcal{R}\left(d\right)=0 \tag{9.32}$$

Function $\mathcal{R}\left(d\right)$ represents the material resistance to the damage evolution by microcrack growth, which can be theoretically determined from experimental investigations. For the sake of simplicity, we consider here an affine function of d, as initially proposed in [39] in the context of macroscopic modeling of isotropic damage:

$$\mathcal{R}\left(d\right)=c_0+c_1 d \tag{9.33}$$

where c_0 and c_1 are two constitutive parameters, respectively defining the initial damage threshold and the kinetics of the damage evolution. These parameters may be identified from experimental data showing progressive degradation of elastic properties during unloading cycles in triaxial compression tests.

Adopting the normality rule, the rates of damage variable d and of sliding vector $\underline{\gamma}$ in the presence of frictional contact are determined by:

$$\dot{d} = \dot{\lambda}^d \frac{\partial f\left(F^d, d\right)}{\partial F^d} = \dot{\lambda}^d \tag{9.34}$$

$$\dot{\underline{\gamma}} = \dot{\lambda}^\gamma \frac{\partial g}{\partial \underline{F}^\gamma} = \dot{\lambda}^\gamma \underline{\upsilon} \tag{9.35}$$

where $\dot{\lambda}_d$ and $\dot{\lambda}_\gamma$ are the multipliers associated with damage and frictional sliding respectively; they are determined by using simultaneously consistency conditions $\dot{f} = 0$ and $\dot{g} = 0$. The unit vector $\underline{\upsilon}$ represents the direction of frictional sliding, defined by $\underline{\upsilon} = \underline{F}^\gamma / \left|\underline{F}^\gamma\right|$.

For the evolution of variable β, which represents the microcrack opening displacement due to frictional sliding of microcracks, two different situations can be singled out:

– frictional sliding without dilatation in smooth microcracks, for which we have $\dot{\beta} = 0$. This leads to an unassociated flow rule for the inelastic deformation $\mathbf{E}^{pl}$;

– frictional sliding with normal dilatation on microcracks with rough faces, for which $\dot{\beta} \neq 0$.

From the physical point of view, the dilatation is related here to the asperity on the microcrack faces and to the misfit of microcrack faces after the unloading of applied stresses (see Figure 9.5). This generally leads to the occurrence of inelastic volumetric strains after a complete unloading.

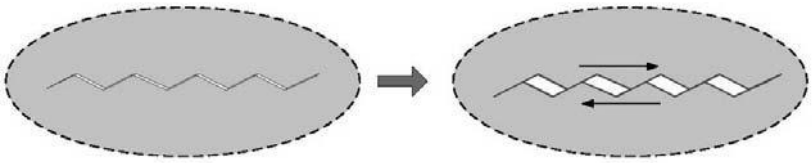

Figure 9.5. *Schematic representation of dilatant crack sliding mechanism*

For simplicity, we also adopt here a normality flow rule for the evolution of $\mathbf{E}^{pl}$. It follows that:

$$\dot{\beta} = \mu_c \dot{\lambda}^{\gamma} \tag{9.36}$$

Subsequently the evolution law of variable E^{pl} reads:

$$\dot{E}^{pl} = \dot{\beta}\left(\underline{n} \otimes \underline{n}\right) + \dot{\underline{\gamma}} \overset{s}{\otimes} \underline{n} = \dot{\lambda}^{\gamma}\left(\underline{\upsilon} \overset{s}{\otimes} \underline{n} + \mu_c \underline{n} \otimes \underline{n}\right)$$

A detailed theoretical analysis of the coupled damage-friction model can be found in Zhu (2006).

9.4. Computational aspects and implementation of the multiscale damage model

We are now interested in implementing the proposed damage-friction coupled model into the finite element software Abaqus. This is performed by means of the provided user subroutine UMAT. In this subroutine, the material Jacobian matrix, $\partial \sum / \partial E$, must be provided for the mechanical constitutive model and the values of stresses and solution-dependent state variables (i.e. the variables d^r, β^r and $\underline{\gamma}^r$ in this study) must be updated at the end of the increment. For this purpose, we need to determine the rate form of the macroscopic stress-strain relation which provides the consistent tangent operator. Then, we will present the local integration of the proposed model.

9.4.1. *Determination of the tangent matrix*

The strategy adopted here consists of starting from the macroscopic stress-strain relation (9.27) and of expressing the macroscopic strain rate $\dot{E}$ as a function of the stress rate:

$$\dot{\mathbf{E}} = \mathbb{S}_t^{\hom} : \dot{\sum} \tag{9.37}$$

The Jacobian matrix can be obtained by an inverse calculation of $\mathbb{S}_t^{\hom}$ [28]. For a given family of closed microcracks, if the damage growth condition and friction sliding criteria are simultaneously verified, we will obtain the following consistency conditions:

$$\begin{cases} \dfrac{\partial g}{\partial \Sigma} : \dot{\Sigma} + \dfrac{\partial g}{\partial \underline{\gamma}} . \dot{\underline{\gamma}} + \dfrac{\partial g}{\partial \beta} \dot{\beta} + \dfrac{\partial g}{\partial d} \dot{d} = 0 \\ \dfrac{\partial f}{\partial \underline{\gamma}} . \dot{\underline{\gamma}} + \dfrac{\partial f}{\partial \beta} \dot{\beta} + \dfrac{\partial f}{\partial d} \dot{d} = 0 \end{cases} \tag{9.38}$$

whereas for a given family of opened microcracks, the consistency condition for damage evolution reads:

$$\frac{\partial f}{\partial \Sigma} : \dot{\Sigma} + \frac{\partial f}{\partial d} \dot{d} = 0 \tag{9.39}$$

Considering relations (9.38) and (9.39), respectively, for the families of closed and opened cracks, as well as the rate form of (9.27), the tangent operator $\mathbb{S}_t^{\text{hom}}$ reads:

$$\mathbb{S}_t^{\text{hom}} = \mathbb{S}^s + \frac{1}{c_1} \sum_{r=1}^{N_o} \left\langle f^r \right\rangle \omega^r \frac{\partial f^r}{\partial \Sigma} \otimes \frac{\partial f^r}{\partial \Sigma} + \sum_{r=1}^{N_c} \left\langle g^r \right\rangle \omega^r \frac{d^r}{\tilde{H}_\gamma^r} \frac{\partial g^r}{\partial \Sigma} \otimes \frac{\partial g^r}{\partial \Sigma} \tag{9.40}$$

with f^r the damage function of the r^{th} family of microcracks:

$$\frac{\partial f^r}{\partial \Sigma} = \left(\frac{1}{H_0} \mathbb{E}^{2,r} + \frac{1}{2H_1} \mathbb{E}^{4,r} \right) : \Sigma, \quad \frac{\partial g^r}{\partial \Sigma} = \underline{\upsilon}^r \overset{s}{\otimes} \underline{n}^r + \mu_c \underline{n}^r \otimes \underline{n}^r ,$$

and

$$\tilde{H}_\gamma^r = H_1 + \mu_c^2 H_0 - \frac{\left\langle f^r \right\rangle (\mu_c H_0 \beta^r + H_1 \underline{\gamma}^r . \underline{\upsilon}^r)^2}{H_0 (\beta^r)^2 + H_1 \underline{\gamma}^r . \underline{\gamma}^r + c_1 (d^r)^3}$$

where $\left\langle x \right\rangle = 1$ when $x > 0$, and zero otherwise.

9.4.2. *Local integration of the model*

Considering the requirements of the user subroutine UMAT in Abaqus, an incremental procedure associated with the rate form of stress-strain relation and based on the strain discretization of the considered loading path is used. Furthermore, a widely-used prediction-correction splitting numerical scheme is adopted, given the

strongly non-linear character of the constitutive law. The scheme from step j to $j+1$ is briefly summarized as follows:

(1) elastic prediction:

For each family of microcracks, allow $d_{j+1} = d_j$, $\beta_{j+1} = \beta_j$, $\underline{\gamma}_{j+1} = \underline{\gamma}_j$;

calculate $\mathbf{E}_j^e = \mathbf{E}_j - \sum_{r=1}^{N} \omega^r \left(\beta^r \underline{n}^r \otimes \underline{n}^r + \underline{\gamma}^r \overset{s}{\otimes} \underline{n}^r \right)$,

then $\mathbf{E}_{j+1}^e = \mathbf{E}_j^e + \Delta\mathbf{E}_{j+1}$ and $\sum_{j+1} = \mathbb{C}^s : \mathbf{E}_{j+1}^e$.

(2) examine the opening-closure condition for each family:

$$F^{\beta^r} = \sum_{j+1} : \left(\underline{n}^r \otimes \underline{n}^r \right) - \frac{H_0}{d_j^r} \beta_j^r$$

(3) determination of increments $\Delta d_{j+1}^r, \Delta \underline{\gamma}_{j+1}^r$ *and* $\Delta \beta_{j+1}^r$:

$F^{\beta^r} > 0$: calculate Δd_{j+1}^r using (9.32) and (9.28) for open cracks;

$F^{\beta^r} \le 0$: examine the frictional sliding criterion (9.30) for closed cracks:

$$\begin{cases} \text{if } g < 0, \text{ then } \Delta d_{j+1}^r = 0, \Delta \underline{\gamma}_{j+1}^r = 0, \Delta \beta_{j+1}^r = 0 \\ \text{if } g \ge 0, \text{ calculate } \Delta \underline{\gamma}_{j+1}^r, \Delta \beta_{j+1}^r \text{ using (9.31)} \\ \text{calculate } f^r : \begin{cases} \text{if } f^r < 0, \text{ then } \Delta d_{j+1}^r = 0; \\ \text{or, calculate } \Delta d_{j+1}^r \text{ using (9.39)} \end{cases} \end{cases}$$

(4) update the variables: $d_{j+1}^r = d_j^r + \Delta d_{j+1}^r$; $\underline{\gamma}_{j+1}^r = \underline{\gamma}_j^r + \Delta \underline{\gamma}_{j+1}^r$; $\beta_{j+1}^r = \beta_j^r + \Delta \beta_{j+1}^r$

(5) update the stress tensor: calculate Σ_{j+1}

9.5. Illustration of the model predictions for shear tests

In order to illustrate the performance of the micromechanical model in various cases (closed frictional microcracks, with and without dilatancy, with and without damage evolution), we should investigate the macroscopic behavior of a material weakened by a family of microcracks with the unit normal $\underline{e}_3$. The damaged material is subjected to a simple shearing path defined by $E_{13} = E_{23}$, which is monotonous or cyclic. To keep the cracks closed, we apply beforehand a compressive stress $\Sigma_{33} = 10$ MPa in the direction perpendicular to the crack plane, i.e. $\underline{e}_3$. The model's parameters used in the simulations are E^s = 33,330 MPa, $\nu^s = 0.23$, $c_0 = 2.5\times10^{-3} J.m^{-2}$, $c_1 = 0.08\ J.m^{-2}$ and $\mu_c = 0.4$. The initial value of the damage is chosen to be equal to $d_0 = 0.1$.

Monotonous loading path

Figure 9.6 shows the comparisons of the mechanical responses predicted by the model for the FCD case (non-dilatant frictional cracks with damage evolution) and FDCD case **(**frictional dilatant cracks with damage evolution).

It is observed that the model, based on the Mori-Tanaka Scheme, predicts a strain hardening response. As expected, volumetric dilatations are obtained in the FDCD case.

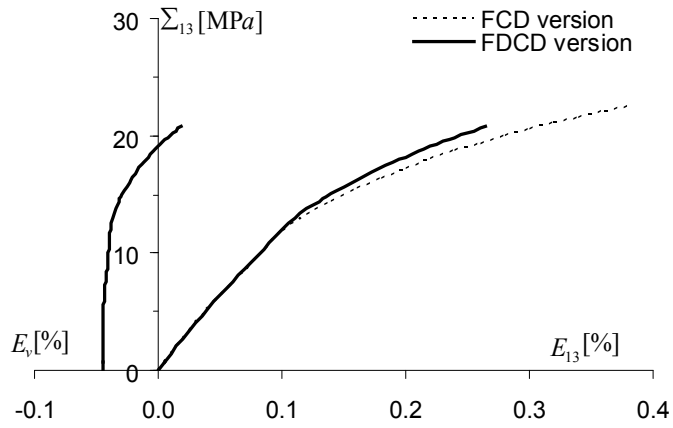

Figure 9.6. *Response (shear strain and volumetric strain) on monotonous loading path predicted by the model. Note the great amount of volumetric strain predicted in the case of dilatant cracks*

Cyclic loading path

The responses predicted by the homogenization scheme for the cyclic loading path are illustrated in Figures 9.7a and 9.7b. From a qualitative point of view, three response phases can be noted as in monotonous loading. Irreversible strains and hysteretic loops during loading-unloading paths are observed as a consequence of the frictional mechanism. Furthermore, the hysteretic loops are closed at the end of the reloading path for the FCD models, similar to those obtained by Lawn and Marshall (1998) in the absence of damage evolution. In contrast, open loops are found for the FDCD models; this is in agreement with the evolution of variable β associated with the volumetric dilatation.

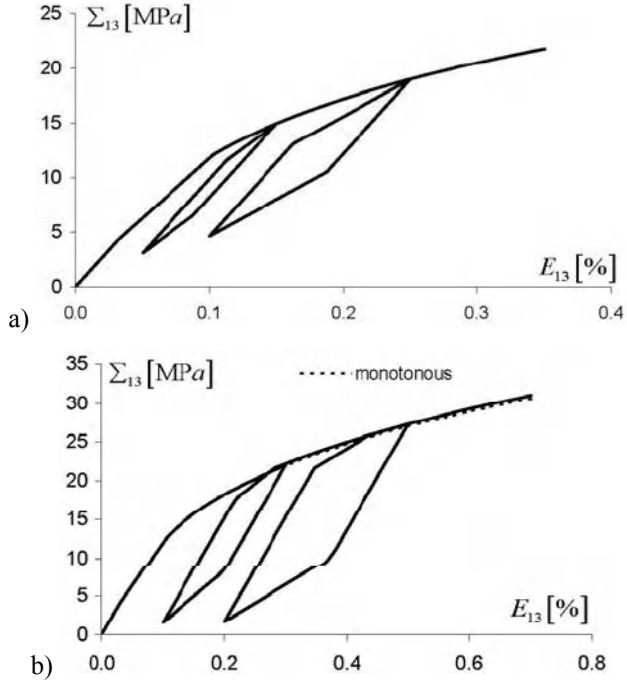

Figure 9.7. *Response on a cyclic loading path predicted by: a) FCD model; b) FDCD model*

9.6. Model's validation for laboratory data including true triaxial tests

In order to provide a preliminary evaluation of the proposed model, we consider in this section the conventional and true triaxial compression tests on two granites (Lac du Bonnet in Canada, Westerly in USA) for which data is available. The

proposed model requires only six parameters with a clear physical meaning for each one. The initial elastic constants E_0 and v_0 can be determined from the linear part of the standard stress-strain curve in a compression test. Parameters c_0 and c_1, involved in the damage criterion, may be determined by evaluating the progressive degradation of the elastic modulus on the unloading stress-strain curves. Friction coefficient μ_c may be evaluated by comparing the mechanical responses with different confining pressures. The initial overall density of microcrack distribution is assumed to be isotropic and characterized by d_0. Its value could be determined from a hydrostatic compression test or, more accurately, from electron microscopy scans.

9.6.1. *Validation by comparison with conventional triaxial compression tests*

The model is first checked by running simulations of conventional triaxial compression tests under different confining pressures. The considered material is known as Lac du Bonnet granite, largely studied in the underground research laboratory for nuclear waste storage in Canada [41-43]. The following parameter values are considered for the simulation: $E^s = 68,000$ MPa, $\nu^s = 0.21$, $c_0 = 3\times10^{-3} J.m^{-2}$, $c_1 = 6\times10^{-2} J.m^{-2}$, $d_0 = 1\times10^{-3}$, $\mu_c = 0.7$. The comparisons of the stress-strain (axial strain E_{11} [%], lateral strain $E_{22} = E_{33}$ [%] and volumetric strain E_v [%]) curves between the experimental data and model predictions are shown in Figures 9.8 to 9.10. It can easily be seen that the main features of quasi-brittle geomaterial behavior, previously mentioned, are correctly described by the model. Moreover, comparisons of numerical predictions between the models with and without friction-based dilatation are also presented. It is observed that the model with dilatation offers a much better prediction then the model without dilatation. Therefore, the macroscopic volumetric dilatancy of these quasi-brittle materials can be physically interpreted as a consequence of the microscopic normal dilatation during frictional sliding along microcracks. In Figure 9.9, some unloading paths are shown. As the microcracks are closed due to compressive stresses and due to the fact that the microcrack sliding is locked by frictional effect, a linear elastic response appears during unloading of the deviatoric stress.

Figure 9.11 shows the simulation of a lateral extension test. In this particular test, the rock sample is first submitted to a hydrostatic stress 60 MPa. The axial stress Σ_{11} is increased in a second stage to a prescribed value. In the last stage, the confining pressure is progressively reduced while the axial stress is kept constant. This test is widely performed in rock mechanics because it approximately reproduces the stress path near the cavity boundary during excavation in axisymmetric conditions. The numerical simulation presented here was performed

for $\Sigma_{11} = 160$ MPa and $\Sigma_{22} = \Sigma_{33} = 60$ MPa . A good agreement is obtained between the test data and the model's predictions. Furthermore, it is noted that in this case the difference between the models with and without dilatation is small.

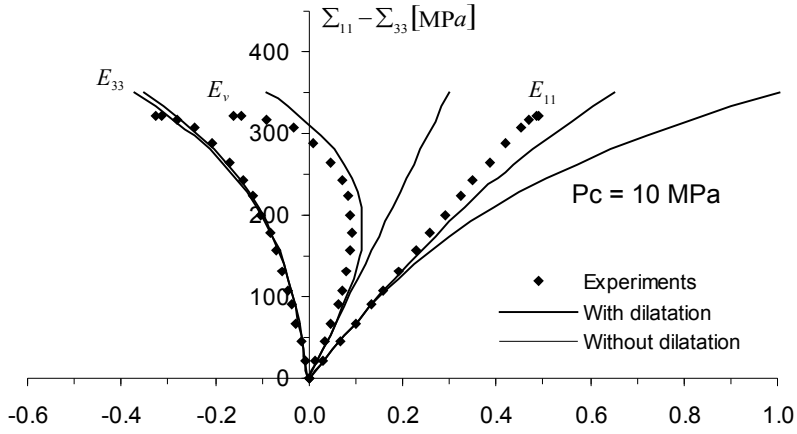

Figure 9.8. *Comparison between data and model's predictions for a triaxial compression test with confining pressure of 10 MPa using the models with and without frictional dilatation*

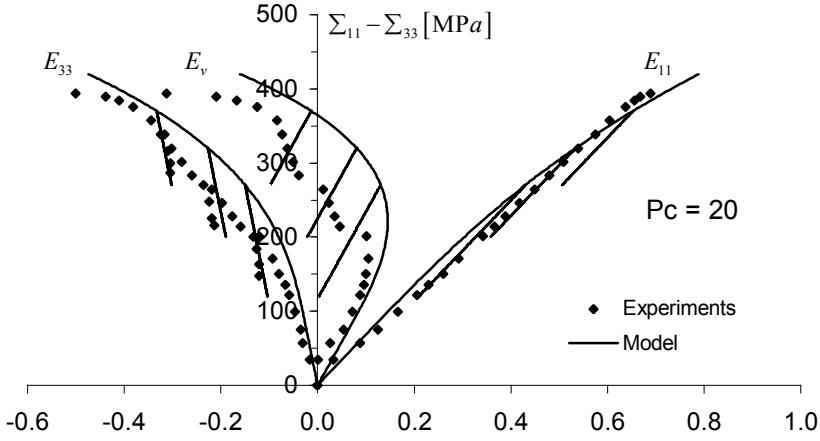

Figure 9.9. *Comparisons between data and model's predictions for a triaxial compression cyclic test with confining pressure of 20 MPa using the model with frictional dilatation*

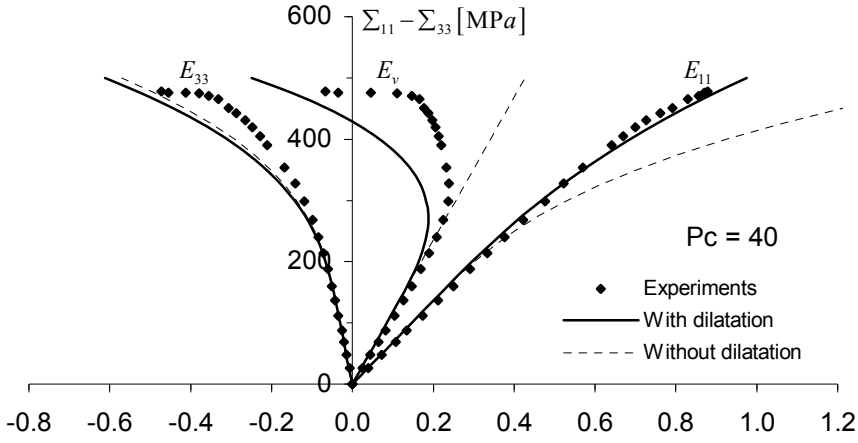

Figure 9.10. *Comparisons between data and model's predictions for a triaxial compression test with confining pressure of 40 MPa using the models with and without frictional dilatation*

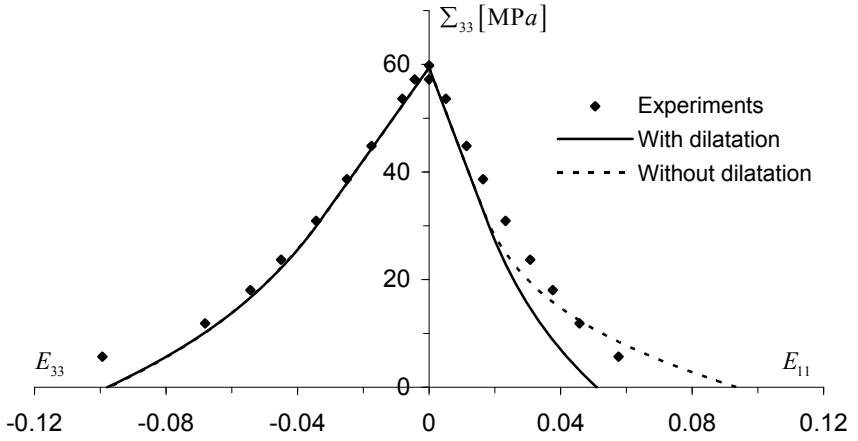

Figure 9.11. *Comparison between data and model's prediction for a lateral extension test*

9.6.2. *Simulations of true triaxial compression tests*

The simulations of conventional triaxial compression tests provide a first validation of the model in the particular case of axisymmetric loading. We now investigate the performance of the model in more general loading conditions. To this

end, we propose comparing numerical predictions and experimental data available from true triaxial compression tests performed on Westerly granite (USA) by Haimson and Chang [44]. The tests were performed on cubic specimens by independently controlling three principal stresses in three axes. We follow a procedure which consists of identifying the model's parameters on a conventional triaxial compression test with a confining pressure of 60MPa and simulating the true triaxial tests. The following values are obtained: $E^s = 68,000$ MPa, $\nu^s = 0.21$, $c_0 = 3\times10^{-3}$ J.m^{-2}, $c_1 = 0.18$ J.m^{-2}, $d_0 = 1\times10^{-3}$, $\mu_c = 0.7$.

The loading path applied in the true triaxial tests is composed of three steps: i) a hydrostatic compression phase until 60 MPa; ii) $\sum_{33}$ being kept constant (60 MPa) and increasing $\sum_{11} = \sum_{22}$ to the prescribed values of 60 MPa, 113 MPa, 180 MPa and 249 MPa; and iii) the value of $\sum_{22}$ and $\sum_{33}$ being kept constant and the value of $\sum_{11}$ increasing from $\sum_{11} = \sum_{22}$ to prescribed values of 747 MPa, 822 MPa, 860 MPa and 861 MPa. The model is now applied to simulate these tests and the comparisons between its predictions and test data are shown in Figure 9.12. An agreement is observed for the different loading paths considered.

It is worth noting that, contrary to phenomenological models, the multiscale model is able to provide not only overall stress-strain responses, but also the anisotropic distribution of the microcrack density parameter. Figure 9.13 shows 3D damage density distributions with the different intermediate principal stress value $\sum_{22}$. Noting o as the original point in the considered space and a as a point on the distribution functions surfaces, the direction of the vector $\overrightarrow{oa}$ corresponds to the family of microcracks with unit normal $\overrightarrow{oa}/\left\|\overrightarrow{oa}\right\|$ and the damage density evaluated by $\left\|\overrightarrow{oa}\right\|$. We notice that as $\sum_{22}$ increases from 60 MPa to 249 MPa, the growth of damage in plane 1-2 is progressively blocked. In addition, the greatest value always occurs in plane 1-3 and the dip angles for all the four tests are always around 62°. This value is slightly different from the experimental data (ranging from 67° to 72°) reported in [43]. The difference may be explained by the fact that the frictional sliding criterion (9.30) is an interfacial criterion and, thus, the intermediate stress $\sum_{22}$ cannot be taken into account for the microcracks with normal vectors within plane 1-3.

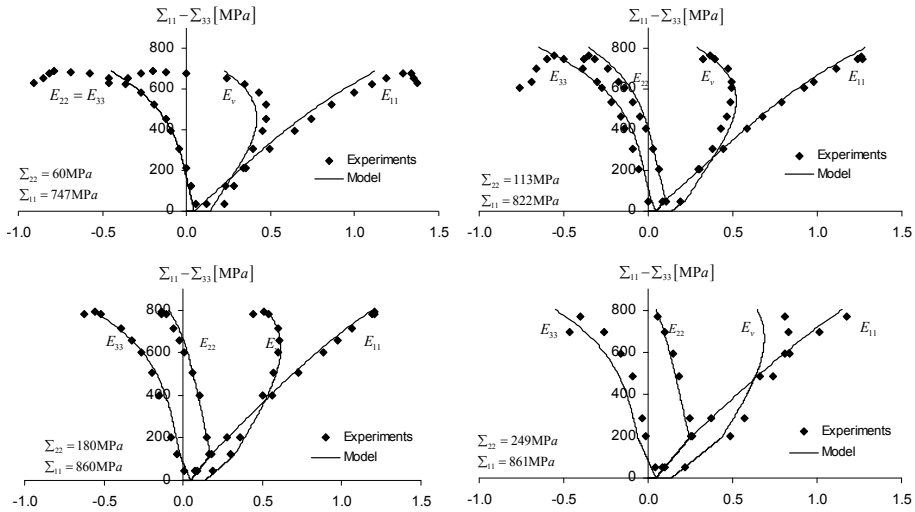

Figure 9.12. *Comparisons of model's predictions with experimental data for true triaxial compression tests on Westerly granite [44]*

9.7. Application on an underground structure: evaluation of the excavation damage zone (EDZ)

After the simulation of laboratory tests, in this section, we will discuss the feasibility of applying the micromechanical model to engineering problems. We propose to study mechanical responses induced by the excavation of a 3.5 m diameter circular tunnel in the context of the Underground Research Laboratory for nuclear waste storage (URL-ACEL Canada). The experiment was conducted at the 420 m level in order to investigate the rock damage process during excavation using a non-explosive technique [41, 43, 45]. The tunnel is subjected to a strongly deviatoric initial stress state as shown in Figure 9.14.

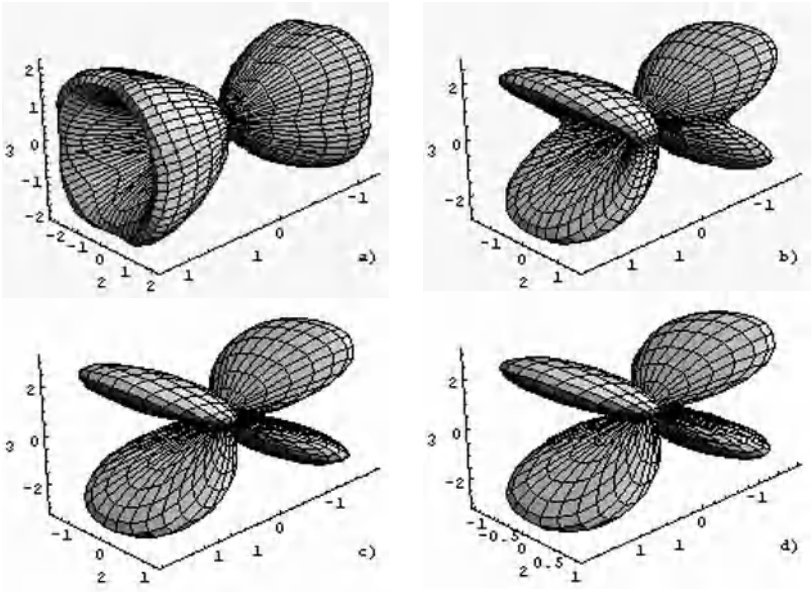

Figure 9.13. *Microcracks density parameter distributions in true triaxial compression tests on Westerly granite: a)* $\sum_{22} = 60$ MPa, $\sum_{11} = 747$ MPa *; b)* $\sum_{22} = 113$ MPa, $\sum_{11} = 822$ MPa *c)* $\sum_{22} = 180$ MPa, $\sum_{11} = 860$ MPa *; d)* $\sum_{22} = 249$ MPa, $\sum_{11} = 861$ MPa

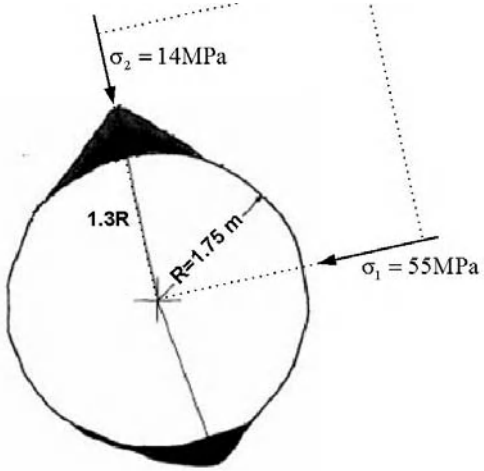

Figure 9.14. *Observing the damaged zones around the tunnel excavation [45]*

Radial displacement evolution and acoustic emission were monitored. *In situ* observations showed two damaged zones in the direction of the minor principal stress (see Figure 9.14). It has been also observed that the size of the damaged zones as well as the radial displacement evolve in time due to time-dependent behavior. However, in this study, only the short term behavior is investigated. Multiscale modeling of the viscous effects accompanying the damage process will be the subject of further investigations.

The initial *in situ* stress state is defined by three principal stresses as follows: $\sigma_1 = 55$ MP*a* , $\sigma_2 = 14$ MP*a* and $\sigma_3 = 48$ MP*a* . The tunnel axis is quasi-parallel to the intermediate principal stress direction. Therefore, 2D modeling was performed under plane strain conditions. Due to the symmetry of the problem, with respect to two principal stresses, only a quarter of the domain is considered. The studied region with the outer boundary of 30×30 *m* was meshed with 900 rectangular elements. The excavation process is simulated by reducing the normal stress on the tunnel wall from its initial value to the atmospheric pressure. The parameters used for the FEM modeling were determined from a uniaxial compression test on the Lac du Bonnet granite. In Figure 9.15, the distribution of the microcrack density parameter around the excavation is shown. The induced damage zone appears localized on the top point of the excavation along the minor principal stress. This is qualitatively in agreement with *in situ* observations. The predicted size of the damaged zone is also close to that observed in place, varying between 0.43 m and 0.52 m [45]. Furthermore, tensile stresses were obtained in numerical predictions in some zones near the tunnel wall (see Figure 9.16). However, the magnitude of the maximum tensile stress (5.3 MPa) is quite small and less than the tensile strength of material which is about 10 MPa. Therefore, the damage is essentially induced by closed cracks due to compressive stresses. The principal mechanism is frictional sliding along microcracks coupled with crack propagation and dilatation.

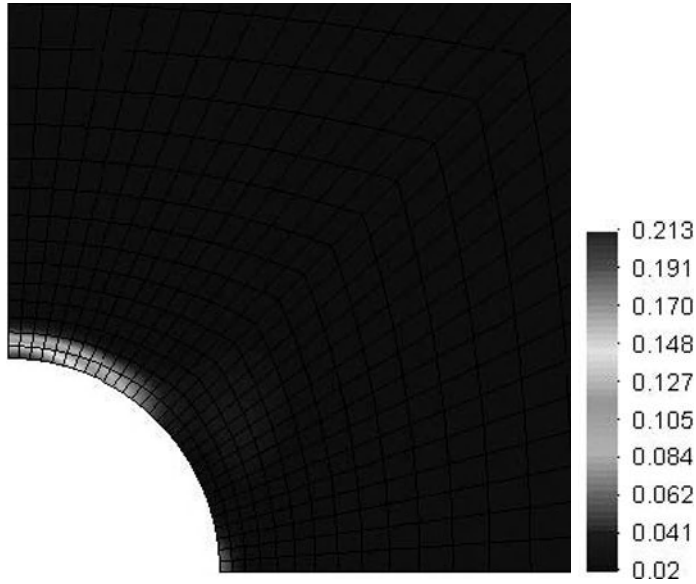

Figure 9.15. *Distribution of the damaged zone*

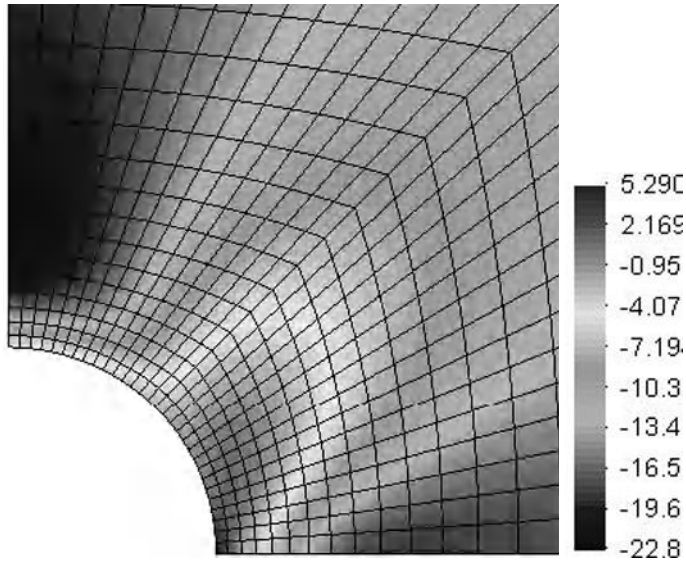

Figure 9.16. *Distribution of the principal stress* Σ_1

In Figure 9.17, we show the radial displacements (convergence) on the tunnel wall in different directions (0° corresponds to the major stress direction). The *in situ* data is obtained by extensometers placed around the excavation [45]. We can point out a good qualitative agreement between the predicted results and *in situ* data.

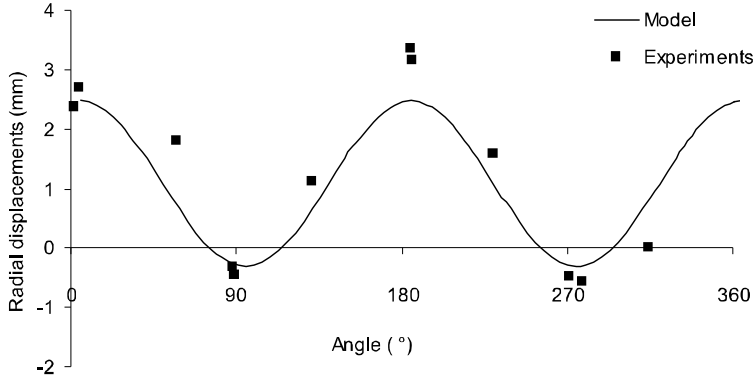

Figure 9.17. *Comparisons of radial convergence between in situ measurement and model prediction*

9.8. Conclusions

This chapter has been devoted to the formulation and application of multiscale anisotropic damage. The materials under investigation are quasi-brittle geomaterials. The model is formulated within a micro-macro framework using a general homogenization procedure, together with a thermodynamics approach of irreversible dissipation mechanisms. An important feature of the model is the incorporation of unilateral effects due to microcrack closure. Coupling of the damage mechanisms with friction phenomena on closed microcrack faces allows us to account for the main features of mechanical behaviors in quasi-brittle geomaterials: non-linear stress-strain relations, volumetric dilatancy, hysteretic behavior, coupling between microcrack growth and frictional sliding. The model contains a small number of parameters and each one contains a physical interpretation. It is applied to two granites and a good agreement between the model's predictions and experimental data for various loading paths has been obtained. The model is also implemented into a standard FEM code. The calculation strategy used for this implementation has been described in detail. An example of a structure has been presented to show the applicability of the micromechanical model to engineering problems. The extension of the model will include, for example, the objective modeling of strain localization as well as the subsequent failure process, the correlation between induced damage and permeability evolution and the time-dependent behavior due to sub-critical microcrack growth.

9.9. References

[1] Brace W.F., Bombolakis E.G. (1963), "A note on brittle crack growth in compression", *J. of Geophys. Res.* 68(12), 3709-3713.

[2] Wawersik W.R., Brace W.F. (1971), "Post-failure behavior of a granite and diabase", *Rock Mechanics*, 3, 61-85.

[3] Nemat-Nasser S. and Horii H. (1982), "Compression-induced non-planar crack extension with application to splitting, exfoliation and rock-burst", *Journal of Geophysical Research*, 87(B8), 6805-6821.

[4] Wong T.F. (1982), "Micromechanics of faulting in Westerly granite", *Int. J. Rock Mech. Min. Sci.*, 19, 49-6.

[5] Kranz R.L. (1983), "Microcracks in rocks: a review", *Tectonophysics*, 100: 449-480.

[6] Stef P.S. (1984), "Crack extension under compressive loading", *Engineering Fracture Mechanics*, 20(3), 463-473.

[7] Horii H. and Nemat-Nasser S. (1985), "Compression-induced microcrack growth in brittle solids: axial splitting and shear failure", *J. of Geophys. Res.*, 90(B4), 3105-3125.

[8] Martin C.D., Chandler N.A. (1994), "The progressive failure of Lac du Bonnet granite", *Int. J. Rock Mech. Min. Sci.*, 31(4), 643-659.

[9] Kamiya T., Tita H., Ishijima Y., Aoki K., Sato T. (1996), "Permeability in anisotropic granite under hydrostatic compression and triaxial compression including post-failure region", in Aubertin M., Hassani F., Miitri H. (eds.), *Rock Mechanics*, Balkema, Potterdam; 1643-1650.

[10] Chen Z., Narayan S.P., Yang Z., Rahman S.S. (2000), "An experimental investigation of hydraulic behaviours of fractures and joints in granitic rock", *Int. J. Rock Mech. Min. Sci.*, 37, 1061-1071.

[11] Souley M., Homand F., Pepa S. and Hoxha D. (2001), "Damage-induced permeability changes in granite: a case example at the URL in Canada", *Int. J. Rock Mech. Min. Sci.*, 38, 297-310.

[12] Bossart P., Meier P.M., Moeri A., Trick T. and Mayor J.C. (2002), "Geological and hydraulic characterisation of the excavation disturbed zone in the Opalinus Clay of the Mont Terri Rock Laboratory", *Engineering Geology*, 66, 19-38.

[13] Oda M., Takemura T., Aoki T. (2002), „Damage growth and permeability change in triaxial compression tests of Inada granite", *Mechanics of Materials*, 34, 313-331.

[14] Shao J.F., Zhou H. and Chau K.T. (2005), "Coupling between anisotropic damage and permeability variation in brittle rocks", *International Journal for Numerical and Analytical Methods in Geomechanics*, 29, 1231-1247.

[15] Chow C.L., June W. (1987), "An anisotropic theory of elasticity for continuum damage mechanics", *International Journal of Fracture*, 33: 3-16.

[16] Ju J.W. (1989), "On energy based coupled elastoplastic damage theories: constitutive modeling and computational aspects", *International Journal of Solids and Structures*, 25(7): 803-833.

[17] Lemaitre J. (1992), *A Course on Damage Mechanics* (2nd ed.), Springer, Berlin.

[18] Chaboche J.L. (1993), "Development of continuum damage mechanics for elastic solids sustaining anisotropic and unilateral damage", *International Journal of Damage Mechanics*, 2: 311-329.

[19] Murakami S., Kamiya K. (1996), "Constitutive and damage evolution equations of elastic brittle materials based on irreversible thermodynamics", *Int. J. Mech. Sci.*, 39(4): 473-486.

[20] Halm D., Dragon A. (1996), "A model of anisotropic damage by mesocrack growth: unilateral effect", *Int. J. Damage Mech.*, 5: 384-402.

[21] Krajcinovic, D. (1996), *Damage Mechanics*, North Holland, Amsterdam, The Netherlands.

[22] Swoboda G., Yang Q. (1999), "An energy-based damage model of geomaterials I and II: deduction of damage evolution laws", *Int. J. Solids Structures*, 36: 1735-1755.

[23] Mura T. (1987), *Micromechanics of Defects in Solids*, (2nd ed.), Martinus Nijhoff Publ., The Hague, Boston.

[24] Nemat-Nasser S., Hori M. (1993), *Micromechanics: Overall Properties of Heterogeneous Materials*, North Holland, Amsterdam, the Netherlands.

[25] Andrieux S., Bamberger Y. Marigo J.J. (1986), "Un modèle de matériau microfissuré pour les roches et les bétons", *Journal de Mécanique Théorique et Appliqué*, 5(3): 471-513.

[26] Gambarotta, L., Lagomarsino, S. (1993), "A microcrak damage model for brittle materials", *Int. J. Solids Structures*, 30(2): 177-198.

[27] Pensée V. Kondo D., Dormieux L. (2002), "Micromechanical analysis of anisotropic damage in brittle materials", *J. Engng. Mech.*, ASCE, 128(8): 889-897.

[28] Zhu Q.Z. (2006), Applications des approches d'homogénéisation à la modélisation tridimensionnelle de l'endommagement des matériaux quasi fragile : Formulation, validation et implémentation numérique. Doctoral thesis (in French), University of Lille I, France.

[29] Mori T., Tanaka K. (1973), "Averages stress in matrix and average elastic energy of materials with misfitting inclusions", *Acta Metal*., 21: 571-574.

[30] Ponte-Castaneda P., Willis J.R. (1995), "The effect of spatial distribution on the behavior of composite materials and cracked media", *J. Mech. Phys. Solids*, 43: 1919-1951.

[31] Budiansky, B., O'Connell, J.R. (1976), "Elastic moduli of a cracked solid", *Int. J. Solids Structures*, 12: 81-97.

[32] Eshelby, J.D. (1957), "The determination of the elastic field of an ellipsoidal inclusion and related problems", *Proc. Royal Soc. London*, A241: 375-396.

[33] Eshelby, J.D., "Elastic inclusions and heterogeneities", *Progress in Solid*, 1961, vol. 2, Chapter 3, North Holland Publishing Co., Amsterdam, The Netherlands.

[34] Dormieux L. and Kondo D. (2005), "Poroelasticity and damage theory for cracked media", in *Applied micromechanics of porous media*, CISM, L. Dormieux and F. J. Ulm (eds.), 153-183.

[35] Barthelemy J.F., Dormieux L., Kondo D. (2003), "Détermination du comportement macroscopique d'un milieu à fissures frottantes", *C.R. Mécanique*, 331: 77-84.

[36] Benveniste Y. (1986), "On the Mori-Tanaka method in cracked bodies", *Mechanics Research Communications*, 13(4): 193-201.

[37] Benveniste Y. (1987), "A new approach to the application of Mori-Tanaka's theory in composite materials", *Mechanics of Materials*, 6: 147-157.

[38] Bazant Z.P., Oh B.H. (1986), "Efficient numerical integration on the surface of a sphere", *Z.A.M.M.*, 66: 37-49

[39] Marigo J.J. (1981), "Formulation d'une loi d'endommagement d'un matériau élastique", *C.R. Acad. Sc. Paris*, II, 292: 1309-1312.

[40] Lawn, B.R., Marshall, D.B. (1998), "Nonlinear stress-strain curves for solids containing closed cracks with friction", *J. Mech. Phys. Solids*, 46(1), 85-113.

[41] Martin C.D., Read R.S., Martino J.B. (1997), "Observation of brittle failure around a circular test tunnel", *Int. Journ. of Rocks Mechanics and Min. Sci.*, 34(7): 1065-1073.

[42] Shao J.F., Hoxha D., Bart M., Homand F., Duveau G., Souley M., Hoteit N. (1999), "Modelling of induced anisotropic damage in granites", *Int. Journ. of Rocks Mechanics and Min. Sci.*, 36: 1001-1012.

[43] Martino J.B., Chandler N.A. (2004), "Excavation-induced damage studies at the Underground Research Laboratory", *International Journal of Rock Mechanics & Mining Sciences*, 41, 1413–1426.

[44] Haimson B., Chang C. (2000), "A new true triaxial cell for testing mechanical properties of rock and its use to determine rock strength and deformability of Westerly granite", *Int. Journ. of Rocks Mechanics and Min. Sci.*, 37: 285-296.

[45] Read R.S., Martin C.D. (1996), Technical summary of AECL's mine-by experiment phase 1: Excavation response, report AECL-11311, COG-95-171.

Constitutive Modeling of Soils and Rocks
Edited by Pierre-Yves Hicher & Jian-Fu Shao

Chapter 10

Poromechanical Behavior of Saturated Cohesive Rocks

10.1. Introduction

This chapter is devoted to the poromechanical modeling of saturated cohesive rocks. Limiting the discussion to this class of materials, we will briefly review the constitutive models developed so far for various coupled poromechanical behavior. In traditional soil mechanics, the pore pressure effect is generally taken into account by using the Terzaghi's effective stress concept. However, it is known that this effective stress concept is not valid for general cases, in particular for cohesive geomaterials. More general approaches should thus be proposed. We will present the fundamental features and general methodologies for modeling three types of behavior of saturated media: poroelasticity, poroplasticity and damage mechanics. As a number of general studies on the modeling of poroelasticity and poroplasticity already exist, we will only recall some basic concepts, emphasizing in particular parameter identification for these two classes of behaviors. Given that modeling damage in saturated porous materials is only a recently developed topic, the field is still largely open and, at the same time, of great interest for many engineering applications. This is why an important part of this chapter is devoted to this topic. Limiting the discussions to macroscopic consideration, we try to provide a general methodology for damage modeling of saturated materials and an example of a constitutive model is given for a saturated porous rock.

Chapter written by Jian-Fu SHAO and Albert GIRAUD.

10.2. Fundamentals of linear poroelasticity

In this section, we begin by presenting the fundamental relations of the linear poroelasticity initially proposed by Biot [BIO 41, 55, 57; COU 91]. The porous medium is seen as an open thermodynamic system exchanging fluid mass with the exterior domain. Limited to isothermal and small deformation cases, the state variables involved are strain tensor ε and fluid mass change per unit initial volume m. Considering a natural initial state (without pre-stress and pressure), the quadratic free energy function is:

$$w(\boldsymbol{\varepsilon}, m) = g_m^0 m + \frac{1}{2}\boldsymbol{\varepsilon} : \mathbf{C} : \boldsymbol{\varepsilon} - \left(\frac{m}{\rho_f^0}\right) M(\mathbf{B} : \boldsymbol{\varepsilon}) + \frac{1}{2} M \left(\frac{m}{\rho_f^0}\right)^2 \tag{10.1}$$

where g_m^0 is the specific free fluid enthalpy and ρ_f^0 the reference volumetric fluid mass. The fourth order tensor $\mathbf{C}$ denotes the elastic stiffness of the porous medium in undrained conditions. The second order tensor B is Biot's coefficient tensor and the scalar parameter M is the Biot modulus. The standard derivative of (10.1) leads to the constitutive relations of linear elasticity:

$$\boldsymbol{\sigma} = C : \boldsymbol{\varepsilon} - M\ \mathbf{B}\left(\frac{m}{\rho_f^0}\right) \tag{10.2}$$

$$(g_m - g_m^0) = -\left(\frac{1}{\rho_f^0}\right) M(\mathbf{B} : \boldsymbol{\varepsilon}) + \left(\frac{1}{\rho_f^0}\right) M \left(\frac{m}{\rho_f^0}\right) \tag{10.3}$$

Using the state law of perfect fluid, relation (10.3) may be rewritten in the following form:

$$(g_m - g_m^0) = \frac{p - p_0}{\rho_f^0} \tag{10.4}$$

$$(p - p_0) = M\left[-\mathbf{B} : \boldsymbol{\varepsilon} + \left(\frac{m}{\rho_f^0}\right)\right] \tag{10.5}$$

Substituting (10.5) for (10.2) leads to the constitutive relations of linear poroelasticity in drained conditions:

$$\boldsymbol{\sigma} = \mathbf{C}^b : \boldsymbol{\varepsilon} - \mathbf{B}\left(p - p_0\right) \tag{10.6}$$

$$\mathbf{C}^b = \mathbf{C} - M(\mathbf{B} \otimes \mathbf{B}) \tag{10.7}$$

where $\mathbf{C}^b$ is the drained elastic stiffness tensor. Relation (10.6) may be rewritten as:

$$\boldsymbol{\sigma}'^{el} = \mathbf{C}^b : \boldsymbol{\varepsilon} \tag{10.8}$$

$$\boldsymbol{\sigma}'^{el} = \boldsymbol{\sigma} + \mathbf{B}\, p \tag{10.9}$$

The second order tensor $\boldsymbol{\sigma}'^{el}$ is called the effective stress for elastic deformation because it is the thermodynamic force associated with the elastic strain tensor.

The following discussion is devoted to the identification of poroelastic parameters. For the sake of simplicity, only an isotropic material is considered:

$$\boldsymbol{\sigma} - \boldsymbol{\sigma}^0 = 2\mu^b \boldsymbol{\varepsilon} + \lambda^b tr(\boldsymbol{\varepsilon})\mathbf{I} - b\left(p - p_0\right)\mathbf{I} \tag{10.10}$$

$$(p - p_0) = M\left[-btr(\boldsymbol{\varepsilon}) + \left(\frac{m}{\rho_f^0}\right)\right] \tag{10.11}$$

$\boldsymbol{\sigma}^0$ and p_0 denote the initial stress and pore pressure at the reference state of deformation. λ^b and μ^b are Lame constants in drained conditions and b is Biot's coefficient.

Four parameters suffice to describe the linear poroelastic behavior: two elastic constants in the drained condition (λ^b and μ^b or equivalently drained Young's modulus E^b Poisson's ratio ν^b) and two coupling parameters b and M. The elastic constants may be identified in the framework of linear elasticity through standard laboratory tests. As for determining the coupling parameters, we see that microstructural analysis applied to saturated porous media leads to the following intrinsic relations [COU 95; DOR 05]:

$$b = 1 - \frac{K_b}{K_s}, \quad \frac{1}{M} = \frac{b - \phi}{K_s} + \frac{\phi}{K_f} \tag{10.12}$$

K_s and K_f are respectively the compressibility modulus of the solid matrix and the fluid. ϕ denotes the connected porosity. Using the constitutive relations of poroelasticity, the following additional relationships may be obtained:

$$b = \frac{1}{B_s}\left(1 - \frac{K_b}{K}\right) \tag{10.13}$$

$$B_s = \frac{bM}{K}, \; K = K_b + b^2 M \tag{10.14}$$

Parameter K is the bulk modulus of a porous medium in undrained conditions, which can be determined from the stress strain curve in an undrained hydrostatic compression test:

$$K = \left(\frac{\Delta\sigma_m}{\Delta\varepsilon_v}\right)_{\Delta m=0} \tag{10.15}$$

where $\sigma_m = tr\sigma/3$ is the mean stress and $\varepsilon_v = tr\varepsilon$ the volumetric strain. In the same test, we can also measure the pore pressure generated by compressive stress, leading to Skempton's coefficient B_s as defined by (see (10.13)):

$$B_s = -\frac{\Delta p}{\Delta\sigma_m} \tag{10.16}$$

An example of Skempton's coefficient measurement is shown in Figure 10.1 for sandstone [KAR 98]. In relation (10.12), K_b is the drained bulk modulus, which may be identified from the stress-strain curve obtained from a drained hydrostatic compression test:

$$K_b = \left(\frac{\Delta\sigma_m}{\Delta\varepsilon_v}\right)_{\Delta p=0} \tag{10.17}$$

In Figure 10.2, typical stress strain curves are shown for drained hydrostatic compression tests on sandstone [KAR 98]. In practice, it is often useful and even recommended to perform a mixed hydrostatic compression test. In such a test, two

loading phases are used: in the first phase, hydrostatic stress (confining pressure) is increased by keeping the pore pressure constant. In the second phase, the pore pressure is increased while the confining stress is kept unchanged. The volumetric strain is measured in each phase. By applying the poroelastic constitutive relations to this loading path, we can express Biot's coefficient as a function of the volumetric strain measured during the two phases by:

$$b = \frac{(\Delta\varepsilon_v)_{\Delta\sigma_m=0}}{(\Delta\varepsilon_v)_{\Delta p=0}} \tag{10.18}$$

Finally, note that the compressibility modulus of solid matrix K_s, is a micro-structural parameter, unlike moduli, K_b and K, which are macroscopic parameters. In practice the modulus (or more precisely, the average value of compressibility of the solid matrix) K_s, may be determined from a specific compression test in which the confining stress and pore pressure are simultaneously increased with $\Delta\sigma_m = \Delta p$. The following relation gives the value of K_s:

$$K_s = \left(\frac{\Delta\sigma_m}{\Delta\varepsilon_v}\right)_{\Delta\sigma_m=\Delta p} \tag{10.19}$$

An example of such a test for sandstone is shown in Figure 10.3 [KAR 98].

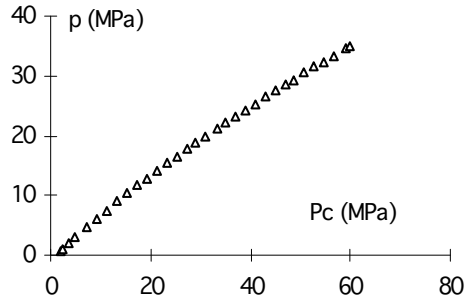

Figure 10.1. *Typical stress-pore pressure curve in undrained hydrostatic compression test on sandstone used for the determination of Skempton's coefficient [KAR 98]*

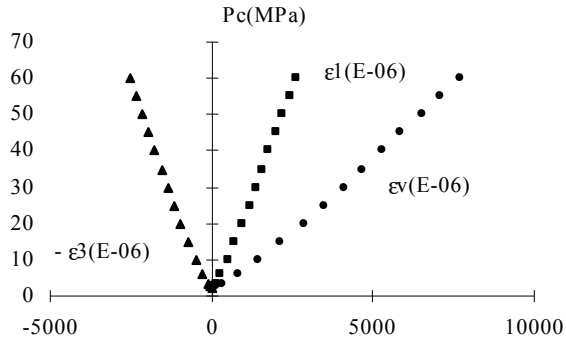

Figure 10.2. *Typical stress strain curves in drained hydrostatic compression test on sandstone [KAR 98]*

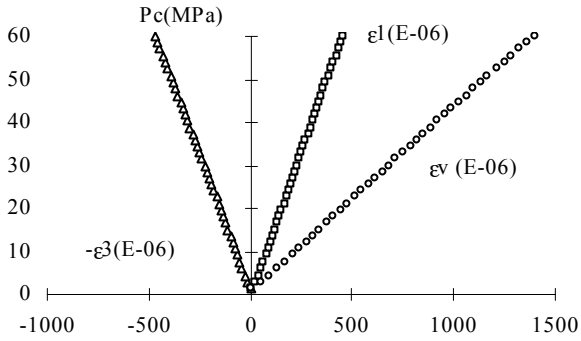

Figure 10.3. *Typical stress strain curves in hydrostatic compression test with* $\Delta\sigma_m = \Delta p$ *on sandstone [KAR 98]*

10.3. Fundamentals of poroplasticity

In this section, we address fundamental features for modeling plastic behavior in saturated porous media. More detailed discussions may be found in [BIO 73; COU 91; COU 95]. Within the framework of small disturbances in a porous medium exhibiting elastoplastic behavior, the strain tensor and fluid mass change are divided into an elastic and a plastic part as:

$$\boldsymbol{\varepsilon} = \boldsymbol{\varepsilon}^e + \boldsymbol{\varepsilon}^p \,,\; m = m^e + m^p \tag{10.20}$$

In practice, it is convenient to use a state variable homogenous with strain to represent irreversible change of fluid mass. Thus the concept of plastic porosity is introduced and defined by:

$$\phi^p = m^p / \rho_f^0 \tag{10.21}$$

The thermodynamic potential for poroelastic medium is extended to include a plastic process:

$$w(\boldsymbol{\varepsilon}^e, m^e, \mathbf{V}_k) = g_m^0 m + \frac{1}{2}\boldsymbol{\varepsilon}^e : \mathbf{C} : \boldsymbol{\varepsilon}^e - \left(\frac{m}{\rho_f^0} - \phi^p\right) M(\mathbf{B} : \boldsymbol{\varepsilon}^e) + \frac{1}{2} M \left(\frac{m}{\rho_f^0} - \phi^p\right)^2 + w^p(\mathbf{V}_k) \tag{10.22}$$

The term $w^p(\mathbf{V}_k)$ denotes locked energy due to plastic hardening, and is a function of internal hardening variables denoted by the set $\mathbf{V}_k$ (scalar for isotropic hardening and tensorial for kinematic hardening). The standard derivative of the thermodynamic potential leads to the constitutive relations of elastoplastic behavior of a saturated porous medium:

$$\boldsymbol{\sigma} - \boldsymbol{\sigma}^0 = \mathbf{C}^b : (\boldsymbol{\varepsilon} - \boldsymbol{\varepsilon}^p) - \mathbf{B}\left(p - p_0\right) \tag{10.23}$$

$$(p - p_0) = M\left[-\mathbf{B} : (\boldsymbol{\varepsilon} - \boldsymbol{\varepsilon}^p) + \left(\frac{m}{\rho_f^0} - \phi^p\right)\right] \tag{10.24}$$

The fundamental Clausius-Duhem inequality for intrinsic dissipation is written as:

$$\boldsymbol{\sigma} : \dot{\boldsymbol{\varepsilon}}^p + p\dot{\phi}^p - \mathbf{A}_k \dot{\mathbf{V}}_k \geq 0\,,\ \mathbf{A}_k = \frac{\partial w}{\partial \mathbf{V}_k} \tag{10.25}$$

Complementary plastic laws are now required to determine the evolution rate of basic state variables ($\dot{\boldsymbol{\varepsilon}}^p, \dot{\phi}^p, \dot{\mathbf{V}}_k$). This may be done by establishing a (dual) plastic dissipation potential. However, considering the time-independent process, plastic complementary laws are defined by a yield function, a plastic potential in the case of unassociated flow and a hardening function. The yield function is an indicative function of a convex elastic domain; it is a scalar function of stresses and thermodynamic forces associated with hardening variables, i.e.:

$$f(\boldsymbol{\sigma}, p, \mathbf{A}_k) = 0 \tag{10.26}$$

For most geomaterials with internal friction, hypothesizing generalized standard materials are not verified. The normality rule for the plastic potential is therefore invalid. We thus have to define a complementary plastic potential and a specific hardening function verifying the dissipation condition (10.25), which could be expressed in the following general form:

$$\dot{\boldsymbol{\varepsilon}}^p = \lambda \frac{\partial g(\boldsymbol{\sigma}, p, \mathbf{A}_k)}{\partial \boldsymbol{\sigma}},\ \dot{\phi}^p = \lambda \frac{\partial g(\boldsymbol{\sigma}, p, \mathbf{A}_k)}{\partial p},\ \dot{\mathbf{A}}_k = \lambda h(\boldsymbol{\sigma}, p, \mathbf{A}_k) \tag{10.27}$$

The complementary plastic laws are constrained by Kuhn-Tucker conditions:

$$\lambda \geq 0\ ,\ f(\boldsymbol{\sigma}, p, \mathbf{A}_k) \leq 0\ \ ,\ \ \lambda f(\boldsymbol{\sigma}, p, \mathbf{A}_k) = 0 \tag{10.28}$$

The plastic multiplier $\lambda \geq 0$ is determined by the plastic consistency condition $\dot{f} = 0$.

The above formulation provides the general framework for elastoplastic modeling of saturated porous media. Note that the yield function, the plastic potential and the hardening law depend independently on the stress tensor, the pore pressure and the conjugated hardening forces. The specific forms of these functions can be found from relevant experimental data. However, experimental identification is usually a difficult task, requiring a series of laboratory tests with complex loading paths. In order to simplify the plastic modeling of porous media, the concept of effective stress formulated in poroelasticity is extended to poroplasticity. Based on the so-called stress equivalence principle, the basic idea is to extend the plastic complementary functions obtained for dry materials to saturated porous media by simply substituting an effective stress tensor for the nominal stress tensor. The essential question is the validity of this concept in the plastic field and how to determine the form of the effective stress. This feature is still an open topic although experimental investigations and micromechanical analyses have been performed [PIE 95; KHE 95; BUH 96; LAD 97; LYD 00]. The conclusion obtained thus far is that the effective stress concept is generally not valid in the plastic field making it impossible to define a general form for such an effective stress. Depending on the microstructure of porous media, the validity of effective stress may be proven only for a few specific cases. For example, for a porous medium with a solid matrix obeying the Von-Mises criterion, we find that the traditional Terzaghi effective stress is valid in the plastic field. In this case, the plastic functions may be formulated with Terzaghi's effective stress to take into account the effect of pore pressure on plastic flow.

For purely macroscopic considerations, some (unproven) kinematic hypotheses may be formulated. For example, it is assumed that plastic porosity is proportional to plastic volumetric strain [COU 91; 95], i.e.:

$$\dot{\phi}^p = \beta \dot{\varepsilon}^p_{kk}\,,\ \beta \in [0,1] \tag{10.29}$$

Coefficient β plays a role similar to Biot's coefficient in poroelasticity, even though its value is generally different. Given this assumption, the intrinsic dissipation inequality becomes:

$$(\boldsymbol{\sigma} + \beta p\mathbf{I}) : \dot{\boldsymbol{\varepsilon}}^p - \mathbf{A}_k \dot{\mathbf{V}}_k \geq 0 \tag{10.30}$$

In view of this, the quantity $(\boldsymbol{\sigma} + \beta p\mathbf{I})$ appears as the thermodynamic force associated with the plastic strain tensor. In this sense, the term $(\boldsymbol{\sigma} + \beta p\mathbf{I})$ is called the effective stress tensor in the plastic field. Accordingly, the plastic potential may be simplified as:

$$g(\boldsymbol{\sigma}, p, \mathbf{A}_k) \equiv g(\boldsymbol{\sigma}'^{pl}, \mathbf{A}_k)\,,\ \boldsymbol{\sigma}'^{pl} = \boldsymbol{\sigma} + \beta p\mathbf{I} \tag{10.31}$$

To complete the formulation, we need to assume that the yield function may also be expressed with the effective stress tensor, i.e.:

$$f(\boldsymbol{\sigma}, p, \mathbf{A}_k) \equiv f(\boldsymbol{\sigma}'^{pl}, \mathbf{A}_k) = 0 \tag{10.32}$$

Within the framework of the above assumptions, we may conclude that the plastic modeling of saturated porous media is formally reduced to the plastic modeling of an equivalent dry material. Finally we note that the value of coefficient β may be determined from specific laboratory tests [YAM 81; KHE 95].

10.4. Damage modeling of saturated brittle materials

Damage due to microcracks is known as an essential mechanism of the inelastic behavior and the failure process in a large class of geomaterials such as rocks and concrete. Over recent decades, a number of research works have attempted the physical characterization and mathematical modeling of brittle damage. Different types of constitutive model, based on either the phenomenological and micromechanical approaches, have been developed. However, most of these constitutive models only focused on damage in dry material subject to mechanical loading. Damage modeling of saturated materials has been discussed more recently and remains open to study. It is known that material damage affects not only

mechanical behavior but also hydromechanical and thermomechanical properties [FAU 91; CAR 98]. In this section, we present some representative results from experimental data and numerical damage modeling in saturated porous media in order to contribute some basic ideas to this large topic.

10.4.1. *Experimental characterization*

The purpose here is to show macroscopic consequences of microcracks on the poromechanical behavior of saturated brittle rocks. A conceptional framework is first defined for constitutive models of damaged porous media in order to explain more clearly the experimental procedures followed and to interpret the results obtained. For the sake of simplicity, an elastic behavior coupled with induced damage is assumed. The damage evolution due to microcrack propagation is the unique dissipation mechanism.

10.4.1.1. *General methodology*

In a fully phenomenological approach, the damage state is represented by internal variables (scalar and tensorial) which may be formally denoted by $\boldsymbol{D}$. The damage variables have to take into account density and orientation of the microcracks [KAC 93; LEM 96]. For the sake of simplicity, it is assumed that the initial behavior of the undamaged material is linear elastic and that the response to unloading at constant damage state is also linear elastic. Assuming the existence of a thermodynamic potential, the constitutive relations of elastic damage behavior of saturated porous media can be deduced in the same way as for dry materials. In a general way, considering that damage affects elastic properties and poroelastic coefficients, the constitutive relations of a damage porous medium in a saturated condition may be expressed as follows:

$$\boldsymbol{\sigma} = \boldsymbol{C}^{bd}(\boldsymbol{D}) : \boldsymbol{\varepsilon} - \boldsymbol{B}(\boldsymbol{D})\, p \tag{10.33}$$

$$\frac{m}{\rho_0^{fl}} = \boldsymbol{B}(\boldsymbol{D}) : \boldsymbol{\varepsilon} + \frac{p}{M(\boldsymbol{D})} \tag{10.34}$$

where $\boldsymbol{C}^{bd}(\boldsymbol{D})$ is the effective elastic stiffness tensor of a damaged material in a drained condition. In the same way, the tensor of Biot's coefficients ***B(D)*** and Biot's modulus, $M(\boldsymbol{D})$ are also functions of damage variables. It is convenient to use the porosity variation as a state variable instead of the change of fluid mass (m/ρ_f^0).

Thus, the free skeleton energy may be separated from the free fluid enthalpy. Relation (10.34) becomes:

$$\phi - \phi_0 = \boldsymbol{B}(\boldsymbol{D}) : \boldsymbol{\varepsilon} + \beta(\boldsymbol{D})\, p \tag{10.35}$$

Coefficient $\beta(\boldsymbol{D})$ thus defines the compressibility of the pores, which is also a function of the damage state.

The time derivative of equations (10.33) and (10.34) gives us the incremental forms of the constitutive relations:

$$d\boldsymbol{\varepsilon} = \boldsymbol{S}^{bt}(\boldsymbol{D}) : d\boldsymbol{\sigma} + \boldsymbol{H}(\boldsymbol{D})\, dp \tag{10.36}$$

$$\frac{dm}{\rho_{\circ}^{fl}} = \boldsymbol{H}^{*}(\boldsymbol{D}) : d\boldsymbol{\sigma} + \frac{dp}{L(\boldsymbol{D})} \tag{10.37}$$

The fourth order tensor $\boldsymbol{S}^{bt}(\boldsymbol{D})$ denotes the tangent elastic compliance of a damaged material in drained conditions, and the second order symmetric tensor $\boldsymbol{H}(\boldsymbol{D})$ defines strain variations due to changes of pore pressure. $\boldsymbol{H}^{*}(\boldsymbol{D})$ is also a second order symmetric tensor producing stress induced change of pore fluid. Finally, scalar modulus $L(\boldsymbol{D})$ gives the relationship between the variation of pore pressure and fluid mass change. It is clear that all the tangent coefficients are functions of the damage state.

We thus assume that there are three symmetry planes in damaged materials, which means that the effects of randomly distributed microcracks may be considered as equivalent to those of three orthogonal microcrack families [KAC 93]. Therefore, it is possible to define three principal directions of damage state, and in the principal damage framework, the tangent compliance tensor $S^{bt}(\boldsymbol{D})$ may be written in the following matrix form:

$$\boldsymbol{S}^{bt} = \begin{bmatrix} \frac{1}{E_1^{bt}} & -\frac{\nu_{12}^{bt}}{E_2^{bt}} & -\frac{\nu_{13}^{bt}}{E_3^{bt}} & 0 & 0 & 0 \\ -\frac{\nu_{21}^{bt}}{E_1^{bt}} & \frac{1}{E_2^{bt}} & -\frac{\nu_{23}^{bt}}{E_3^{bt}} & 0 & 0 & 0 \\ -\frac{\nu_{31}^{bt}}{E_1^{bt}} & -\frac{\nu_{32}^{bt}}{E_2^{bt}} & \frac{1}{E_3^{bt}} & 0 & 0 & 0 \\ 0 & 0 & 0 & \frac{1}{2G_{23}^{t}} & 0 & 0 \\ 0 & 0 & 0 & 0 & \frac{1}{2G_{31}^{t}} & 0 \\ 0 & 0 & 0 & 0 & 0 & \frac{1}{2G_{12}^{t}} \end{bmatrix} \tag{10.38}$$

Coefficients E_k^{bt} and ν_{ij}^{bt} are the Young's moduli and Poisson's ratios of the damaged material in drained conditions respectively, while G_{ij}^{t} are the shear moduli. In a similar way, the coupling coefficient tensor $H(\boldsymbol{D})$ may be expressed as:

$$\mathbf{H}(\mathbf{D}) = \begin{bmatrix} \frac{1}{H_1} & 0 & 0 \\ 0 & \frac{1}{H_2} & 0 \\ 0 & 0 & \frac{1}{H_3} \end{bmatrix} \tag{10.39}$$

In rock mechanics, basic laboratory tests are usually performed on cylinder samples. In this particular case, a transversely isotropic behavior is assumed. If axis x_1 is parallel to the cylinder axis, we obtain the following relations:

$$E_2^{bt} = E_3^{bt},\ \nu_{12}^{bt} = \nu_{13}^{bt},\ \nu_{21}^{bt} = \nu_{31}^{bt},\ \nu_{23}^{bt} = \nu_{32}^{bt},\ G_{12}^{t} = G_{31}^{t},\ H_2 = H_3 \tag{10.40}$$

and the incremental constitutive equations are written as:

$$d\varepsilon_{11} = \frac{1}{E_1^{bt}} d\sigma_{11} - \frac{2\nu_{12}^{bt}}{E_2^{bt}} d\sigma_{22} + \frac{1}{H_1} dp \tag{10.41}$$

$$d\varepsilon_{22} = d\varepsilon_{33} = -\frac{\nu_{21}^{bt}}{E_1^{bt}} d\sigma_{11} + \left(\frac{1-\nu_{23}^{bt}}{E_2^{bt}} \right) d\sigma_{22} + \frac{1}{H_2} dp \tag{10.42}$$

$$\frac{dm}{\rho_0^{fl}} = \frac{1}{H_1^*} d\sigma_{11} + \frac{2}{H_2^*} d\sigma_{22} + \frac{1}{L} dp \tag{10.43}$$

The above equations may be inverted to give incremental stresses versus incremental strains and pore pressure:

$$d\sigma_{22} = \left(\frac{E_2^{bt}}{1 - 2\nu_{21}^{bt}\nu_{12}^{bt} - \nu_{23}^{bt}} \right) (d\varepsilon_{22} + \nu_{21}^{bt}\, d\varepsilon_{11}) - b_2^t\, dp \tag{10.44}$$

$$d\sigma_{11} = \left(E_1^{bt} + \frac{2\,\nu_{21}^{bt}\,\nu_{12}^{bt}\,E_1^{bt}}{1 - 2\nu_{21}^{bt}\nu_{12}^{bt} - \nu_{23}^{bt}} \right) d\varepsilon_{11} + \left(\frac{2\,\nu_{21}^{bt}\,E_1^{bt}}{1 - 2\nu_{21}^{bt}\nu_{12}^{bt} - \nu_{23}^{bt}} \right) d\varepsilon_{22} - b_1^t\, dp \tag{10.45}$$

The two Biot coefficients b_1^t and b_2^t may be given in terms of measurable quantities:

$$b_1^t = \left(\frac{E_1^{bt}}{1 - 2\nu_{21}^{bt}\nu_{12}^{bt} - \nu_{23}^{bt}} \right) \left(\frac{1-\nu_{23}^{bt}}{H_1} + \frac{2\nu_{21}^{bt}}{H_2} \right) \tag{10.46}$$

$$b_2^t = \left(\frac{E_2^{bt}}{1 - 2\nu_{21}^{bt}\nu_{12}^{bt} - \nu_{23}^{bt}} \right) \left(\frac{\nu_{12}^{bt}}{H_1} + \frac{1}{H_2} \right) \tag{10.47}$$

Thus, in the case of axisymmetric conditions, the tangent poroelastic behavior of damaged porous media are determined by 8 independent parameters, which are dependent on the damage state. These parameters are E_1^{bt}, E_2^{bt}, ν_{12}^{bt}, ν_{21}^{bt}, ν_{23}^{bt}, G_{12}^t, H_1 and H_2. The tangent Biot's coefficients may be determined from relations (10.46) and (10.47). Therefore, experimental investigations consist of evaluating the 8 parameters for different states of damage.

Type of testing	Loading condition	Constitutive relations	Measurable coefficients
Drained triaxial compression (with and without unloading cycles)	$d\sigma_{22} = d\sigma_{33} = 0$ $dp = 0$ $d\sigma_{11} \neq 0$	$d\varepsilon_{11} = \frac{1}{E_1^{bt}} d\sigma_{11}$ $d\varepsilon_{22} = -\frac{\nu_{21}^{bt}}{E_1^{bt}} d\sigma_{11}$ $\frac{dm}{\rho_\circ^{fl}} = \frac{1}{H_1^*} d\sigma_{11}$	E_1^{bt}, ν_{21}^{bt} H_1^*
Increase and decrease cycles of radial stress σ_{33} in drained triaxial compression	$d\sigma_{11} = 0$ $dp = 0$ $d\sigma_{33} = d\sigma_{22} \neq 0$	$d\varepsilon_{11} = -\frac{2\nu_{12}^{bt}}{E_3^{bt}} d\sigma_{33}$ $d\varepsilon_{33} = \left(\frac{1-\nu_{23}^{bt}}{E_3^{bt}} \right) d\sigma_{33}$ $\frac{dm}{\rho_\circ^{fl}} = \frac{2}{H_2^*} d\sigma_{33}$	$\frac{1-\nu_{23}^{bt}}{E_3^{bt}}$ $\frac{\nu_{12}^{bt}}{E_3^{bt}}, H_2^*$
Increase or decrease of pore pressure during triaxial compression (drained or undrained)	$d\sigma_{11} = 0$ $d\sigma_{33} = d\sigma_{22} = 0$ $dp \neq 0$	$d\varepsilon_{11} = \frac{1}{H_1} dp$ $d\varepsilon_{33} = \frac{1}{H_3} dp$ $\frac{dm}{\rho_\circ^{fl}} = \frac{1}{L} dp$	H_1, H_3 L

Table 10.1. *Loading conditions and coefficients measured in various tests*

Generally, four typical loading paths may be performed:

– drained triaxial compression test with and without unloading cycles;

– drained triaxial compression test with increase of pore pressure at different levels of deviatoric stress;

– drained triaxial compression test with extension of radial stress at different levels of deviatoric stress;

– undrained triaxial compression with decrease of pore pressure at different levels of deviatoric stress.

In Table 10.1, we summarize the loading conditions, the constitutive relations concerned and the measurable coefficients for various loading paths.

10.4.1.2. *Some representative results*

We present here some typical results obtained from sandstone. It is composed of 95% quartz and the average porosity is about 20% [KAR 98]. This material is extensively studied due to its quite homogenous microstructure and sensitivity to induced damage. The typical mechanical behavior of sandstone has been investigated in [IKO 90, KHA 95, KAR 00]. In this section, only the poromechanical behavior is discussed. The main purpose is to show the consequences of damage on the poromechanical response of a damaged material.

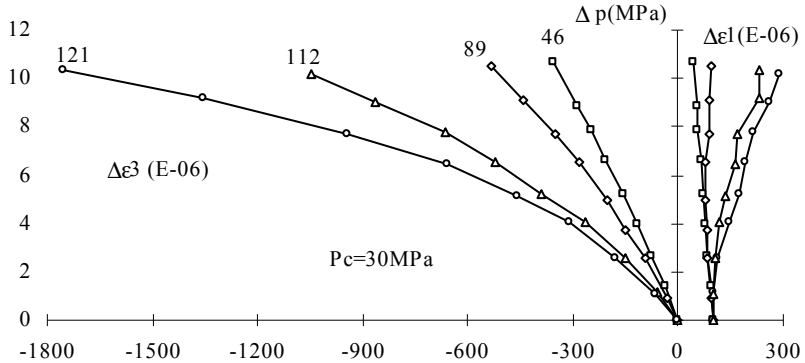

Figure 10.4. *Variation of axial and radial strains with pore pressure at different values of deviatoric stress [KAR 98]*

A first series of results has been obtained from a triaxial compression test in which pore pressure was increased at different values of deviatoric stress. In this test, the sample was first subjected to a conventional triaxial compression phase until a given value of deviatoric stress was reached. Then, the axial and radial stresses are held constant and fluid is injected into the sample. The pore pressure magnitude was limited to a third of the confining pressure in order to avoid extra propagation of microcracks. Invoking microcrack space distribution, the purpose of this test was to show induced anisotropy of poromechanical behavior. Several tests have been performed by [KAR 00]. The results obtained from a test with a confining pressure of 30 MPa are shown in Figure 10.4.

We can see that if the increase in pore pressure is performed at a level of deviatoric stress larger than the damage threshold, further propagation of

microcracks is generated by the increased pore pressure. Accordingly, the variations of the axial and radial strains are non-linear and anisotropic ($\Delta\varepsilon_1 \neq \Delta\varepsilon_3$). However, if the injection is performed at a level of deviatoric stress lower than the damage threshold, i.e. inside the elastic domain, linear and isotropic strains are obtained depending on the increasing pore pressure ($\Delta\varepsilon_1 = \Delta\varepsilon_3$). The results obtained from the series of tests appear to agree with this analysis. As most microcracks are oriented along the axial direction, the variation of axial strain is always smaller than that of radial strain. The difference between these two orientations is intensified as the level of induced damage increases. Furthermore, for a very high level of damage, a compressive incremental strain may be obtained in the radial direction due to an increase of pore pressure. This indicates a very strong induced anisotropy by microcracks. Using the initial slope of the strain variation curves at the beginning of the fluid injection, we can determine the coupling parameters (H_1, H_2, L) as defined in the previous section [KAR 00].

A second example involves an undrained triaxial compression test. In the first stage, the sample is subjected to conventional undrained compression until a given value of deviatoric stress is reached. Pore pressure is progressively generated by applied deviatoric stress. Then the pore pressure is decreased and axial and radial strains are measured. Note that the diminution of pore pressure corresponds to elastic unloading, leading to linear elastic strain responses. However, the initial slopes of strain curves represent the effective poroelastic behavior and should thus depend on the damage state (or equivalently on the level of deviatoric stress applied). In Figure 10.5, strains and pore pressure are presented as dependent on deviatoric stress. The pore pressure increases at a first stage and then decreases in a second stage. Such a decrease in pore pressure is a consequence of volumetric dilatation induced by the growth of microcracks. In Figure 10.6, strain variations are shown with the decrease in pore pressure. Clearly, linear variations are obtained and the slopes of the curves become smaller as the level of deviatoric stress increases. Moreover, the slope of the radial strain is much smaller than that of the axial strain. This seems to confirm induced anisotropy of poroelastic behavior of damaged material.

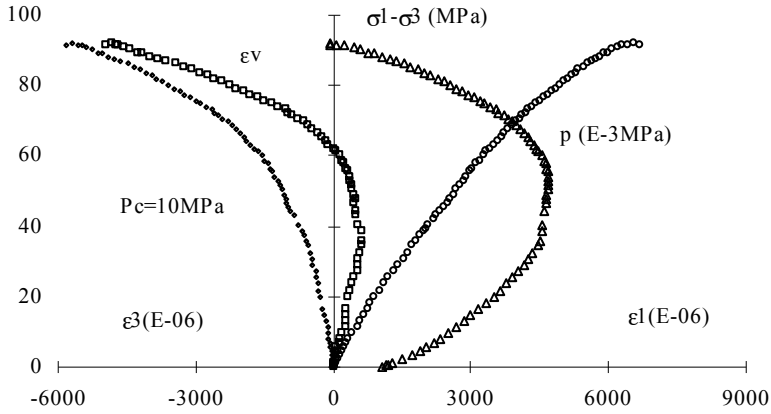

Figure 10.5. *Strains and pore pressure versus deviatoric stress in an undrained triaxial compression test [KAR 98]*

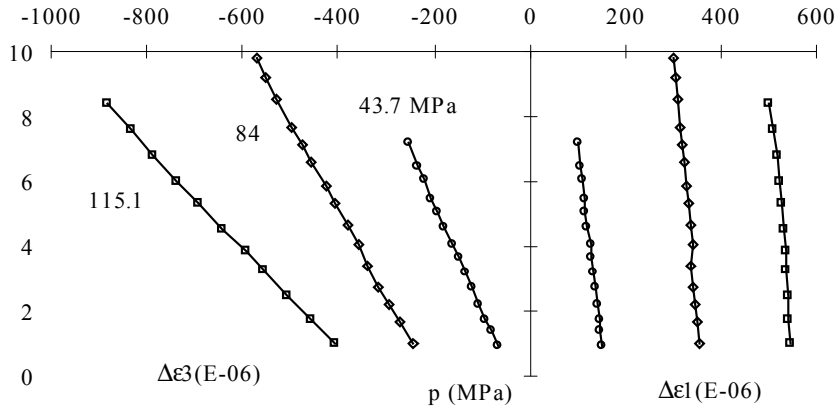

Figure 10.6. *Variations of axial and radial strains with pore pressure decrease during undrained triaxial compression test [KAR 98]*

Finally, an example is given to show the determination of the tangent Biot's coefficient during a drained triaxial compression test that uses the procedure presented in the preceding section. However, a geometrical limitation is placed on cylinder samples. Due to geometrical symmetry, it is impossible to distinguish radial and tangential directions. For example, as it is impossible to determine v_{23}^{bt} and then

deduce E_3^{bt} and ν_{12}^{bt} (see Table 10.1), a strong simplification is usually introduced. It is assumed that $\nu_{23}^{bt} = \nu_0^b$ in order to estimate the tangent Biot's coefficients. Representative results are given in Table 10.2 for a test performed with a confining pressure of 20 MPa [KAR 00]. From these results, the following observations are in order:

– at a low level of deviatoric stress, the values of tangent Biot's coefficients are smaller than the initial value obtained from a hydrostatic compression test (around 0.8) [KAR 00]. This decrease in Biot's coefficient may be related to the closure of the initial microcracks by applied deviatoric stress. The fact that the decrease in the axial direction is larger than that in the radial direction is in agreement with this analysis;

– after a short phase of decrease, the tangent Biot's coefficient in the radial direction increases continuously, as a consequence of the growth of microcracks which are essentially oriented in the axial direction;

– the tangent Biot's coefficient in the axial direction continuously decreases until a high level of deviatoric stress is reached and starts to increase only when the deviatoric stress is close to peak strength. This clearly indicates an anisotropic distribution of microcracks which generates an induced anisotropy in the tangent Biot's coefficients.

$\frac{\sigma_1 - \sigma_3}{(\sigma_1 - \sigma_3)_{pic}}$	27%	39%	52%	63%	74%
b_1^t	0.434±.042	0.368±.037	0.355±.036	0.296±.036	0.306±.037
$d\,b_1^t / b_1^t$	9.6%	10.1%	10.2%	12.3%	12.1%
b_2^t	0.611±.042	0.593±.040	0.606±.041	0.675±.046	0.770±.054
$d\,b_2^t / b_2^t$	6.8%	6.8%	6.8%	6.8%	7.0%

Table 10.2. *Tangent Biot's coefficients for different values of deviatoric stress (Pc=20 MPa) [KAR 98]*

10.4.2. *Numerical modeling*

This section is now devoted to constitutive damage modeling in saturated porous media. The general framework is first exposed, and an example of a constitutive model is then presented. Note that only phenomenological approaches will be discussed here.

10.4.2.1. *General framework*

Under phenomenological approaches, damage is represented by internal variables. In order to describe anisotropic damage, tensorial damage variables are needed. Second and fourth order tensors are generally used. For the sake of simplicity, only a second order symmetric damage tensor is involved here [KAC 93], which can be decomposed to a spectral form with its three principal directions:

$$\boldsymbol{D} = \sum_{i=1}^{3} D_i \, V^i \otimes V^i \tag{10.48}$$

where V^i is the unit vector normal to the i^{th} family of microcracks and D_i denotes the microcrack density. By adopting this representation, we can see that the damaged material exhibits an orthotropic behavior defined by its three principal directions.

In a direct formulation, the state variables used are strain tensor ε, Lagrangian porosity change $(\phi - \phi_0)$ and damage tensor $\mathbf{D}$. The thermodynamic potential is split into two parts, the free energy of the skeleton and the free enthalpy of the pore fluid:

$$\psi(\varepsilon, \phi - \phi_o, \mathbf{D}) = \psi_s(\varepsilon, \phi - \phi_o, \mathbf{D}) + \psi_f \tag{10.49}$$

The basic Clausius-Duhem's inequality is written as:

$$\Phi_1 = \sigma : \dot{\varepsilon} + p\dot{\phi} - \dot{\psi}_s \geq 0 \tag{10.50}$$

The standard derivation of thermodynamic potential (10.50) leads us to the following state equations:

$$\sigma = \frac{\partial \psi_s}{\partial \varepsilon}, \; p = \frac{\partial \psi_s}{\partial \phi}, \; \mathbf{Y}^d = -\frac{\partial \psi_s}{\partial \mathbf{D}} \tag{10.51}$$

In order to specify the expression of the free energy function, some assumptions need to be made. The initial behavior of the undamaged material is linearly elastic and the anisotropy is entirely induced by the directed distribution of microcracks. Moreover, linear poroelastic behavior is also assumed for a constant damage state. Thus, the free energy of the skeleton is in quadratic form on ε and ϕ. Finally, neglecting interactions between microcracks [KAC 93, HAL 96], the thermodynamic potential is linear in $\mathbf{D}$. Thus, by extending Biot's poroelasticity, the following form of the thermodynamic potential is proposed:

$$\psi_s = \psi_{s1}^{\phi} + \psi_{s2} = \frac{1}{2}\varepsilon : \mathbf{C}^{\phi d}(\mathbf{D}) : \varepsilon - (\phi - \phi_0)(\mathbf{B}^0 : \varepsilon) + \frac{1}{2}N^0(\phi - \phi_0)^2 - C_1^{\phi}(\phi - \phi_0)(\mathbf{D} : \varepsilon) + \frac{1}{2}C_2^{\phi}(tr\mathbf{D})(\phi - \phi_0)^2 - C_3^{\phi}(\phi - \phi_0)(tr\mathbf{D})tr\varepsilon \tag{10.52}$$

Second order tensor $\mathbf{B}^0$ and scalar coefficient N^0 denote poroelastic coefficients of undamaged material. Three parameters C_1^{ϕ}, C_2^{ϕ} and C_3^{ϕ} are introduced to characterize the influence of damage on poroelastic coefficients. Fourth order tensor $\mathbf{C}^{\phi d}$ denotes the effective elastic stiffness of the damaged material at constant porosity. From (10.52), the thermodynamic force associated with damage can be deduced, which is a second order tensor depending on the strains and variation of porosity. In practice and in view of experimental identification, it is more convenient to use pore pressure as a driving variable instead of the change of porosity. Thus, it is proposed to write a complementary formulation through a partial Legendre transformation with respect to the change of porosity. The thermodynamic potential takes the following form (the reference pore pressure is zero for convenience):

$$\psi^* = \psi - p(\phi - \phi_0) = \psi_s^*(\varepsilon, p, \mathbf{D}) + \psi_f \tag{10.53}$$

$$\psi_s^* = \psi_{s1}^b + \psi_{s2}^* = \frac{1}{2}\varepsilon : \mathbf{C}^{bd} : \varepsilon - p(\mathbf{A}^0 : \varepsilon) - \frac{1}{2}\beta^0 p^2 - C_1^p(\mathbf{D} : \varepsilon)p - \frac{1}{2}C_2^p(tr\mathbf{D})p^2 - C_3^p\, tr\mathbf{D}\, tr\varepsilon\, p \tag{10.54}$$

Accordingly, the state equations are given by:

$$\sigma = \frac{\partial \psi_s^*}{\partial \varepsilon} = \mathbf{C}^{bd} : \varepsilon - \left[\mathrm{A}^0 + C_1^p\mathbf{D} + C_3^p\, tr\mathbf{D}\,\mathbf{I} \right] p \tag{10.55}$$

$$\phi - \phi_0 = -\frac{\partial \psi_s^*}{\partial p} = \left[\mathbf{A}^0 + C_1^p\mathbf{D} + C_3^p\, tr\mathbf{D}\,\mathbf{I} \right] : \varepsilon + \left[\beta^0 + C_2^p\, tr\mathbf{D} \right] p \tag{10.56}$$

$$\mathbf{Y}^d = \mathbf{Y}^{d1} + \mathbf{Y}^{d2} = -\frac{\partial \psi_{s1}^b}{\partial \mathbf{D}} + C_1^p p\varepsilon + \frac{1}{2}C_2^p\, p^2\,\mathbf{I} + C_3^p\, p\, tr\varepsilon\,\mathbf{I} \tag{10.57}$$

We can easily see that the second order tensor $\mathbf{A}^0$ is the initial Biot's coefficient tensor and that β^0 is the initial coefficient of pore compressibility. Three parameters C_1^p, C_2^p and C_3^p, which are respectively dual to C_1^ϕ, C_2^ϕ and C_3^ϕ, characterize the influence of damage on poroelastic coupling coefficients. Fourth order tensor $\boldsymbol{C}^{bd}$ denotes the drained elastic stiffness of the damaged material. In (10.57), we can see that the thermodynamic force associated with damage is independently related to strain and pore pressure.

Comparing (10.55) and (10.56) with the standard linear anisotropic poroelasticity [THO 91; CHE 97], we may deduce the following relations:

$$A_{ij}(\mathbf{D}) = A_{ij}^0 + C_1^p\, D_{ij} + C_3^p\, tr\mathbf{D}\,\delta_{ij} \tag{10.58}$$

$$\beta(\mathbf{D}) = \beta^0 + C_2^p\, tr\mathbf{D} \tag{10.59}$$

These relations clearly define the poroelastic coefficients of material with induced damage. Three coefficients should be determined from relevant experimental data. However, a micromechanical analysis allows some theoretical estimation to be made. In fact, the application of homogenization techniques on porous media shows that the poroelastic properties are directly related to those of the constituents and to the microstructure [DOR *et al*. 06]. For example, for initially isotropic materials, we obtain [LYD 00]:

$$A_{ij} = \delta_{ij} - \frac{1}{3K_s} C_{ijkl}^{bd}\delta_{kl} \tag{10.60}$$

$$\beta = \frac{1}{K_s}\left(\frac{1}{3}tr(\mathbf{A}) - \phi\right) \geq 0 \tag{10.61}$$

where K_s is the compressibility modulus of the solid matrix. According to these relations, identifying the poroelastic behavior can lead to the determination of effective elastic properties of the damaged material $C^{bd}(\mathbf{D})$.

The evolution of the damage variable is determined by a pseudo-potential of dissipation. In the case of time-independent dissipation, the dissipation potential becomes an indicative function of the convex elastic domain and its boundary is

defined by the damage criterion in the space of the thermodynamic forces conjugate to damage.

$$f_d(\mathbf{Y}^d, \mathbf{D}) \leq 0 \tag{10.62}$$

and the damage evolution law is:

$$\dot{\mathbf{D}} = \lambda_d \frac{\partial f_d}{\partial \mathbf{Y}^d} \tag{10.63}$$

Parameter $\lambda_d \geq 0$ is determined by the damage consistency condition $\lambda_d \dot{f}_d = 0$. The damage dissipation is verified by the fundamental inequality:

$$\mathbf{Y}^d : \dot{\mathbf{D}} \geq 0 \tag{10.64}$$

The specific form of the damage criterion should be based on relevant experimental investigation. However, it is noted that experimental identification is generally a delicate task.

10.4.2.2. *An example of a damage model*

An example of an anisotropic damage model for saturated media is presented. As previously mentioned, the essential step is to determine the effective elastic stiffness tensor of a damaged material. Based on the previous works by Kachanov [KAC 93] and Halm *et al*. [HAL 96], the following free energy function of the dry skeleton material (without fluid) may be used:

$$\psi_{s1}^b = \frac{\lambda_0}{2}(tr\varepsilon)^2 + \mu_0 tr(\varepsilon.\varepsilon) + a_1\, tr\varepsilon\, tr(\varepsilon.\boldsymbol{D}) + a_2\ tr(\varepsilon.\varepsilon.\boldsymbol{D}) \tag{10.65}$$

where λ_0 and μ_0 are Lame's elastic constants of undamaged material. Two parameters a_1 and a_2 characterize the degradation of elastic properties due to damage. From the derivative of (10.65), the effective elastic stiffness of damaged material can be deduced:

$$\begin{aligned} C_{ijkl}^{bd} &= C_{ijkl}^{b0} + a_1(\delta_{ij} D_{kl} + D_{ij} \delta_{kl}) \\ &\quad + \frac{a_2}{2}\left[\delta_{ik} D_{jl} + \delta_{il} D_{jk} + D_{ik}\delta_{jl} + D_{il}\delta_{jk}\right] \end{aligned} \tag{10.66}$$

$\mathbf{C}^{b0}$ denotes the initial elastic stiffness tensor of undamaged material and the thermodynamic force associated with damage is given by:

$$\begin{aligned}\mathbf{Y}^{d} &= \mathbf{Y}^{d1} + \mathbf{Y}^{d2} = -a_1(tr\varepsilon)\varepsilon - a_2(\varepsilon.\varepsilon) \\ &\quad + C_1^p p\varepsilon + \frac{1}{2}C_2^p\, p^2\,\mathbf{I} + C_3^p\, p\, tr\varepsilon\,\mathbf{I}\end{aligned} \tag{10.67}$$

Note that the thermodynamic potential given in (10.65) is a simplified version of a more general expression deduced from micromechanical analysis [PEN 05]. In this simplified version, unilateral effects have been neglected. Since experimental identification of the damage force is generally difficult, a pragmatic approach for determining damage evolution is preferred. Based on the principles of linear fracture mechanics, we propose to relate the damage evolution to the propagation of microcracks. Therefore, the damage tensor components are expressed as:

$$\boldsymbol{D} = \sum_{k=1}^{N} m_k \left(r_k^3 - r_0^3\right)(\vec{n}\otimes\vec{n})_k\ ,\ r_k = \frac{\hat{a}_k}{b}\ ,\ r_0 = \frac{\hat{a}_0}{b} \tag{10.68}$$

where $\hat{a}_k$ and m_k are, respectively, the average length and number (density) of the k^{th} family of microcracks, with $\vec{n}_k$ being the unit normal vector. In this definition, an initial isotropic distribution of microcracks with the average length $\hat{a}_0$ is assumed. Parameter b defines a critical length of microcracks for coalescence.

A crack propagation criterion remains to be defined. In the spirit of fracture mechanics, this criterion is formulated with applied stresses and pore pressure. Based on the work by Costin [COS 87], it is assumed that any family of microcracks can be replaced by a fictitious single crack subjected to mode I propagation. The propagation is controlled by the deviatoric stress field which is the driving force for propagation and the hydrostatic stress which acts as a confining effect. For instance, the following criterion is proposed:

$$\sqrt{r}\left[\sigma_n'^{T} + f(r)\left(\vec{n}.\boldsymbol{S}.\vec{n} + a_3(1-r)p\right)\right] - C_r = 0 \tag{10.69}$$

$$\sigma_n'^{T} = \vec{n}.\sigma'^{T}.\vec{n} = \vec{n}.(\sigma + p\mathbf{I}).\vec{n}\ ,\ \mathbf{S} = \sigma - (\sigma_{kk}/3)\mathbf{I} \tag{10.70}$$

Tensor σ'^{T} denotes the effective stress defined by Terzaghi. The corrective term $(1-r)p$ is introduced to describe an anisotropic effect of pore pressure on crack propagation. Parameter C_r defines material resistance to propagation. Function $f(r)$ plays a double role in this criterion. It first defines the proportionality between the macroscopic deviatoric stress field and the local tensile stress. Secondly, the variation of $f(r)$ describes the material hardening/softening during crack propagation. It increases monotonically when the crack density is smaller than ($r < 1$). After this critical point ($r \geq 1$), it becomes stationary (as in perfect plasticity) or decreases (as in strain softening) to produce an unstable crack propagation. The specific form of function $f(r)$ may be experimentally and numerically determined. As a first approximation, the following simple function may be used:

$$f(r) = \begin{cases} t/r, & r < 1 \\ t, & r \geq 1 \end{cases} \tag{10.71}$$

The detailed procedure for determining the model's parameters is given in [BAR 00].

In Figure 10.7, a simulation example is shown, corresponding to a drained triaxial test with stages of pore pressure increase at different levels of deviatoric stress, as previously mentioned. In order to study the influence of the pore pressure on the crack propagation criterion, two comparative simulations have been performed, with ($a_3 \neq 0$) and without ($a_3 = 0$) respectively, taking into account the anisotropic effect. From these results, we can first conclude that linear poroelasticity is not able to describe the experimental evidence, even in a qualitative way. The results obtained by the anisotropic damage model are qualitatively in agreement with experimental data. The numerical predictions are significantly improved by taking into account the anisotropic effect of pore pressure.

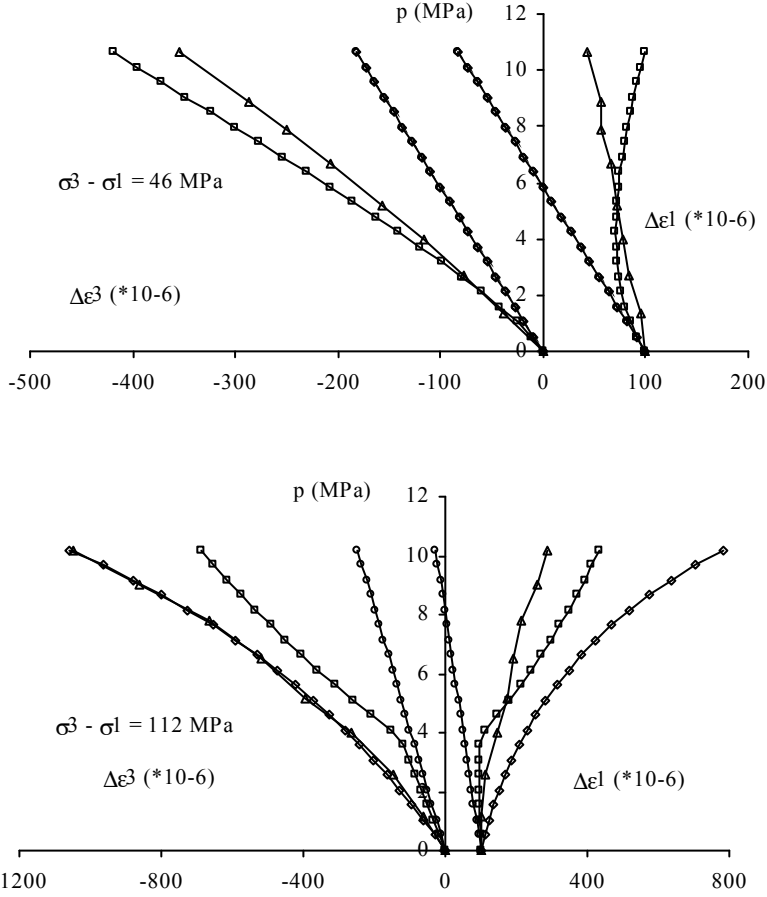

Figure 10.7. *Variation of axial and radial strain with increase of pore pressure - comparisons between numerical predictions and experimentale data for two values of deviatoric stress (46 and 112 MPa) under a confining pressure of 30 MPa: triangle – experiment, square – proposed mode* $a_3 \neq 0$ *l, rhombus – simplified model with* $a_3 = 0$ *, circle – linear poroelasticity, from [BAR 00]*

10.5. Conclusion

Some basic features for damage modeling in saturated porous media have been presented. Basic experimental investigations have also been discussed. However, this topic is still an open issue. Recent advances have been made in recent years both in phenomenological approaches and micromechanical analyses.

10.6. References

[BAR 00] BART M., SHAO J.F. and LYDZBA D., "Poroelastic behavior of saturated brittle rock with anisotropic damage", revised version submitted to *International Journal for Numerical and Analytical Methods in Geomechanics* (2000).

[BIO 41] BIOT M.A., "General theory of three dimentional consolidation", *J. Appl. Phys*., vol. 12, p. 155-164 (1941).

[BIO 55] BIOT M.A., "Theory of elasticity and consolidation for a porous anisotropic solid", *J. Appl. Phys*. 26, 182-185 (1955).

[BIO 57] BIOT M.A. and WILLIS D.G., "The elastic coefficients of the theory of consolidation", *J. Appl. Mech.*, vol. 28, p. 594-601 (1957).

[BIO 73] BIOT M.A., "Non linear and semi-linear rheology of porous solids", *J. of Geophy. Res.*, vol. 78, no. 23, p. 4924-4937 (1973).

[BUH 96] DE BUHAN P. and DORMIEUX L., "On the validity of the effective stress concept for assessing the strength of saturated porous materials: a homogenization approach", *J. Mech. Phys. Solids*, 44, 1649-1667 (1996).

[CAR 98] CARMELIET J., "On the poro-visco-elastic and damage coupling in non saturated media", in *Proc. of Biot Conference*, Thimus *et al.* (eds.), Balkema, Rotterdam, 41-46, (1998).

[CHE 97] CHENG A. H.-D., "Material coefficients of anisotropic poroelasticity", *Int. J. Rock Mech. Min. Sci.*, vol. 34, no. 2, 199-205 (1997).

[COU 91] COUSSY O., *Mécanique des Milieux Poreux*, Editions Technip, Paris (1991).

[COU 95] COUSSY O., *Mechanics of Porous Continua,* Wiley, New York (1995).

[DOR 05] Dormieux, L. and Kondo D., "Poroelasticity and damage theory for cracked media", in *Applied Micromechanics of Porous Media*, CISM lecture notes, L. Dormieux and F.J. Ulm (eds.), Springer, 153-183 (2005).

[FAU 91] FAUCHET B., "Analyse poroplastique des barrages en béton et de leur fondation, Rôle de la pression interstitielle", Doctoral thesis, Ecole Nationale des Ponts & Chaussées (1991).

[HAL 96] HALM D. and DRAGON A., "A model of anisotropic damage by mesocrack growth; unilateral effect", *Int. J. of Damage Mechanics*, vol.5, 384-402 (1996).

[IKO 90] IKOGOU S., Etude expérimentale et modélisation du comportement d'un grès, Doctoral thesis, Lille University of Science and Technology (1990).

[KAC 93] KACHANOV M., "Elastic solids with many cracks and related problems", in *Advances in applied mechanics*, vol. 30, Hutchinson and Wu (eds.), NY, 259-445 (1993).

[KAR 98] KARAMI M.H., Etude expérimentale du comportement poromécanique d'une roche endommageable, Doctoral thesis, Lille University of Science and Technology (1998).

[KAR 00] KARAMI M.H., SIBAI M. and SHAO J.F., "Une étude expérimentale du comportement poromécanique d'une roche fragile saturée", *Revue Française de Génie Civil*, vol. 4, no. 1, 109-142 (2000).

[KER 95] KERBOUCHE R., SHAO J.F. and SKOCZYLAS F., "On the poroplastic behaviour of porous rock", *European. J. of Mech., A/Solids*, 14, no. 4, 577-587 (1995).

[KHA 95] KHAZRAIE R., Etude expérimentale et modélisation de l'endommagement anisotrope des roches fragiles, Doctoral thesis, Lille University of Science and Technology (1995).

[LAD 97] LADE P.V. and DE BOER R., "The concept of effective stress for soil, concrete and rock", *Géotechnique*, 47(1), 61-78 (1997).

[LEM 96] LEMAITRE J., *A Course on Damage Mechanics*, second edition, Springer (1996).

[LYD 99] LYDZBA D. and SHAO J.F., "Study of poroelasticity material coefficients as response of microstructure", *Mechanics of Cohesive-Frictional Material*, vol. 5, no. 2, 149-171 (1999).

[LYD 00] LYDZBA D. and SHAO J.F., "Micromechanical study on the validity of stress equivalence principle for saturated porous media, Part I: Micro-homogeneous skeleton material", submitted to *Comptes Rendus de L'Académie des Sciences*, Paris, Série Iib (2000).

[LYD 00] LYDZBA D. and SHAO J.F., "Micromechanical study on the validity of stress equivalence principle for saturated porous media, Part II: Arbitrary skeleton material", submitted to *Comptes Rendus de L'Académie des Sciences*, Paris, Série Iib (2000).

[ORT 94] ORTEGA B. and DE G., Développement d'une cellule triaxiale haute pression pour essais sur roches poreuses saturés. Application aux grès, Doctoral thesis, Joseph Fourier University - Grenoble I (1994).

[PEN 02] PENSEE V., KONDO D. and DORMIEUX L., "Micromechanical analysis of anisotropic damage in brittle materials", *J. Engng. Mech.*, ASCE, 128(8), 889-897 (2002).

[PIE 95] PIETRUSZCZAK S. and PANDE G.N., "On the mechanical response of saturated cemented materials – Part I: Theoretical considerations and Part II: Experimental investigation and numerical simulations", *International Journal for Numerical and Analytical Methods in Geomechanics*, vol. 19, 555-571 (1995).

[SHA 98] SHAO J.F., "Poroelastic behaviour of brittle rock materials with anisotropic damage", *Mechanics of Materials*, 30, 41-53 (1998).

[SHA 04] SHAO J.F., LU Y.F. and LYDZBA D., "Damage modeling of saturated rocks in drained and undrained conditions", *Journal of Engineering Mechanics*, ASCE, 130(6), 733-740 (2004).

[SIB 90] SIBAI M., Etude de l'interaction fluide-squelette dans les roches méthodes expérimentales et modélisation, Doctoral thesis, Lille University of Science and Technology (1989).

[THO 91] THOMPSON M. and WILLIS J.R., "A reformulation of the equations of anisotropic poroelasticity", *J. Appl. Mech. ASME*, 58, 612-616 (1991).

[YAM 81] YAMADA S.E., SCHATZ J.F., ABOU SAYED A. and JONES A.H., "Elasto-plastic behavior of porous rock under undrained condition", *Int. J. Rock Mech. Min. Sci. & Geomech. Abstr.*, vol. 18, p. 177-179 (1981).

Constitutive Modeling of Soils and Rocks
Edited by Pierre-Yves Hicher & Jian-Fu Shao

Chapter 11

Parameter Identification

11.1. Introduction

The use of a constitutive model, particularly in finite element calculations for geotechnical problems, requires a methodology to be developed which identifies parameters, adapted to both the internal structure of the model and the available test data. The identification method must lead, so far as possible, to an objective determination of the model parameters, which means that it has to be user independent. In most cases, it consists of a better use of the available experimental data in order to obtain a set of parameters that is the best compromise for the model's response along all the known loading paths. According to the problem which has to be treated, this compromise can give more importance to the response along specific loading paths.

Developing such a methodology for a given model requires at first an analysis of all the parameters, their physical meaning, their possible value interval, and their eventual link with the usual geotechnical parameters. They can usually be divided into two groups:

1) parameters having a direct link to experimental behavior: for example, the Young's modulus and the Poisson's ratio in elasticity, the friction angle and the dilatancy angle in plasticity;

2) "numerical" parameters: for example, in the case of an elastoplastic model, the parameters controlling the shape of the yield surface or the evolution of the hardening variables.

Chapter written by Pierre-Yves HICHER and Jian-Fu SHAO.

The determination method can vary from one group to another. For the first group, a direct approach based on the experimental curves in well controlled laboratory tests, such as triaxial and oedometer tests, is usually possible and straightforward. However, it has to be well controlled and in agreement with the concepts at the basis of the model. For example, the definition of the friction angle in the Mohr-Coulomb elastic-perfectly plastic model is different from the one in the Cam-Clay model or any derived model such as Hujeux's model (see Chapters 3 and 4). In the first case, the model introduces the peak friction angle, while in the second case, we use the friction angle at the perfect plasticity state (critical state). These two angles are the same for contractant materials, but are different for dilatant ones.

Another example concerns the determination of the elastic modulus for every elastoplastic model. It is now well established that the elastic domain for a soil is restrained to very small deformations ($\varepsilon < 10^{-5}$ to 10^{-4}). Therefore, the elastic properties can be measured only with specific tests (instrumented triaxial cells, resonant columns, etc.). Conventional elastic parameters are measured from traditional tests at higher strain amplitudes, usually around 10^{-3}. It is in that case better to use an unloading curve whenever it is available rather than the initial slope of the loading curve, which corresponds to the development of plastic as well as elastic strains. The moduli measured in that case are much smaller than those obtained in very small deformations and cannot be used in analyses requiring small strain amplitudes, such as seismic case studies for example. We have to remember that, even for high stress levels, the value of the elastic modulus can play a non-negligible role on the overall response of a non-homogenous boundary value problem, as shown in [DAR 95]. In the parameter identification process itself, the choice of the elastic parameters can influence the determination of some other parameters, in particular the "numerical" parameters. This is particularly true when the identification procedure is conducted using stress paths along which the model response is strongly influenced by the elastic constants. This is not the case for a drained triaxial test, but is for an undrained triaxial test. In this loading, the condition of no volume change corresponds for the elastoplastic response to the relation $d\varepsilon_v^e + d\varepsilon_v^p = 0$, which means that the amplitude of the plastic volumetric strain is of the same order of magnitude as the elastic one, leading to a marked influence of the elastic parameters on the model response.

The determination of the "numerical" parameters usually requires a method adapted to each model. They can be classified under three categories: analytical methods, correlation methods and optimization methods.

11.2. Analytical methods

These methods involve using the mathematical formulation of the model equations in order to obtain a set of analytical expressions leading to a system of linear equations whose unknowns are the required parameters. Usually, these equations correspond to particular stress and strain states, such as the peak or the asymptotic value of the deviatoric stress, the change in sign of the volume change increment or the inflection point in the volume change curve, the instant slope values at different points of the stress-strain curve, etc.

It is a simple approach which has the advantage of staying close to the model's inner structure and which provides good results if the set of experimental results does not present strong incoherency. It has been used with success by different authors; see for example the work of Mestat *et al*. [MES 00] with Nova's elastoplastic model.

This approach can be enriched by the analytical study of the plastic yield condition, verified by a large number of experimental points, which enables a well written set of parameters to be obtained by an appropriate statistic treatment. Based on this method, Laigle developed a program for determining Hujeux's model parameters, called DELUGE.

The least squares methods, which can also be classified within this kind of approach, consist generally of using simple, often linear, relations in well chosen diagrams in order to obtain a direct determination of one of the model parameters (for example the slope of the linear relation). We can cite the work of Duncan and Chang [DUN 70] who transformed a hyperbolic relation into a linear one; the work of Lade [LAD 88] adapted to his model; the work of Kolymbas [KOL 91] for his hypo-elastic model. However, not all the constitutive models are adapted to the use of such an approach and we have to be careful with the use of some diagrams which can amplify the effect of experimental errors.

11.3. Correlations applied to parameter identification

Until now, empirical correlations have successfully offered some links between the physical properties (nature of the constituents, grain size distribution, etc.) and the mechanical properties of soils. Most of the common parameters used in soil mechanics have thus been related in this way to parameters linked to the nature of the materials. A methodology of connecting properties of the discontinuous medium and properties of the equivalent continuous medium has been developed by Biarez *et al*. [BIA 77 BIA 89, BIA 94]. Some results are presented in Chapter 2. This approach has been extended to the determination of constitutive model parameters

by Hicher and Rahma [HIC 94]. The main objective of this method is not to replace the experimental determination of the parameters, but to give a first estimate of a set of parameters for a given soil, which can afterwards be used as an objective initial set for a more precise determination, as for example in an optimization procedure (see section 11.4). The correlation framework can also provide us with the value of a given parameter when the available data is not sufficient to obtain the entire set of parameters. It can also allow us to take into account the special heterogenities of a natural soil deposit.

We present here an example of the construction of correlations applied to the determination of the parameters of Hujeux's model (see Chapter 4). The setting up of correlations between physical and mechanical properties consists of creating an implicit link between characteristics of the discontinuous medium (DM) made of grains and those of the equivalent continuous medium (CM). The mechanical properties of the latter will thus depend on a set of parameters representative of the discontinuous medium which can be classified into different groups:

1) mechanical properties of the grains:

– mechanical properties of each individual grain. For most purposes, linear isotropic elasticity can be assumed (two parameters E_g and ν_g). If not, a more complex constitutive model has to be developed with plasticity, damage, etc. This is particularly the case for elevated stresses when grain ruptures take place.

– mechanical properties of the contact between grains: intergranular friction (one parameter of friction φ) and possibly intergranular glue (see Chapter 2).

2) geometrical boundary conditions:

– grain geometry: shape characterized by the angularity coefficient, the surface state, etc.; the size and grain size distribution characterized by several parameters (d_{90}, d_{60}, d_{60}/d_{10}, etc.);

– arrangement of the grains: the compacity of the arrangement can be represented by a scalar, such as the void ratio *e* or the porosity *n*. The anisotropic aspect is more complex to define. We can use for example the statistical orientation of the tangential planes at grain contact or the fabric tensor.

These different parameters, representative of the discontinuous medium, can be classified into two categories: a set of parameters which can be considered as constant in the absence of grain ruptures, called nature parameters; parameters representative of the grain arrangement which evolve with the loading history. Table 6.1 summarizes the different elements and allows us to propose a basic equation for the construction of correlations:

NATURE (DM) + COMPACITY (DM) – RHEOLOGY (CM)

Properties of the discontinuous medium			→	Properties of the continuous medium
Properties of the grains	+	Grain assembly	→	$\sigma_t \rightarrow \varepsilon_t\ (\sigma, \varepsilon, \dot{\sigma}, \dot{\varepsilon})$
Nature and geometry of the grains + mechanical Eg, vg 2R		4 contacts $K = \frac{27}{8}\sqrt{3} = 5.85$	→	Semi-cubic elastic modulus ξ(Eg, vg, R – K) ε_i σ_i $\overline{\sigma_i}$ $\varepsilon_i = \frac{W}{R}$ $\xi = \frac{Eg}{1 - vg^2}\frac{3}{4K}$
		12 contacts $K = \sqrt{2} = 1.4$		
λ (ψ, angularity, $\frac{d60}{d10}$)	×	1/e	→	$tg\ \emptyset = \lambda \frac{1}{e}$
$0.11 + 0.0037 \times Ip$	×	σ	→	Cu
$130\ d^2_{10\ cm}$	×	$\left(\frac{e}{e_{max}}\right)^2$	→	Permeability K (cm/s)

Table 11.1. *Relations between discontinuous and continuous media*

As it is difficult to identify all the parameters representative of the discontinuous medium, the nature of soils can be synthesized by a particular arrangement of the constituents in response to suitable normalized mechanical tests: maximum and minimum void ratio e_{max} and e_{min} for sands, Atterberg's limits w_l and w_p for fine soils. These nature parameters can be combined with a parameter representative of the grain arrangement:

density index $I_D = (e_{max} - e)/(e_{max} - e_{min})$ or consistency index $I_c = (w_l - w)/(w_l - w_p)$

These mixed parameters are representative of the mechanical state of the discontinuous medium and the second basic equation can be written as:

MECHANICAL STATE (DM) – RHEOLOGY (CM)

Given this approach, it is possible to construct correlations either between parameters representative of the discontinuous medium, for example between nature parameters and mixed parameters, or between parameters of the discontinuous medium and parameters of the continuous medium. In the latter case, we have to distinguish between parameters independent of the grain arrangement: which are sometimes called intrinsic parameters, and parameters dependent on both nature and arrangement which evolve with the mechanical state. In particular, they are dependent on the initial state of the material at the beginning of the loading and thus have to be calibrated according to this initial state.

Along these lines, Hicher and Rahma [HIC 94] have developed correlations applied to the determination of parameters of Hujeux's model (see Chapter 4) in a simplified version called Cyclade [AUB 82]. This simplified version contains 10 parameters which can be classified in two groups:

1) parameters directly related to experimental behavior: E, ν and n for non-linear elasticity; β, p_{c0} and ϕ for perfect plasticity;

2) "numerical" parameters: b which controls the shape of the yield surface, r^{el} which defines the initial size of the elastic domain; a and α which control the evolution of the hardening variables.

21 sands, with a large variety of physical properties, were selected from the *Modelisol* database [FAV 91]. Around 150 drained and undrained triaxial tests were available for these 21 sands, tested at different initial densities. For each material, the same procedure was used for parameter determination. Parameters of group 1 were first measured as closely as possible from experimental data. Parameters of group 2 were then estimated using an optimization programme called *Adelap* [MEI 92]. The quality of the numerical simulations was estimated according to certain criteria, such as the initial slope, the peak and plateau levels, the peak abscissa of the stress-strain curve and the amplitude of the contraction and dilatancy of the volumetric change curves. Figure 11.1 presents an example of numerical simulations of drained and undrained triaxial tests on Ham River Sand [BIS 66] with an optimized set of parameters. Only two parameters E and p_{c0} are dependent on the initial state of the material, all the others are considered as intrinsic and depend only on the soil physical characteristics.

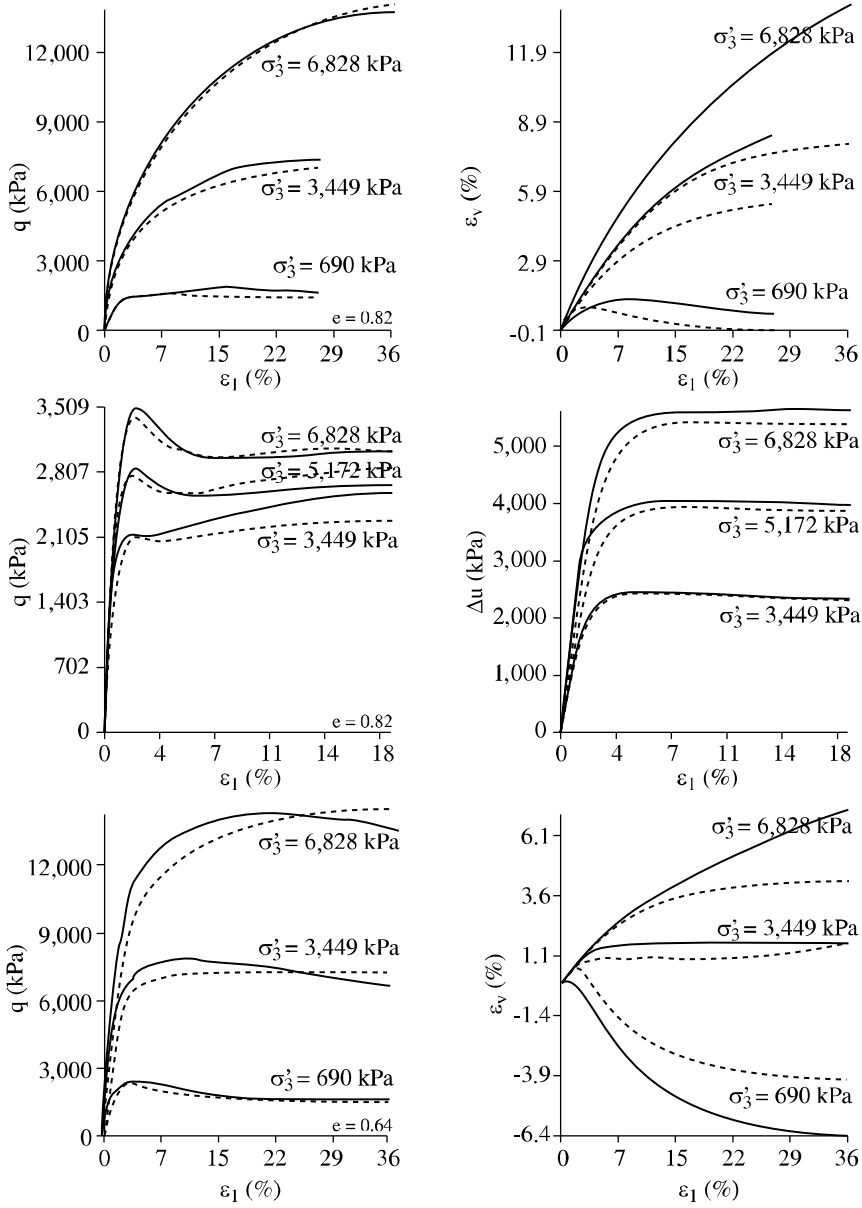

Figure 11.1. *Numerical simulations (dashed lines) of drained and undrained triaxial tests on Ham River Sand. Experimental data (continuous lines) after [BIS 66]; parameter identification by optimization procedure*

Correlations were then constructed by using a statistical approach composed of two methods: the principal component analysis and the multiple regression analysis. They gave mathematical links between model parameters and parameters of the discontinuous medium with a probability in a confidence range estimated at 95%. Correlations for elasticity and perfect plasticity parameters already exist [BIA 94], the main interest of this approach lies in its capacity to produce correlations for the "numerical" parameters. As an example, the results obtained for parameters *b* and *a* are presented below.

Parameter *b* controls the shape of the yield surface. It can vary between 0 and 1. For $b = 1$, the shape is similar to the yield surface of the Cam-Clay model. Values close to 1 are therefore suitable for clayey materials. For $b = 0$, we obtain a Mohr-Coulomb type yield surface. Therefore, small values of *b* ($b < 0.3$) are more suitable for sandy materials. In this study, all the tested materials being sands, obtained values of b were all located between 0.1 and 0.3. The principal component analysis showed a strong dependency with e_{max}, e_{min} and the grain size distribution, in particular d_{10}. This last parameter indicates that the percentage of fine particles has a significant influence on the shape of the yield surface. The proposed relation is the following:

$$b = 0.5e_{max} - 0.84e_{min} - 0.02d_{10}(mm) + 0.2 \quad R = 0.93$$

Parameter *a* controls the evolution of the hardening variable, which is a function of the deviatoric plastic strain. It thus has a great influence on the non-linearity of the stress-strain relationship. For sands, its values are between 10^{-3} and 10^{-2}. The principal component analysis showed a strong dependency with the grain size. The correlation equation takes this effect into account by means of the mean size coefficient d_{60}, completed by a parameter which can be related to the whole granulometry range, here e_{min}:

$$\log a = 0.35\log d_{60}(mm) + 0.93e_{min} - 3.37 \quad R = 0.97$$

In order to validate this approach, an *a priori* determination of the model parameters based on these correlations was performed for a sand outside of the database. Elastic parameters and the friction angle were determined directly from the experimental curves while the other parameters were determined by using the correlation equations. The result of the simulation, presented in Figure 11.2, is quite satisfactory and has been improved in a second step using an optimization technique. The final value of each parameter is well located within the standard deviation obtained by the statistical analysis.

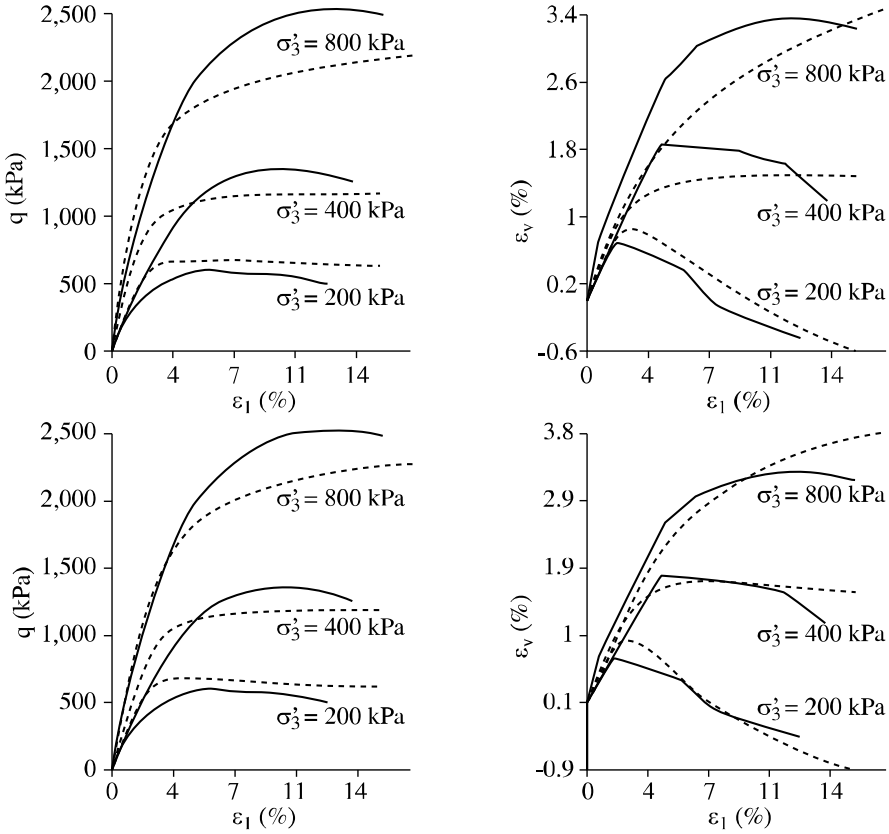

Figure 11.2. *Validation of correlations: a) initial set of parameters, b) optimized set of parameters. Continuous lines: experimental results, dashed lines: numerical simulations*

This method has been applied with success to other materials [DAO 99]. The construction of correlation models provides *a priori* an initial set of parameters and facilitates the use of an optimization technique by reducing the variation interval of each parameter for any given soil. It is also a very useful complement to a determination by inverse analysis (as will be seen later in this chapter).

11.4. Optimization methods

When some of the model parameters cannot be determined either by direct analysis of the experimental curves or by an analytical method, the usual approach to attempt them is by curve fitting. However, this is often time consuming and the

result can be strongly user dependent. We thus have to develop methods which are more objective and this is usually done by means of an optimization technique coupled or not to a statistical analysis which takes into account any experimental errors. This approach is based on the inverse problem theory [TAR 87]. The optimization process consists of minimizing a given function, called the cost function, which depends on the whole set of parameters and measures the distance between experimental results and numerical simulations.

The database can be diverse in origin. The first approaches in soil mechanics [MEI 89, PIC 91, SHA 91] were developed for laboratory test data, mainly drained and undrained triaxial tests. In recent years, *in situ* testing data, mainly pressiometer tests, have been included [CAM 93, HIC 96, ZEN 01, RAN 03, YIN 07].

11.4.1. *Numerical formulation*

Traditionally, we would resolve a mechanical problem by calculating response R of a mechanical system S subjected to actions A. This can be written:

actions (X) – system (S) – response (R)

System S includes constitutive model M and its parameters P. These problems, known as direct problems, can be mathematically expressed by:

$$R = F(P, X, B, C)$$

where F represents a functional calculus connecting R (to be determined) to S (known), B represents all the boundary conditions of the problem and C all the constants of the problem, such as the initial state.

In the inverse problem, one part of the information constituting system S is unknown. In the case of parameter identification, parameters P of constitutive model M are unknown. Therefore, we need complementary information which is given by our knowledge of response R (or at least a part of it), corresponding here to mechanical test results. The inverse problem is thus defined such that:

$$P = F^{-1}(R^*, X, B, C)$$

where R^* represents a set of experimental data. It is usually impossible to obtain an explicit solution to this equation which requires the construction of an optimization procedure, consisting of minimizing the difference between the experimental data R^* and the calculated response R_C.

The inverse problem, as defined above, is mathematically formulated by introducing a "cost" function which measures, for a given set of parameters, the distance between the model simulation R_C and the experimental response R^* made of a series of experimental data. This "cost" function L can be written:

$$L = \Sigma_1^N L_i \text{ with N: number of tests in the database}$$

$$L_i = 1/(t_1 - t_0)\int_{t0}^{t1} || R^*(t) - R_C(t) || \, dt$$

where the notation $|| \ldots ||$ represents a norm in the space variable, $t_1 - t_0$ is the time of observation and $R^*(t) - R_C(t)$ is the difference at time t between experimental and numerical data for tests i.

In practice, the experimental data correspond to a set of discrete data obtained at specific times. Thus, the integral in the previous equation can be replaced by a sum of the number of measurements. The "cost" function is thus defined by using a Euclidean norm and by introducing a weighting matrix D:

$$L_i = 1/m_i \Sigma_1^{mi} (R^*(t_j) - R_C(t_j))^T D (R^*(t_j) - R_C(t_j))$$

with m_i the number of observation times t_j for test i.

Diagonal weighting matrix D is introduced to transform the observable variables into adimensional quantities. The quality of the measure is taken into account at this point by choosing as diagonal terms in this matrix the square of the inverse of the error estimate, within the measure of each variable. Thus, the weighting coefficients can be defined in an objective manner, which enable us to give more weight to values measured with good accuracy.

It is also possible, in the definition of the "cost" function, to attribute a given weight to each test. We can therefore give more importance to specific loading paths, closer to the actual problem, or penalize some tests which are considered as being of poor quality. We can also give more weight to certain parts of the experimental curve in order to assure a better determination of some given parameters.

Different numerical methods have been proposed for the resolution of a minimization problem. We can find in Tarantola [TAR 87] the description of the most commonly used methods. Among them, the Gauss-Newton method seems to be well adapted when response R_C is a derivable function of parameters P, which is the case for determining model parameters from laboratory simple tests or from non-homogenous tests which can be described by an analytical solution (see following section). The numerical treatment of the minimization problem can lead to several

solutions or to a solution which is physically unacceptable (values of parameters outside the current intervals). In particular, the function can have several local minima and under these conditions, the calculation procedure can converge towards a different solution according to the initial set of parameters. To overcome this difficulty, it is necessary to start the numerical process with an initial set of parameters well adapted to the nature of the material. For this purpose we can use one of the methods described earlier (analytical method, correlations, etc.) and/or base the choice on the previous knowledge of the model users.

Before starting the optimization procedure, it is also necessary to check if the model response along stress paths corresponding to those present in the database is significantly affected by the parameters to be determined. If this is not the case, it will be necessary to enrich the database or to accept that some of the parameters are given *a priori* values. More complex problems can also exist in case of a coupling effect of some parameters. The whole procedure requires a real strategy of parameter identification as well as controlling the numerical tools used for this purpose.

11.4.2. *Examples of parameter identification by means of laboratory testing*

When the database is made of laboratory tests, we can usually obtain a set of responses R^* corresponding to well documented material behavior along well controlled loading paths. The optimization procedure thus consists of minimizing the difference between experimental results and numerical simulations. The division of the whole set of parameters into two groups as defined earlier allows us in general to identify directly a first group of parameters and to reserve the optimization procedure to the second group. In fact, the numerical problems described earlier (local minima, etc.) can be more easily avoided if the number of parameters to be determined is smaller. Therefore, for a given model, we have to adapt the identification method to the type of tests available in the database by a classification of the parameters according to their influence along different loading paths.

Several studies lead to the construction of calculation programmes adapted to different models. We can cite for example the ADELAP program [MEI 89] for the Cyclade model and the PARASOL program [PIC 91] for Hujeux's model. We present below an approach developed by Shao *et al.* [SHA 91] which takes into account a certain degree of uncertainty on the experimental data, R* being in that case an assembly of random variables.

The example presented here concerns the parameter identification of a constitutive model for porous rocks [SHA 91]. It is an elastoplastic model with two plastic mechanisms, which contains 13 parameters. In order to construct the inverse method applied for their determination, we divide the parameters into two groups:

the first group contains parameters that can be determined directly from conventional experimental data (compressive triaxial tests), such as the cohesion and the friction angle; the second group includes the "numerical" parameters, whose determination requires a specific treatment of the experimental data, such as the hardening parameters. The inverse analysis is specially developed for the parameters of the second group. The method takes into account the uncertainties in the experimental data. The problem to be solved consists of maximizing the intersection between two probabilistic density functions of the Gaussian type.

The efficiency of the method was at first tested on three important model parameters. Numerical simulations were created from a given set of parameters and taken as representative of the material behavior. Then, the parameter values were modified and the inverse method was applied in order to minimize the difference between the stress-strain relations obtained by this new set of parameters and the reference one. The results proved the inverse method to be efficient in terms of calculation time and solution stability.

Then, two examples were chosen. The first example concerns a hydrostatic test used to determine the three parameters of the pore collapse mechanism associated with a compressive triaxial test used to determine the five parameters of the deviatoric mechanism. The uncertainty in the experimental data was estimated to be 10%. The results of the optimization procedure are presented in Figure 11.3.

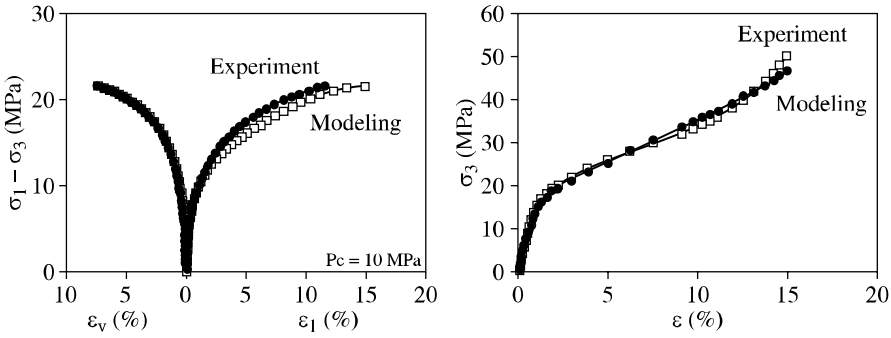

Figure 11.3. *Chalk parameter identification. Elastoplastic model with isotropic and deviatoric mechanisms*

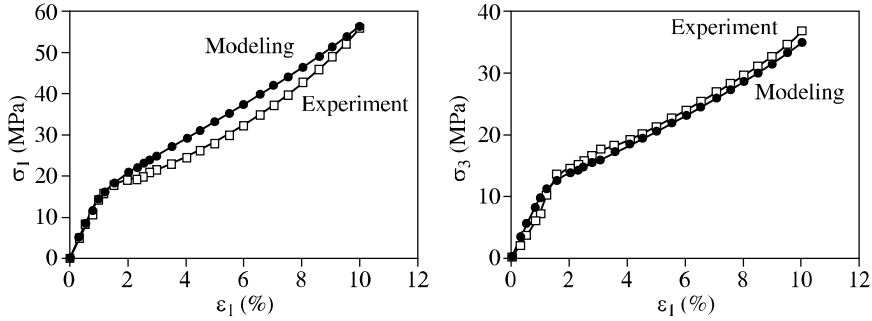

Figure 11.4. *Chalk parameter identification from oedometer test*

In the second example, an oedometer test is used to determine the eight parameters of the model. Satisfactory results could be obtained (Figure 11.4). However, the stability and the uniqueness of the solution become more difficult to achieve when the number of parameters increases. We have to specify that the quality of the solution is directly linked to the quality of the experimental data expressed in terms of mean values D_m and variance S_1. From a statistical point of view, the response quality improves when a greater number of repeated tests are made. Under these conditions, the inverse method gives the most probable values of the parameters.

11.4.3. *Parameter identification from in situ testing*

Data obtained from laboratory tests can be biased for different reasons: poor representativeness of the sampling, remolding of the specimens due to boring, extraction and transport. In order to overcome these difficulties, *in situ* testing is often recommended. Furthermore, *in situ* testing is now far more developed in site investigation because of its cost effectiveness.

We thus have to develop appropriate methods in order to identify the parameters of the adopted constitutive model from *in situ* test data. A direct identification is impossible in this case, since the stress and strain fields are non-homogenous and the measures are made at specific points. Therefore, an inverse method is necessary. In geophysics, such approaches were developed many years ago and could now be extended to geotechnical problems. They enable us to determine the elastic properties of a soil formation from the measurement of wave propagation in the ground (cross-hole testing for example). However, these tests have up to now been limited to mechanical characteristics at very small strains. More recently, inverse analysis methods have been developed and applied to the pressuremeter test, which corresponds to the expansion of a cylindrical cavity within the soil. The advantage of this specific test among other *in situ* tests is that it gives information on the soil

behavior in a large range of strain amplitudes, from small deformation up to failure, with boundary conditions well controlled and easy to reproduce in a numerical simulation. The plane strain condition hypothesis in the direction of the boring axis can usually be assumed as well as the symmetry condition around the same axis, which leads to a 1D loading condition easy to implement in a numerical simulation. Analytical solutions can be obtained for simple constitutive models, such as the elastic-perfectly plastic Mohr-Coulomb model [MON 94, YU 91]. For more complex models, the numerical simulation requires the use of a finite element code.

The analysis of the pressuremeter test shows that there are some difficulties in interpreting the results, due to its mode of execution. The main difficulty concerns the remolding due to boring. Menard's pressuremeter, most commonly used, requires a preliminary boring, before the introduction of the probe. This testing procedure leads to an unloading of the soil near the cavity wall and a more or less important remolding of the soil, which influences the initial part of the pressure-displacement curve. This difficulty can be overcome by the use of a self-boring pressuremeter (PAF or Camcometer). The work by Cambou *et al.* [CAM 93] has shown the influence of the loading mode, in particular on the modulus values, by means of numerical simulations using the CJS model (see Chapter 4). The conclusion of this work is that the identification of the elastic modulus can be carried out by using the pressure-volume curve obtained by a self-boring pressuremeter without considering the initial part up to $\Delta V/V = 2.5\%$. Another, more rigorous, procedure consists of realizing an unloading-reloading cycle and identifying the elastic properties from this cycle. However, this procedure is not applied in routine tests.

Another important aspect concerns the drainage condition for saturated soils with low permeability. Several analyses [CAM 91, HIC 96, RAN 03, ZEN 99] have shown that Menard's pressuremeter test could be considered as totally drained for a permeability $k > 10^{-5}$ m/s and totally undrained for $k < 10^{-10}$ m/s. For intermediary values of k, it is necessary to use a coupled numerical simulation in order to take into account partial consolidation of the soil around the probe. This aspect has been examined with great care in the works of Hicher and Michali [HIC 96] and Rangeard *et al*. [RAN 03] for self-boring pressuremeter tests in clayey soils.

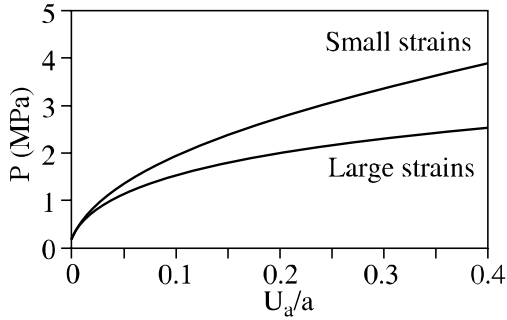

Figure 11.5. *Numerical simulations of the pressuremeter curve using the Mohr-Coulomb model in small and large deformations*

The determination of the parameters of the elastic-perfectly plastic Mohr-Coulomb model from pressuremeter tests has been treated by Dano *et al*. [DAN 01] from the analytical formulation proposed by Yu and Houlsby [YU 91] in large deformations. This last hypothesis has a significant consequence on the pressure-volume curve, as shown in Figure 11.5 by comparison to the one proposed by Monnet *et al*. [MON 94] for small deformations. We can see that the two curves become different for radial deformations u_a/a (radial displacement/initial radius) greater than few percent. Using the formulation proposed by Yu and Houlsby, the equation of the pressuremeter curve can be written as follows for a cohesive-frictional material:

$$\frac{U_a}{a} = \frac{P - P_0}{2G}$$

The maximum pressure corresponding to the plastic condition is:

$$P_{pl} = C.\cos\varphi + P_0.(1+\sin\varphi)$$

We have the following relations:

$$\varepsilon_r = \mathrm{Ln}\left(\frac{dr}{dr_0}\right) \qquad \varepsilon_\theta = \mathrm{Ln}\left(\frac{r}{r_0}\right)$$

$$G = \frac{E}{2(1+\nu)} \qquad M = \frac{E}{1-\nu^2} \qquad Y = \frac{2C.\cos\varphi}{1-\sin\varphi}$$

$$\beta = \frac{1+\sin\psi}{1-\sin\psi} \quad \gamma = \frac{\alpha(\beta+1)}{(\alpha-1)\beta} \quad \alpha = \frac{1+\sin\varphi}{1-\sin\varphi} \quad \delta = \frac{Y+(\alpha-1)P_0}{2(1+\alpha)\beta}$$

$$\eta = \exp\left\{\frac{(\beta+1)(1-2\nu)[Y+(\alpha-1)P_0][1+\nu]}{E(\alpha-1)\beta}\right\}$$

$$\xi = \frac{2\delta(1-\nu)}{\beta(\alpha-1)}\left[\alpha\beta+1-\frac{\nu(\alpha+\beta)}{1-\nu}\right]$$

$$R = \frac{(1+\alpha)[Y+(\alpha-1)P]}{2\alpha[Y+(\alpha-1)P_0]}$$

The analytical expression of the pressuremeter curve takes the following form:

$$\frac{U_a}{a} = \left\{\frac{R^{-\gamma}}{(1-\delta)^{\frac{1+\beta}{\beta}} - \left(\frac{\gamma}{\eta}\right)\Lambda_1(R,\xi)}\right\}^{\frac{\beta}{1+\beta}} - 1$$

$$\Lambda_1(x,y) = \sum_{n=0}^{\infty} A_n^1$$

$$A_n^1 = \frac{y^n}{n!}\ln x$$

$$A_n^1 = \frac{y^n}{n!(n-\gamma)}\left[x^{n-\gamma}-1\right]$$

$$P_{pl} = 2G\delta + P_0 = \frac{Y+(\alpha-1)P_0}{1+\alpha} + P_0$$

The results presented in Figure 11.6 show the influence of each model parameter: Young's modulus E, friction angle φ, the dilation angle ψ, cohesion c, as well as the influence of the initial horizontal stress P_0 on the pressuremeter curve.

We can see that each parameter affects the whole curve, which makes identifying several parameters simultaneously difficult.

An optimization method based on the Newton-Gauss algorithm has been developed and used to treat several examples [DAN 01]. The results show the difficulty of identifying several parameters simultaneously, as discussed previously. The "cost" function presents local minima and the whole procedure thus leads to a final solution which depends on the initial set of parameters. To overcome this problem, an optimization procedure has been developed for non-cohesive frictional materials only. It requires the use of a pressuremeter test with an unloading-reloading cycle from which the elastic modulus is at first determined. Then, a correlation between the dilation angle and the friction angle is used, in order to center the optimization on the sole friction angle. This procedure has given good results. Figure 11.7 presents an example of two simulations obtained by the use of this optimization procedure from tests realized by Mokrani [MOK 91] in the calibration chamber on Hostun RF sand. The result of the optimization process gives friction angle values in accordance with those obtained by triaxial tests (Table 11.2).

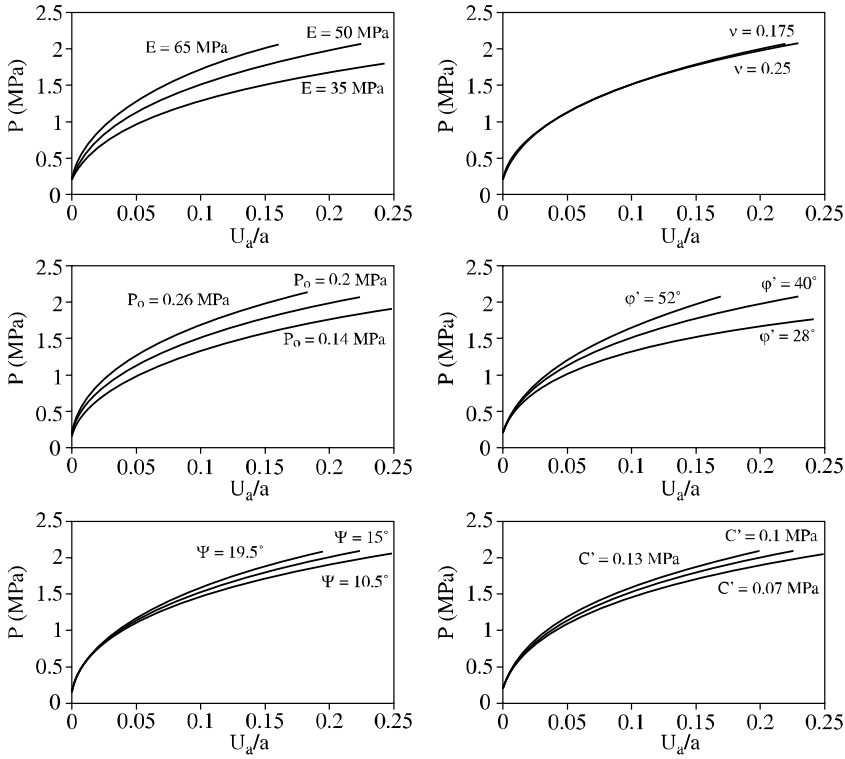

Figure 11.6. *Influence of Mohr-Coulomb model's parameters on the pressuremeter curve*

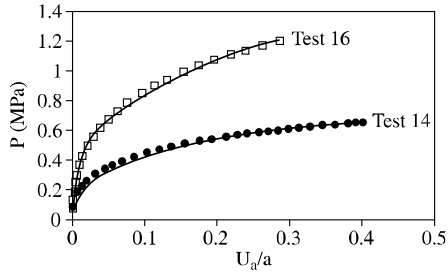

Figure 11.7. *Optimization of Hostun Sand parameters from pressuremeter tests*

Test	**σ'_v**	**p_0**	**γ**	**I_d**
	kPa	kPa	kN/m^3	%
14	200	84	14.4	41
16	500	130	14.9	54
Test	E_p	E_{triax}	$\alpha = \psi / \varphi$	φ'_{triax}
	MPa	MPa		(°)
14	25	26	0.15	35.4
16	79	57	0.25	34

a) *Test characteristics*

Test	**Imposed value**	**Correlation used**	**Optimization results**
14	E = 26 MPa	$\psi = \varphi' - 30$	$\varphi'_{opt} = 33.6°$
14	E = 25 MPa	$\psi = \varphi' - 30$	$\varphi'_{opt} = 33.9°$
14	E = 26 MPa	$\psi = 0.15\varphi'$	$\varphi'_{opt} = 32.7°$
14	$\varphi'_{triax} = 35.4°$	$\psi = \varphi' - 30$	E = 21.1 MPa
16	E = 57 MPa	$\psi = \varphi' - 30$	$\varphi'_{opt} = 36.1°$
16	E = 79 MPa	$\psi = \varphi' - 30$	$\varphi'_{opt} = 33.4°$
16	E = 57 MPa	$\psi = 0.25\varphi'$	$\varphi'_{opt} = 34.4°$
16	$\varphi'_{triax} = 34°$	$\psi = \varphi' - 30$	E = 72.9 MPa

b) *Optimization results*

Table 11.2. *Results of optimization tests and comparison with values obtained from triaxial tests*

For a cohesive-frictional material, the simultaneous identification of c and φ from one test is not possible, but can be obtained if two tests at two different depths are available. For each test, a series of coupled values of c and φ are derived. The solution is obtained for the couple which is the solution for the two tests (Figure 11.8 [CAM 93]).

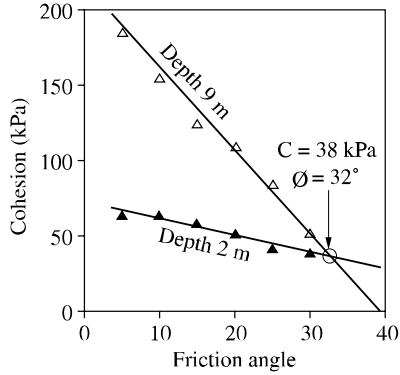

Figure 11.8. *Determination of cohesion and friction angle from two pressuremeter tests at different depths*

When the chosen constitutive model does not allow us to obtain an analytical expression of the pressuremeter curve, it is necessary to use a numerical approach by means for example of a finite element code. Zentar *et al*. [ZEN 01] and Rangeard *et al*. [RAN 03] have developed this type of approach and have applied it to the modified Cam-Clay model (see Chapter 3). For this purpose, they have used two codes: CESAR_LCPC, a finite element code, for the numerical simulation of the pressuremeter test, and SiDoLo (simulation and identification of constitutive models) [CAI 94], an optimization code for the parameter optimization process. The algorithm used to resolve the non-linear optimization problem combines two traditional minimization techniques: the steepest descent method at the beginning of the process, in order to improve the initial estimation of the parameters and a variant of the Levenberg-Marquardt method [NOU 85] in order to accelerate the convergence in the final phase of the identification. The coupling of the two codes was performed by the development of an interface code, InCeSi.

The soils which can be modeled by the Cam-Clay model are essentially saturated soft clays. Under these conditions, the finite element calculation has to be coupled in order to consider the permeability of the material. The identification procedure can be realized only with parameters which affect the numerical response in a significant way. A parametric study of the modified Cam-Clay parameters on the pressuremeter curve have shown that the shear modulus G, the critical state constant M and the

preconsolidation pressure p'_{c0} greatly affect the numerical response, whereas the Poisson's ratio ν and the plastic consolidation coefficient β ($\beta = \lambda - \kappa$) have little influence. The identification method was thus applied in order to determine *G, M* and p'_{c0}. The results showed the impossibility of determining simultaneously the two parameters *M* and p'_{c0}, due to the fact that the pressuremeter results are expressed in terms of total stresses while the model is expressed in terms of effective stresses. In order to overcome this difficulty, the pore pressure measured at a given point near the probe was introduced as a complementary result. In these conditions, the three parameters *G*, *M* and p'_{c0} could be simultaneously correctly identified. Where this new information is not available, as in most cases for a common pressuremeter test, the complementary information can come from an oedometer test performed on the same material. The values of β and p'_{c0} can be identified directly from the oedometer test results and *G* and *M* can be identified afterwards using an inverse analysis on the pressuremeter test results.

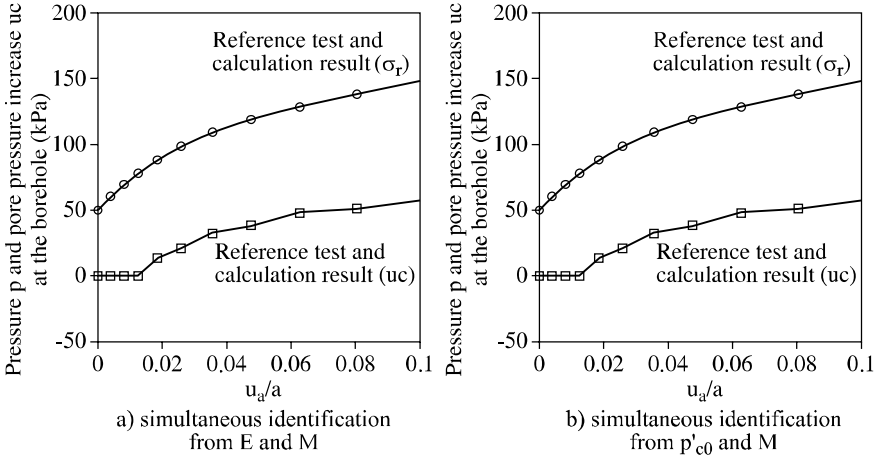

Figure 11.9. *Validation of the identification procedures of Cam-Clay model's parameters from pressuremeter curves: a) identification from the sole pressure-volume curve; b) identification from the pressure-volume curve and the pore pressure evolution at a point near the apparatus*

This method has been successfully applied in order to determine the parameters of Saint Herblain Clay, a soft clay from the Loire Valley, in the vicinity of Nantes. The parameter values obtained from pressuremeter tests are in agreement with those determined by a direct analysis of triaxial tests (Figure 11.10).

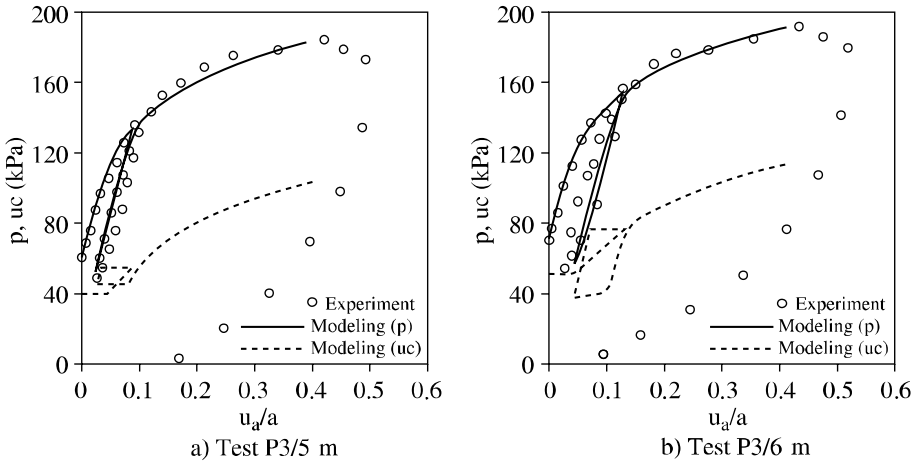

Figure 11.10. *Identification of parameters E and M for Saint Herblain Clay*

Rangeard *et al*. [RAN 03] have developed an identification procedure in order to identify mechanical parameters and permeability simultaneously from pressuremeter tests with strain holding stages. The mechanical parameters are identified, as presented previously, on the pressuremeter curve, and then, with the obtained optimized set of parameters, the permeability is derived from the pore pressure dissipation curve during a strain holding stage. Few iterations need to be realized on the two optimization procedures in order to obtain both mechanical parameters and permeability. Figure 11.11 shows an example of the final optimization step on both the pressuremeter curve and pore pressure dissipation during a strain holding stage on a Saint Herblain Clay sample. The validation of the whole procedure was performed by comparing the parameter values obtained after optimization to values of the same parameters obtained by direct analysis of oedometer and triaxial tests. A very good agreement could be achieved.

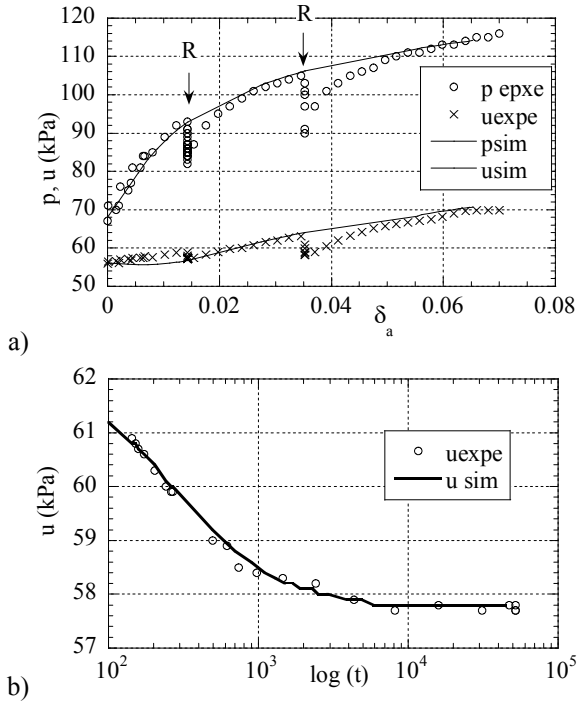

Figure 11.11. *Comparison between experiment and simulation of pressuremeter test: (a) pressuremeter curve and pore pressure evolution; (b) pore pressure dissipation during strain holding stage*

The procedure has been extended in order to be applied to a viscoplastic model, the EVP-MCC model developed by Yin *et al*. [YIN 07] (see Chapter 7). The parameters of the viscoplastic model are the same as in the Cam-Clay model, but two more parameters N and μ have been added to take into account the clay viscous behavior. The inverse analysis is thus more difficult to carry out. The shear modulus is at first determined by the initial slope of the radial stress-radial strain curve. The other parameters can be determined by using pressuremeter tests with three levels of strain rate. The coupling effect between M and p'_{c0} requires a special treatment to determine both of them separately. A first assumption is made on the value of M. For a given value of M, the values of p'_{c0}, N, μ and permeability k can be found after a convergence of the optimization procedure made on the three loading curves at different strain rates and the pore pressure dissipation during a strain holding stage. The same procedure is repeated for different values of M until the overall convergence of the optimization process, which is obtained when the difference between experimental data and calculation results becomes sufficiently small and

stable, according to a criterion which enables the calculation of the overall error between experimental and numerical results. Figures 11.12 and 11.13 show a final result obtained from this procedure applied to the Saint Herblain Clay.

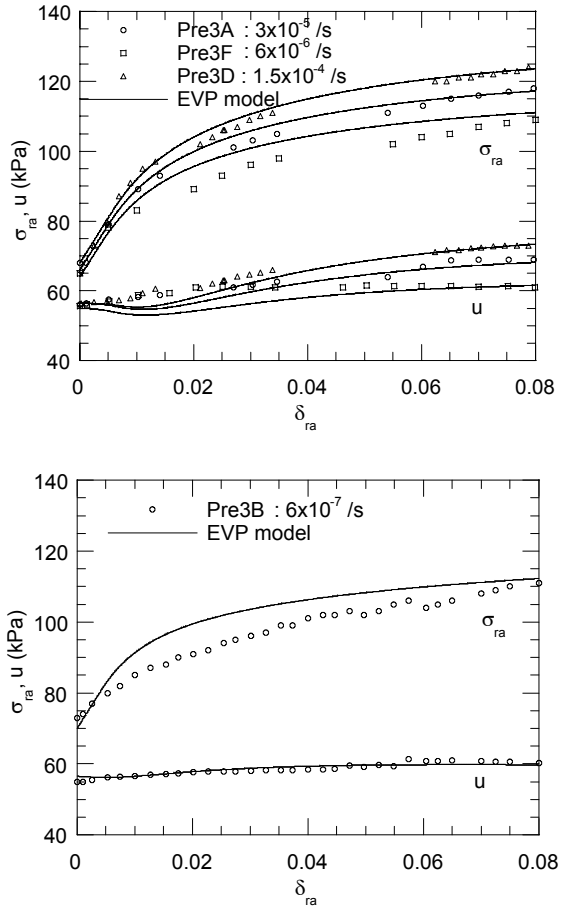

Figure 11.12. *Comparison between experiment and simulation of pressuremeter strain rate tests*

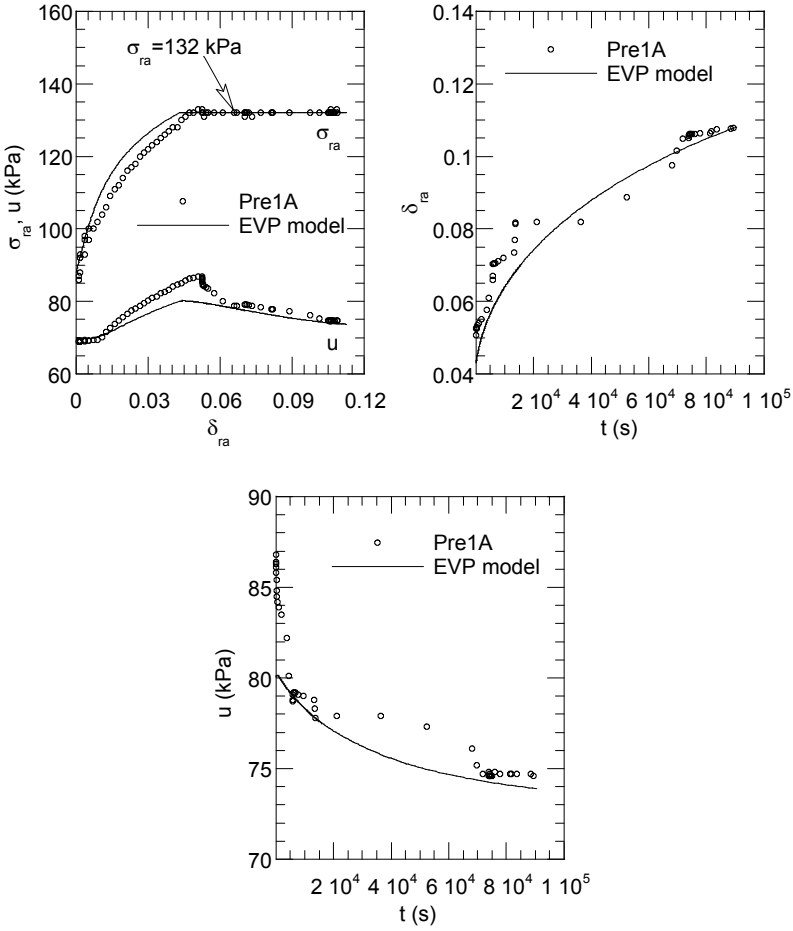

Figure 11.13. *Comparison between experiment and simulation of a pressuremeter creep test*

Cambou *et al*. [CAM 93] have developed a similar approach by constructing a specific optimization code, called Press'ident, and applying it to the determination of the parameters of two different models: the Duncan-Chang hypoelastic model and the elastoplastic CJS model (see Chapter 4). After the extraction of the parameters, they simulated the displacements of the soil during the construction of a nuclear power plant and a tunnel made from soft soil. A good agreement between numerical results and *in situ* measures was obtained.

11.5. Conclusion

The methodology of determining model parameters has to be considered at the same time as the model construction. This is a necessary step for its use in finite element codes applied to geotechnical projects. This methodology has to be based on experimental data obtained through traditional laboratory or *in situ* tests, and while it should be adapted to the structure of each model, it must enable, as completely as possible, an objective determination, i.e. independent of the user.

When experimental data comes from laboratory tests, several approaches are possible and can be established more or less easily, depending on the nature of the parameter to be identified. When all or part of the data comes from *in situ* tests, only an inverse analysis method based on numerical optimization techniques can adequately be used. The inverse analyses are often difficult to achieve because the character of the numerical problem is badly written. It is therefore recommended that at least part of the data should come from laboratory tests.

The good quality of the latter is an indispensable factor for a successful identification. The quality of each individual test can be taken into account at different levels of the identification process: a greater weight given to certain tests or to certain parts of the tests; introduction of the data uncertainty in the optimization technique. It is also important to define the testing procedure to account for both the problem to be solved and the identification procedure to be envisioned.

11.6. References

[AMA 97] AMADEI B. and STEPHANSSON O., *Rock Stress and its Measurement*, Chapman & Hall, 2–6 Boundary Row, London, SE1 8HN, UK, 1997.

[AUB 82] AUBRY D., HUJEUX J.C., LASSOUDIÈRE F. and MEIMON Y., "Prediction with an elastoplastic model including multiple mechanisms for cyclic soil behaviour", *Int. Workshop on Constitutive Relations for Soils*, pp. 249-259, Grenoble, 1982.

[BIA 77] BIAREZ J. and FAVRE J.L., Statistical estimation and extrapolation from observations, Reports of organizers, Spec. Session 6, IX ICSMFE, Tokyo, vol. 3:505-509, 1977.

[BIA 89] BIAREZ J., FAVRE J.L., HICHER P.-Y. and RAHMA A., "Correlations for granular media, classification logic and connection between classes", *Powders and Grains*, Biarez and Gourvès (eds.), Balkema, pp. 201-209, 1989.

[BIA 94] BIAREZ J. and HICHER P.-Y., *Elementary Mechanics of Soil Behaviour*, Ed. Balkema, 1994.

[BIS 66] BISHOP A.W., "The strength of soils as engineering materials", *Geotechnique*, vol. 16, no. 2, pp. 99-112, 1966.

[CAI 94] CAILLETAUD G. and PILVIN P., *Identification and Inverse Problems Related to Material Behaviour, Inverse Problems in Engineering Mechanics*, Bui, Tanaka *et al*. Eds., Balkema, pp. 79-86, 1994.

[CAM 91] CAMBOU B., SOEGIRI S., FAY J.B., LE TIRANT P. and NAUROY J.F., "Pressiomètre avec mesure de pression interstitielle", *10th European Conference on Soil Mechanics and Foundation Engineering*, vol. 1, pp. 45-48, Florence, Italy, 1991.

[CAM 93] CAMBOU B. and BAHAR R., "Utilisation de l'essai pressiométrique pour l'identification de paramètres intrinsèques du comportement d'un sol", *Géotechnique*, no. 63, 1993.

[DAN 01] DANO C. and HICHER P.-Y., "Interpretation of *in situ* pressuremeter tests in grouted soils", *Int. Conf. IN SITU 2001*, Bali, Indonesia, 2001.

[DAO 99] DAOUADJI A., Modélisation de l'influence de la rupture des grains sur le comportement des matériaux granulaires, Doctoral thesis, Ecole Centrale de Paris, 1999.

[DAR 95] DARVE F., HICHER P.-Y. and REYNOUARD J.M., *Mécanique des Géomatériaux*, Hermes, 1995.

[DUN 70] DUNCAN J.M. and CHANG C.Y., "Non linear analysis of stress and strain in soils", *J. Soil Mech. and Found. Div., ASCE*, vol. 96, SM5, pp. 1629-1653, 1970.

[FAV 91] FAVRE J.L., HICHER P.-Y. and KÉRILIS J.M., "Modelisol: a database for reliability analyses", in *Geotechnique 6th ICASP*, Mexico, 1991.

[HIC 94] HICHER P.-Y. and RAHMA A., "Micro-macro correlations for granular media. Application to the modelling of sands", *Eur. J. Mech., A/Solids*, vol. 13, no. 6, pp. 763-781, 1994.

[HIC 96] HICHER P.-Y. and MICHALI A., "Identifying soil parameters by means of laboratory and in-situ testing", *Computers and Geotechnics*, vol. 19, no. 2, pp. 153-170, 1996.

[KOL 91] KOLYMBAS D., "Computed-aided design of constitutive laws", *Int. J. for Num. and Anal. Methods in Geomechanics*, vol. 15, pp. 593-604, 1991.

[LAD 88] LADE P.V., *Double Hardening Constitutive Model for Soils, Parameter Determination and Predictions for Two Sands, Constitutive Equations for Granular Non-cohesive Soils*, Saada and Bianchini (eds.), Balkema, pp. 367-383, 1988.

[LEE 64] LEEMAN E.R., "The measurement of stress in rock", *J. South Afr. Inst. Mining Metall.*, 65, pp. 45-114, 1964.

[MEI 92] MEIMON Y., Modèles pour le comportement des fondations d'ouvrages types marins, Research notes, University of Lille, 1992.

[MES 00] MESTAT Ph. and ARAFATI N., Modélisation des sables avec la loi de Nova: détermination des paramètres et influence sur les simulations, LPC bulletin, no. 225, pp. 21-40, 2000.

[MOK 91] MOKRANI I., Simulation physique du comportement des pieux à grande profondeur en chambre de calibration, Doctoral thesis, INPG, 1991.

[MON 94] MONNET J. and KHLIF J., "Etude théorique de l'équilibre élasto-plastique d'un sol pulvérulent autour du pressiomètre", *Revue Française de Géotechnique*, 67, pp. 3-12, 1994.

[NOU 85] NOUGIER J.P., *Méthodes de Calcul Numérique*, Masson, Paris, 1985.

[PIC 91] PICCUEZZU E., Lois de comportement en géomécanique. Modélisation, mise en œuvre, identification. Doctoral thesis, Ecole Centrale de Paris, 1991.

[QUI 99] QUIERTANT M., Etude des contraintes naturelles dans les roches: Influences des comportements anélastiques, Doctoral thesis, University of Lille I, 1999.

[SHO 91] SHAO J.F, DAHOU A. and HENRY J.P., "Application de la théorie des problèmes inverses à l'estimation des paramètres des modèles rhéologiques", *Revue Française de Géotechnique*, no. 57, pp. 75-80, 1991.

[TAR 87] TARANTOLA A., *Inverse Problem Theory*, Elsevier, 1987.

[YIN 07] Yin Z.Y. & Hicher P.Y. **"**Identifying Parameters Controlling Soil Delayed Behaviour from Laboratory and In Situ Pressuremeter Testing", *International Journal for Numerical and Analytical Methods in Geomechanics*, 2007.

[YU 91] YU H.S. and HOULSBY G.T., "Finite cavity expansion in dilatant soils: loading analysis", *Geotechnique*, 41, vol. 2, pp. 173-183, 1991.

[ZEN 99] ZENTAR R., Analyse inverse des essais pressiométriques. Application à l'argile de Saint – Herblain, Doctoral thesis, University of Nantes and Ecole Centrale de Nantes, 1999.

[ZEN 01] ZENTAR R., HICHER P.-Y. and MOULIN G., "Identification of soil parameters by inverse analysis", *Computers and Geotechnics 28*, no. 2, pp. 129-144, 2001.

Constitutive Modeling of Soils and Rocks
Edited by Pierre-Yves Hicher & Jian-Fu Shao

List of Authors

Jean BIAREZ
Formerly
MSS-MAT
Ecole Centrale de Paris
Grande Voie des Vignes
92295 Chatenay-Malabry cedex
France

Emmanuel BOURGEOIS
Division for Soil and Rock Mechanics and Engineering Geology
Laboratoire Central des Ponts et Chaussées
58 boulevard Lefebvre
75732 Paris cedex 15
France

Bernard CAMBOU
LTDS
Ecole Centrale de Lyon
36, avenue Guy de Collongue
69130 Ecully
France

René CHAMBON
Laboratoire 3S-R
Joseph Fourier University, BP 53
38041 Grenoble cedex 9
France

Félix DARVE
Laboratoire 3S-R
Joseph Fourier University, BP 53
38041 Grenoble cedex 9
France

André DRAGON
LMPM
UMR CNRS and Ecole Nationale Supérieure de Mécanique et d'Aéronautique
1 avenue Clément Ader
86961 Futuroscope Chasseneuil
France

Albert GIRAUD
Laboratoire de Physique et Mécanique des Matériaux
Institut Supérieur de Génie Mécanique et Productique,
University of Metz
57045 Metz cedex 01
France

Pierre-Yves HICHER
Institut de Recherche en Génie Civil et Mécanique
UMR CNRS 6183, Ecole Centrale de Nantes
44321 Nantes cedex 3
France

Djimédo KONDO
Laboratoire de Mécanique de Lille
UMR8107 CNRS, Lille University of Science and Technology
59650 Villeneuve d'Ascq
France

Farid LAOUAFA
INERIS (Institut National de l'environnement industriel et des risques)
Parc technologique ALATA, BP.2
60550 Verneuil-en-Halatte
France

Philippe MESTAT
Laboratoire Central des Ponts et Chaussées
58 boulevard Lefebvre
75732 Paris cedex 15
France

Vincent PENSEE
University of Paris-East
Laboratoire de Mécanique
5 bd Descartes, 77454 Marne-la-Vallée
France

Philippe REIFFSTECK
Division for Soil and Rock Mechanics and Engineering Geology
Laboratoire Central des Ponts et Chaussées
58 boulevard Lefebvre
75732 Paris cedex 15
France

Isam SHAHROUR
Laboratoire de Mécanique de Lille (CNRS, UMR 8107)
University of Lille 1
59650 Villeneuve d'Ascq
France

Jian-Fu SHAO
Laboratoire de Mécanique de Lille
UMR8107 CNRS, Lille University of Science and Technology
59650 Villeneuve d'Ascq
France

Shou-Yi XIE
Laboratoire de Mécanique de Lille
UMR8107 CNRS, Lille University of Science and Technology
59655 Villeneuve d'Ascq
France

Qizhi ZHU
Laboratoire de Mécanique de Lille
UMR8107 CNRS, Lille University of Science and Technology
59650 Villeneuve d'Ascq
France

Constitutive Modeling of Soils and Rocks
Edited by Pierre-Yves Hicher & Jian-Fu Shao

Index